Structural Performance of Prestressed Precast High Speed Railway Bridges using High Performance Concrete

by Bradley Matthew Pring

MEng ACGI

A thesis submitted to

Imperial College London

for the degree of

DOCTOR OF PHILOSOPHY

Department of Civil and Environmental Engineering

Imperial College of Science, Technology and Medicine

London SW7 2AZ, United Kingdom

November 2019

Declaration

I declare that this thesis consists of my own work. Any material used from published or unpublished sources is referenced accordingly.

Abstract

Bridges often need to conform to strict alignment rules for high speed railway (HSR) lines. Generally, the bridges are constructed either from prestressed concrete or steel-concrete composite. Prestressed concrete bridges can be constructed by precast methods, which offer benefits in economies of scale, quality and construction times for long repetitive viaducts. However, currently precast construction utilises conventional concrete strengths, leading to thicker, heavier cross sections to resist the load. High performance concrete (HPC), with its increased strength, can be implemented to reduce the precast segment weights, subsequently reducing substructure and transportation capacities. However, lighter sections could lead to decks more prone to vibrations exceeding acceleration limits. Therefore, the implementation of HPC requires further research, addressed in this thesis, using the most sophisticated and realistic numerical models of the bridge, vehicle, track, wheel-rail interaction and rail irregularities, identified in literature.

A suitable benchmark bridge is selected and analysed from a database of concrete HSR bridges. This analysis finds that using track irregularities with wheel-rail contact is mandatory for accurate bridge accelerations, leading to up to 3.75 times larger accelerations than equivalent moving load models. Furthermore, sectional deformations have been found to be non-negligible, with beam element bridge models incapable of exhibiting the wide frequency content of the acceleration response seen in shell elements. A subsequent parametric analysis reduces the geometrical cross sectional dimensions of the precast components, implementing HPC to maintain the structural capacities.

The applicability of the acceptable parametric analyses are tested on other bridges, determining more general conclusions for HPC inclusion in HSR bridges. Appropriate reductions in geometry (web, bottom flange and top flange thicknesses down to 66, 75 and 75% of the original value respectively), are identified from the response of the bridge and vehicle, by using HPC up to 96 MPa, contributing to up to 22% lighter precast elements. Appropriate design guidance is subsequently made for better design of HSR bridges to incorporate HPC into precast solutions.

Acknowledgements

First and foremost, I would like to thank my supervisor, Dr. Ana Ruiz-Teran. Your guidance over the course of the PhD and Masters projects has been outstanding, and this work would not be possible without you, *Gracias*! Secondly, this research was enabled by the funding and support of EPSRC and Laing O'Rourke, especially Adam Locke and Phil Robinson, who have helped to establish the link of this work to the industry.

Having spent a considerable time in the Skempton building over the last eight years, there are countless people who have helped me along the way. Special mention to Laura and Andi, who for almost eight years have been true friends! In addition, the support staff including Tina, Anna and Louise of the undergraduate office and Sarah of the research office, have always been there to help and brighten the gloomy wet London days! For the office, past and present, you have all been so friendly and I wish you all the best with your futures. Jiajia and Sophie you both never failed to liven the day. Javi and Luke, it is a shame that we started years apart, but I have cherished our friendship, *Long Live Balloon Matt.* It is testament to the kindness of people of the department, that it is very hard to narrow down my appreciation to a few people, and even if I have not mentioned you by name, let it be known that you have all truly helped in some way!

Mental breaks are key to motivation and focus and being a part of outdoor club has helped to provide that. I can not thank you all enough and special mention to the multiple years of fun with Tom, Mimis, Ioana, Joanna, Salomé, Gareth, Todd, Jonny, Rose, Micol, Maria, Aina, Leonie and Lizzie! Beyond outdoor club, special mention to Jim, Tim, Matt, Alex, Dave, Jineesha, Loren, Arka, Conor and Jeff, with whom friendship has progressed beyond university!

I would like to thank Mum, Dad and Fran for their support. We may not meet as often as you would have all liked, but I am very thankful for your support, care and love! It is because of the way you have guided me over the past 26 years that I have achieved this! To the rest of my extended family, I am also grateful for your love and support! Finally, Elina you have been with me throughout this experience. I have enjoyed and look forward to more adventures, travel and relaxing with you. Thank you for all your patience and I appreciate you! *Es tevi milu!!!*

3

Contents

List of Figures

List of Tables

Nomenclature

Abbreviations

Acc	Acceleration
CWR	Continuous Welded Rail
DAF	Dynamic Amplification Factor
Disp	Displacement
DOF	Degrees of freedom
FASTSIM	Fast Algorithm for the Simplified Theory of Rolling Contact
FE	Finite Element
FRA	Federak Railroad Administration
HPC	High Performance Concrete
HSR	High Speed Rail
S11	Normal stress in the longitudinal direction
S22	Normal stress in the direction in the shell plane perpendicular to the longitudinal direction
SNCF	Société Nationale des Chemins de fer Français
U2	Lateral displacement
U3	Vertical displacement
UEL	User Element (ABAQUS)
Veh	Vehicle
WRI	Wheel-Rail Interaction

Bridge

α	Rayleigh damping constant
$\bar{z}$	Sectional vertical centroid from base of superstructure [m]
β	Rayleigh damping constant

ζ_n	Damping ratio [-]
A_c	Area of concrete [m^2]
A_{mb}	Cross sectional area of of Macalloy bar [mm^2]
E_{mb}	Modulus of elasticity of Macalloy bar [GPa]
$f_{bt,i}$	The frequency of the ith significant bridge mode for ballasted track [Hz]
$f_{f,i}$	i^{th} modal bridge frequency with track structure and vehicle mass [Hz]
f_n	Modal frequency [Hz]
$f_{s,i}$	i^{th} modal bridge frequency without track structure nor vehicle mass [Hz]
$f_{st,i}$	The frequency of the ith significant bridge mode for slab track [Hz]
I_{yy}	Second moment of area about y axis [m^4]
I_{zz}	Second moment of area about z axis [m^4]
k_{mb}	Axial stiffness of Macalloy bar [kN/mm]
L_{mb}	Length of Macalloy bar [m]
M_{rd}	Design moment resistance [MNm]
n_0	Fundamental vertical frequency of bridge [Hz]
V_{rd}	Uncracked design shear resistance [MN]

Concrete

α_E	Factor based on the type of aggregate for Young's modulus calculation[-]
E_{ci}	The concrete modulus of elasticity at a concrete age of 28 days [GPa]
f_{ck}	Characteristic strength of the concrete [GPa]
w/c	Water-cement ratio

Irregularities

ω_l	The lower spatial frequency considered for the irregularity profile [m^{-1}]
ω_n	The spatial frequency of the nth sinusoidal component of the irregularity [m^{-1}]
ω_u	The upper spatial frequency considered for the irregularity profile [m^{-1}]

ψ_n	Random phase angle for irregularity generation $[rad]$
A_a	Roughness parameter for calculation of alignment irregularity
A_n	Amplitude of the sinusoidal irregularity component $[m]$
A_v	Roughness parameter for calculation of vertical and cross level irregularities
b_0	Half the wheelset width $= 0.75\,m$
$r(x)$	Longitudinal spatial variation of the irregularity $[m]$

Dynamic Behaviour

$f_{\mathrm{v}i}$	Resonant frequencies for the ith harmonic $[Hz]$
$v_{c1,in}$	Cancellation speeds $[m/s]$
$v_{r1,in}$	Resonant speeds $[m/s]$

Wheel-Rail Interaction

$\bar{F}_{tx}$	Tangential longitudinal wheel rail contact force using Kalker's linear method $[kN]$
$\bar{F}_{ty}$	Tangential lateral wheel rail contact force using Kalker's linear method $[kN]$
$\bar{F}_t$	Magnitude of the Kalker's Linear tangential force $[kN]$
δ	Penetration between the wheel and rail $[m]$
$\dot{\delta}_0$	Initial rate of change of penetration between wheel and rail $[m/s]$
$\dot{\delta}$	Rate of change of penetration between wheel and rail $[m/s]$
$\dot{\mathbf{R}}^{\mathbf{w}}$	Velocity vector of wheelset $[m/s]$
$\dot{\mathbf{r}}^{\mathbf{w}}$	Directional velocity vector of contact point $[m/s]$
$\omega^{\mathbf{w}}$	Angular velocity vector of wheelset $[rad/s]$
$\mathbf{n}^{\mathbf{r}}$	Direction vector of the normal wheel rail force
$\mathbf{t}_{\mathbf{x}}^{\mathbf{r}}$	Longitudinal direction vector of the longitudinal tangential force
$\mathbf{t}_{\mathbf{y}}^{\mathbf{r}}$	Lateral direction vector of the lateral tangential force
$\mathbf{u}_{\mathbf{cp}}^{\mathbf{w}}$	Position vector of contact point with respect to the wheelset centre $[m]$
μ	Coulombs coefficient of friction [-]
ν_{wr}	Poisson's ratio of the wheel and rail material
ϕ	Wheel rail spin creepage [-]

θ_c Angle between the horizontal plane and the plane of contact

θ_{wr} Angle linked to wheel rail curvatures [°]

ζ_x Wheel rail longitudinal creepage [-]

ζ_y Wheel rail lateral creepage [-]

$A(S)$ Combined wheel-rail curvatures in x direction at contact point location S $[m^{-1}]$

a_e, b_e Semi axes dimensions of the contact ellipse $[mm]$

$B(S)$ Combined wheel-rail curvatures in y direction at contact point location S $[m^{-1}]$

$B_f(S)$ Smoothed rail curvature for wheel rail contact problem $[m^{-1}]$

$B_{mod1}(S)$ Modified combined wheel-rail curvatures in y direction at contact point location S $[m^{-1}]$

$B_{mod2}(S)$ Modified combined wheel-rail curvatures in y direction at contact point location S $[m^{-1}]$

BYQ Bogie-side lateral to vertical force ratio

c_{11}, c_{22}, c_{23} Kalker coefficients

C_H Damping coefficient for normal contact force $[kN/m^{3/2}]$

e_{res} Coefficient of restitution between the wheel and rail

E_{wr} Young's modulus of elastic of the wheel and rail material $[MPa]$

F_{nd} Wheel rail contact damping force normal to contact surface $[kN]$

$F_{ne,t-\Delta t}$ Normal wheel-rail contact force using hertz method for time step previous to current time step $[kN]$

F_{ne} Normal force between the wheel and rail from Hertz law $[kN]$

F_n Combined normal Hertzian contact force and damping contact force $[kN]$

F_{tx} Longitudinal tangential force using heuristic approach $[kN]$

F_{ty} Lateral tangential force using heuristic approach $[kN]$

F_t Magnitude of the Heuristic tangential force $[kN]$

G_{wr} Shear modulus of wheel rail contacting surfaces

K_{bma} Coefficient related to wheel-rail curvatures $[m^{-1}]$

K_{bpa} Coefficient related to wheel-rail curvatures $[m^{-1}]$

K_H Hertzian Spring stiffness $[kN/m^{3/2}]$

K_{mat}	Coefficient related to wheel rail material for use in the wheel rail contact problem
K_s	Linearised Hertzian contact stiffness $[kN/mm]$
l_0	Approximate ellipse width $[mm]$
m	Coefficient used in the calculation of the wheel rail contact
n	Coefficient used in the calculation of the wheel rail contact
$Q_{w,0}$	Static vertical wheel force v
Q_w	Vertical wheel force $[kN]$
r	Coefficient used in the calculation of the wheel rail contact
$R_{rx}(S)$, $R_{ry}(S)$	Radii of curvature of the rail in x and y directions at contact point S $[m]$
$R_{wx}(S)$, $R_{wy}(S)$	Radii of curvature of the wheel in x and y directions at contact point S $[m]$
S_{1R}, S_{2R}	Surface parameters relating to the rail
S_{1W}, S_{2W}	Surface parameters relating to the wheel
V	Forward velocity of the vehicle $[m/s]$
X^G, Y^G, Z^G	Global coordinate system
X^{R_L}, Y^{R_L}, Z^{R_L}	Local coordinate system of the left rail
X^{R_R}, Y^{R_R}, Z^{R_R}	Local coordinate system of the right rail
X^W, Y^W, Z^W	Local coordinate system of the wheelset
Y_{lim}	Lateral Track force Limit $[kN]$
Y_w	Lateral wheel force $[kN]$
YQ	Lateral to vertical track force ratio [-]

Chapter 1

Introduction

This thesis presents a study into the implementation of high performance concrete (HPC) into prestressed, precast high speed railway (HSR) bridges. The implementation of these concretes will enable several benefits over conventional concrete, with impacts greater than to just the bridge deck design. For example, but not limited to, improvements in bridge deck transportation and reduced substructure design capacity, as a consequence of the reduction of the self-weight that may be achieved. As a consequence of that, the dynamic response may be amplified. Therefore, in order to gain understanding about their dynamic response under HSR traffic loading, comprehensive and realistic numerical models are required. This chapter introduces the background to the subject briefly, before presenting the objectives of this research. Finally, the outline of the content of this thesis is provided at the end of this chapter.

1.1   Background and Motivation

High speed railways are found in many countries around the world. The development of these lines has stemmed from the first HSR line to be built in Japan, between Tokyo and Osaka, in 1964 (Smith, 2003). A HSR line is defined by many factors, but the widely accepted definition is a general minimum line speed exceeding $250\,km/h$ for a new line specifically built for HSR and $200km/h$ for existing lines upgraded from slower speeds (Leboeuf, 2018). So called Maglev (magnetic levitation) trains are not considered as HSR, as they use a wheel-less technology that spreads the weight over a wider region than the concentrated HSR wheel loads (Li et al., 2016).

In the United Kingdom (UK), there is currently one dedicated HSR line, known as High Speed One (HS1), operating at $300\,km/h$ and linking London to the Channel Tunnel and hence the European HSR network (Bennett, 2007). Further lines have been upgraded to

Country	Operational		Planned		Country	Operational		Planned	
	Length	Max Speed	Length	Max Speed		Length	Max Speed	Length	Max Speed
Qatar*	-	-	180	350	Germany	1571	300	438	300
China	31043	350	8535	350	Italy	896	300	205	300
India	-	-	508	320	Netherlands	90	300	-	-
Indonesia	-	-	712	300	Norway	-	-	333	250
Iran	-	-	3104	250	Poland	224	200	1082	350
Israel	-	-	85	250	Portugal	-	-	596	350
Japan	3041	320	596	260	Russia	-	-	2970	400
Kazakhstan	-	-	1011	250	Spain	2852	300	1965	300
Malaysia**	-	-	350	320	Sweden	-	-	750	320
Saudi Arabia	453	300	-	-	Switzerland	144	250	15	250
South Korea	887	305	49	300	UK	113	300	550	360
Taiwan-China	354	300	-	-	**EUROPE**	9096	320	12721	400
Thailand	-	-	2878	250	Australia	-	-	1749	350
Turkey	594	250	6242	300	Brazil	-	-	511	300
Vietnam	-	-	1600	350	Canada	-	-	290	250
ASIA	36372	350	29976	350	Egypt	-	-	1210	?
Austria	263	250	352	250	Mexico	-	-	210	300
Baltic	-	-	870	240	Morocco	200	320	1114	320
Belgium	209	300	-	-	South Africa	-	-	2390	300
Czechia	-	-	810	350	USA	735	240	2351	350
Denmark	-	-	60	250	**OTHER**	935	320	9825	350
France	2734	320	1725	320	**WORLD**	46403	350	52522	400

Table 1.1: Table of the current and planned lengths [km] and maximum operating speeds [km/h] of countries around the world currently with or planned to have dedicated HSR lines as of 2019 (*link to Bahrain; **link to Singapore)

run at 200 km/h and so are also classified as high speed. Particularly applicable to this thesis, a new HSR line, High Speed Two (HS2), has begun construction between London and Birmingham (with plans for later phases to extend further north), with planned speeds up to 360 km/h, which would make it among the fastest HSR lines in the world (Leboeuf, 2018; Durrant, 2015). In the design of this HS2 line, the use of precast solutions, with modular and accelerated construction techniques have been explicitly promoted. Similar drivers are currently guiding the design of HSR lines in other countries.

Globally, China has the highest usage of HSR, both in terms of number of users, with 800 million passengers per year in 2015 (Leboeuf, 2018), as well as in total track length, as seen in Table 1.1 (UIC, 2019). Globally, as of 2019 there was a HSR network length of 46403 km, with a further 52522 km planned (UIC, 2019). This shows the global spread of HSR and the high growth of the industry.

The strict alignment and longitudinal constraints required for HSR lines means that a significant proportion of the design will require bridges and tunnels to traverse the existing landscape. For example, in Taiwan, 73% of a HSR line was constructed using prestressed concrete viaducts (Tai et al., 2010a). When constructing viaducts of many spans, repetitive design leads well to the manufacture of precast spans, helping to achieve benefits from economies of
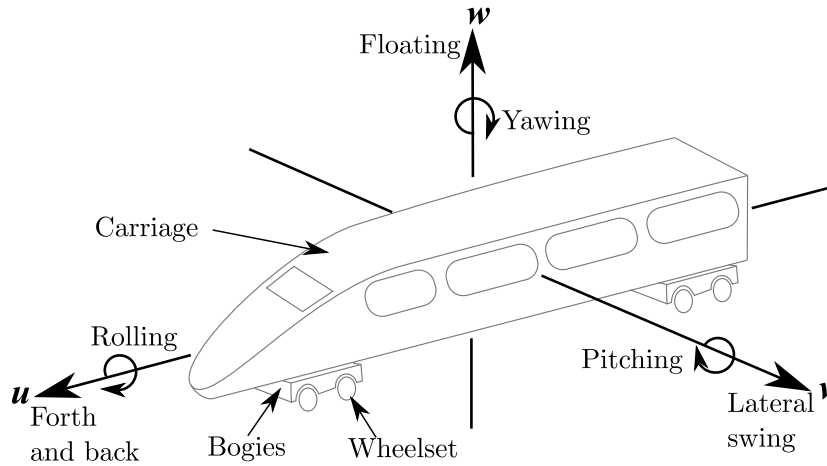
Figure 1.1: Train dynamic motions

scale, speed of construction, site safety and quality. The implementation of precast construction is already used for HSR bridges. However, the construction of these bridges tends to use conventional concrete strengths, leading to bulky solutions with high mass. These large and heavy elements need to be transported from the precast plant to the construction site and lifted in place to their final location. Through the use of high performance concrete (HPC) the cross section can be designed with thinner elements, reducing the span mass, and improving the prospects of precast construction. Nevertheless, these lighter structures would be more prone to vibrations under the HSR traffic loading, due to the lower mass in Newton's Second Law, which therefore requires further study.

Precedent for using HPC precast solutions in bridges comes from highway bridges, where many existing bridges are constructed with this material. However, HSR bridges are exposed to a very different type of loading in comparison. The ratio between traffic and permanent loads are larger in HSR bridges than in road bridges. In addition, train vehicles will enter a bridge at higher velocities, at fixed lateral locations (where the rail is located), and will have fixed distances between axles. In comparison, vehicles on highway bridges will enter at lower speeds, with lower loads per wheel, with a larger spatial variation in the transverse direction within the lanes and a random pattern of axle distances due to the variety of vehicles and distances between them. This makes HSR bridges more susceptible to resonance problems, which generally results in stockier, stiffer and heavier cross sections. In addition, in HSR bridges there are strict requirements for the vibrations of the bridge to guarantee the train safety minimising the probability of derailment.

A high speed train vehicle normally consists of three main body types as seen in Figure 1.1: the carriages, bogies and wheelsets. Firstly, the carriage is the largest body and the passengers are seated within it. The bogie, which is sometimes excluded, is found between the carriage and wheelsets. The bogie holds two wheelsets and houses mechanisms to provide braking and traction forces, whilst also helping to steer the train around curves. Finally, the wheelsets

sit on the rails and through rotation provide a forward motion to the train. Connecting the bodies there are layers of suspension, comprising springs and dampers, which improve passenger comfort and help to steer the vehicle. These suspension layers are defined as the primary suspension, which is found between the wheelset and the bogie, helping to steer the train, and the secondary suspension, which is found between the bogie and the carriages, mainly functioning for the passenger comfort.

Trains are required to have very high comfort levels for passengers in comparison with a road vehicle. Definition of the motions of the train is important in the study of the vehicle dynamics. A set of three perpendicular axes (u, v, w), can be used to define the six degrees of freedom (DOF) of the vehicle motion, with three displacements (forth and back, lateral swing and floating) and three rotations (rolling, pitching and yawing). Axis u is defined in the direction of travel, v perpendicular to u and horizontal, and w perpendicular to u and v. This can be seen in Figure 1.1.

The modelling of the vehicle is one of five important considerations for the development of a HSR dynamic bridge model. The other four are the dynamic bridge model, the interaction between the wheels of the train and the rails, the irregularities found deviating the rails from a perfect profile and alignment, and a method to obtain the numerical solution (Zhang et al., 2008; Antolin et al., 2012). Nowadays, numerical models developed by researchers and powerful structural analysis packages can enable modelling of the whole train and all its suspension systems in conjunction with the track and the bridge structure in a very accurate and detailed manner. Through these models, the implementation of HPC, allowing lighter precast decks in HSR bridges, can be investigated. The idea is to make the precast elements as light as possible (by implementing HPC), without penalising their dynamic behaviour and hence not making them too prone to vibrations.

1.2   Research Objectives

This thesis is focused on the study of the dynamic structural response of high-speed railway bridges, with lighter HPC precast decks. The implementation of HPC could lead to lighter sections, which are easier to transport and to set out in place on site, but which may be more prone to vibrations. Whilst the study of HSR bridges is well documented, the level of detail required in modelling each component varies significantly between literature. Deciding on the modelling processes is a substantial part of the problem to be solved, before a study on the use of HPC in the bridge can be initiated. Hence, the main objectives of the research are:

- To perform an extensive literature review, compiling the main design characteristics of HSR bridges using precast concrete solutions, the material properties of HPC, the main characteristics of the high speed trains, the properties of the track and irregularities

and finally the interaction between the wheels of the train and the rails, as well as the existing theories and methodologies to model all these elements.

- To develop a sophisticated dynamic finite element (FE) model, including the whole train, train tracks and the wheel-rail interaction, to analyse the structural response of these bridges under the dynamic loading scenarios, with an assessment of the sensitivity of the key input modelling parameters.

- To investigate the structural dynamic behaviour of a benchmark bridge, followed by performing parametric analyses through implementing HPC into this bridge to maintain existing structural capacities, whilst reducing its weight through changes to the geometrical bridge properties such as the web and flange thickness, continuity, and bridge depth.

- To evaluate and compare the structural behaviour of different bridge cross sections, and apply similar parametric analysis to these bridges to incorporate HPC.

- To gain understanding about the structural behaviour of these bridges and to provide appropriate design recommendations.

Furthermore, the findings of this thesis are to be disseminated into papers to be published in scientific journals.

1.3 Thesis Outline

There are seven chapters in this thesis. Excluding this chapter, the outline of the remaining thesis is described as follows.

The literature review is presented in Chapter 2. This includes a detailed analysis and compilation of models previously used for bridges, train vehicles, track structure, track irregularities, wheel-rail interaction, the properties of HPC and some specific design criteria for HSR bridges. Within this chapter there is also a study of existing HSR bridges constructed using concrete, particularly precast elements, showing a comparison of the characteristics of each solution, enabling an appropriate benchmark case to be later chosen.

Chapter 3 focuses on the general methodology used in this thesis. This includes the selection of a benchmark case bridge to focus the analysis on. The chapter will follow on to identify how the track, train, irregularities and wheel-rail interaction are modelled.

Based on the methodology presented, Chapter 4 initiates the analysis of the benchmark bridge. The model is analysed considering the sensitivity of modelling parameters, and seeks to clarify contradicting sources from literature. The bridge model is analysed to determine optimal

computational efficiency and response accuracy. Different loading models are compared, to determine their appropriateness, based on the dynamic responses and the computational requirements. The analysis also considers the range of properties found in literature for the track and vehicle to study the effects of varying the stiffness of components, on the bridge and vehicle dynamics.

Chapter 5 considers the parametric analysis of the benchmark case bridge cross section identified in Chapter 3. The bridge is analysed using the best modelling approach determined in Chapter 4, to firstly establish an initial dynamic performance, for a range of vehicle velocities, for both a single span and a three spanned case. After establishing the initial cases, both the one span and three spanned bridge cases are subjected to detailed parametric analysis focusing on changing the geometrical properties of the precast elements, whilst increasing the strength. Through introducing HPC, to maintain the structural capacity of the bridge, suitable parameters for lighter precast decks are identified.

Chapter 6 studies three existing bridges, with precast decks, of different cross sections to incorporate the parametric changes identified by Chapter 5 into other bridge types. This requires identification of the initial dynamic performance of each benchmark bridge before implementation of HPC into the precast decks to create lighter cross sections are considered and investigated. The conclusions made in Chapter 5 are then determined whether they are appropriate for these other bridge types as well.

Finally, Chapter 7 concludes the work of this thesis, identifying and summarising the findings of the preceding chapters. It also identifies avenues for further study and recommendations for the updating of codes.

Chapter 2

State-of-the-Art

This chapter evaluates the current literature, to establish what studies need to be carried out for the solving of the problems of this thesis. It will also investigate the current state of the art of HSR bridges. Included are previous studies on the bridge, vehicle, track, wheel-rail interaction and material models.

2.1 Railway Bridges

Bridges are an important part of many HSR lines, due to strict geometrical requirements for the vertical and lateral alignment. In some cases the line can consist primarily of bridges. For example, in Taiwan, $251\ km$ of a total line length of $345\ km$ used bridges, 73% of which are precast full span box girders (Tai et al., 2010a).

In comparison with a highway bridge, the traffic loading is much heavier and sudden, although less continuous over the time, leading to stockier span to depth ratios in HSR bridges. The repeating distance of axles on a train can also lead to resonance problems in a bridge (see Section 2.7.5.1). Railway bridges are often flatter, as they must conform to stricter vertical curvature control than highway bridges.

2.1.1 Materials

Current HSR bridges generally use either composite (steel and concrete) or prestressed concrete for construction materials. Longer spans tend to use composite construction, very short spans use reinforced concrete and the rest prestressed concrete (Hseih and Wu, 2014). Direct comparison of the performance between the materials is difficult for a comparable bridge, but generally the dynamic response (measured using accelerations and Dynamic Amplification

Factors (DAF)) of a concrete bridge is better than a comparable composite bridge. This is due to the larger mass which makes it less prone to suffer significant vibrations. However, an important factor is the running speed of the vehicle compared to the critical speed (defined as the speed at which resonant vibration may occur (Frýba, 2001)), the latter tends to be higher in concrete bridges. It is seen in Kim et al. (2011), that the running speed of the vehicles achieved today can still match the critical speed within prestressed concrete bridges. Study of composite bridges is beyond the scope of this thesis.

2.1.2 Construction Methods

The main construction methods for concrete bridges can be split into two categories: in-situ construction and prefabricated construction. In-situ construction, consists of construction at the location of the final position of the structure, whereas prefabricated construction tends to include casting the concrete in a different location and transporting elements to site. For in-situ construction, methods include full-span casting, balanced cantilever and incremental launching methods. Prefabricated construction typically uses either full span placement or segmental methods (explained further in Section 2.1.2.1).

In-situ methods are the more traditional and are more financially viable for small scale production. These methods are more time intensive, require more site space to cast and construct and often require a larger workforce. However, it does allow more design flexibility between bridges. This thesis focuses on precast construction which is detailed further in the next section.

2.1.2.1 Precast Bridge Construction

In cases where standardisation of bridges is possible, cast in-situ methods become less economical, such that for a sufficient number of spans, prefabricated methods become achievable by reducing the construction costs through economies of scale. These savings must cover the initial set-up costs of a precasting factory for it to be financially viable. Many cross sections are of existing standard sizes. Changing of the shape of the cross sections can be achieved via placing of inserts into existing moulds to reduce the geometry of the existing sections.

Precasting of concrete reduces on-site construction times, with the structure sufficiently cured by the time it is placed in position, so further construction processes such as post-tensioning and placing of further spans can continue. It also can be constructed in a wider range of weather conditions, leading to smaller possible construction delays. Precasting methods can reduce the disruption of bridges constructed in proximity to other infrastructure due to its speed and reduced falsework requirements. The process can be controlled better than in-situ methods, which can lead to higher quality, better riding comfort levels, lower maintenance costs
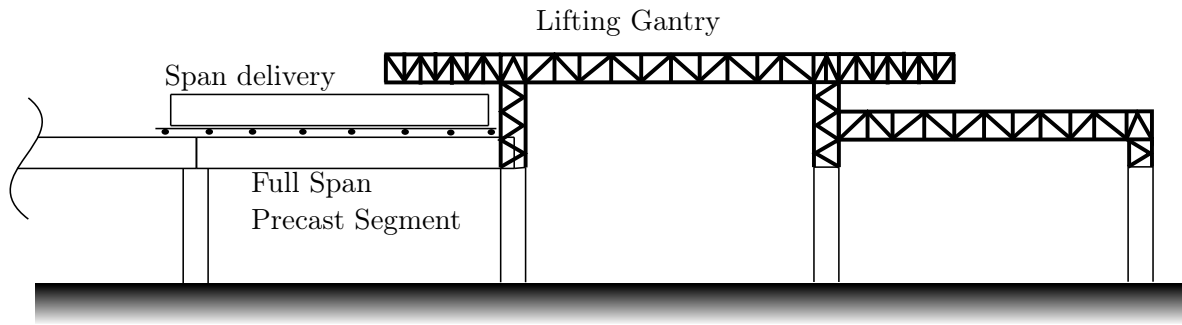
Figure 2.1: Figure showing the full span erection of a precast box girder

and more influence on the prestressing loads. Generally, the durability of the construction can be increased, although the joints between precast elements need to be carefully designed due to small tolerances and durability issues. This is particularly the case for segmental construction where epoxy resins and post-tensioning are used to join segments. Disadvantages of precast construction include a lack of design flexibility and a requirement for heavy lifting equipment, which for some cases may lead to the critical load design to be for construction rather than during the railway vehicle loading (Morgan Girgis and Tadros, 2007; Rosignoli, 2014a; Hseih and Wu, 2014).

As previously mentioned, there are two methods commonly used in precasting bridges. Firstly, segmental construction involves splitting the span into multiple segments (typically a few metres long) that are easy to transport, before post-tensioning together in-situ, a process commonly used in France (Combault, 2013). However, this method is not included within the scope of this thesis, due to the complex interactions of the joints between segments. The alternative, full span construction, uses one segment that is the full length of the span and placed into position. This can either consist of a single segment that is the whole bridge cross section or use longitudinal elements (precast beams) that are later topped by a slab on site. There are many challenges with using forms of full span precasting (as seen in Figure 2.1 (Rosignoli, 2014b)). As bridge sections are very heavy, they require dedicated machines such as span launcher or portal carriers to carry the precast element and place them into position (Rosignoli, 2014b). To support the structure during transportation, the beams are often pre-tensioned.

When using precast beams, transverse diaphragms are frequently used at support sections. The precast beams support a slab which the track is placed on. Generally this slab is added as either fully cast-in-place, or partially cast in-situ (partial depth slab), which uses thin precast panels placed over the beams as permanent formwork and topped with a cast-in-place slab (FHWA, 2005). Less commonly, the slab is constructed with precast panels that are the full depth of the slab, utilising grout filled shear pockets to connect the mechanical shear connectors of the precast beam to the slab. According to Morgan Girgis and Tadros (2007), using full depth panels may increase the life of the bridge as the slab can be prestressed, use high performance concrete and have the benefits in quality that comes with use of prefabricated

cross section	name	key
	Box girder	a
	Dual U-Beam	b
	Straight sided box girder	c
	Triple webbed box girder	d
	Voided slab	e

Table 2.1: Different types of cross section used in the bridge database and Figure 2.2

elements. This method has not been found to have been used in HSR bridge design, but examples have been found in highway bridges.

2.1.3 Cross sections

A database of published HSR bridges from around the world has been compiled by the author (see Appendix A). The bridges are split into categories based on characteristics such as construction method and cross section type, with the properties then compared. The cross sectional categories are described in Table 2.1, with the comparison of properties made in Figure 2.2. It can be clearly seen that there is an upper span length of around $45\,m$ for the precast bridges due to construction constraints (mainly transportation). Continuous bridges are found to be more common in the database than simply supported, single span cases. When focusing on the span to depth ratios shown in Figure 2.2a, precast solutions are found to be stockier than the cast in-situ solutions. Precast solutions tend to have slenderness ratios between 1/11 and 1/14, whereas cast in-situ solutions range between 1/14 and 1/16.

The thickness of the webs in general is between 1/5 and 1/9 of the depth, with some exceptions when there are more than two webs per cross section (Figure 2.2b). The majority of web thicknesses are between 0.4 and 0.6 m. It is also apparent that the precast solutions are thinner than cast in-situ, which could be due to the shorter spans associated with the precast methods.

The use of the dual U-beams shows considerably smaller bottom flange widths (Figure 2.2c), and the thicknesses of the bottom flange not directly correlated to its width. The widths of the bottom flange tend to be greater than $5\,m$. The thickness of the bottom flange also shows very little correlation to the span length (Figure 2.2d), with most of the thicknesses between 0.3 and 0.4 m.

Precast HSR beam bridges will generally conform to approximate span to depth ratios. According to Montagut (2010) spans of up to 30 to 35 m can be achieved in simply supported

(a) Cross section depth against bridge span

(b) Web thickness against bridge depth

(c) Thickness of bottom flange against its width

(d) Thickness of the bottom flange against the bridge depth
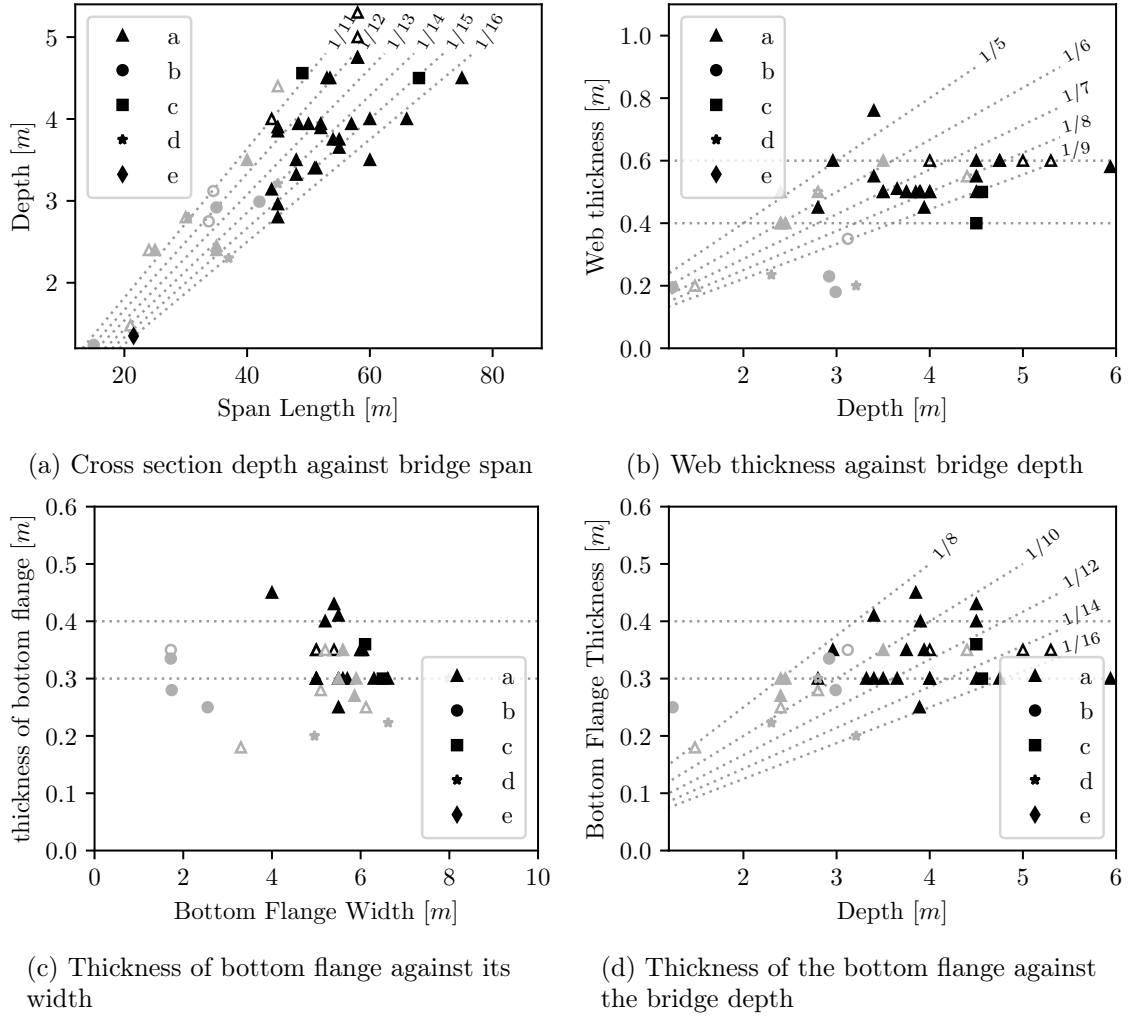
Figure 2.2: Different comparisons of bridges from the bridge database (Appendix A). The shape of the data point refers to the cross section in Table 2.1. Solid markers refer to continuous bridges and hollow are simply supported. Grey colours represent precast construction and black is cast in situ.

bridges, with depth to span ratios between 1/10 and 1/12. Through post-tensioning for continuity, up to $40\,m$ spans can be achieved, with more slender profiles such that the depth to span ratio reaches between 1/14 and 1/15.

Precast beams have many different forms and shapes, and include U-beam, I-beam, T-beam and Y-beam. The typical span ranges of these prospective solutions are shown in Figure 2.3 (FIB, 2004; Pacadar, 2015), which consider any vehicle loading type, not just railway bridges. Therefore, the maximum spans are likely to be smaller for railway bridges as they tend to be less slender. The use of U-beams is the most popular type of precast beam used in HSR bridges, due to its torsional resistance and attractive design (Gray et al., 2003). Section depths typically vary from 0.8 to $2.6\,m$, and at least one U-beam should be used per track supported. For the same span, I-beam bridges require greater depths, larger number of beams and transverse diaphragms at supports, hence the more frequent use of U-beams. However, U-beams are heavier, with a higher initial cost due to higher capacity lifting equipment and a less standardised design (Tierra Armada, 2012; Gray et al., 2003). All of these bridges require completion through topping with a slab.
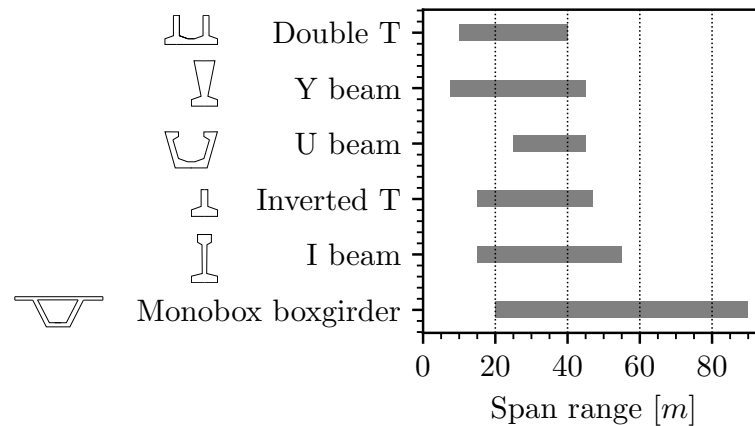
Figure 2.3: Potential precast bridge span lengths comparison

From Figure 2.2, it appears the majority of published HSR solutions use a box girder, matching the claims of Hseih and Wu (2014). When precast these commonly use the full span method, where the whole cross section is precast. Common variations of the box girders are shown in Figure 2.4. The spans can be up to $45\,m$ long, often limited by transport methods. However, through post tensioning to make continuous, several longitudinal precast beams of the full box girder cross section can be joined to reach spans of up to $90\,m$, which has previously been achieved in highway bridges (FIB, 2004). According to Montagut (2010), the use of box girder bridges can lead to depth to span ratios of generally 1/12 to 1/14, but occasionally up to 1/17. A haunched profile close to the support sections can half the depth in the middle of the span, which has been demonstrated in Spain (Llombart Jaques et al., 2014b). However,

(a) Standard box girder   (b) Double celled box girder   (c) Straight sided Box girder
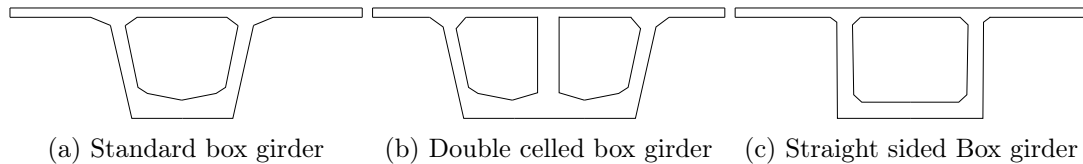
Figure 2.4: Box girder solutions

this value is based on cast-in-place solutions and examples of precast construction indicated stockier solutions (Tai et al., 2010b).

The majority of solutions use the standard solution shown in Figure 2.4a. For wide decks or if the bridge requires a higher level of stiffness and shear strength, a double cell box girder can be used (Figure 2.4b). This may take the form of two precast U-beams placed adjacently, transversely joined by prestressing bars and topped by a slab (Montaner Fraguet et al., 2014), or by the full cross section being precast (Miotti et al., 2003). Alternatively, a single cell box girder could be used with inclined struts linking the cantilevered slab flanges back to the box, reducing the transverse bending and providing additional stiffness (Marí and Montaner, 2000).

Although the previous cross sections are most popular, other sections are possible. Trough bridges, with an example in Figure 2.5, allows the train to run in the base of a wide U shape beam without an additional slab being constructed. This method reduces noise pollution without a need for sound barriers (Rosignoli, 2014b), and also reducing the running height of the train. It has had some limited use in HSR, particularly for the Modena viaducts in Italy, with further rail use in Belgium (Staquet et al., 2004).
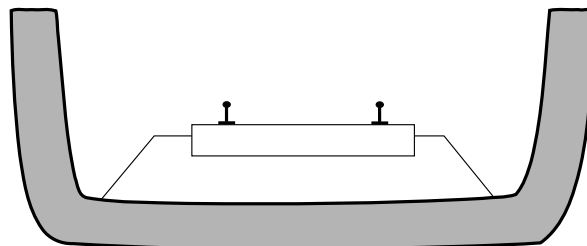
Figure 2.5: Sketch of shape of U shaped Trough bridge, with ballasted track shown inside

2.1.4 Longitudinal Continuity and Articulation

The longitudinal scheme of a bridge can be classified as simply supported, continuous or integral. Continuous bridges are constructed without joints between intermediate spans. They can also be materialised by a combination of post-tensioned bars and a cast in-situ joint (with high strength concrete or epoxy) to connect the precast bridge beams together (FIB, 2004). Continuous railway bridges offer lower vibration response and therefore a better dynamic performance than simply supported bridges (Goicolea-Ruigómez, 2008).

Integral bridges are constructed without expansion joints between intermediate spans or between the end spans and the abutments. Bearings are also eliminated in this type of bridge. However, evidence of the use of this method for HSR with a precast solution has not been found.

The continuity of the rail over joints is often ignored for the dynamic analysis due to the relatively low rail stiffness compared to the bridge (Majka and Hartnett, 2009). However, rail-structure interaction is studied for longitudinal actions such as braking, acceleration, thermal expansion and long-term bridge deformations (creep and shrinkage). These actions introduce stresses into the rail, so to avoid rail expansion joints on the bridge, the distance from a fixed support to a bridge expansion joint is limited to $90\,m$ for concrete bridges ($60\,m$ for steel-concrete composite bridges) (Calgaro et al., 2010b).

Through vehicle braking and accelerating, large horizontal forces are required to be transported from the deck into the foundations. The horizontal load can be transferred through a stocky pier, an abutment or V shaped piers, all of which need to be stiff enough to transfer the horizontal load.

When piers are slender they may need modelling for the dynamic effects of the bridge. This is normally the case for tall viaducts. The flexibility of the pier can lead to larger lateral displacements of the bridge (Antolín et al., 2010; Antolin et al., 2012). Where piers have previously been modelled, the model of the bridge deck and piers tend to use simple beam element models (Antolín et al., 2010; Antolin et al., 2012). Alternatively, the stiffness of the piers, abutments, bearings and foundations are represented by springs attached to the support conditions for beam element models of simply supported bridges, when modelled by Simões et al. (2008), Reis et al. (2008), Cuadrado et al. (2008) and Ramondenc et al. (2008). In a shell element bridge deck model, Moliner et al. (2012) incorporates the bearings by applying vertical stiffness to the shell elements in the support regions. It was found that the vertical accelerations decreased with a decreasing connection stiffness, but it was found that the effects of the bearing model is negligible. However, modelling of pier stiffness has not yet been made when studying a bridge using three dimensional shell elements in current literature. This may be as some literature consider piers to be stiff enough to neglect modelling (Au et al., 2002; Dinh et al., 2009; Zhang et al., 2010; Antolín et al., 2013).

As abutments consist of different material to the bridge deck, so they can have different stiffnesses. This can create a change of running profile for the track such as that described by Hess (2008). However, the transition is not found to be modelled in literature.

2.1.5 Bridge Modelling

The modelling of the bridge structure itself depends largely on the focus of the investigation. For design studies or research focusing on the vehicle dynamics, it often is the case that the bridge is modelled by simple beam elements, ranging from two dimensional Euler-Bernoulli (Gabaldon et al., 2008), and Timoshenko methods (Lou et al., 2012) to three dimensional beam element models (Montens and Huyard, 2008). The beam is characterised by the bridge cross-sectional properties, such as the area, second moment of areas, torsional rigidity and centroids. It offers an approximate solution to the bridge response without a lot of computational cost.

In order to capture the cross-sectional deck deformations, we can use shell elements (Delgado et al., 2009). These elements, used by Song et al. (2003) among many others, are often preferred over the solid elements, used by Kwasniewski et al. (2006) and Xia et al. (2003), as they have the ability to model the bridge more accurately for the same computational time. Theoretically, solid elements could be used, but the usage is limited with current computing capacity, as once these models are appropriately calibrated through the sensitivity analysis, an extremely large number of elements is required, so the computational time becomes unrealistic for complex dynamic modelling. Modelling with shell elements requires significantly fewer elements for accurate analysis, leading to smaller computational time for comparable results. In addition, the more realistic representation gained from using 3D solid elements, rather than shells, has very little implication for the dynamic analysis problems raised during the design of these bridges.

2.1.6 Conclusions related to Bridges in Literature

From this study of literature, precast HSR bridges utilise a wide variety of bridge types and construction methods. The type of bridge used in this thesis is presented in the methodology, however to model the bridge, literature suggests the following:

- The use of shell elements for the most computationally efficient and accurate solution

- The use of beam elements to model simple cases of the bridge, or when using more complicated vehicle models

- Ignoring the flexibility of the piers if they are stocky

- Ignoring the stiffness of the bearings in the model

- That continuous bridges will give rise to smaller accelerations

Train	Country	Type	V_{max} [km/h]
Thalys	France, Belgium, Germany	A	320
AVE S100	Spain	A	300
Eurostar	France, Belgium, UK	A	300
ICE2	Germany	C	280
ICE3	Germany	C	330
ETR-500	Italy	C	300
Virgin	UK	C	200
TALGO 350	Spain	R	300
TGV Duplex	France	A	320
700T	Taiwan, China	C	300
N700	Japan	C	300

Table 2.2: Table of trains, country of operation, layout type and maximum operating velocity. A=Articulated, C=Conventional, R=Regular

(a) Articulated   (b) Conventional

(c) Regular
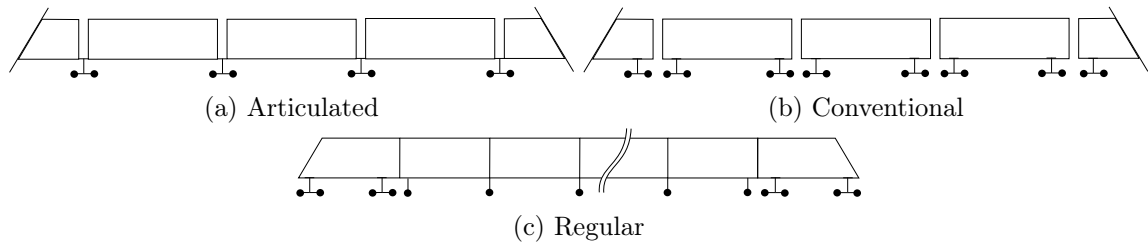
Figure 2.6: The three types of train layout

2.2   Train-Vehicle Models

There are many different types of train vehicle, each with different wheel-axle spacings, component masses and suspension stiffnesses. Table 2.2 shows a selection of different high speed rolling stock and the maximum speed each operates at from around the world (Goicolea and Gabaldón, 2008). The vehicles can be broadly placed into three categories, based on the wheel layout. Articulated vehicles have bogies shared between carriages, with each bogie having two wheelsets. Contrastingly, conventional vehicles do not share bogies, so instead have two bogies per carriage and two wheelsets per bogie. Finally, regular trains do not feature bogies, with wheelsets directly connected to the carriages. These trains can be seen in Figure 2.6.

Vehicles have previously been modelled in a variety of different ways to suit the desired outcome. Some models are very simple, just a set of moving loads, whereas others can model the whole train system, from the wheelset up to the flexibility of the carriages themselves.

2.2.1   Point Load Methods

The simplest method of modelling is through a set of moving point loads, as seen in Figure 2.7a. Analytical models of moving point loads on beams have been achieved from Timoshenko (1922), Smith (1988) and Frýba (2001). The model of Frýba allows determination of the bridge acceleration, deflection and bending moment from moving point loads. Compared to real data, the calculated numerical values were on average 10% higher.

Yang et al. (2004a), stated that although the moving load model is widely used in literature, it ignores the interaction between the bridge and the moving vehicle and hence is only suitable for situations where the vehicle mass is small compared to the mass of the bridge, and with the vehicle response an undesired output. Further, Martin (2008) finds this type of modelling unsuitable for bridges with spans less than $40\,m$ as it neglects mass interaction. This is similar to BS EN 1991-2:2003 (2010), which suggests that in bridges with spans less than $30\,m$, the interaction of the mass of the bridge with the vehicle mass is important.

2.2.2   Moving Mass Models

In order to incorporate the effects of the vehicular mass, some models incorporate a moving mass model, as seen in Figure 2.7b. This is useful for situations where vehicle mass is large in proportion with the bridge mass for which differences between moving load and moving mass models can raise by up to 80% (Akin and Mofid, 1989) (although the moving mass to bridge mass ratio here is much larger than realistically found for railway bridges). The lack of a vehicle in this model, means the vehicle motion cannot be determined, which is according to Yang et al. (2004a), important for HSR in the presence of track irregularities.

2.2.3   Sprung Mass Model

A sprung mass model, as seen in Figure 2.7c, incorporates a mass suspended by either a spring or a spring and damper, which moves along the bridge with the velocity of the train. It allows incorporation of the mass effects (Delgado et al., 2008; Goicolea and Gabaldón, 2008), and also some simple vehicle dynamics. Models include a mass hung from a spring (Yang et al., 2004a), an unsprung mass attached to a sprung mass and multiple layers of sprung mass (quarter or half bogie models). The wheelset mass is unsprung, with the carriage mass either incorporated by an additional sprung layer, combined with the bogie mass or as a moving load on top of the wheelset mass (Vale and Calçada, 2014).

Yang et al. (2004a) compared different values of vehicle suspension stiffness and damping using a sprung mass model. It was concluded higher damping led to higher vertical acceleration of the sprung mass and the bridge had a reduced response. Variation of the suspension stiffness
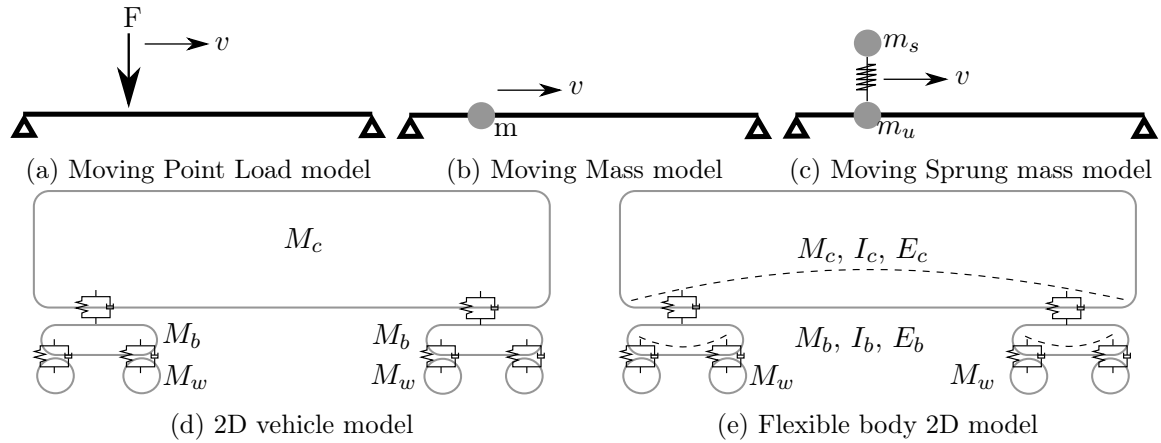
Figure 2.7: Some of the vehicle model types found in literature

of the sprung mass was found to have a negligible impact on the bridge response, but was important for the dynamics of the sprung mass (Yang et al., 2004a). A drawback of the sprung mass model is that the vehicle motion does not include pitching motion which is important especially in the presence of rail track irregularities (Yang et al., 2004a).

2.2.4 Two dimensional Vehicle Model

When modelling in two dimensions (Yang et al., 2004a; Lou, 2005), the sprung mass model can be modified to connect the components of the vehicle, with a rigid beam connecting the bogie sprung masses, such that they are linked like a real carriage (as seen in Figure 2.7d). This incorporates the pitching motion, important in the determination of the vehicle response. Similar findings of the sensitivity to suspension stiffness and damping for this vehicle model as were found by Yang et al. (2004a) as in Section 2.2.3. The impact of this model compared with sprung mass models is negligible for bridge response, but it was found that the vehicle accelerations were increased (Lou, 2005, 2007).

2.2.4.1 Consideration of Flexible Bodies

The idea of a flexible body is shown in Figure 2.7e. Chen et al. (2015) considered the linking rigid bodies of the carriage and bogies to be flexible. Good correlation of the dynamic vehicle response with experimental data was found (Zhai and Sun, 1994), but the vehicle was not run across a bridge, so the impact on bridge dynamics was not determined. This research appears to be more concerned with vehicle response.

2.2.5 Complete Vehicle Models

The two dimensional models expressed previously have limitations. Forces are only available in one plane, with lateral actions ignored. Yang et al. (2004a), Xu et al. (2004) and Zhang et al. (2008) are among many to extend the train vehicles to three dimensions. Some of the common assumptions of the models made in these sources are:

1. Car bodies and bogies have five DOFs each, with the movement in the longitudinal direction restrained by the velocity of the train which runs at a constant speed.

2. Each vehicle consists of a rigid carriage body, two rigid bogies and generally four rigid wheelsets, each component joined by viscoelastic elements (with linear properties).

3. The connection between a bogie and its wheelsets (the primary suspension system) consist of both vertical, longitudinal and lateral springs and dampers, which are placed at both sides of the bogie.

4. The second suspension system acts between the car body and the bogies.

In general the carriages are modelled independently in literature, except for certain articulated trains (Zhang et al., 2008). The mass and the inertial moments of the bodies are lumped at their respective centres of mass (Kwark et al., 2004; Majka and Hartnett, 2008; Dinh et al., 2009; Ju, 2012). Some sources allow deformations of the bodies, for example the wheelset in Dinh et al. (2009), but the significance of this on the bridge or vehicle response is not disclosed and it is rarely used in literature. Due to the constant velocity modelling, the horizontal acceleration and braking forces are usually studied in combination with vertical loads in a static analysis (BS EN 1991-2:2003, 2010).

According to Zhang et al. (2008) the main difference between models is the number of degrees of freedom (DOF) allocated to each of the wheelsets. For example, in Xu et al. (2004) and Yang et al. (2004a), three DOF are allocated for each wheelset, restraining the yaw, pitching and longitudinal DOF, resulting in 27 DOF for each vehicle (carriage: 1×5, bogies: 2×5, wheelsets: 4×3). Alternatively, both Dinh et al. (2009) and Antolín et al. (2010, 2013) allocate 4 DOF to the wheelsets, with rotations around the main axle (pitching) and longitudinal DOF suppressed, resulting in a vehicle model with 31 DOF in total (carriage: 1×5, bogies: 2×5, wheelsets: 4×4). A diagrammatic model of the vehicle from Antolín et al. (2013) is shown in Figure 2.8.

Due to the sharing of bogies in articulated trains there is interconnection between carriages. This invalidates assumption of independence of carriages (Song et al., 2003; Xia et al., 2003; Kwark et al., 2004; Lee and Kim, 2010). In this case, additional visco-elastic elements exist between carriages. Examples of regular train layout full vehicle models used in literature were not found.
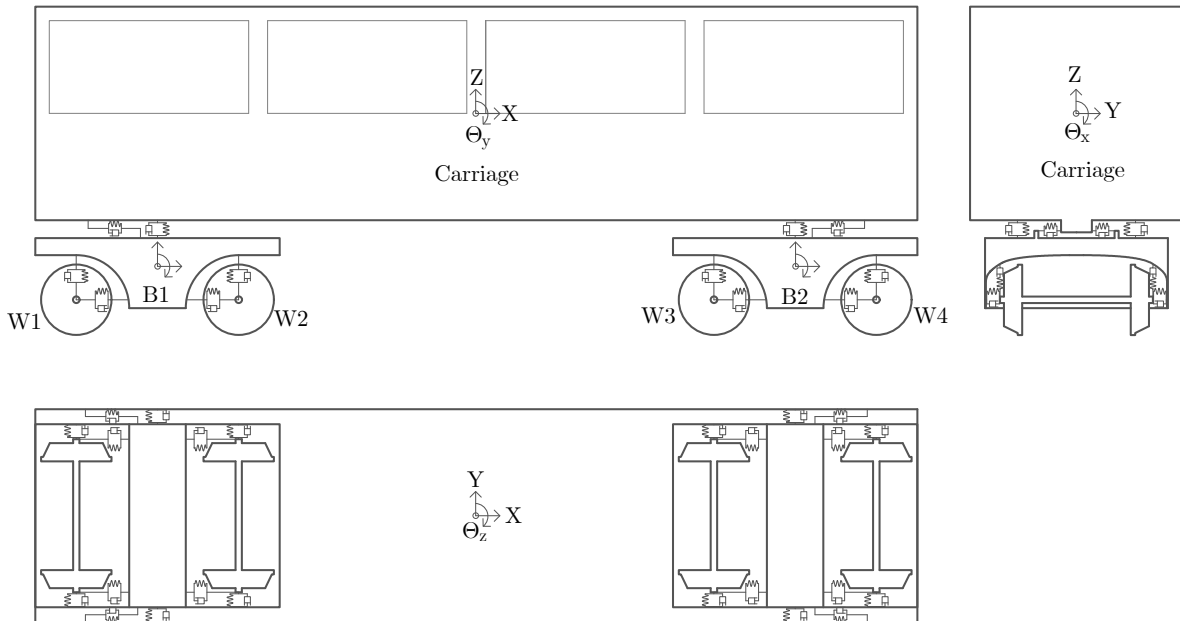
Figure 2.8: An example of a three dimensional vehicle model

2.2.5.1 Use of Full Vehicle Models in Literature

In some cases the full vehicle model is used in conjunction with a simple beam bridge model (Antolín et al., 2010, 2013). In these sources, no comparison was made between the model and experimental or other method results was made, so it is not possible to conclude whether this level of detail was appropriate, either for the vehicle or bridge response.

Alternatively, the full vehicle model is sometimes used with beam or frame elements in a three dimensional lattice (Kwark et al., 2004; Lee and Kim, 2010). Kwark et al. validates the three dimensional vehicle model with experimental methods on the actual bridges under construction, concluding that the three dimensional model with interaction between vehicle and bridge appeared to be necessary for the bridge response. However, Lee and Kim finds that the full vehicle model is not necessary for all carriages, employing a hybrid model of moving point loads and full vehicle models for different carriages, achieving a 25% computational saving, although this underestimates the displacement dynamic amplification factor by up to 3%. Lee and Kim (2010) found that although the full train was 20 carriages long, the 16 carriage model offered satisfactory representation.

By including the three dimensional model, there is the ability to be able to test the derailment safety of the train, using a series of vertical to lateral force ratios, whereas this is not possible in two dimensional analyses (Yang et al., 2004a) (See Section 2.7.2 for more information on derailment).

2.2.6 Vehicle Modelling Parameters

A wide selection of data found in literature in describing the vehicle properties has been established in Appendix C. It can be seen in this Appendix that there are some common properties between vehicles. For example, the vertical primary stiffness of a carriage tends to be lower than the lateral and longitudinal stiffnesses. However, the database also shows a lack of consistency between vehicles. Despite, the large amount of data, only a few vehicles have all data provided, including dimensions. Hence, the choice for modelling the real vehicle in this thesis is limited.

2.2.7 Eurocode Dynamic Load Models

As explained in Section 2.2, there are many different vehicles. In order to satisfy the loading that all variations of these trains cause, load models are generated to encompass the possible load profiles. European lines have to conform to the Technical Specifications for Interoperability (TSI) standards (Commission Regulation (EU), 2014), which ensure that the design of train lines is adequate for any of the types of trains in operation in the European Union (EU).

For BS EN 1991-2:2003 (2010), two High Speed Load Models (HSLM) have been developed, HSLM A and HSLM B, covering European train load dynamic signatures. The criteria to determine which HSLM to use is expressed in BS EN 1991-2:2003 (2010). A graph comparing the dynamic signature of some real trains with HSLM A has been compiled by the author and is shown in Figure 2.9. This compares the wavelength against the force component associated with that wavelength. These wavelength can be converted into a frequency by using the vehicle velocity, which allows comparison of the loading frequencies with the modal frequencies of the bridge, identifying the regions of concern for resonant behaviour. This means that although the wavelength of $15\,m$ has a low level of associated force, it does not necessarily mean a bridge of this length will be okay, due to the variation in speed of the vehicles.

Gabaldón et al. (2008) compared the vertical bridge accelerations numerically generated for different real trains with the universal trains provided by HSLM A, for a $22.5\,m$ spanned, precast double box girder bridge. For the real train, Virgin, at $220\,km/h$ the accelerations generated exceed the envelope of accelerations caused by the HSLM A trains, but this was not a determinate factor for design. However, Gabaldón et al. (2008) notes that the envelope capabilities of the universal trains have not been proven for statically indeterminate structures, which could lead to, in another case, a critical peak in accelerations and then an inadequate design.
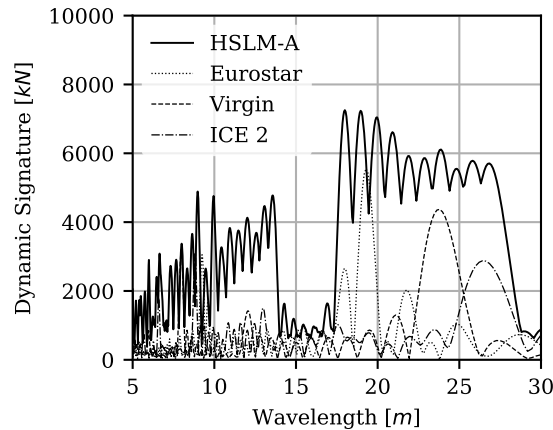
Figure 2.9: Comparison of the dynamic signatures of the high speed trains, Eurostar (articulated), Virgin (conventional) and ICE2 (conventional), with the dynamic envelope of the HSLM-A models (inspired by Goicolea et al. (2006))

2.2.8   Conclusions related to Vehicles in Literature

From the literature, it is suggested that a moving point load model is inappropriate for spans less than $30\ m$, due to mass interaction. The use of flexible bodies is the most advanced, but is utilised in situations focusing on vehicle response. For obtaining and studying the vehicle response the vehicle should be included in the model. The implementation of the whole train within the model has rarely occurred in conjunction with a detailed model of the bridge (through a shell element model), as it is mostly modelled with beam elements. Different vehicles have been found to induce different responses with load models utilised to cover the loading of the variety of different train types.

2.3   Track Model

The track is an important subsystem of the global vehicle-track-bridge system. By track we refer to all of the components between the vehicle and the bridge. This includes the rail, rail pads, fasteners, sleepers and either ballast (for ballasted track which in some literature includes further layers of subballast and subgrade, separate to the ballast layer), or a slab (for slab track). There are multiple ways to define these layers according to literature, depending on what the level of detail and aim of the study is. There are also differences that will arise between the modelling of ballasted track and a slab-track (nonballasted track), although according to Dinh et al. (2009), the former is more widely implemented in reality.

The track life cycle is a maximum of around 50 years, compared to bridge design lives typically in excess of 100 years (BS EN 1991-2:2003, 2010). Therefore, this has to be considered in the design, for example, by including a separation layer between the waterproofed bridge structure
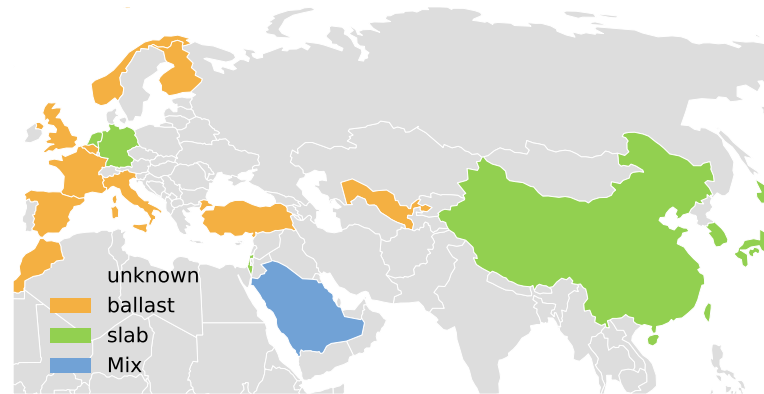
Figure 2.10: Ballast usage in different countries around the world, compiled by the author with data taken from Fagan (2016), Alamaa (2016), Miura et al. (1998), Nurmikolu (2012), Kufver and Gåsemyr (1999) and Aripov et al. (2016)

and the track system. This removes the composite action between the two components and enables replacement of the track structure.

2.3.1 Ballasted Track vs Slab-Track

Traditionally railway track has included a ballasted bed, but recent trends have been towards a slab track (Fagan, 2016). Some of the benefits of ballasted over slab track are: lower initial costs, a more flexible structural system, good noise absorption, speed of construction, improved water drainage and wider load distribution. On the contrary, slab track has the following advantages over ballasted track: smaller long term track movement, higher resistance to lateral movements, a lower train running height, a lower lifetime cost due to reduced maintenance costs (particularly important on HSR bridges), smaller weight, increased passenger comfort for a given maintenance level and higher capacity to resist axle loads (Esveld, 1997; Fédération internationale du béton. Task Group 6.5., 2006; Bastin, 2006; Bezin et al., 2010). In addition, the lack of ballast removes the long-term mass gain from material in the voids and removes the potential for dislodged ballast material from causing damage to the wheels and rails.

Many countries with HSR, use a combination of slab-track and ballasted track, with different segments of the lines utilising different tracks (Fagan, 2016). The predominant track usage in countries with HSR and published data, is shown in Figure 2.10. Often due to the high initial costs and small construction tolerances with some ballastless methods, the wider use of this system has been inhibited (Esveld, 1997). In addition, it is a relatively young system, such that the real long term cost-benefits are not fully known yet.

2.3.2 Embankment to Bridge Track Transition

An important consideration in the design of a track is in the location of the transition between the bridge and the embankment. In this area the bridge can be stiffer than the surrounding ground (Esveld, 1997). This can cause changes in the vertical alignment of the track from the bridge to abutment, potentially causing large dynamic forces, particularly a problem for the vehicle behaviour (Esveld, 1997). In addition, the train crossing the bridge causes rotation at the deck ends. This rotation can cause problems for the track (Fumey et al., 2002). Additional structural transitional components may be added to the bridge to span the joint, smoothing the discontinuity between the abutment and the bridge (Fumey et al., 2002; SSF Ingenieure, 2016).

2.3.3 Modelling the Track

Modelling of the track has been found to be important to the vehicular dynamic response in particular, with Yang et al. (2004a) finding the vehicle particularly sensitive to ballast stiffness changes when travelling at low speeds. Despite this, other authors (Xia et al., 2003; Antolín et al., 2013) ignore all of the track components, assuming that the track and the bridge deck deflect and accelerate together. This method is the least computationally expensive, using the fewest number of elements, but neglects the load distribution and elastic effects of the track.

Modelling of the rail is sometimes used when modelling in two dimensions when studying the longitudinal stresses introduced to the rail and substructure from horizontal actions and temperature changes. This uses longitudinal elastic linear and non-linear springs between the rail beam and the bridge beam (Ramondenc et al., 2008; BS EN 1991-2:2003, 2010). When studying vertical loading, a series of vertical springs may support the rail beam (Winkler foundation model). However, these models require additional parameters to represent the longitudinal track stiffness (Zhaohua and Cook, 1983; Song et al., 2003).

A four layer track model is required to represent the rail, rail pad, sleeper and ballast in greater detail (Wu and Thompson, 2002; Kargarnovin et al., 2005). The rail pad and ballast can be modelled by viscoelastic elements. It was found in Kargarnovin et al. (2005), that a linear approach was accurate enough to describe track impacts on the vehicle comfort levels. The sleepers are modelled as a lumped mass in these models. Longitudinal and lateral springs between the ballast can be incorporated (Wen et al., 2009), as seen in Figure 2.11. This allows transfer of longitudinal and lateral loads to the bridge.

The values used for some of the parameters in these track models are shown in Table B.1 of Appendix B. It is seen in this table that the values used for different parameters vary significantly between different sources, particularly the railpad stiffness. This is partly down to different stiffness of railpads being used for different types of track.
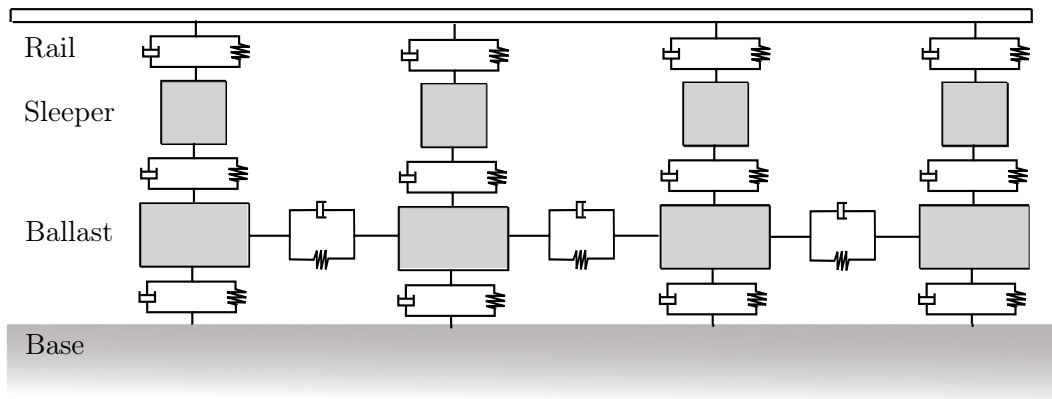
Figure 2.11: Side view of the full track model, adapted from Wen et al. (2009)

Slab tracks are less commonly found to be modelled in literature. De Man (2002) and Proença et al. (2011), models in two dimensions a beam for the rail, connected to a discrete slab below, of $6.5\,m$ long (which is also modelled by a beam), connected to the bridge underneath. Viscoelastic elements are used between the elements of the rail and slab, to model the railpads, and between the slab and the bridge to represent a waterproof membrane layer. However, these are the only sources found to use this method. Dinh et al. (2009) uses a slab track model, but ignores elastic effects of the track system. Very few other researchers have been found to model ballastless tracks.

2.3.4 Conclusions related to the Track in Literature

Track models are different for ballasted and slab track. Slab track appears to be where industry is moving towards. Ballasted track is more commonly modelled in literature, with models limited for slab track. Significant variation in complexity of models in literature occurs, but studied literature finds this has the greatest effect on the vehicle and not bridge dynamics. Therefore, it is useful to see the impact of the track properties and a comparison of the two tracks on the bridge.

2.4 Wheel-Rail Interaction

According to Yang et al. (2004a), it is the definition of the contact between the wheel and the rail, that allows the coupling of the bridge and vehicle models. The degree of complexity of the Wheel-Rail Interaction (WRI) models varies among literature. For moving point load models, the interaction does not need to be modelled. Therefore, the models expressed in this section refer to the three dimensional vehicle models.

At the simplest level the wheels of the vehicle are set on a perfectly guided predefined path

(Song et al., 2003; Xia et al., 2003). Alternatively, a linear model (Xu et al., 2004; Yang et al., 2004a), can allow a relative velocity and displacement between the wheel and rail, but linearise the wheel and rail profiles. A more complex model considers the real profiles of the wheel and rail, which is a much more realistic way to describe the contact problem and this also allows contact between the wheel flange and the rail, which keeps the wheelset between the rails (Nguyen et al., 2009; Antolín et al., 2010; Antolin et al., 2012).

In general, for the consideration of the force transfer between the wheels and the track, there are two types of force that are modelled. The normal force acts perpendicular to the contact point and the tangential force acts in the surface plane of the contact. The order of solving the wheel rail interaction problem is performed by solving in order the: 1) contact position, 2) contact area, 3) normal force and 4) tangential forces (Antolin et al., 2012).

2.4.1   Contact Position

Before finding the contact area, the position of the contact needs to be defined. This enables the properties of the contact area to be calculated. This position may be found by the point at which the two bodies come into contact, or by the largest penetration between the two bodies (neglecting the deformation of the bodies). It is possible for multiple points of contact to occur simultaneously as found in Piotrowski and Chollet (2005). Methods used to find the point of contact can vary from searching at discrete points and interpolating between points, to using equations to solve the contact (Shabana et al., 2005).

2.4.2   Contact Area

There are two different approaches for solving the contact area. The first is to assume that the contact is an elliptical area, and the second is assuming that the contact area is non-elliptical (Antolín, 2013).

In general a contact area between two identical spherical deformable bodies would be circular. Due to the changing curvatures of the profile of the wheel and rail, non-elliptical contact areas are found. However, the area is often assumed to be an ellipse or series of ellipses (Piotrowski and Chollet, 2005). Formulations to calculate the shape and size of the contact patch have been given in multiple papers (Antolín et al., 2012; Shabana et al., 2004). This depends on the normal load, the Poisson's ratios and the Young's moduli of both materials in contact, and uses Hertz's Contact theory (as explained in detail in Section 2.4.3.1) (Antolín et al., 2012).

Consideration of a non-elliptical contact area is less commonly used in literature. To model this, the area may be approximated as multiple elliptical contact regions (Pascal and Sauvage, 1993; Piotrowski and Chollet, 2005), or the actual area split into strips (Ayasse and Chollet,

2005). Multiple points of contact may occur as a result of the assumptions in Hertz theory (Hertz, 1882), that the curvature is constant and bodies non-conforming, which in reality the contact between rails and wheels can invalidate. For non-conforming contact, the shapes of the contacting bodies are different, such that a point of contact can be determined. In contrast, an example of conforming contact would be a sphere inside a spherical socket, where contact would occur everywhere simultaneously, whereas non-conforming contact would be a cube in the same socket, such that contact only occurs in discrete locations. Alternatively, a method of semi-Hertzian contact could be employed. In this case, Hertz theory only applies in the direction of travel and not in the transverse direction. It again can solve cases where curvature is not constant, and the method has been solved for in both Ayasse and Chollet (2005) and Quost et al. (2006)

2.4.3   Normal Force

After finding the contact between the wheel and rail, the next step to solving the WRI is to solve the normal contact. The normal force is split into methods that consider an elastic contact, normally using elliptical Hertz contact, and those that use a simpler rigid contact.

2.4.3.1   Elastic Normal Contact

The use of elastic theory for the determination of the contact requires iteration to solve the equations (Xia et al., 2012). The majority of elastic solutions use Hertz theory. There are certain assumptions of the theory outlined by Hertz, and translated to be expressed in English by Antolín et al. (2012) (Hertz, 1882). These are:

1. The surface of both interacting bodies can be approximated by a quadratic function near to the patch of contact

2. The contact patch is dimensionally small in comparison to the radius of curvature of both of the bodies at the point of contact

3. Only one contact patch is considered for each interaction of the wheel and rail

4. The surfaces at contact are continuous and that the shapes of the two contacting bodies are non-conforming

5. The two bodies only have small deformations and these remain elastic

6. At positions far from the contact patch boundaries, the stresses (normal and tangential) are zero

7. The mechanical properties of the materials constituting two bodies are identical, which allows independent study of the tangential and normal contacts.

The contact force between the two bodies is determined from the apparent penetration between the two bodies. The normal force is then found to be a force perpendicular to the surface of contact between the two bodies. Although this penetration does not really exist, it is a representation of the local deformation of the bodies on contact. This is normally used in a non-linear Hertzian contact equation (Shabana et al., 2004; Antolín et al., 2012; Xia et al., 2012), expressed as:

$$F_{ne} = K_H \delta^{3/2} \tag{2.1}$$

where F_{ne} is the normal force [kN], K_H the non-linear Hertzian contact stiffness [$kN/mm^{3/2}$] and δ the representative penetration between the two bodies [mm].

Alternatively, the expression can be linearised (Antolín et al., 2012) as in Equation 2.2, instead relying on a stiffness, K_s [kN/mm]. This is predetermined as in Equation 2.3, from the non-linear Hertzian stiffness, K_H, using the penetration calculated under a static self weight load δ_s [mm] such that the equation then becomes:

$$F_{ne} = K_s \delta \tag{2.2}$$

$$K_s = K_H \delta_s^{1/2} \tag{2.3}$$

Separation between the rail and the wheel can occur when the normal contact force becomes zero (Sun and Dhanasekar, 2002; Kargarnovin et al., 2005; Dinh et al., 2009; Nguyen et al., 2014). The definition of the parameter K_H, for the Hertzian contact stiffness, is not uniformly defined across the different literature. Kargarnovin et al. (2005) predefines the value of K_H as a constant based on specific track and rail conditions. However, Sun and Dhanasekar (2002), Nguyen et al. (2014), Antolín (2013), Shabana et al. (2007) and Antolín et al. (2012) all define it by a relationship between the wheel and rail, assuming that the material of the contacting wheel and rail are identical.

Variations used by Shabana et al. (2004), Shabana et al. (2005) and Torstensson and Nielsen (2011) couple the spring with a nonlinear damper, allowing contact damping. This additional damping force represents the resistance to the rate of penetration of the two bodies.

However, Nielsen and Oscarsson (2004) and Zhu et al. (2007, 2009) argue that the nonlinear Hertzian normal force model is inaccurate, proposing the Adaptive Wheel Rail Contact Model. Despite better accuracy claims, this method is not widely used in literature and is not compared in terms of computational requirements.

2.4.3.2 Rigid Normal Contact

The rigid contact (or constraint) approach, is more simplistic and it does not allow for the derailment (Xia et al., 2012; Shabana et al., 2004). It takes as input the displacements of

Source	Contact type	Normal contact	Tangential contact
Li et al. (2005)	Rigid	-	-
Majka and Hartnett (2008)	Rigid	-	-
Zhang et al. (2008)	Rigid	-	-
Liu et al. (2009a)	Rigid	-	-
Song et al. (2003)	Rigid	-	-
Lou (2005)	Rigid	-	-
Yang and Wu (2001)	Rigid	-	-
Vale and Calçada (2014)	Linear-2D	Linear Hertz	n/a
Kargarnovin et al. (2005)	Non-linear-2D	Non-linear Hertz	n/a
Dinh et al. (2009)	Linearised	Non-linear Hertz	Linear theory
Antolin et al. (2012)	Non-linear	Non-linear Hertz	FASTSIM
Goicolea and Antolín (2011)	Non-linear	Non-linear Hertz	USETAB
Antolín et al. (2013)	Non-linear	Non-linear Hertz	USETAB

Table 2.3: Selection of Wheel-Rail Contact models being used in literature for bridges

the bridge and the rail, including the displacements due to irregularities and the hunting motion. From this equation based approach to the positioning of the wheels, the forces can be determined by a set of lagrangian multipliers (Zaazaa et al., 2009). The formulation is widely used for bridges in literature due to its simplicity, as shown by Table 2.3.

According to Xia et al. (2012), this method has been widely verified by many in literature. Due to the inability to naturally develop hunting motion with this method, hunting motion is a prescribed displacement (Antolín et al., 2012). The number of DOF in the constraint approach is reduced as the wheels only have 5 DOF possible with respect to the rail, whereas in the elastic approach there are 6 possible DOF for the wheel relative to the rail (Shabana et al., 2004). A similar rigid approach is also employed by Song et al. (2003) but defines the force acting on the bridge based on the forces that act on the wheels, taking into account the sprung and unsprung masses.

2.4.4   Tangential Force

Due to the movement of the wheel relative to the rail, friction plays a part in the interaction. The tangential force (sometimes known as the creep force), is essentially the friction force acting within the plane of the contact surface, perpendicular to the normal force. The tangential force is important for the consideration of the lateral hunting motion, derailment issues and as a result a closer determination of the ride quality (Shen et al., 1983). It is part of the causation of the yawing motion of the wheelset, so as such will impact the dynamic performance of the vehicle and therefore the ride quality. It is important to note that at no point on the contact patch can the tangential stress (a shear stress) exceed the normal stress at that point multiplied by the friction coefficient as given in Coulombs law (Antolín et al., 2010, 2012).

The tangential force is often lower than the maximum allowed. If the wheel was not rotating about its axis, but was still moving forwards, this would be considered full slip, and the tangential forces would be maximum. Due to the conical nature of the wheel, with a constant rotation of the wheelset, the points of wheel in contact will be travelling at different velocities based on the different radii at the point of contact. The relative differences in the velocity between the wheel and rail in the contact patch (nondimensionalised and known as creepages), if zero, would result in a wheel in full adhesion with no tangential forces. The creepages between the wheel and rail are calculated in the lateral, longitudinal and the rotational planes between the wheel and rail (Antolín et al., 2012).

The tangential force has many different methods to calculate it. Some of the most well used and common models are proposed by Kalker, whose models are confirmed by others in literature according to Garg and Dukkipati (1984), but there are other proposed models that have been used. These models are discussed further here.

2.4.4.1 Kalker's Linear theory

The most simple tangential contact is the linear theory, of which Kalker's Linear theory is the most prominently used linear theory (as described in Antolín et al. (2012) who references the original text of Kalker (1967)). This theory assumes that every point on the ellipse is under an adhesion situation, with no slippage. With this theory, due to the neglecting of the creep forces, Coulomb's friction law may not be satisfied. This method has very small computation times, but it is unrealistic for anything but small creepages in the prediction of the tangential force, and it is for these larger creepages that the linear theory violates Coulomb's law.

2.4.4.2 Heuristic approach

Some manipulation can be made of the linear theory as outlined by Antolín et al. (2012), which applies a correction to the forces to satisfy Coulomb's law (Shen et al., 1983; Shabana et al., 2007). This can modify the tangential forces such that they do not exceed the maximum value given by Coulomb's theory.

The approach taken by Shen et al. (1983), improves an earlier theory by Johnson and Vermeulen (Garg and Dukkipati, 1984) by incorporating the influence of the spin. This theory is used by Zhang et al. (2008) and Wen et al. (2009), but according to (Polach, 2005) is less accurate than Polach's approach despite similar times for computation. However, these methods are not widely used in literature.

2.4.4.3   Polach's Method

An advanced method is the Polach's method (Polach, 1999). It has advantages over Kalker's Simplified theory through shorter computational time (up to 17 times shorter (Polach, 1999)), making it more suitable for complicated multi-body simulations (Six et al., 2015).

The method assumes that the tangential stress grows linearly, in the adhesion zone, with distance from the leading contact edge (Polach, 2005). It differs from the Linear Kalker method by including slip, so the maximum force is limited to Coulomb's theory. Antolín (2013) found that the Polach method is not accurate for high values of rotational (spin) creepage.

2.4.4.4   Kalker's Simplified Theory

A more complicated theory is Kalker's simplified theory. The accuracy of the simplified method is much closer to that of the exact theory compared to the linear theory, and to implement this theory an algorithm is required for which Kalker (1982) proposes a Fast Algorithm for the Simplified Theory of Rolling Contact (FASTSIM) (Garg and Dukkipati, 1984; Antolín et al., 2010; Torstensson and Nielsen, 2011). This method is one of the most widely used algorithms due to its speed of computation and accuracy, as it is a factor of 100 times less computationally expensive than the most accurate theory (exact theory of rolling contact)(Garg and Dukkipati, 1984), however Kalker (1982) finds FASTSIM to only be 15-25 times faster. Errors are found to be less than 15% compared to Kalker's Exact Rolling Contact Theory (Antolin et al., 2012).

In order to solve the algorithm the contact area is split up into a series of longitudinal strips, each strip being discretised into the same number of cells. The equations to calculate the stress are calculated at the centre of each cell, integrating over its area starting from the leading edge of the ellipse. This leads to longer computational times than the preceding methods explained. Although not used by Antolín (2013), this solution is claimed to be accurate enough for most solutions, but it does not list any exceptions where it is not suitably accurate. Although most work of FASTSIM focuses on the assumption that the contact area is an elliptical shape, adaptations have been made for other shapes, such as the one by Quost et al. (2006).

2.4.4.5   Kalker's Exact Theory

The most exact theory that has been created is Kalker's Exact Three-Dimensional Rolling Contact Theory (also known as variational theory). This is often used as the benchmark of comparisons for accuracy with other models through it's program, CONTACT (Kalker, 1990; Antolín, 2013; Vollebregt, 2016). In this theory, the contact problem is solved with a theory of virtual work, and as a result the method is very computationally expensive. Hence, it is

not used for solving dynamic problems in practice. The increased accuracy comes from a lack of limiting assumptions of the spin creepage and contact areas (Garg and Dukkipati, 1984).

2.4.4.6 USETAB

As the use of Kalker's Variational theory is too demanding computationally, a method is proposed where lookup tables are created based on the creepages and elliptical semi-axes, such that for a given ellipse and creepage the values for the forces can be found. The forces in the lateral and longitudinal direction and the moment about the perpendicular to the contact surface (spin) are pre-calculated for the different input variables of creepages, normal force, friction coefficient and semi-axes values using the variational theory. This significantly reduces the computational times. However, interpolation is often required to find the forces for the exact set of input variables (Antolín, 2013). This reduces the potential accuracy (Shabana et al., 2004; Antolín et al., 2013). Large tables will still add significant computational time, and small tables will reduce accuracy, so a trade-off is required when using this model (Polach, 1999).

2.4.5 Wheel Hunting Behaviour

The irregularities are a possible cause of wheel hunting in the vehicle. Wheel hunting movement (sometimes known as nosing motion), can occur due to the shape of the wheels, and their position on the rail (Xia et al., 2012). The shape of the running surface of the wheels results in an off-centre wheelset leading to one wheel running with a larger running radius than the other. As a result, yawing and lateral motions of the wheelset occur in an attempt to reach equal running radius, causing lateral and yaw oscillation motion. At critical instability limit speeds (Antolin et al., 2012), the motion may become uncontrollable and resonate, causing a derailment risk and large lateral impact forces (Zaazaa et al., 2009), but this is more of a train manufacturing problem. On straight track this hunting motion is one of the major factors in causing lateral movements of the bridge (Antolín et al., 2010). Overall, the hunting motion can cause lateral resonant problems in the bridge if the frequencies of the vehicle lateral oscillation and lateral bridge modes align (Zhang et al., 2012).

In elastic nonlinear contact models, this motion can occur naturally. However for less complex contact models, either an additional force has to be applied asin BS EN 1991-2:2003 (2010), or the motion predefined (Goicolea and Antolín, 2011).

2.4.6 Conclusions related to the Wheel-Rail Interaction in Literature

The interaction is the most complex part of the study. It is necessary to incorporate for accurate vehicle responses, but also to introduce variation in vertical and horizontal loads. It allows the inclusion of irregularities to create a non-perfect running case. It requires a full vehicle model, and increases computational time. The most appropriate, documented and tested normal contact model is the nonlinear Hertzian model, with an elastic approach offering better vehicle dynamics then a rigid contact approach. The tangential methods have to be studied further to determine which model to progress with.

2.5 Irregularities

As highlighted in Section 1.1, irregularities are one of the five important considerations in the modelling of trains over bridges (Zhang et al., 2008). Despite this, many sources do not include irregularities in the work (Antolín et al., 2010). The effects of irregularities are inconclusive, with differing conclusions from different sources.

The effect of irregularities on the dynamics of the system are varied across literature. Yang et al. (2004a) finds that they have a negligible impact on the vertical accelerations of the bridge, but the lateral bridge response and the vehicle dynamics are significantly affected. However, work by Cantero et al. (2016) concludes that irregularities, particularly in the short wavelengths increase the vertical bridge accelerations. In the case of different track qualities, the poorer the quality, the worse the vehicle and lateral bridge responses are, yet the vertical bridge response is unaffected (Au et al., 2002; Yang et al., 2004a; Wu et al., 2010). The lateral irregularities here are found to be the predominant cause of the change to the lateral bridge response (Yang et al., 2004a; Majka and Hartnett, 2009), but the cross level irregularity also has an impact (Garg and Dukkipati, 1984). The change in response according to Xia et al. (2000), does not extend to the lateral bridge displacement, which remains unaffected. Yang et al. (2004a) claims the opposite, that the lateral displacements are impacted by poorer quality track.

Irregularities may arise as isolated irregularities, often found around track features such as switches, turnouts, crossings, bridges and other special track work (Hamid et al., 1983). Alternatively, more continuous track variations include random track irregularities and rail corrugations.

Long wavelength irregularities ($> 100\,m$) often originate in the construction, intermediate wavelengths ($1.5 - 50\,m$) from track degradation and short wavelengths ($< 1.5\,m$) from manufacturing processes (Yang et al., 2004a; Hamid et al., 1983). The faster the traffic runs across the rails the higher the rate of degradation (Berawi, 2013). Track maintenance tends to rec-
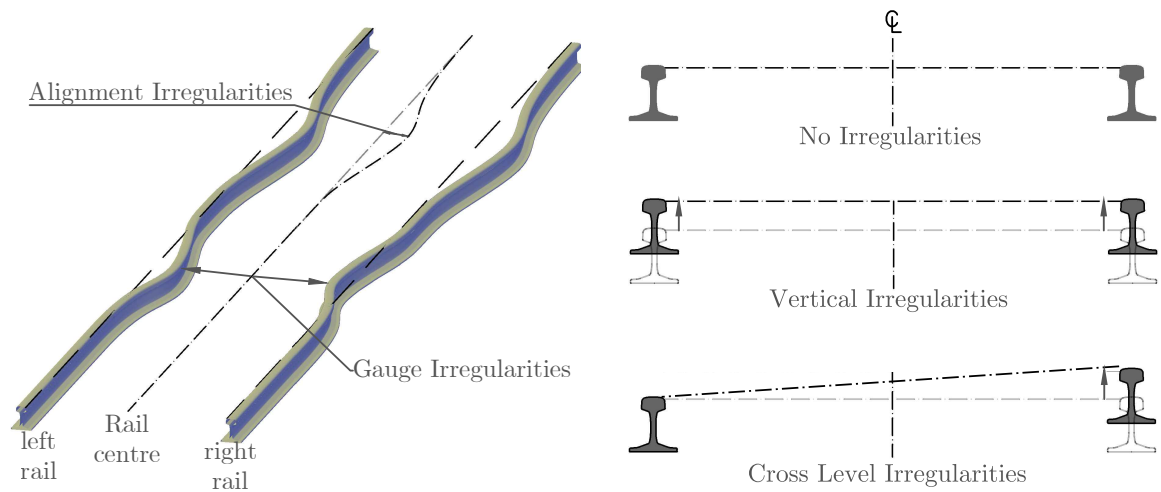
(a) Definitions of the gauge and alignment track (b) Definitions of the vertical and cross level track
irregularities   irregularities

Figure 2.12: Irregularity definition

tify irregularities when exceeding the limits seen in Section 2.5.4. The degradation rate of the
track can be studied, but this is often only performed in analysis focusing on rail degradation,
as tracks will be maintained to a certain threshold level of quality (Berawi, 2013).

2.5.1   Definitions

There are four types of track geometry irregularity (Garg and Dukkipati, 1984; Li et al., 2005;
Yang et al., 2004a; Xia et al., 2012), related to:

The vertical profile: It is the deviation of the average height of the rail from the intended
height.

The horizontal alignment: It is the deviation of the centre of the two rails from the in-
tended centre.

The cross level: It is the unintended differences in elevation between the two rails.

The gauge: It is the deviation from the intended gauge of the horizontal distance between
the two rails measured on a plane $1.5\,cm$ below the railhead top.

These irregularities are shown in Figure 2.12. The gauge irregularity is commonly ignored, as
it has negligible impacts on analysis (Song et al., 2003; Xu et al., 2004; Yang et al., 2004a; Li
et al., 2005). The cross level irregularity should not be confused with the cant of the track as
the cant is an intended difference between the vertical heights of the two tracks to help steer
vehicles round curves and the irregularity is unintended.

2.5.2 Random Track Geometry Variations

The definition of random track geometry irregularities is commonly made in one of two ways: it can be defined by a random function such as a power spectral density function (Song et al., 2003; Li et al., 2005; Dinh et al., 2009; Au et al., 2002), or it can use real data (Xia et al., 2000; Xu et al., 2004; Xia and Zhang, 2005; Zhang et al., 2008). Real data is often site specific, depending on the local maintenance and track operating speeds, and is very limited.

Power Spectral Density (PSD) functions, give rise to a series of amplitudes for different wavelengths. For irregularities, these amplitudes and wavelengths can be used in sinusoidal functions, superimposing different wavelengths to generate random profiles. Each PSD is calculated for a range of wavelengths, based on the highest and lowest frequencies considered to contribute to the irregularities of the track (Yang et al., 2004a).

According to Song et al. (2003), the irregularities produced by the PSD functions depend on the railway characteristics of the country, and are often proposed by organisations from within that country such as the Société Nationale des Chemins de fer Français (SNCF) in France or the Federal Railroad Administration (FRA) in the USA. As highlighted within these models, the speed of the line is an important consideration as tracks of higher operating speeds will tend to have better quality. Five of the common PSD functions are known as the FRA, German, Chinese, SNCF and Braun functions (Berawi, 2013). The SNCF and Braun functions only have capabilities for defining the vertical irregularities, whereas the FRA, German and Chinese functions can account for all four irregularities. The FRA and German functions are discussed in the following sections, with further detail on the generation of the PSD functions defined in Appendix F.

2.5.2.1 FRA PSD Function

These equations are the most commonly used in literature, utilising the class of tracks using proposed by the Federal Railroad Administration (FRA) (Hamid et al., 1983). The FRA define classes 1-9 of track qualities, where class 1 is poorest quality and class 9 the best. PSD functions have been defined up to class 6, a quality corresponding to a line speed of up to $177\,km/h$ (Berawi, 2013). Classes 7-9 apply to track qualities allowing high speed operation, but are yet to be defined due to the age of the publication predating HSR implementation (Hamid et al., 1983). Despite the claims by Dinh et al. (2009), the highest quality PSD defined (class 6) is unlikely to be suitable for HSR lines.

2.5.2.2   German Rail PSD Function

Another commonly used PSD function is the German one (Li et al., 2005; Zhang et al., 2010; Berawi, 2013). There are two types: the German Rail Spectrum of Low Irregularity (GRSLI) and German Rail Spectrum of High Irregularity (GRSHI). These can simulate the irregularities of modelling a bridge that runs HSR vehicles with design velocities up to $350\,km/h$. Some variation of the model exists with different coefficients given for the generation of the PSD (Claus and Schiehlen, 1998; Cuadrado et al., 2008). Irregularities generated from the Claus and Schiehlen (1998) model, is found to match well the real irregularities measured for a Deutsche Bahn Train travelling at $250\,km/h$, although Liu et al. (2009b) questions the suitability of the German Spectra, instead proposing a modified PSD, supposedly more suitable to model real track in Germany.

2.5.2.3   Generating the irregularities from the PSD

Conversion of the PSD function into the track irregularities can be performed with either the Monte-Carlo method or the spectral representation method. The Monte-Carlo method (Podworna, 2014), is essentially an inverse Fourier transform (Zhang et al., 2001). The expression used can be seen in 2.4.

$$r(x) = \sum_{n=1}^{N} \sqrt{4S(\omega_n)\Delta\omega}\cos(\omega_n x - \phi_n) \tag{2.4}$$

$$\Delta\omega = (\omega_{max} - \omega_{min})/N \tag{2.5}$$

$$\omega_n = \omega_{min} + \delta\omega(n-1) \tag{2.6}$$

where $r(x)$ is the longitudinal spatial variation of the irregularity $[m]$, ω_n is a circular frequency found in the frequency range of the PSD being converted $[rad]$, $S(\omega_n)$ is the PSD value for the particular frequency, x the longitudinal coordinate $[m]$, $N=$ the number of frequency points between the upper and lower limits of the frequency range (ω_{max} and ω_{min} respectively $[rad]$). The random phase angle (ϕ_n) $[rad]$ is a uniformly distributed between 0 and 2π, and each irregularity type should have independent angles (Zhang et al., 2001).

The alternative spectral representation method (Claus and Schiehlen, 1998; Yang et al., 2004a; Antolín et al., 2012), gives different results to the other model. It is shown in Equation 2.7.

$$r(x) = \sqrt{2}\sum_{n=0}^{N-1} A_n \cos(\Omega_n x + \phi_n) \tag{2.7}$$

where $\Omega_n = n\frac{\Omega_{max}}{N}$ $[rad]$, for $n = 0, 1, 2, \ldots, N-1$, where Ω_{max} $[rad]$ is the upper circular

frequency considered for the PSD spectrum; and:

$$A_n = \begin{cases} 0 & n = 0 \\ \sqrt{\frac{1}{\pi}(S(\Delta\Omega) + \frac{4}{6}S(0))\Delta\Omega} & n = 1 \\ \sqrt{\frac{1}{\pi}(S(2\Delta\Omega) + \frac{1}{6}S(0))\Delta\Omega} & n = 2 \\ A_n = \sqrt{\frac{1}{\pi}S(\Omega_n)} & n > 2 \end{cases} \tag{2.8}$$

According to Yang et al. (2004a) the final results of the generation of the irregularity profile may not be satisfactory, due to the superposition of random components. Hence, they may require some form of normalisation to ensure the maximum irregularity peaks are representative.

2.5.3 Periodic Irregularities

According to Frýba (1996), in addition to the irregular random irregularities, there are periodic irregularities that may be experienced that can cause resonance problems. This is due to the regular repeating distance of the axles causing periodic excitation by isolated irregularities. These periodic irregularities include corrugations and isolated irregularities of the track, as well as wheel flats.

2.5.3.1 Isolated Irregularities

Whilst the typical track variations can be described by PSD functions, the random process of the PSD not able to pick up particular local irregularities. These local irregularities include features generated by special track work or physical features in the track such as switches, crossings and rail joints. The frequency of occurrence of the irregularity depends on the causation (Garg and Dukkipati, 1984). If occurring in regular patterns they can cause resonance problems (Hamid et al., 1983; Garg and Dukkipati, 1984). However, there is little reference or use of these isolated irregularities with respect to the dynamics of a bridge in literature. This could be due to the limitation of the positioning joints and features that can cause periodic irregularities on a bridge (Frýba, 1996).

In general rail joints are not a problem for bridge dynamics. Modern tracks utilise Continuous Welded Rail (CWR) especially for HSR, which enables long distances between joints. Rail joints required for expansion are not normally allowed on bridges (Frýba, 2001), but in long viaducts they may be necessary, so then have to be especially designed for safety and maintenance issues (Delhez et al., 1995; Matsumoto and Asanuma, 2008; Hseih and Wu, 2014).

2.5.3.2 Corrugations

Rail corrugations are another periodic type of irregularity of the rail, caused from track degradation after initial imperfections and impacting the vertical profile of the rail. Corrugations take the form of particularly prominent sinusoidal variation (with one dominant period, as opposed to superposition of multiple periods as found in random irregularity generation) (Frýba, 1996). They can lead to damage of the track and the vehicle as well as to cause vibration which translates to noise. Lou (2005) and Torstensson and Nielsen (2011) find that they could cause resonance affects on the vertical superstructure accelerations, but previous study by Yang et al. (2004a) suggests negligible effects to the vertical bridge dynamics.

2.5.3.3 Wheel Flats

Defects to the profile in the wheelsets can cause a dynamic response due to the driving rotation of the wheel causing the imperfection to regularly become in contact with the rail. These defects, commonly called wheel flats, can be created during heavy braking, which causes the locking and subsequent sliding and wear to the wheels (Sun and Dhanasekar, 2002; Wu and Thompson, 2002).

2.5.4 Track Variation Limits

Due to maintenance, the irregularities on a track will be smoothed and reduced beyond a certain threshold, as expressed in regional codes (BS EN 13848-5:2017, 2017). There are three types of limit: the alert limit (maintenance is planned as part of the regular maintenance schedule if exceeded), intervention limit (corrective maintenance is required before the next inspection) and immediate action limit (action taken immediately if exceeded due to safety problems). The limits are made in reference to individual isolated irregularities with respect to the mean value of the track geometry and the standard deviation of the variations of track defined over a set track length. Information is given for gauge, alignment and longitudinal profile, with the cross level not given directly but linked to the twist and cant limits.

2.5.5 Conclusions related to the Irregularities in Literature

From the literature, random irregularities are the more commonly utilised in these kinds of models. Periodic irregularities generally have a cause that is not present on a bridge due to the resonating effect, and when present requires more complex analysis and design. Therefore, this thesis should use random irregularities, but it is uncertain how the random irregularities generated by PSD functions compare to the variation limits given in codes and guidelines, and hence testing of this should occur.

2.6 High Performance Concrete

High performance concrete (HPC) can be defined in a variety of ways. According to Nawy (2001) and Aitcin (1998), it should display very high fluidity, with low or negligible permeability, high workability and optimised performance characteristics over conventional concrete. These properties differentiate it from just a high strength concrete (FIB, 2008). It is generally considered to have a compressive strength in the range of $50\,MPa$ to $150\,MPa$, although design values in codes are found to consider strengths up to $120\,MPa$. This is due to the strengths up to this point having sufficient experimental results to draw relationships from.

Fundamentally, the constituent materials are the same as that used in traditional concrete. Concrete traditionally used to have water-cement ratios around 0.65, however the use of plasticisors allow reduction to around 0.4 for traditional concrete strengths. For HPC the water cement ratio falls below 0.4, typically near to 0.2 (FIB, 2008). However, this reduction in the water content leads to a reduction in the hydrated materials, which in turn increases how brittle the concrete is. The stronger the concrete, the more brittle it becomes as a result.

2.6.1 Modulus of Elasticity

For low stress and strain levels, the material can be modelled linearly by the Modulus of Elasticity E_{ci}. The value of the Modulus of Elasticity for HPC can be determined by Equation 2.9 as given by the FIB (2008).

$$E_{ci} = E_{c0} \cdot \alpha_E \left(\frac{f_{ck} + 8MPa}{10MPa} \right)^{1/3}, \tag{2.9}$$

where: E_{ci} is the modulus of elasticity at a concrete age of 28 days [GPa], f_{ck} is the characteristic strength of the concrete [MPa], $E_{c0} = 20.5$ [GPa] and α_E is a factor based on the type of aggregate used in the concrete mix. This equation differs slightly from the one given in BS EN 1992-1-1:2004 (2004), however both the one presented and this alternative give similar results.

The modulus of elasticity depends on the constituent materials, particularly those in the aggregate. Hence, models with no adjustment according to the constituent materials are found to be inaccurate (Aitcin, 1998). This adjustment in aggregate type can lead to increases in the elasticity modulus of up to 20% and decreases of 30% compared to the values provided. The reference value used is for quartzite aggregate. Due to the variability in the constituent materials, it is recommended by FIB (2008) to have tests to determine the specific modulus of elasticity for the concrete being used. This is also recommended in BS EN 1991-2:2003 (2010) for conventional concrete, limiting the concrete modulus of elasticity to the value for compressive strength of $50\,MPa$, unless tests are performed to prove otherwise.

Reinforcement Ratio [%]	C30 (w/c ≈ 0.65)	C80 (w/c ≈ 0.35)	C120 (w/c ≈ 0.25)
0.0	2350	2450	2500
1.0	2400	2500	2550
2.0	2450	2550	2600

Table 2.4: The mass densities of concrete as specified by FIB (2008), where the reinforcement ratio is the ratio of the volume of reinforcement bars to the concrete volume and w/c is the water-cement ratio.

In the case where the stress or strain rate in compression or tension exceeds certain thresholds (FIB, 2008), the formulations above become less valid. This is as the modulus of elasticity is enhanced for very short impact loads, compared to that of static loads (FIB, 2008). It is found under numerical simulation by Aied and González (2011), that for a singular $100\,kN$ moving load, at a velocity of $35\,m/s$, on a concrete beam $10\,m$ long and $0.65\,m$ deep, the rate of strain was sufficient for the modulus of elasticity is enhanced above the static response. In this case the velocity was lower than in HSR.

2.6.2 Poisson's Ratio

The determination of the Poisson's ratio of HPC is difficult, so as such, only limited estimates are known for the values. Some literature estimates that the Poisson's ratio is between 0.18 and 0.24 (Aitcin, 1998) or between 0.14 and 0.26 (FIB, 2008), varying with stress. The latter source suggests that a good design estimate of the value is 0.2 if exact value cannot be used.

2.6.3 Density

BS EN 1990:2002 +A1:2005 (2010) defines the reinforced concrete unit weight as $25\,kN/m^3$ ($2548kg/m^3$), with $24\,kN/m^3$ ($2446kg/m^3$) from plain concrete and $1\,kN/m^3$ from reinforcement. With the decreasing ratio of water to cement for strength increases the concrete microstructure changes which affects the density. In addition, the decreasing water can reduce the fluidity of the concrete (FIB, 2008), possibly entrapping more air, which can change the density of the concrete by 1%.

Approximate concrete densities can be obtained based on the strength and reinforcement density as given by FIB (2008) and shown in Table 2.4. These values are based on concrete with entrapped air content of 2%. The values shown are intended to be interpolated between to get densities for concrete strengths between those shown. Despite the values given, it is recommended that tests are carried out on the specific concrete used due to the high dependence on the constituent materials.

2.6.4 Creep, Shrinkage and Thermal Effects

The existing models of creep and shrinkage cannot simply be extrapolated to the higher strengths. This is as changes in the microstructure of concrete affect the shrinkage and creep behaviour. The reduced porosity lead to reduced effects of shrinkage and creep in HPC. However, published research into this topic is limited and hence the models of creep and shrinkage are not well defined, limited by the amount of data that is available (FIB, 2008). Despite this, FIB does propose formulas for the shrinkage and creep behaviour. In this FIB work, it is also considered that the thermal expansion coefficient is taken as the same as in BS EN 1992-1-1:2004 (2004) for normal strength concrete.

2.6.5 HSR Bridges Constructed with HPC

From a thorough literature search, it can be concluded very few bridges have been published for the HSR industry, where their strength is explicitly stated to be within the range of HPC, or at least their construction has not been widely disseminated. For example, the twin viaduct segmental bridge in Avignon (Radiguet, 1999), uses $52\,MPa$ concrete. A further rail bridge (Kojundic, 2007), found in Utah, uses HPC of 48 MPa for a small bridge with span $13.1\,m$. This rail bridge however is not a HSR bridge, the strength is not in the HPC range and other bridge properties are not given. Within highway bridges, HPC is more widely found to have been used.

2.6.6 Ultra High Performance Concrete

Ultra High Performance Concrete (UHPC) is a new material with multiple variants, such as Ultra High Performance Fibre Reinforced Concrete(UHPFRC), that according to Tang (2004), should be less referred to as a concrete and more as a new material altogether. Commonly this material has fibres within it which help improve the structural strength to strengths commonly between $150\,MPa$ and $300\,MPa$ (Buitelaar, 2004). The use of UHPC can have advantages in section sizes, with the lack of reinforcing bars reducing the concrete cover depths (Resplendino, 2011).

Some guidelines for the design with UHPC can be found in AFGC (2013). Further guidelines are expected soon by the FIB, which should gain the benefits of the material developed further in the last 15 years (Almansour and Lounis, 2011). However, these guidelines are very generic and different manufacturers can achieve very different properties.

According to Almansour and Lounis (2011), several bridges have been constructed using UH-PFRC in Europe, which include several highway bridges in France, and other parts of the world, and multiple pedestrian bridges. However no rail bridges have been found to use the

material. Almansour and Lounis (2011) finds that the use of UHPFRC allows the reduction of concrete by up to two thirds the volume of ordinary concrete when constructing a bridge, with fewer beams of smaller size required to support the deck. This means there is massive potential for the use of UHPC in rail bridges.

2.6.7 Conclusions related to the Concrete Material in Literature

The mass and stiffness of HPC change with strength, and this can be utilised to simulate the increasing strength of concrete in models. Good linearity in the stress strain relationship for low stresses and strains, enables the concrete model to be linearly modelled for service loads. It can also be seen from literature that higher strengths of HPC have not widely been published to have been used in HSR bridges, enabling this work to establish novel results. The lack of results published may be due to the industry having a reluctance to try novel methods, due to the high cost of failure.

2.7 Specific Design Constraints for HSR Bridges

This section highlights some of the specific design constraints within codes for HSR bridges, particularly focusing on the dynamic modelling.

2.7.1 Load Combinations for Persistent Situations

For the design to the Eurocodes, the vehicles are modelled by moving point loads. Different combinations of load models are expressed in Table 6.11 of BS EN 1991-2:2003 (2010), taking into account the direction of the loading and number of tracks to be loaded. The combinations apply to static models, with dynamic models only requiring the loading of one track per bridge. The positioning of the tracks should be considered to be in the least favourable possible location on the bridge. Considerations for curved bridges require centrifugal forces from the vehicle to be added.

2.7.2 Derailment

Determining whether a vehicle may derail is possible when using a nonlinear vehicle bridge interaction model (Antolín et al., 2013). Yang et al. (2004a) states five limits that determine the derailment and the safety assessment for trains. They are found as the axle load decrement ratio (δQ), the lateral track force (Y_{lim}), single wheel lateral to vertical force ratio (SYQ), wheelset lateral to vertical force ratio (YQ) and bogie-side lateral to vertical force ratio (BYQ).

Many of these limits are used by other literature (Dinh et al., 2009; Ju, 2012; Six et al., 2015; Zhang et al., 2008). The ratio of δQ depends on the vertical static and dynamic contact forces, and the Y_{lim} force depends on the static vertical force to determine an upper bound to the lateral force available. The other three ratios are all a direct comparison between the vertical and lateral forces in the wheels or wheelsets. With the exception of the δQ ratio, these ratios are found to be dependent on the track quality and train velocity.

When not considering a full vehicle model, it is the bridge accelerations that are the only indicator for the derailment safety, as explained in Section 2.7.3.1. In the unfortunate case when derailment occurs, the bridges are designed such that the loads of the derailment process incur are accounted for, as per BS EN 1991-2:2003 (2010).

2.7.3 Serviceability Limit State

2.7.3.1 Bridge Accelerations

The acceleration of HSR bridges is often the constraining design factor (Calgaro et al., 2010b). BS EN 1991-2:2003 (2010) specifies that the bridge deck must not have accelerations above a certain threshold. These values are widely used in literature, for the vertical deck acceleration as $0.35g$ (or $3.5\,m/s^2$) for ballasted track, and $0.5g$ (or $5\,m/s^2$) for non-ballasted track (BS EN 1991-2:2003, 2010). Ballasted track has a lower limit to ensure the ballast stability, as destabilisation can cause long term track damage (either from ballast thrown or settling) and potential vehicle damage from dislodged ballast. Both accelerations limits include a factor of safety (FOS) of 2 (Salcher et al., 2014). The slab track limit of $0.5g$ ($1.0g$ without FOS) is related to the acceleration causing derailment.

According to BS EN 1991-2:2003 (2010), the acceleration demands, to be compared to the limits, take into account a low pass filter, removing high frequency acceleration components. This filter is as follows:

$$f_f = \max\left(30, 1.5f_1, f_3\right) \qquad [\text{Hz}] \qquad (2.10)$$

where f_f is the cutoff frequency, f_1 is the frequency of the fundamental bending mode and f_3 is the frequency of the third bending mode (all in Hz).

Chinese codes have a limit to the lateral acceleration of a HSR bridge of $1.4\,m/s^2$ (Xia and Zhang, 2005; Zhang et al., 2008), which is not found in BS EN 1991-2:2003 (2010). The reasoning behind this limit is not found in literature.

2.7.3.2 Vehicle Accelerations

The vehicle accelerations from within the carriage are used to determine the riding comfort of the vehicle. Very good comfort is considered as vertical accelerations below $1\,m/s^2$, and acceptable vertical accelerations would be anything below $2\,m/s^2$ (BS EN 1992-2:2005, 2005). Despite the lateral accelerations being sensitive to the presence of irregularities (Majka and Hartnett, 2009), they are not limited in BS EN 1992-2:2005 (2005). According to Zhang et al. (2008), the Chinese codes limit the vertical carriage acceleration to $1m/s^2$, and laterally to $1.3m/s^2$.

2.7.3.3 Deformations

Excessive bridge deflections can cause changes to the track profile increasing rail stress and potentially causing vehicle running problems (Calgaro et al., 2010a). The maximum vertical deflection of the bridge varies between $L/600$ (BS EN 1990:2002 +A1:2005, 2010), and $L/1800$ (Dinh et al., 2009), where L is the span of the bridge. BS EN 1991-2:2003 (2010) also limits the relative vertical displacement between the bridge and the adjacent construction to $2\,mm$ under the variable loads for line speeds over $160\,km/h$. In addition, the longitudinal deflection is limited to either 8 or 10 mm for vertical loading, and between 5 and 30 mm under horizontal loads. The variation in values arise from different bridge and rail set-ups, with more detail in BS EN 1991-2:2003 (2010).

2.7.4 Fatigue

The track and in particular the rails can undergo fatigue due to their heavy dynamic loading (Sun and Dhanasekar, 2002; Wu and Thompson, 2002). However, this is beyond the scope of many HSR bridge studies as the lifespan of the track is shorter than the bridge and relatively easily replaced. According to Eurocode 2 (BS EN 1992-2:2005, 2005), the fatigue for concrete bridges is calculated based on the stresses in the concrete, the design fatigue strength of the concrete and various factors relating to the loading type. With prestressed concrete bridges, ensuring the section remains fully prestressed under service loads helps to avoid fatigue problems. The fatigue damage characteristics depends on the material and is determined using load model 71 and a series of fatigue trains from BS EN 1991-2:2003 (2010). Also the design should consider excessive dynamic effects which increase the fatigue damage, through dynamic amplification factors.

2.7.5   Dynamic Behaviour

Both the resonance and cancellation phenomenon relate to the behaviour of the bridge under the forced vibration stage, but can influence the behaviour in the free vibration stage. If the free vibrations from multiple loads are in phase, then resonance can occur, resulting in an amplified response. Whereas if they are out of phase by half a period, the free vibration response will cancel out, leaving a cancellation effect (Yang et al., 2004b). The formulas expressed below are based on a simply supported bridge.

2.7.5.1   Amplification Effects

Resonant speeds are speeds at which, due to an excitation frequency matching one of the natural frequencies of the bridge, amplifying the accelerations and deflections of the bridge (Podworna, 2014). Equation 2.11 shows the first method used to calculate the resonant speeds $v_{r1,in}$, where n is the mode of bridge vibration that is being considered ($n = 1, 2, 3, \dots$) and i stands for the particular harmonic of that mode of vibration ($i = 1, 2, 3, ..., 1/2, 1/3, 1/4, ...$) (Xia et al., 2014; Goicolea et al., 2008).

$$v_{r1,in} = \frac{f_n d}{i} \qquad [m/s] \tag{2.11}$$

where d is the regular repeating distance between the loads $[m]$ and f_n is the nth modal frequency of the bridge $[Hz]$. This formula can be inverted (Equation 2.12), such that for a given vehicle velocity v, the frequencies that this excites are given by f_{vi} $[Hz]$, where $i = 1, 2, 3 \dots$ is the harmonics of the driving frequency.

$$f_{vi} = \frac{vi}{d} \qquad [Hz] \tag{2.12}$$

A second resonant set of speeds $v_{r2,n}$ is found in Equation 2.13 relating the span of the bridge L to the natural frequencies of the bridge (Frýba, 2001). This was also subject to extensive studies by Madrazo-Aguirre (2016) for an advanced formulation applied to highway bridges. However, it was found by Frýba (2001) that the speeds associated with this method are much higher than possible for HSR and therefore are not generally as applicable.

$$v_{r2,n} = \frac{2L f_n}{n} \qquad [m/s] \tag{2.13}$$

Resonance may also occur in the lateral direction due to the action of hunting motion matching the lateral frequencies of the bridge. This utilises a formula very similar to Equation 2.11, but instead of the train length it uses the dominant wavelength of the hunting motion (Xia et al., 2006). Cuadrado et al. (2008) suggests that the lateral response of the bridge does not become resonant under normal conditions, as the vehicles lateral frequencies were found to be

less than $1\,Hz$, smaller than the minimum frequency of the first lateral mode which is required by BS EN 1991-2:2003 (2010) to be at least $1.2\,Hz$.

2.7.5.2 Cancellation Effects

Under cancellation phenomenon the residual response of bridge under load is minimal. With different repeating distances associated with a vehicle (for example both the wheel spacing and carriage spacing), multiple critical speeds can be very close to each other. If one of these critical speeds displays cancellation effects and one resonant, the resonance effect at this velocity is reduced. As a result some critical velocities of the train vehicle will not display expected resonant effect because of the cancellation effect (Lou, 2007). This effect also known as a resonance disappearance effect (Xia et al., 2014). There are multiple forms of cancellation, like with resonance. The first cancellation velocity $v_{c1,in}$ $[m/s]$(Equation 2.14) (Xia et al., 2014), is based on any regular repeating train distance d $[m]$, such as the distance between wheels, bogies or vehicles.

$$v_{c1,in} = \frac{2df_n}{2i-1} \qquad \text{for} \qquad i = 1,2,3... \qquad [m/s] \tag{2.14}$$

The other commonly quoted cancellation speed is defined in Equation 2.15, with the frequency of the mode f_n $[Hz]$ and length of bridge, L $[m]$, contributing to the cancellation velocity of $v_{c2,in}$ $[m/s]$, for different harmonics of $i = 1,2,3,\ldots$ (Xia et al., 2014). This formula is expanded further by Madrazo-Aguirre (2016), but in both cases the corresponding critical velocities are generally above those possible for HSR.

$$v_{c2,in} = \begin{cases} \frac{2Lf_n}{2i-1} & \text{for} \quad n = 1,3,5 \quad \text{but} \quad n \neq 2i-1 \\ \frac{2Lf_n}{2i} & \text{for} \quad n = 2,4,6; \quad \text{but} \quad n \neq 2i \end{cases} \qquad [m/s] \tag{2.15}$$

2.8 Conclusions to the State-of-the-Art

From this chapter some key points have been identified from the literature which help to form the basis of the analysis for the rest of this thesis. These are found as:

- The use of shell elements are the most computationally efficient and accurate solution to model the bridge with, but beam elements can be used to complement this.

- The use of a full vehicle model with mass is necessary for vehicle accelerations to be determined, and particularly for short spans less than 30 m where mass interaction has a large effect. Otherwise point load models are currently appropriate.

- Slab track is the solution that the industry is tending towards using, but ballasted track is the existing common solution. A wide range of track properties exist with varying opinions on their effects on bridge and vehicle dynamics.

- Wheel-rail interaction allows accurate vehicle response and variation in the vertical and lateral wheel loads. It also allows the introduction of irregularities. There are many different approaches available to tackle the interaction problem.

- Irregularities can have several causes, resulting in different shapes and patterns of the imperfections to the rail. They are best modelled by a random PSD function in the absence of real data.

- HPC is a material with strengths above 50 MPa, and has a linear response for low stress and strain values. The current literature has very little focus on the use of this material for HSR bridges.

From this chapter many existing models currently exist, but the challenging aspect is incorporating them together, as each one is complex on its own. The results of incorporating each of the complicated models for the bridge, vehicle, wheel-rail interaction, irregularities and the track, is a new approach, with unknown effects.

Chapter 3

Methodology

In this chapter, the general methodology to be carried forward will be defined. This includes the bridge, the train, the track and their respective models, as well as the interaction between the track and the vehicles.

3.1 Bridge

In Section 2.1.3, a database of bridges identified from the literature were compared. These comparisons can be useful in determining the appropriate benchmark cases, which are analysed in depth and are then carried forward as the basis for the parametric analysis. As before, the bridges are coordinated into groups by cross sectional shape, represented again in Table 3.1. Comparison between the span length and the depth is seen in Figure 3.1 for the chosen bridges.

For this thesis, the bridge in Figure 3.1 highlighted by the blue marker will be used, due to its completeness in design given by the literature in comparison with other models. This will be used for the analysis in Chapters 4 and 5. The bridge properties are explained in more detail in Section 3.1.2. It also has a span and slenderness similar to other precast bridges of the same type (as seen in Figure 3.1). This is also the case for further properties of the bridge not shown in the figure such as the web and bottom flange thickness, depth and the width of the bottom flange. In addition, this design was applicable to the requirements of HS2 in the UK, and as a result the conclusions can be more relevant to industry and the sponsors of this thesis.

In Chapter 6, a precast single celled box girder, precast dual celled box girder and a trough bridge are analysed. The single celled box girder is highlighted by the red marker and the double celled box girder by the green marker in Figure 3.1. The trough bridge is a unique shape and hence is not in the database, nor the figure. The details of these bridges are
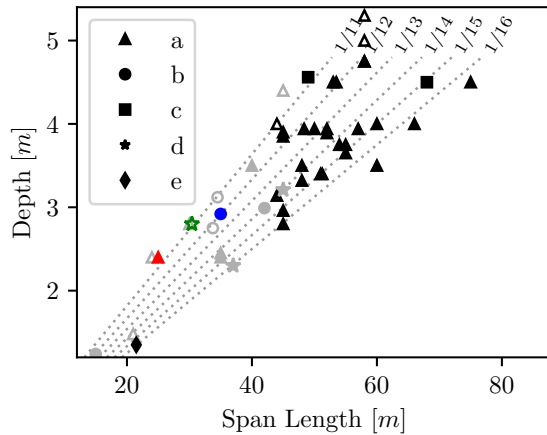
Figure 3.1: Bridge span against cross section depth. The shape of the point refer to the cross section in Table 3.1. Solid markers refer to continuous bridges and hollow are simply supported. Grey colours refer to precast construction and black is cast insitu

Table 3.1: Different types of cross section in the bridge database

cross section	name	key
	Box girder	a
	Dual U-Beam	b
	Straight sided box girder	c
	Triple webbed box girder	d
	Voided slab	e

expressed further in Chapter 6. These particular bridges were chosen due to a completeness of the design within published literature, as well as displaying similar properties to other similar bridges through comparison in the bridge database.

3.1.1 Modelling of the bridge

When it comes to modelling the bridge, finite element methods, using ABAQUS (Dassault Systèmes SIMULIA Corp., 2014), were chosen to determine the results of a dynamic model. An assessment was made to determine the best way to model the bridge using finite elements. As mentioned in Section 2.1.5, the available methods are beam elements, shell elements or solid elements. As literature suggested, the use of shell elements, complemented with beam elements for verification is used to model the bridge.

3.1.1.1 Beam Element models

As a computationally inexpensive model, these elements are appropriate for determining an estimate of the accelerations in the bridge. These models can be used as a first approximation to define the critical speeds (amplification speeds) for which the maximum accelerations are induced. This can identify velocities to use the shell element models where a more precise solution is required. The formulation for the beam element model is as shown in Figure 3.2.

The approach for the beam element model is to model the section in two separate beam
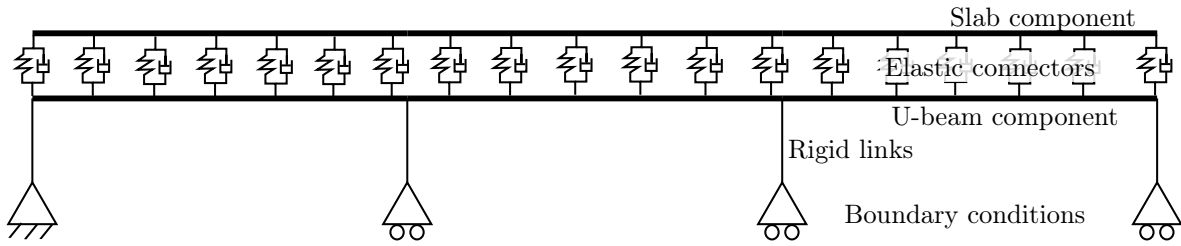
Figure 3.2: Visualisation of the beam element model of the three span bridge (benchmark case)

element components. The two components, one representing the slab and the other the U-beams, allows for an account for the slip between the precast beams and the cast in-situ slab. The section properties of the slab and the U-beams are input to the beam element profile using a *BSP* file in Abaqus (Dassault Systèmes SIMULIA Corp., 2014). Non-structural masses are applied to represent top-side equipment and the track system. Having separate beam element components for the precast U-beams and the slab, with the *BSP* file, also allows for the inclusion of the different concrete strength materials for the U-beam and the slab.

The beam elements used in Abaqus are 'B31' elements, which allow modelling in a three dimensional space, are linear and use Timoshenko beam theory. This choice is partially limited by the use of the *BSP* file. The links between the slab and U-beam components are created through connectors with elastic and damping properties. The links are explained in more detail in Section 4.1.7.

To account for the boundary conditions coming from the bearings located at the base of the beam and not the centroid of the section, a rigid link (using the *BEAM* section), connects a node located at the location of the bottom of the beam to the corresponding node in the U-beam component.

The vertical vehicle loads are applied to the slab beam elements as concentrated loads. The effect of the movement of the load is introduced by applying a time based amplitude to each load.

3.1.1.2 Shell Element models

The use of shell elements allows local deformations and stresses to be determined. In this thesis, the main complex and comprehensive models use shell elements. They utilise the four-noded *S4R* shell element in Abaqus. In comparison, it is a linear shell formulation as opposed to the quadratic formulation of the eight-noded *S8R* element, but as a result requires significantly less computational time. The detailing for the creation of the model in shell elements is outlined within Section 3.1.2.
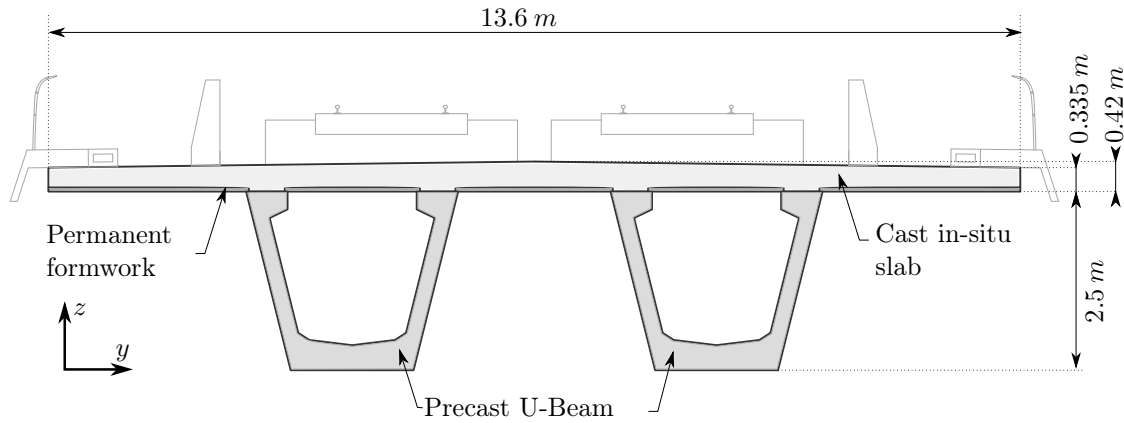
Figure 3.3: Cross section of chosen dual U-beam bridge
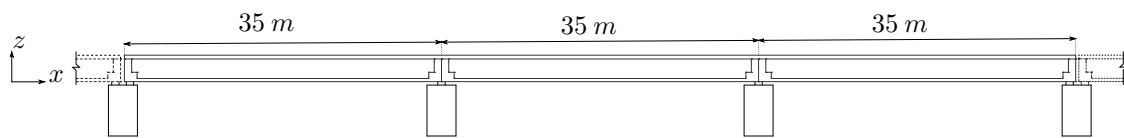
Figure 3.4: Longitudinal section of chosen dual U-beam bridge

3.1.2 Double U-Beam Section Solution

This design is obtained from Laing O'Rourke as a typical tender bridge design for the new high speed two (HS2) line in the United Kingdom. The design was made in a joint venture, also with WSP and Ramboll. The bridge is made from concrete, using two precast, prestressed 'U' shaped beams (U-beam), overlain with permanent formwork which allows casting of an in-situ top slab. The cantilevering permanent is usually supported by being connected to the adjacent formwork to provide stability. The U-beams are longitudinally tied together with the 1030 Macalloy bars to create continuity over the support sections (Macalloy, 2017), with an epoxy resin complementing the bars. The longitudinal elevation of the bridge is shown in Figure 3.4, with more detail on the connection between U-beams found in the upcoming section on the diaphragm.

The cross section of the bridge is shown in Figure 3.3. Each span is $35\,m$, as seen in the longitudinal section in Figure 3.4, with the three span continuous bridge studied. With a constant depth of $2.92\,m$, it results in a depth to span ratio of $1/12$. The properties of the whole section are shown in Table 3.2.

Section Property	Whole section	Isolated U-beam section
$A_c\ [m^2]$	8.60	1.913
$I_{yy}\ [m^4]$	8.607	1.374
$I_{zz}\ [m^4]$	102.9	1.664

Table 3.2: Whole section and U-beam cross section properties

	C35	C60
Reinforcement ratio [%]	2.0	1.6
Material density [kg/m^3]	2460	2490
Modulus of elasticity [GPa]	33.3	38.8
Poissons ratio [-]	0.2	0.2

Table 3.3: Concrete Material Properties

Property	Rail	Prestressing
Density [kg/m^3]	7800	7800
Modulus of elasticity [GPa]	210	195
Poissons ratio [-]	0.3	0.3

Table 3.4: Steel Material Properties

3.1.2.1   Materials

The precast components use C60 concrete, whereas the cast in-situ slab utilises the lower strength C35 concrete. The concrete properties have been taken from FIB (2008), as explained in Section 3.2. The properties are outlined in Table 3.3.

The structural concrete also contained steel. This steel is used in rebar, the rails and also prestressing tendons. The rebar properties are incorporated in the properties of the concrete. As this is a linear concrete model, this removes the nonlinearity and complexity of including rebar as discrete elements. The prestess material properties are detailed in BS EN 1992-1-1:2004 (2004), and the rail steel in BSI Group (2011). Hence, the steel properties as outlined in Table 3.4

3.1.2.2   Boundary Conditions

According to the tender bridge design (Laing O'Rourke, 2016), the articulation should be as in Figure 3.5. However this arrangement disagrees with conventional alignments. The horizontal action due to braking and acceleration are extremely large in HSR bridges. The most conventional arrangement is fixing the longitudinal displacements of the deck at one of the support sections by means of prestressing the deck into the abutment, allowing for longitudinal displacements at all the other support sections. For viaducts, like this benchmark case, there is not necessarily an abutment, so the deck is fixed into the piers. This leads to large bending moments being induced in the piers from horizontal actions, requiring stockier piers to have the flexural capacity. In this benchmark case, the deck is fixed at the middle two piers, which restricts the bridge from expanding under thermal and concrete long term deformation effects. Hence, a more realistic modified articulation shown in Figure 3.6a, with the plan view shown in Figure 3.6b, is used in this thesis. A comparison of the boundary conditions is made in Section 4.1.5.

Figure 3.5: Original articulation of bridge

(a) Simple modified articulation of bridge

←—○—→ Longitudinally free bearing
● Fixed bearing

(b) Articulation of bridge plan view
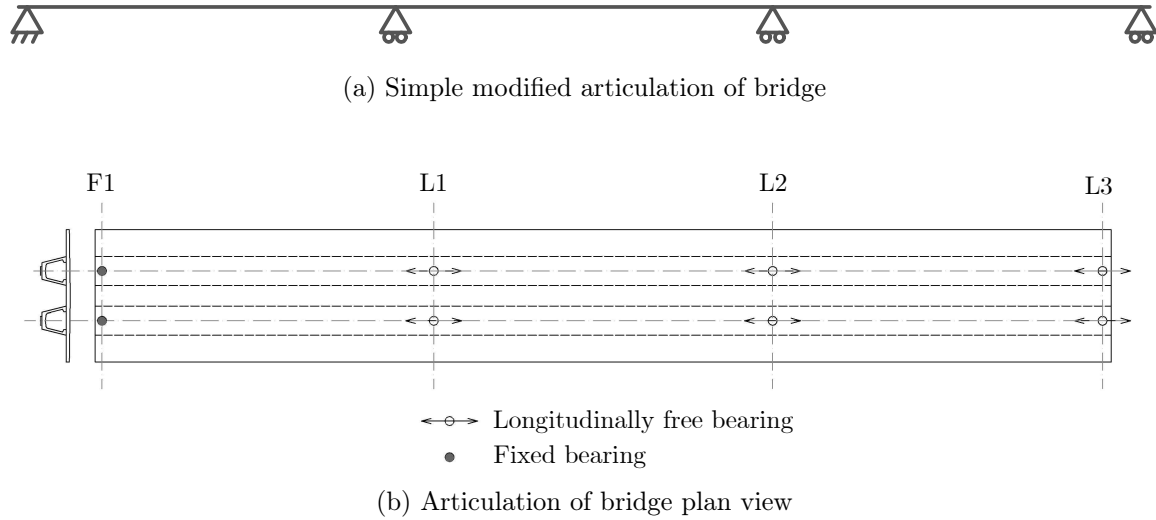
Figure 3.6: Modified articulation of bridge

3.1.2.3 Modelling of Boundary Conditions

The modelling of the boundary conditions takes place by applying displacement constraints to a series of nodes in a line. This line is found across the lateral centroid of the bearing pads, as seen in Figure 3.7. The full bearing pad was not restrained as this would be unrealistic, ignoring the elasticity and allowable rotations of the bearing pads. Due to uncertainty of the size of the bearing pads, a comparison was made to determine the appropriate size, as analysed in Section 4.1.5. As mentioned in Section 2.1.4, horizontal transfer of load is required by the pier, and due to the low height (max $7\,m$), and the stocky section of the piers in this design, the study of the piers themselves will not be made.

3.1.2.4 Prestress

The bridge is prestressed through 128 pre-tensioned strands per beam. The strands have an initial prestress force of $219\,kN$, and an area of $150mm^2$, leading to an initial stress of $1460\,MPa$, although losses and the debonding of strands over certain parts of the bridge changes the force in the cross section. The losses and prestress arrangement is described in Appendix E.

The prestressed strands are modelled with a *REBAR* layer in Abaqus (Dassault Systèmes SIMULIA Corp., 2014), and an applied initial stress. This is available to use when using shell elements. The *REBAR* layer superimposes on top of the existing shell, without removing the material from the shell. Therefore the prestress material properties are accordingly modified. A comparison is made in Section 4.1.6 to determine the impacts of the prestress on the bridge and vehicle behaviour. Post-tensioning is also added for establishing continuity, using Macalloy

(a) Three Dimensional realisation of the bearing location under the diaphragm of the precast beam

(b) Representation of the boundary conditions acting along the edge of elements at the midpoint of the bearing location
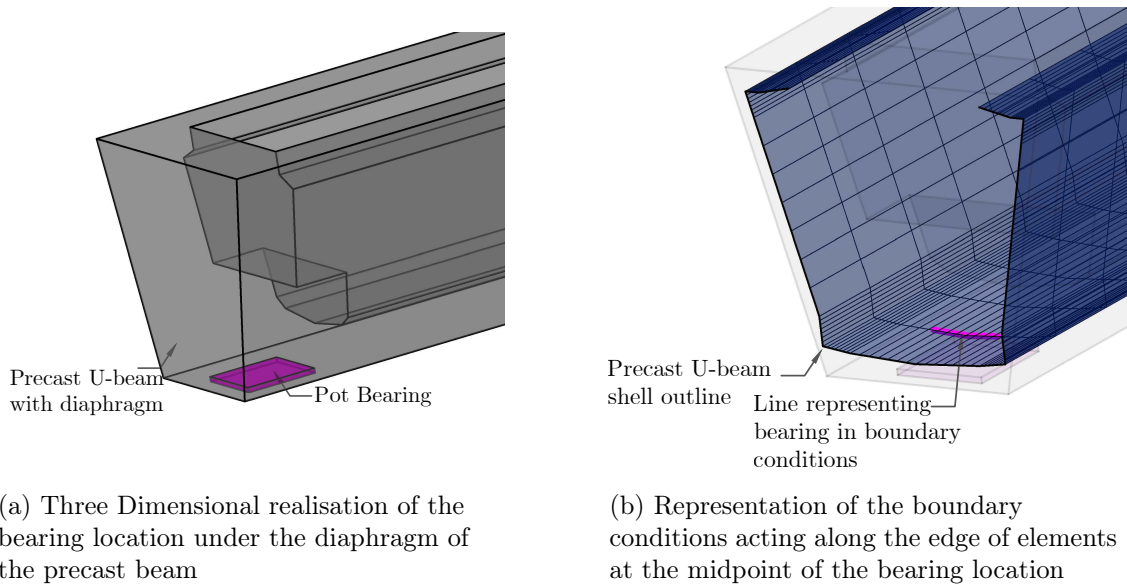
Figure 3.7: Visualisation of bearing conditions

bars (Macalloy, 2017) over the supports where continuity is required, and described further in the next section.

3.1.2.5 Diaphragm

Diaphragms are present in the design, enabling transfer of both the shear forces from the webs of the U-beams and the horizontal forces applied to the concrete slab to the bearings, as well as allowing connection between beams for continuity. Shells in the vertical plane tied to the existing beam shell elements represent this diaphragm.

Connection between beams longitudinally through the diaphragms are done as in Figure 3.9, using five $47\,mm$ and six $32\,mm$ diameter 1030 Macalloy bars (Laing O'Rourke, 2016). This is combined with use of a high strength epoxy fill and shear keys to the end of the diaphragm. The shear keys and the epoxy are ignored in the dynamic model as it is too complicated to be included in this scope and it is not expected to significantly change the response. This assumption of excluding this epoxy resin between diaphragms is tested by a simple calculation. It uses the stiffness of the different parts of the bridge U-beam, as seen in Figure 3.8a. By introducing a thin $100\,mm$ layer of resin at the central support, the deflection under load of the beam is compared. The resin modulus of elasticity of E_2 is varied as a ratio to the concrete modulus of elasticity E_1. The loading arrangement for this test is shown in Figure 3.8b.

From TECROC Products (2006), it can be found that epoxy resins can have strengths of around $12\,MPa$, which corresponds to E_2/E_1 of about 0.4. This would result in deflections being up to 2.5% higher from this assumption, as seen in Figure 3.8c. This value is acceptable, but the difference in deflections is significantly smaller when the non-linear impacts of the
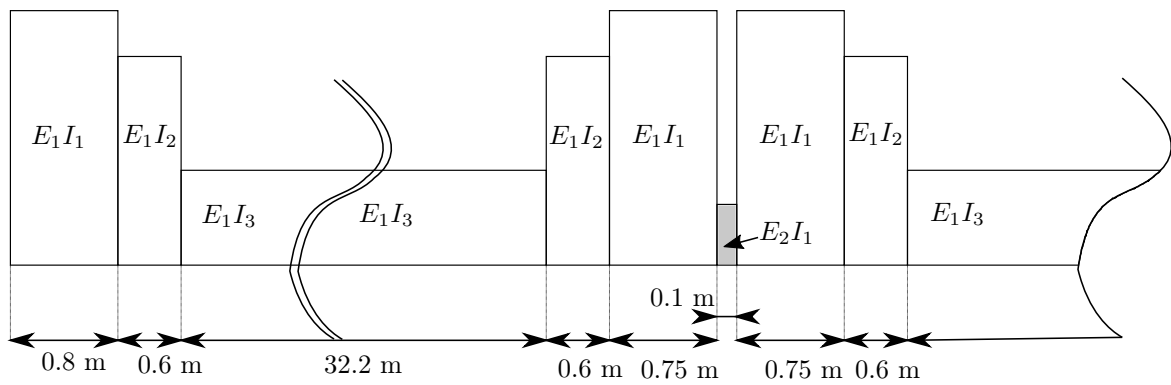
(a) Stiffness of each section of the bridge, considering the both concrete and Epoxy elasticity modulus
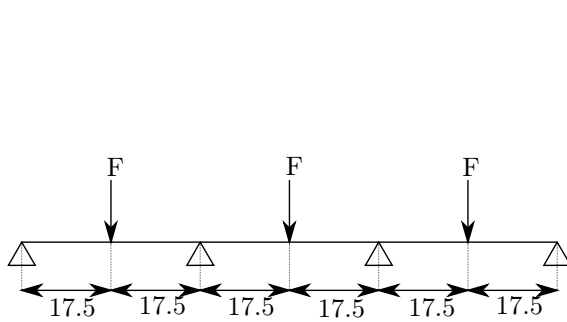
(b) Diagram showing loading configuration for this test
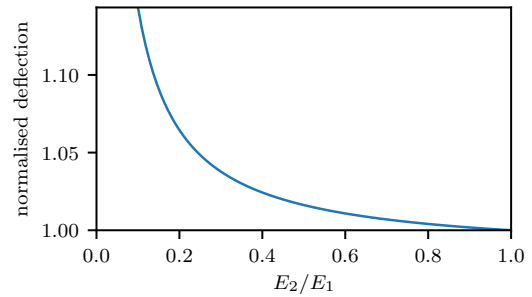
(c) Variation of the deflection at midspan of middle span for different ratios of elasticity modulus

Figure 3.8: Model used to test the diaphragm assumption of ignoring epoxy resin
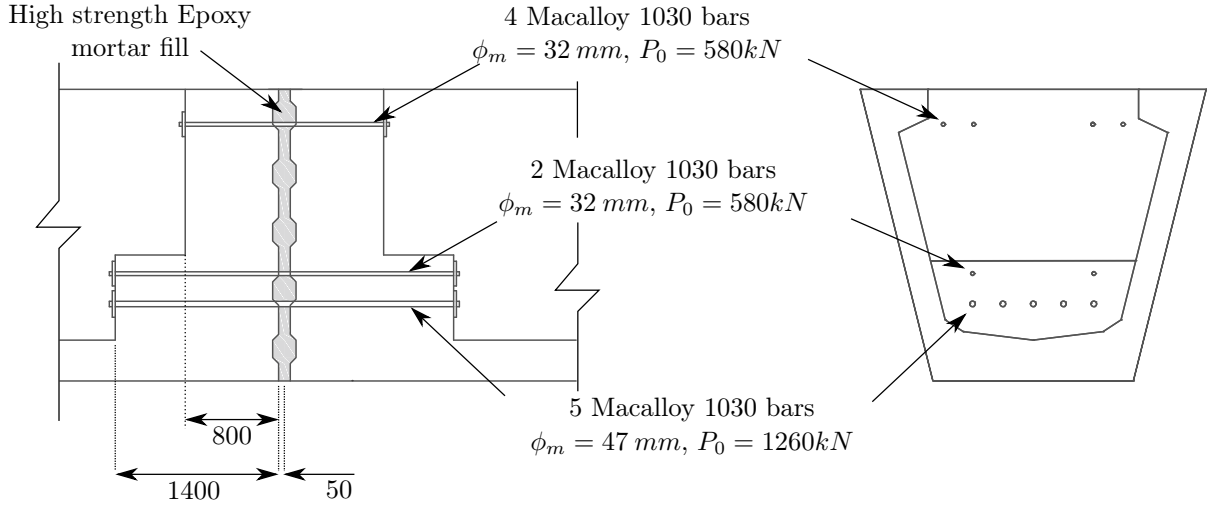
Figure 3.9: Detailed cross section of the diaphragms and the inter U-beam connection, with all dimensions in mm

prestressing bars and the moment redistribution over the central supports are taken into account, reducing the magnitude of the hogging bending moment in this weaker epoxy region.

To model the longitudinal connection between beams, a comparison is made between the modelling of a fully tied connection with no relative displacement and a connection using prestressed Macalloy Bars allowing relative displacement. The lower five bars are of diameter $47\,mm$ and the remaining six $32\,mm$. They are stressed to $685\,MPa$ (corresponding to forces of $1260\,kN$ and $580\,kN$ respectively). To model, the Macalloy bars are represented by springs (using $CONN3D$ elements in ABAQUS (Dassault Systèmes SIMULIA Corp., 2014)). As a result of this method, additional mass associated with the bars is not included in the model. The stiffness of the springs is determined by the axial stiffness of the bars, calculated using Equation 3.1.

$$k_{mb} = \frac{E_{mb}A_{mb}}{L_{mb}} \tag{3.1}$$

Where k_{mb} is the axial stiffness of the bar $[kN/mm]$, A_{mb} is the cross-sectional area of the bar $[mm]$, E_{mb} is the modulus of elasticity of the bar [GPa] and L_{mb} is the length of the bar $[m]$.

The comparison in Figure 3.10 shows that the impact of the inclusion of the prestressed bars is minimal on the accelerations of the bridge. The frequency of the first three bending modes in Table 3.5 also shows minimal change. Therefore, although the accelerations change due to the inclusion of the Macalloy bars to model the connection between U-beams, neither model shows consistently larger accelerations. However, at the same time the computational time increases by between 12 and 20% with the Macalloy bar modelling (from 510 minutes with the rigidly tied method compared to 600 minutes). This increase in computational time, but very little change in response, means that it is assumed that the rigidly tied method can represent the end connection.
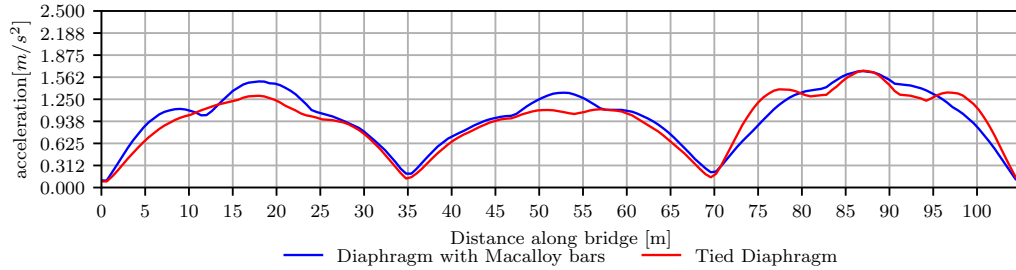
Figure 3.10: Comparison of the bridge vertical acceleration with distance along bridge for different diaphragm connection details

Vertical Bending Mode	Rigidly Linked	Macalloy Bars Modelled
1	3.7764	3.7389
2	11.391	11.205
3	17.067	16.952

Table 3.5: Comparison of modal frequencies [Hz] of the bridge for different diaphragm connections.

3.1.2.6 Mesh

To accurately model the beam of the bridge in shells, a program was developed in Python to find the section properties of shell elements of the U-beam. This adjusted the positions and thickness of elements such that the shell element sectional properties matched the values of the true U-beam, as compared in Table 3.6.

An example of the shell geometry representing the U-beam is shown in Figure 3.11. The top two corners have material properties reduced by a factor of 0.89 to match the overall section properties, due to material overlap in these regions. The simple geometry of the slab does not necessitate such a complex program to determine the shell thickness.

The mesh is refined such that the results are converged, but not over refined which would lead to longer computational times. This leads to a mesh for the whole bridge of 10707 elements. From a mesh sensitivity analysis, optimisation occurs such that localised regions have higher refinement. This considers the location of connections and loading. The beam is meshed as in Figure 3.12a accounting for a finer mesh around the support regions, with the cross sectional mesh profile as shown in Figure 3.12c.

In the slab the longitudinal spacing of the elements is defined by the sleeper spacing, which is $0.6\,m$ in this thesis. This results in a mesh profile as in Figure 3.12b, with an arrangement in the cross section as shown in Figure 3.12d. Nodes are positioned at connecting points between the slab and the beams, hence varying element width. Analysis on the suitability of this mesh is made in Section 3.1.2.7. The connection between the slab and the U-beam is discussed in

Section Property	Shell Model	Real U-Beam
A_c $[m^2]$	1.913	1.913
I_{yy} $[m^4]$	1.374	1.374
I_{zz} $[m^4]$	1.664	1.664
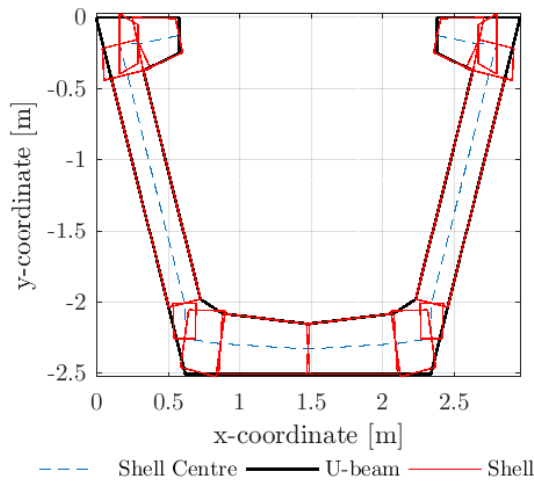
Figure 3.11: U-beam shell and cross section comparison

Table 3.6: Comparison between real and modelled U-Beam properties
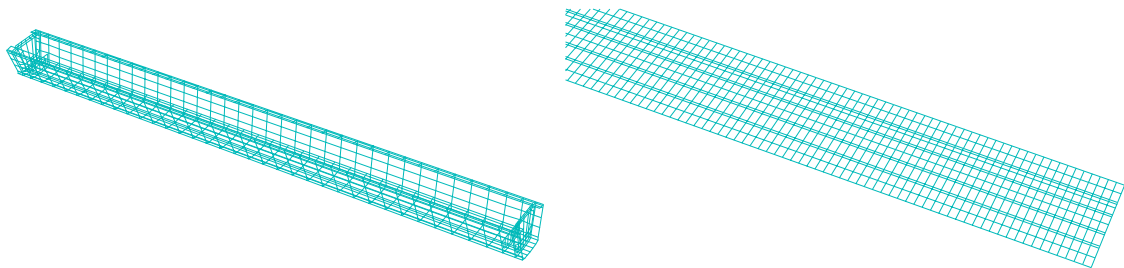
(a) Mesh shape of beam

(b) Mesh shape of portion of slab
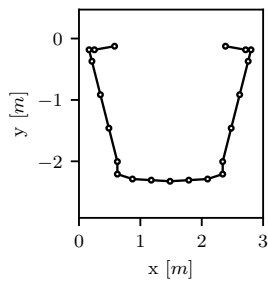
(c) Cross section of mesh of beam, nodes shown by circles and elements by lines
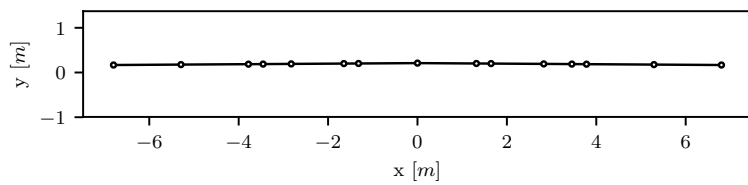
(d) Cross section of mesh of slab, nodes shown by circles and elements by lines

Figure 3.12: Visualisation of the mesh

Number of	Size [m]		Stress		Deflection		Acceleration	
Elements	x	yz Plane	MPa	%	mm	%	m/s^2	%
8391	1	2	-12.47	0.9	11.69	0.6	0.346689	4.6
8907	1	1	-12.52	0.5	11.62	0.0	0.34465	5.1
10707	optimised		-12.46	1.0	11.61	0.1	0.36109	0.6
38584	0.3	0.3	-12.58	0.0	11.64	0.2	0.365756	0.6
297132	0.1	0.1	-12.58	-	11.62	-	0.363427	-

Table 3.7: Mesh sensitivity analysis for the benchmark case bridge at a point in the third span of the bridge, for different numbers of elements as determined by the element size prescribed in the longitudinal x direction and in the cross sectional yz plane (accelerations at midspan of the slab, normal stress in the longitudinal direction and vertical deflection in the bottom flange of the U-beam).

Section 4.1.7.

3.1.2.7   Mesh Size Sensitivity

Determining an appropriate and efficient mesh is key to modelling. Sufficient accuracy must be achieved, but also be balanced with the computational time. Different mesh refinements were tested, with results from a selection shown in Table 3.7, with a focus on the bridge vertical accelerations, deflections and longitudinal normal stress caused by a single carriage of the real train with irregularities, displayed in Figure 3.13a. Due to the close results between the different element sizes, the results are focused on a small section at midspan of the third span of the bridge. This selection shows that the chosen size, of 10707 elements, provides a good match with the finer mesh sizes (with 38584 and 297132 elements for a globally applied mesh size of 0.1 m and 0.3 m respectively) for the vertical accelerations. For the stress and vertical displacement shown in Table 3.7, the difference of this model to the finely meshed models is small and so it is acceptable to use this model. The more coarse meshes with fewer elements, show greater errors for accelerations despite better computational times, justifying the chosen mesh size is appropriate. The chosen mesh size was optimised by each edge, using edge seeding in Abaqus (Dassault Systèmes SIMULIA Corp., 2014), which means the mesh size is not uniform in either the x direction or the yz plane.

In addition to testing the element size, the element types have been compared. The standard shell elements used in the model are *S4R* elements. These are 4 noded shell elements with reduced integration. Alternatively, and compared in Figure 3.13b is the use of *S8R* elements, which are 8 noded reduced integration quadratic elements and *S8R5*, which is an 8 noded quadratic reduced integration element with 5 degrees of freedom per node. Both these elements are more accurate in calculation, however they are more computationally expensive, and the change in accelerations from using them is very small, hence it is justified to use *S4R* elements in this work.
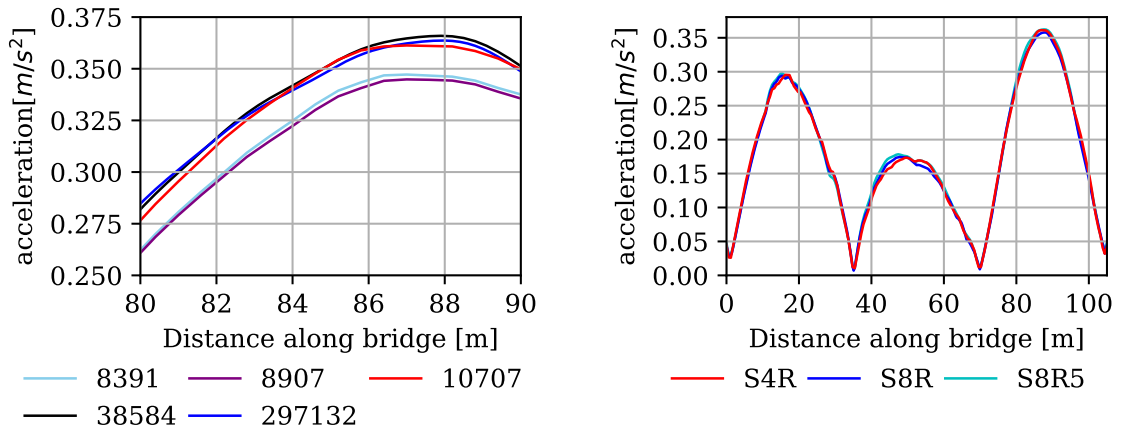
(a) Comparison of different mesh sizes, focused the region of middle of the third span

(b) Comparison of different element types

Figure 3.13: Analysis on the maximum filtered vertical accelerations of the bridge for the sensitivity of the elements

Using the $S4R$ elements with the optimised mesh and moving point loads, modelling the simulation of an eight carriage train over the three spanned bridge, takes between 60 and 90 minutes. Considering the interaction between the wheel and rail, and including the irregularities and the track, instead of moving point loads, increases the computational time to between 24 and 36 hours. Timings vary depending on the resonant behaviour of the bridge and vehicle speed. These timings are based on a desktop PC with a Intel Core i7 processor with 32 GB of RAM.

3.1.3 Filtering

According to BS EN 1991-2:2003 (2010) the maximum limits to the accelerations are applied for acceleration frequency components up to the higher of 30 Hz, the third modal frequency or $1.5 \times n_0$, where n_0 is the fundamental frequency. This requires a Fourier transform, a low pass filter to the frequency domain, and then an inverse Fourier transform. This potentially excludes significant modes contributing to the maximum vertical acceleration. However, the filtering is intended to remove high frequency components that would not impact the derailment safety of the vehicle for which the limits exist.

A comparison of the maximum vertical accelerations along the length of the bridge with and without irregularities with a frequency cut off of $30Hz$ and a higher frequency of $45Hz$ is made in Figure 3.14. When considering irregularities the filtering frequency has a big impact. This is due to the inclusion of higher frequency bridge modes that are activated by the inclusion of the irregularities, which is explained further in Section 4.3.3.

Comparison of the frequency components with and without irregularities (Figure 3.15) clearly
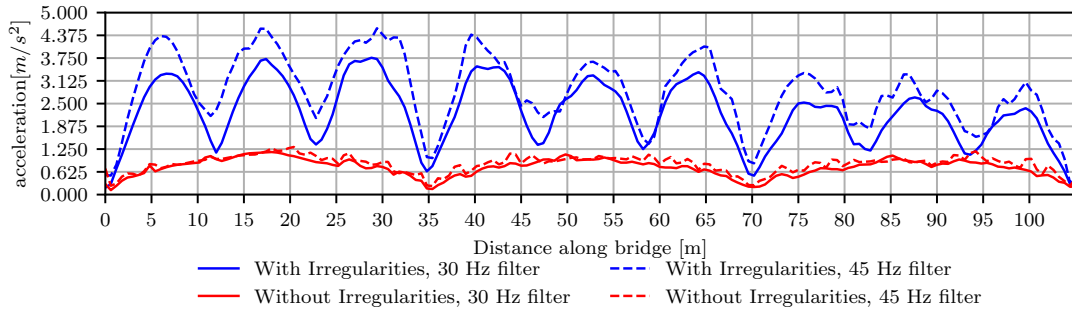
Figure 3.14: Comparison of different low-pass filters on vertical bridge accelerations along the length of the bridge
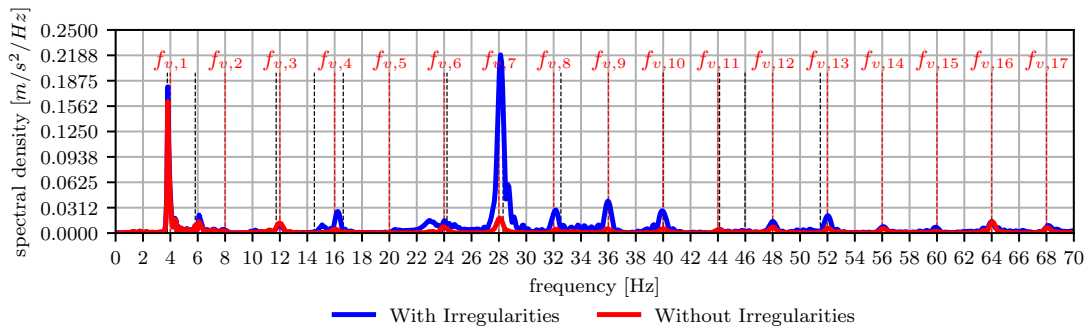
Figure 3.15: Comparison of Fourier transform of the vertical accelerations at midspan of the first span of the bridge with and without irregularities

shows higher contribution to the accelerations from the higher modes for the case with irregularities. However, the contributions above $30\,Hz$ are not as significant as those below the limit in this case. Combined with a lack of publications on the origin of the limits to the frequency components, the BS EN 1991-2:2003 (2010) frequency limit will be kept for this work.

A comparison of the maximum peak accelerations at midspan of the first span with root mean square (RMS) accelerations of different time windows in Figure 3.16, shows that filtering at $30\,Hz$ is approximately equal to an RMS acceleration with the time window of 3 seconds for the accelerations with irregularities and that without irregularities the RMS values do not fall
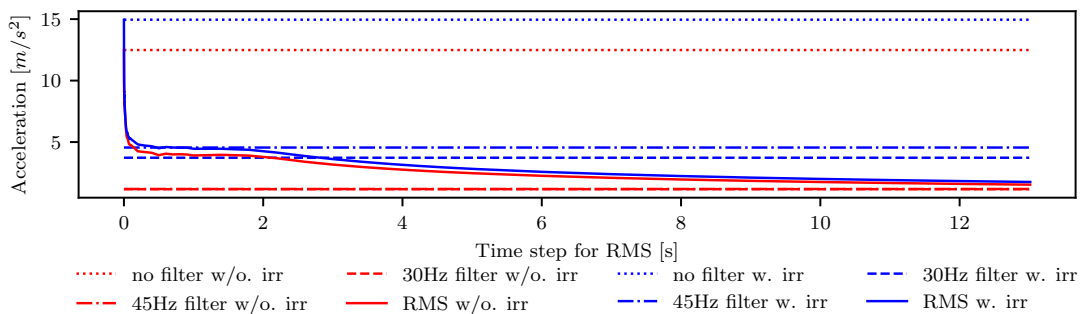
Figure 3.16: Comparison of maximum Fourier-filtered values with RMS values
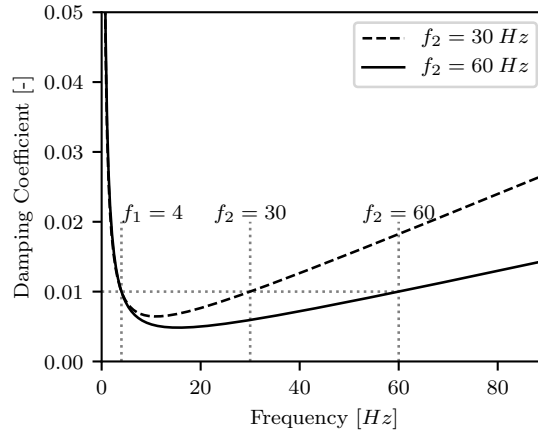
Figure 3.17: Rayleigh damping coefficients as a function of the location of the frequency control points

below the level of the filtered accelerations. The RMS accelerations of the bridge with and without imperfections are very similar for a time window larger than 0.15 seconds. However, codes do not prescribe limits to the RMS accelerations, so they will not be further studied.

3.1.4 Damping

Damping in this thesis takes the form of Rayleigh damping, which is a material damping. This applies different damping coefficients to different modal frequencies as by Equation 3.2.

$$\zeta_n = \frac{\alpha}{4\pi f_n} + \pi f_n \beta \tag{3.2}$$

According to BS EN 1991-2:2003 (2010), a lower bound estimate of damping must be used, taking the damping ratio (ζ_n) to be 1% for this type of bridge. A comparison to 2% damping is made in Section 4.1.2. The frequencies used to determine the Rayleigh coefficients of α and β, are open to interpretation. The fundamental frequency, f_1, is the first primary bending mode and is usually used as one of the frequencies to set the coefficients. The second frequency used, f_2, is in some cases (Kandge, 2007), taken as the frequency at which 95% of the modal mass is found below. In this thesis that accounts to about $60\,Hz$. On the contrary, considering only the frequencies of acceleration considered in BS EN 1991-2:2003 (2010) is up to $30\,Hz$ in this model. Other Rayleigh damping models Bathe (1996); Zhang et al. (2010), also use a mode with known damping coefficient, perhaps the second or third bending mode, for f_2, which corresponds to near to $30\,Hz$ in the latter case. A comparison of the second frequency being located at $30\,Hz$ and $60\,Hz$ is made in Section 4.1.2.

3.2   Materials

The bridges focused on are made from concrete. The focus of this thesis is on the introduction of high performance concrete (HPC) into the bridge. The material properties used in this thesis are as defined in Section 2.6. The changes in concrete strength result in changes to the modulus of elasticity as by Equation 2.9 of Section 2.6.1 and the mass as by Table 2.4 of Section 2.6.3. Despite BS EN 1991-2:2003 (2010) limiting the modulus of elasticity to the value found at compressive cylinder strength of $50\,MPa$ for strengths of concrete over this strength, it is allowed to use enhanced values when confirmed by trial mixes. Hence, the relationship defined in Equation 2.9 of Section 2.6.1, has been assumed to be representative for concrete strengths exceeding this.

3.3   Vehicle

The vehicle modelled in this thesis is a conventional train called the Siemens Velaro (Antolín, 2013; Antolin et al., 2012). Each of the vehicle bodies are assumed and modelled rigid in Abaqus, as is standard from the literature. This is achieved through the *RIGID BODY* input line command. The mass (*MASS*) and inertia (*ROTARYI*) of each of the rigid bodies is then assigned to the centre of mass of each vehicle body as point masses and inertias.

The modelling of the suspension systems between bodies was carried out in Abaqus through the use of connector elements, (*CONN3D2*) with assigned stiffness and damping coefficient. The central node of the wheelset is the location at which the user element (which is required to model the wheel rail interaction) is connected to the vehicle in Section 3.5.7.

The vehicle model follows the assumptions expressed in Section 2.2.5. In addition further assumptions are:

5. The wheelsets have 4 DOF each, with the forward motion and the rotation about the axle restrained.

6. The mass and inertias of each carriage in the train are the same and remain constant thoughout analysis

7. The distance between the carriages is constant and there is no connection between the carriages (as it is a conventional style train vehicle layout)

Assumption 6 arises from a lack of data on the differences in vehicle characteristics for carriages which provide traction to purely passenger carriages. As expressed in some literature, with conventional trains, assumption 7 can be valid as carriages can be treated independently.
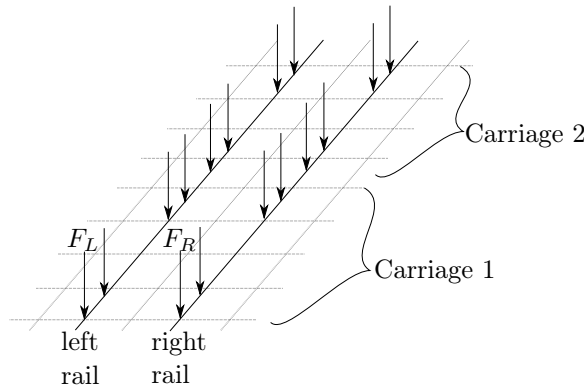
Figure 3.18: Forces used in a simple point load model directly onto the slab representing a real train

x [m]	F_L [kN]	F_R [kN]
$0 + n \cdot Ca_L$	89.69	89.69
$2.5 + n \cdot Ca_L$	89.69	89.69
$17.375 + n \cdot Ca_L$	89.69	89.69
$19.875 + n \cdot Ca_L$	89.69	89.69

Table 3.8: Point load representation of the Siemens vehicle, where: n is the number of the carriage from $n = 0 \ldots N - 1$, N is total number of carriages, Ca_L is the distance between centres of carriages ($= 25$ [m]), and F_L & F_R are the vertical forces [kN] on the left and right wheel respectively

This is only appropriate as the vehicle is moving at a constant velocity. Under acceleration or braking loads this assumption would have to be modified.

The chosen Siemens Velaro train had one of the most complete vehicles outlined in literature, as highlighted in Appendix C. The properties of this vehicle are given in detail by Figure C.1 and Tables C.1 and C.2 of Appendix C.

A comparatively simple model, to the full vehicle model, comprising of moving point loads is made, based on the vehicle weight. The forces and distances of this moving point load model are shown in Table 3.8, and is visually represented in Figure 3.18.

In this thesis, the vehicle will always move across the bridge in the positive x-direction, unless otherwise stated. This means moving from the left to the right on any diagrams or graphs presented. The direction of travel will impact the response of the spans, as can be found in the section on boundary condition comparison (Section 4.1.5).

3.4 Track

In this thesis slab track will be studied, due to many of the high speed railway lines in the world using this type of track (Section 2.3) and the current tendency in using this system due to its benefits. However, due to the mix of ballast and slab track in use around the world, a comparison will be made in Section 4.2.

(a) Ballast Track   (b) Slab Track
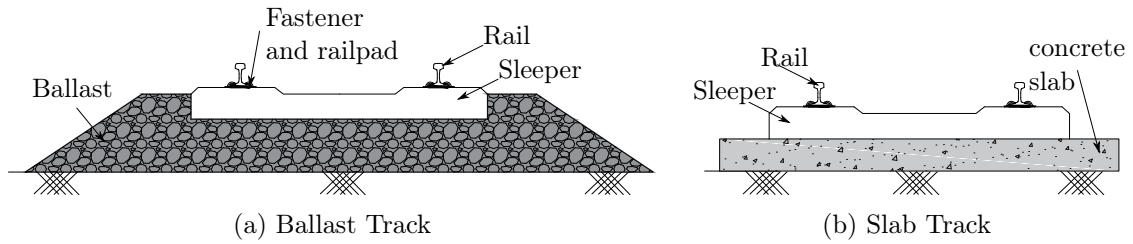
Figure 3.19: Comparison of the two track types

3.4.1   Track Types

The differences between the slab and ballasted tracks are seen in Figure 3.19. The ballast track is considered a less stiff material, hence the ballast is considered an elastic material, whereas the concrete slab in slab track is far stiffer, being composed of solid reinforced concrete. Additionally, the mass of the track systems are not considered the same as the ballasted layer is normally thicker and will change weight in its lifetime, as it traps fine material in the ballast voids from the environment, but the slab track will have a more consistent lifetime weight.

In order to model the track, Figure 3.20 shows the comparison of the two track type models. For the ballasted model the rail is modelled by a series of *'B31'* beam elements, which allow the longitudinal load distribution from the vehicle deck. Below the rail is the railpad, modelled by springs and dampers in all three component directions (using connector elements, *'CONN3D'* in ABAQUS). The railpad connects a rail node to a node with mass. This node represents the mass of the sleeper and 50% of the ballast mass. This node is connected to the bridge deck by another set of springs and dampers that represent the ballast stiffness. Finally, a non-structural mass is applied to the bridge deck to model the remaining 50% of the ballast mass, which is modelled as unsprung.

The slab track models the rail and railpad in the same way. However, the railpad is directly fastened to the bridge, removing this node with mass and additional spring elements. As a result, the sleeper mass is unsprung in this model and instead is distributed uniformly as a non-structural mass within the region of the track. Finally, in addition to the sleeper mass, the mass of the concrete track slab, taken as $0.24m$ thick (Proença et al., 2011), is applied as a non-structural mass to the bridge deck. The concrete track slab itself is not assumed to add any rigidity to the bridge slab, as has been found to previously been assumed in literature (Dinh et al., 2009; Lou et al., 2012). This is as vertically the stiffness is very large, so is assumed rigid, and longitudinally the track is separated from the bridge deck by waterproofing membrane layers, so there is minimal rigidity.

(a) Ballast Track model

(b) Slab Track model
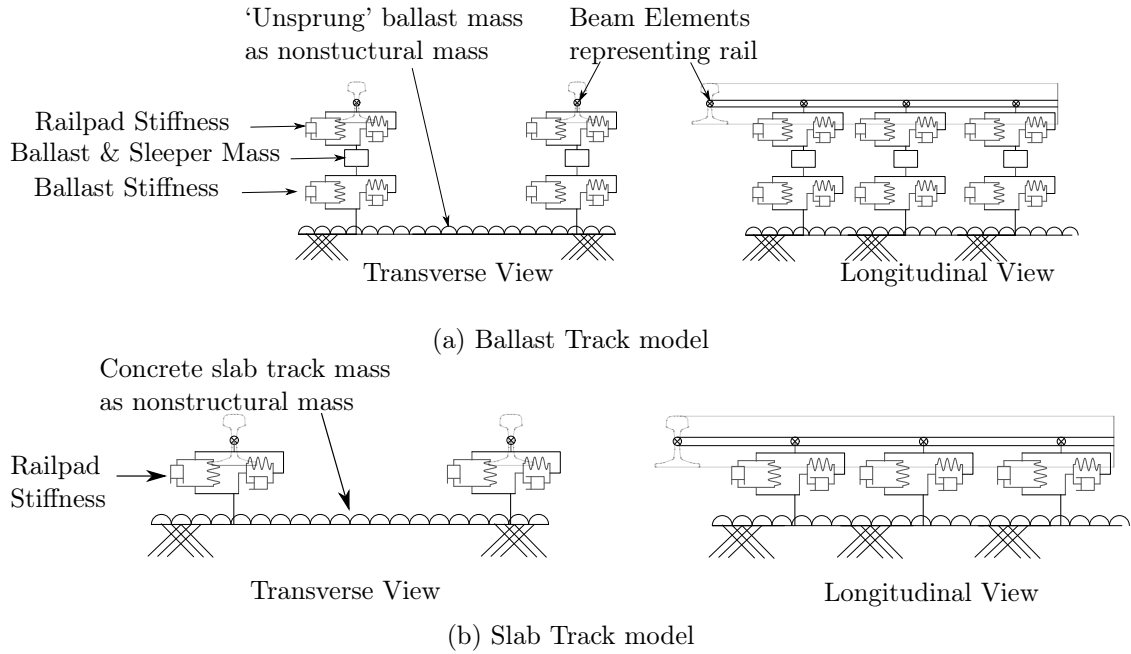
Figure 3.20: Comparison of the models for the two track types

3.4.2 Other Deck Components

On the top of the bridge deck slab there are other materials that are not part of the track. These include parapets and protection barriers. The mass of these is placed into the model as a nonstructural mass on top of the shell elements representing the deck slab.

3.5 Wheel-Rail Contact

The most complicated part of the model is the contact between the rail and the wheels of the train vehicle. This section will expand on the material presented in the literature review in Section 2.4 and explain the intricacies of the calculation of the contact between the wheel and rail. The full process used to calculate the wheel-rail interaction is shown in Figure 3.21.

3.5.1 Definitions

At the point of contact, there is a normal force (acting perpendicular to the contact patch plane), and tangential forces (acting in the plane of the contact patch), which are seen in Figure 3.22. With the wheelset modelled as a rigid body, the location of all potential contact points is linked to the central point of the wheelset. In addition, as the deformation of the cross section of the rail is neglected, the location of the rail contact point can be determined with respect to the central point of the rail. This gives rise to the local coordinate systems
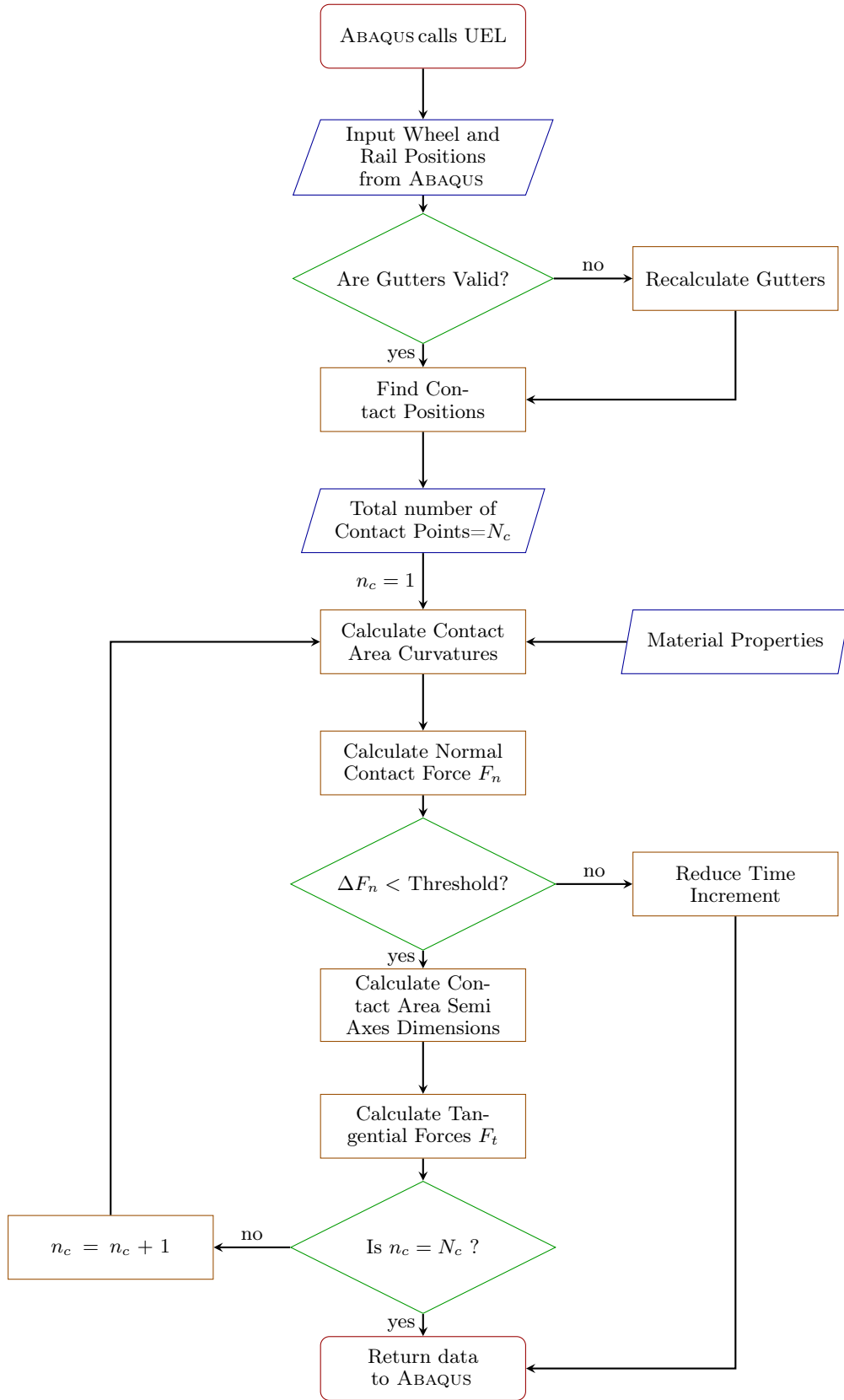
Figure 3.21: Flow chart of the processes involved in the wheel rail contact
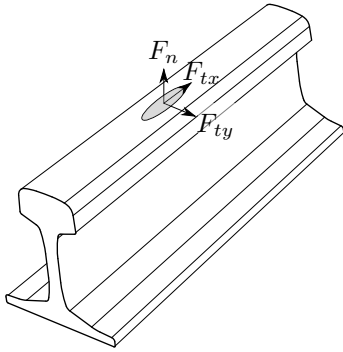
Figure 3.22: Direction of forces at the contact patch on the rail
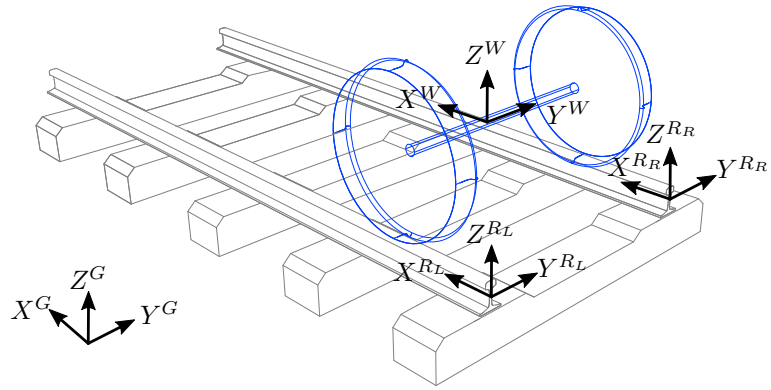
Figure 3.23: Local coordinate systems of the left (X^{R_L}, Y^{R_L}, Z^{R_L}) and right (X^{R_R}, Y^{R_R}, Z^{R_R}) rails, the wheelset (X^W, Y^W, Z^W), and connection to the global coordinate system (X^G, Y^G, Z^G)
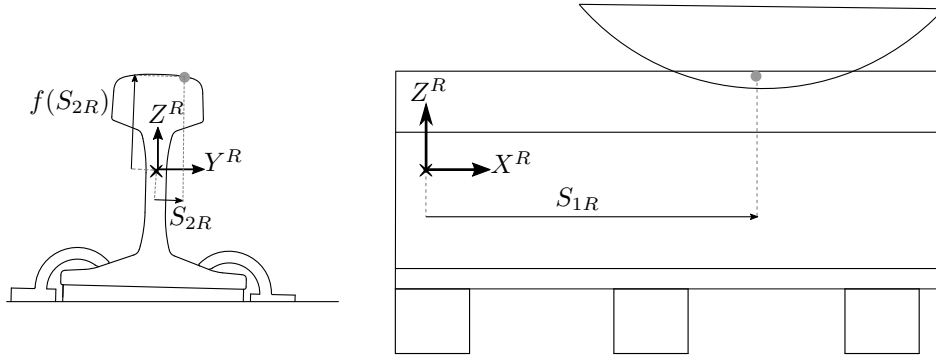
Figure 3.24: Surface parameter definition for the rail

in Figure 3.23, showing the coordinate systems for the left and right rails and the wheelset respectively.

The location of the contact point on both the wheel and rail are defined with local surface parameters in respect to the local coordinate systems, as used in the discrete methods proposed by Pombo and Ambrósio (2006) and Shabana et al. (2004). For the rail, the local surface parameters used, S_{1R} and S_{2R}, are defined as shown in Figure 3.24. S_{1R} represents the longitudinal coordinate of the contact point on the rail and S_{2R} the lateral coordinate of the contact point with respect to the local coordinate system for the rail. The vertical coordinate of the contact point can be determined as a function of the S_{2R} local coordinate, due to the assumption that the cross section of the rail remains rigid.

To determine the location of the contact point on the wheel, the local coordinate system is defined by the surface parameters S_{1W} and S_{2W}, as seen in Figure 3.25. The local coordinate system of the wheelset, defined by X^W, Y^W and Z^W, rotates with the rotation of the wheelset. Hence, S_{2W} represents the angle from direction of the X^W axis, to the plane of the wheel containing the contact point. Finding the plane with the contact point is simplified in this
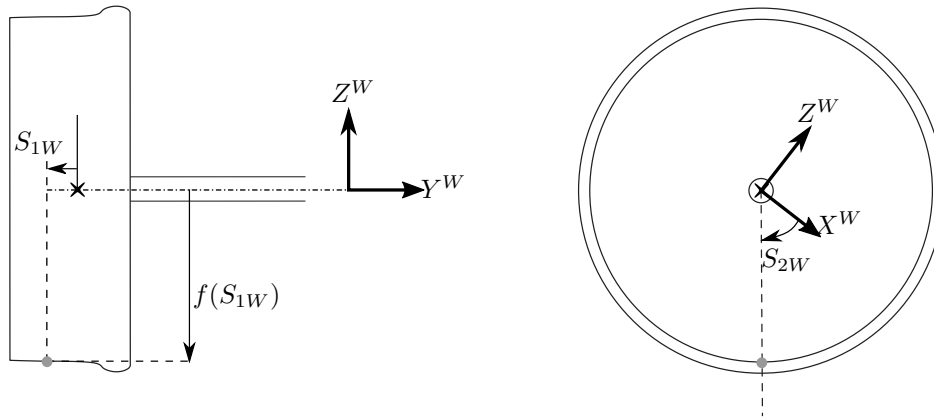
Figure 3.25: Surface parameter definition for the wheelset
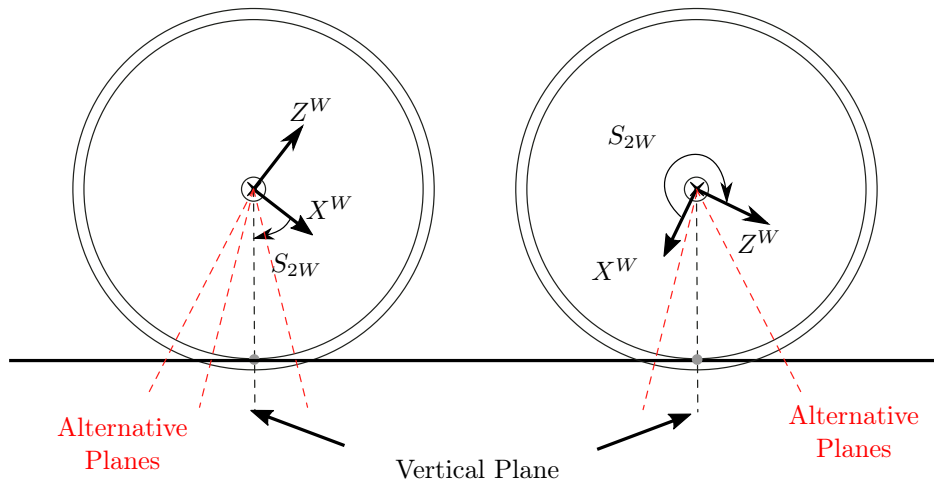
Figure 3.26: Surface parameter definition for the wheelset

thesis, by assuming that it is the vertical plane, therefore containing the lowest point of the wheelset (Figure 3.26). However, expansion could be made to study further planes to more accurately determine the contact point. Within the plane defined by the S_{2W} coordinate, the lateral coordinate in which the contact occurs is represented by the S_{1W} coordinate. Again the vertical position of contact is known as a function of this coordinate, due to the assumed rigidity of the wheel. For more detail on the definition of the surface parameters and local coordinates, see Pombo and Ambrósio (2006) and Shabana et al. (2004).

3.5.2 Location of contact point

As explained in the literature review (Section 2.4.1), the first stage to establishing the wheel rail contact is to establish the position and area of contact. This requires a definition of the wheel and rail geometry, which are expressed in Appendix D (BS EN 13715:2006+A1:2010, 2011; BS EN 13674-1:2011+A1:2017, 2011). As part of the contact area definition, first the location of the contact point needs to be determined, the process of which is explained here.

(a) Running surface contact penetration   (b) Flange surface contact penetration
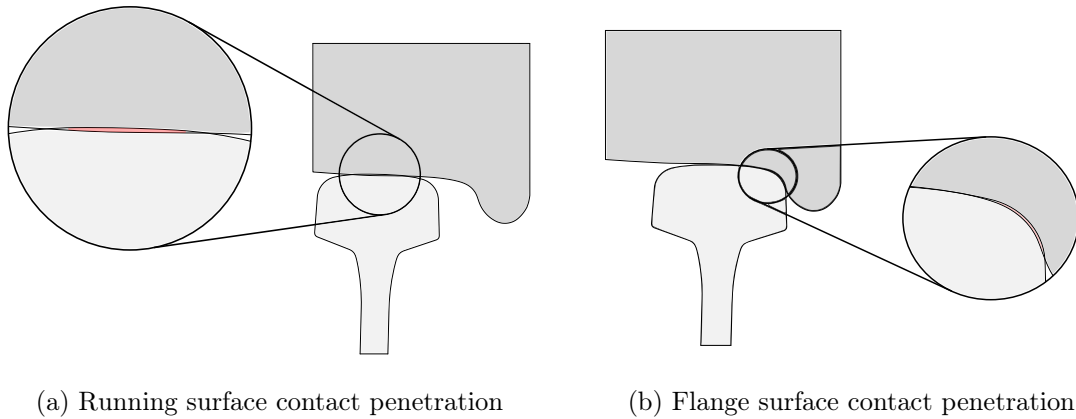
Figure 3.27: Different methods of determining the contact point

3.5.2.1   Position of contact point

Using the global position of the wheelset and rails, in conjunction with the local coordinate systems and surface parameters, the position of the contact point can be found. This uses the relative position of the wheel and rail to find the virtual penetration between the two contacting bodies. The elastic contact formulation used in this thesis, uses the penetrations to calculate the contact area and forces. The penetration, which is the overlap between the two bodies (Figure 3.27), are based on an imagining of the elastic deformation of the contacting bodies under force, compensating for the fact that these bodies are modelled as rigid.

The penetrations between the wheel and rail, used to define the contact point location, are determined iteratively. Taking the global positions and displacements of the wheel and rail, and the geometry of the irregularities at the contact point (later explained in Section 3.5.6), the penetration between the bodies is calculated at coarse discrete points defined by the rail surface parameter. Where penetration is found, refinement is made to the coarse discrete points to model the penetration profile with higher resolution. These discrete points are then interpolated with a cubic function, to determine the final coordinate on the rail of the maximum penetration. From this coordinate, the corresponding coordinate on the wheel is also found. This process is shown in Figure 3.28.

Although obtaining the penetration profile between the bodies is relatively easy, representing the location of the contact point is not. The shape of the penetration may not lend itself to be well modelled by a single contact point, as it may have multiple peaks in penetration. This is particularly a problem, as the contact area used to formulate the forces at the contact point, is defined by an ellipse, which with only one contact point may not represent the penetration profile well. This can be seen in Figure 3.29, where modelling the contact from the ellipse only at the peak penetration (point D), would not represent the true penetration well. Some previous research has accepted the inaccuracies with modelling at a single point of contact (Antolín et al., 2010), but it was found in this work to be a cause of modelling errors when
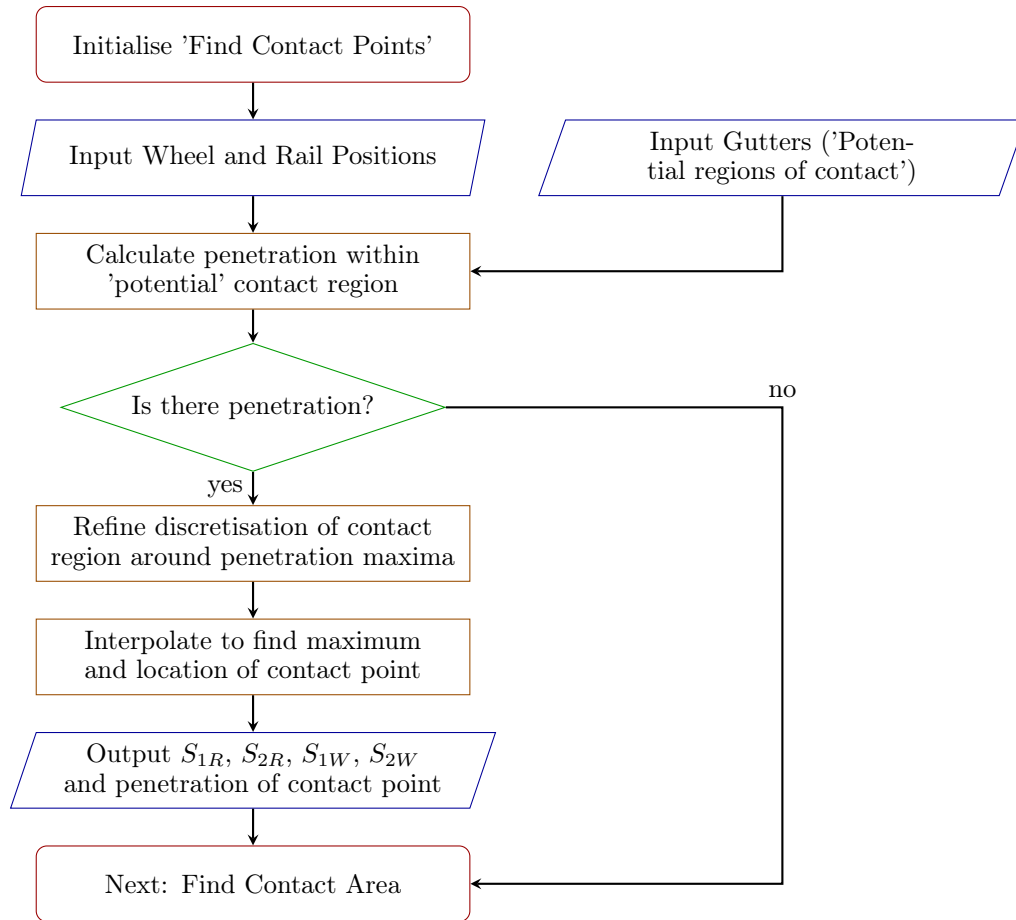
Figure 3.28: Process of determining the penetration
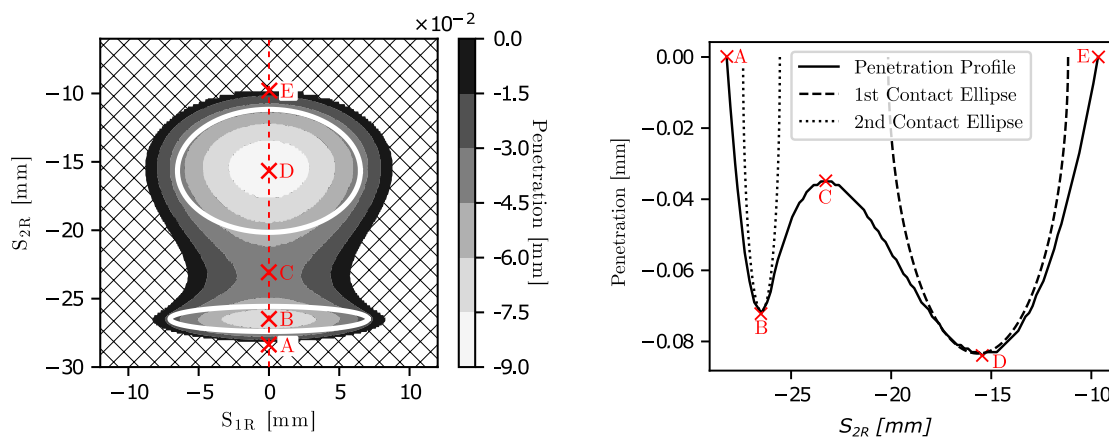
(a) Contour plot of the penetration, showing the centre of the contact ellipses

(b) Penetration in the two dimensional plane given by the line A-E of Figure 3.29a

Figure 3.29: Actual penetration between a contacting wheel and rail, for a given force and position of the wheel and rail. Also showing contact two possible contact ellipses to model the penetration, centred at points B and D
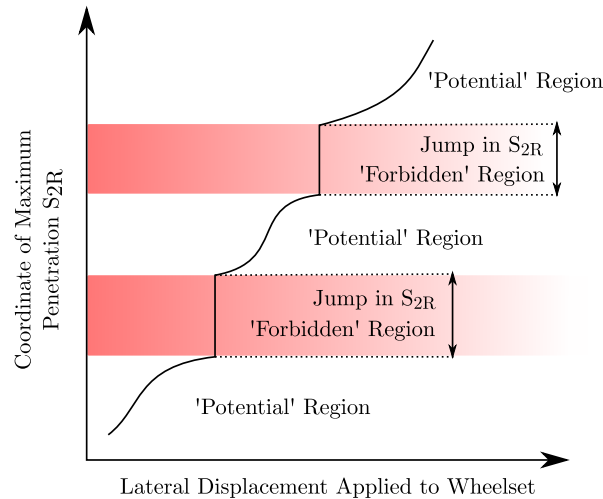
Figure 3.30: Simulated process of determining the 'forbidden' and 'potential' S_{2R} contact ranges

the position of contact changes significantly, which is further explained in Section 3.5.2.2. A solution was found using work by Pascal and Soua (2016), which allowed multiple points of contact to be defined per wheel rail pair. In this work it was found sufficient to limit to a maximum of four potential contact points per wheel-rail pair.

The method used here and by Pascal and Soua (2016), involves splitting the cross section of the rail up into 'potential' and 'forbidden' contact point regions (also known as gutters). These regions are calculated based on the position of the wheel and rail. For a given position, the S_{2R} coordinate on the rail of the maximum penetration is recorded. Then a series of imaginary lateral displacements are introduced to the wheel, recording the S_{2R} coordinate of the maximum penetration for each displacement (Figure 3.30). From this process, it is found that the maximum penetration is never located within certain S_{2R} ranges. This is a result of the geometry of the wheel and rail, which means the maximum penetration cannot occur in this 'forbidden' contact point range. The ranges of S_{2R} that allow contact are the 'potential' regions. Refinement of the imaginary lateral displacements applied in finding these locations, is required to accurately find the regions. These are valid for the specific wheelset yawing and rolling rotations. Hence, if the rotation of the wheelset changes significantly the regions have to be recalculated.

For the determination of the wheel-rail contact points, if penetration is found within a region, then the largest penetration within each and every region is defined as a contact point. As a result, the process of determining the maximum penetration explained earlier in this section and in Figure 3.28, is applied in each region of 'potential' contact. An example of the regions of contact are shown on the rail in Figure 3.31, with green being the 'potential' contact regions and red the 'forbidden' regions. Figure 3.32 shows how this can be used to define two contact points, even when there is only one distinct peak, allowing a better representation of the penetration profile by two ellipses (this is explained more in Section 3.5.3).
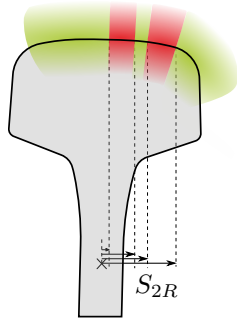
Figure 3.31: Visualisation of the regions in which contact point is allowed to be located: green=allowed, red=not allowed
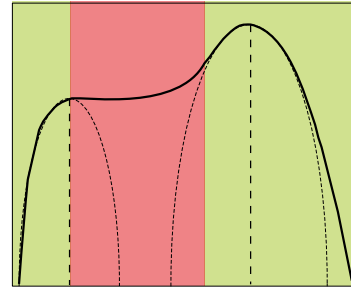
Figure 3.32: Profile of penetration for a given force and location of the wheel and rail, with two contact points/ellipses, one located at the maximum penetration in each 'potential' contact region (green)

3.5.2.2 Jumping of contact point

The simplest and most computationally efficient method to model the contact is to use just one contact point per wheel-rail pair, as done previously by Antolín et al. (2010). However, errors were found to occur in calculation when using this method. This was because for many given forces and wheel-rail positions, the penetration profile has dual peaks, as visible in Figure 3.33. Due to the discrete time increment, in one time step (for example from t_1 to t_3) the location of the contact point can jump from one location (CP1) to another (CP2). In this case, with the change in location comes a significantly different sized ellipse, which in turn affects the Hertzian stiffness, K_H (Section 3.5.4.1) and then the contact forces. This means that with the change in location of the contact point, although the value of the penetration may not change significantly between the time increments, the normal force can change significantly. This change in normal force unrealistically acts as an impact, and the sudden increase in force causes a modelling error. It is therefore necessary to model multiple contact points.

Another drawback of the one contact point method, is the potential for a situation such as in time step t_2 of Figure 3.33. Here, two locations (CP1 and CP2) have identical penetrations. Modelling with one contact point would result in requiring a method to preferentially select one of these points, which then neglects the other equally viable contact point.

3.5.3 Area of contact

As expressed in the literature review (Section 2.4.2), the contact area for elastic contact models is generally approximated as an ellipse. With the interaction model in this thesis having potentially multiple points of contact per wheel-rail pair, an ellipse is required for each contact point. This can help approximate a non-elliptical contact area, as shown in Figure 3.29a. In this figure, the contact ellipses are shown in white for the contact points B and D,
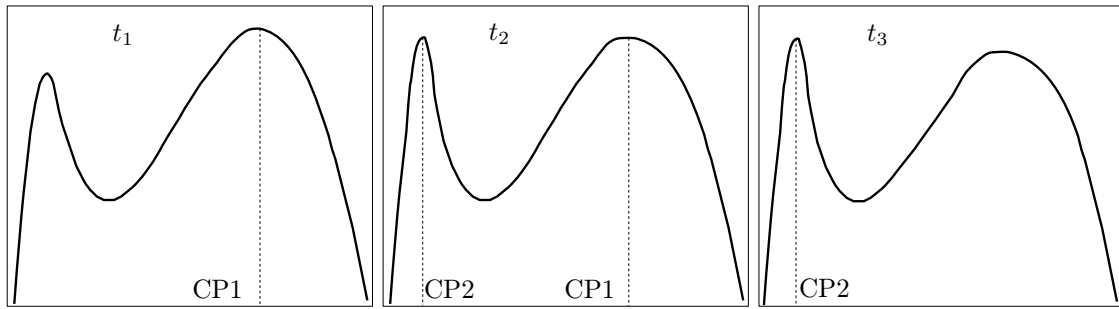
Figure 3.33: The jumping of contact points from CP1 to CP2 in a single contact point problem, with the changing penetration profile between the wheel and rail shown here. Shown for times $t_1 < t_2 < t_3$

(a) Two interacting three dimensional spherical bodies

(b) Overlap between two bodies shown in two dimensions with the contact ellipse location and the corresponding penetration (δ)
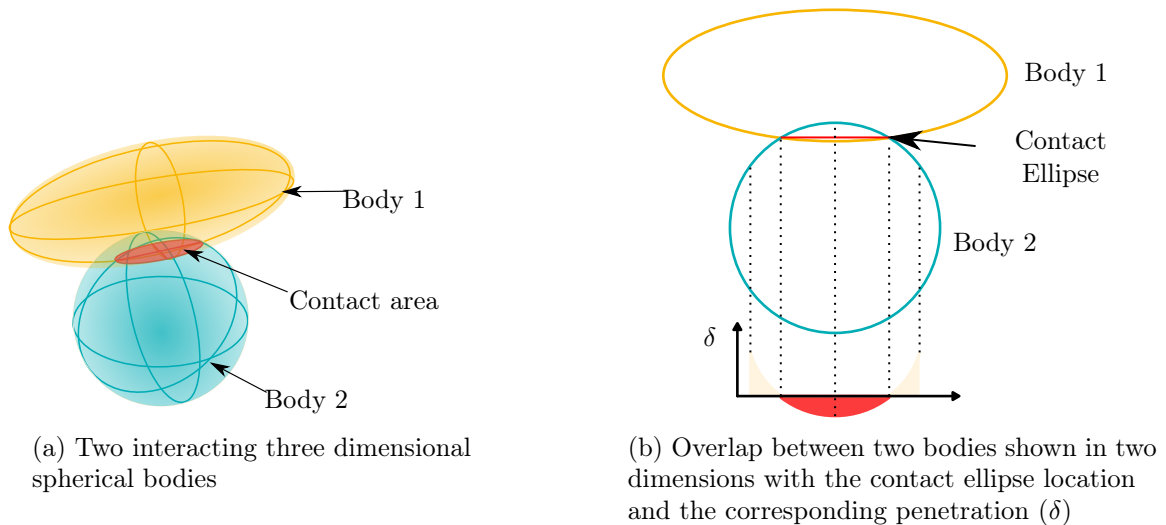
Figure 3.34: Hertz theory of two inter-penetrating bodies

against the real penetrating area in the background. The ellipses are centred at the locations of maximum penetration for each potential contact region, but they do not extend to the boundary where the real penetration is zero. This is due to the variation in the curvatures of the wheel and rail, which causes the non-elliptical penetration area, that is difficult for the extent of the ellipse to match. Nonetheless, multiple ellipses provide a better approximation of the penetration area than one ellipse.

The calculation of the ellipse contact area comes from Hertz theory (Hertz, 1882), which is regularly used in wheel-rail contact. Originally this theory represented the area of penetration between two ellipsoids as seen in Figure 3.34a. This is simplified to two dimensions in Figure 3.34b, with the variation of the penetration (δ) between the two bodies indicated. The theory uses the curvatures of the two contacting bodies at the contact point (i.e. the wheel and the rail), with the corresponding penetration to determine the ellipse size. The ellipse size, indicated by the semi axes dimensions a_e and b_e (Figure 3.35), can be determined by Equations 3.3 and 3.4 (Shabana et al., 2007). However, these depend on the normal force between the wheel and rail, F_{ne} (Equation 3.19), and can therefore not be calculated until after the normal
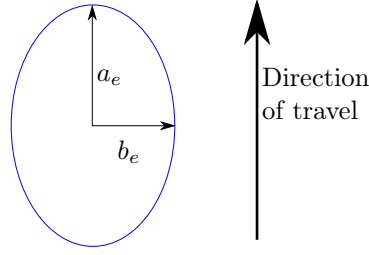
Figure 3.35: The dimensions of the semi axes of the contact ellipse with respect to the direction of travel

force is known. However, due to the complexity of the problem, this force depends on many of the same parameters that define the ellipse semi-axes. Therefore, the common parameters used in the definition of the the semi axes and normal force are defined within this section and are calculated first, before the the normal force and then the dimensions of the contact ellipse semi-axes can be found.

$$a_e = m \left(3\pi F_{ne} \left(K_{mat} \right) / 4 K_{bpa} \right)^{\frac{1}{3}} \tag{3.3}$$

$$b_e = n \left(3\pi F_{ne} \left(K_{mat} \right) / 4 K_{bpa} \right)^{\frac{1}{3}} \tag{3.4}$$

The coefficients m and n of Equations 3.3 and 3.4 are found in Table 3.9, using the angle θ_{wr} (Hertz, 1882) as defined by Equation 3.5. Alternatives to using this table have been proposed by (Shabana and Sany, 2001), but not used in this thesis. Also, K_{mat} is a coefficient related to the material properties of the wheel and rail (Equation 3.8), and K_{bpa} is a coefficient related to the wheelset and rail curvatures at the contact point (Equation 3.6). For the calculation of the angle θ_{wr}, a further coefficient related to wheel and rail curvatures at the contact point, K_{bma} is required (Equation 3.7).

$$\theta_{wr} = cos^{-1} \left(K_{bma} / K_{bpa} \right) \tag{3.5}$$

$$K_{bpa} = A(S) + B(S) \tag{3.6}$$

$$K_{bma} = B(S) - A(S) \tag{3.7}$$

$$K_{mat} = \frac{2 \left(1 - \nu_{wr}^2 \right)}{\pi E_{wr}} \tag{3.8}$$

Here, ν_{wr} is the Poisson's ratio and E_{wr} is the modulus of elasticity of the wheel and rail. These values are 0.2 and $200\,GPa$ respectively. Although the grades of steel that a wheel and rail are made from may in fact be different resulting in different properties, it is widely assumed that the material properties are identical (Antolín et al., 2013).

The coefficients related to wheel-rail curvature, $A(S)$ and $B(S)$, are sums of the curvatures in the x and y direction respectively, and equal to:

$$A(S) = \frac{1}{2} \left(\frac{1}{R_{wx}(S)} + \frac{1}{R_{rx}(S)} \right) \tag{3.9}$$
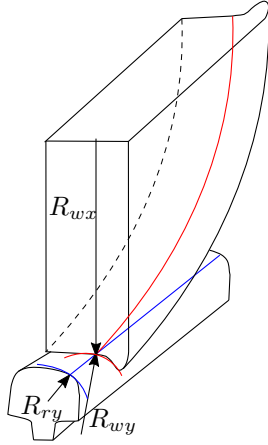
θ_{wr} [°]	m	n	r	θ_{wr} [°]	m	n	r
2.0	22.243	0.169	0.179	38.0	2.233	0.553	0.801
6.0	9.788	0.255	0.327	46.0	1.889	0.611	0.861
10.0	6.611	0.311	0.428	54.0	1.636	0.671	0.909
14.0	5.078	0.356	0.508	62.0	1.441	0.733	0.946
18.0	4.155	0.394	0.574	70.0	1.285	0.800	0.973
22.0	3.531	0.429	0.632	78.0	1.157	0.873	0.990
26.0	3.077	0.462	0.682	86.0	1.048	0.955	0.999
30.0	2.731	0.493	0.726	90.0	1.000	1.000	1.000

Figure 3.36: Curvatures of the wheel and rail

Table 3.9: Values of m, n and r as a function of θ_{wr} (Hertz, 1882; Antolín, 2013)

$$B(S) = \frac{1}{2}\left(\frac{1}{R_{wy}(S)} + \frac{1}{R_{ry}(S)}\right) \qquad (3.10)$$

where $R_{wy}(S)$ and $R_{wx}(S)$ are the principal wheelset radii of curvature in the x and y direction at the location of the contact point, S, and $R_{ry}(S)$ and $R_{rx}(S)$ are the principal radii of curvature of the rail at the contact point (S). This is shown in Figure 3.36. If the radii of curvature is situated on a convex curve, it is assigned a negative value, with concave curves assigned positive values. As such many of the $R_{wy}(S)$ values are negative. With wheelset rotation, the longitudinal axis of the wheelset and the rails will not necessarily be aligned. This requires adjustment to the K_{bpa} and K_{bma} coefficients, to account for the difference between the longitudinal axes. However, as this work focuses on straight track, this angle is small, so the variation of these coefficients is negligible and hence this adjustment is not performed. For curved track, the adjustment would be required, as the difference between the angles is larger.

3.5.3.1 Modified curvature 'B'

Due to the convex curvature represented by R_{wy}, the summation of curvatures in the y direction (Equation 3.10), can be negative or close to zero at the point of contact (see the original line of Figure 3.37a). This results in the calculation of unrealistic, elongated ellipse semi axes for the contact area, because a combined curvature, $B(S)$, of zero would essentially mean that the surfaces were conformal. This would invalidate the assumption in Hertz theory (Hertz, 1882), that the two objects have non-conformal shapes. The cause of this problem is the distinct changes in curvature of the rail as seen in Figure 3.37b.

As the determination of the ellipse size depends on the curvatures at the contact point, large changes in the ellipse size can occur for a small change in the contact point location, due to
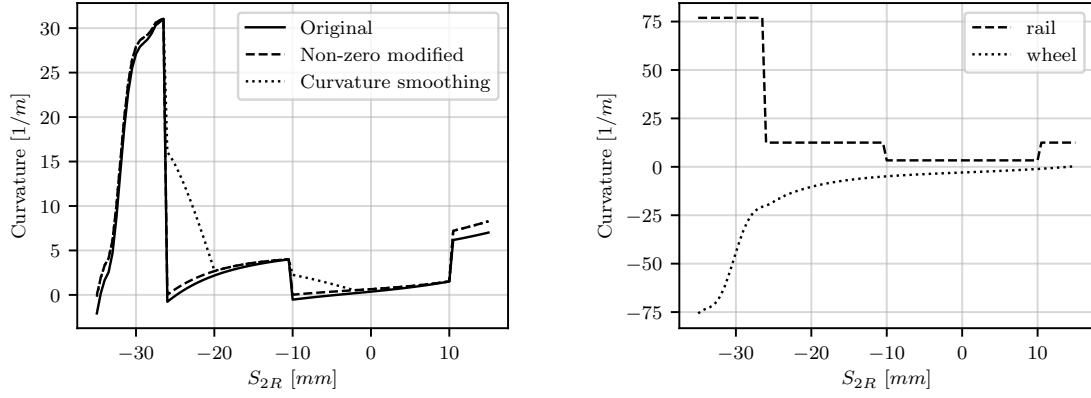
(a) Variation of the curvature, B, with surface parameter S_{2R} showing the effect of the modification

(b) Separate curvatures of the rail and wheel

Figure 3.37: Curvatures used for the calculation of the B curvature

the jumps of the combined curvature seen in the original line of Figure 3.37a. Moreover, for a contact point located close to a jump in curvature, the ellipse shape will take the dimensions generated by that point, and ignore the very different dimensions that would be generated if the contact point was on the other side of the jump in curvature. This leads to disparity between the real penetration area and the ellipse generated. Furthermore, the curvatures across the width of the ellipse may vary significantly.

To avoid the problems caused by jumps, variation across the ellipse and potentially negative curvature, modification and smoothing of the combined curvature $B(S)$, previously defined by Equation 3.10, is made in this section. Firstly, the combined curvature, $B(S)$, in Equation 3.10, is modified to ensure the value is greater than zero, as was similarly performed by Piotrowski and Chollet (2005). Secondly, smoothing is performed to reduce the magnitude of the jumps in curvature found in the discontinuous regions caused by the distinct changes in the rail curvature. These two steps are seen in Figure 3.37a, as firstly the 'Non-zero modified' line and secondly the 'Curvature smoothing' line. This modified $B(S)$ provides ellipses that match the properties of the real penetration much better, and avoids computational errors generated by the negative or close to zero combined curvatures.

To first ensure that the B curvature is greater than zero, the following modification is made:

$$B_{mod1}(S) = B(S) - \frac{S - S_1^+}{S_2 - S_1^+} B_{min}(S_1^+) \tag{3.11}$$

where $B_{mod1}(S)$ is the modified curvature value at location S and $B(S)$ is the curvature determined in Equation 3.10 at location S. The values of S and S_1^+ are shown in Figure 3.38. S is the coordinate (in terms of surface parameter S_{2R}), of the contact point. For this coordinate of the contact point, the extent of S_{2R} for which the rail curvature is constant is
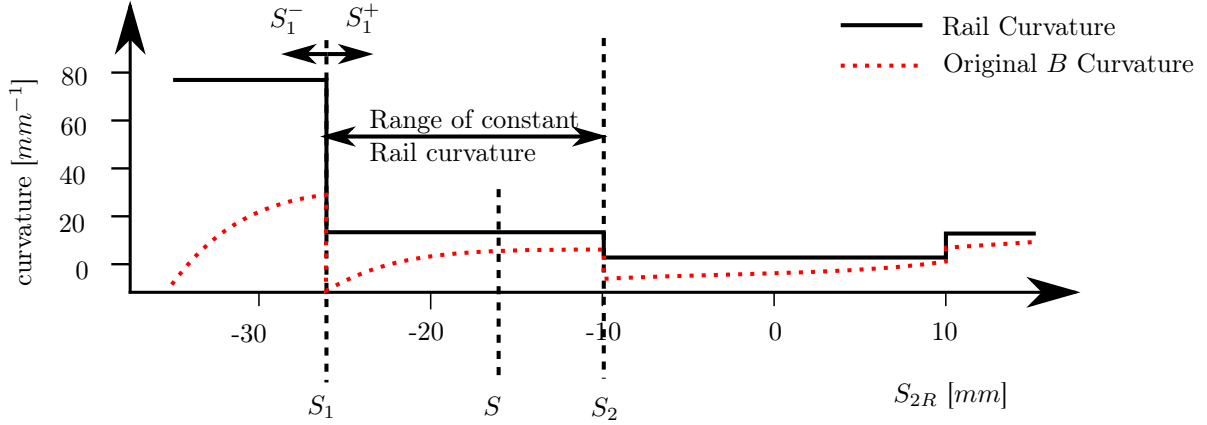
Figure 3.38: Indication of the method used in determining the rail curvatures for calculation of the two modifications of the B curvature

bound by the coordinates S_1 and S_2. S_1 is located at the side of this range for which the combined curvature 'B' is minimal. Due to the discontinuity in the rail curvature, S_1^+ is found to the right of the discontinuity (the smaller rail curvature), and S_1^- to the left (leading to a larger rail curvature). $B_{min}(S_1^+)$ is the curvature at coordinate S_1^+, as determined by Equation 3.12, which is where the combined curvature is at a minimum within the range of constant rail curvatures. This modification is only made when the value of $B(S_1^+)$ is negative, as it is not required in other cases.

$$B_{min}(S_1^+) = \begin{cases} \frac{1}{2}\left(\frac{1}{R_{wy}(S_1^+)} + \frac{1}{R_{ry}(S_1^+)} \right), & \text{if } B(S_1^+) < 0 \\ 0, & \text{if } B(S_1^+) \geqslant 0 \end{cases} \qquad (3.12)$$

where $R_{wy}\left(S_1^+\right)$ and $R_{ry}\left(S_1^+\right)$ are the wheel and rail curvatures at corresponding to the coordinate S_1^+. Due to the constant geometry of the rail, the values of S_1 and S_2 can be predefined based on the coordinate of the contact point S. As such they are defined by:

$$\begin{cases} S_1 = 10.23, & S_2 = 26.03, & \text{if} & 26.03 \geqslant S > 10.23\,mm \\ S_1 = -10.23, & S_2 = 10.23, & \text{if} & 10.23 \geqslant S > -10.23\,mm \\ S_1 = -26.03, & S_2 = -10.23, & \text{if} & -10.23 \geqslant S > -26.03\,mm \\ S_1 = -36.00, & S_2 = -26.03, & \text{if} & -26.03 \geqslant S > -36\,mm \end{cases} \qquad (3.13)$$

The second modification, smoothing the $B(S)$ curvature over the discontinuity, results in the final modified curvature value $B_{mod2}(S)$. This changes the value of $B(S)$ used in Equation 3.11, from being defined by Equation 3.10 to Equation 3.14 for the modified curvature value

$B_{mod2}(S)$.

$$B_{mod2}(S) = B_f(S) + \frac{1}{2R_{wy}(S)} - \frac{S - S_1^+}{S_2 - S_1^+} B_{min}(S_1^+) \tag{3.14}$$

where the value $B_f(S)$ comes from a smoothing of the curvatures of the rail as in Equation 3.15:

$$B_f(S) = \begin{cases} \frac{1}{2} \left[\frac{1}{2} \left(1 + \frac{|S-S_1|}{l_0} \right) \frac{1}{R_{ry}\left(S_1^+\right)} + \left(1 - \frac{1}{2} \left(1 + \frac{|S-S_1|}{l_0} \right) \right) \frac{1}{R_{ry}\left(S_1^-\right)} \right], & |S - S_1| < l_0 \\ \frac{1}{2R_{ry}(S)}, & |S - S_1| \geqslant l_0 \end{cases} \tag{3.15}$$

Here, the value l_0 is a distance representing the range over which the rail curvature is smoothed. It is linked to an approximate calculation of the ellipse semi lateral axis value.

$$l_0 = n \left(3F_{ne,t-\Delta t} \pi K_{mat} / \left(4 \left(A(S) + B_{mod1}(S) \right) \right) \right)^{\frac{1}{3}} \tag{3.16}$$

where $F_{ne,t-\Delta t}$ is the normal force calculated by Equation 3.19 from the previous time step, and n is approximated from the Table 3.9 using $B_{mod1}(S)$ in place of $B(S)$ for Equations 3.6 and 3.7.

The new value of curvature, B_{mod2}, is used in place of $B(S)$, which affects Equations 3.3 through to 3.7. This changes Equation 3.6 to Equation 3.17 and likewise Equation 3.7 to Equation 3.18. The modified formulation is used for the rest of this thesis. This removes the problem of local conformal contact invalidating assumptions for Hertz theory (Section 3.5.4.1).

$$K_{bpa} = A(S) + B_{mod2}(S) \tag{3.17}$$
$$K_{bma} = B_{mod2}(S) - A(S) \tag{3.18}$$

3.5.3.2 Flange Contact

In this thesis the contact is always assumed to occur within the vertical plane (Section 3.5.1 and Figure 3.26). However, this method neglects any contact that may occur outside of this plane, particularly between the wheel flange and the rail, as a result of yawing motion of the wheelset. When this contact occurs in front of the lateral axis of the wheel, it is deemed a lead contact and when behind this axis it is a lag contact. Some models have made a case for the use of these lead and lag contacts (Shabana et al., 2005), as shown in Figure 3.40. However, this thesis does not introduce this into the model, as it requires searching for contact across multiple planes given by the surface parameter S_{2W}. This is much more computationally expensive, and as the straight track reduces the amount of wheelset yawing, the contact outside of the vertical plane is ignored.

Despite modelling within this vertical plane, flange contact is still possible, and is calculated
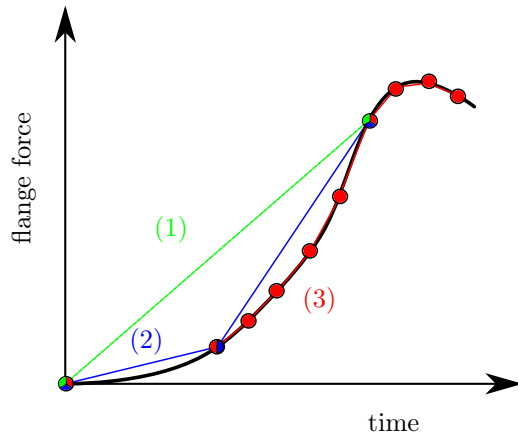
Figure 3.39: Modelling of the time step near flange contact
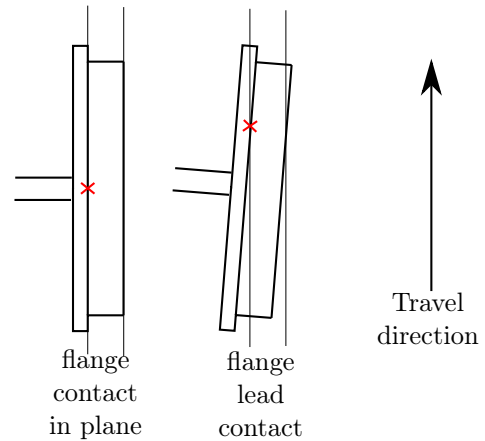
Figure 3.40: Flange contact when lag/lead contact is possible

in the same way as for the rest of the rail using the 'potential' regions (gutters) of possible contact. However, unlike contact between the normal running surfaces of the wheel and rail, the rate of change in penetration, and hence force, for contact between the wheel flange and the rail is much higher. This means that for the normal time step, a sudden increase in force, both laterally and vertically can occur. This problem creates computational errors due to the sudden increase of force, and hence this is resolved by reducing the time step when the force increment is too large until the increment in force is manageable. Figure 3.39 shows this problem. In the first time step (1) the increment in force is large. Hence, a smaller time increment is chosen (2), which leads initially to a sufficiently small increase in force. However, on the second iteration of this time increment, the force increases significantly. Hence, further refinement of the time step occurs (3), which proves to be sufficiently small, such that the incremental increase in force is manageable. The flange contact force variation with time is then satisfactorily represented. After the flange contact force reduces the time step is increased to the standard modelling time step. This is as the smaller time step is only used in the case of flange contact; when contact occurs elsewhere the time step is larger.

3.5.4   Normal Force

Once the parameters associated with the contact area are calculated, the normal force can be calculated. The normal force acts perpendicular to the contact surface of the rail and wheel as defined by a plane tangential to the contact point, as seen by the directions in Figure 3.41. Although there are different methods to calculate the normal force, as found in Section 2.4.3, the most commonly used and appropriate for elastic contact is the Hertz nonlinear method.
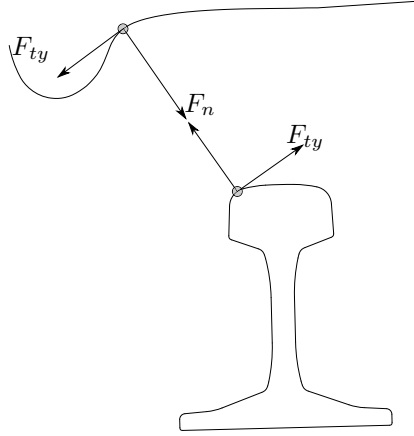
Figure 3.41: Direction of contact forces in wheel and rail

3.5.4.1 Hertz method

The nonlinear Hertz contact approach follows the method expressed in Section 2.4.3. The normal force is found by Equation 3.19.

$$F_{ne} = K_H \delta^{3/2} \tag{3.19}$$

The stiffness of the contact, K_H is then found by Antolín (2013):

$$K_H = \frac{2}{3} \left(\frac{E_{wr}}{(1 - \nu_{wr}^2)\, r^{\frac{3}{2}} K_{bpa}^{\frac{1}{2}}} \right) \tag{3.20}$$

where r is also defined as a function of θ_{wr} as in Section 3.5.3 and is found in Table 3.9. It is at this point that the calculation of the semi-axes of the contact ellipse (a_e and b_e, Equations 3.3 and 3.4), can be calculated, as it is required for the calculation of the tangential forces.

3.5.4.2 Normal damping

This wheel-rail interaction also includes a damping force acting in the normal direction (Magalhães et al., 2016). This helped provide computational stability to the model. This formulation makes use of the term $\dot{\delta}$, which is the rate of change of the penetration with respect to time. The normal damping force is found as:

$$F_{nd} = C_H \delta^{3/2} \tag{3.21}$$

where C_H is a function of the contact stiffness and the relative rate of penetration (Magalhães et al., 2016):

$$C_H = K_H \frac{3\left(1 - e_{res}^2\right)}{4} \frac{\dot{\delta}}{\dot{\delta}_0} \tag{3.22}$$

where e_{res} is the coefficient of restitution between the two materials, taken conservatively as 0.7 (Güttler et al., 2012). $\dot{\delta}_0$ is the rate of penetration between the two bodies when they first come into contact at that contact point. As a result, the overall normal force between the wheel and rail is found as:

$$F_n = F_{ne} + F_{nd} = (K_H + C_H)\,\delta^{\frac{3}{2}} \tag{3.23}$$

3.5.5 Tangential Forces

The last part of the WRI contact problem is the tangential force. This relies on the parameters of the contact ellipse dimensions defined by a_e and b_e and the normal force F_{ne} (excluding the damping force), to have been previously calculated within the contact problem. The choice of the contact model used is the most divisive part of the contact problem amongst previous literature (Section 2.4.4). The method chosen in this thesis is the heuristic approach outlined by (Shen et al., 1983; Shabana et al., 2007). This was chosen as it is computationally much quicker than FASTSIM (Kalker, 1982), the exact three-dimensional theory of rolling contact (Kalker, 1979), and more widely available than USETAB (Kalker, 1990). Finally, through the comparison of methods shown in Section 3.5.5.1, it is found to be more accurate than Kalker's linear and Polach's methods, with similar calculation times. It is comparable to the accuracy of FASTSIM (except when the spin creepage is high), but the calculation time of the heuristic method is much lower (Shabana et al., 2007; Shen et al., 1983; Kalker, 1991).

Through the heuristic method, the tangential forces (F_{tx} and F_{ty}) are calculated by firstly using Kalker's linear method, to calculate the unrestricted tangential forces ($\bar{F}_{tx}$ and $\bar{F}_{ty}$), which do not conform to Coulomb's friction law. This is shown in Equation 3.24:

$$\begin{bmatrix} \bar{F}_{tx} \\ \bar{F}_{ty} \end{bmatrix} = -G_{wr} a_e b_e \begin{bmatrix} c_{11} & 0 & 0 \\ 0 & c_{22} & \sqrt{a_e b_e} c_{23} \end{bmatrix} \begin{bmatrix} \zeta_x \\ \zeta_y \\ \phi \end{bmatrix} \tag{3.24}$$

Here, the coefficients c_{11}, c_{22} and c_{23} are so called Kalker coefficients, obtained from Table 3.10, as a function of the ratio of the ellipse semi axes dimensions (a_e and b_e) and the Poisson's ratio of the wheel and rail (ν_{wr}). G_{wr} is the shear modulus of the wheel and rail material, taken by the value of $83.3\,GPa$. ζ_x and ζ_y are the creepages in the longitudinal and lateral respective directions, and ϕ is the spin creepage about the perpendicular axes to the contact plane (for the definition see Section 2.4.4), as calculated through the vector Equations 3.25 to 3.27. These vector equations take into account all of the components of velocity at the contact point to convert into a creepage value.

$$\zeta_x = \frac{\dot{\mathbf{r}}^{\mathbf{w}} \mathbf{t}^{\mathbf{r}}_{\mathbf{x}}}{V} \tag{3.25}$$

$$\zeta_y = \frac{\dot{\mathbf{r}}^{\mathbf{w}} \mathbf{t}_{\mathbf{y}}^{\mathbf{r}}}{V} \qquad (3.26)$$

$$\phi = \frac{\dot{\mathbf{r}}^{\mathbf{w}} \mathbf{n}^{\mathbf{r}}}{V} \qquad (3.27)$$

Here, V is the forward velocity of the vehicle, $\dot{\mathbf{r}}^{\mathbf{w}}$ is a vector of the components of velocity of the contact point as defined in Equations 3.28 and 3.29, $\mathbf{t}_{\mathbf{x}}^{\mathbf{r}}$ is the longitudinal tangential direction vector to the contact patch, $\mathbf{t}_{\mathbf{y}}^{\mathbf{r}}$ the lateral tangential direction vector to the contact patch, and $\mathbf{n}^{\mathbf{r}}$ the directional vector of the normal to the contact patch (Equation 3.30). These directional vectors align with the longitudinal and lateral tangential force and the normal force respectively.

$$\dot{\mathbf{r}}^{\mathbf{w}} = \dot{\mathbf{R}}^{\mathbf{w}} + \dot{\omega}^{\mathbf{w}} \times \mathbf{u}_{\mathbf{cp}}^{\mathbf{w}} \qquad (3.28)$$

$$\begin{bmatrix} \dot{r}_x^w \\ \dot{r}_y^w \\ \dot{r}_z^w \end{bmatrix} = \begin{bmatrix} R_x^w \\ R_y^w \\ R_z^w \end{bmatrix} + \begin{bmatrix} \dot{\omega}_x^w \\ \dot{\omega}_y^w \\ \dot{\omega}_z^w \end{bmatrix} \times \begin{bmatrix} u_{x,cp}^w \\ u_{y,cp}^w \\ u_{z,cp}^w \end{bmatrix} \qquad (3.29)$$

$$\mathbf{t}_{\mathbf{x}}^{\mathbf{r}} = \begin{bmatrix} 1 \\ 0 \\ 0 \end{bmatrix} \qquad \mathbf{t}_{\mathbf{y}}^{\mathbf{r}} = \begin{bmatrix} 0 \\ \cos\theta_c \\ \sin\theta_c \end{bmatrix} \qquad \mathbf{n}_{\mathbf{y}}^{\mathbf{r}} = \begin{bmatrix} 0 \\ -\sin\theta_c \\ \cos\theta_c \end{bmatrix} \qquad (3.30)$$

Here, θ_c is the angle of the plane of the contact ellipse from the horizontal plane as shown in Figure 3.42. $\dot{\mathbf{R}}^{\mathbf{w}}$ is a directional vector of the velocities in the component directions of the centre of the wheelset, R_i^w, with i being the component direction (x, y, z). Similarly, $\dot{\omega}^{\mathbf{w}}$ is the vector of rotational velocities $\dot{\omega}_i^w$ at the centre of the wheelset, defined around each component axis (x, y, z), again represented by the subscript i. Finally, the vector $\mathbf{u}_{\mathbf{cp}}^{\mathbf{w}}$, assembles the distances $(u_{i,cp}^w)$ from the centre of the wheelset to the contact point in each component direction, based on the local coordinate system (X^W, Y^W, Z^W).

From the unrestricted tangential forces defined in Equation 3.24, modification is required to make the heuristic model conform to Coulomb's friction law. Firstly this requires the calculation of the total unrestricted tangential force $\bar{F}_t$:

$$\bar{F}_t = \sqrt{\left(\bar{F}_{tx}\right)^2 + \left(\bar{F}_{ty}\right)^2} \qquad (3.31)$$

The upper bound to the tangential force, based on Coloumb's friction law, is calculated by a function of the normal force (F_{ne}) and the coefficient of friction between the wheel and rail $(\mu$, taken as 0.2). This would only realistically be reached if the wheel was fully sliding along the rail without any rolling. Hence, Shen et al. (1983) proposes the following upper bound to
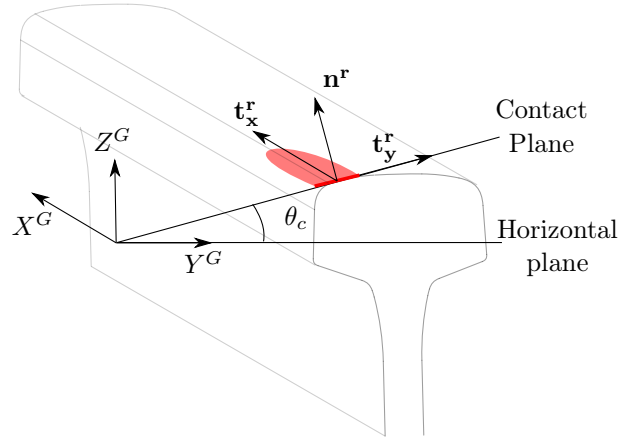
Figure 3.42: Directions of the tangential and normal vectors with respect to the contact patch, at an angle, θ_c to the horizontal plane, for the calculation of the creepages

$\nu_{wr} =$	c_{11}			c_{22}			c_{23}			$\nu_{wr} =$	c_{11}			c_{22}			c_{23}		
	0	0.25	0.5	0	0.25	0.5	0	0.25	0.5		0	0.25	0.5	0	0.25	0.5	0	0.25	0.5
a_e/b_e										b_e/a_e									
0.1	2.51	3.31	4.85	2.51	2.52	2.53	0.33	0.47	0.73	1.0	3.4	4.12	5.2	3.4	3.67	3.98	1.33	1.47	1.63
0.2	2.59	3.37	4.81	2.59	2.63	2.66	0.48	0.6	0.81	0.9	3.51	4.22	5.3	3.51	3.81	4.16	1.44	1.57	1.77
0.3	2.68	3.44	4.8	2.68	2.75	2.81	0.61	0.72	0.89	0.8	3.65	4.36	5.42	3.65	3.99	4.39	1.58	1.75	1.94
0.4	2.78	3.53	4.82	2.78	2.88	2.98	0.72	0.82	0.98	0.7	3.82	4.54	5.58	3.82	4.21	4.67	1.76	1.95	2.18
0.5	2.88	3.62	4.83	2.88	3.01	3.14	0.83	0.93	1.07	0.6	4.06	4.78	5.8	4.06	4.5	5.04	2.01	2.23	2.5
0.6	2.98	3.72	4.91	2.98	3.14	3.31	0.93	1.03	1.18	0.5	4.37	5.1	6.11	4.37	4.9	5.56	2.35	2.62	2.96
0.7	3.09	3.81	4.97	3.09	3.28	3.48	1.03	1.14	1.29	0.4	4.84	5.57	6.57	4.84	5.48	6.31	2.88	3.24	3.7
0.8	3.19	3.91	5.05	3.19	3.41	3.65	1.13	1.25	1.4	0.3	5.57	6.34	7.34	5.57	6.4	7.51	3.79	4.32	5.01
0.9	3.29	4.01	5.12	3.29	3.54	3.82	1.23	1.36	1.51	0.2	6.96	7.78	8.82	6.96	8.14	9.79	5.72	6.63	7.89
										0.1	10.7	11.7	12.9	10.7	12.8	16.0	12.2	14.6	18.0

Table 3.10: Creepage coefficient values of c_{11}, c_{22} and c_{23} as a function of a_e, b_e and ν_{wr} (Kalker, 1990)

the tangential force ($F_{t,u}$):

$$F_{t,u} = \begin{cases} \mu F_{ne} \left[\left(\frac{\bar{F}_t}{\mu F_{ne}} \right) - \frac{1}{3} \left(\frac{\bar{F}_t}{\mu F_{ne}} \right)^2 + \frac{1}{27} \left(\frac{\bar{F}_t}{\mu F_{ne}} \right)^3 \right], & \bar{F}_t \leqslant 3\mu F_{ne} \\ \mu F_{ne}, & \bar{F}_t > 3\mu F_{ne} \end{cases} \tag{3.32}$$

From the upper bound tangential force magnitude ($F_{t,u}$), the tangential force from the heuristic method, complying to Coulomb's law, can be calculated in the longitudinal (F_{tx}) and tangential (F_{ty}) directions:

$$\begin{bmatrix} F_{tx} \\ F_{ty} \end{bmatrix} = \frac{F_{t,u}}{\bar{F}_t} \begin{bmatrix} \bar{F}_{tx} \\ \bar{F}_{ty} \end{bmatrix} \tag{3.33}$$

This ends the process of calculating the wheel rail contact problem. The normal and tangential forces are calculated individually for each contact patch, and they are calculated within the User Defined Element of ABAQUS (Dassault Systèmes SIMULIA Corp., 2014), as expressed in Section 3.5.7.
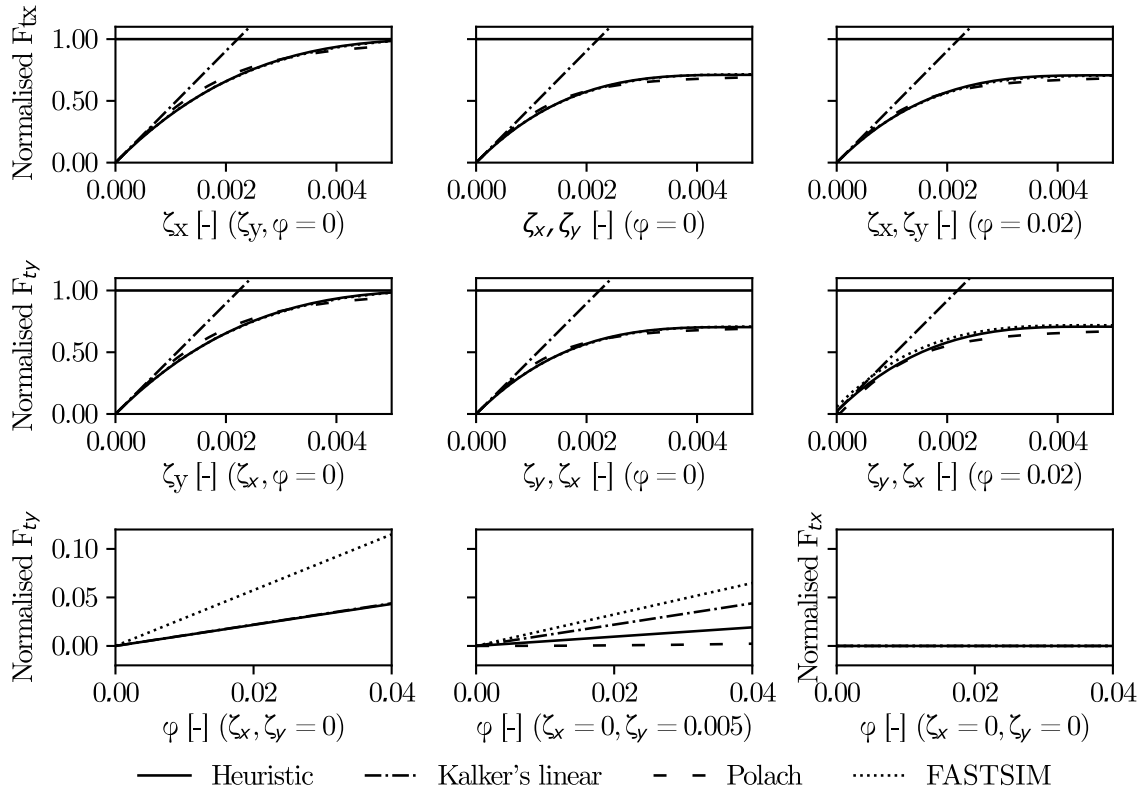
Figure 3.43: Comparison of tangent models, showing the tangential forces F_{tx} and F_{ty} normalised with respect to the maximum possible tangential force given by Coulombs friction law (νF_{ne}). These forces are varied through different creepage combination values, as defined under the x axis of each graph.

3.5.5.1 Comparison of Tangential Models

To decide on the appropriate tangential model to use in this thesis, a comparison of some of the available methods were made. The chosen heuristic method was compared to Kalker's simplified method (FASTSIM) (Kalker, 1982), Polach's method (Polach, 1999) and Kalker's linear method (Kalker, 1967). Other possible methods such as USETAB and the exact three dimensional theory (CONTACT) were unable to be obtained. FASTSIM is thereby the most accurate method compared. The lateral and longitudinal tangential forces are shown for the different models in Figure 3.43, for a range of combinations of creepage values (as defined on the x axis of each graph). The tangential forces were calculated using a given normal force ($F_{ne} = 80\,kN$), and ellipse semi axes (a_e and b_e of $6.6\,mm$ and $2.5\,mm$ respectively). These values were chosen based on a simulation of a train vehicle on the bridge, using the resulting average ellipse size and force over time. Under this simulation the creepage values between the wheel and rail were recorded and averages of 0.48×10^{-3}, 0.093×10^{-3} and 0.028 were found for the values of ζ_x, ζ_y and ϕ respectively. These averages were used to define the range of creepage values that the tangential forces were calculated over in Figure 3.43.

As can be seen from the comparison in Figure 3.43, Kalker's linear approach is very inaccurate for creepages larger than 0.001. It also shows that Polach's method, the FASTSIM method and the heuristic approach generally produce similar results, although the results produced by the heuristic approach are much closer to the FASTSIM method. In cases of low or no spin creepage, the FASTSIM and heuristic approaches are indiscernible. When the spin creepage is large and the other creepages small, there are large differences between the models.

In the case of the FASTSIM method, computational times were found to be between two and four times longer than the times required for the Polach, Linear and heuristic approaches (which had similar computational calculation times). Considering the computational time and the small difference in the tangential forces when considering a representative combination of creepages, ellipse dimensions and normal force, justification of using the heuristic model in this thesis is made.

3.5.6 Irregularities

The irregularities used in this thesis come from the definitions of the German Rail Spectrum of Low Irregularity as set out by Li et al. (2005). This is a power spectral density function method, utilising the combination of sinusoidal components to generate an irregularity profile. It uses the spectral representation method, as follows, to convert the PSD into a spatial domain:

$$r(x) = \sqrt{2} \sum_{n=1}^{N} A_n \cos(\omega_n x + \psi_n), \qquad (3.34)$$

where $r(x)$ is the irregularity value at longitudinal rail coordinate x, ψ_n is a random phase angle for the nth spatial frequency and ω_n is the spatial frequency of the nth sinusoidal component of the irregularity (units: m^{-1}).

$$\omega_n = \omega_l + (n - 0.5)\,\Delta\omega \qquad (3.35)$$

where $\Delta\omega = (\omega_u - \omega_l)\,/N$, ω_u and ω_l refer to the upper and lower spatial frequencies considered for the irregularity profile and N is the total number of frequencies considered.

The value of A_n which is the amplitude of the sinusoidal irregularity component comes from:

$$A_n = \sqrt{2S\left(\omega_n\right)\Delta\omega} \qquad (3.36)$$

where $S\left(\omega_n\right)$ depends on the irregularity such that:

$$\text{Alignment irregularity:} \quad S\left(\omega_n\right) = \frac{A_a\omega_c^2}{\left(\omega_n^2 + \omega_r^2\right)\left(\omega_n^2 + \omega_c^2\right)} \qquad (3.37)$$

$$\text{Vertical irregularity:} \quad S\left(\omega_n\right) = \frac{A_v\omega_c^2}{\left(\omega_n^2 + \omega_r^2\right)\left(\omega_n^2 + \omega_c^2\right)} \qquad (3.38)$$

$$\text{Cross-Level irregularity:} \quad S\left(\omega_n\right) = \frac{\left(A_v/b_0^2\right)\omega_n^2\omega_c^2}{\left(\omega_n^2 + \omega_r^2\right)\left(\omega_n^2 + \omega_c^2\right)\left(\omega_n^2 + \omega_s^2\right)} \tag{3.39}$$

where b_0 is half the wheelset width ($b_0 = 0.75\,m$), and the parameters A_a and A_v relate to the track quality (equal to 2.19×10^{-7} and $4.032 \times 10^{-7}\,m\,rad$ respectively). The values of ω_s, ω_r and ω_c are 0.4380, 0.0206 and 0.8246 rad/m respectively.

This irregularity generating method was chosen after the findings of the literature review in Section 2.5, making use of the German high speed irregularity spectra. Again, gauge irregularities have little effect. Hence, only the cross-level, vertical and alignment irregularities are used in this thesis.

As found in Cantero et al. (2016), the bridge response is affected more by the irregularities in the D1 range of $3-25\,m$ (BS EN 13848-5:2017, 2017). The higher wavelengths were previously found to impact more on the vehicle accelerations. Hence, irregularities of the D1 wavelength range were the only ones modelled in this thesis (between 3 and 25 m). Longer wavelengths would be in the range of the bridge span and due to the small affect they supposedly have on vehicle and bridge dynamics, they have been ignored.

The irregularities are precalculated using by using predetermined random phase angles in the calculation. Each irregularity, along with its moving mean and standard deviations (both based over a length of 200 m) are plotted in Figure 3.44. Due to guidelines referencing the rate of twist, this has been plotted as a derivation of the cross level irregularity. The mean value is not necessarily zero as the profiles are adjusted to remove an initial discontinuous change in the running surface.

The peak to mean limits for the alignment, twist and vertical irregularities are shown as the Alert Limit (AL) for speeds between 300 and 360 km/h, as mentioned in Section 2.5.4. The standard deviation limits are the AL for speeds up to 300 km/h, as higher speeds and other limits are not given. It can be seen from Figure 3.44, that all the irregularities have reasonable variation in the mean to peak values. For the standard deviation, it can be seen that the variation is slightly higher than the limits, but as this is only the AL there could be further deterioration before fixing, justifying this additional variation in these irregularities. Comparison of the chosen vertical profile is shown, compared to the variation generated by 100 different sets of random phase angles in Figure 3.45. By taking the peak maximum and minimum values of each variation of the irregularity, the median maximum and minimum are calculated and plotted by the 50% lines. The chosen profile has a peak maximum and minimum elevation that is fairly consistent with these median values. This shows that the chosen profile is representative of the variation that different phase angles can introduce.

Seven combinations of irregularities have been created. These are compiled in Table 3.11. Each of the components of irregularity have been isolated and then combined into *Combined set 1*. This allows comparison and determination of the effects of each component. Then a
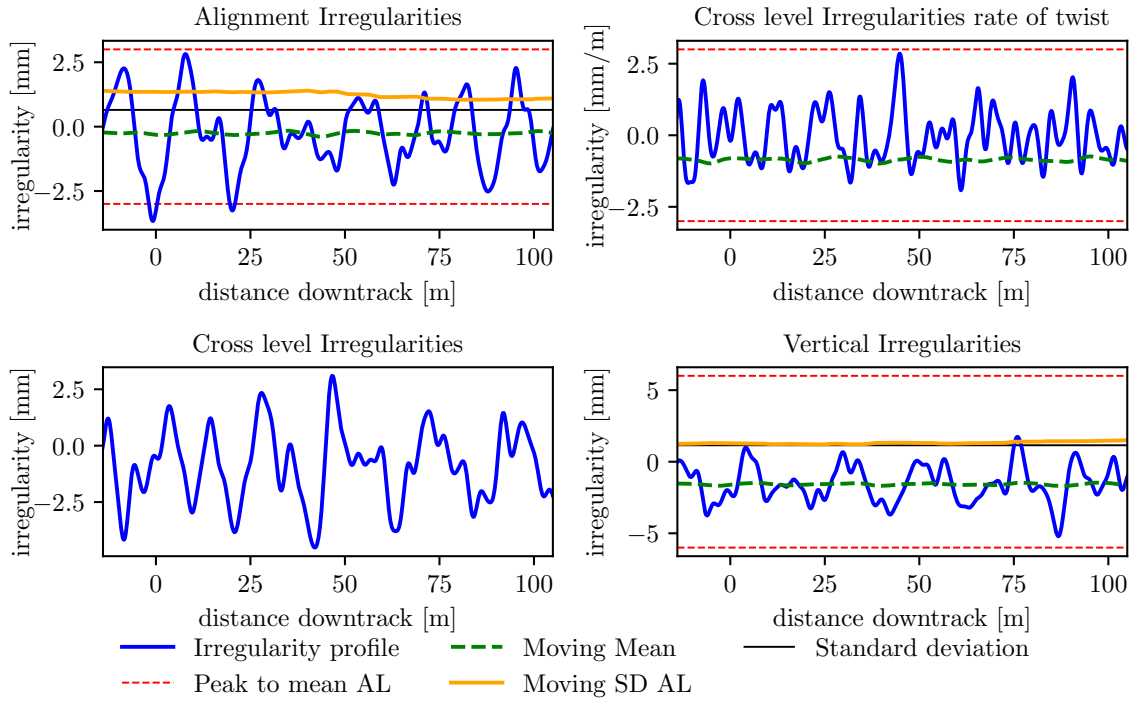
Figure 3.44: Comparison of a chosen irregularity profile case with the limits in BS EN 13848-5:2017 (2017); BS EN 13848-6:2014 (2014). Also showing the moving mean and standard deviations (SD) of the irregularity profile based on the length 100 m
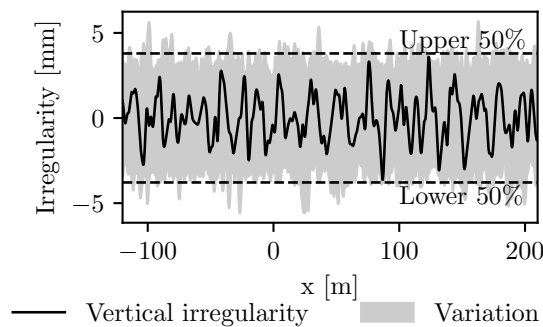
Figure 3.45: Vertical irregularity profile shown against variation caused by different phase angles on the irregularity profile. Comparison is made to the median of the maximum (upper 50%) and minimum (lower 50%) peak values of the profiles with different phase angles

Irregularity model	Alignment	Cross-level	Vertical
None			
Alignment only	(1)		
Cross Level only		(1)	
Vertical only			(1)
Combined set 1	(1)	(1)	(1)
Combined set 2	(2)	(2)	(2)
Combined set 3	(3)	(3)	(3)

Table 3.11: The irregularity combinations. (1) represents the values generated by Li et al. (2005); (2) is the same as (1) but with different phase angles; (3) represents the same phase angles as (1) but the amplitudes are doubled. Blank cells indicate this form of irregularity is not included in this set.
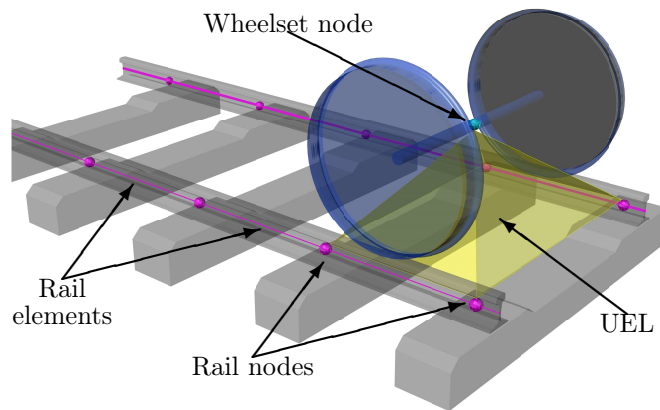
Figure 3.46: Three dimensional representation of the UEL, showing the rail nodes as pink spheres and the wheelset node as the blue sphere

comparison of the combined sets are made, comparing a different set of random phase angles (ψ_n) for *Combined set 2* and then double the component amplitudes (A_a and A_v) in *Combined set 3*.

In this thesis, apart from where specified otherwise, models using irregularities will be making use of *Combined Set 1*. This may only be noted as *with irregularities*, rather than specifying the specific set.

3.5.7 Modelling

Modelling of the wheel rail interaction used the capabilities of the 'User Defined Element' (UEL) subroutine of ABAQUS (Dassault Systèmes SIMULIA Corp., 2014), as previously suggested as a solution by Antolín (2013) and Antolín et al. (2013). It enables the forces to be transmitted to nodes of the element based on the relative position of the nodes.

Each element consisted of five nodes, one for the centre of the wheelset and four for the rail, as
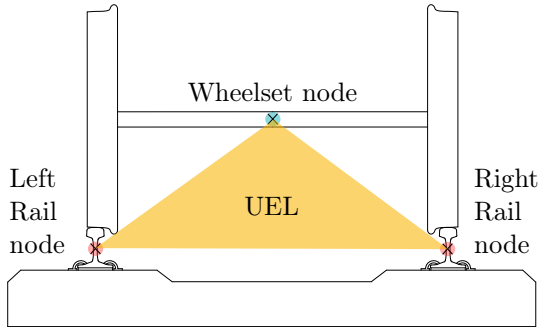
Figure 3.47: Two dimensional representation of UEL
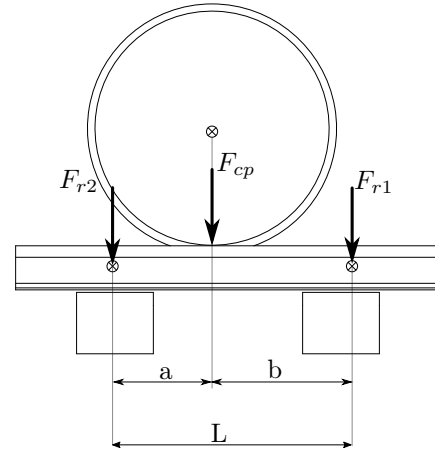
Figure 3.48: Distribution of force between two rail nodes when contact point is between them

shown in Figure 3.46. A three noded UEL (Figure 3.47), with all three nodes moving forwards with the train, created modelling problems. This is due to this method requiring the use of surface interaction between a node and a surface, which did not transfer the horizontal forces from the wheel into the rail. By using five nodes the user element directly connects to the rail nodes, removing the problematic surface interaction.

The UEL is encoded in the computing language Fortran, to convert the position of the rail and wheel nodes into forces generated through pre-described wheel-rail interaction method. The forces are converted to the global coordinate system, X^G, Y^G and Z^G. This is used to create a local force vector and local stiffness matrix which are input to the global force vector and global stiffness matrix by ABAQUS, which then is solved to find the displacements. In the UEL chosen, the UEL is only active when the wheel node is located between the rail nodes of the element. The force, located at the contact point, is distributed to the activated rail nodes as in Figure 3.48, and Equations 3.40 and 3.41 (Antolín, 2013). To model the whole length of track, each longitudinal pair of rail nodes for the left and right rails has a UEL connected with each wheelset of the train. Deactivation of some of the UEL elements occurs when they are not of significance, improving computational times.

$$F_{r2} = F_{cp} \cdot b/L \tag{3.40}$$

$$F_{r1} = F_{cp} \cdot a/L \tag{3.41}$$

The use of this user element for a train of eight carriages, on the three spanned benchmark bridge when including irregularities leads to a computational time to model the train to cross the vehicle of between 32 and 36 hours. By contrast, the same bridge modelled using moving point load models will take between 1 and 1.5 hours to complete a simulation. This shows the very significant computational times associated with using this model.

3.6 Conclusions to the Methodology

This chapter has focused on the general methodology used in this thesis. The chapter identified a benchmark bridge, the double U-beam bridge, for studies in the following chapters. A detailed modelling approach to the bridge was given, with justification made for the choice of element type, mesh size, diaphragm connections and the filtering of the bridge accelerations. It was identified that the Siemens Velaro vehicle was the most appropriate real train to model in this thesis due to the completeness of the model data in existing literature. The approach to modelling it was also identified for the finite element program ABAQUS. Two different track models were shown, one for the ballast and one for the slab track. These models will be compared in the following chapter.

The majority of the chapter focused on the methodology behind the wheel rail contact. The approach followed an elastic normal contact formulation, using a heuristic tangential contact method. Problems whilst modelling were identified in order to aide future researchers with the development of their model. The standard irregularities used in this thesis, in conjunction with the wheel rail contact, where also identified and found to be suitable in comparison with the current maintenance limits. The chapter finishes by identifying the method used to incorporate the wheel-rail interaction into the finite element software, by using a UEL.

Chapter 4

Models for the Dynamic Analysis of HSR bridges

This chapter tests the models used in this thesis, comparing coefficients to determine their sensitivity, and testing assumptions. This allows confidence in the models carried forward to the parametric analysis. The models presented in this thesis incorporate some of the most complicated models in the literature, used for different subsystems and that have not been found to have been used together before. Through establishing which models are unnecessary, due to negligible effects on the response parameters that are important for this study, helps to increase computational efficiency by using simpler models.

4.1   Bridge Model

This section tests the models associated with the bridge. The bridge considered herein is the dual U-beam bridge with three $35\,m$ spans (unless otherwise stated), as described in Section 3.1.2.

4.1.1   Slab Accelerations

With vertical accelerations often being design critical, determining where these accelerations are highest, within the region of interest on the slab, is key to efficient modelling. For the vertical accelerations, Figure 4.1 shows the maximum filtered (according to Section 3.1.3) acceleration found at each location on the slab. As established in Section 3.3, the train is moving in the positive x direction, and in this case along the track positioned in the positive y coordinates. The highest accelerations are along the edges of the slab. However, this area is beyond the extent of the track systems for both slab track and ballasted track, for which the
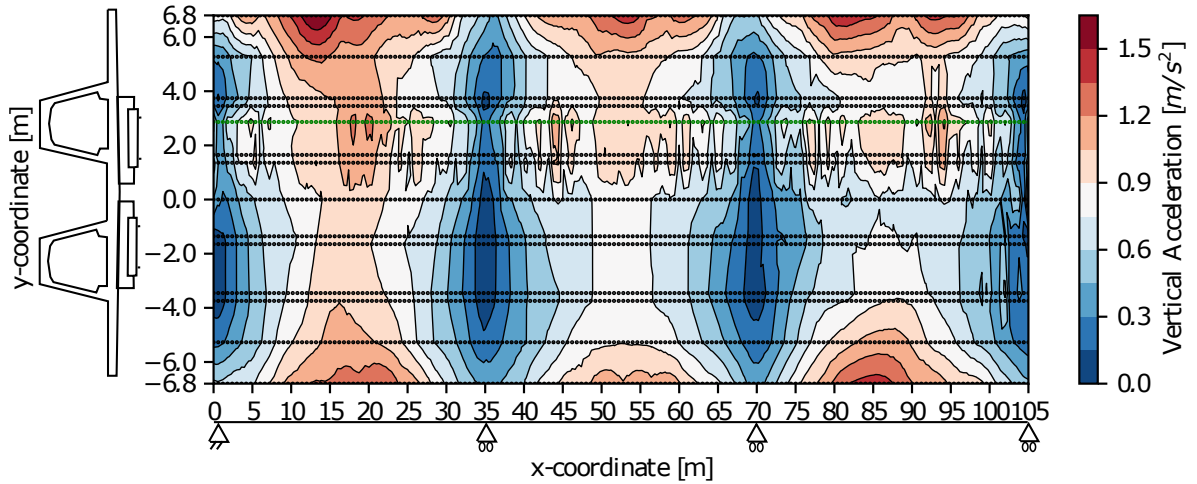
Figure 4.1: Filtered maximum vertical acceleration contour plot across the slab for a single train running on slab track, with vehicle moving left to right as explained in Section 3.3
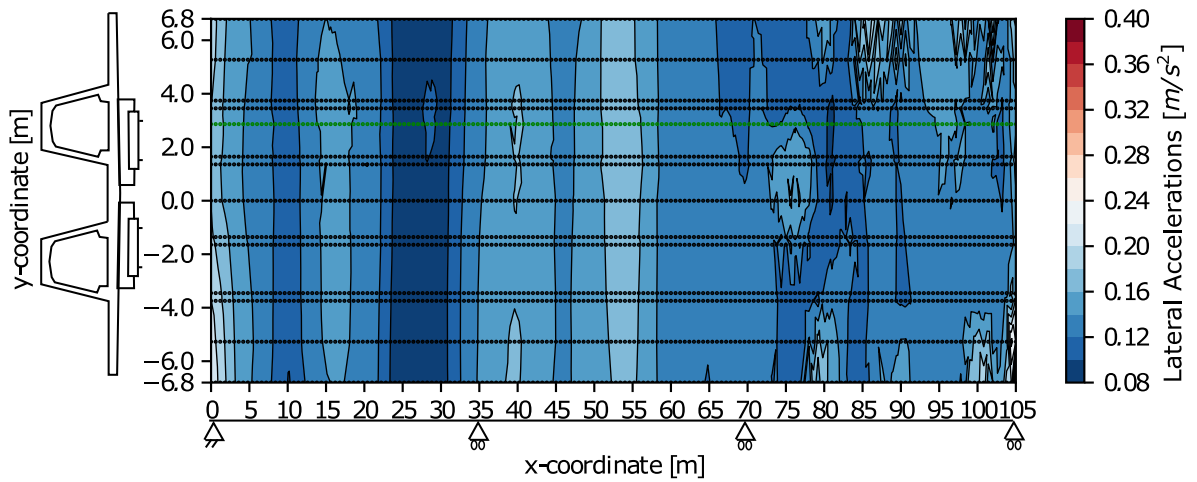
Figure 4.2: Filtered maximum lateral acceleration contour plot across the slab for a single train running on the track

acceleration limits prescribed in BS EN 1991-2:2003 (2010) are intended. Hence, the highest set of accelerations within in the applicable area on the slab is at the centre of the beam. This is coincidentally the set of nodes that correspond to those underneath the track.

Henceforth, the bridge accelerations will be taken and compared from the line of nodes in the slab below the track, as highlighted by the green nodes in Figure 4.1. Consideration of the lateral accelerations (Figure 4.2) shows little difference across the lateral direction, enabling the same line of nodes identified before (green line) to be used as representative values for both vertical and lateral accelerations. In the case where two trains are running in opposing directions, the maximum filtered vertical accelerations at the edges of the slab are even more pronounced (Figure 4.3). Within the confines of the track, local peaks can be found along the line of nodes highlighted by green and yellow. Therefore, these two lines of nodes shall be compared for determining the maximum acceleration in the slab when running two vehicles.
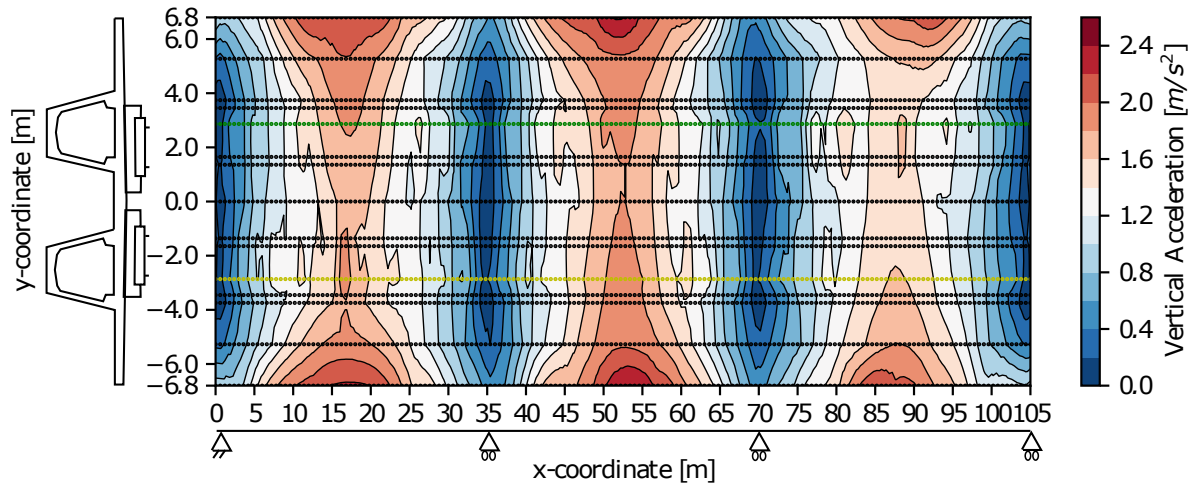
Figure 4.3: Filtered maximum vertical acceleration contour plot across the slab for two trains running in opposite directions on slab track (for the positive-y track, train is travelling in the positive x direction; for the negative-y track, train is travelling in the negative x direction).
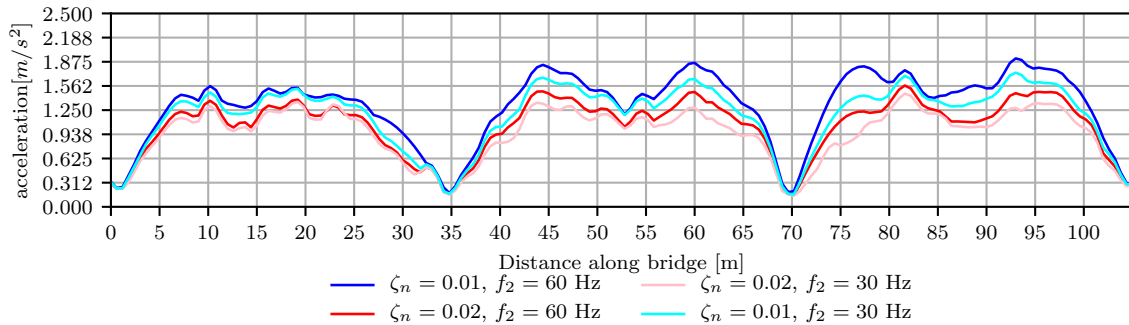
Figure 4.4: Comparison filtered vertical accelerations along the length of bridge with different damping properties, for velocity of $360\,km/h$

4.1.2 Comparison of Damping Coefficients

As established in Section 3.1.4, Rayleigh damping is used in this model. The effects of changing the damping coefficient (between damping ratios of 1 and 2%) and the frequencies which define the Rayleigh curve (30 and 60 Hz) are investigated herein.

The results seen in Figure 4.4 show that 1% damping, as expected yields larger accelerations than 2%. This highlights the importance of selecting the correct damping coefficients and not overestimating them. Hence, as per BS EN 1991-2:2003 (2010), 1% shall be used as to not over-damp the system. Likewise, increasing the second frequency point for the Rayleigh coefficients, from 30 to 60 Hz, increases accelerations experienced by up to 20%. This is as expected, and for conservative design, this bridge is assigned Rayleigh coefficients calculated with a second frequency at 60 Hz.
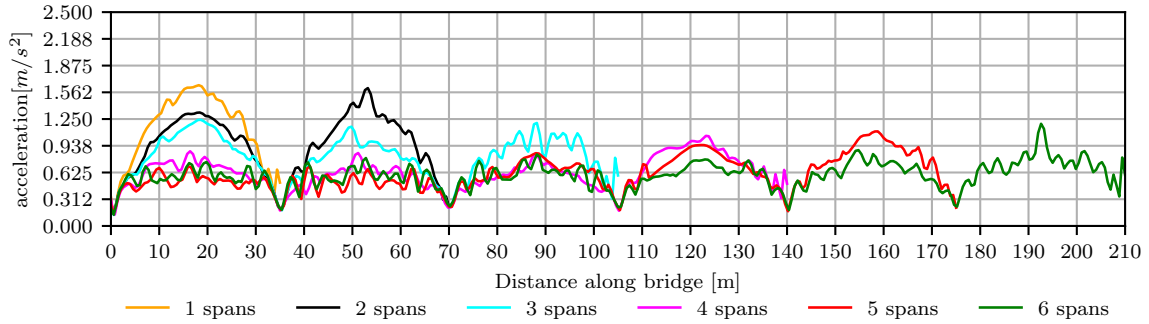
Figure 4.5: Variation in the filtered vertical acceleration along the length of the track at $360\,km/h$ for different numbers of spans

Number of spans	1	2	3	4	5	6
Frequency $[Hz]$	3.94	3.84	3.78	3.67	3.44	3.10

Table 4.1: Comparison of the frequency of the fundamental vertical bridge mode frequency with number of spans

4.1.3 Number of Spans

Although the chosen bridge is three spanned, comparison is made to the impact of the number of spans on the maximum filtered vertical bridge accelerations, as seen in Figure 4.5. Comparison of the vertical acceleration along the length of the bridge for each number of spans, with the first pier considered fixed (i.e. restraining movements in the longitudinal direction). In addition, the response under moving point load models is shown. As expected, the simply supported version (one span), yields the largest accelerations. The two spanned bridge actually yields similarly high results, particularly in the second span. For spans longer than two, the three span bridge actually forms a good approximation to the results in the other spans.

Whilst the previous figure focused on only $360\,km/h$ ($100\,m/s$), Figure 4.6, looks at the maximum filtered vertical acceleration along the length of the bridge with different velocities. Again the simply supported case results in the highest accelerations, followed by the two span case and then the following number of spans result in similar maximum accelerations. The one and two span cases show the most variation with velocity and this can be reflected in the natural frequencies shown in Table 4.1. The lower number of spans have higher fundamental frequencies, such that their critical resonant speeds are within the range of speeds investigated. Although the frequency of the fundamental mode decreases with increasing number of spans, the increasing number of spans results in multiple frequencies displaying similar modal shapes, some with similar frequencies to the fundamental modal frequency for the one span case. Only the first frequency value is shown. However, the reduction in the frequency is a result of both transverse deformations and as the boundary conditions are located at the base of the U-beams, not at the centre of mass. If modelled by beam elements, with boundary conditions applied at the centre of mass, the fundamental frequency will be identical between the number
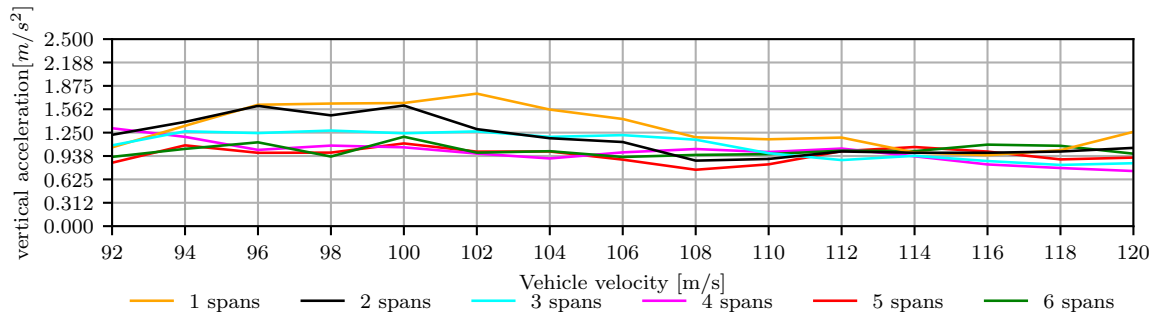
Figure 4.6: Variation in the maximum filtered vertical acceleration at any point in the length of the track for different velocities for different numbers of spans
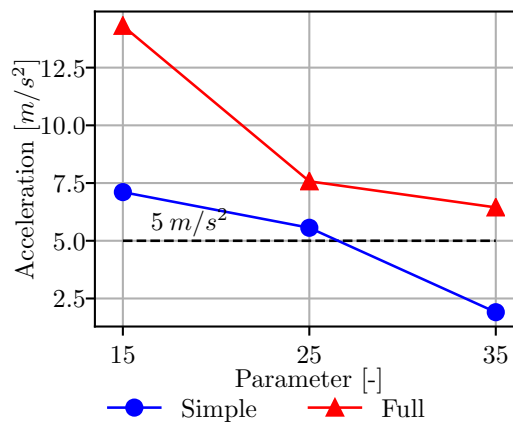
Figure 4.7: Variation of the maximum vertical filtered acceleration, for all velocities, found at any point along the length of the one spanned bridge, for different span lengths of the same L/14 slenderness.

of spans. The results here show that a three spanned bridge can be relatively representative of larger number of spans, although shifting of modal frequencies requires a range of speeds to be tested. In addition, one and two spanned bridges appear to show similar accelerations.

4.1.4   Comparison of Span Lengths

In this section, justification is sought to the choice of $35\,m$ as a span length. For this study, the use of a one span variation of the bridge model is used. The original slenderness of the U-beam is L/14. By maintaining this slenderness, whilst proportionally changing the span length, the thickness of the flanges, the height of the web and amount of prestress of the U-beam, to maintain this slenderness. As a result three spans are compared: 15, 25 and 35 m, as shown in Figure 4.7.

From Figure 4.7, it can be clearly seen that reducing the span length, whilst maintaining the

slenderness increases the accelerations. Due to changing frequencies of the bridge, in line with Section 3.1.3, the cut off frequency increases beyond 30 Hz for the smaller span lengths, to 36.5 and 50 Hz for 25 and 35 m spans respectively. These frequencies are necessary to include the contribution from the third bending mode, displaying three half sine waves per span. Hence, it is found to be appropriate to use the 35 m span. On the basis of longer spans having lower accelerations for the same slenderness, a case could be made to extend to longer spans such as 45 m. However, these longer spans then require more careful considerations for transportation, as this is either at the limit or exceeding the lengths possible for road transportation.

4.1.5   Comparison of Boundary Conditions

Following from Section 3.1.2.2, this section presents a comparison of the modelling approaches to boundary conditions. According to the design drawings (Laing O'Rourke, 2016), the three spanned bridge segment of the viaduct is longitudinally fixed at two points (both of the central piers). This is unusual in industry and hence a modified version is proposed, with only one longitudinally fixed point, at the beginning of the bridge segment (an abutment or a pier in the case of a long viaduct). In the case this point is an abutment, it allows better transfer of horizontal loads to foundations, resisting the high bending response initiated on the piers in the initial case. Alternatively, for a case where the studied bridge segment is in the middle of a viaduct, this will lead to the one fixed point to be a pier, which then requires a high bending capacity. However, the modified articulation allows for the central span to expand and contract more freely with shrinkage, creep and thermal variations. The comparison between articulations is made with both a tied and an elastic beam-slab connection (which is studied later in Section 4.1.7).

Firstly, using a tied beam-slab connection, the maximum filtered vertical accelerations generated by the two articulations, for a vehicle velocity of 360 km/h, is shown in Figure 4.8, using the full vehicle model with irregularities. Clearly, the case with one longitudinally fixed point results in higher accelerations, which is due to a greater resonant effect, because of matching of the bridge fundamental frequency and the loading frequency based on the vehicle velocity and axle spacing. The frequencies of the first three modes are shown in in Table 4.2. On the other hand, the lateral accelerations are found to be higher for two fixed points (Figure 4.9). Nonetheless, these accelerations are less of a concern for bridge design as they are lower and less safety-constrained, with no limits found in BS EN 1991-2:2003 (2010).

Secondly, study of the boundary conditions using an elastic beam-slab connection, shows different results (Figure 4.10). The change in beam-slab connection also changes the bridge frequencies, leading to larger vertical accelerations in the case when longitudinally fixed in two locations. The change in frequencies means that the fundamental frequency is no longer resonant for the case of one longitudinally fixed point. Due to the more realistic articulation including only one fixed point, which is used for the remainder of this thesis, but the results
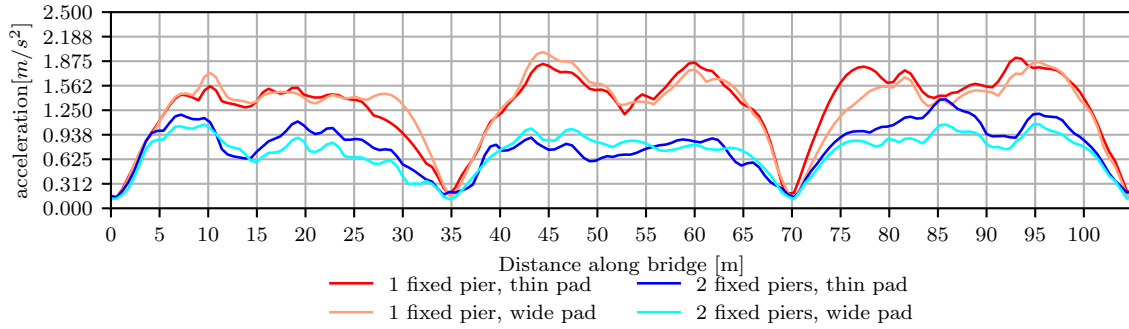
Figure 4.8: Comparison of the effects of different types of articulations and boundary condition lengths on the maximum filtered vertical bridge accelerations along the length of the bridge for a tied slab-beam connection, for a vehicle velocity of $360\,km/h$
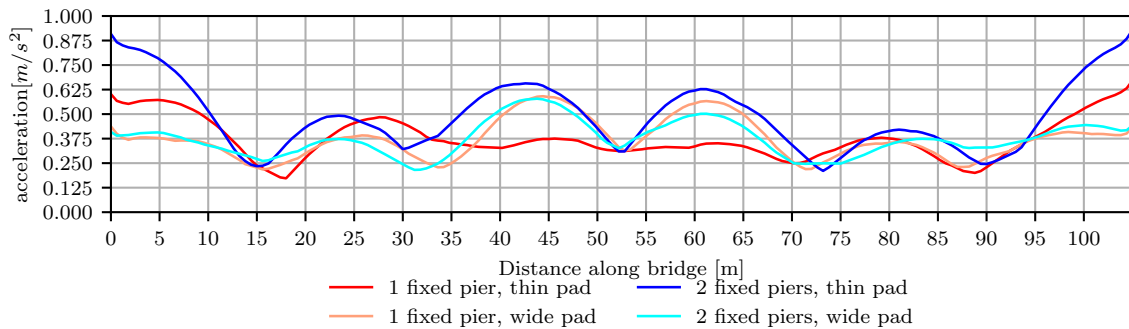
Figure 4.9: Comparison of the effects of different types of articulations and boundary condition lengths on the lateral bridge accelerations along the length of the bridge, for a vehicle velocity of $360\,km/h$

show the high sensitivity of the results to the boundary conditions and resonant effects.

In addition to comparing the type of articulation, the width of the bearing pad is compared. The difference in the vertical accelerations is small, but slightly higher with the thinner pad (Figure 4.8). In contrast, when studying the lateral accelerations (Figure 4.9), the reduction in the width of the pad results in greater variation in the lateral accelerations, with neither showing dominantly higher lateral accelerations. Hence, the smaller pads are chosen as they were modelled at a more realistic width of $0.8\,m$.

4.1.5.1 Comparison of the Location of the Fixed Point

A comparison here is made to study the impact of the location of the longitudinally fixed pier, for a three spanned bridge segment within a viaduct. This concurrently displays the impact of changing the running direction of the vehicle on the bridge dynamics (if the fourth pier is fixed that is akin to the first fixed but with the vehicle running in the opposite direction). This can be seen in Figure 4.11.
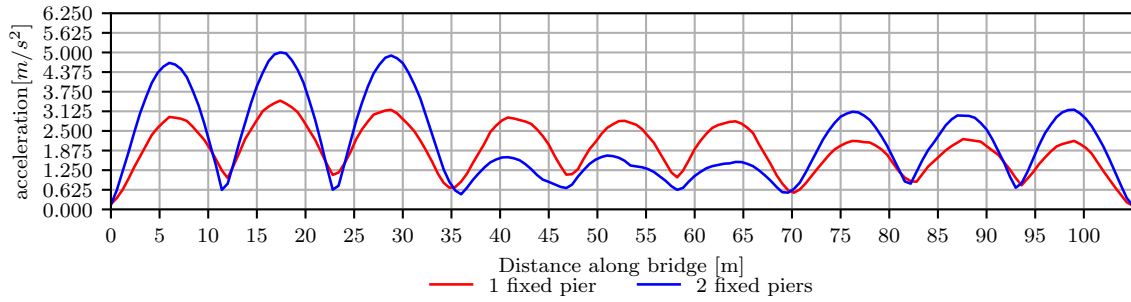
Figure 4.10: Comparison of the effects of different types of articulations on the maximum filtered vertical bridge accelerations along the length of the bridge for an elastic slab-beam connection, for a vehicle velocity of 360 km/h

Mode	Shape	Tied slab		Elastic slab	
		1 Fixed	2 Fixed	1 Fixed	2 Fixed
1		4.04	4.90	3.79	4.58
2		4.88	5.04	4.49	4.66
3		6.45	6.92	5.88	6.18

Table 4.2: Comparison of the natural frequencies of the bridge for different boundary conditions. Tied and elastic slab refer to Section, 4.1.7. 1 Fixed and 2 Fixed refer to the number of longitudinally fixed boundary conditions for the different articulations explained in Section 3.1.2.2.
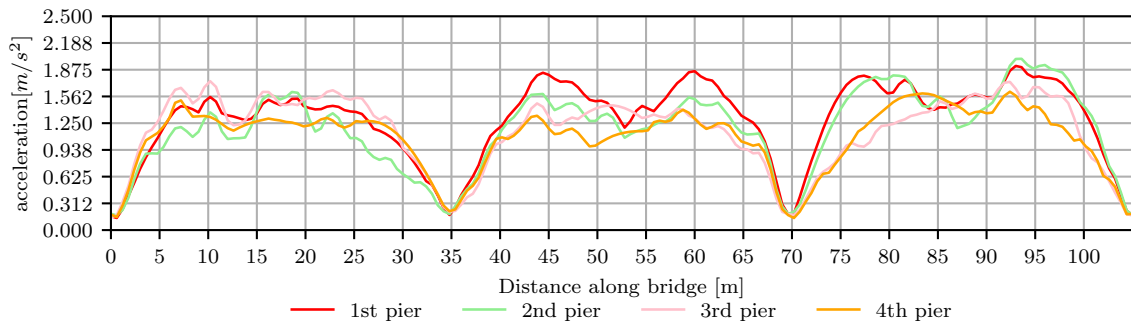
Figure 4.11: Comparison of the impact of changing the pier that is fixed on the filtered vertical accelerations, for a train velocity of 360 km/h

From Figure 4.11, it can be seen that there is no significant increase in the accelerations by fixing other piers. It appears that having the last pier fixed results in slightly lower accelerations and that having the first pier fixed results in generally higher values. Fixing the second pier results in similar results to fixing the first pier. As a result, the fixing of the first pier is appropriate for continuation of studies. This is also more realistic of the solutions used in practice, for occasions when the bridge segment is connected to an abutment. In this case, the the deck is prestressed against the abutment, to resist horizontal braking and acceleration forces.

4.1.5.2   Support motion

Over the support, as seen in Figure 4.9, the lateral accelerations are not zero, nor a minimum as would be expected. This is despite lateral constraints being enforced on the bridge at every support location. However, the constraints are only imposed at the base of the U-beams, to mimic a built structure, where there may not be an abutment to connect to at the end of the span. As a result, a comparison of the lateral accelerations and deflections over the first support is made in Figure 4.12.

From Figure 4.12b, it can be seen that the maximum filtered accelerations in the slab are relatively constant at about $0.6 \, m/s^2$. This could be a concern as to the lateral stability of the train with derailment. However, the lateral displacements, as seen in Figure 4.12a, are small compared to lateral rail irregularities and hence unlikely to cause derailment and hence are satisfactory.

4.1.6   Prestress Comparison

Following from Section 3.1.2.4, where the methodology on the prestress was outlined, this section will outline a comparison of the impacts of different prestresses. This will involve comparing two time dependent sets of values of prestress, with a case where there is no prestress in the bridge.

The losses in the pre-stressing strands are calculated, taking into account the transition length at the anchorage, concrete elastic shortening, concrete shrinkage, concrete creep and steel relaxation. Two models are compared for this with stresses at 30 days and 70 years compared, due to the difference in the stresses resulting from concrete creep and shrinkage as well as steel relaxation. The calculation of the losses in stress is shown in Appendix E.

The effect on the accelerations would come from possible changes in frequency of the bridge and also possibly changes in the profile of the bridge creating changes to the track profile (although this would be managed in reality by track maintenance). However, It was found

(a) Maximum lateral displacements

(b) Maximum filtered lateral accelerations

Figure 4.12: Variation of the values of displacement/acceleration laterally with different locations in the cross section, with the vehicle passing over the right side of the cross section.

Figure 4.13: Influence of different prestress aged stresses on the bridge acceleration along the length of the bridge

(a) Influence of different prestress aged stresses on the vertical vehicle accelerations in the rear carriage with time

(b) Maximum vertical vehicle acceleration in each carriage compared against prestress force age

Figure 4.14: Comparison of the impact of prestress ages on carriage vertical accelerations for vehicle travelling at $360\,km/h$

that the natural frequencies of the bridge did not change by more than 0.01% in all the cases of prestress. Through inspection of the maximum vertical accelerations along the length of the bridge in Figure 4.13, it is found that there is no discernible change by including the various prestressing forces. Therefore the prestressed forces do not have an effect in the dynamic response under traffic loading studied in this thesis, and therefore, there is not a need to be included in the models used to analyse this particular response, with the corresponding benefit of using simpler models. However, the prestressing strands, represented by the *REBAR* layer, does need to be included to include the stiffness and mass this material adds to the bridge. The only noticeable change of the various prestressing forces on the accelerations are found in the vehicle accelerations (Figure 4.14a), where the impact of the different forces on the vertical deformation of the bridge, impacts the vertical train accelerations. Figure 4.14b shows that consistently throughout the train the accelerations are higher in the vehicle when there is no prestress in the bridge.

4.1.7   Shear Connection

In real life, the connection between the bridge U-beam and the cast in-situ slab is realised through the bonding of concrete to protuding U-shaped reinforcement bars. In addition, the roughness of the concrete increases the amount of friction between the surfaces compared to concrete-steel interfaces of composite bridges. No existing literature was found on how to model this interaction between concrete surfaces in a simple manner, without introducing contacts or unsuitable solid elements, which would have complicated in turn a model which is already extremely computationally demanding. Therefore, this section makes a comparison between a full interaction and partial interaction at the interacting surface.

Modelling of the full interaction is achieved by a rigid tie between the contiguous surfaces,
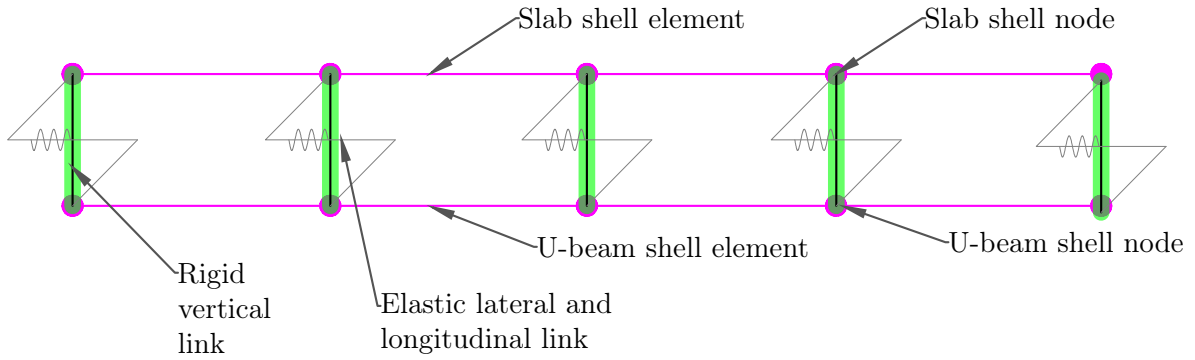
Figure 4.15: Connection representation of the slab shell elements to the beam shell elements at interface

which assumes no relative displacement between the two surfaces. Partial interaction allows some relative displacement, but limited by elastic forces representing the protruding rebar. In this section the partial interaction uses a model based on a steel beam - concrete slab connection realised through shear studs, as found in Turmo et al. (2015). Hence, it is likely an upper bound to the relative displacement, as it neglects surface friction and the full interacting strength of the protruding U-shaped bars, as the shape of the studs does not include the horizontal part of the U-shaped bars.

For the partial interaction model, each protruding U-shaped bar is assumed to be equivalent to two shear studs from the model by Turmo et al. (2015). Details for the number of protruding U-shaped bars are not given in the bridge design, so based on Turmo et al. (2015) it is assumed to be one U-shaped bar spaced at 0.3 m for each contiguous surface. As in Turmo et al. (2015) the vertical relative motion between the slab and beam is restrained, allowing for only longitudinal and lateral displacements. The stiffness of the connection is modelled as both laterally and longitudinally $170000\,kN/m$ per single vertical bar of the U-shape bars (shear studs in the aforementioned cited model). The value is not explained by how it is obtained, nor are the exact dimensions of the stud given, so it is not possible to convert the stiffness of the stud to a stiffness for the protruding U-shaped bars, however, the cross sectional areas of the shear studs and this U-shape reinforcement bars are comparable. Hence, the value is taken directly from Turmo et al. (2015). It is computationally modelled as in Figure 4.15, with springs being placed between adjacent nodes.

A comparison between the accelerations generated under moving point load models with full and partial interaction methods in Figure 4.16 shows that the partial interaction method increases the accelerations in general across the full length of the bridge. Comparing the different speeds with the different interaction methods as in Figure 4.17, shows a similar first peak around $97\,m/s$ ($349\,km/h$). However, the elastic method shows a secondary peak at or above $141\,m/s$ which is not reflected in the tied method. This is indicative of the additional mode activated around $141\,m/s$ having different frequencies between the elastic and tied methods. This is explained through the activation of bridge mode 30 with a frequency of 17.5
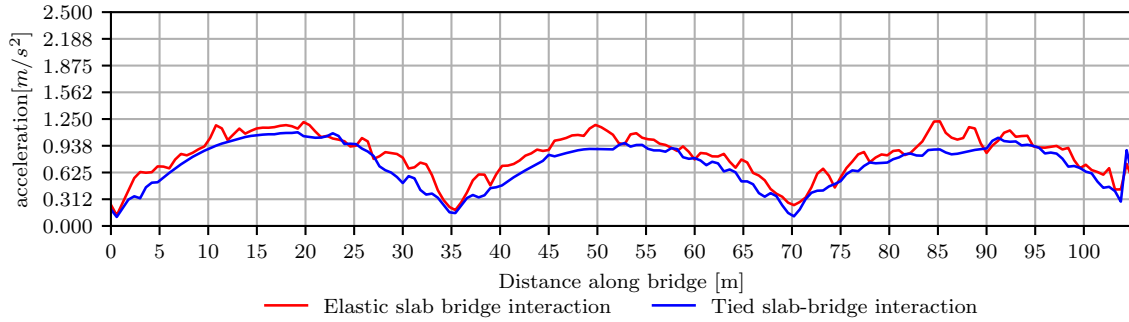
Figure 4.16: Comparison of vertical accelerations along length of bridge with different beam-slab interaction at 360 km/h
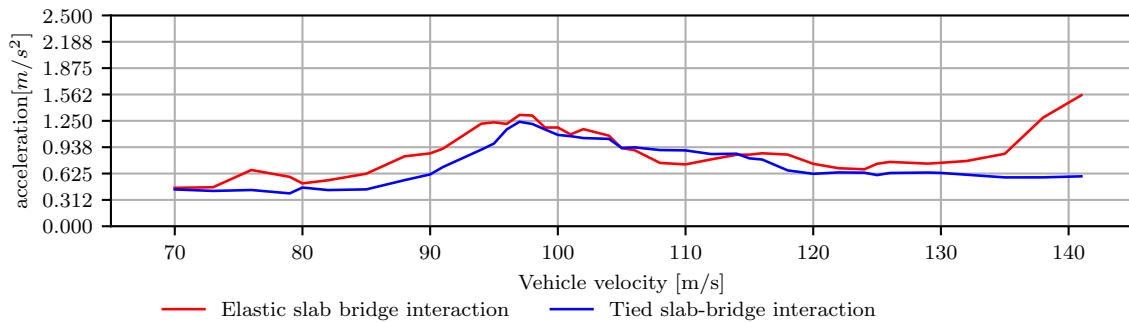
Figure 4.17: Comparison of vertical accelerations against velocity at $x = 17.5\,m$ with different beam-slab interaction

Hz as shown in Figure 4.18 (frequencies in Table 4.3). This is from the coinciding of a loading frequency and the bridge modal frequency for the elastic case. However, $141\,m/s$ ($508\,km/h$) is much larger than the design speed of the bridge ($120\,m/s$) and therefore is not needed to be considered in design.

Even though the elastic method results in slightly higher accelerations, the difference in the peak acceleration with velocities in the design range of speeds is small (about 4%). In addition, the elastic model is in fact the more computationally efficient model. The tied method has 50% longer computational times, hence, the shear connection between the slab and the beam will be modelled by the elastic method.

4.1.8   Bridge Validation

The comparison of the bridge model to real data was not possible in this thesis. This is as many current infrastructure owners deem this information sensitive and confidential, and monitoring costs may be high. Therefore comparison of the bridge models using shell and beam elements have been compared to identify whether they have similar responses, and deflections and moments checked against hand calculations to check for similar responses. In
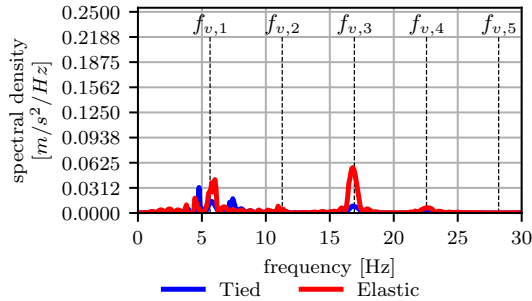
Figure 4.18: Comparison of vertical accelerations in the frequency domain for vehicle moving at $141 m/s$, for the elastic and tied slab-beam connection.

Mode	Shape	Elastic freq [Hz]	Tied freq [Hz]
1		3.79	4.04
2		4.48	4.88
3		5.88	6.45
15		11.66	13.18
30*		17.50	19.39
64		28.36	32.88

Table 4.3: Comparison of the bridge frequencies of the tied and elastic slab approaches (*) this has a similar mode shape but different flange displacements and amplitudes to mode 15

addition, the many components of the whole model (bridge, vehicle, track and interaction models), have been verified by the source authors. The sensitivity of the element size and element type was made in the methodology in Section 3.1.2.7. In addition to the element size, the time step size also needs to be validated, as is done in the following section.

4.1.8.1 Time Step Sensitivity

In order to model the dynamic response accurately, the time step needs to be appropriate. With element sizes longitudinally being 0.6 m, as determined by the sleeper spacing, a vehicle travelling at $100 \, m/s$ $(360 \, km/h)$ will move over that element in $6 \times 10^{-3} \, s$. Hence to make sure the load is transferred into the bridge at this location, the time step should be sufficiently smaller than this. In addition, with frequencies of $30 \, Hz$ needed to be recorded, this requires a time step of $6 \times 10^{-3} \, s$ to have at least 10 data points per cycle to accurately record the data. A comparison between the time step of $5 \times 10^{-4} \, s$ and $1 \times 10^{-4} \, s$ is made in Figure 4.19. This shows no difference in the filtered responses. Moreover, the time step cannot be larger than $5 \times 10^{-4} \, s$ as this creates computational instability for the user element to model the vehicle-track interaction, so this is the critical condition that determines the time step.
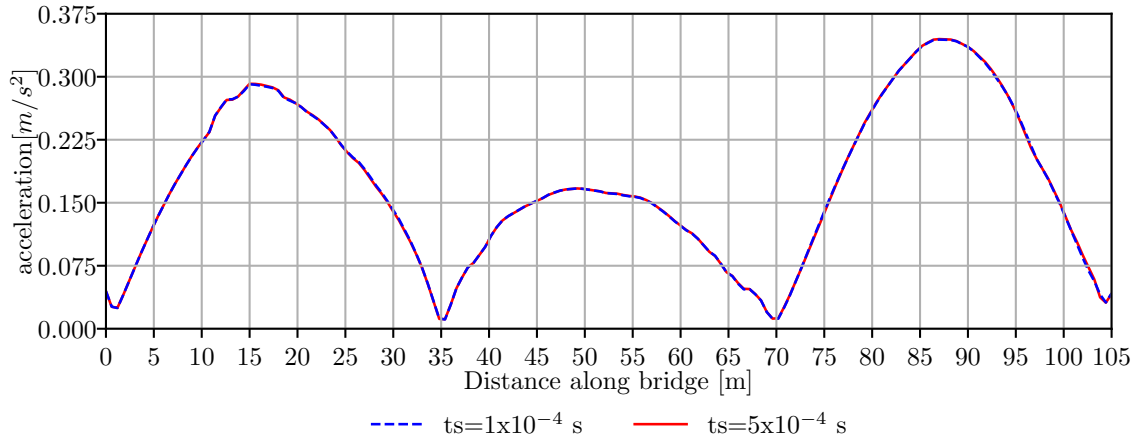
Figure 4.19: Comparison of the accelerations from different timesteps used for the dynamic analysis

Model	Elastic stiffness $[MN/m]$	Damping stiffness $[kN\,s/m]$
Upper Bound	500	75
Median	100	40
Lower Bound	60	15

Table 4.4: Variation of the properties of the railpad for the slab track models

4.2   Track Modelling Sensitivity

As identified in the literature review, Section 2.3, the track seemingly had more of an impact on the vehicle behaviour than the bridge, but still impacted the bridge dynamics. With the use of three dimensional shell models in this thesis, this section determines if these conclusions still agree. This section looks at the different variations considered for the models associated with the track.

4.2.1   Slab Track

Following the model outlined in Section 3.4.1, the stiffness and damping of the springs connecting the rail to the bridge are varied in the slab track model. This is to see the sensitivity to the stiffness and damping. The values are taken from the upper bound, lower bound and median of values found in literature (see Appendix B) and are shown in Table 4.4. These values refer to the railpad stiffness and in other parts of this chapter the median values are taken. The values given are those for the vertical direction. The lateral and longitudinal springs are considered to be 30% of this value as expressed in Vale and Calçada (2014).

Comparison of the stiffness of the railpads for the slab track in Figure 4.20, includes a rigid track model. This is a model based on the assumption that the stiffness of the railpads is
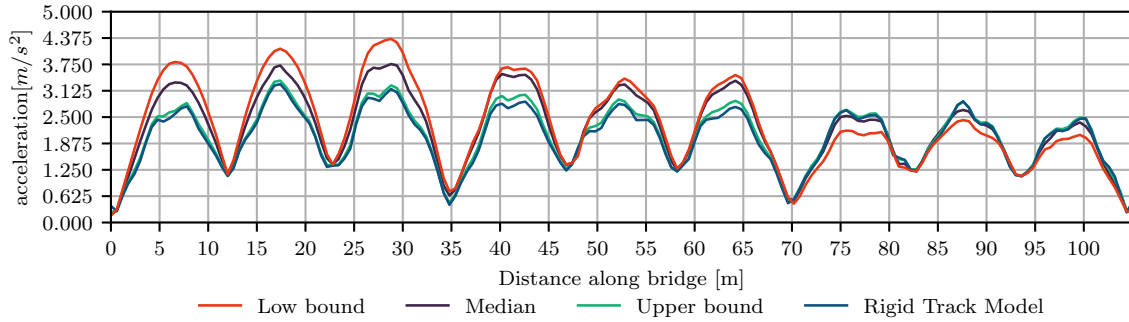
Figure 4.20: Comparison of the vertical accelerations for the comparison of railpad stiffness for the slab track
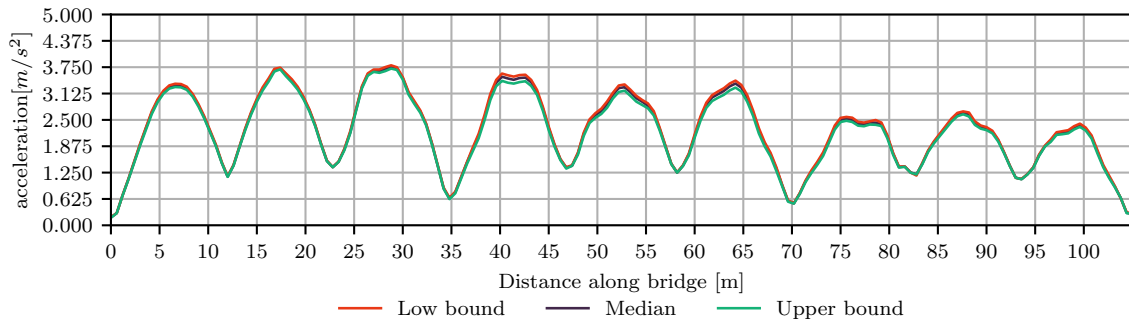
Figure 4.21: Comparison of the vertical accelerations for the comparison of railpad damping for the slab track

infinitely stiff. It shows that the rigid model is a close response to the upper bound model. More significantly there is a considerable difference in the bridge accelerations depending on the railpad stiffness. This is possibly as a result of a softening in stiffness of the railpad leading to less spreading of the load between sleepers. This maybe resolved by a comparison with a non-linear spring, but that is too complex for the model to work effectively and literature data on the nonlinear properties has not been found.

Considering the damping of the railpad, the value of damping seemingly makes no difference to the vertical accelerations of the bridge as seen in Figure 4.21. As a result the median level will be used for both the damping and the stiffness of the railpad as it is an average of all values found in literature.

4.2.2 Ballasted Track

Comparison of the ballasted track properties looks at the elastic stiffness, damping stiffness and the mass properties of the ballast layer. Again this takes the form of comparing the median value in literature with the upper and lower bounds (see Appendix B). As there is no set ballast mass, the mass comparison will investigate different depths and densities of the

Model	Elastic stiffness [kN/m]	Damping stiffness [kN s/m]	Ballast Density [kg/m³]	Ballast Depth [m]	Ballast Mass per Area [kg/m²]
Upper Bound	5.38×10^5	120	2600	0.45	1170
Median	1.0×10^5	60	1800	0.45	810
Lower Bound	2.29×10^4	40	1800	0.3	540

Table 4.5: Variation of the properties of the ballast for the ballasted track models.
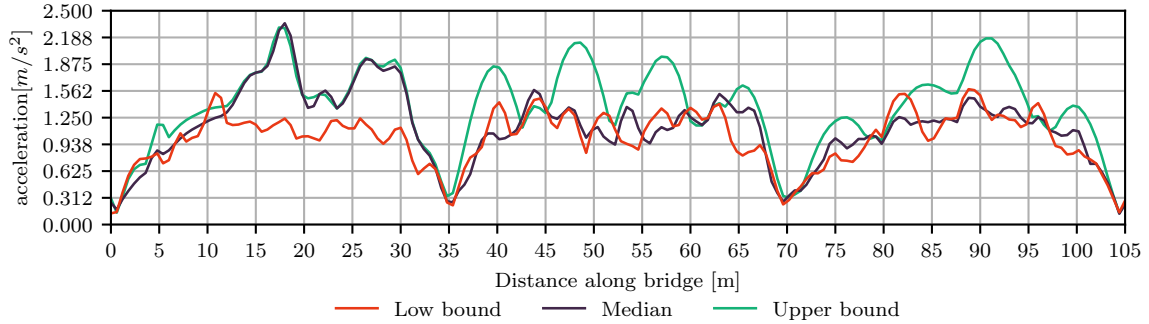
Figure 4.22: Comparison of the filtered vertical accelerations with the ballast elastic stiffness

ballast as defined in Table 4.5.

It can be seen from Figure 4.22 that the ballast stiffness can have a significant affect on the response of the bridge. The lower the stiffness the lower the accelerations experienced. This is potentially due to the lower stiffness making the ballast softer and so smoothing the variation of forces transmitted from the vehicle-rail contact to the bridge itself. This indicates it is important to get an accurate model of the elasticity of the ballast when modelling it.

From Figure 4.23, it becomes clear that the damping of the ballast has less of an affect than the stiffness of the ballast on the bridge response. It shows a slight increase in response for less damping. The findings are that the ballast damping values are less important to be accurate
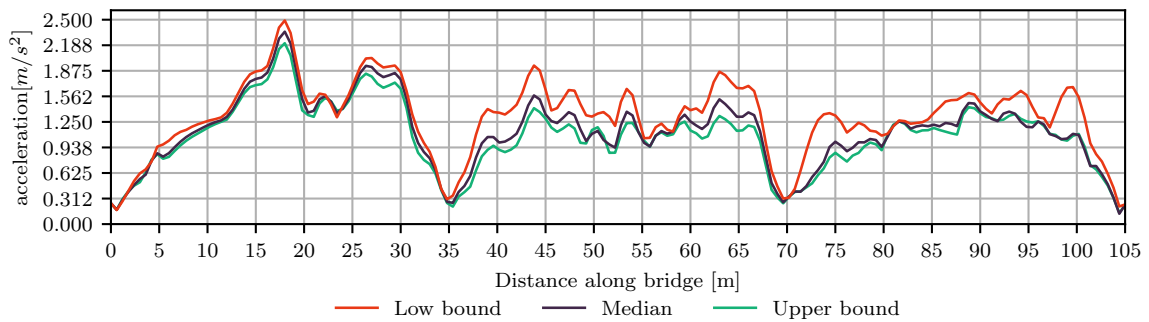
Figure 4.23: Comparison of the filtered vertical accelerations with the ballast damping stiffness
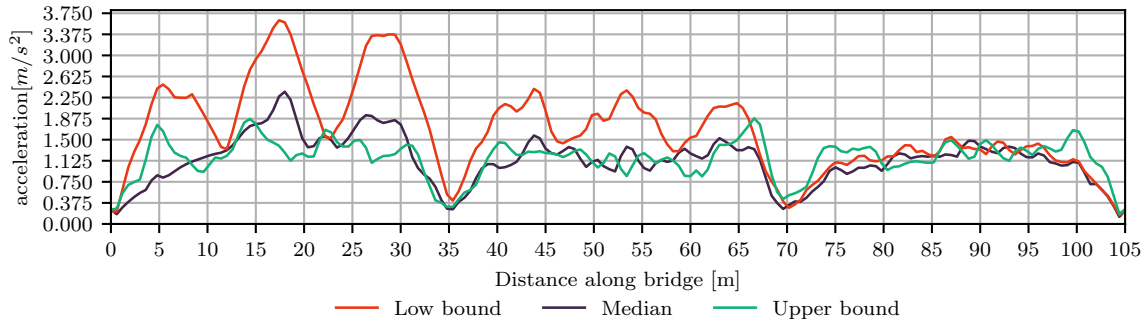
Figure 4.24: Comparison of the filtered vertical accelerations with the ballast mass

than the elasticity.

The ballast mass has a significant affect on the bridge response. This is shown in Figure 4.24, which shows that the lower bound has the highest accelerations. This is partly a function of the natural frequency, as reducing the mass of the track will change the natural frequency. In the case of the lower bound, this results in bridge frequencies matching with loading frequencies and hence the response is more resonant. In addition, accelerations would be expected to increase with lower mass, as due to Newton's Second Law, a lower mass will lead to higher acceleration for a given force ($F = ma$). This suggests that the weight of the ballast needs to be accurately modelled. However, this creates difficulties as the mass of ballast will change with time, which means a range of ballast masses should need to be studied to determine the effects on the frequency and therefore accelerations.

4.2.3   Track Model Comparison

An interesting study is the direct comparison of the ballast and slab tracks. The comparison of the variation of the maximum accelerations along the length of the bridge for all the models studied for the slab and ballasted tracks, is shown in Figure 4.25. This shows that the ballasted models have a higher variation than the slab track models. However, this is partly down to the variation of the mass in the ballasted track comparison. Therefore, a model of the ballasted track, with median stiffness and damping properties, but the same mass as a slab track is introduced for comparison. When comparing the results without the variation in mass, as in Figure 4.26, the variation is much smaller than before for the ballasted track. The slab track leads to higher accelerations in this particular case of $100 \ m/s$ ($360 \ km/h$). This is because the change in mass, changes the modal frequencies of the bridges, as seen in Figure 4.27. $f_{st,i}$ represents the ith significant modal frequency of the slab track and $f_{bt,i}$ represents the same for ballasted track.

The variation in the frequencies causes this change in the accelerations as shown in Figure 4.28, which shows the frequency components of the acceleration signal at the midspan of the
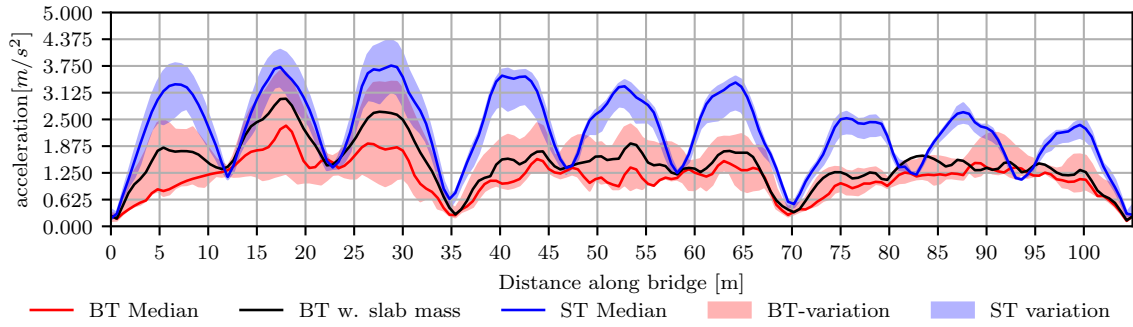
Figure 4.25: Comparison of the maximum filtered vertical acceleration for the slab track (ST) and ballasted track (BT) for all variations of track properties, for a vehicle velocity of $100 m/s$. Also includes the ballasted track with the mass of the slab track median mass as a comparison
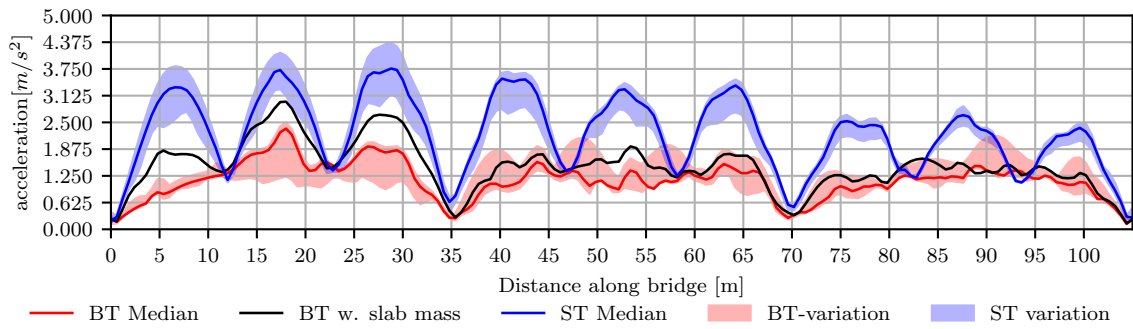
Figure 4.26: Comparison of the maximum filtered vertical acceleration for the slab track (ST) and ballasted track (BT) for all non-mass variations of slab and ballast track properties, for a vehicle velocity of $100 \, m/s$. However, it does include the ballasted track with the median slab track mass as a comparison

(a) $f_{bt,1} = 3.70$ Hz, $f_{st,1} = 3.79$ Hz

(b) $f_{bt,2} = 4.38$ Hz, $f_{st,2} = 4.48$ Hz

(c) $f_{bt,27} = 15.95$ Hz, $f_{st,27} = 16.08$ Hz

(d) $f_{bt,63} = 27.29$ Hz, $f_{st,63} = 28.36$ Hz
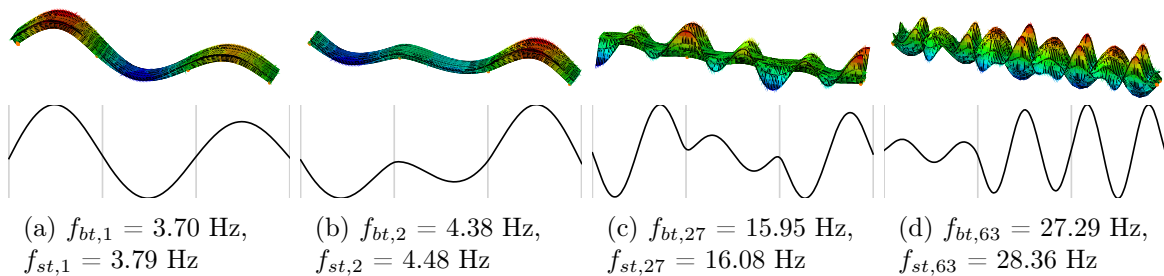
Figure 4.27: Comparison of significant modes in slab track - ballasted track comparison, with the full mode in three dimensions on top and the simplified mode shape underneath it
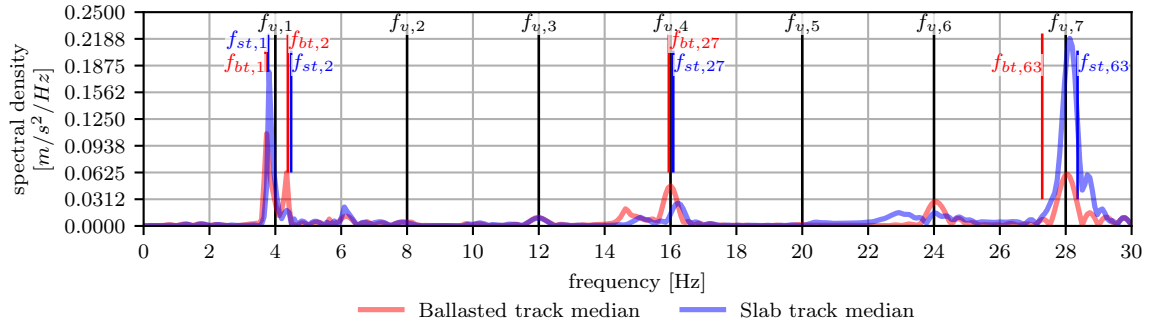
Figure 4.28: Comparison of the frequency component of acceleration, at $100\,m/s$, at midspan of the first span, for the two track type models. Also showing the resonant frequencies (f_{vi}) related to the axle spacing and velocity, and selected bridge modal frequencies for ballasted track ($f_{bt,i}$) and the slab track ($f_{st,i}$)

first span. This shows that the slab track modes are closer to the resonant speed frequencies, f_{vi} of the loading for $i = 1$ and $i = 7$ where the component of acceleration is largest. Hence, the accelerations in the slab track are higher than ballasted track for the operating speed of $100\,m/s$ ($360\,km/h$). This appears to be the case in the situation shown in Figure 4.26, where the case of the ballasted track mass being equal to the slab track mass shows that the mass is not the only determining factor in resulting in larger accelerations in the bridge under slab track.

With no clear preference for the type of high speed track used and due to the benefits outlined in the literature review (Section 2.3.1), slab track will continue to be used. The slab track model uses less elements as well, resulting in a computationally quicker model. The higher mass of ballasted track tends to reduce the natural modal frequency of the bridge. As the slab track fundamental frequency appears to be in the range of the design operating speed, this results in the higher accelerations found. Therefore in addition to aforementioned reasoning for picking slab track to model, it will also represent a case where accelerations are expected to be higher, and therefore more conservative.

4.3   Wheel-Rail Interaction Modelling Sensitivity

This section first verifies the wheel rail contact model, then explores the sensitivity of the vehicle and bridge response to both the wheel-rail interaction models and the irregularities found in the rails.

Property	Value
Mass per unit length	29805.3 kg/m
Lateral Bending Rigidity	1520.8 $GPa\,m^4$
Polar Inertia	50.0 m^4
Vertical Bending Rigidity	229.7 $GPa\,m^4$
Torsional Rigidity	21.7 $GPa\,m^4$

Table 4.6: The bridge properties for this validation model reproduced from Antolín et al. (2013)

4.3.1 Wheel-Rail Contact Model Verification

Validation of the whole model is difficult as there is a lack of published data of built high speed railway bridge acceleration response (as it is considered sensitive information by infrastructure owners), or the bridge and vehicle data needed to replicate it. However, Antolín et al. (2013) does make a computational model, verified against data by Zhang et al. (2008). This compares different vehicle-bridge interaction models to the measured data. It is claimed that the figures shown are at 270 km/h, however analysing this data it appears that the graphs published are taken from the resonant speed of 231.5 km/h (64.2 m/s). Therefore a comparison of a moving point load model and the full vehicle model with irregularities is made to the results of the non-linear model by Antolín et al. (2013) for the vertical accelerations and the vertical deflections, at the midspan location specified in the paper.

The properties of the bridge are shown in Table 4.6 such that the first natural vertical modal frequency is 7.57 Hz, first torsional modal frequency 11.68 Hz and the first lateral modal frequency is 19.50 Hz. The irregularities modelled are the same as used in the other sections of this chapter, and the vehicle has the same mass properties as in the Antolín et al. (2013) paper.

The results show good agreement with the results in Antolín et al. (2013). There is similar shape and amplitudes for the deflections (Figure 4.29a). Figure 4.29b shows the major component of the acceleration is from the 7.57 Hz first bending mode, although this has been unable to be compared to the Antolín et al. model due to a lack of data. The vertical accelerations of the interaction models of this thesis (Figure 4.29c) show a slightly smaller peak, and more variation but again the general shape is in agreement. This shows that the vehicle-track models established in this thesis have good agreement with those established in literature.

4.3.2 Wheel Forces

In many guidelines the forces in the wheels are studied to determine if there is a risk to the vehicle of derailment. There are many different methods to study this, including the

(a) time history of midspan vertical displacement

(b) Frequency component of midspan vertical accelerations

(c) Time history of filtered midspan vertical accelerations
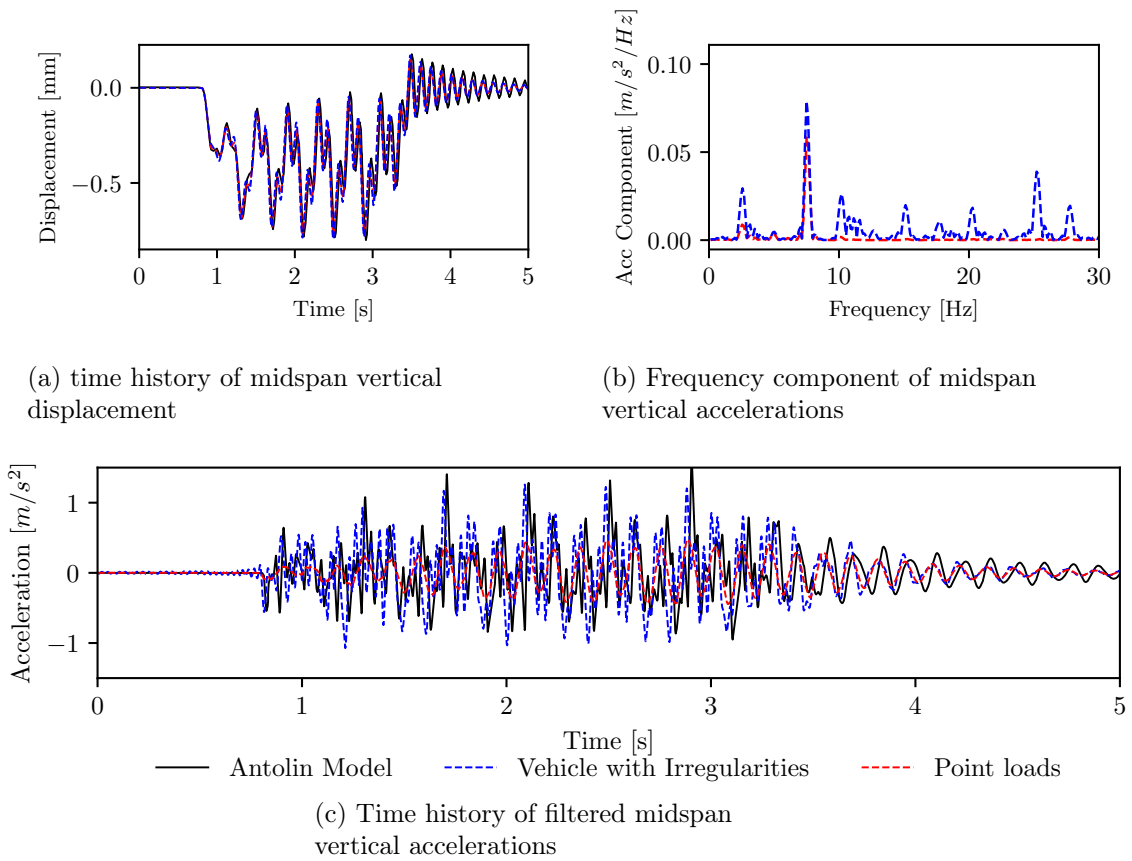
Figure 4.29: Comparison of the interaction models of this thesis with the nonlinear model from Antolín et al. (2013)
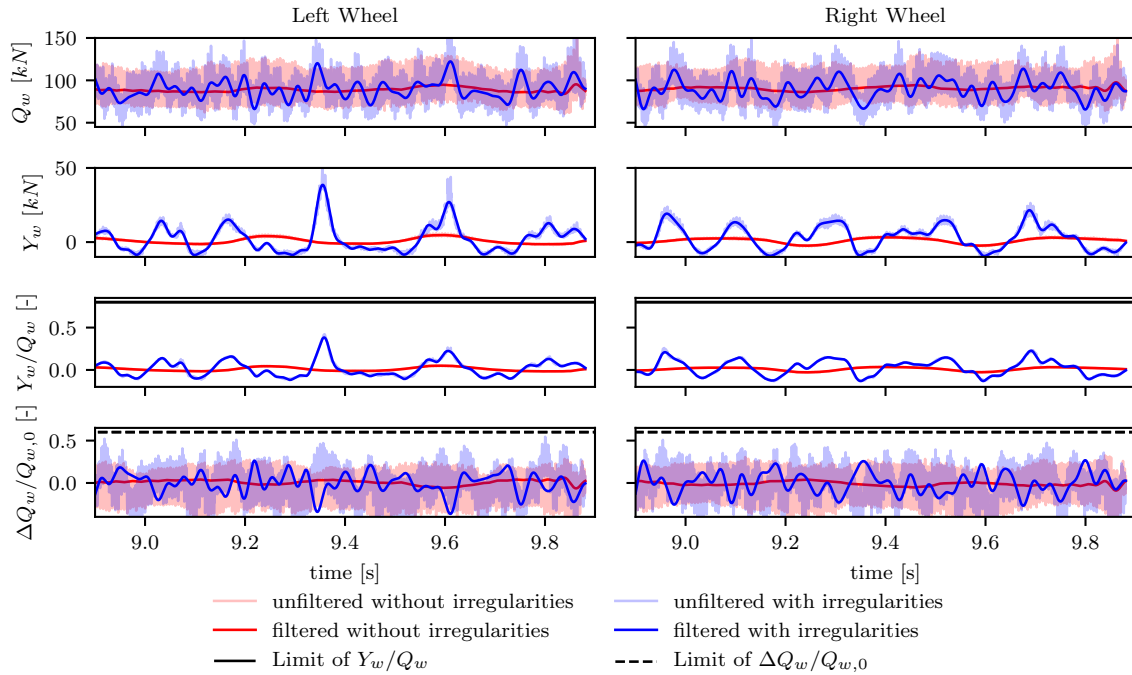
Figure 4.30: Comparison of the left and right wheel forces for a model with irregularities and without irregularities, as well as study of the limiting ratios

derailment factor of Y_w/Q_w and the offload factor $\Delta Q_w/Q_{w,0}$, where Y_w is the lateral wheel force, Q_w is the vertical wheel force, $Q_{w,0}$ the static vertical wheel force, and as a result $\Delta Q_w = Q_w - Q_{w,0}$. The limit for the derailment factor is 0.8, allowable for a period less than 15 ms (Arvidsson, 2018). For the offload factor the forces should be filtered with a low pass filter of 20 Hz, but the ratio should not exceed 0.6 (Arvidsson, 2018; Zhang et al., 2008; BS EN 14363:2016, 2016). These limits are commonly used in both numerical models and experimental live test work, although the origins are unclear.

It would be ideal to check the forces against these limits for each simulation as an additional check. However, for the current model setup it is computationally expensive to study the wheel forces for every simulation. It increased the computational time by above 400%, and hence was very inefficient. As a result a study into the wheel forces for the vehicle has been conducted with and without irregularities for this benchmark case to see if it is generally a concern or not.

Study of the wheelset forces, as shown in Figure 4.30 shows that the correct filtering of the forces removes a considerable amount of vertical variation. When considering the ratios of the forces, it shows that the filtered values are significantly below the limits in both cases, and hence it is justifiable that the forces are not studied in all cases.
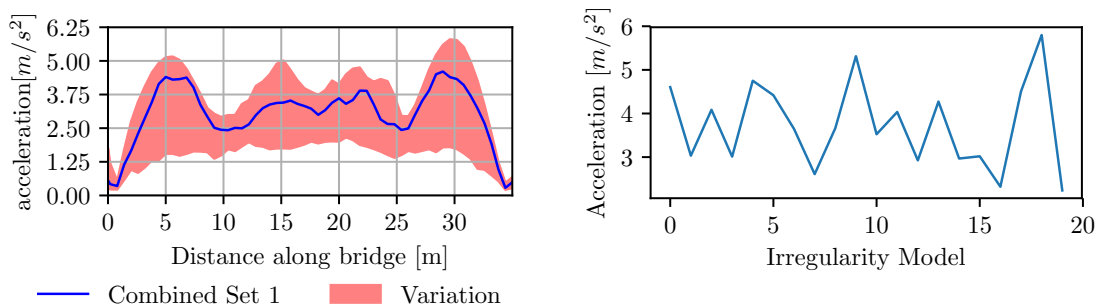
(a) Comparison of the vertical acceleration response along the length of the bridge for *Combined Set 1* against the variation provided by 19 different irregularity sets due to different phase angles.

(b) Comparison of the maximum vertical acceleration for any point along the bridge, between the 19 variations in phase angle and the *Combined Set 1* model (which corresponds to irregularity model 0)

Figure 4.31: Comparison of acceleration response for different irregularity profile phase angles for the one spanned dual U-beam bridge, for a vehicle velocity of $360\,km/h$

4.3.3   Effects of Irregularities

Firstly, it must be determined if the response from the irregularities used are representative. This is further to the work presented in Figure 3.45 of Section 3.5.6, which showed that the size of the irregularities were representative. Through variation of the random phase angles associated with the irregularities, but keeping the amplitudes of the frequency components the same, the variation of the acceleration response is shown in Figure 4.31. Figure 4.31a shows the response of the maximum acceleration response along the length of the bridge (using the one spanned case), where *Combined set 1* compared with the variation provided by another 19 irregularity profiles. In addition, the maximum acceleration response at any point along the bridge for these 19 cases and the *Combined set 1* irregularities, is compared in Figure 4.31b. These figures show considerable variation in the accelerations coming from different irregularity profiles. However, for all cases they provide significantly larger acceleration response than the moving point load model. Unfortunately, due to the high computational time required to run one model, it is not possible to run with multiple different phases of irregularities for each case, so only the *Combined set 1* will be used.

Using the irregularities prescribed in Section 3.5.6, a comparison is made to identify which components of the irregularities impact which characteristic of the bridge response. This utilises the combination of irregularities previously defined in Table 3.11. By comparing the maximum accelerations at the middle of the first span under the different irregularities for different velocities (Figure 4.32), it is clear that there are greater accelerations with irregularities in all cases for the speed of $100\,m/s$ ($360\,km/h$). Therefore comparing the maximum vertical accelerations along the length of the bridge at $360\,km/h$, as in Figure 4.33, it is apparent that *Combined set 1* shows similar maximum accelerations to the *Vertical only* set. The other two component sets, *Alignment only* and *Cross Level only*, have contributions similar to the

Figure 4.32: Comparison of maxiumum filtered vertical accelerations of the vertical bridge accelerations at the midspan of the first span for different irregularities
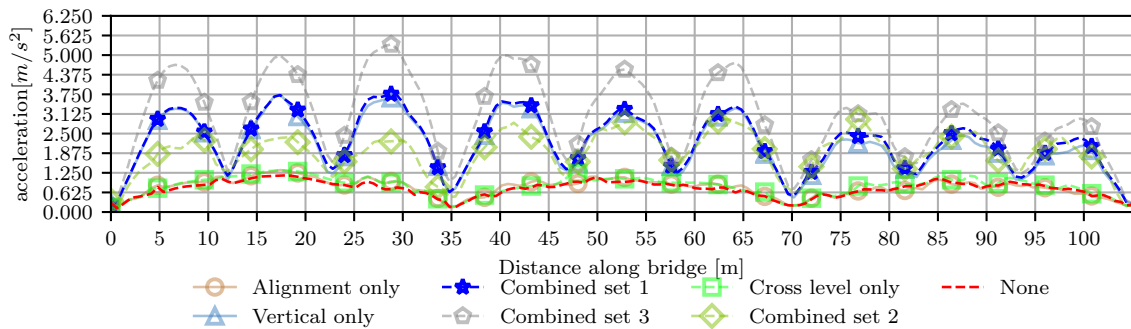
Figure 4.33: Comparison of the filtered maximum vertical bridge acceleration magnitudes along the length of the bridge with different types of irregularities at 360 km/h

case without irregularities. This indicates that the vertical irregularities have the greatest contribution to the vertical accelerations, and despite cross level irregularities working in the vertical plane, they have little affect.

Comparing the three combined sets, *Combined set 3* clearly shows larger accelerations as could be assumed by the larger amplitude irregularities. Interestingly, *Combined set 2* with its different phase angles shows lower accelerations than the same amplitude irregularities of *Combined set 1*. Contrastingly, Figure 4.34, running at 432 km/h, shows that in some locations *Combined set 2* has higher accelerations than both other combined sets.

Considering the comparison between the *Combined set 1* and *None* irregularity sets, it is clear there is a substantial increase in vertical accelerations when the irregularities are considered. This is particularly significant considering the fact that these irregularities were found to be acceptable according to BS EN 13848-5:2017 (2017) in Section 3.5.6, and therefore are likely to occur on HSR lines. It can be seen that to calculate the accurate vertical accelerations, the consideration of irregularities is essential, with their consideration only possible through use of a full vehicle model. Using the moving point load models, as used in practice for design of HSR bridges, are not accurate enough for the calculation of deck accelerations, providing significantly lower results. When comparing the time history of the vertical acceleration in the
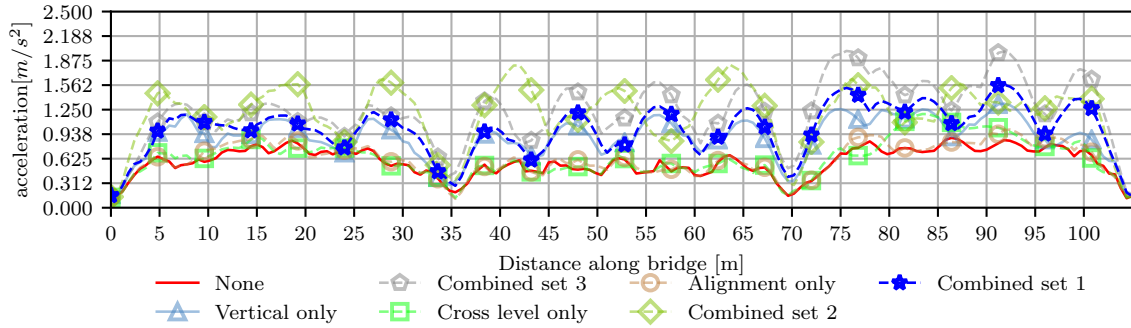
Figure 4.34: Comparison of the filtered maximum vertical bridge acceleration magnitudes along the length of the bridge with different types of irregularities at 432 km/h
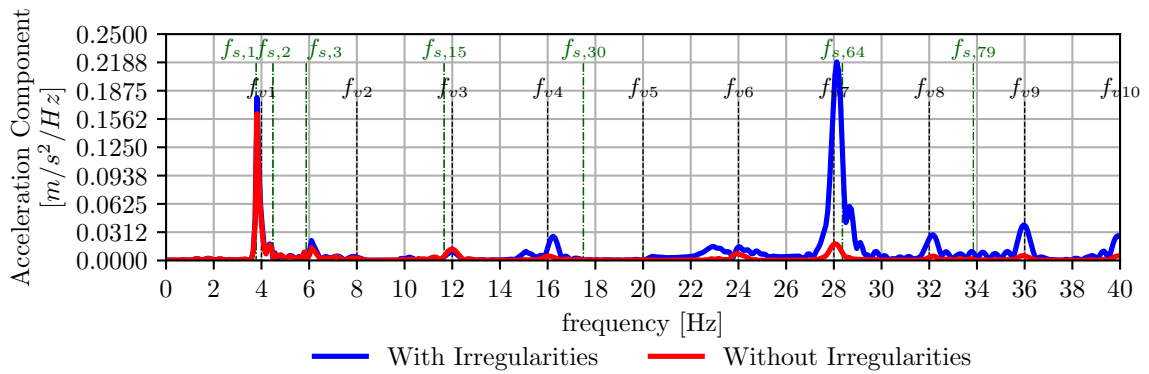
Figure 4.35: Comparison of the component frequencies of the vertical bridge accelerations at the midspan of the first span at 360 km/h with and without irregularities, showing the loading frequencies f_{vi} and the bridge frequencies $f_{s,i}$
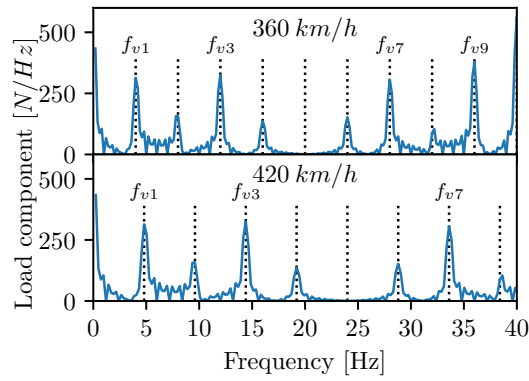
Figure 4.36: Frequency component of the vehicle loads acting at a fixed location on the rail for moving point loads for both $360\,km/h$ and $432\,km/h$
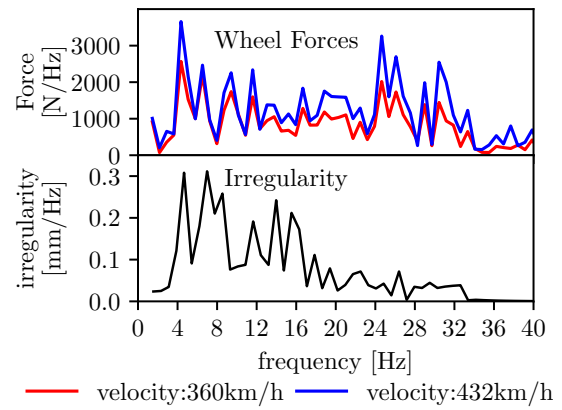
Figure 4.37: Frequency component variation of the wheel-rail force for two velocities in comparison with the corresponding irregularity variation. The frequencies are normalised to $360\,m/s$ for comparison

frequency domain at the midspan of the first span, as in Figure 4.35, there is clear increase in the contribution by irregularities. However, this contribution is not equal, and the contribution is greater at higher frequencies particularly at 28 Hz.

Considering that the whole train model, the bridge model and the train speed are identical for both cases, with and without irregularities, the peak in the amplitude of the accelerations for the 28 Hz frequency component, when the imperfections are considered, must have a causation or be activated by the irregularities. Considering a fixed point on the rail, a train vehicle, modelled using moving point loads, crossing that point would define a load function over the time. Converting this force-time history into the frequency domain, shows the resonant loading frequencies, f_{vi}. The dominant factors in finding the resonant loading frequencies, are a repeating vehicle distance (the length of the carriage) and the vehicle velocity. However, other repeating distances such as the axle and bogie spacings, influence the amplitude through interactions of cancellation and resonant effects, such that not every resonant loading frequency has the same contributions. This is represented in Figure 4.36, using a load magnitude that is fixed, neglecting the variation found when modelling the vehicle dynamics. It is well known that when these loading frequencies match the structural bridge frequencies, resonant responses may be activated. Here, the f_{v7} frequency has a high contribution for the velocity of $360\,km/h$ at 28 Hz, however for $432\,km/h$, f_{v7} is found at 33.6 Hz. From Figure 4.35 it is clear a structural frequency is at 28 Hz, which is matched by the larger contribution from f_{v7} at this frequency for a vehicle velocity of $360\,km/h$. Hence, resonant effects are activated at this velocity. However, it alone does not explain why the amplification is much larger by including the vertical irregularities, than modelling without them or with a set of moving point loads. This requires a deeper study of the irregularities and wheel forces, presented

(a) With Irregularities   (b) Without Irregularities
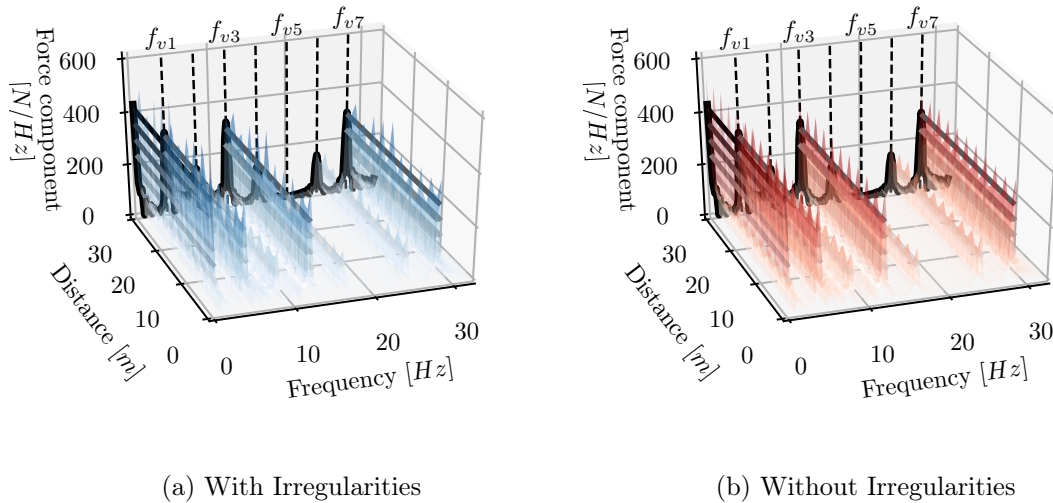
Figure 4.38: Frequency components of the vehicle loads, acting at different fixed locations on the rail along the length of the bridge, considering both fixed magnitude moving point loads (in black) and variable magnitude wheel loads due to using vehicle-bridge dynamic models (shades of blue for models including irregularities and red for models without the irregularities) for a vehicle velocity of $360\,km/h$

herein, to understand this particular phenomenon.

Figure 4.37 shows the variation of the vertical force of one wheel as it moves forward in the frequency domain (obtained by modelling the vehicle, so here the force can vary with time), as it passes over the bridge and irregularities for both $432\,km/h$ and $360\,km/h$. The frequency component of the $432\,km/h$ force variation is normalised to $360\,km/h$, in order to make a direct comparison (i.e. the horizontal axis for $360\,km/h$ covering 0 to 40 Hz, whereas 0 to $40 \times 120/100 = 48$ Hz for $432\,km/h$). In addition, the variation of the vertical irregularity as the wheel-rail pair move along the bridge at $360\,km/h$, is also shown in the frequency domain. Here, it can be seen that the variation in the wheel force, has peaks at similar normalised frequencies for both velocities. This indicates a relationship between the frequency component of the irregularity and the force. The variation of the force appears to also be higher for the higher velocity. Study of the irregularity frequency components shows that there is significant variation in the irregularity component between 4 and 20 Hz, some smaller variation between 20 and 33 Hz and no variation at frequencies above this. This is as a result of the minimum irregularity wavelength being $3\,m$, which for a velocity of $360\,km/h$ ($100\,m/s$) corresponds to a frequency of 33 Hz. Study of the wheel force variation again shows much smaller variation for normalised frequencies greater than 33 Hz. This indicates a direct link between the wheel force variation and the irregularities.

Study of the force experienced at a fixed point on the rail, due to a passing train, in the frequency domain is shown in Figure 4.38, for cases where the vehicle and bridge dynamics are modelled, hence allowing a variation in the force, unlike previously seen in Figure 4.36
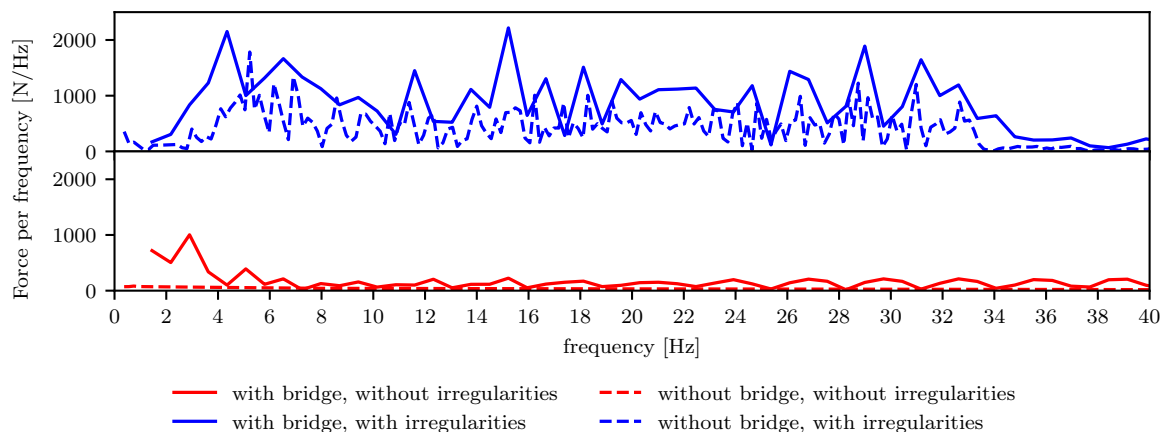
Figure 4.39: Comparison of the frequency components of the wheel force with and without the bridge and irregularities in the frequency domain

which used a fixed magnitude. Figure 4.38a shows a case where the irregularities are considered in the vehicle bridge dynamics, and Figure 4.38b when the train vehicle passes over the bridge and track with no irregularities present. In these figures, the frequency contributions of the force are plotted at a range of locations along the first span of the bridge, as one location would not be representative of the whole span, due to the variation in force. In addition, the equivalent force variations for a constant magnitude of force are shown in black, whereas the variable force due to the dynamic vehicle-bridge model is shown in shades of blue for the case with irregularities and red for the case without. The two figures show that the contributions of the variable force at 28 Hz, although not constant with location along the bridge, have values very close to those of the constant magnitude force (in black). There is very little difference between these contributions with and without the irregularities. This shows that the contribution of the increased acceleration components around 28 Hz, for the inclusion of irregularities is not due to an amplification of the contribution of the loading frequency component.

In order to have a better understanding about the additional contribution to the accelerations at 28 Hz, when including irregularities, for a vehicle velocity of $360\,km/h$, the force between a wheel and rail as it moves along the track has been represented in the frequency domain. For comparison, this uses models both with and without the irregularities, for a train vehicle running over the benchmark bridge (with bridge) and also over a rigid embankment (without bridge). The variation in forces arises because here the bridge and vehicle dynamics are modelled, hence the force is allowed to vary unlike in a moving point load model. Here, the rigid embankment is modelled as a fixed platform, with the same track and irregularities on top. This allows study of the influence of the bridge on the wheel force variation. It can be seen in Figure 4.39 that when the train crosses the bridge, without irregularities in the track, the contribution to the variation in wheel forces comes mainly from frequencies lower than 5 Hz. This variation comes from the displacement profile of the bridge, which is not perfectly

flat, as there are initial deflections due to self-weight and prestress, as these actions are applied before the train crosses the bridge. In contrast, when the irregularities are considered present in the track, the wheel forces have components across all the frequency domain, regardless of if the train is crossing a bridge or an embankment. Therefore it is clear the origin of this effect is not in the bridge itself, but in the interaction between the train dynamics and the irregularities. However, despite the phenomenon not being caused by the bridge structure, the force variation has a very clear effect on the bridge accelerations.

The enrichment of the force variation, found across the frequencies to which the irregularities vary (4-33 Hz for a velocity of 360 km/h, due to the wavelength of irregularities being between 3 and 25 m, see Figure 4.37), causes the increase in accelerations across all modes of this frequency range (see Figure 4.35). It is the combination of this with the high resonant loading component at 28 Hz matching the structural bridge modal frequency, leading to the particularly high contribution. Therefore, only when the irregularities are included, and the vehicle transfers onto the bridge a wide range of variable force frequency content, the matching between the loading bridge frequencies at 28 Hz produce resonant effects, with a large amplification of the bridge accelerations. However, without irregularities, the frequency content of the force variation transmitted through the wheelset is very limited, and does not reach the frequency value at which the loading matches the bridge frequencies, preventing the appearance of a resonant effect.

The wheel force variation can be confirmed to be the cause by running a point load model of the train, with the real variation of the wheel forces as the amplitude (Force variation model). This leads to a similar acceleration response of the bridge to that of the full vehicle model with irregularities (Figure 4.40), with the same modal frequency components being activated, as is expected (Figure 4.41). As previously compared in Figure 4.37, the force variation had peaks at the same normalised frequencies, but different amplitudes between the two speeds. Similar locations of peaks can be noted in the irregularity profile, but with again differing amplitudes. Considering that the force variation due to irregularities is necessary for the higher mode excitation, when the loading and bridge frequencies match, the possibility of developing a method to include this variation in the forces in a moving point load model without running the full vehicle model for all velocities, has been explored, without success, due to the complexity of the problem involving the wheel-rail contact and the train dynamics. Nonetheless, if a method is found, this could create an easier alternative to model the contribution of the irregularities and force variation in industry, without such complicated models.

A contribution of the variation in wheel forces from irregularities to the bridge excitation was made before in Cantero et al. (2016), where it is stated that the irregularities cause a small increase in the accelerations of the bridge. However, that model is a two dimensional bridge model, with the increase in accelerations from irregularities in this thesis significantly larger, contradicting the initial conlusion by Cantero et al. (2016). Unlike the Cantero et al. paper, here it can be seen that there is a link between the complexity of the frequency content in
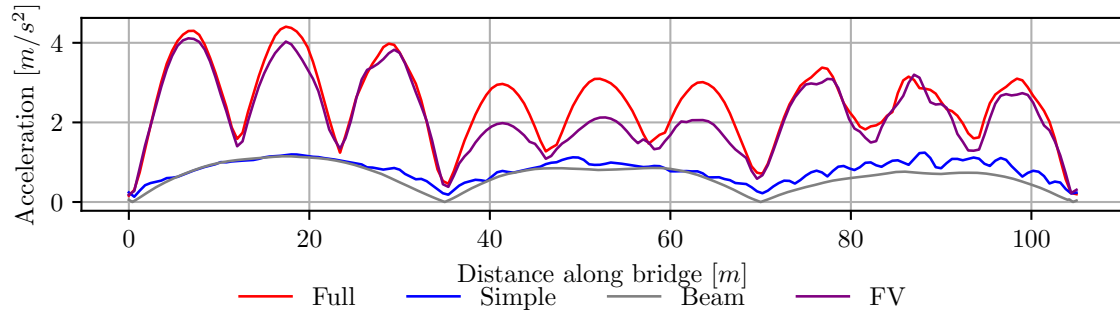
Figure 4.40: Maximum vertical bridge accelerations along the length of the bridge, for a velocity of $360\,km/h$, comparing a moving point load of fixed magnitude, the full vehicle model with irregularities and a moving point load model incorporating the vertical force variation.
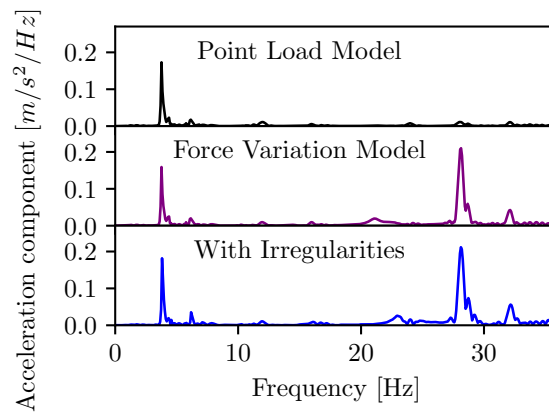
Figure 4.41: Frequency component of vertical acceleration at midspan of first span for $360\,km/h$ for models in comparison with the force variation model
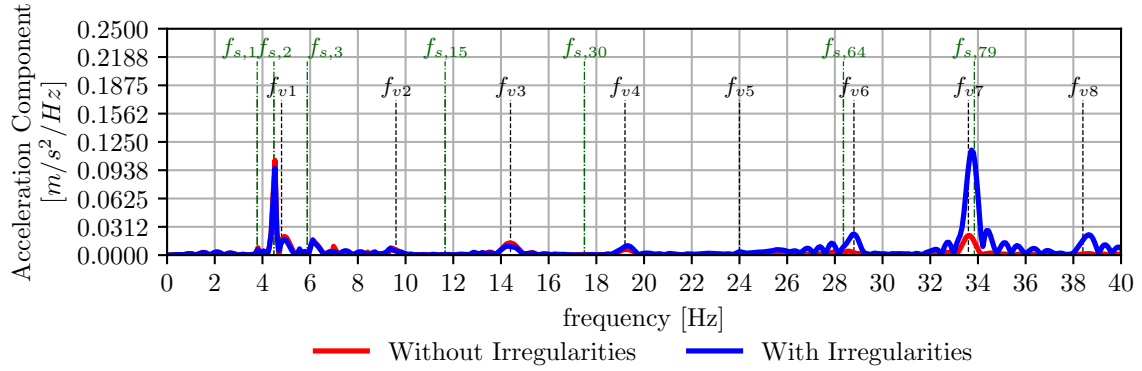
Figure 4.42: Comparison of the component frequencies of the vertical bridge accelerations at the midspan of the first span at 432 km/h with and without irregularities, showing the loading frequencies f_{vi} and the bridge frequencies $f_{s,i}$
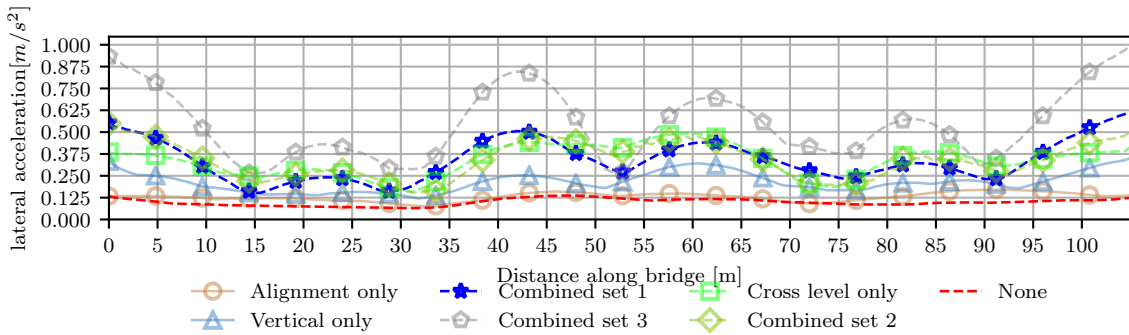
Figure 4.43: Comparison of the filtered maximum lateral bridge acceleration magnitudes along the length of the bridge with different types of irregularities at 360 km/h

wheel forces from irregularities, and matching of a resonant loading frequency (f_{v7}) and bridge modal frequency ($f_{s,64}$), for the velocity of $360\,km/h$, causing the increase in accelerations.

This effect can be seen again in Figure 4.42, at the higher speed of $432\,km/h$ ($120\,m/s$). At this speed the loading frequencies are shifted, such that f_{v7} shifts from 28 Hz to 33.6 Hz ($28 \times 432/360$). This was seen previously in the peak in the loading frequency for $432\,km/h$ in Figure 4.36. This leads to the matching of the f_{v7} frequency with a different bridge modal frequency, $f_{s,79}$. As concluded before, this resonant effect between the train loading and the bridge is only activated when there are rail irregularities as they introduce a wider frequency content in the vertical loading at the wheels. Nevertheless, for this particular case, the bridge modes activated by f_{v7} are later filtered out following Eurocode recommendations (Section 3.1.3), as the frequency is above 30 Hz

The consideration of the effects of different irregularity sets on lateral bridge accelerations is seen at $360\,km/h$ in Figure 4.43. From the *Alignment only* set, it can be seen that their affect is minimal again. Instead the main variation for the lateral accelerations comes from the cross level irregularities. There is also some contribution from the vertical irregularities.
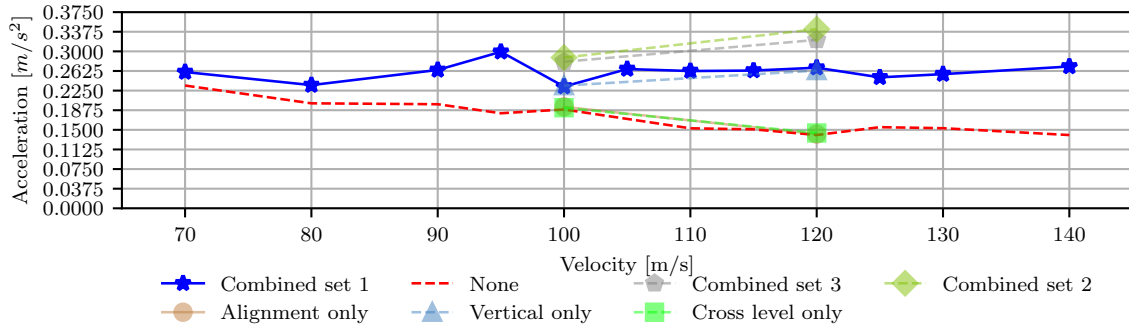
Figure 4.44: Comparison of maximum vertical accelerations in the rear carriage of the vehicle under different irregularities. Accelerations taken from the centre of mass of the vehicle.
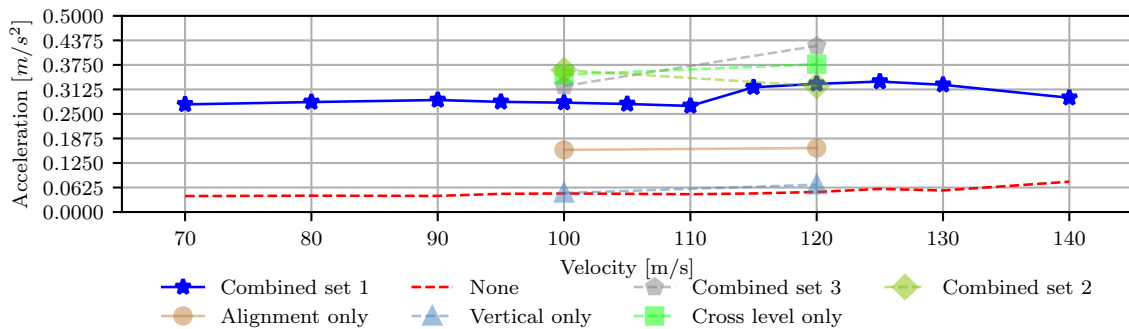
Figure 4.45: Comparison of maximum lateral accelerations of the rear carriage of the vehicle for different irregularities. Accelerations taken from the centre of mass of the vehicle.

This is partially down to the location of the tracks on the slab inducing some twisting which will cause lateral accelerations. In addition, the cross level irregularities tend to cause high lateral forces in the wheels which then get transferred into the bridge.

The impact of the irregularities on the rear carriage vertical (Figure 4.44) and lateral (Figure 4.45) accelerations, indicates that the irregularities have a much greater affect on the lateral accelerations than the vertical. It shows that the vertical accelerations in the vehicle are increased predominantly by vertical irregularities. It also shows that the case of no irregularities has a relatively high level of accelerations, coming from the deformed profile of the bridge due to permanent loading. The lateral accelerations appear to be from a combination of the alignment and cross level accelerations, with the impact of the alignment irregularities more clear on the vehicle than on the bridge.

As seen in Figure 4.46, the decomposition of the vehicle accelerations shows activation of frequencies in the region of $5\,Hz$ for the irregularities that caused significant lateral accelerations in the carriage. For the vertical accelerations, there is a peak around $1\,Hz$ and then later peaks around $5\,Hz$ again. The frequency of the modes of the vehicle, f_{ti}, are obtained by anchoring the wheels of the train. Relevant modes that show carriage activation, as this is where the vehicle accelerations are obtained, are indicated in Figure 4.46. It shows that the lateral
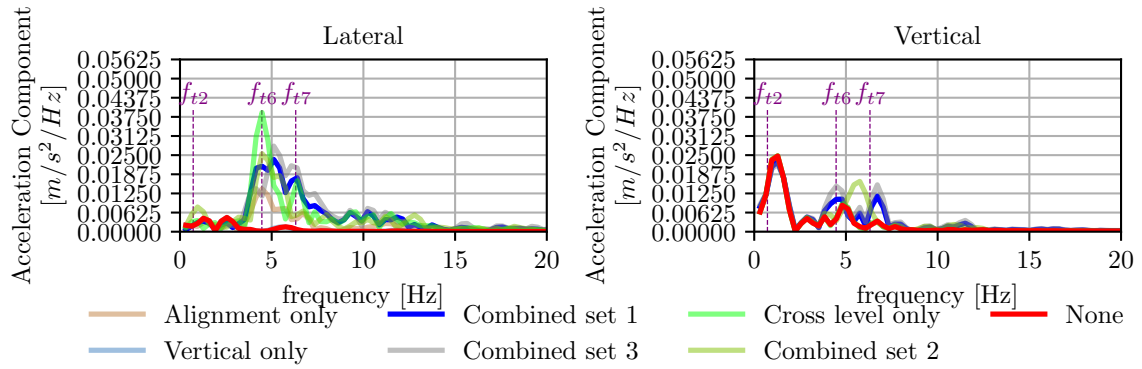
Figure 4.46: Comparison of frequency domains of the vertical and lateral carriage accelerations, where f_{ti} are frequencies associated with the vehicle dynamics
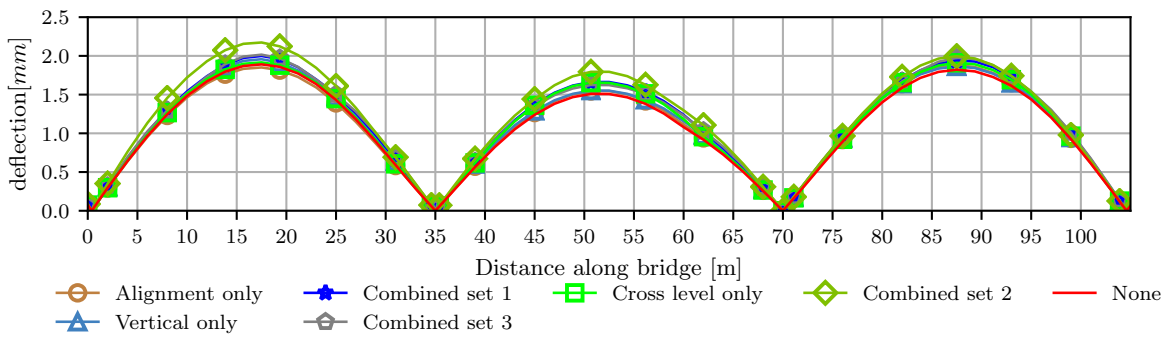
Figure 4.47: Comparison of maximum filtered vertical deflection along the length of the bridge for vehicles comprising different irregularities

carriage accelerations appear to be focused around the f_{t6} frequency, which corresponds to a carriage forward motion, not lateral motion, so there may be an additional lateral frequency component at a similar frequency that is related to the wheel-rail interaction and hence not picked up as part of this simple frequency analysis. The majority of the vertical response comes from the f_{t2} mode which is a vertical carriage mode. f_{t7} also shows some contribution and is an additional vertical carriage mode.

Finally, a comparison of the maximum vertical accelerations along the length of the bridge shown in Figure 4.47, indicates that although the accelerations may be considerably larger for the case with irregularities the deflections are much more similar.

As a result of this analysis into irregularities, the impact of each component of the irregularity on the bridge and train has been identified. It has been seen that the inclusion of irregularities is necessary to model the higher level of accelerations induced. Although a selection of irregularity variations would be needed to identify the average response, time and computational restraints mean that only one set of irregularities can be tested efficiently, which therefore for consistency will continue to be *Combined set 1*. This set of irregularities will be the set used to demonstrate cases with irregularities in this thesis unless otherwise stated.
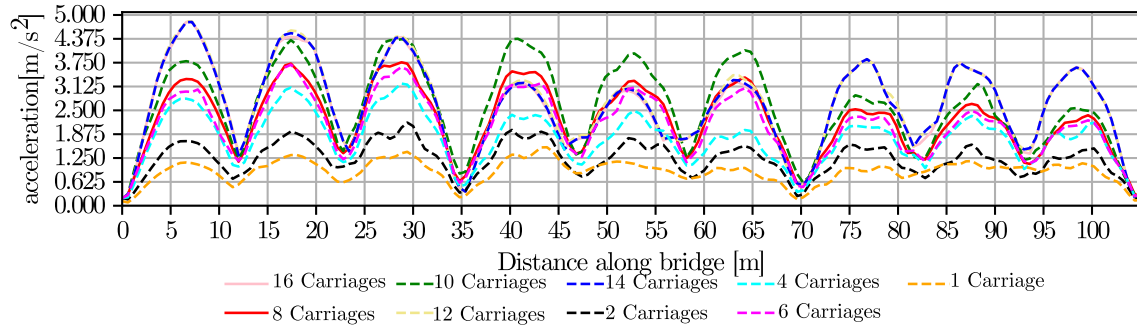
Figure 4.48: Comparison of maxiumum filtered vertical accelerations along the length of the bridge for vehicles comprising different numbers of carriages

4.4 Vehicle

The vehicle determines the loading for the bridge. To have a good understanding of the behaviour of the vehicle-bridge system, a sensitivity analysis is carried out on the parameters involving the vehicle. This uses the vehicle outlined in Section 3.3.

4.4.1 Number of Carriages

Whilst the standard number of carriages chosen is the configuration of eight carriages of the Siemens Velaro train, an investigation is carried out looking at the influence of more carriages in the vehicle. This is important as sometimes future developments will lead to longer trains, as well as the availability of a sixteen carriage model (Siemens, 2018; Railway Technology, 2018). The decision to have standard eight carriage train was purely computational, it takes more than double the amount of time to run a sixteen carriage rather than an eight carriage train.

Comparing the vertical accelerations along the length of the bridge at 360 km/h, with irregularities for different numbers of carriages, as in Figure 4.48, shows that the train of twelve carriages provides the greatest magnitude of acceleration. Surprisingly this is larger than trains of longer length, possibly as a result of the weight of the following carriages reducing the acceleration response. In addition, it can be seen that the use of eight carriages, results in a slightly smaller but similar set of maximum accelerations to the trains of fourteen and sixteen carriages. This justifies the use of eight carriages to represent both the standard length trains. The reason for not modelling the rest of analysis with ten carriages is that this is not the design length of the train, which is commonly either eight or sixteen carriages long due to
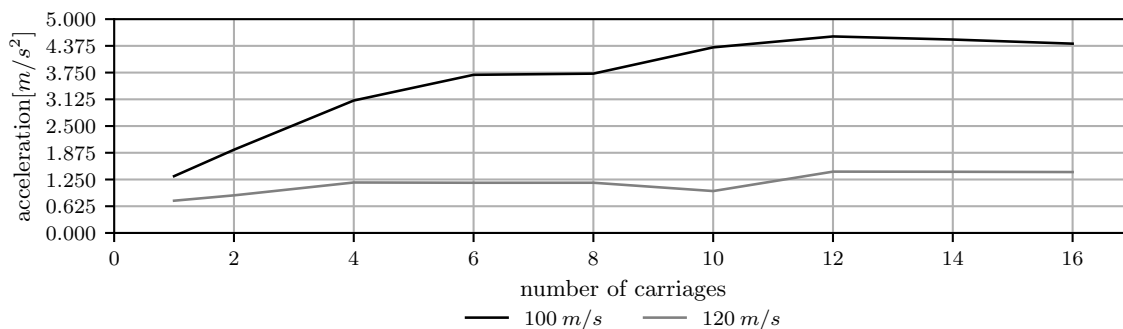
Figure 4.49: Comparison of maximum filtered vertical accelerations along the length of the bridge for vehicles comprising different numbers of carriages
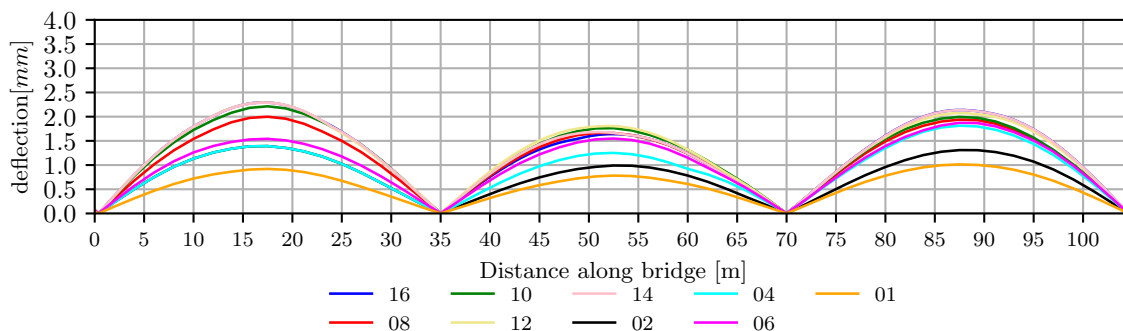
Figure 4.50: Comparison of vertical deflections along the length of the bridge for vehicles comprising different numbers of carriages

the train set up. Also, the more carriages, the more computationally demanding to complete analysis.

Comparison of the filtered vertical accelerations versus the number of carriages for different velocities at the midspan of the first span, as seen in Figure 4.49 shows that the number of carriages is important at resonance. When using the velocity of $360 \, km/h$ ($100 \, m/s$), a resonant speed, the number of carriages clearly impacts the vertical accelerations. However, when looking at $432 \, km/h$ ($120 \, m/s$), the accelerations have a much smaller magnitude of acceleration as well as a smaller rate of change of acceleration. This is due to the fact that the resonance effect for $120 \, m/s$ is at 34 Hz and therefore is neglected due to filtering, as explained before in Section 3.1.3.

Finally, comparing the deflections in Figures 4.50 and 4.51, it can be seen that there is very little difference in the vertical deflections for numbers between eight and sixteen carriages. The greatest difference coming from trains less than eight carriages long, again justifying the use of eight carriages as representative. Interestingly in Figure 4.50, the deflection in the first span is the same for two and four carriages, but the displacements vary between these vehicle lengths for the other spans.
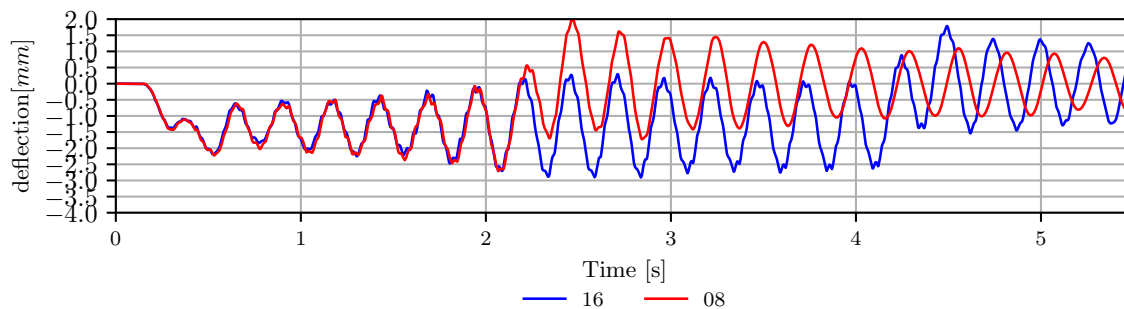
Figure 4.51: Comparison of vertical deflections with time for both 8 and 16 carriages, for a velocity of 360 km/h, at midspan of the first span. The 16 carriage train leaves the bridge at 4.2 seconds

4.4.2   Running Two Trains

Whilst the analysis so far has been focused on one vehicle on the track, there is a possibility of two vehicles running on the bridge at once. In BS EN 1991-2:2003 (2010), it is only required to run a dynamic analysis with one vehicle on the bridge. However, it is important to understand whether this is an acceptable assumption to make. An investigation has been carried out running two vehicles in opposite directions crossing the vehicle at the same time. This is done at $360 \, km/h$.

4.4.2.1   Concurrent entering

The first study involves looking at how the bridge system performs when the vehicles enter the bridge at opposite ends, at the same time. This is studied using the bridge and vehicle model with and without irregularities, also considering the comparison to moving point loads on the bridge. It can be seen in Figure 4.52 that when one track is loaded and the effect of irregularities are ignored, the accelerations are just over half of that when dual tracks are loaded. However, when the effect of irregularities is taken into account, the accelerations are found to be lower when dual tracks are loaded, than when a singular track is loaded. In order to understand why this is the case, a study into the affect of a delay on entering was performed. This is to determine whether the vehicles are causing a resonant or cancellation effect, particularly considering the reduction of accelerations in the case where irregularities were considered, which as previously discussed, the irregularities activate higher modes.

4.4.2.2   Delayed entering

By delaying the time that the second train enters the bridge, the accelerations along the length of the bridge have been plotted against the delay in Figure 4.53. A snapshot of this vertical
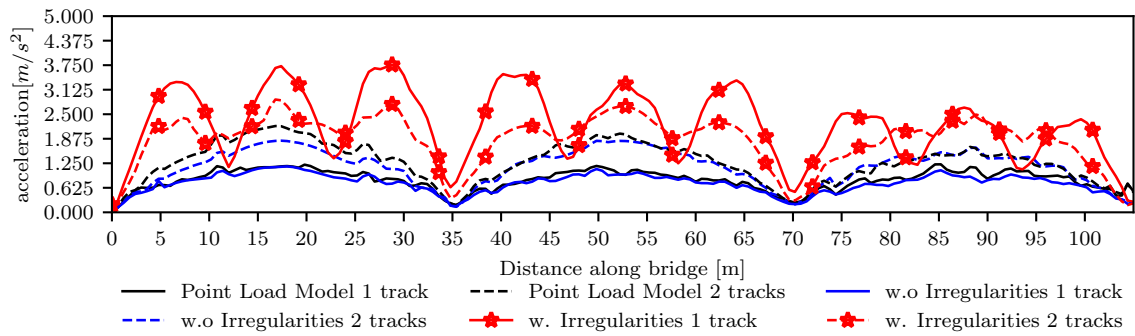
Figure 4.52: Comparison of maxiumum filtered vertical accelerations of the vertical bridge accelerations along the length of the bridge for one and two trains with and without irregularities. Also for comparison a moving point load model is compared.
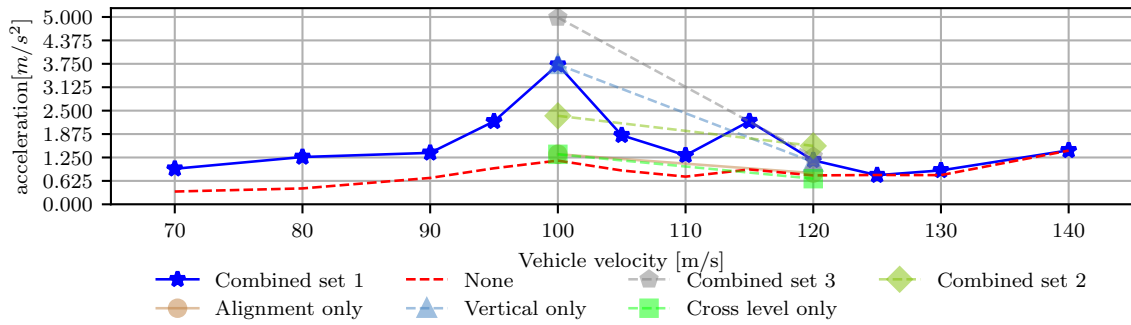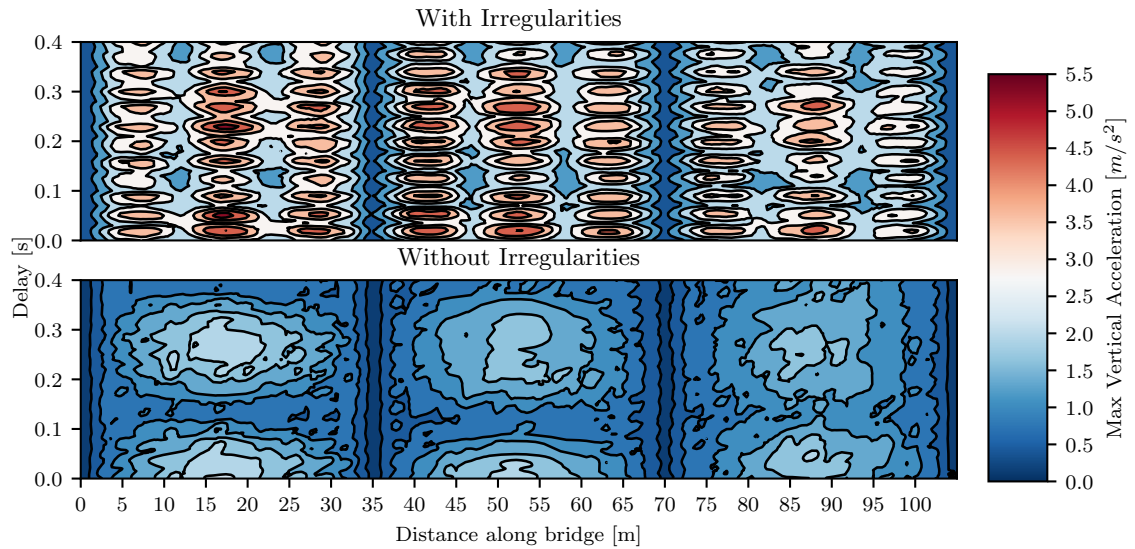

Figure 4.53: Comparison of maximum filtered vertical accelerations of the vertical bridge accelerations along the length of the bridge versus the delay for the second train to start moving across the bridge in the opposite direction.
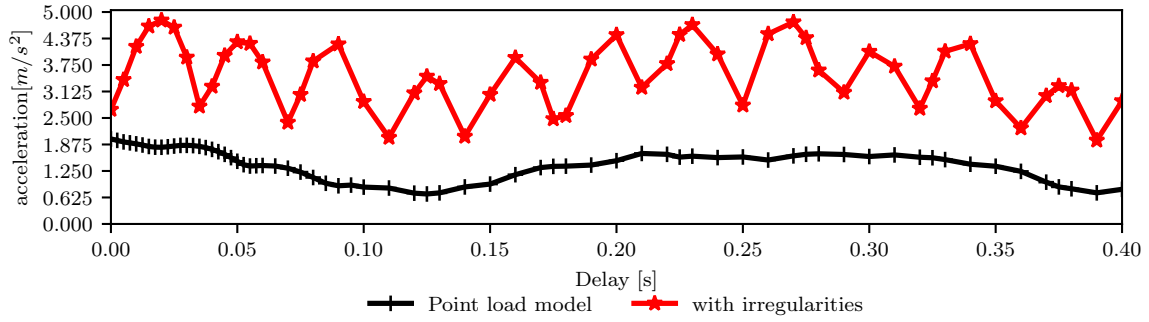
Figure 4.54: Comparison of vertical accelerations with delay at midspan of the 2nd span
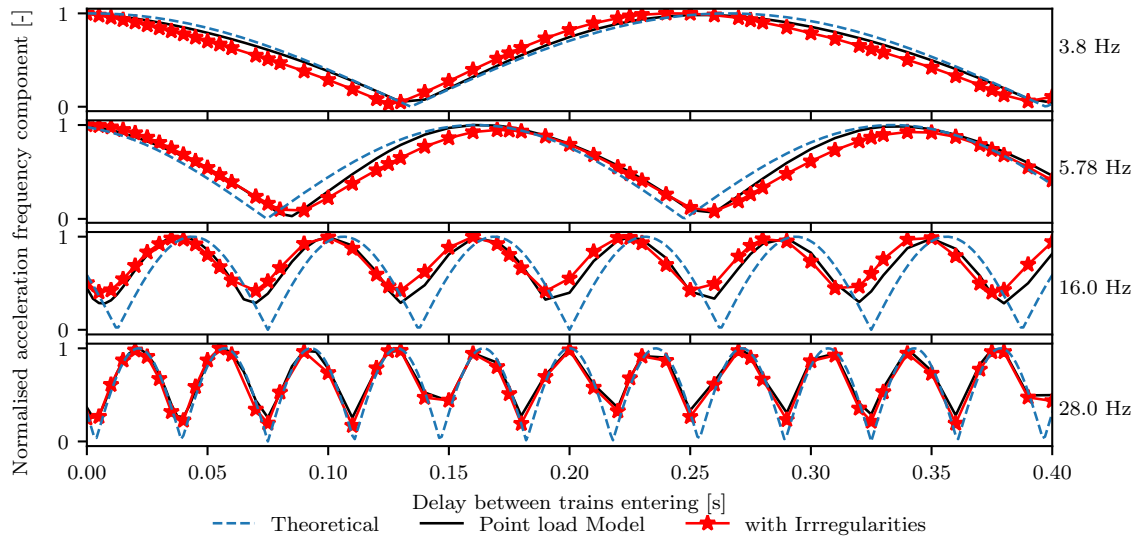
Figure 4.55: Comparison of different normalised frequency components of the vertical bridge acceleration at midspan of the second span

acceleration variation with delay has been taken at x=52.5 m (midspan of the middle span) in Figure 4.54. These two figures show that the simple point load model, which matches well with the no irregularity model, has a period of variation around 0.25 seconds delay. This corresponds to 4 Hz, which is around the primary resonant frequency of the bridge at 360 km/h. In contrast the variation of the accelerations, when considering irregularities, follows both a 0.25 second period delay and a much shorter period, close to 0.037 seconds. This is close to the modal frequency activated by the irregularities of 28 Hz.

As previously seen, for the velocity of 360 km/h, the frequency content of the force interacts with a matching of the loading frequency f_{v7} and the bridge frequency $f_{s,64}$, causing amplification of the acceleration response. As in this section two vehicles are running across the bridge in opposite directions, the contribution of this mode varies due to the additional cancellation and amplification effects introduced by the second vehicle. Figure 4.55 shows the variation of the acceleration component for different frequencies, using acceleration data from the midspan

(a) Symmetric modes   (b) Anti-symmetric modes
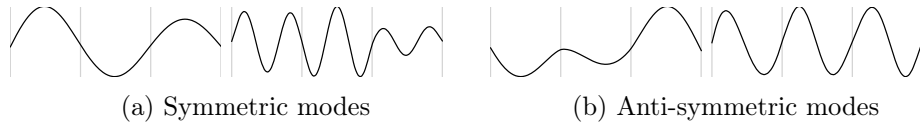
Figure 4.56: Visualisation of symmetric and anti-symmetric modes for dual track analysis

of the middle span at a velocity of 360 km/h. Here, the simple point load model is compared to the vehicle model with irregularities and a theoretical model. These frequency components are shown to vary with delay, and the contributions of each model normalised to its maximum value, allowing comparison between models and theoretical contributions, even though the full model with irregularities generates much larger accelerations, as shown in Figure 4.54. The hypothesis here is that due to the huge computational requirements of the full vehicle model with irregularities, especially when modelling two vehicles, an appropriate tool is required to estimate the delay that will lead to maximum response.

Study of the component frequencies contributing to the larger response of the singular vehicle crossing the bridge, will enable an approximate delay to be studied for maximum response with two vehicles. For example, using the simple or theoretical models, study is made of the variation of the normalised components of acceleration at 3.8 Hz and 28 Hz, which were previously seen to be the frequencies contributing significantly to the vertical acceleration response of the singular full vehicle model with irregularities. These two frequency components have maximum contributions close to aligning for delays of both 0.02 and 0.24 seconds. When studying the actual acceleration variance with delay in Figure 4.54, these delays lead to the largest bridge accelerations. Hence, the tool can eliminate the need to model the full vehicle model for all possible delays. Use of the theoretical model is preferential over the simple model for this prediction as although the point load model has much lower computational times then the full model, the times are still significant. The theoretical contribution of a bridge modal frequency component is calculated using the following Equation:

$$
A\left(f, de\right) = \begin{cases} \mathrm{abs}\left(\cos(\pi \cdot f \cdot \left(de + \frac{1}{f}\left(\left[L \times f\right]\%V\right)\right)\right) & \text{if mode is symmetrical} \\ \mathrm{abs}\left(\cos(\pi \cdot f \cdot \left(de + \frac{1}{f}\left(\left[L \times f\right]\%V\right) + 0.5\right)\right) & \text{if mode is anti-symmetrical} \end{cases}
$$
(4.1)

where $A\left(f, de\right)$ is the component of acceleration for the frequency f and delay de. $\left[L \times f\right]\%V$ represents the non integer remainder of $L \times f$ when divided by the velocity of the vehicle V, where L represents the total length of the bridge. The term symmetrical mode and anti-symmetrical mode refers to the modal shapes of the bridge at that frequency. Examples of the symmetrical and anti-symmetrical modes are shown in Figure 4.56.

Hence, it can be determined that the reason for the smaller accelerations for the irregularity model when trains entered concurrently on dual track rather than on single track in Figure 4.52, is that the 28 Hz mode with this delay is reduced in contribution by a cancellation effect

from the interaction of the loading of the two tracks. This is opposite to the effect of the 4 Hz mode, which experiences a peak in contribution with concurrent entering, coinciding with a resonance of the loading, hence increasing the response of the dual track moving point load model with respect to the single track.

4.4.3 Vehicle Characteristics Sensitivity

Comparison of the upper, median and lower bounds of the primary and secondary, suspension stiffness and damping stiffness values based on different literature values (as found in Appendix C) and compared to the Siemens Velaro train values proposed by Antolín (2013) is made in this section. The Siemens train is labelled as *Antolin Model* in these analyses.

4.4.3.1 Primary Suspension

Model	Stiffness $[kN/m]$		
	$k_{p,x}$	$k_{p,y}$	$k_{p,z}$
Antolin Model	120×10^3	12500	1200
Upper Bound	55000	12500	3280
Median	35696	4880	1480
Lower Bound	9000	640	590

Table 4.7: Primary suspension stiffness comparison values

The first set of analysis studies the primary suspension values. The values implemented are stated in Table 4.7. The values come from a database of literature values as found in Appendix C. Unfortunately due to computational problems, the lower bound of the primary stiffness was too low for this model and hence caused modelling convergence problems. This was caused by the force between the wheel and rail being too large, which could be a result of the reduction of stiffness enabling more horizontal movement of the wheelsets.

It can be seen from the variation in Figure 4.57a that the larger the primary suspension values the smaller the vertical accelerations in the bridge, although the difference is relatively small, especially when the speeds are not near resonance as shown by Figure 4.57b. However, the small difference that does occur seems to come from the activation of the mode around 28 Hz (Figure 4.57e), which as the primary stiffness helps to control the forces in the wheelset, again indicates that this mode is activated by a contribution from the wheel forces.

The vehicle accelerations are also relatively similar in the vertical direction (Figure 4.57c), but in the lateral direction the median model shows the highest lateral vehicle accelerations. This could be down to the lower stiffness increasing the lateral movement (Figure 4.57d). This is significant as the primary suspension is used to help steer the vehicle and keep it on the
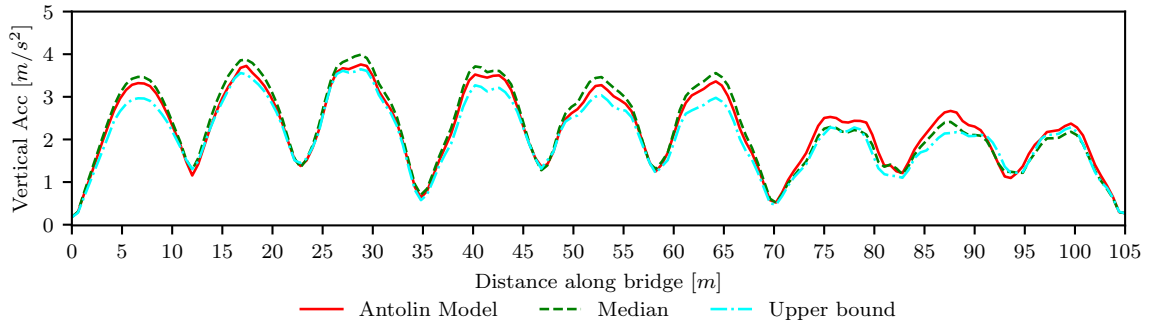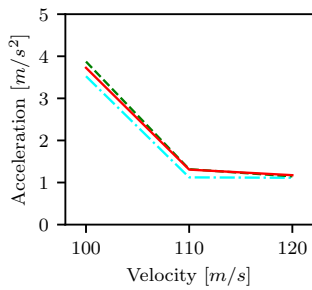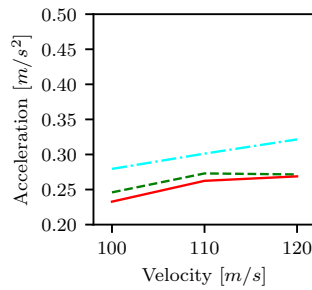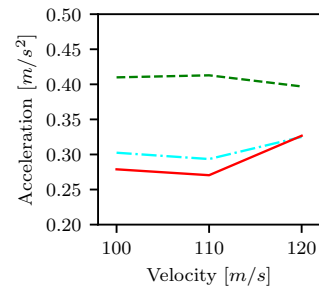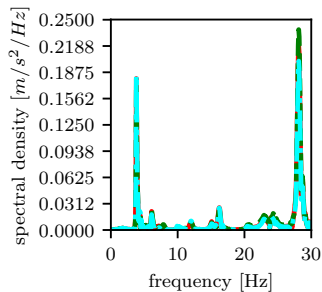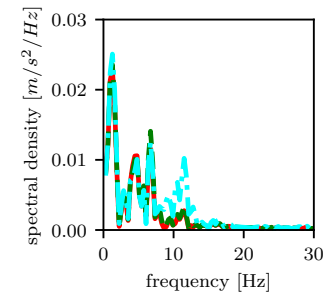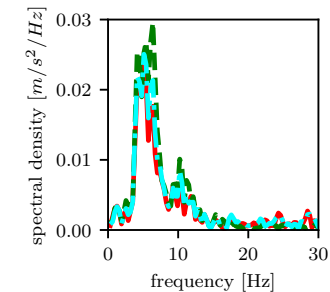
Figure 4.57: Comparison the effects of varying the primary suspension values on: a) the vertical bridge acceleration along the length of the bridge at 360 km/h; b) Variation of filtered vertical bridge acceleration at midspan of the first span with velocity; c) Variation of vertical vehicle acceleration with velocity; d) Variation of lateral vehicle acceleration with velocity; e) Bridge vertical acceleration at midspan of first span in frequency domain at 360 km/h; f) Rear vehicle vertical acceleration in frequency domain at 360 km/h; g) Rear vehicle lateral acceleration in frequency domain at 360 km/h

track. The frequency domains (Figures 4.57f and g), of the accelerations of the vehicle at 360 km/h, do not show any significant change in the location of the peaks, showing that the modes contributing to the vehicle accelerations have not changed.

Overall, the effects of changing the primary suspension stiffness on the bridge and vehicle dynamics is relatively small, and the response by the Siemens train is matched closely by other primary suspension stiffnesses in literature. This is significant as some of the Siemens train values are high compared to the rest of literature, however the response is still reasonable.

4.4.3.2 Primary Damping

Comparison of the variation of the damping coefficients expressed in Table 4.8 is visualised in Figure 4.58. From Figure 4.58a it can be noted that the impact of increasing the damping can cause the vertical accelerations in the bridge, but not the vehicle to be higher. This reflected in Figure 4.58b, which shows the same pattern, especially under the resonant characteristics of 100 m/s (360 km/h). The reasoning for this could be that the damping restricts the ability for the wheelset to react and move relative to the bogie, therefore transferring more variation in force into the bridge when there is a relative displacement between the two wheelsets sharing a bogie, possibly caused by either irregularities or bridge deflections. This is shown in Figure 4.58e, which shows that there is variation in the modal contribution to the 28 Hz mode, which was considered to be caused by the wheel forces.

Model	Damping Stiffness $[kN \cdot s/m]$		
	$c_{p,x}$	$c_{p,y}$	$c_{p,z}$
Antolin Model	27.9	9	10
Upper Bound	48	27.9	80
Median	12	9	19.8
Lower Bound	0	0	2.93

Table 4.8: Primary suspension damping stiffness comparison values

In contrast the vehicle accelerations shown in Figures 4.58c and d, show very little impact of the damping on the carriage accelerations. This is unsurprising as the primary damping system primarily helps to steer the vehicle, and this is a straight track that is being modelled. The lack of effects on the carriage is also indicative of the purpose of this level of suspension. This is also shown in Figures 4.58f and g which do not change significantly for the different damping values.

It is worth recalling that the primary damping is between the bogie and the wheelset and hence there is another layer of suspension between the bogie and the carriage where the changes accelerations can be absorbed before reaching the passengers. Again overall the Siemens train proves to have a good representation of the damping stiffness in comparison
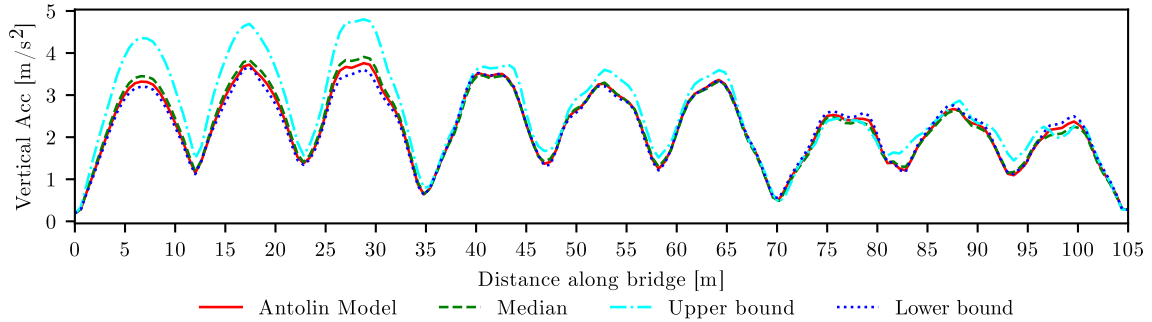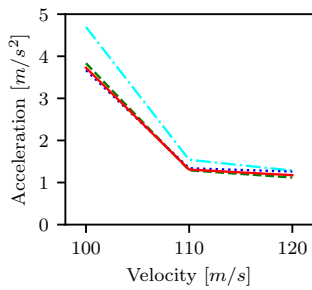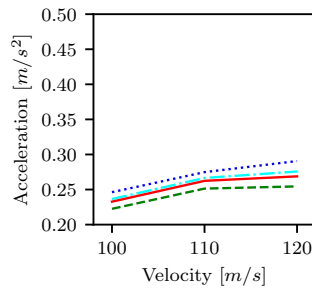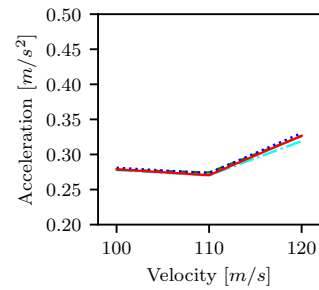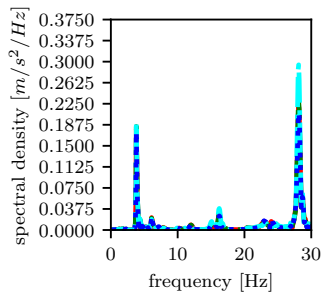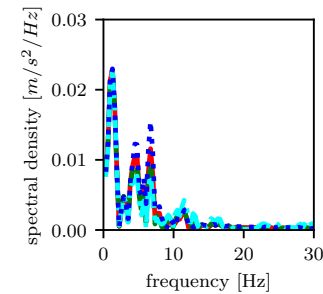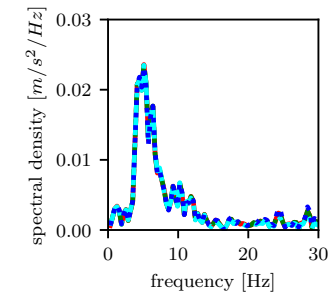
Figure 4.58: Comparison the effects of varying the primary suspension damping values on:a) the vertical bridge acceleration along the length of the bridge at 360 km/h; b) Variation of filtered vertical bridge acceleration at midspan of the first span with velocity; c) Variation of vertical vehicle acceleration with velocity; d) Variation of lateral vehicle acceleration with velocity; e) Bridge vertical acceleration at midspan of first span in frequency domain at 360 km/h;f) Rear vehicle vertical acceleration in frequency domain at 360 km/h; g) Rear vehicle lateral acceleration in frequency domain at 360 km/h

with other literature.

4.4.3.3   Secondary Suspension

The secondary suspension level, acting between the carriage and the bogie is not directly linked to the wheelsets. Hence its impact on the wheelset forces will be minimal. Therefore, the likelihood of changes in the secondary suspension effecting the bridge are small. This is backed up by Figures 4.59a and b. The difference between the maximum vertical accelerations is barely discernible, for the different stiffnesses outlined in Table 4.9. This is further noticed in the near identical modal contributions to the vertical accelerations in Figure 4.59e.

Model	Stiffness [kN/m]		
	$k_{s,x}$	$k_{s,y}$	$k_{s,z}$
Antolin Model	12000	240	350
Upper Bound	316	316	1440
Median	210	160	530
Lower Bound	100	39.2	33

Table 4.9: Secondary suspension stiffness comparison values

In contrast to the impact on the bridge, the impact of the suspension stiffness on the carriage accelerations is much larger. The higher the stiffness the larger the accelerations, with the upper bound showing significantly higher vertical accelerations in Figure 4.59c. The decomposition in the frequency domain of the vertical acceleration, as seen in Figure 4.59f, shows significantly higher amplitudes of the contributing frequencies to the acceleration but no noticeable shift in frequency. The lateral accelerations do not show so much variation in Figure 4.59d, but still indicate higher stiffnesses lead to higher accelerations. The lower variation is also seen in Figure 4.57g. The value chosen for $k_{s,x}$ by Antolín (2013) is very high and above the upper bound considered based on other values in literature. This value is repeated in Antolin et al. (2012), so is unlikely to be a mistake in print. However, the use of this value for the Antolin Model, produces a response similar to the median and lower bound values. Hence, as the Siemens model train is within the range of the accelerations given by the upper and lower bounds, it is appropriate to use this model. However, this sensitivity shows the importance of modelling the correct vehicle secondary stiffnesses in order to calculate the correct vehicle response.

4.4.3.4   Secondary Damping

The final study into the vehicle sensitivity looks at the secondary damping stiffness. The values used in this study are found in Table 4.10. The lower bound models did not converge computationally, due to flange-rail contact, and hence have been excluded from the results.
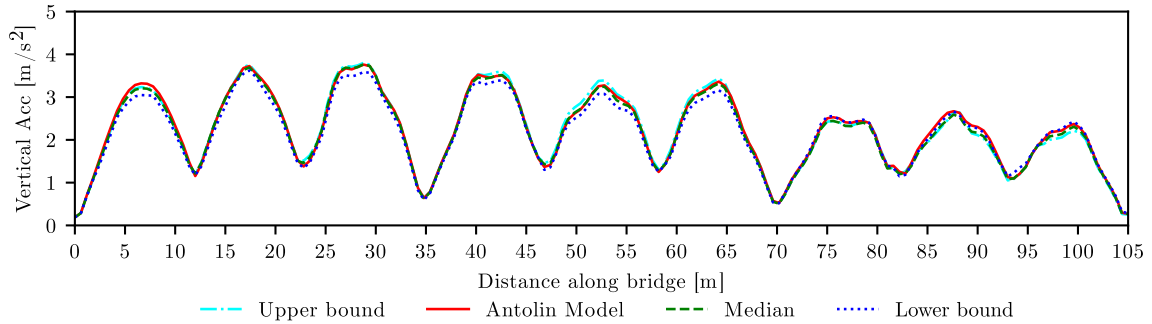
(a)
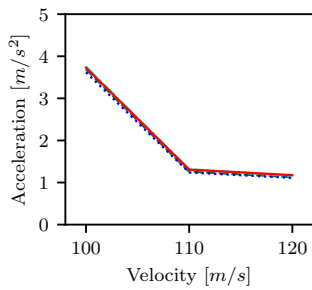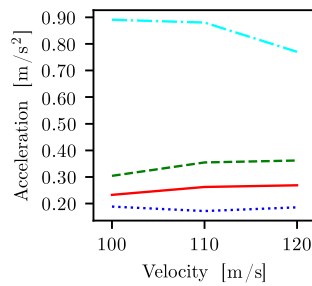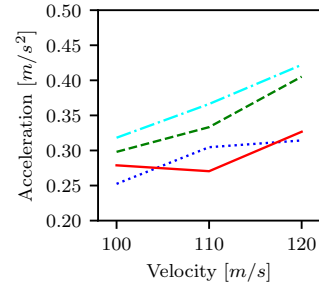
(b)   (c)   (d)
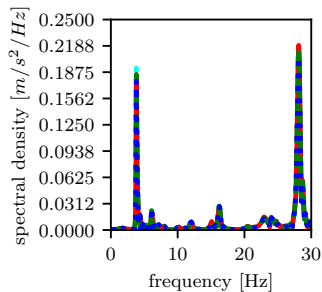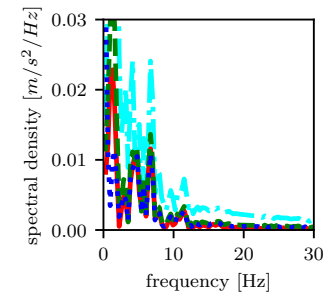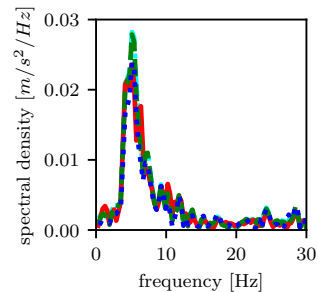
(e)   (f)   (g)

Figure 4.59: Comparison the effects of varying the secondary suspension values on: a) the vertical bridge acceleration along the length of the bridge at 360 km/h; b) Variation of filtered vertical bridge acceleration at midspan of the first span with velocity; c) Variation of vertical vehicle acceleration with velocity; d) Variation of lateral vehicle acceleration with velocity; e) Bridge vertical acceleration at midspan of first span in frequency domain at 360 km/h;f) Rear vehicle vertical acceleration in frequency domain at 360 km/h; g) Rear vehicle lateral acceleration in frequency domain at 360 km/h
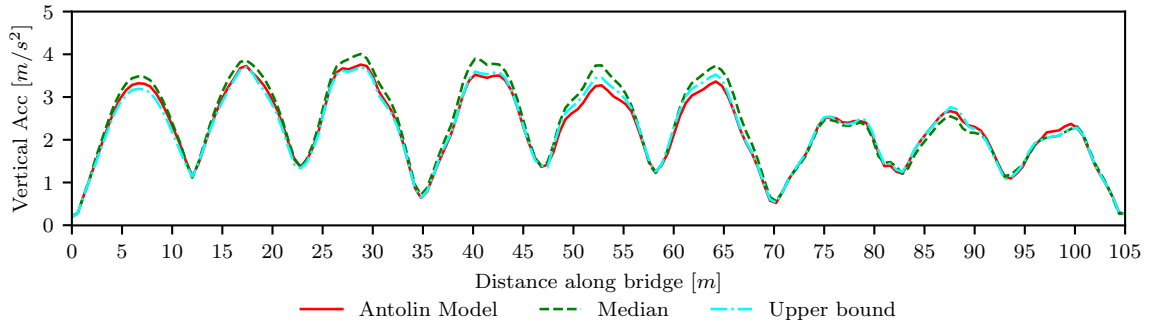
(a)
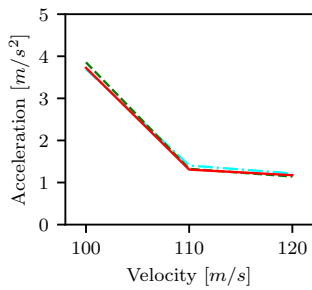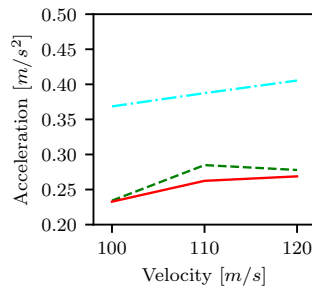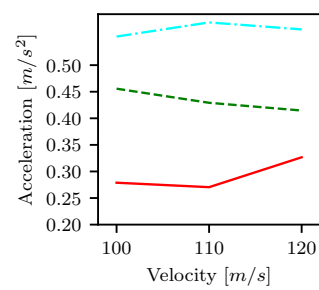
(b)   (c)   (d)
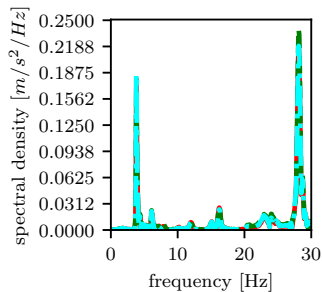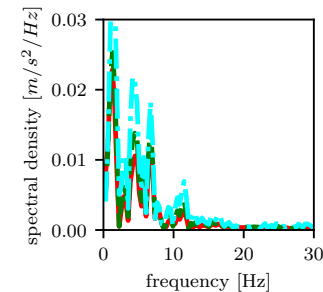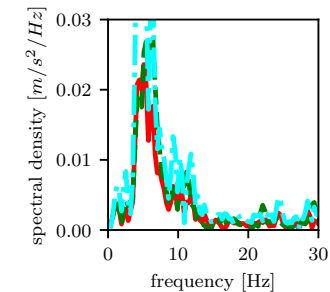
(e)   (f)   (g)

Figure 4.60: Comparison the effects of varying the secondary suspension damping values on: a) the vertical bridge acceleration along the length of the bridge at 360 km/h; b) Variation of filtered vertical bridge acceleration at midspan of the first span with velocity; c) Variation of vertical vehicle acceleration with velocity; d) Variation of lateral vehicle acceleration with velocity; e) Bridge vertical acceleration at midspan of first span in frequency domain at 360 km/h; f) Rear vehicle vertical acceleration in frequency domain at 360 km/h; g) Rear vehicle lateral acceleration in frequency domain at 360 km/h

This may have been due to the lack of damping allowing the carriage to turn more freely, which may enable hunting motions to develop.

Model	Damping Stiffness $[kN \cdot s/m]$		
	$c_{s,x}$	$c_{s,y}$	$c_{s,z}$
Antolin Model	600	30	20
Upper Bound	600	72	90
Median	180	30	34.2
Lower Bound	30	1.23	0

Table 4.10: Secondary suspension damping stiffness comparison values

The secondary damping stiffness affects the bridge vertical accelerations a small amount as can be seen in Figure 4.60a. The effect though is small, and probably is linked to the rate of movement of the train, as to adapt to the deflections of the bridge and the irregularities, becomes slower with higher damping. Figure 4.60b shows even less variation in the bridge accelerations, which is reflected in the near identical modal contributions to the vertical accelerations seen in Figure 4.60e. However, again the carriage accelerations in Figures 4.60c and d are greatly affected by the secondary damping stiffness, as they were by the secondary elastic stiffness. The frequency component contributions are much more variant in the vertical case and in the lateral direction as seen in Figures 4.60f and g. This is more prominent in the lateral accelerations. It is probably due to greater force transfer into the vehicle with the higher damping stiffnesses. Also the Antolin Model shares the same value as the upper bound for $c_{s,x}$, however the results of the Antolin model show much smaller response than the upper bound for all cases. This indicates the negligible effect the variation of this coefficient has on the vehicle-bridge dynamics. In conclusion the Siemens train model by Antolín (2013), performs similarly to values from literature and hence is appropriate to use.

4.5   Alternative Models

Where in the previous sections all models have focused on the bridge being composed of shell elements and the vehicle being either the full Siemens Velaro vehicle model, or a representation of the vehicle by moving point loads, this section looks at other alternatives.

4.5.1   Alternative Loading Models

When considering the moving load model representation of the vehicle in the previous sections, this includes also removing the track as well as the vehicle, but ensuring that the mass of the track is still represented in the bridge. In this section a comparison between moving load models on the bridge, with and without the track is made. This compares four cases. The
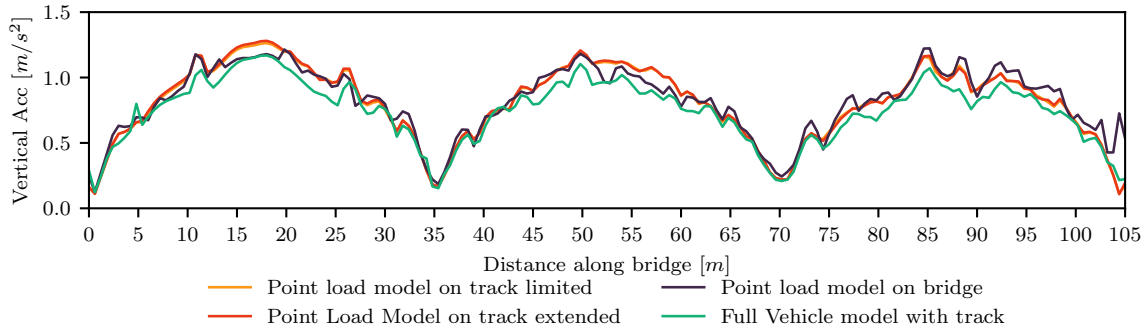
Figure 4.61: Comparison of the filtered maximum vertical accelerations along the length of the bridge for different loading types at 360 km/h

first uses moving point loads directly applied to the track. Secondly, the track is modelled and the moving point loads travel along the full length of the track including beyond the extent of the bridge, whereas in the third case, the same model is used but the moving point loads are limited to the extent of the bridge. Finally a comparison is made to a moving vehicle model without irregularities.

It can be seen in Figure 4.61 that the point load models have similar maximum accelerations, and that the full vehicle model has a slightly smaller response, but still similar. The smaller response in the case of the vehicle being modelled could be from the mass of the vehicle interacting with the bridge mass, and altering the fundamental natural frequency of the bridge as mentioned in Cantero et al. (2016). Alternatively it could be due to the vehicle being modelled allowing alternative loads to be transferred into the bridge. Nonetheless, the difference is small and as such the point load model without track is an appropriate indication of the vehicle model without irregularities.

When looking at the same data in the time domain, at the midspan of the first span, as in Figure 4.62, it shows that the exclusion of the track results in a small shift in the free vibration frequency of the structure, which shows the accelerations becoming increasingly out of phase. This is due to the affect on the bridge of the track, which acts to restrain the bridge a little, as well as allowing transfer of loads from the train into the bridge via the rail even after the train has left the bridge. As a result there is a change in the frequency of the bridge when modelling the tracks, as expressed in Table 4.11. Different mode shapes undergo different changes in the frequency, not consistently larger or smaller for the inclusion of the track. It can be seen that the impact of the moving loads extending on the track beyond the length of the bridge has little effect compared to loads just within the track nodes within the limits of the bridge. However, the maximum accelerations are not occurring in the free vibration phase, and the forced vibration period shows good correlation between the three models. Due to the additional time required to model the track (40%) in the moving point load models, and the small difference in the resulting accelerations, it is more appropriate to model the bridge without including the track for the simple models.

Mode	Shape	Number of tracks modelled		
		0	1	2
1		3.79	3.82	3.87
2		4.49	4.10	4.16
3		5.58	4.49	4.51

Table 4.11: Shift of frequency by including the tracks on bridge when calculating frequency
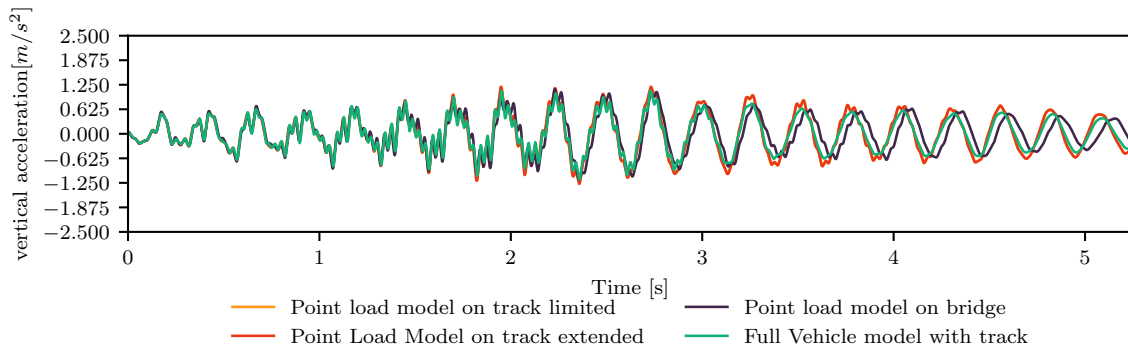
Figure 4.62: Comparison of the time history of the filtered maximum vertical bridge accelerations at the midspan of the first span at 360 km/h of different load types.

Considering that the moving point load model without the track is an appropriate model to compare the vertical accelerations at 360 km/h for the vehicle model without irregularities, a comparison across different velocities is made in Figure 4.63. This shows a good match between the vertical accelerations between the two models, especially at higher velocities. Due to higher computational demand for the full model, there is a smaller speed resolution for this model than the point load model, hence the larger variation in the point load model accelerations with velocity. From this figure it is clear that the bridge vertical dynamic performance can be approximated by the point load model for all speeds for perfect tracks without irregularities.
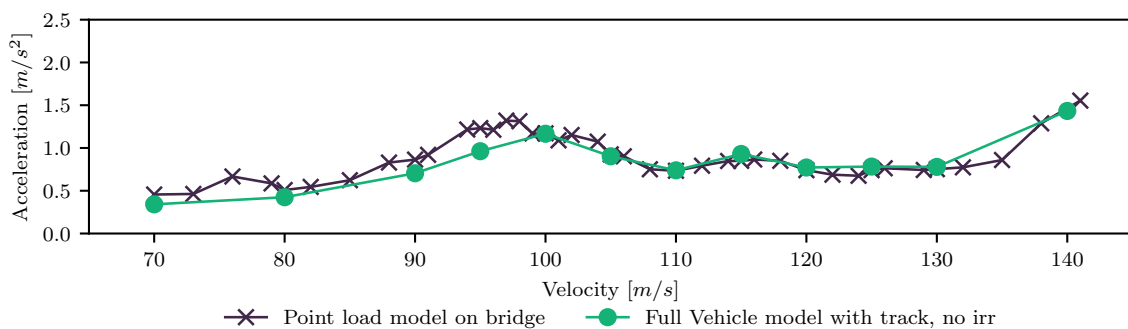
Figure 4.63: Comparison of the filtered maximum vertical accelerations at midspan of the first span for different velocities with different loading types
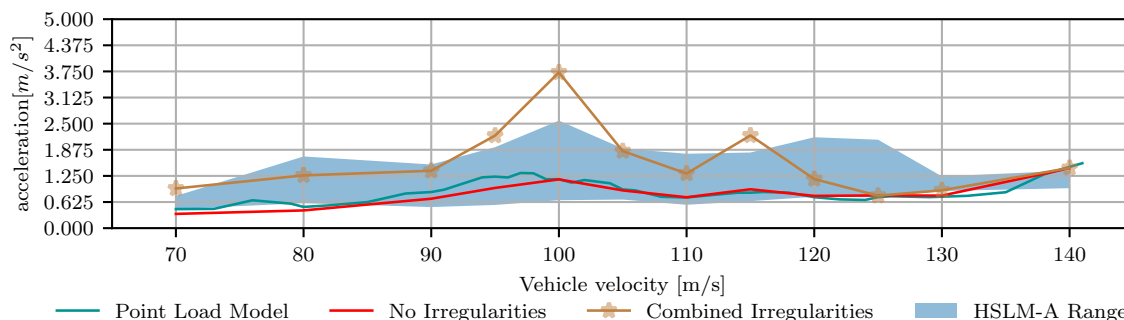
Figure 4.64: The filtered maximum vertical accelerations for models with and without irregu-larities in comparison with moving point load models for a real Siemens Velaro train and the Eurocode HSLM models

Whereas in this work, the model has focused on the real train model, BS EN 1991-2:2003 (2010) specifies a series of moving load models to test the bridge dynamics. These models are designed to encompass all variations of train weights and configurations. Figure 4.64 compares the Siemens train to the HSLM-A models from BS EN 1991-2:2003 (2010). From this figure it can be seen that at resonant speeds this real train with irregularities results in larger vertical accelerations than the load model. Although the use of HSLM-A models neglect the impact of irregularities, they were designed such that the response of the collection of load models is representative of the full possible range of vehicles crossing the bridge. So it could be important in developing an approximation of the axle spacing that causes the critical resonant responses, due to the variation in axle spacing incorporated in the HSLM models. This axle spacing could then be correlated to a real train for which the full vehicle model with irregularities can simulate. However, currently there is not enough available information on the wide range of real trains, to use this approach with the full vehicle in this thesis. It does however, highlight the importance of testing the bridge model with real trains to incorporate the irregularities, which can cause higher accelerations than the HSLM-A envelope of loading suggests.

4.5.2   Alternative Bridge Model

Using the beam element models considered in Section 3.1.1.1, a comparison is made between the shell element models and the beam element models. Due to the complicated nature of the bridge boundary conditions, the lateral performance is not well matched by the beam element model. Nonetheless, the vertical accelerations are relatively well matched, partly as the fundamental vertical frequencies are within 1%.

As seen in Figure 4.65, the accelerations of the beam model and the shell model with point loads is well matched. Due to the difference in the accelerations in the bridge between the slab and the actual U-beams, both have been plotted for the shell bridge models. This is chosen as unlike in the beam element model, there is no node at corresponding centroid of
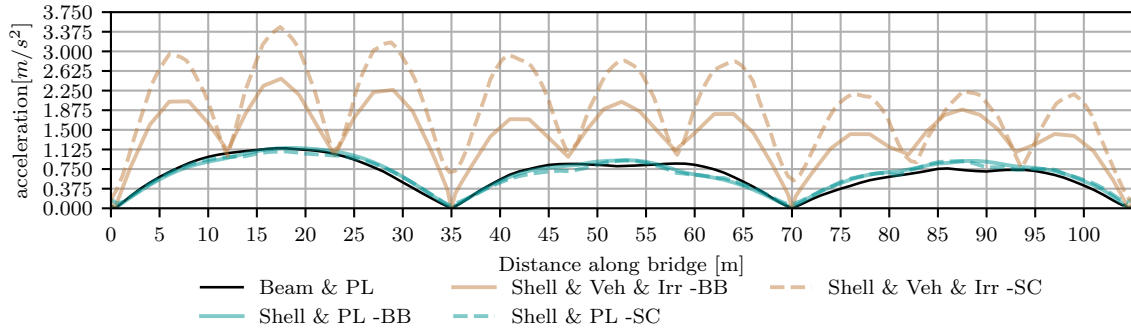
Figure 4.65: Comparison of filtered maximum vertical accelerations in shell bridge models and beam bridge models along the length of the bridge at 360 km/h. *PL* stands for moving point loads as opposed to *Veh* which signifies the model uses real vehicles with irregularities (*Irr*). *SC* represents the values taken from the centre of the slab, *BB* being values taken from the bottom of the beam under the loaded track.
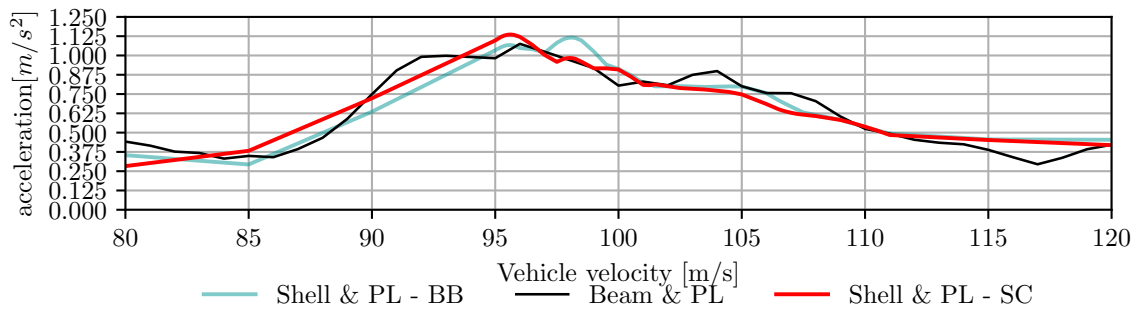
Figure 4.66: Comparison of filtered maximum vertical accelerations in shell bridge models and beam bridge models at midspan of the first span with different vehicle velocities, using only moving point load models (*PL*), hence not including irregularities. *SC* represents the values taken from the centre of the slab, *BB* being values taken from the bottom of the beam under the loaded track.

mass for the shell elements, and averaging from other nodes is inappropriate due to the large transverse deformations in the shell elements. It shows that the accelerations along the bottom of the U-beam are similar to those in the slab. However, when considering irregularities, the accelerations found by modelling using shell elements, are much smaller in the bottom of the U-beam than they are in the slab. These accelerations with irregularities are only able to be picked up by using shell element models, as these allow local vibrations of the cross section, which are mainly focused in the slab. These higher frequency modes are unable to be captured through a beam model, with beam models not allowing transverse deformations.

Finally, comparison of the vertical accelerations against velocity between the beam and shell bridge models using moving point loads is shown in Figure 4.66. The velocity that the shell element models are calculated at are refined such that they find the peaks accurately, but are coarsely modelled where peaks are not expected. This is done at the midspan of the middle
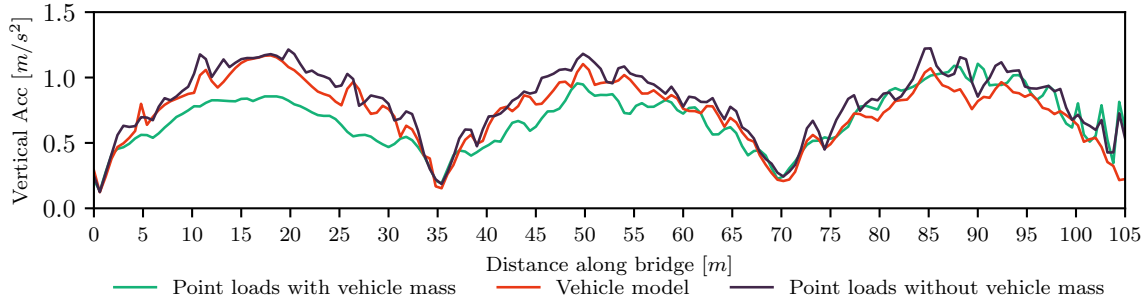
Figure 4.67: Comparison of the maximum filtered vertical accelerations along the length of the bridge for a vehicle moving at 360 km/h, testing the effects of the mass of the vehicle being incorporated

span. It indicates that the beam element model can provide an estimate of the velocities that activate resonant effects for low frequency modes. However, it is obvious from the previous results in this chapter, that higher frequency modes, only found with shell element models, can be activated by irregularities, which were not modelled here. Hence, it is required that for an accurate response of the bridge, accelerations must be determined by the shell element model coupled with irregularities.

4.5.3   Distributed Vehicular Mass

The mass of the train is not insignificant in comparison with the bridge mass. Each carriage (including the passengers, bogies and wheelsets), has a mass of 73040 kg, whereas the mass of one span of the bridge deck, including the track and other topside equipment is 1127350 kg. Per unit length, this results in a ratio of vehicle to bridge mass of 9%. To investigate whether this mass has an impact on the bridge response, the mass of the train is distributed along the track as a nonstructural mass.

The nonstructural mass takes the value of 781.6 kg/m^2, spread over a track width of 3.74 m and over the full bridge length of 105 m. This equates to the mass of 4.2 train carriages (each train carriage is 25 m long), spread over the length of the bridge. Then the dynamic response is tested with moving point loads. This is compared to the moving point load model without the additional mass and the full vehicle model without irregularities. The aim of this is to compare the models, as a full vehicle model is not as easily constructed in real world, as a moving point load model. This is seen in Figures 4.67 and 4.68.

As can be seen from Figure 4.67, including this vehicle mass as a continuous mass along the bridge yields smaller maximum filtered accelerations across most of the bridge. Study of Figure 4.68 shows that the response of the model with the distributed train mass has significantly different response. This is not as small as the difference due to the exclusion of the track,
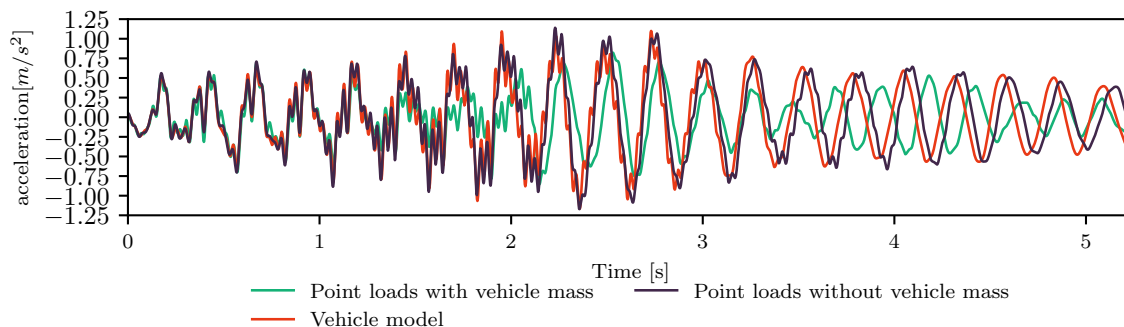
Figure 4.68: Comparison of the time dependent filtered vertical acceleration of the midspan of the first span of the bridge with a vehicle moving at $360\,km/h$, testing the effects of the mass of the vehicle being incorporated

and indicates that the change in frequency caused by the inclusion of this mass is significant. The fundamental bending mode's frequency changes from $3.79\,Hz$ in the model without the additional mass to $3.63\,Hz$ in the model with the addition of the vehicle mass. According to Cantero et al. (2016), the fundamental frequency of the bridge varies with the position of the vehicle on the bridge. This changing frequency, and the difference in the frequencies with the full mass of the vehicle and with no vehicle mass explains the reduced resonant effect at $360\,km/h$, causing the smaller response experienced.

As a result, due to the reduction in accelerations by adding the track mass, it is not recommended to include the mass of the vehicle as a fixed non structural mass along the length of the track.

4.6   Conclusions for this Chapter

The conclusions of this section allow the models to be progressed with justification into parametric analysis of the bridge. In terms of the bridge design, it has been found:

- The vertical accelerations in the slab are largest on the lateral edges, and under the loaded track, but only the latter is relevant to the vehicle running safety.

- Rayleigh damping with a coefficient of 1% fixed at 4 Hz and 60 Hz shall be used in this thesis as it is the most conservative of those tested, accounts for 95% of modal mass and is the value assigned by BS EN 1991-2:2003 (2010).

- A three span bridge is relatively representative of the accelerations of longer bridges, and one span bridge represents the maximum accelerations of a two span bridge as well.

- The condition where the intermediate piers are both longitudinally fixed leads to smaller

accelerations than the case where the first pier has longitudinally fixed boundary conditions.

- The vehicle entering and travelling over the longitudinally fixed pier first leads to larger accelerations than when the last pier travelled across is longitudinally fixed

- Although the slab has lateral accelerations that are not zero over the supports, the maximum lateral deflection is very small, so not a concern for derailment

- The prestress force has no affect on the bridge dynamics, only onto the vehicle dynamics due to prestress associated changes in the running profile of the track. Therefore the prestress force does not need to be modelled, but the prestressing steel must be modelled for the additional stiffness this provides to the section.

- The connection between the slab and the precast beams is to be modelled as partial interaction, as the full interaction model led to longer computational times, but little difference between the results of the two models.

For modelling the track, the following conclusions have been made:

- The railpad stiffness coefficient impacts the vertical accelerations of the bridge, with lower stiffness leading to larger accelerations.

- The railpad damping coefficient leads to no discernible change in the bridge dynamics.

- The ballast stiffness also impacts the vertical accelerations of the bridge, but the lower the stiffness, the lower the acceleration.

- The ballast damping stiffness has a small effect on the bridge dynamics, but not significantly.

- The ballast mass affects the bridge dynamics significantly, due to its impact on the bridge modal frequencies.

- From the models tested the ballasted models lead to lower accelerations in the bridge than the slab track models

Modelling of the track will utilise slab track for the remainder of this thesis, as these models are found to be less computationally demanding. Despite the larger accelerations associated with this model, the safety limit to vertical bridge accelerations is also higher, and the trend in industry is towards slab track over ballasted tracks.

In the region of the wheel-rail interaction, the following conclusions could be made:

- Consideration of the wheel forces under a resonant speed showed that the risk of derailment from these forces was small, and hence the need to test the computationally expensive wheel forces versus derailment limits is not required in the rest of the thesis.

- Vertical irregularities had the greatest effect on the vertical accelerations of the bridge

- Lateral accelerations in the bridge were mainly impacted by the cross-level irregularities

- Vertical irregularities were those to have the biggest impact on the vertical accelerations in the vehicle, but cross level and alignment irregularities impacted the lateral vehicle accelerations

- Introducing the irregularities induces a wide frequency content in the wheel-rail forces, which contributes to the amplification of resonant bridge modes that meet vehicle driving frequencies, which are not activated when irregularities are not present. This can lead to significant increases in the bridge accelerations.

As a result of this analysis irregularities are still required to be studied in the models in this thesis as they have significant effects on the bridge dynamics, despite being computationally expensive.

Study of the vehicle has led to the following conclusions:

- An 8 carriage train vehicle induces lower accelerations than a 16 carriage train on the bridge by a maximum of 16%. However it is much more computationally efficient than the 16 carriage train, and is a standard length of carriages, so will be proceeded with.

- Running two vehicles simultaneously in opposite directions across the bridge can lead to almost doubling of accelerations in the bridge. This depends on the delay between the vehicles entering and the corresponding contribution of modes under resonant or cancellation effects. An equation was proposed to determine whether a contributing mode is in a resonant or cancellation phase with a particular delay.

- The vehicle primary stiffness has little affect on the bridge behaviour, but more significant effects on the vehicle behaviour

- The primary damping does have a limited affect on the bridge dynamics, but little effect on the vehicle behaviour

- The secondary stiffness and damping have little to no affect on the bridge dynamics, but significant impacts on the vehicle dynamics.

Considering the modelling of the whole system, some conclusions are:

- A beam bridge model can adequately have a first estimate of the behaviour of the bridge without irregularities

- A moving point load model can predict the behaviour of a bridge under a vehicle without irregularities well

- A moving point load model with the wheel force variation from irregularities can predict the response of the bridge well without the need to model the full vehicle model. However, a method of pre-determining the force variation based on the irregularities has not been found, so the model with the vehicle still has to be run to obtain the wheel forces.

- Inclusion of the track elements on the bridge does not have a significant impact on the dynamics of the bridge, but alters the frequency slightly.

- Inclusion of the full vehicle mass on the bridge whilst using point load models, is not equivalent to the full vehicle model, and not including this mass, when using moveable point load models, gives a better representation of the results found by a full vehicle without irregularities.

From this chapter, some recommendations can be made to update the codes and guidelines for modelling HSR bridges. These are:

- Clarification must be made on the type of bridge model used. Currently no reference is made to the complexity of the bridge model. It is evident from literature many authors use beam models, but this chapter shows these are inadequate at estimating the local deformations of the slab, as proven by shell element models, particularly when modelling using a full model with irregularities. This lack of clarity could lead to insufficient design, with high accelerations. However, it is recognised that the use of beam elements is more accessible, so different acceleration limits should be established for different complexities of models.

- Updating of the high speed load models. The real vehicle used in this chapter was shown to exceed the accelerations given by the range of vehicle covered by the HSLM load model. This could lead to unacceptable bridge accelerations for irregularities that are also considered acceptable in the codes.

In addition, it was found that numerical instabilities could form within the models, under certain cases. For example:

- The time step of the model using wheel-rail interaction and a vehicle had to be much smaller than a point load model to avoid computational errors.

- The primary suspension stiffness and secondary damping coefficient must be sufficiently large to avoid errors associated with wheel flange contact.

As a result, the next chapters shall use the Siemens Velaro train, on a slab track. The bridge shall be modelled using shell elements, with beam element models used to identify potential speeds of resonance. The connection between the precast U-beams should be using a tied formulation in ABAQUS, whereas the connection between the beams and the slab shall be an elastic connection. This is due to computational benefits. Finally, irregularity models shall be used in order to determine the full extent of the accelerations.

Chapter 5

HSR Bridges with Dual U-Beam Cross Sections

This chapter focuses on the response of HSR bridges with dual U-beam cross sections. In order to get a deep and sound understanding about their response, in addition to the analysis of the benchmark case, a comprehensive parametric analysis has been conducted. As the U-beams are precast, and the slab cast in-situ, focus will be made to the reduction of the amount of materials used in the precast beams through the implementation of high performance concrete, as saving weight here will contribute to the greatest benefits for transportation, crane capacities and subsequent reduction in the demands of other structural members that form part of the substructure.

5.1   Methodology

The bridge as outlined in Section 3.1.2, is used here as a benchmark case. For different components of the bridge, the geometry is reduced by a factor and the concrete strength increased by another factor, with the intention of counterbalancing the effect in terms of structural capacity, and then analysed. The increase in concrete strength is determined such that the moment resistance, shear resistance and vertical bending stiffness of the beam are maintained at values similar to the benchmark case values. The geometry cases studied are the beam web thickness, bottom flange thickness, combined bottom flange and beam thickness, and section depth. The cases are first studied in a simply supported version of the bridge (using one span), which as shown in Section 4.1.3 is representative of the accelerations found in both the one and two span cases. If the parameter studied is feasible, then it is studied for the three span continuous case. In all cases the span length is maintained at $35\,m$, which is the original span length and was established as the most suitable span length in Section 4.1.4.

Model	Analysis Type	Bridge Model		Loading Model	
		Beam	Shell	Moving Loads	Full Vehicle
Beam	Dynamic	✓		✓	
Static	Static		✓	✓	
Simple	Dynamic		✓	✓	
Full	Dynamic			✓	✓

Table 5.1: Characteristic of the different model types, showing the element type used for the bridge model, loading model used (Full Vehicle includes the wheel-rail interaction and irregularities) and the analysis type.

For determining the effects of the parametric analysis, dynamic amplification factors (DAF) and accelerations are studied. The DAF are studied on the both lateral (U2) and vertical (U3) displacements, the direct normal stress in longitudinal direction (S11), which is induced by longitudinal bending and axial response, and the normal stress in the element plane perpendicular to the longitudinal direction (S22), which is induced by transverse bending. Positive direct stresses are tensile stress. Only the component of the stresses developed under the traffic loading, not accounting for the impacts of gravity, prestress or long term concrete behaviour, are compared herein. The static model results, shown and used in the DAF calculations, are the stresses and displacements experienced when running the vehicle across the bridge in a static rather than dynamic analysis.

Comparison of four types of model is made in his section. These are *Beam, Static, Simple* and *Full*. These models differ as explained through Table 5.1.

5.2 Single span Benchmark Case

Using the same cross section as the continuous bridge, the single span bridge was previously shown to exhibit larger accelerations (Section 4.1.3). To study the DAF and accelerations for parametric analysis, critical locations for the study of these values are established in this section. The stress in the beam will be critical in the bottom flange of the precast U-beam, whereas the deflection and acceleration requirements are based on impact to the running safety of the vehicle, and so will be based in the slab. The accelerations were previously identified to be critical along the length of the bridge under the track in Section 4.1.1.

5.2.1 Bridge Displacements

The impact of the model type on the bridge vertical deflection can be seen in Figure 5.1. It shows considerably higher maximum vertical deflections in the dynamic models, influenced by the resonant speed at $100\,m/s$. The highest deflections are found at the midspan of the edge of the flange on the slab on the loaded side. The lack of symmetry laterally across the

(a) *Static* Model   (b) *Simple* Model   (c) *Full* Model
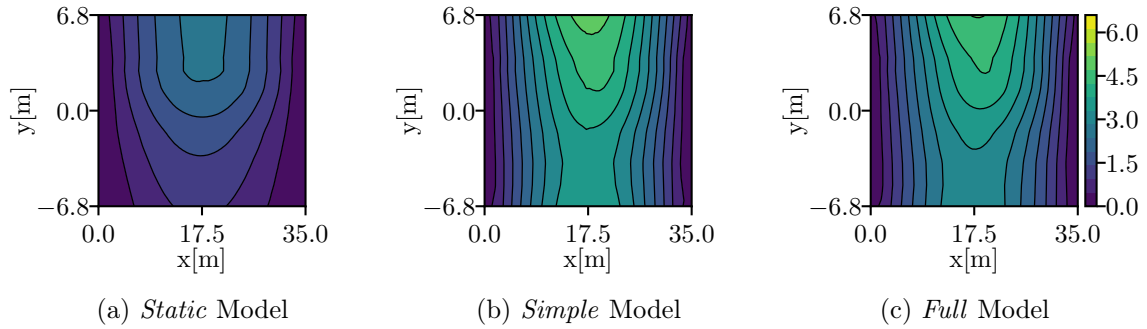
Figure 5.1: The vertical displacements (U3) in the slab $[mm]$ at $100\,m/s$

(a) *Static* Model   (b) *Simple* Model   (c) *Full* Model
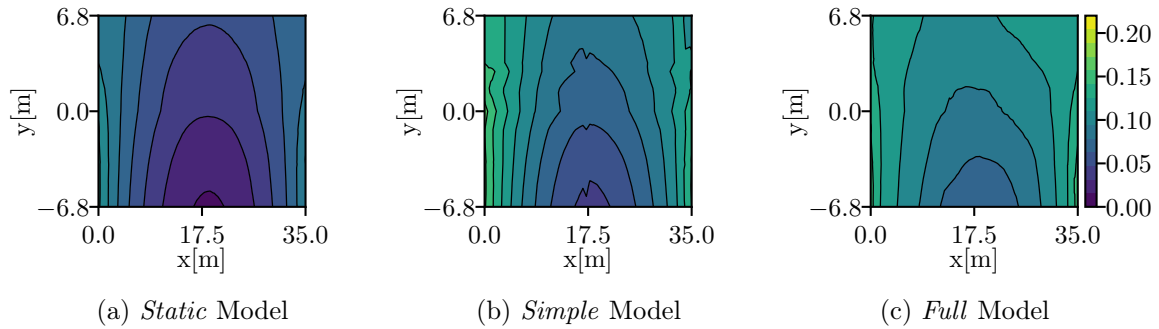
Figure 5.2: The lateral displacements (U2) in the slab $[mm]$ at $100\,m/s$

bridge indicates the deck slab is distorting. Compared with the limits on bridge deflection of $L/600$ (BS EN 1990:2002 +A1:2005, 2010), where L is the bridge span, the maximum vertical deflection under loading is no more than $6\,mm$ in the case shown, whereas the limit would be $58\,mm$.

Laterally, the maximum displacements in the slab appear to be located at the ends of the span, although these deflections are still very small. This can be seen in Figure 5.2. This is due to contribution of distortion modes. Introduction of thicker diaphragms can be used to control lateral displacements, for which under analysis not shown here, a thicker diaphragm proved to lower the lateral displacements.

The DAF of the displacements are shown in Figure 5.3 (vertical) and Figure 5.4 (lateral). They show the DAF of the *Full* model, with the *Simple* model providing very similar results. The low displacement, especially in the static case, close to the end spans leads to high DAF here in the vertical deflection case. Likewise, high DAF are found in the centre of the bridge on the unloaded side for the lateral displacement. As a result, the vertical deflection DAF shall be compared at the midspan where the largest deflection is found.

The variation of the DAF with velocity can be found in Figure 5.5a. The vertical deflection has a peak at around $100\,m/s$ which is consistent with a resonant speed. There is good correlation between the DAF and the actual deflections between the *Full* and *Simple* models. The lateral
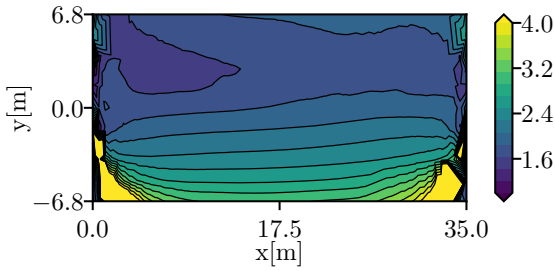
Figure 5.3: The DAF for vertical deflections in the slab at $100\,m/s$ for the *Full* vehicle dynamic model
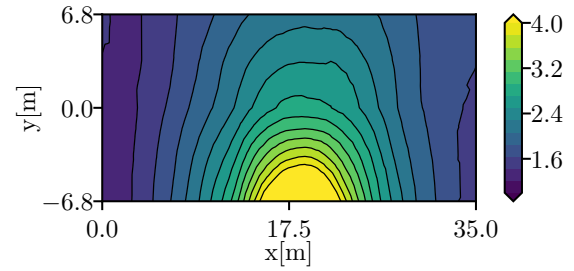
Figure 5.4: The DAF for lateral displacements in the slab at $100\,m/s$ for the *Full* vehicle dynamic model
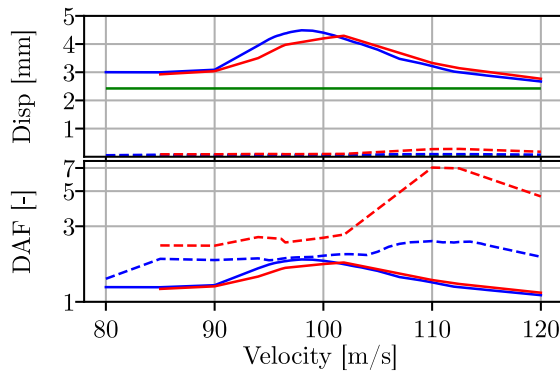
(a) Variation in actual displacement and DAF with velocity at midspan under the track, using a logarithmic scale for the y axis of the DAF
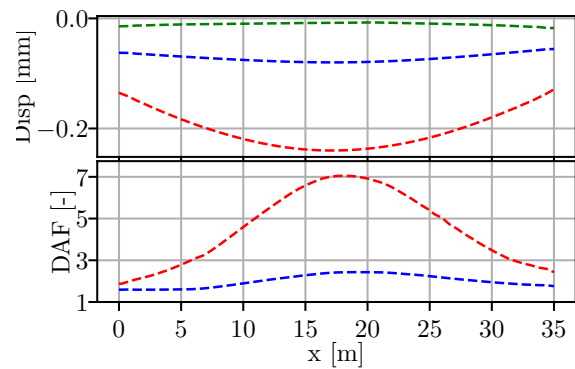
(b) Variation in actual displacement and DAF along the bridge length, for a velocity of $110\,m/s$ under the track

Figure 5.5: Benchmark case DAF variation of displacement for the single span, simply supported bridge

displacement is consistently low for all tested velocities, but the DAF shows that there is a peak around $110\,m/s$, especially exacerbated by the *Full* model. For this velocity, the actual lateral displacement and DAF are shown in Figure 5.5b. This shows a peak in the lateral displacement at midspan rather than the end spans, due to a lateral mode being activated. As the static case has a relatively low midspan deflection, this contributes to the high DAF found.

It is therefore appropriate to look at the displacements at the midspan as this is where the largest vertical and lateral displacements occur, although they are at different velocities, as they are linked to different resonant effects. Laterally, due to the irregularities and amplification of the displacement by the *Full* model, there are disparities between this loading type and the *Simple* model. However, vertically the two loading methods match well for displacements, despite the inclusion of irregularities leading to much higher vertical accelerations than in the

(a) Variation of S11 stress   (b) Variation of S22 stress
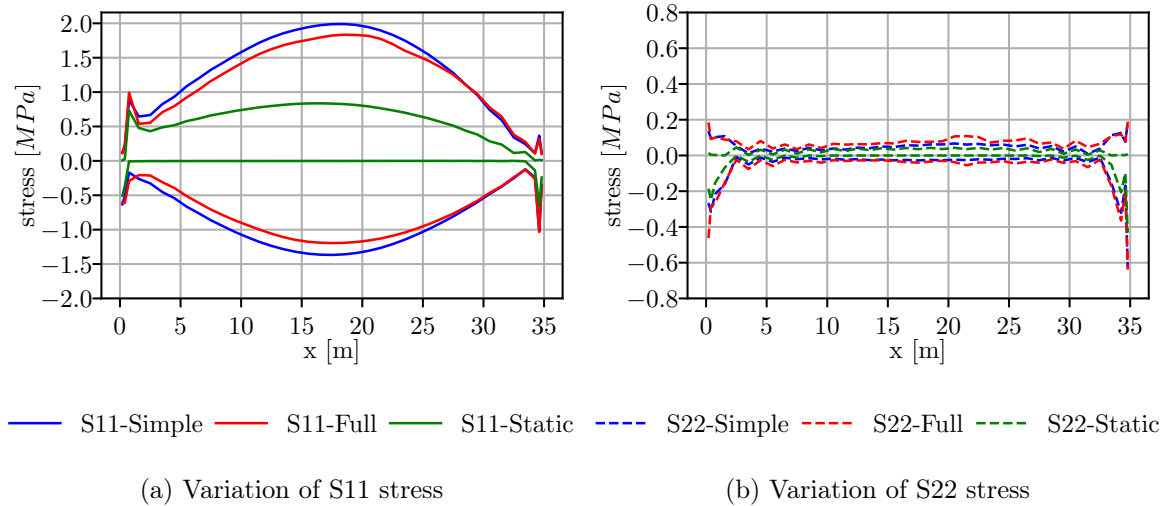
Figure 5.6: Variation of U-beam stresses along the length of the bridge in the bottom flange at $100\,m/s$

Simple model.

5.2.2 U-Beam Stress

Due to the changes in the properties of the U-beam investigated in this chapter, it is important to investigate the stresses in the beam itself. The stresses are studied where they will be closest to tension in the beam (in the bottom). Studying along the length of the beam (Figure 5.6), it is seen the direct stress S11 (Figure 5.6a), has a greater variation, due to the primary bending direction. The variation between model types of the S11 stress is greatest at the midspan and relatively small at the span ends. The S22 stress variation (Figure 5.6b), also taken from the bottom flange of the U-beam, is found to be comparatively low, with some slightly higher variation around the supports.

The corresponding DAF along the beam length for the S11 stress is seen in Figure 5.7a. It can be seen that the DAF is not largest at the largest stress variation level. This is as the static stress variation is very small at the end spans, which magnifies the DAF in these regions. It is most appropriate to take the DAF from the location with the highest stresses, which is found at the midspan. Hence, in Figure 5.7b, the stresses and DAF values are compared at midspan for different velocities. A peak in the S11 stress and DAF around $100\,m/s$ is consistent with the resonant speed of the first bending mode. Despite lower stresses, the DAF for S22 stress is a similar order of magnitudes to the S11 stress DAF, but with different peak locations. The lateral bending affects the S22 stresses more and hence the different peaks are related to lateral modes.

It is apparent that the S11 stresses offer similar responses for both the *Full* model and the *Simple* model. For the S22 model there is greater disparity between the *Simple* and *Full*

(a) Variation of S11 stress DAF at $100\,m/s$ along the length of the bridge

(b) Variation of S11 and S22 stresses and stress DAF with velocity at midspan of the bridge
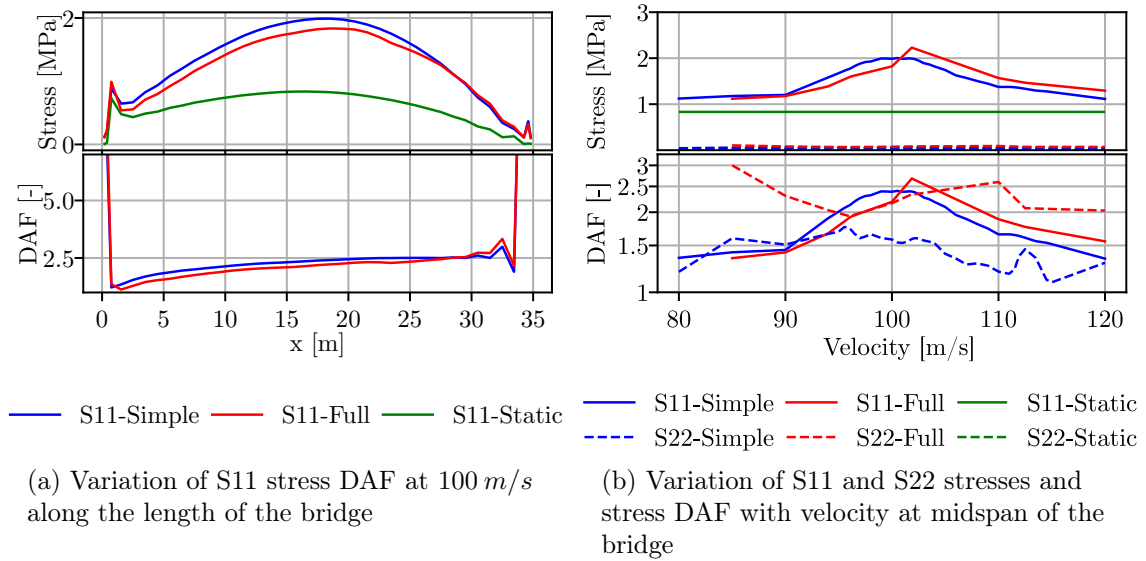
Figure 5.7: Variation of U-beam stress DAF in the bottom flange

DAF, which is consistent with the increase in lateral bridge displacement by the inclusion of a vehicle and irregularities. The magnitude of the S22 stresses are insignificant compared to the S11 stresses and hence will not be further studied in these cases. It can be seen that for further study, the operating velocity of $100\,m/s$ is a good speed to compare at, along with the midspan of the bridge.

5.3 Single Span Parametric Analysis

This section focuses on the parametric analysis performed on the single span, simply supported bridge. The influence of the web and bottom flange thicknesses, the depth of the bridge and a combination of suitable parameters are studied herein.

5.3.1 Web Thickness

Theoretically, the web thickness could allow the largest parameter changes. This is as the thickness of the web will have the least impact on the beam stiffness, as it is closer to the centroid of the section than the flanges. The changes take place as in Figure 5.8. As the web thickness is reduced, the strength of concrete is increased, to maintain the moment resistance (M_{rd}), shear resistance (V_{rd}) and the second moment of area of the section (EI_{yy}).

Significant benefits to the weight can be made. This can be seen in Figure 5.9, where the bending stiffness of the beam increases slightly, but the mass of the beam reduces by up to 11% for a web thickness that is 66% the width of the original.
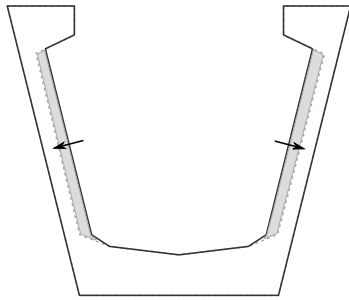
Figure 5.8: The web thickness changes
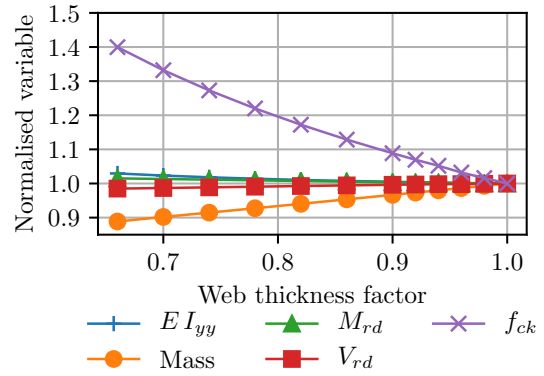
Figure 5.9: Variation of bridge properties with web thickness

5.3.1.1 Modal Contribution

First under the study of the single span case, we investigate the frequencies. This studies the modal shapes of predominant vertical bending modes, in particular the fundamental, 2nd and 3rd modes, which have one, two and three half sine waves per span respectively, as seen in Figure 5.10.
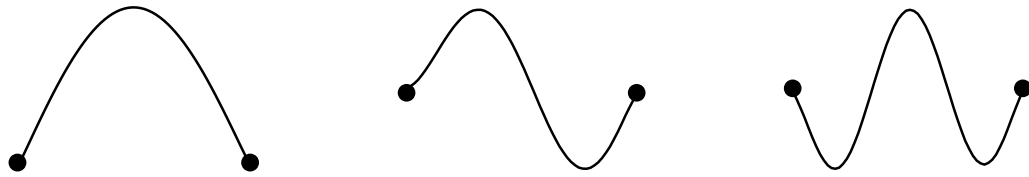
(a) First bending mode   (b) Second bending mode   (c) Third bending mode

Figure 5.10: Single span, simply supported bridge mode shapes (nodes indicate the bridge supports)

The variation of the frequency with parameter has been shown in Figure 5.11. The bridge frequencies are calculated both with and without the consideration of the track and vehicular mass (as a distributed mass proportional to the weight of train per unit length). The inclusion of the distributed mass of the vehicle was determined in Section 4.5.3, to not be relevant to the acceleration response of the bridge, however it is included as a reference in this parametric analysis, in order to test if this conclusion is still valid when the bridge mass is reduced. Frequencies including the vehicle mass are denoted by $f_{f,i}$ and those without the mass by $f_{s,i}$, where i is the mode number. The mode number (i) may change between parametric cases as the changing geometry of the section alters the mode number for which the modes of one, two and three half sine waves per span are found.
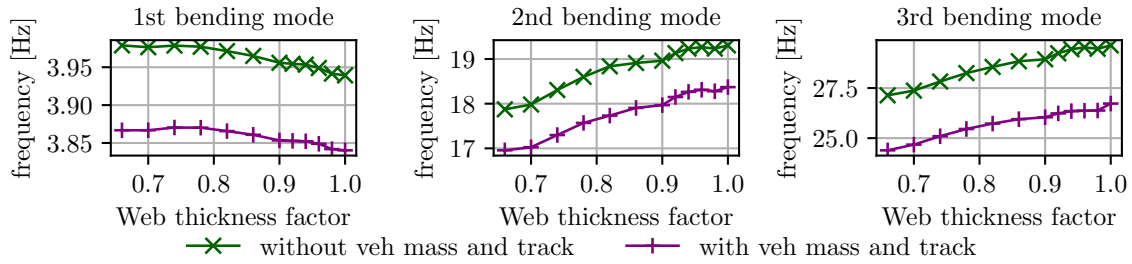
Figure 5.11: Frequency variation of the single span bridge modes with web thickness parametric analysis. Frequencies without the vehicle mass and track are akin to the *Simple* model and with the vehicle mass and track are similar to the *Full* model

Interestingly, the fundamental frequency increases with decreasing thickness, as expected due to the lower mass and higher stiffness (Figure 5.9) for the reduced web thickness. However, the majority of other modal frequencies, including ones not shown, decrease with the thickness of the web changing. The higher the frequency of the mode, the gap between the two frequency methods increases non proportionally.

5.3.1.2   Vertical Bridge Accelerations

As described previously in Section 2.7.3.1, the vertical accelerations are often found to be the constricting factor in design. Hence, seeing how the maximum slab deck accelerations change with the reduction of the web thickness (and the corresponding increase to the concrete strength), is key to this parametric analysis. Figure 5.12 shows the maximum magnitude of vertical filtered acceleration for any velocity under $432\,km/h$ and at any location along the length of the track on the slab and how that varies with the web thickness. The accelerations are all above the threshold value of $5\,m/s^2$ for slab track in the *Full* vehicle model case, as the bridge is not explicitly designed to be a single span, simply supported structure, so is less restrained than required. In the *Simple* model, a reduction of web thickness leads to a slight increase in accelerations as the web thickness reduces, however, the level of accelerations under the *Full* vehicle model stay similar for the reductions in web thickness. This suggests that the reduction in web thickness has limited impact on the bridge accelerations. There is a localised reduction in the maximum acceleration for the *Full* model for the web thickness being 66% of the original thickness, and this is due to decoupling of modes, so therefore leading to a reduction in the peak acceleration. This coupling of modes can be seen in Figure 5.16, where for all the parameters shown, there are two prominent peaks.

Further to the maximum filtered vertical accelerations anywhere, the accelerations are studied specifically at one velocity of $100\,m/s$ and at the midspan location of $17.6\,m$. Comparison in Figure 5.13 shows steady increase in the *Simple* model accelerations, but a peak in the *Full* vehicle accelerations between web thicknesses 86% and 90% of the original. This is due to in
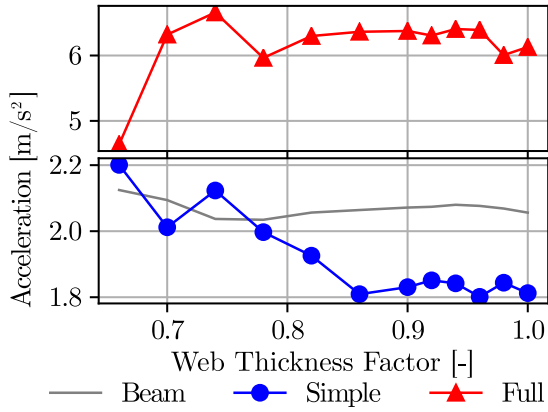
Figure 5.12: Maximum filtered vertical acceleration at any point on the bridge slab under the track, for any velocity under $432\,km/h$ for different web thicknesses
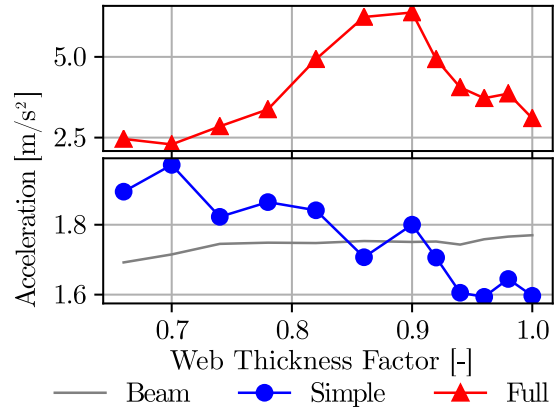
Figure 5.13: Maximum filtered vertical acceleration at midspan on the bridge slab under the track, at $100\,m/s$ for different web thicknesses
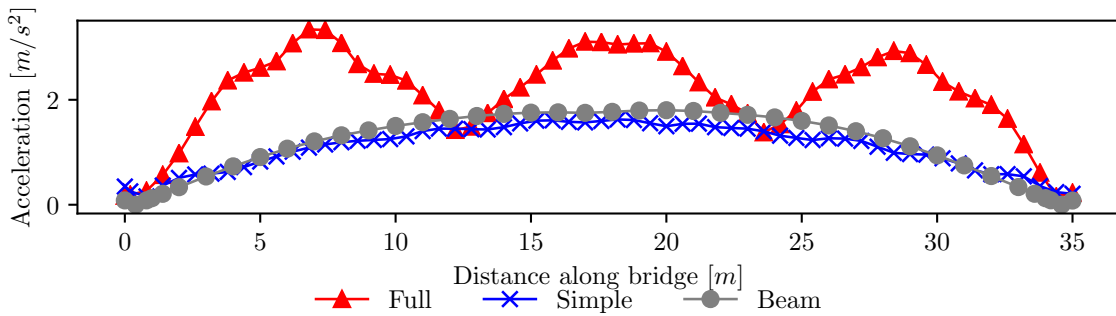
Figure 5.14: Comparison of the maximum vertical accelerations along the length of the bridge under the benchmark case for a one span bridge

these parametric cases, the bridge natural frequencies shift, therefore at $100\,m/s$ the resonant loading frequency of f_{v7} becomes closer to the third bending mode of the bridge ($f_{s,24}$ or $f_{s,26}$).

Previous studies on the dual U-beam bridge accelerations in this thesis, focused on the three spanned case. For this one span case, the maximum filtered vertical accelerations along the bridge length, at velocity of $100\,m/s$, for the benchmark case, can be seen in Figure 5.14. This shows that there is the similar exacerbated response with the *Full* vehicle, due to the activation of the third bending mode as described in Section 4.3.3. The maximum acceleration is generally found in the midspan of the bridge, although the localised peaks can cause higher accelerations elsewhere.

The midspan maximum filtered vertical accelerations are shown against velocity for various parameters in Figure 5.15. This shows how the accelerations in the *Simple* model peak at very similar velocities, with a very slight increase in the velocity as the thickness decreases. This
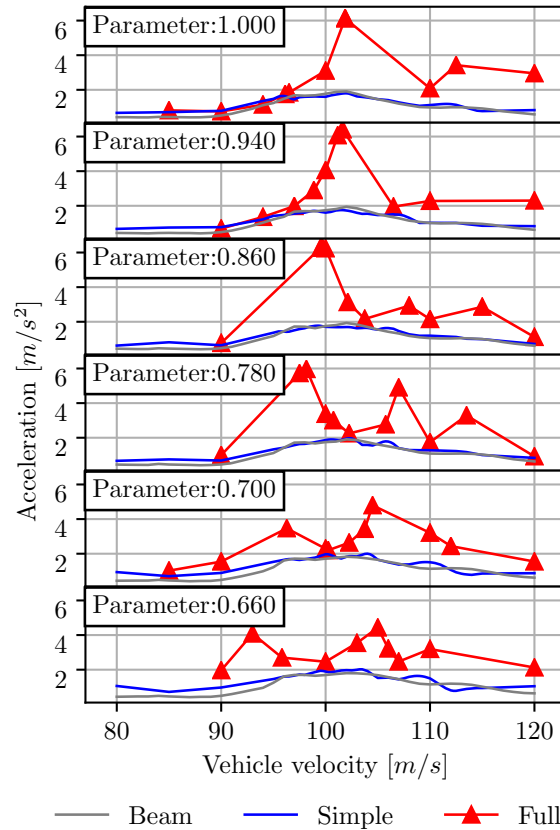
Figure 5.15: Comparison of the filtered maximum vertical accelerations with velocity of the bridge for changing web thicknesses, taken at midspan

is consistent with the very similar frequencies with a very small increase, for the fundamental mode, which is the resonant bridge mode activated at this peak in the *Simple* model, as the thickness decreases. For the *Full* model the velocity of the peak changes with parameter, which is a function of the changing frequency of the mode with three half sine waves per span, and the resulting coupling and decoupling of activation of both this and the fundamental modes. The velocity for which the peak occurs in the *Full* model reduces as the web thickness reduces, consistent with the change in frequency of this third bending mode ($f_{s,24}$). However, for reductions lower than 0.86 a second peak is observed, which occurs at a higher speed, ending up generating a larger response. This secondary peak arises due to the shifting frequencies of the bridge modes, leading to reduced combined activation of the first bridge mode ($f_{s,1}$) and the third bridge mode ($f_{s,24}$ or $f_{s,26}$) for the same speed, and instead coupling of another, higher frequency bridge mode, with the first bridge mode, becomes possible due to bridge frequency shifting, which leads to a further resonant speed peak.

Understanding why the accelerations increase is fundamentally due to the natural modal frequencies of the bridge. Figure 5.16 shows the frequency components of acceleration for velocities that produced the largest accelerations for selected parameters. It shows the large
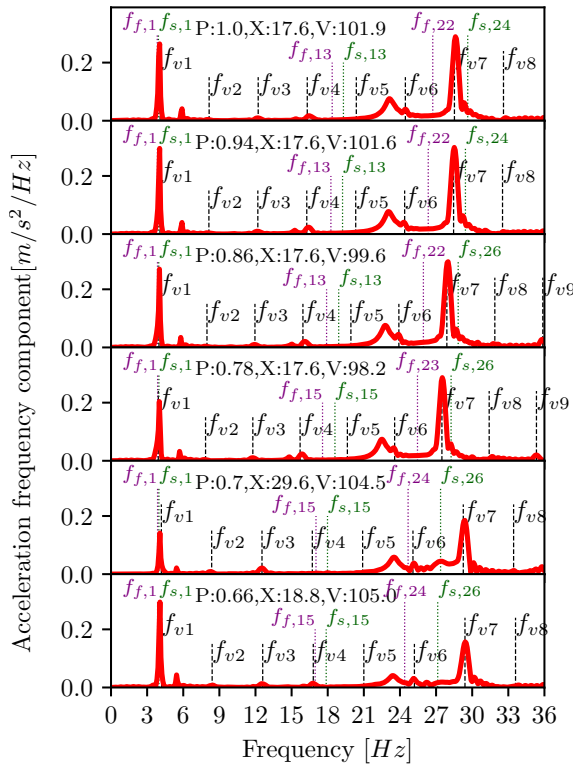
Figure 5.16: Comparison of the frequency components of the filtered maximum vertical accelerations for the particular velocity (V, $[m/s]$) and location along the length of the bridge (X, $[m]$ from the end span), that lead to the maximum vertical acceleration for each web thickness parameter (P). Also showing the resonant loading frequencies (f_{vi}, black dashed lines), and selected bridge frequencies without the track and vehicle mass ($f_{s,i}$, green dotted lines) and with the track and distributed vehicle mass ($f_{f,i}$, purple dotted lines)
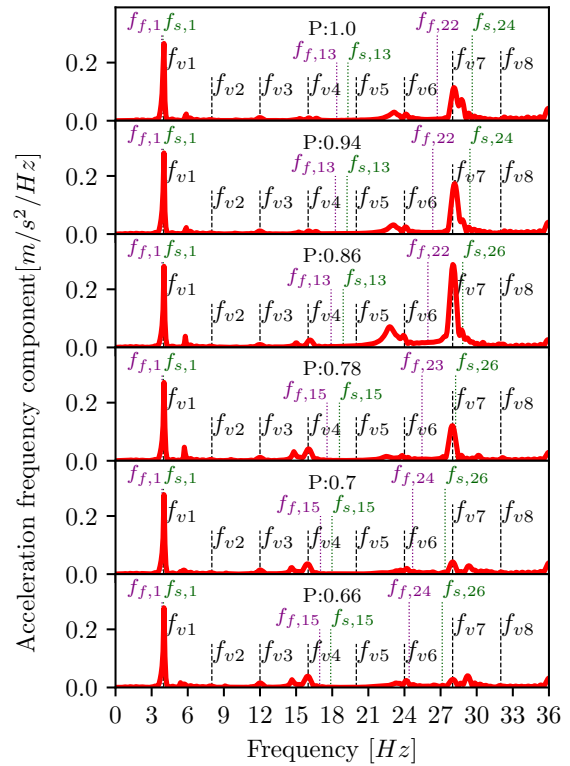
Figure 5.17: The frequency components of the vertical acceleration at midspan for a velocity of $100\,m/s$ for a selection of web thickness parameters (P). Also showing the resonant loading frequencies (f_{vi}, black dashed lines), and selected bridge frequencies without the track and vehicle mass ($f_{s,i}$, green dotted lines) and with the track and distributed vehicle mass ($f_{f,i}$, purple dotted lines)

contributions due to the coupling of the first (f_{v1}) and seventh (f_{v7}) resonant loading frequencies, with the bridge modal frequencies related to one and three half sine waves per span ($f_{s,1}$ and $f_{s,24}$ respectively). With a reducing parameter, the frequency shift is shown by the reducing contribution of the first mode to the maximum vertical acceleration. It can be seen by the location of the peaks that the frequencies including the full vehicle mass distributed along the track ($f_{f,i}$) are still not representative of the frequency of vibration of the response of the bridge, as per the conclusions in Section 4.5.3.

Comparison of the frequency components of bridge acceleration for vehicle velocities of $100m/s$ in Figure 5.17, shows the more significant shift in the frequency of the third bridge mode ($f_{s,24}$ or $f_{s,26}$) and the reducing contribution of that mode, which leads to the shape of Figure 5.13. When the 7th driving frequency is close to the third bending mode ($f_{s,24}$ or $f_{s,26}$), this mode heavily influences the response.

When the web thickness is 70% of its original, the maximum acceleration in Figure 5.16 is shown to have significant contributions from a mode higher than the third bridge mode. This is from a torsional-vertical hybrid bending mode, for which the frequency has shifted lower by this frequency.

Overall, from the relatively stable accelerations no clear results can be obtained for the cut-off point for the benefits of reduction in web thickness on the bridge deck for the single span case, but it becomes apparent that the web thickness can be reduced with a corresponding increase in concrete strength with no apparent bound.

5.3.1.3 U-Beam Stress

The stress in the beam will vary with the parameter as well. Through reduction in the web thickness the stress and DAF of the S11 stress in the bottom flange (most critical location), is seen to stay relatively consistent (Figure 5.18). Contrastingly, the S22 stress is seen to increase, and the corresponding DAF increases significantly with a reduction in the web thickness. This is due to a reduction in the corresponding lateral stiffness, and changes in the lateral and torsional modal frequencies leading to larger lateral responses. Therefore, with the reduction of the web thickness, both the stress induced by the load and the capacities are not modified, when the reduction of the thickness is counterbalanced by an increment of the concrete strength, by the amount established in Figure 5.9.

5.3.1.4 Bridge Displacements

Comparison of the DAF of the deflections in the slab show that the vertical deflection DAF insignificantly increases with decrease in web thickness (Figure 5.19). On the other hand

(a) Variation in stresses and DAF in the bottom flange of the beam at midspan, for the velocity under $432\,km/h$ ($120\,m/s$) that leads to maximum DAF, using a logarithmic scale for the y axis of the DAF

(b) Variation in stresses and DAF in bottom flange of the beam at midspan, for a velocity of $360\,km/h$ ($100\,m/s$), using a logarithmic scale for the y axis of the DAF
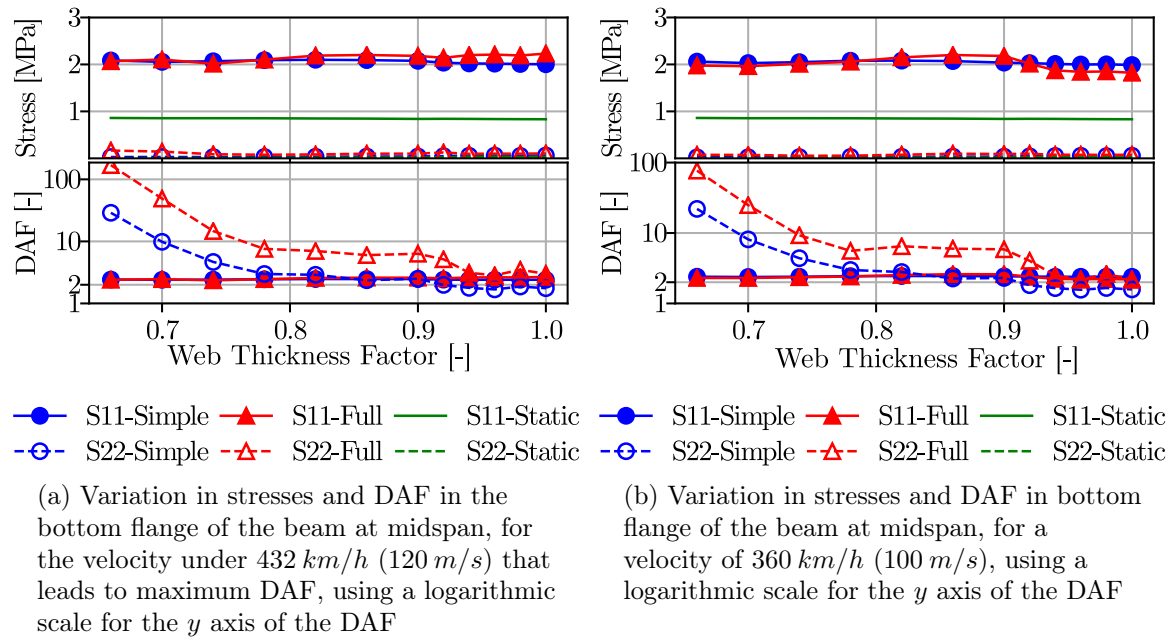
Figure 5.18: Variation of DAF for stress in the bottom flange of the U-Beam for web thickness reductions for the single span, simply supported bridge

the lateral DAF increases particularly when the web thickness is 74% of the original. This is due to the shifting of the lateral mode to a frequency matching a loading frequency here. However, this increase in DAF does not correspond to a significant increment of the lateral displacement, with values found to be less than $0.5\,mm$ still.

5.3.1.5   Summary of the Web Thickness Reductions

The models show that the thickness in the webs can be decreased with a corresponding increase in the concrete strength, shown in Figure 5.9, with maximum accelerations not increasing significantly, the structural demands remaining constant and the capacities being maintained or increased. The DAF of the stress is relatively constant in all locations for the critical normal stress S11, and the deflection in the slab constant, apart from for the lateral displacement which shows large DAF but small actual values. With the accelerations being the limiting factor the decrease in web thickness can seemingly be matched by increase in concrete strength to maintain bending moment resistance capacity, shear resistance capacity and vertical section stiffness, until the thickness of the webs is limited by other construction constraints (such as spacing for reinforcement bars, fire resistance, minimal construction thicknesses or temporary loading conditions on the webs).

(a) Variation in the displacement DAF in the slab at midspan at a location under the track for the velocity under $432\,km/h$ $(120\,m/s)$ that causes maximum displacement, using a logarithmic scale for the y axis of the DAF

(b) Variation in displacement DAF in the slab at midspan at a location under the track for $360\,km/h$ $(100\,m/s)$, using a logarithmic scale for the y axis of the DAF
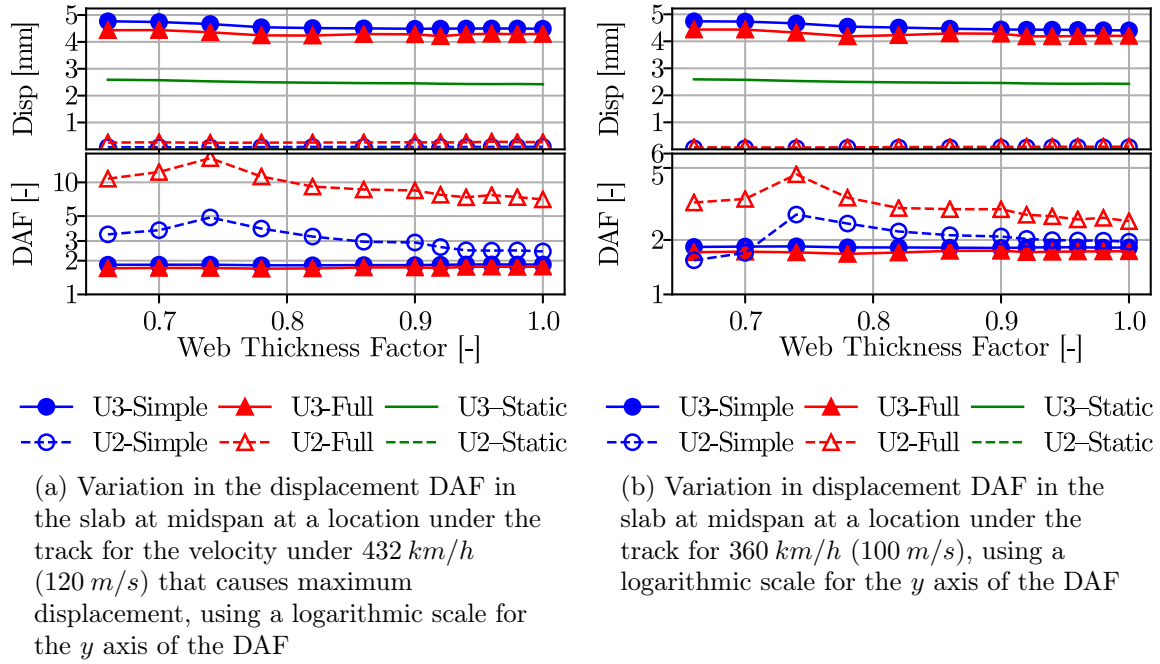
Figure 5.19: Variation of the slab displacement with web thickness parameter

5.3.2   Bottom Flange Thickness

Changes to the bottom flange thickness are compared in this section. The changes to the bottom flange are as shown in Figure 5.20. Through these variations, the concrete strength changes and weight savings are shown in Figure 5.21. As the thickness was reduced, the strength of concrete was increased for the precast elements to maintain the structural capacities (M_{rd} and V_{rd}) of the bridge. The modelling procedure limited the thickness of the bottom flange thickness to 0.75 of the original, lower thicknesses caused computational errors, in part due to the prestressing bars in the bottom flange not having enough space. The potential changes in mass are not large at a maximum of 5% shown, but the increase in concrete strength is also just a little over a 20% to achieve this, which is reasonable.

5.3.2.1   Modal Contribution

The frequencies of the three modes shown in Figure 5.10 of Section 5.3.1.1, vary with the bottom flange thickness as shown in Figure 5.22. Unlike for the web thickness, the decrease in bottom flange thickness leads to decreases in the frequency of the fundamental mode and increases the frequencies of the other modes. This is initially unexpected as the mass decreases and the rigidity of the U-beam is maintained. However, as the bridge is supported by the bearings at the base of the U-beams, the distance to the centroid of the section is important, and in this case the centroid is lowered as the bottom flange thickness is reduced. This has two results, the distance between the centroids of the slab and U-beams increases, increasing the
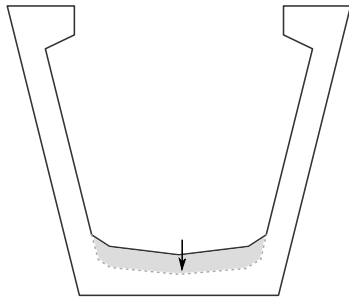
Figure 5.20: Bottom flange variation
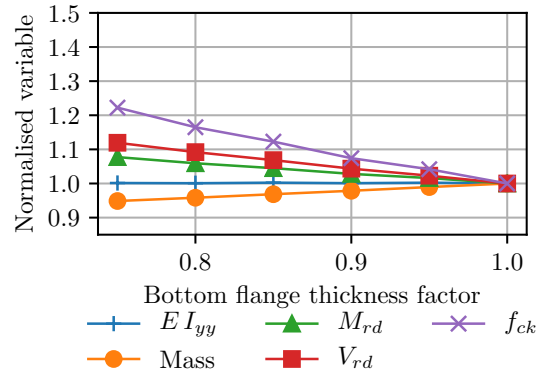
Figure 5.21: Variation of the mass, stiffness and concrete strength with variation of the bottom flange thickness
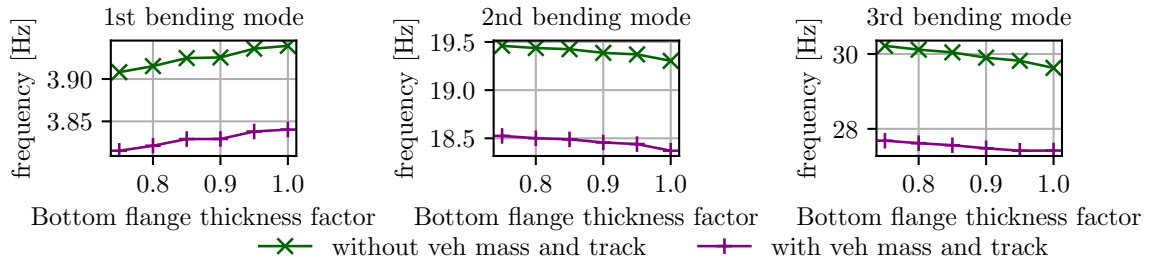
Figure 5.22: Variation of the frequency of the three main bending modes with bottom flange thickness, in the single span, simply supported case. Frequencies without the vehicle mass and track are akin to the *Simple* model and with the vehicle mass and track are similar to the *Full* model

overall rigidity of the cross section and the lowering the global centroid closer to the boundary conditions, which in turn increases the effective stiffness, leading to the higher frequency.

5.3.2.2 Vertical Bridge Accelerations

The vertical accelerations here show some decrease with decreasing thickness, for the *Full* vehicle model. This is in both the case where the maximum acceleration at any location or velocity is chosen (Figure 5.23) or when focused on the accelerations at midspan for the velocity of $100 \, m/s$ (Figure 5.24). In the case of the *Simple* loading model, the maximum accelerations at any velocity under $432 \, km/h$ ($120 \, m/s$), do not change significantly with the bottom flange thickness. However when focusing at the accelerations at midspan, for the velocity of $360 \, km/h$ ($100 \, m/s$), these accelerations are shown to increase with reductions to the thickness.

The maximum accelerations for any velocity under $432 \, km/h$ ($120 \, m/s$), (Figure 5.23), de-
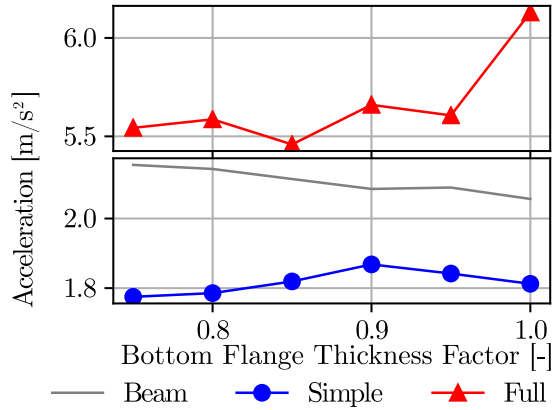
Figure 5.23: Maximum filtered vertical acceleration at any point on the bridge slab under the track, for any velocity under $432\,km/h$ ($120\,m/s$), for different bottom flange thicknesses
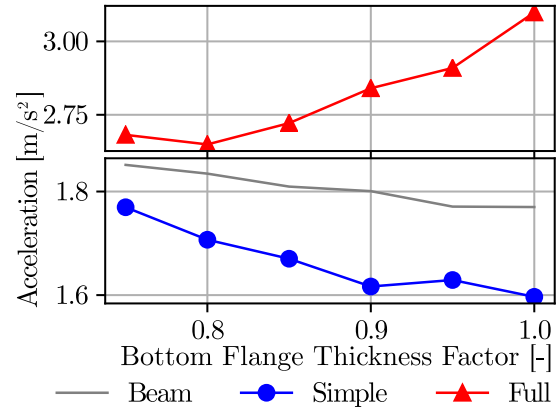
Figure 5.24: Maximum filtered vertical acceleration at midspan on the bridge slab under the track, at $360\,km/h$ ($100\,m/s$) for different bottom flange thicknesses

crease slightly with decrease in the bottom flange thickness, which is down to decoupling of the activation of the modes containing one and three half sine waves per span ($f_{s,1}$ and $f_{s,24}$). Figure 5.25, shows how in the benchmark case the contributions to the maximum acceler-ations are relatively equal between the bridge modes with one ($f_{s,1}$) and three ($f_{s,24}$) half sine waves per span. However, for the thinnest thickness of the bottom flange, at 75% of the original thickness, the contribution of the mode with one half sine wave ($f_{s,1}$) is about half the contribution of the bridge mode of three half sine waves ($f_{s,24}$). This is as a result of the changing of the frequencies of these modes, leading to them becoming decoupled, as they are not both resonant at the same velocity, hence reducing the overall maximum accelerations. The range of velocities modelled is shown in Figure 5.26, which indicates the drifting of the peak in acceleration to the high velocities for a smaller thickness.

5.3.2.3   U-Beam Stress

The stress DAF in the bottom flange is shown to vary as in Figure 5.27. The DAF for the S11 stress is seen to be relatively consistent, with the actual stress increasing slightly with decrease in thickness. For the S22 stress, the DAF value decreases for a reduction in the thickness of the bottom flange, as a function of reducing lateral modal contribution, although the actual stress contribution remains very small. As previously seen the *Simple* loading model can seemingly represent the *Full* loading model.

Figure 5.25: Comparison of the frequency components of the filtered maximum vertical accelerations for the particular velocity (V, $[m/s]$) and location along the length of the bridge (X, $[m]$ from the end span), that lead to the maximum vertical acceleration for each bottom flange thickness parameter (P). Also showing the resonant loading frequencies (f_{vi}, black dashed lines), and selected bridge frequencies without the track and vehicle mass ($f_{s,i}$, green dotted lines) and with the track and distributed vehicle mass ($f_{f,i}$, purple dotted lines)

Figure 5.26: Variation in maximum vertical acceleration with velocity, at midspan, for different thicknesses of the bottom flange
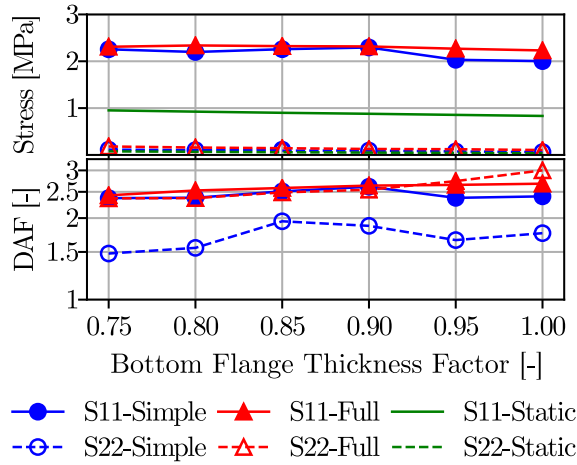
Figure 5.27: Variation of actual and DAF stress in the bottom flange of the U-beam for changes to the bottom flange thickness for the single span bridge at midspan for the velocity that leads to maximum stress, using a logarithmic scale for the y axis of the DAF
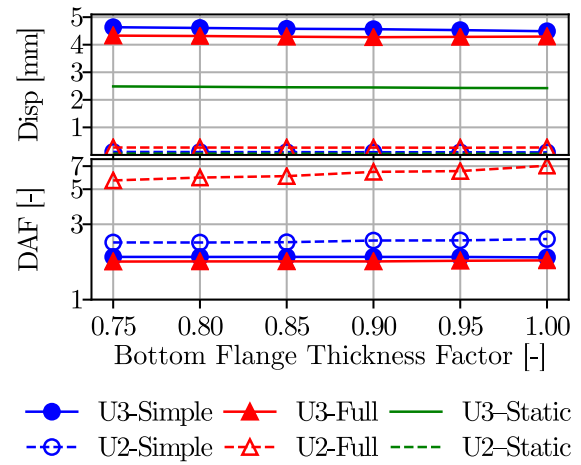
Figure 5.28: Variation in displacement DAF, in the slab at midspan under the track, for changes to the bottom flange thickness parameter, for velocities under $432\,km/h$ that cause maximum displacement, and using a logarithmic scale for the y axis of the DAF

5.3.2.4   Bridge Displacements

The DAF of displacement of the slab under the track is compared in Figure 5.28. It can be seen here that again the DAF is not dependent on the thickness of the bottom flange, particularly in the vertical case. In addition, the actual vertical deflection is very consistent for different thicknesses. In the lateral case, the inclusion of irregularities in the *Full* vehicle model, leads to significant lateral DAF, which appear to reduce for thinner values of bottom flange thickness, but the actual displacement generating these large DAF values is small.

5.3.2.5   Summary of the Reduction in the Bottom Flange Thickness

The change in bottom flange thickness does not offer as significant weight savings as the web thickness, but the savings are still useful, as the concrete strength needs only small increases to maintain the rigidity. Stress, deflection and accelerations in the bridge appear to not be limiting on the bottom flange thickness, making it a plausible location for saving material.

5.3.3   Depth

The U-beam is modified in this section to reduce the depth and simultaneously therefore increase its slenderness. It is expected that this would therefore increase the accelerations.
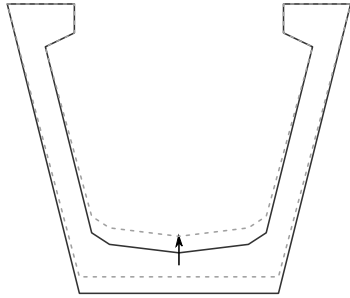
Figure 5.29: Depth variation
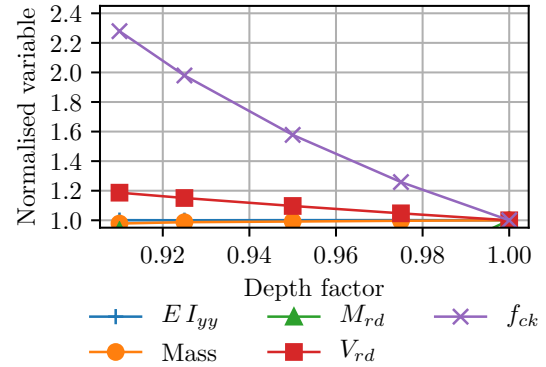
Figure 5.30: Variation of the mass, stiffness and concrete strength with variation of the section depth

Increasing the depth would have the opposite effect of reducing the accelerations, but deeper sections are undesirable, as they complicate transportation, reduce the vertical clearance, and are more aesthetically unsightly. This is done by reducing the height of the web as per Figure 5.29. The weight, stiffness and concrete strength changes associated with the changes are shown in Figure 5.30. This shows that the mass of the U-beam changes very little, and large increases in the concrete strength are required to maintain a level of stiffness, moment resistance and shear resistance in the section. The depth is limited in its ability to be reduced by the maximum strength of concrete available. In addition, beyond a reduction to 0.91, the method used to model the cross section of the bridge requires modification, with the changes making it harder to directly compare to the benchmark case.

5.3.3.1 Modal Contribution

The frequencies of the three modes shown in Figure 5.10 of Section 5.3.1.1, vary with the section depth as shown in Figure 5.31. The relationship to a reduction in depth is similar to that of a reduction in the bottom flange thickness, with the reducing frequency as mass reduces and rigidity of the U-beam remains constant again explained by the changing centre of mass of the whole bridge.

5.3.3.2 Vertical Bridge Accelerations

The vertical accelerations do not change significantly with the reduction in depth for the *Full* vehicle model, as seen in Figure 5.32. In the case of *Simple* point load modelling and not the *Full* vehicle model, the accelerations slightly increase with a reduction in depth, but have a decrease for the smallest depth.
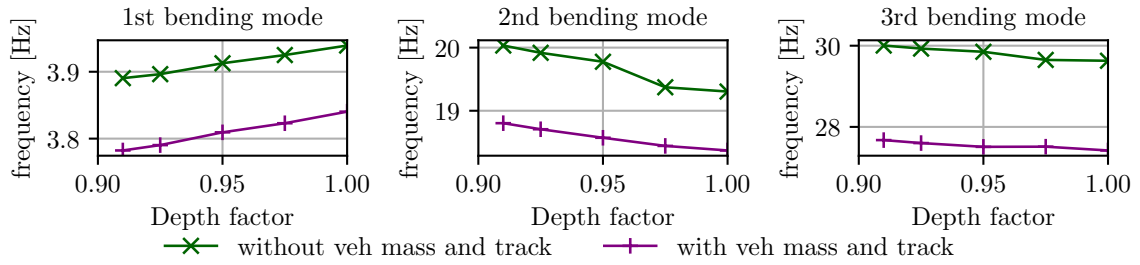
Figure 5.31: Variation of the frequency of the three main bending modes with bottom flange thickness, in the single span, simply supported case. Frequencies without the vehicle mass and track are akin to the *Simple* model and with the vehicle mass and track are similar to the *Full* model
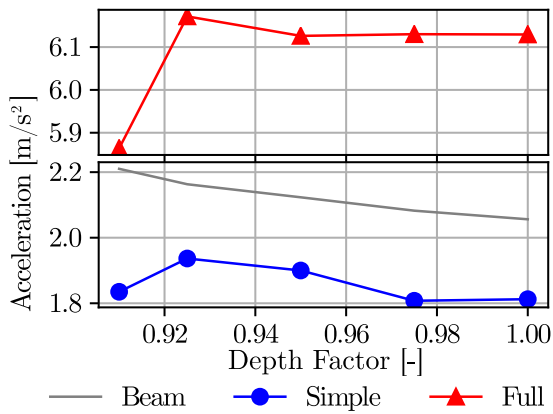
Figure 5.32: Maximum filtered vertical acceleration at any point on the bridge slab under the track, for any velocity under $432\,km/h$ ($120\,m/s$), for different depths
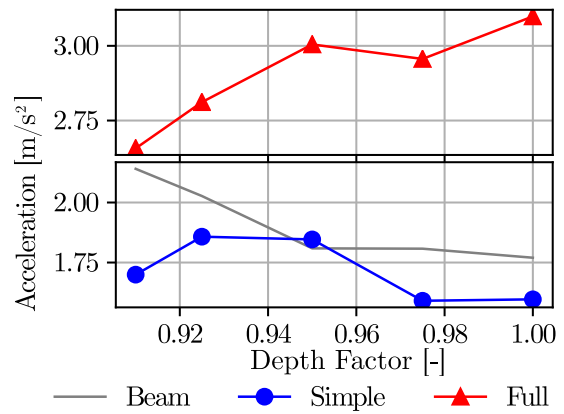
Figure 5.33: Maximum filtered vertical acceleration at midspan on the bridge slab under the track, at $360\,km/h$ ($100\,m/s$) for different depths
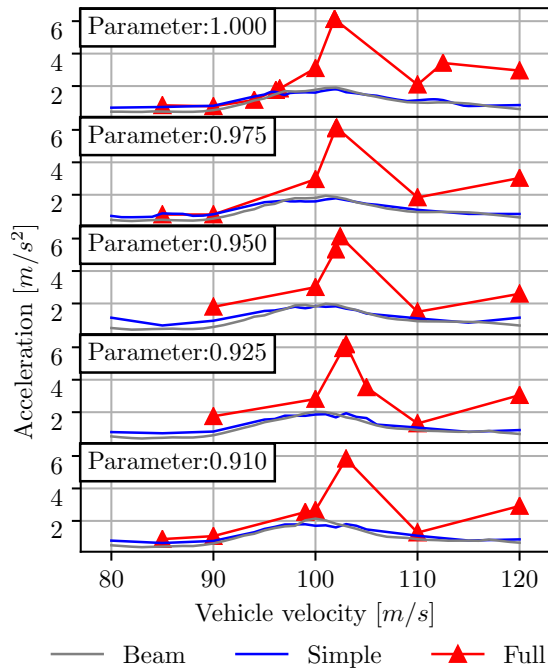
Figure 5.34: Variation in vertical acceleration with velocity for different depths, with the acceleration taken at midspan
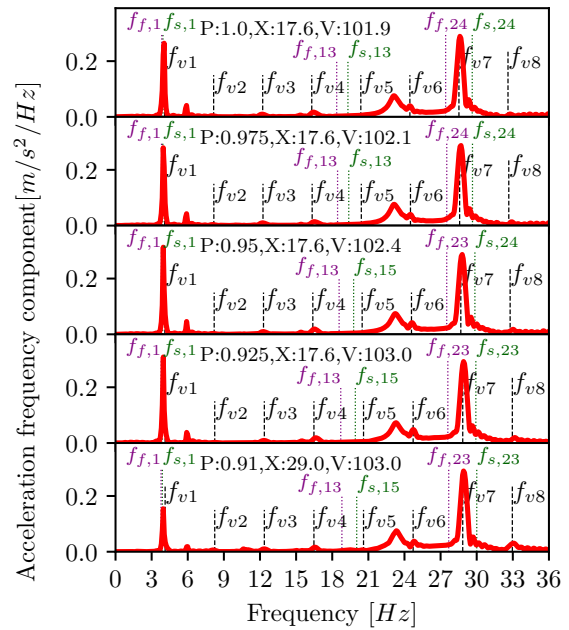
Figure 5.35: Comparison of the frequency components of the filtered maximum vertical accelerations for the particular velocity (V, $[m/s]$) and location along the length of the bridge (X, $[m]$ from the end span), that lead to the maximum vertical acceleration for each depth parameter (P). Also showing the resonant loading frequencies (f_{vi}, black dashed lines), and selected bridge frequencies without the track and vehicle mass ($f_{s,i}$, green dotted lines) and with the track and distributed vehicle mass ($f_{f,i}$, purple dotted lines)

Focus on the operating speed (Figure 5.33), shows decreasing accelerations in the *Full* model, as the third mode shifts further away from the driving frequency, but the *Simple* model shows some small increase as the depth decreases. Overall, from Figure 5.34, it appears that the peak acceleration for the *Full* model is shifting to higher velocities, consistent with the increase in frequency of the third mode with decrease in depth.

In Figure 5.32, it is evident that there is a decrease in the accelerations for the *Full* vehicle model at the 0.91 depth value. This is due to the decoupling of the modes, such that at the peak acceleration, the first mode ($f_{s,1}$) has a smaller contribution, whilst the bending mode of three half sine waves ($f_{s,23}$ or $f_{s,24}$), has a similar contribution between all parametric cases, which shows the decoupling of the activation of these two bridge modes (Figure 5.35).

5.3.3.3   U-Beam Stress

Study of the DAF for the stress, shows that the DAF in the bottom flange is relatively constant for different depths as seen in Figure 5.36. This is the case for both S11 stresses and S22. The S22 stress values are still small, however the actual S11 stress values show a rise of up to 20% in the stress in the bottom flange with decrease in depth, with similar results in both the *Simple* and *Full* models. This is meaningless on its own due to the smaller depth. It would be required to integrate the stress response across the whole section to determine the moment demand to compare with the capacity. A rough calculation of the change in the moment is made by the increment in stress divided by both the increment in the modulus of elasticity and the increment in the depth. For the depth value of 0.91, the stress increases by an increment of 20% and the modulus of elasticity is increased by 31%. As a result, a rough calculation to the increment in the moment is shown by $1.2/(1.31 \times 0.91) = 1.01$. This shows the increase in the moment demand is very small.

5.3.3.4   Bridge Displacements

The deflection, as seen in Figure 5.37, has relatively constant DAF vertically, but laterally is varied. The vertical deflection itself increases slightly with the depth reduction, but laterally the displacements are found to be small. Therefore, deflections appear not to be of large concern in this parametric case.

5.3.3.5   Summary of the Depth Reductions

Reductions of the depth of the bridge offers poor value. High concrete strength increases are required to maintain section stiffness, shear resistance and moment resistance. The material savings are also small, with the weight saving small. On the contrary, accelerations do not
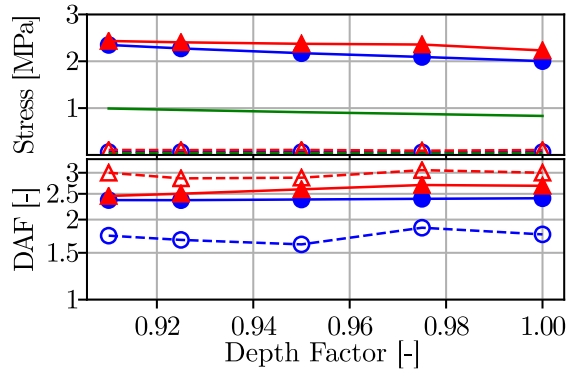
Figure 5.36: Variation of actual and DAF stress in the bottom flange for changes to the depth in the single span bridge. Values taken at midspan for the velocity under $432\,km/h$ that leads to maximum stress, and using a logarithmic scale for the y axis of the DAF
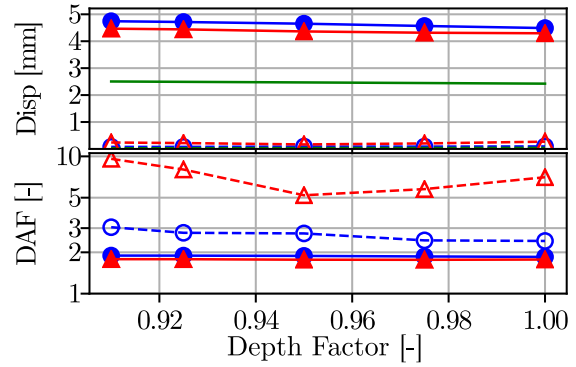
Figure 5.37: Variation in displacement DAF, at a location on the slab at midspan under the position of the track, with reductions to the depth parameter, for the velocity under $432\,km/h$ that causes the maximum displacement, and using a logarithmic scale for the y axis of the DAF

increase for the *Full* vehicle model under changes in depth, although the *Simple* loading model does show an increase in accelerations. The DAF of the normal stress and vertical deflection are relatively consistent, and although the actual value of the stress increases, the resulting moment demand does not seem to, so these are also not of concern. Due to the low weight saving, it is not recommended that a study of the depth be carried out on the continuous bridge, as it offers little benefits for precasting.

5.4 Continuous Bridge Benchmark Case

Study of the stresses and displacements are made in this section of the three spanned bridge using U-beams. This allows identification of the locations to test for the DAF with different parameters.

5.4.1 Bridge Displacements

The maximum vertical displacements of the slab are shown in Figure 5.38, for the three loading cases. It shows as expected maximum displacement in the middle of each of the spans, with the ultimate maximum under the track found in the end spans. The dynamic models show much higher deflections than the static model, which is due to the near resonant speed that

(a) *Static* Model   (b) *Simple* Model   (c) *Full* Model
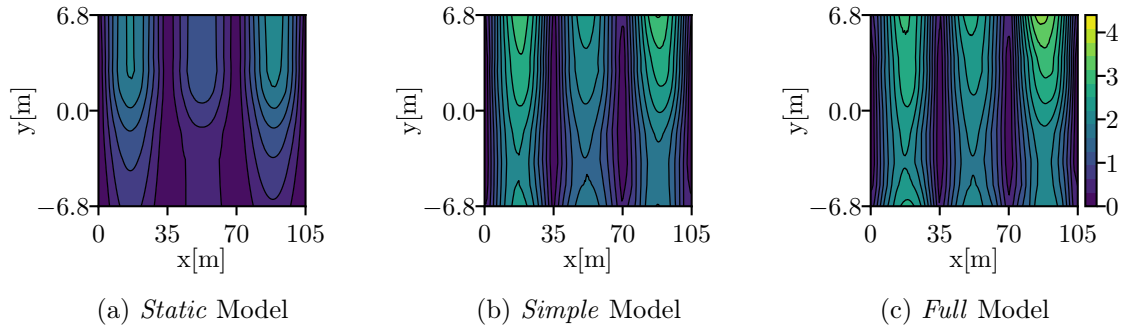
Figure 5.38: The vertical displacements (U3) in the slab for the continuous bridge $[mm]$

(a) *Static* Model   (b) *Simple* Model   (c) *Full* Model
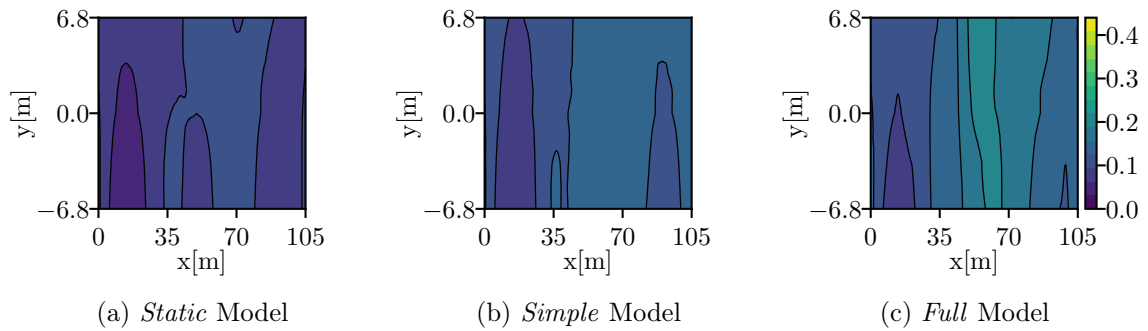
Figure 5.39: The lateral displacements (U2) in the slab for the continuous bridge $[mm]$

the contour plots represent $(100 \, m/s)$.

The lateral displacements (Figure 5.39) are much smaller than the vertical, as in Section 5.2. These displacements have a small increase over the end spans, although this is hard to see in the figure. In addition, support sections over intermediate piers do not lead to significant reductions in the displacement, due to twisting and lateral displacement modes covering the full length of the bridge. The DAF corresponding to the *Full* model for the vertical displacement is shown in Figure 5.40. Here it is seen that the DAF is significantly higher on the unloaded side, which is as a result of the low static displacement at this location. The DAF that is meaningful is that under the loaded track line. This is as it has higher deflections and influences the running behaviour of the vehicle.

Variation of the displacement DAF with the velocity is shown in Figure 5.41. It shows a peak vertical displacement for both the *Simple* and dynamic cases at a speed just under $100 \, m/s$ and a rise in the DAF for lateral displacements around $110 \, m/s$, signifying a lateral resonant speed here. This shows importance of the dynamic model incorporating all speeds for accurate determination of the DAF. Interestingly the vertical DAF has similar DAF values between the *Simple* and *Full* models, whereas the lateral DAF has much higher DAF for the *Full* model, due to the irregularities enhancing the lateral dynamic motion.
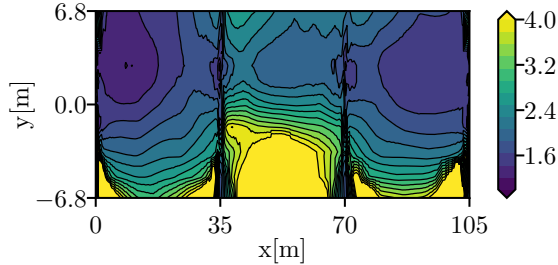
Figure 5.40: The DAF for vertical deflections in the slab at $100\,m/s$ for the *Full* vehicle dynamic model with a continuous bridge
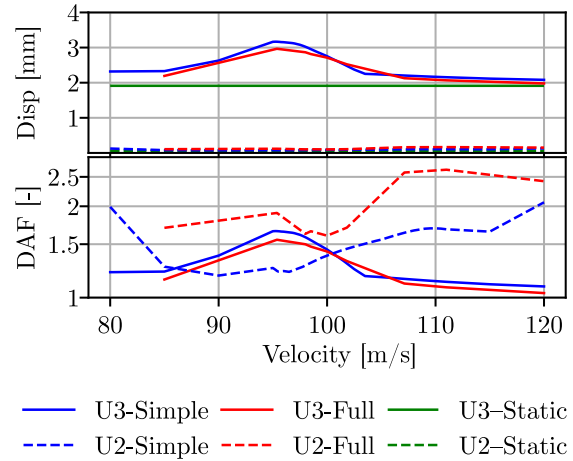
Figure 5.41: Variation of the displacement DAF, at midspan of the first span, with velocity for the continuous bridge, using a logarithmic scale for the y axis of the DAF

5.4.2 U-Beam Stress

The change in stress in the beams is compared here along the full length of the continuous bridge in the base of the beam. It can be seen in Figure 5.42a, that the S11 stress is, as expected largest in the middle of the spans, coinciding with the largest vertical deflection. The DAF is maximum near the supports, as here the stress from static loading is very small. The *Full* model leads to slightly higher stress values in comparison with the *Simple* model. From the stress response it is appropriate to choose midspan locations for study of variation of the stress and DAF with velocity or parameter due to the larger magnitude of the stress at this location. The first span shows the higher stress out of the three spans.

The S22 stress is found to be small, with maximum values of stress up to $0.5\,MPa$ near support regions, but mostly below $0.1MPa$ elsewhere. The variation of the stress with velocity (Figure 5.42b), again shows correspondence to the displacements (Figure 5.41). There is a strong correlation between the *Simple* and *Full* models in the S11 direction, with the S22 stress response significantly different between models. However, the S22 stress response is much smaller, and less of a design concern.

5.5 Continuous Bridge Parametric Analysis

Under the consideration of the three spanned continuous bridge studied in the benchmark case in Section 5.4, the web thickness and bottom flange thickness are again investigated in this section. The depth is not studied, due to the lack of weight savings offered.

(a) Variation in the maximum tensile S11 stress variation and DAF from the vehicle loading, in the bottom flange of the U-beam, along the full length of the bridge, for a velocity of $100\,m/s$

(b) Variation in the actual stress and DAF with velocity, in the bottom flange of the U-beam at midspan of the first span, using a logarithmic scale for the y axis of the DAF
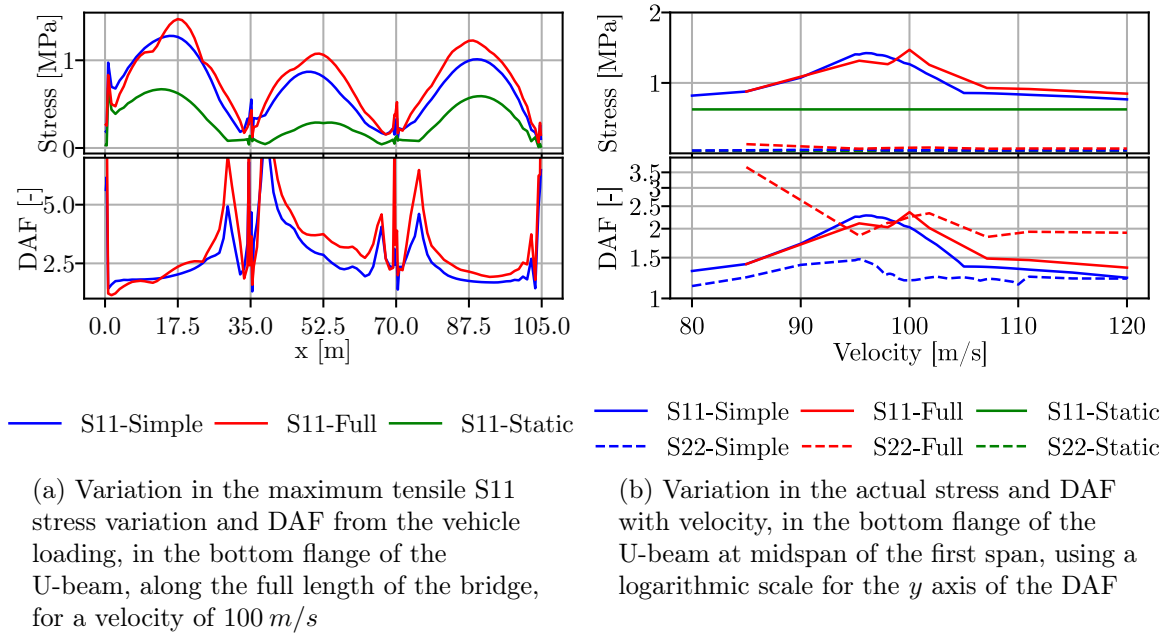
Figure 5.42: Variation in the beam stresses and DAF in the bottom flange
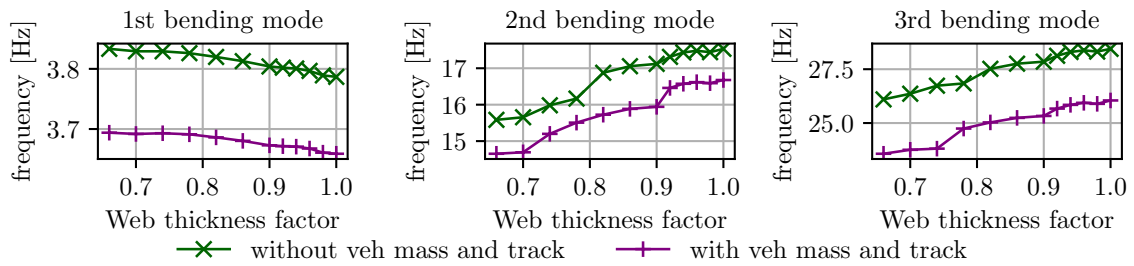
Figure 5.43: Comparison of how the frequency of certain modes varies with web thickness for the continuous bridge case. Frequencies without the vehicle mass and track are akin to the *Simple* model and with the vehicle mass and track are similar to the *Full* model

5.5.1   Web Thickness

Changes to the web thickness, follow the same changes as seen in Section 5.3.1. As a result the same benefits for the mass can be found.

5.5.1.1   Modal Contribution

For the continuous bridge the frequencies are slightly different to the one span case, and as such the frequencies are as shown in Figure 5.43. However, they show similar relationships with the single span web thickness, although different values, that change with the parameter as in the single span case. The corresponding mode shapes are also shown in Figure 5.44

(a) First bending mode   (b) Second bending mode   (c) Third bending mode
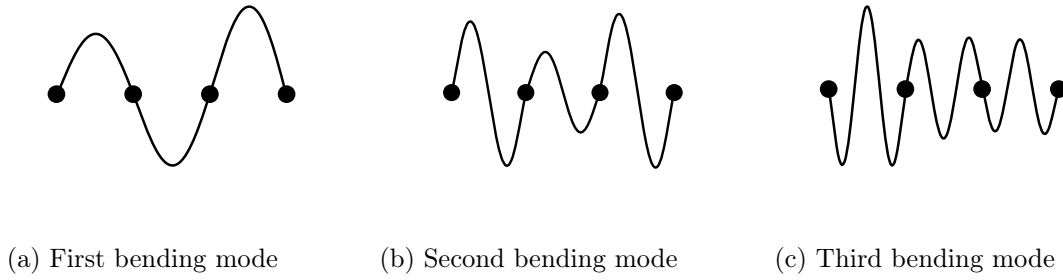
Figure 5.44: Continuous bridge mode shapes
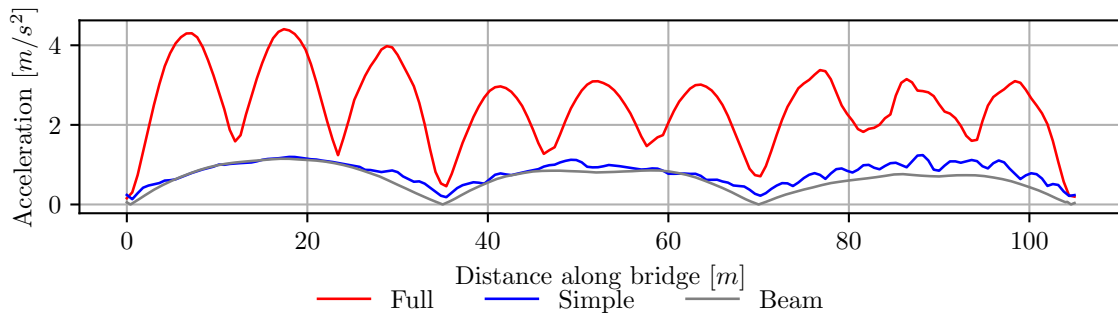
Figure 5.45: Maximum filtered vertical accelerations along the bridge for three spanned continuous bridge at $100\,m/s$, for the benchmark case.

5.5.1.2 Vertical Bridge Accelerations

With the vehicle moving in the positive x direction again, for the velocity of $100\,m/s$, the maximum acceleration is found at the midspan of each span for the *Simple* and beam load models, whereas in the case of the *Full* vehicle dynamic model with irregularities, the maximum acceleration is found at midspan of the first span, with three local peaks per span. This is seen in Figure 5.45. The reason for the first span having a larger response is that the mode activated by this *Full* vehicle model shows a larger contribution in the first span.

Study of the accelerations with changing parameter and velocity as in Figure 5.46, shows that in this case the bridge accelerations increase in the *Simple* model case, up to a 78% thickness, where the acceleration then decreases again. For the *Full* vehicle model, apart from localised lows, the accelerations continue to increase, such that at 66% of the thickness the bridge accelerations are about to exceed the limits for slab track. Further reductions in thickness were not possible without changing the way in which the cross section was modelled, which would have led to greater variability in the results.

Furthermore, study of the variation in accelerations with web thickness at the fixed location of the midspan of the first span, combined with the operating speed of $100\,m/s$, is shown in Figure 5.47. It highlights a decrease in accelerations as the web thickness increases, which is primarily a result of the reduction in the frequency and hence contribution of the third
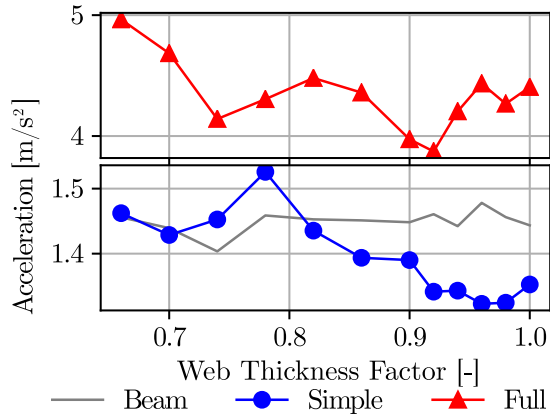
Figure 5.46: Variation in maximum filtered acceleration at any point along length of bridge for all velocities under $432\,km/h$ ($120\,m/s$), for different web thicknesses
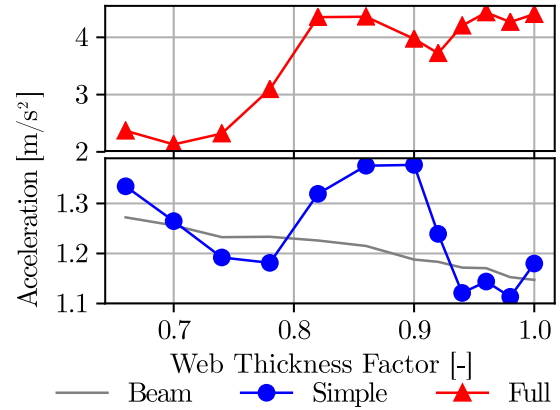
Figure 5.47: Variation in maximum filtered acceleration at midspan of the first span for a velocity of $100\,m/s$ for different web thicknesses

bending mode for this studied velocity.

The appropriateness of the use of $100\,m/s$ as a case study is again as a result of it being the operating speed and consistently the velocity for the peak acceleration of the *Simple* and *Beam* models. The shifting peak of the *Full* dynamic model with respect to velocity is shown in Figure 5.48. It can be seen that in the *Full* model the peak is moving to lower speeds, which is similar to as seen in the corresponding single span case. From Figure 5.49, it can be seen that the modal bridge frequencies shift and contributions from other modes can still be high. This is particularly noticeable for parameters of 0.78 and 0.7. In the case of the web thickness parameter being 0.7, the acceleration components show much smaller peaks, which is contradictory with Figure 5.46, as this parameter leads to the second largest accelerations. However, this is due to a larger spread of frequency components for this parametric case (Figure 5.49), which also coincides with the maximum acceleration being found at an x coordinate of 41.4 m. This puts it 6.4 m into the second span, hence not at midspan. Figure 5.49 also shows that for parametric cases between 1 and 0.78 the maximum acceleration was found at midspan of the first span (given by the coordinate 17.4 m), whereas in the parametric case 0.7 it is at a coordinate of 41.4 m and in parametric case 0.66 it is at a coordinate of 6.6 m. This indicates the shifting location of the maximum acceleration due to the fact that the first $(f_{s,1})$ and third $(f_{s,67})$ bending modes are not both resonant for the same velocity.

5.5.1.3 U-Beam Stress

Consideration of the stress DAF in the beam is seen in Figure 5.50, showing the influence of changing web thickness. As before the DAF of the S11 stress barely changes, but the S22
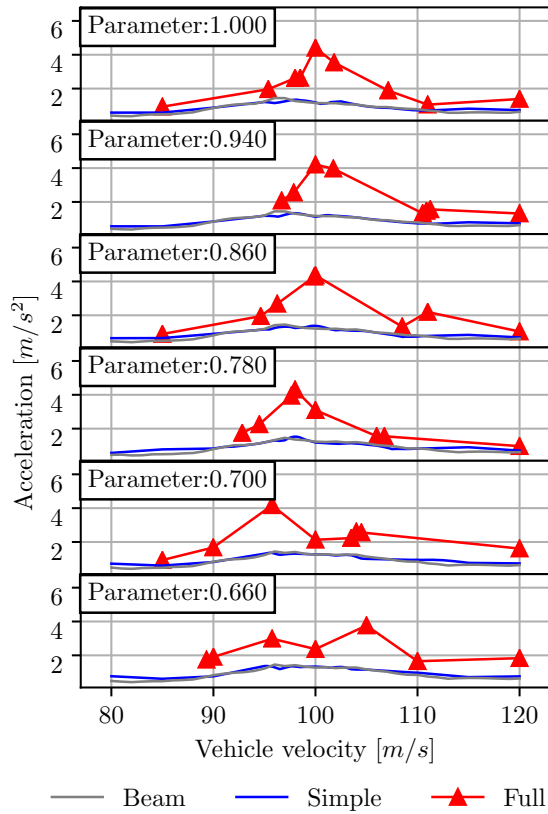
Figure 5.48: Variation of the maximum vertical accelerations with velocity, at midspan of the first span of the three spanned continuous bridge, with reductions to the web thickness
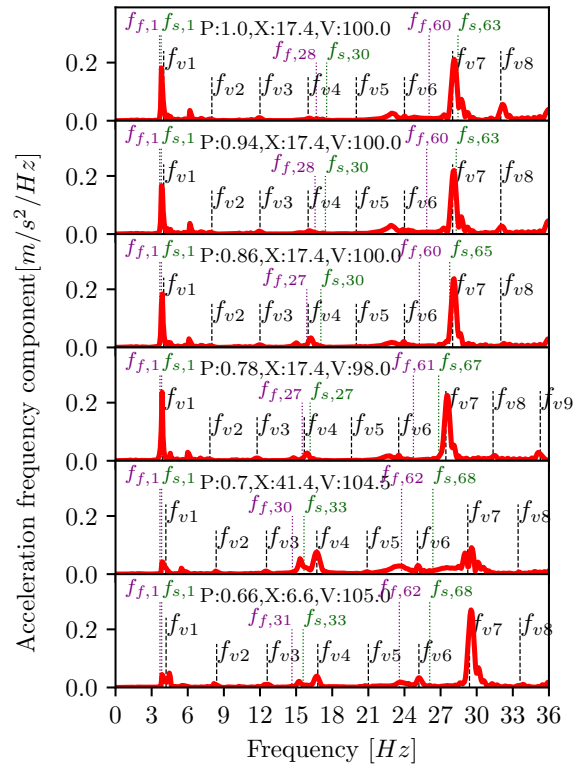
Figure 5.49: Comparison of the frequency components of the filtered maximum vertical accelerations for the particular velocity (V, $[m/s]$) and location along the length of the bridge (X, $[m]$ from the end span), that lead to the maximum vertical acceleration for each web thickness parameter (P). Also showing the resonant loading frequencies (f_{vi}, black dashed lines), and selected bridge frequencies without the track and vehicle mass ($f_{s,i}$, green dotted lines) and with the track and distributed vehicle mass ($f_{f,i}$, purple dotted lines)
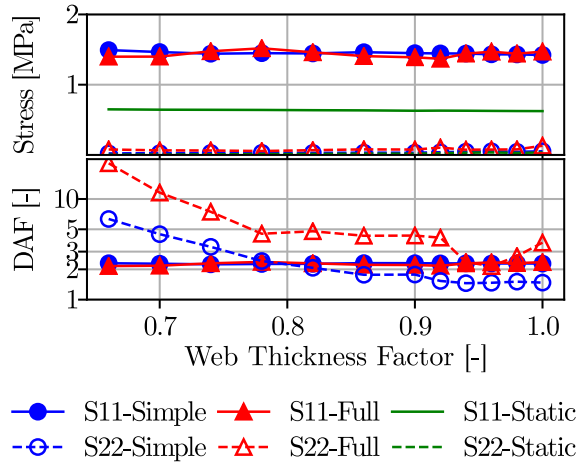
Figure 5.50: Variation of maximum stress DAF with web thickness reduction, taken from the bottom flange of the U-beam, at midspan of the first span, for the velocity under $432\,km/h$ that leads to the greatest stress, using a logarithmic scale for the y axis of the DAF
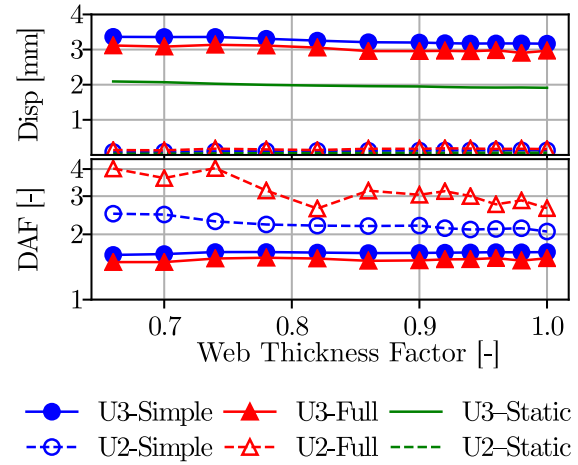
Figure 5.51: Variation of maximum actual displacement and DAF with web thickness reductions, taken from the slab at midspan of the first span, for the velocity under $432\,km/h$ that leads to the greatest displacement, and using a logarithmic scale for the y axis of the DAF

stress DAF increases significantly. This is due to low initial static S22 stress and activation of lateral modes. Like in the single span case the S11 stress is near constant.

5.5.1.4   Bridge Displacement

The maximum displacement in the slab at the midspan of the first span is shown in Figure 5.51. This takes into account all velocities studied. The actual vertical displacement varies very little, although it increases slightly with reduced web thickness. The *Simple* and *Full* models give similar displacement responses as well. Laterally, the actual displacements are small, but consideration of the DAF shows increase with smaller thickness of web. This is particularly the case for the *Full* model.

5.5.1.5   Summary of the Web Thickness Reductions

The accelerations in the bridge approach the limit for slab track with a web thickness of 0.66. This highlights a possible upper bound to the amount of material to be able to save from webs. In terms of the DAF, the actual stress and DAF do not increase significantly with consideration of the critical S11 stress. The S22 stress is found to still be much lower but due to lateral action, the DAF is much higher. This is reflected in the lateral displacement DAF, which increases for decreasing web thickness. Vertically though it remains constant. As
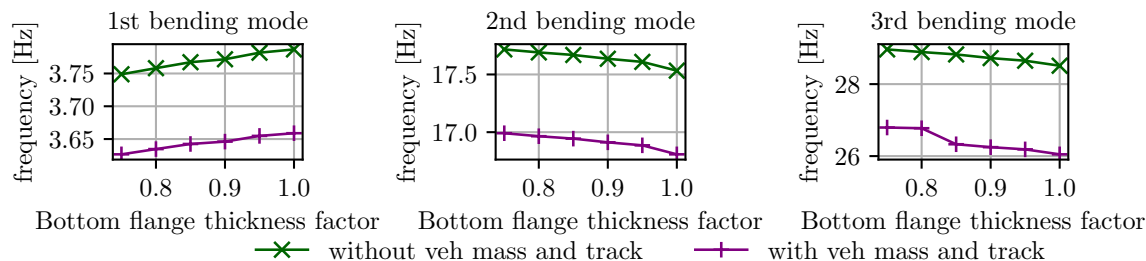
Figure 5.52: Comparison of how the frequency of certain modes varies with bottom flange thickness for the continuous bridge case. Frequencies without the vehicle mass and track are akin to the *Simple* model and with the vehicle mass and track are similar to the *Full* model

the lateral motion is small and not therefore critical, this makes the web thickness changes suitable for use.

5.5.2 Bottom Flange Thickness

Changes to the bottom flange thickness, follow the same changes as seen in Section 5.3.2. As a result the same benefits for the mass can be found.

5.5.2.1 Modal Contribution

Again, the frequencies of the variation in the bottom flange thickness are slightly different to the single span case (Figure 5.52). Similar relationships are found with the single span bottom flange thickness, such that the frequency of the first mode decreases with decreasing thickness, whilst other modes increase. These mode shapes were shown in Figure 5.44.

5.5.2.2 Vertical Bridge Accelerations

Consideration of the maximum vertical accelerations anywhere along the length of the bridge under the track for any tested velocity under $432\,km/h$ ($120\,m/s$), is shown in Figure 5.53. It can be seen that apart from the benchmark case value the *Full* model accelerations show steady increase in value with reducing thickness. In contrast, focus on only the first span midspan at $100\,m/s$ (Figure 5.54), shows steady decrease in the acceleration with bottom flange thickness, due to the shifting modal frequencies. For both figures the *Simple* model has accelerations that stay within a range of $0.1m/s^2$, and hence can be considered relatively consistent.

Study of the velocities show a shifting vertical acceleration peak in the *Full* model to higher velocities (Figure 5.55). Through the decomposition of the frequency component of the max-
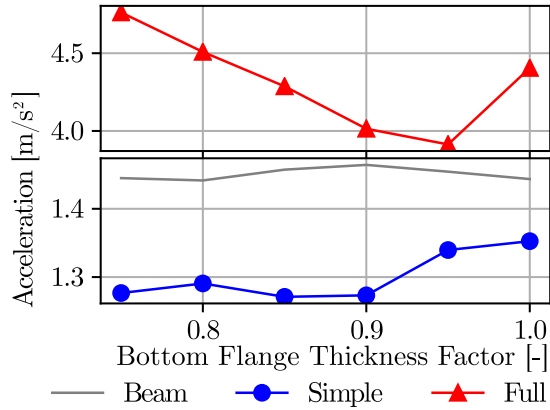
Figure 5.53: Variation in maximum filtered acceleration at any point along length of bridge for all velocities under $432\,km/h$ $(120\,m/s)$ for different bottom flange thicknesses
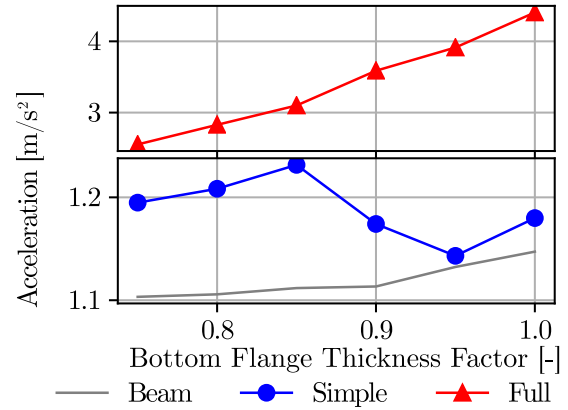
Figure 5.54: Variation in maximum filtered acceleration at midspan of the first span for a velocity of $100\,m/s$ for different bottom flange thicknesses

imum accelerations at the midspan of the first span, it can be seen in Figure 5.56 that the maximum acceleration found in the *Full* case initially has equal contribution from first $(f_{s,1})$ and third $(f_{s,64})$ bridge modes, but with reducing thickness, the contribution becomes increasingly dominant of just the third bending mode around $27 - 29$ Hz. This results in the maximum acceleration being no longer located at midspan of the first span, but at the coordinate of $28.8\,m$ which is about $L/6$ from the end of the first span, as can be seen by the x coordinate for which the maximum acceleration is decomposed at for each parametric case in Figure 5.56.

5.5.2.3 U-Beam Stress

The stress S11 in the bottom flange increases as the thickness is reduced (Figure 5.57). However, the static stress also increases, such that the DAF is relatively stable. Like seen in the single span case the DAF for the S22 stress is more variable, but this is a result of the relatively low static stress and lateral mode activation. However, variation of the bottom flange thickness is found to have little effect on the stress response.

5.5.2.4 Bridge Displacements

The displacement DAF of the slab for variation of the bottom flange is shown in Figure 5.58, showing the maximum DAF for all velocities under $432\,km/h$ $(120\,m/s)$. Unlike for the web thickness changes there is no distinct change in the lateral displacement DAF with reduction in the thickness. The influence of irregularities and small static lateral displacement leads to
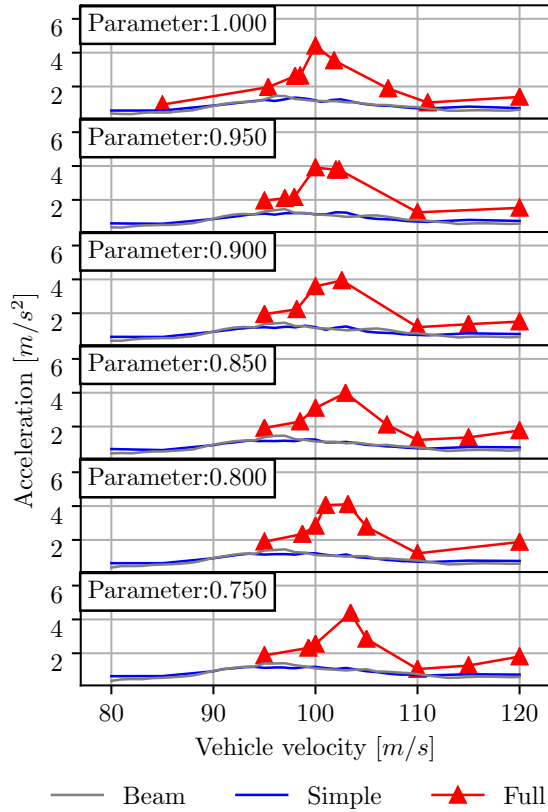
Figure 5.55: Variation of the maximum filtered vertical accelerations with velocity, for different bottom flange thickness changes, taken from the midspan of the first span for the three spanned continuous bridge
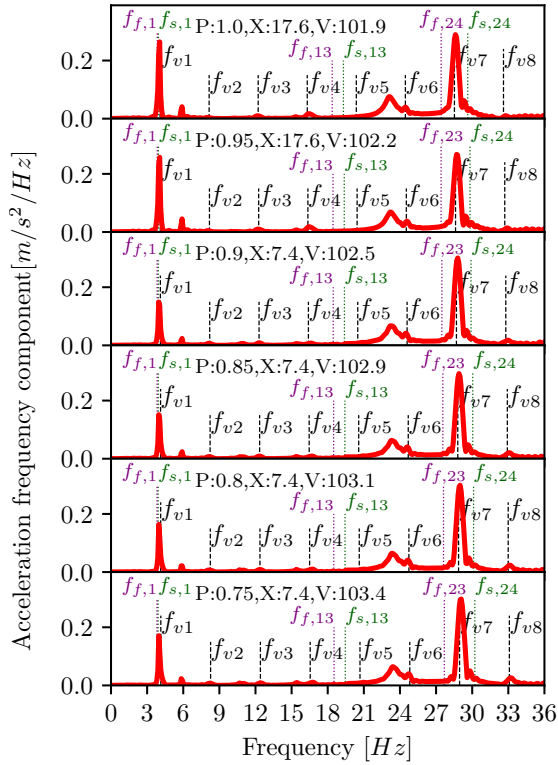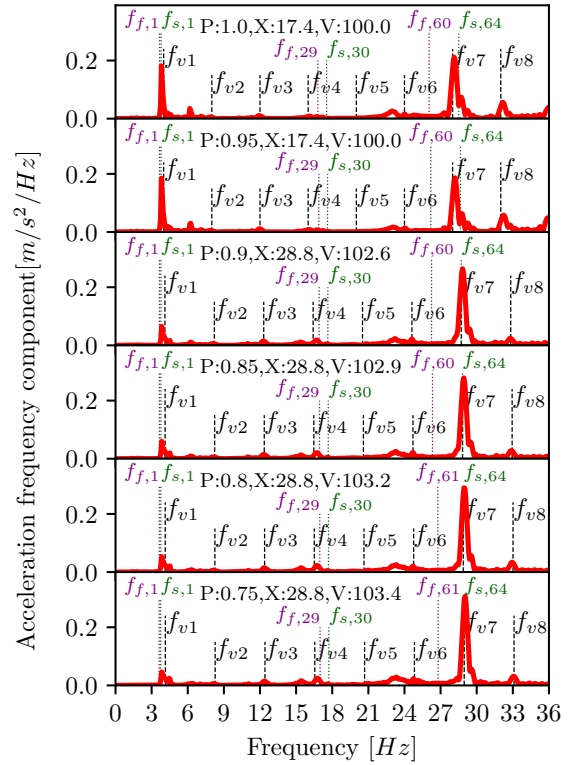
Figure 5.56: Comparison of the frequency components of the filtered maximum vertical accelerations for the particular velocity (V, $[m/s]$) and location along the length of the bridge (X, $[m]$ from the end span), that lead to the maximum vertical acceleration for each bottom flange thickness parameter (P). Also showing the resonant loading frequencies (f_{vi}, black dashed lines), and selected bridge frequencies without the track and vehicle mass ($f_{s,i}$, green dotted lines) and with the track and distributed vehicle mass ($f_{f,i}$, purple dotted lines)
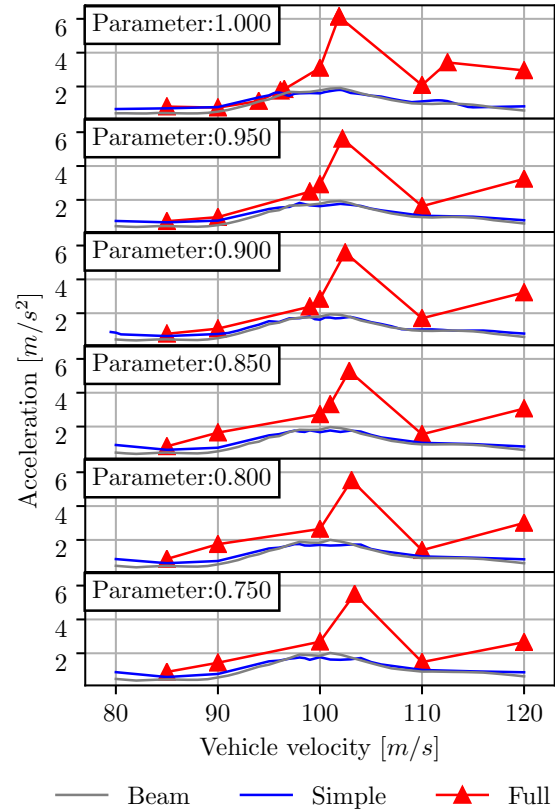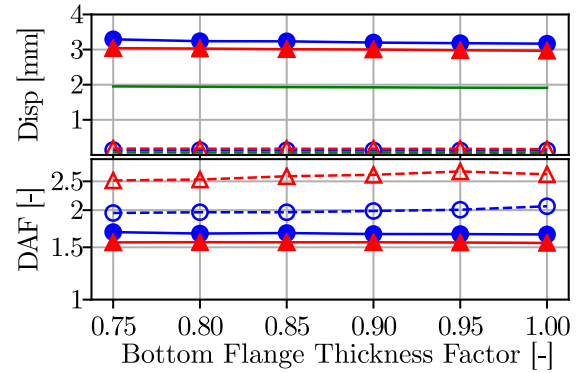
Figure 5.57: Variation of actual and DAF stress with bottom flange thickness variation, with values taken at the bottom flange of the U-beam at the midspan of the first span, for the velocity under $432\,km/h$ leading to the largest DAF, and using a logarithmic scale for the y axis of the DAF

Figure 5.58: Variation of actual and DAF displacements with bottom flange thickness variation, for values taken from the slab at midspan of the first span, for the velocity under $432\,km/h$ leading to the greatest DAF, and using a logarithmic scale for the y axis of the DAF

a substantial difference between the *Simple* and *Full* models. Vertically there is very little change in the DAF between loading models nor for different thicknesses.

5.5.2.5 Summary of the Bottom Flange Thickness Reductions

The maximum accelerations are found to increase with reducing bottom flange thickness. Whilst the *Full* model accelerations do not exceed the limits, they are tending towards it, with computational methods limiting the extent to which the bottom flange thickness can be reduced.

Small increases in the S11 stress are matched by the static stress such that the DAF for the variation in stress stays constant. The DAF for the displacements are less sensitive compared to changes in web thickness, with the *Simple* load model providing a good estimation of the vertical DAF *Full* model for all thicknesses, but the lateral DAF requires the *Full* vehicle model to capture the effects of the irregularities on the lateral displacements. From the accelerations and the DAF it appears that reductions up to 75% of the original thickness of the bottom flange, are viable for the reduction in mass of a U-beam.

Model	Parameters		
	Web Thickness	Bottom flange thickness	Concrete strength
BC	1	1	1
C1	0.66	0.75	1.46
C2	0.66	0.75	1.56
C3	0.66	0.75	1.66
BF1	1.0	0.75	1.22
W1	0.66	1.0	1.40

Table 5.2: Parameters used in the models compared in the combined web and bottom flange models
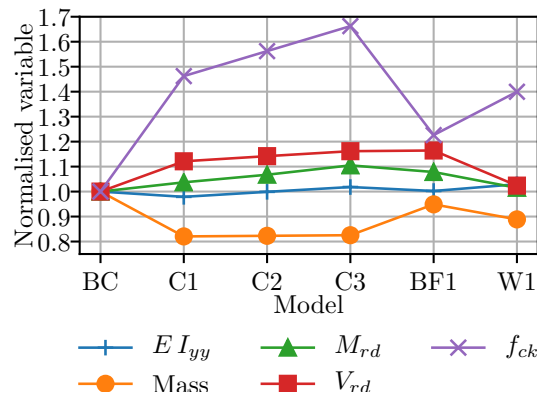
Figure 5.59: The mass, stiffness and concrete strength changes with combined web and bottom flange thickness changes

5.5.3   Combined Bottom Flange and Web Thickness Reductions

As the bottom flange and web thickness changes offered good ability to save weight and material with an increase in the concrete strength, this section investigates combining the two parametric models together, for a small selection of cases. These cases are detailed by Table 5.2, with *C2* representing the concrete strength required to maintain the structural rigidity when combining a web thickness of 66% with a bottom flange of 75%, with the *C1* and *C3* cases representing 10% variations on this concrete strength. For comparison it is compared to the results of the benchmark case study (BC), the ultimate web thickness reduction of 66% and bottom flange thickness reduction of 75%.

The combination of the web and the bottom flange thicknesses leads to the U-beam masses of 82% of the original (Figure 5.59), with some small variations with the different concrete strengths, which is a very significant weight saving. The capacities of the bridge are also shown to be similar or higher than the benchmark in all parametric cases.

The frequencies of the bridge with the combined web and bottom flange thickness changes, appear to follow similar relationships to the web thickness for the higher modes, with the frequencies appearing similar in comparison to the bottom flange thickness. For the fundamental
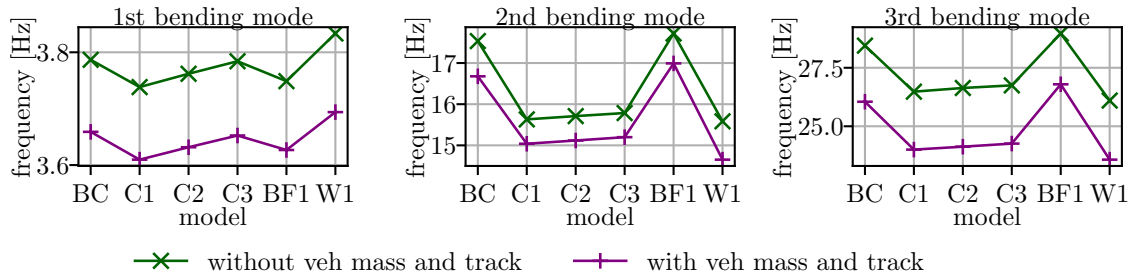
Figure 5.60: The frequency changes with models for the combined web and bottom flange changes. Frequencies without the vehicle mass and track are akin to the *Simple* model and with the vehicle mass and track are similar to the *Full* model

modal frequency, the frequency is similar to the bottom flange thickness.

5.5.3.1   Vertical Bridge Accelerations

Consideration of the vertical accelerations for a velocity of $100\,m/s$ at midspan of the first span is shown by Figure 5.61. The accelerations for all the *Full* model cases are found to be much lower than the original benchmark case (BC). This is due to the shift in frequencies, reducing the resonant response from particularly the third bending mode at this velocity, and shifting the location of the maximum acceleration. On the contrary the maximum response seen along the length of the bridge for all velocities under $432\,km/h$ ($120\,m/s$) (Figure 5.62) shows $C3$ and $C2$ with similar accelerations to the web ($W1$) and bottom flange ($BF1$) cases, higher than that of the benchmark case (BC). Yet the $C1$ model shows a lower response than the benchmark case (BC) model. This is a result of the decoupling of the first ($f_{s,1}$) and third bridge modes (between frequencies of $f_{s,63}$ and $f_{s,68}$, depending on the parametric case), such that one velocity does not activate both modes simultaneously.

When considering the *Simple* model the accelerations are always lower than that of the *Full* model as previously found, but unlike the *Full* model, the *Simple* accelerations are slightly higher for the $C1$, $C2$ and $C3$ bridge than in the BC bridge. This is from the dominant fundamental mode dominating the response, with the changing mass and stiffness of the bridge contributing to the increased response.

The decoupling of the modes is evidenced in Figure 5.63, that still shows peaks of the acceleration for the *Full* model velocity, but with reduced amplitude for the $C1$ model. Consideration of the component frequencies of the maximum accelerations (Figure 5.64), reinforces this theory, as for $C1$, the maximum response found on the bridge has minimal contribution from the first ($f_{s,1}$) and third (about $f_{s,68}$) bridge bending modes, instead contributions from around the second bending mode and slightly higher than the third bending mode contribute, which are hybrid modes. This figure also shows the change in the location of the maximum location, as the location (x), that the maximum acceleration is split into its frequency components for
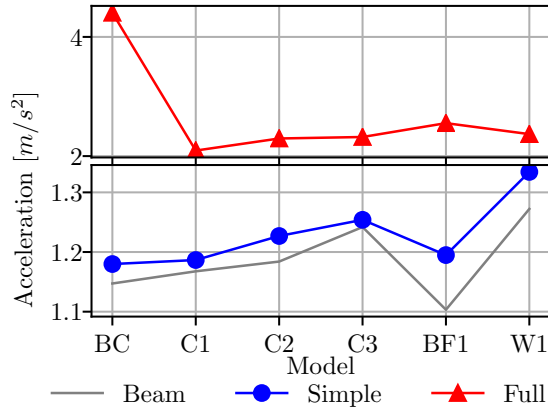
Figure 5.61: Maximum accelerations at midspan of the first span for combined web and bottom flange thickness changes at $100\,m/s$
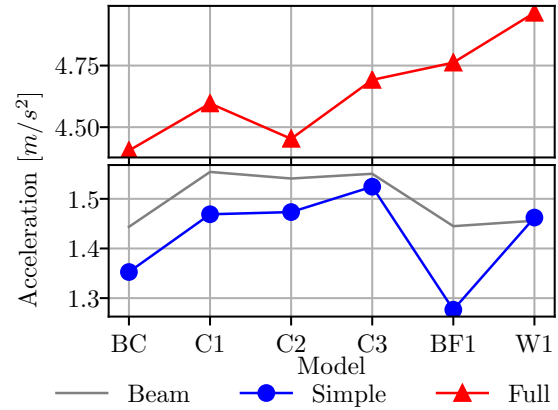
Figure 5.62: Maximum accelerations along length of bridge under track, for combined web and bottom flange thickness changes for all velocities under $432\,km/h$ ($120\,m/s$)

each parametric case varies. It does show that the maximum is always in the first span, as all x coordinates are less than the span length of 35 m. However, the location of the maximum varies between midspan (17.4 m), and L/6 from either end of the first span (6.6 and 28.8 m), which is consistent with peaks due to the third bridge bending mode ($f_{s,68}$), of three half sine waves per span.

Overall, the accelerations are found to be lower than the limits and therefore the combined adjusted web and bottom flange thickness bridge model is acceptable from the aspect of accelerations, with both the *Full* and *Simple* vehicle loading models.

5.5.3.2 U-Beam Stress

The stress S11 in Figure 5.65, is seen to have some small variation in the actual stress values between models. However, the DAF value stays the same, and the increase in the stress is no more than 20% from the benchmark case models, yet the strength of concrete increases by over 50%, which would cover this increase in stress. Looking at the S22 stress (Figure 5.66), the values of stress are found to be lower in the combined thickness model cases, but all of the S22 stress values are very small to have influence.
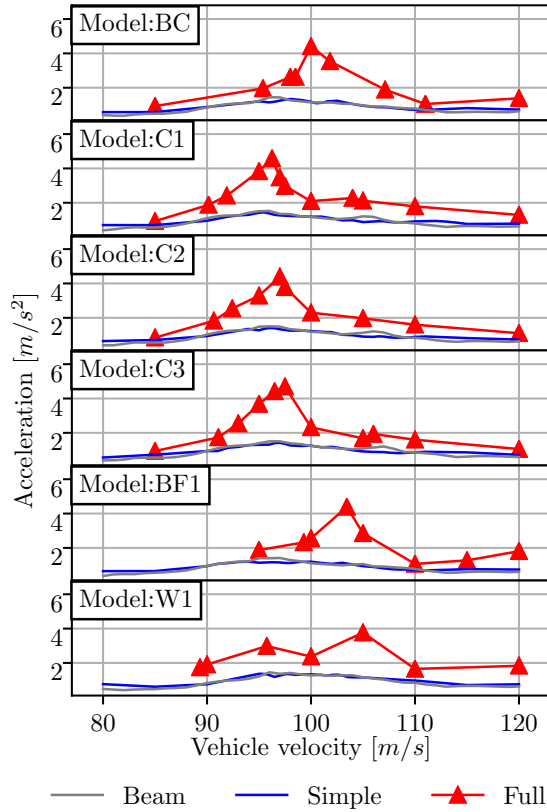
Figure 5.63: Variation of the accelerations at midspan of first span for the different models and velocities
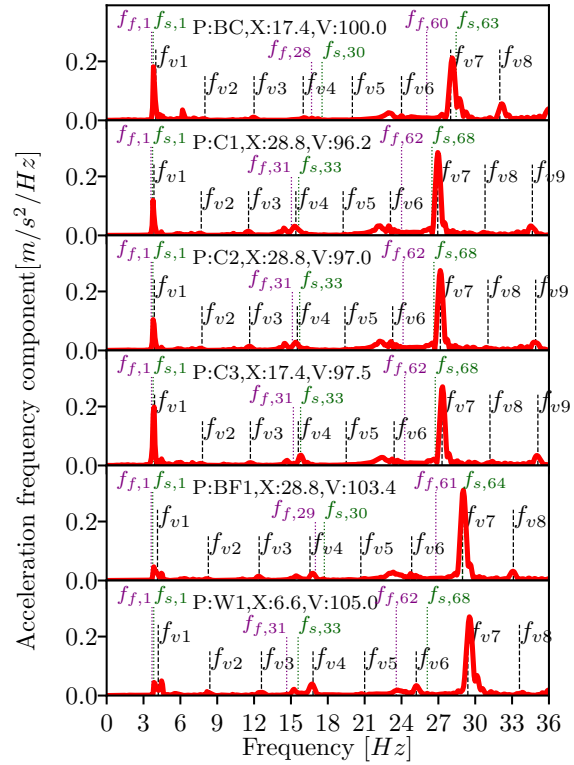
Figure 5.64: Comparison of the frequency components of the filtered maximum vertical accelerations for the particular velocity (V, $[m/s]$) and location along the length of the bridge (X, $[m]$ from the end span), that lead to the maximum vertical acceleration for each model (P). Also showing the resonant loading frequencies (f_{vi}, black dashed lines), and selected bridge frequencies without the track and vehicle mass ($f_{s,i}$, green dotted lines) and with the track and distributed vehicle mass ($f_{f,i}$, purple dotted lines)
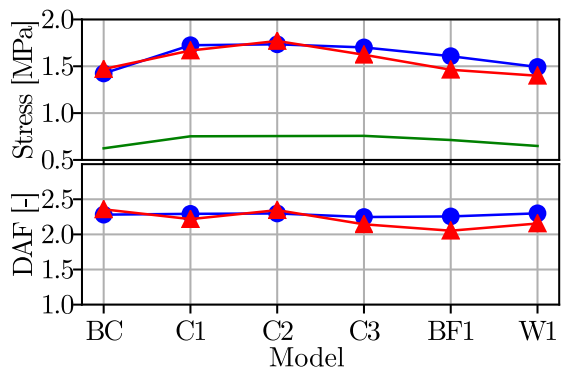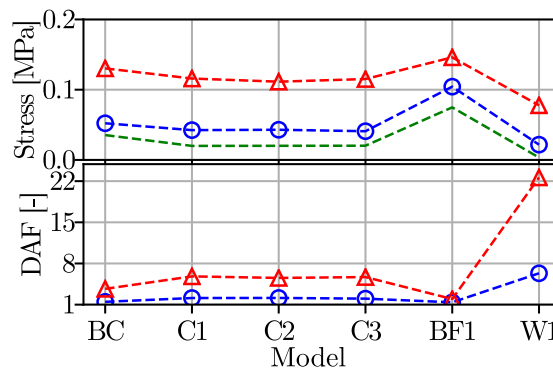
Figure 5.65: Variation of the actual and DAF S11 stress values with model, taken from the bottom flange of the U-beam at midspan of the first span, for the velocity under $432\,km/h$ that leads to the maximum stress

Figure 5.66: Variation of the actual and DAF S22 stress values with model, taken from the bottom flange of the U-beam at midspan of the first span, for the velocity under $432\,km/h$ that leads to the maximum stress

5.5.3.3 Bridge Displacements

The vertical displacement of the bridge slab at midspan of the first span is found to be relatively constant between models (Figure 5.67). Laterally, the displacement is more variant than the vertical direction, especially in the DAF, which is due to the lateral response being amplified under certain loading velocities. The bridge displacements here are seen not to be of concern as they are well below the $L/600$ limit vertically and very small laterally.

5.5.3.4 Vehicle Accelerations

The vehicle accelerations are an indication of the passenger comfort level. With the *Full* vehicle it becomes possible to analyse these. As can be seen from Figure 5.68, the vehicle accelerations are very similar vertically between models, with the variation of acceleration for different vehicle velocities very small (max variation $0.008m/s^2$). By contrast the lateral vehicle accelerations are more variant with variation of $0.07m/s^2$, but this is still small, and the maximum values both laterally and vertically are well within the comfort levels required (Section 2.7.3.2). The vehicle comfort levels are as a result not a concern.
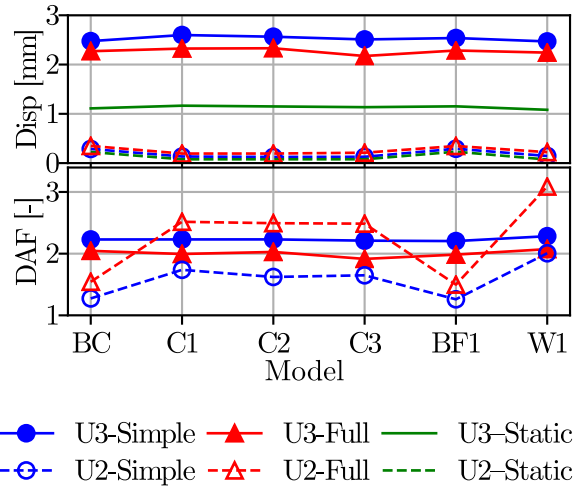
Figure 5.67: Variation of the displacement of the bridge with each parametric case, studying the displacements in the slab at midspan of the first span, for the velocity under $432\,km/h$ that leads to the maximum displacement

(a) Vertical vehicle acceleration

(b) Lateral vehicle acceleration
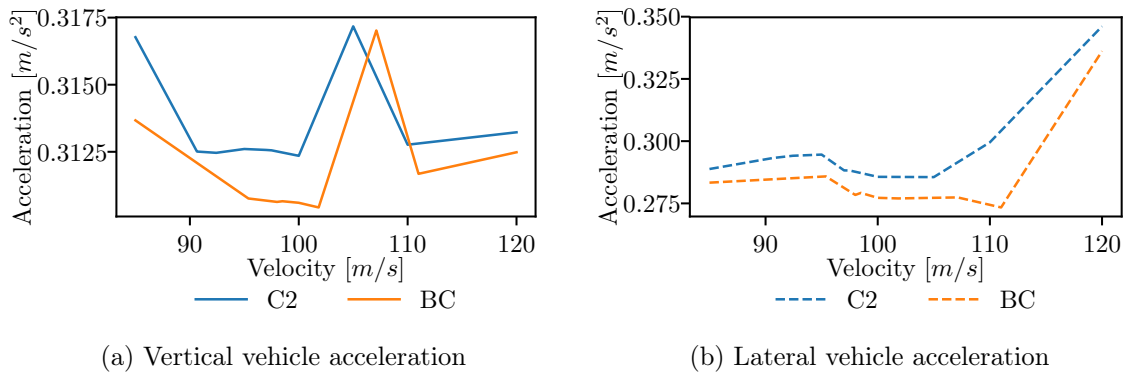
Figure 5.68: Variation of the maximum vehicle accelerations, taken at the centre of mass of the carriages, for each velocity for the cases *BC* and *C2*
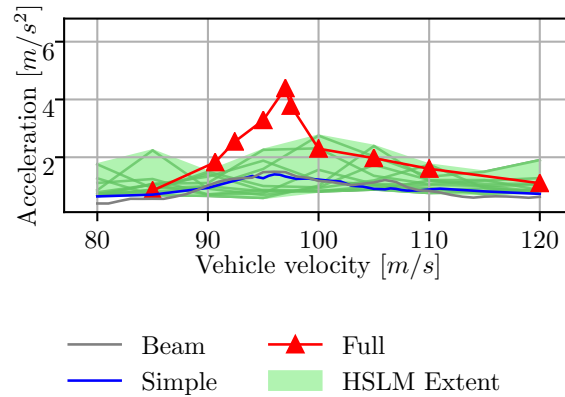
Figure 5.69: The combined web and bottom flange model C2, acceleration variation with velocity at midspan of first span with the HSLM models

5.5.3.5   HSLM Dynamic Load Models

With the combined web and bottom flange thicknesses proving a potentially viable option for use of higher strength concretes under the real train load, consideration of the dynamics of the bridge under the HSLM A models is made. This covers all the potential train models (see Section 2.2.7). Although it ignores the consideration of the irregularities, as it only uses *Simple* moving point loads, it is the current design standard for bridge dynamic analysis. As can be seen from Figure 5.69, the HSLM load model provides significantly larger accelerations than found in the *Simple* load model, however crucially still lower than the limits to acceleration and the *Full* vehicle model with irregularities.

5.5.3.6   Summary of the Combined Web and Bottom Flange Reductions

The combined model of web and bottom flange thickness variation is shown to be successful in reducing the precast mass by 18% and the total bridge structure mass by 8%, whilst also maintaining satisfactory bridge accelerations with the *Full* vehicle model, as well as the moving point load HSLM models. In addition the accelerations in the vehicle were found to be unaffected by the changes in the bridge model. In order to maintain the rigidity of the bridge model under the changes in thickness, an increase in concrete strength by 56% was required, which would correspond to a concrete strength of 94 MPa. The displacements change very little and are within limits prescribed, and the variation in stresses despite increasing by up to 20%, maintain constant DAF and are below the corresponding increase in concrete strength.

5.6   Conclusions for this Chapter

This parametric analysis has led to conclusions based on the displacement, stress and accelerations. They are outlined in this section.

Study of the displacements have led to the conclusions:

- By maintaining the structural rigidity, the displacements of the bridge vertically are minimally influenced by geometry changes.

- The lateral displacements can vary significantly in percentage/DAF terms due to activation of lateral and torsional modes, but magnitude of change is of order of a tenth of a millimetre, hence still insignificant.

- This lateral response is amplified more by the *Full* vehicle model, due to the lateral components of the loads that are not present in the *Simple* moving point load model.

- The magnitude of deflection of the bridge is matched well between the *Simple* and *Full* models.

- The DAF is consistent between the loading models vertically, although horizontally the small increase in lateral displacement from the lateral resonance leads to a mismatch between models.

Considering the maximum stress variation in the beam when a high speed train crosses the bridge, it was found that:

- The variation in stress from the dynamic loading was maximum in the midspan of the beams, with the bottom flange displaying a more critical stress, as expected

- The actual stress variation was seen to increase in the bottom flange (by up to 20%), particularly when a reduction was applied to the bottom flange thickness.

- The S11 stress (the normal stress in longitudinal direction) was found to suffer the larger stress variations due to traffic loading.

- The S22 stress (normal stress in plane of shell perpendicular to longitudinal direction), is mainly affected by transverse bending and lateral displacements. This creates differences between the *Full* and *Simple* model results, in particular the DAF, which is very high due to low static stress variation. The actual magnitude of the stress changes for S22 stresses are similar and very small.

- For both the S11 and S22 actual stresses, modelling using the *Simple* method provides a similar stress response to the *Full* model, removing the need to model using the *Full* model to account for the stress response.

The following conclusions were made based on the general bridge vertical accelerations:

- As highlighted in the previous chapter, the use of the *Full* model with irregularities leads to amplification of higher modes, which contributes to higher accelerations.

- For the bridge modelled with a single span, under the *Full* model, the vertical accelerations do not change significantly from the original values of the benchmark case when a reduction of the cross section is introduced and counterbalanced by an increment of the concrete strength.

- Under the continuous bridge, reductions to the thicknesses generally lead to increased accelerations.

- With frequencies of the bridge for modes containing one half sine wave and three half sine waves, are found to be positioned such that both bridge modes are activated by resonant loading frequencies (f_{v1} and f_{v7}) for the same velocity. This leads to a coupling of resonant responses, increasing the resonant acceleration response. This is particularly evident in the benchmark case, and in some other parametric cases. Through reductions to the geometry, the modal frequencies change, such that only one bridge mode is activated by the resonant loading frequencies for the same velocity, reducing the resonant response in some cases. The response of these bridge modes is then decoupled. However, prediction of this decoupling of the modes to achieve reduced acceleration responses, by changing the modal frequencies through reductions to the geometry is very complicated, and a method has not been found.

- With the *Simple* loading model, accelerations were seen to increase with reductions in thickness. Under the *Simple* model, the higher modes have much smaller contributions than in the *Full* model, but these modes still influence the maximum acceleration. As a result, the mode coupling and decoupling, can still cause some small localised peaks in acceleration for parameter changes.

Some consideration was made to the vehicle accelerations. It was found that they vary in the lateral direction slightly with models, but by very small amounts. Vertically the difference is very small, such that the vehicle accelerations are not of concern to the parametric study.

Consideration of the dynamic response under the moving HSLM model, showed higher acceleration responses than the bridge under the *Simple* model, but still significantly lower than the response found under the *Full* train model. This shows the importance of the *Full* vehicle model, including the rail irregularities, using real trains in the study of accelerations.

Considering the parametric analysis, the following conclusions are found:

- Modelling of changes to the bottom flange achieved a viable thickness 75% of the original value, with a concrete strength increased by 22.6%.

- Likewise the web thickness changes found a thickness of 66% of the original to be achievable, with a concrete strength increased by 40%.

- Reductions to the depth, although they maintained acceleration levels, were not found to be viable due to the small material savings, and large increases in concrete strength required to maintain the structural rigidity.

- A combination of the 75% thickness of the bottom flange and 66% of the web thickness is identified as a viable solution. It leads to mass savings of 18% for the precast elements and 8% for the whole bridge mass, for a 56% increase in the precast concrete strength. The maximum accelerations are very similar to the original benchmark case model in this case.

Chapter 6

Parametric Analysis of Alternative Bridge Cross Sections

Analysis of the dual U-beam HSR bridge in the preceding chapter led to several conclusions regarding the ability to change the geometry to primarily achieve a mass reduction, whilst maintaining the structural and dynamic performance of the bridge. In this chapter, these conclusions are studied after being applied to other real precast HSR bridge cross sections in use around the world. The aim is to determine if the conclusions are valid for different bridge types. Study is made on three existing benchmark bridges of different cross sectional types: the viaducts of segment 2.2 of the Kyung-bu HSR line (South Korea, Single celled box girder, continuous), the Piacenza Viaduct (Italy, Double-celled box girder, simply supported), and the Modena Viaducts (Italy, 'Omega'/Trough profile, Simply Supported). These have been selected after comparison to other similar cross sections, with the chosen bridges showing normal representative characteristics (see Section 3.1), and also having enough relevant information published to use the design.

6.1 Viaducts of the Kyung-bu HSR line

The bridge studied in this section is from South Korea, published by Kim et al. (2000) and Dong Kang and Suh (2003), where full span precasting was implemented on a section of the alignment. This type of bridge construction has also been used elsewhere, for example in Japan and Taiwan (Amarume et al., 2003; Tai et al., 2010a). In real life, a range of longitudinal arrangements and continuity arrangements were utilised, but in this section focus will be made to a continuous bridge of three spans, each $25\,m$ long. For construction, these spans were pretensioned individually before transportation to location by a gantry carrier, installed with a launching girder, then establishing continuity through post-tensioning and a concrete joint

232
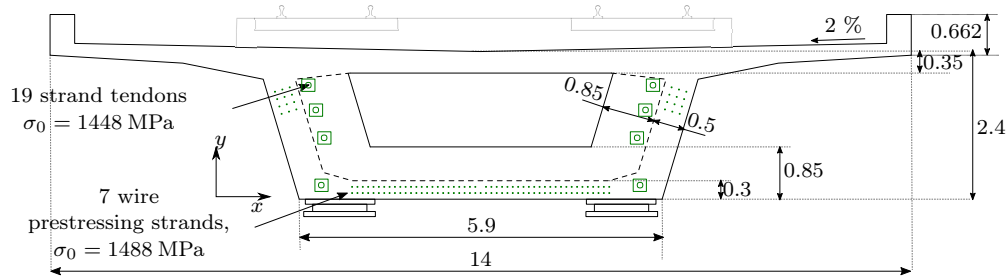
Figure 6.1: The Kyung-bu HSR line bridge cross section, dimensions in m
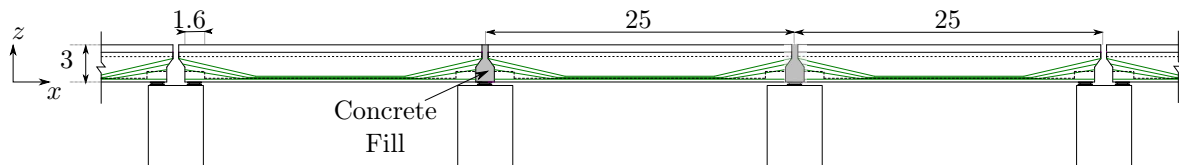
Figure 6.2: The Kyung-bu HSR line bridge longitudinal alignment, dimensions in m

infill.

It was found that the temporary loading conditions of this bridge determined the design (Dong Kang and Suh, 2003). This requires locally higher densities of reinforcement in the locations where fixings for the lifting of the precast span by the gantry carriers and launching girders are found. Although the parametric design will maintain the shear and moment resistance of the section, ensuring that the bridge continues to be able to resist the construction loads, local problems, for example the fixings for lifting, are beyond the scope of the project and hence would require further detailed design after the parametric analysis.

6.1.1   Initial Design

The initial cross section is shown in Figure 6.1 and the horizontal alignment shown in Figure 6.2. The bridge has design details as expressed in Table 6.1. The chosen solution leads to the sectional properties at midspan as found in Table 6.2. In the support regions, the thickness is increased in the bottom flange from $300\,mm$ to $850\,mm$ and in the webs from $500\,mm$ to $1350\,mm$. This is for horizontal stability, transfer of loads to the supports and anchoring of prestress. Under the parametric analysis the dimensions of the support sections are maintained. Although not expressed in the drawings of the authors (Kim et al., 2000; Dong Kang and Suh, 2003), the articulation of the bridge is assumed to be as in Figure 6.3, restricting the longitudinal displacement at the first pier that the vehicle crosses. This bridge is found in a viaduct consisting of many spans, hence the longitudinally fixed bearings and end spans are not necessarily at abutments, requiring short, stocky piers to transfer horizontal load to the ground. In this model again the vehicle is always moving in a positive longitudinal (x) direction.

Span length, L		25 m
Concrete strength, f_{ck}		40 MPa
Prestressing steel strength, f_{pk}		1860 MPa
Initial prestressing force	Pre-tension	219 kN
	Post-tension	3370 kN
Prestress Area	Pre-tension	150 mm^2
	Post-tension	2660 mm^2
Distance between track centrelines		5.1 m
Vehicle operating velocity		300 km/h
Span to Depth Ratio		10.4

Table 6.1: Selected data for Kyung-bu viaducts

M_{rd} [MNm]	128.9	I_{yy} [m^4]	7.519	A_c [m^2]	8.964
V_{rd} [MN]	7.592	I_{zz} [m^4]	107.0	$\bar{z}$ [m]	1.633

Table 6.2: Kyung-bu cross sectional properties at midspan

The bridge is designed to hold two tracks, with $5.0\,m$ between the respective centrelines. The track is assumed to be a ballastless slab track, hence accelerations should be limited to $5\,m/s^2$ for safety requirements. Design requirements for this specific bridge limited the deflection to span ratio to the UIC code ratio of 1/1700 (Dong Kang and Suh, 2003). The operating velocity is 300 km/h, hence the design speed is 360 km/h. Additionally, a project specific passenger comfort level, limited the vehicle accelerations to 0.5 m/s^2.

Prestress is added at two stages. Pretensioning, through 7 wire strands of 15.7 mm diameter, is used to give enough support for the processes involved with construction. This uses 99 longitudinal strands in the bottom flange and 12 within each web. The prestressing force is not specified, and so is assumed to be 219 kN per strand (78% of the characteristic breaking strength). Post-tensioning for continuity uses four, 19 strand tendons in each of the webs, with all except the bottom pair deviated at two locations. Over continuous supports the tendons are anchored in the adjacent diaphragm to provide continuity. A force of 379 $tons - force$ per tendon is specified in Dong Kang and Suh (2003), which corresponds to an approximate force of 3370 kN per tendon. The prestressing layout can be seen in Figures 6.1 and 6.2.
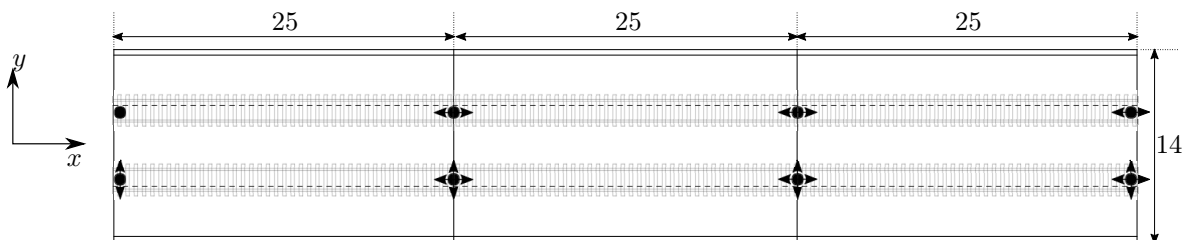
Figure 6.3: The Kyung-bu HSR line bridge articulation. Arrows indicate unrestricted motion of the bearing, dimensions in m

Number of Elements	Element Size [m]		Stress		Displacement		Fundamental Frequency	
	X	YZ Plane	[MPa]	%	[mm]	%	[Hz]	%
5172	0.6	0.6	-2.06	1.8	-4.52	0.6	4.849	0.2
8250	0.3	0.6	-2.06	1.7	-4.48	0.2	4.849	0.0
46569	0.2	0.2	-2.03	0.4	-4.49	0.1	4.852	0.0
186357	0.1	0.1	-2.02	-	-4.52	-	4.853	-

Table 6.3: Mesh sensitivity of the Kyung-bu model. Prescribed element size is shown in the cross sectional plane (YZ Plane) and longitudinal direction (X)

6.1.2   Modelling of Kyung-bu Viaduct

This bridge is modelled using shell elements as in preceding chapters. As the span is fully precast, there is no connection required to be modelled between the slab and the beam as they are precast as one entity, which differs from the dual U-beam bridge that required modelling of an elastic layer to simulate the slab-beam connection (as in Section 4.1.7). In addition, the beam element model used for comparison, uses only one layer of beam elements, unlike the two layered beam element model seen in Section 3.1.1.1. For the *Full* model, with the vehicle, track and irregularities, the vehicle-track interaction model used is the same as previously.

For the shell element model, stresses, frequencies and displacements are compared between different sized element models to verify the mesh size. The number of elements in the model is shown as an indicator of the computational demand. This is seen in Table 6.3, with the prescribed size of discretisation of the elements in the cross sectional plane (YZ Plane) and longitudinally (X) shown. The values of the frequency of the fundamental mode, the longitudinal normal stress and the vertical displacement are compared with values obtained by a very fine mesh, to determine the convergence. Due to the inefficiency of the fine mesh models, these were not analysed dynamically to obtain the convergence of accelerations. The differences between the mesh sizes for the studied variables indicate very small differences, so the model with 8250 elements was chosen.

To obtain the shell positioning and thicknesses, such that the properties of the modelled bridge match the properties of the real cross section, a similar process was performed to that of Section 3.1.2.6. The simple geometry resulted in a good shell element match, with the shell positioning and thicknesses shown in comparison to the real cross section in Figure 6.4. The size of each shell is not indicative of the refinement of the element mesh, but rather the thickness applied to the shells in that region.

The natural frequencies and mode shapes displaying one, two and three half sine waves per span, are shown in Figure 6.5. These modes, denoted by $f_{s,i}$, where i is the mode number, are calculated using frequency analysis in ABAQUS, without including the vehicular mass. For the later study of the bridge acceleration frequency components, comparison is made to modes incorporating the vehicular mass as a distributed non-structural mass along the length
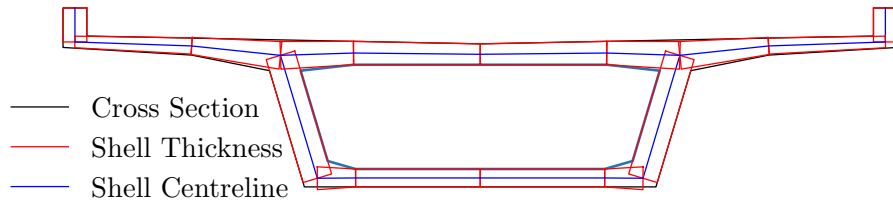
Figure 6.4: Thicknesses applied to the shells of the Kyung-bu viaducts, in comparison with the actual cross sectional profile

(a) $f_{s,1} = 6.16$ Hz   (b) $f_{s,28} = 19.4$ Hz   (c) $f_{s,34} = 23.2$ Hz
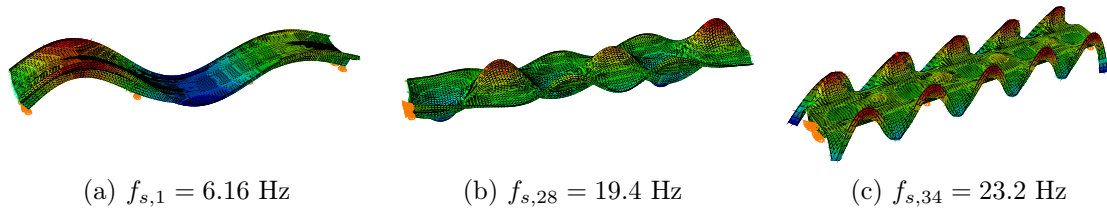
Figure 6.5: Modal shapes of first three half-sinusoidal bending modes of the Kyung-bu viaduct

of the track (and denoted by $f_{f,i}$). The frequency of the first mode ($f_{s,1}$), displaying one half sine wave per span, is around 50 % larger than found in the dual U-beam benchmark case. As multiple modes display characteristic shapes of two or three half sine waves per span, the selected modes ($f_{s,28}$ and $f_{s,34}$ for two and three half sine waves per span respectively) are the modes that display this behaviour for the whole cross section and not locally in the slab. Even still, a larger deformation occurs in the slab than the webs or bottom flange. This is due to the low number of intersections between webs and the slab (four webs in the U beam bridge, two in this one), which results in higher transverse flexibility of the slab.

6.1.3 Benchmark Case Results

In this section, the analysis focuses on identifying areas of the bridge to study further in the parametric analysis. It also identifies a control test to compare results of the parametric analysis back to the original, in order to determine the impact of the parametric analysis.

6.1.3.1 Bridge Vertical Accelerations

The study of the accelerations focuses on the top flange of the bridge as this is where the tracks are located and hence are most applicable to the limits of the vertical accelerations. Comparison of the maximum filtered vertical acceleration along the whole of the top flange of the bridge is shown in Figure 6.6. It shows that the maximum is along the longitudinal
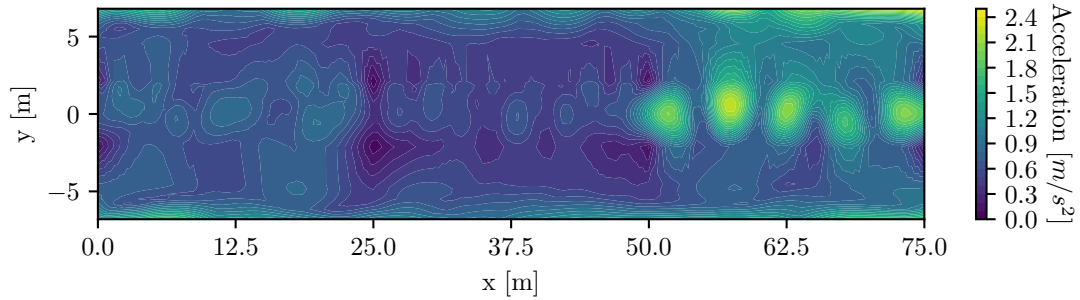
Figure 6.6: Maximum filtered vertical acceleration across the whole bridge on the top flange using the *Simple* model for a vehicle velocity of 88 m/s (317 km/h) (which is identified in Figure 6.7 as the velocity leading to largest accelerations in the *Simple* model)
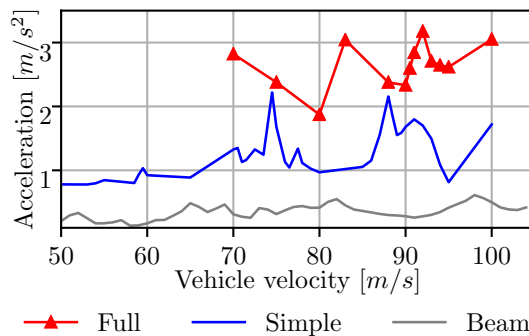
Figure 6.7: Variation of the maximum filtered value of the vertical acceleration from the length of the Kyung-bu bridge with changing velocity

centreline of the top slab. Multiple peaks in the acceleration are found in the third span (between 50 and 75 m), including peaks close to the support. This is due to the flexibility of the slab and the smaller diaphragm present in this bridge compared to the previous dual U-beam bridge, leading to less rigidity to the slab.

Comparison of the maximum vertical acceleration found along the length of the bridge for a variety of velocities is shown in Figure 6.7. This clearly shows that the higher peaks are associated with the *Full* model. The beam model shows considerably lower accelerations than the shell element models, which indicates that the shell response is increased by the sectional deformations that a beam element cannot model. The maximum accelerations are below the limits required to be maintained, hence there is potential for an increase in accelerations to be allowed in the parametric analysis. The maximum acceleration generated by the *Simple* model occurs at a velocity of 88 m/s (317 km/h), whereas the maximum for the *Full* model occurs at 92 m/s (331 km/h).

Comparison of the accelerations along the length of the bridge is made at velocities of 88 m/s (317km/h) and 92m/s (331km/h) in Figures 6.8 and 6.9 respectively. These figures show considerable difference between the *Simple* and *Full* models, although both lead to accelerations

below the $5\,m/s^2$ limit.

Further study of the accelerations induced in the bridge by the vehicle travelling at $88\,m/s$ ($317\,km/h$) can show that for the *Simple* model there are approximately four peaks per $25\,m$ span, however the *Full* model does not show this. This suggests activation of a mode shape with four vertical half sine waves per span. To consider what modes are contributing, a modal analysis was taken at $x = 60\,m$. This corresponds to a peak in the *Simple* model accelerations, and close to a peak for the *Full* model, as seen in Figure 6.8.

The modal analysis is shown by Figure 6.10. Both the *Simple* and *Full* models show a peak corresponding to a matching of the resonant loading frequency f_{v2} with the $f_{s,3}$ (or $f_{f,2}$ if considering the distributed vehicle mass) modes. These modes are variations on the fundamental frequency (i.e. one half sine wave per span). Of the contributions by the *Simple* model, this is the only major peak within the applicable frequency range ($< 30\,Hz$). However, for frequencies higher than $21\,Hz$ there is non-negligible contribution to the accelerations, without forming peaks. In addition, at $35\,Hz$ there is a huge contribution from a mode which displays behaviour of four sine waves per span. This contribution is filtered out for being high frequency, but it is possible that this mode is fundamentally influencing the bridge behaviour and therefore contributing to the accelerations. An inadequate time step, would possibly be a cause of the frequencies not being adequately filtered, but this is not the cause of this problem, as the time step is less than 5×10^{-4} seconds, corresponding to a sampling rate of 57 samples per wavelength of a $35\,Hz$ mode.

For the *Full* model at $88m/s$ ($317km/h$), a significant peak is found at $21Hz$, which contributes to the two acceleration peaks per span, due to the proximity of the f_{v6} mode to the $f_{s,31}$ mode (Figure 6.12a). This is another mode that displays two half sine waves per span, matching well with the maximum acceleration variation along the bridge length. Peaks in the contribution around the f_{v7} mode indicate some mode being activated. The modal frequency in proximity is the $f_{f,38}$ frequency, which is a vertical slab mode with three half sine waves per span. However, the contribution of this mode is not significant enough to lead to three peaks in acceleration per span for the *Full* model for this velocity.

Study of the accelerations induced by the vehicle at $92\,m/s$, as shown in Figure 6.9, shows relatively consistent peak accelerations along the length of the bridge for the *Full* model, and slightly larger in the third span for the *Simple* model. Within this third span, there are three peaks in acceleration for both models, indicating a contribution from a mode displaying three half sine waves per span. Decomposition into the frequency domain at midspan of the third span is shown in Figure 6.11. For both models, the frequency spectrum shows a large and main contribution from around the f_{v7} frequency. This frequency corresponds with modal shapes $f_{f,42}$, $f_{f,43}$ and $f_{s,38}$. The modes $f_{f,42}$ and $f_{f,43}$ include the vehicle mass but the deformations associated with these modes are primarily from the cantilevered edges to the slab at the midspan section (Figure 6.12d), and hence are unlikely to be the cause of the
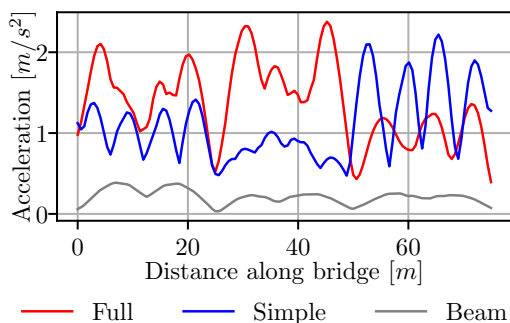
Figure 6.8: Variation of filtered maximum vertical accelerations along the length of the bridge for a velocity of 88 m/s for the Kyung-bu Viaduct
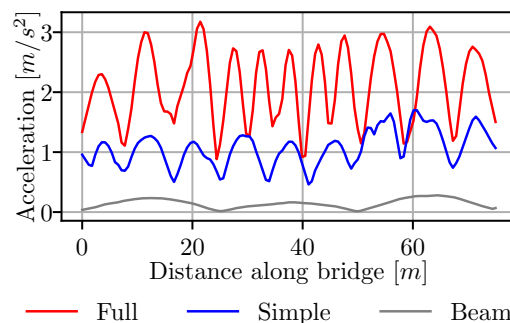
Figure 6.9: Variation of filtered maximum vertical accelerations along the length of the bridge for a velocity of 92 m/s for the Kyung-bu Viaduct

acceleration contribution along the centreline of the slab. Instead, it is likely that the $f_{s,38}$ mode is the main mode contributing to the response as it has three half sine waves per span (Figure 6.12b), similar to the acceleration pattern seen. The amplification of this mode in the *Full* model case is similar to the amplification seen by the models in preceding chapters at the same resonant loading frequency, f_{v7}.

From the study of the vertical bridge accelerations for the Kyung-bu viaduct, it is clear that the parametric study needs to incorporate the *Full* vehicle model to find a more accurate response of the bridge, due to the higher accelerations associated with it. Due to the smaller accelerations associated with the beam model, because of the lack of sectional deformations, these will not be studied in the parametric analysis for the Kyung-bu Viaduct as they do not represent the bridge accelerations well. The high flexibility of the slab, due to only two webs also leads to a larger number of vertical slab modes, which can cause particularly high accelerations in the *Full* model when combined with a resonant loading speed. It also displays a larger contribution to the accelerations for the *Simple* model for the higher frequencies, something that was not seen in the preceding chapters. Finally, although incorporation of the vehicular mass in frequency analysis reduces the frequency of these modes ($f_{f,i}$) in comparison to the corresponding modes without the vehicular mass ($f_{s,i}$), it is found that the vehicular mass does not influence the frequency of the bridge response, which is consistent with the outcomes of the previous two chapters. Therefore only the bridge frequencies determined using a *Simple* model that excludes the distributed vehicular mass, will be compared with the acceleration components in the parametric analysis.

6.1.3.2   Bridge Displacements

The maximum displacement due to the dynamic variable loads introduced are found in the first and last spans of the bridge at midspan. As a result, the vertical displacements from
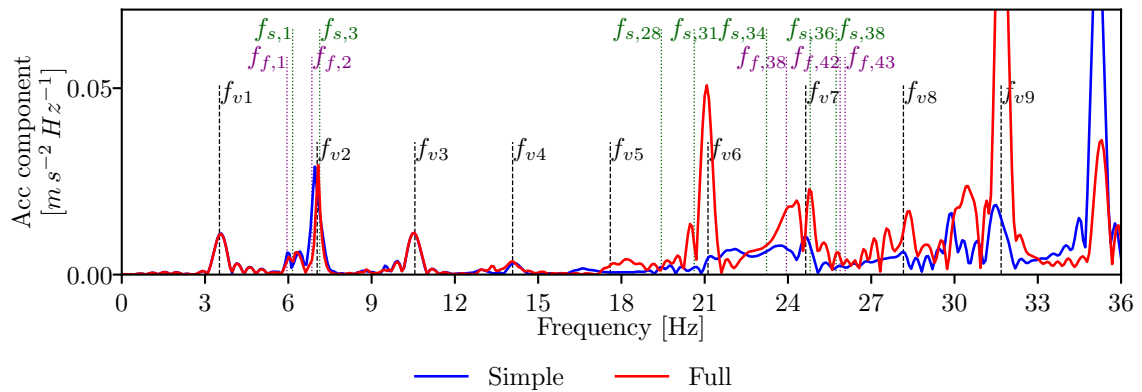
Figure 6.10: Frequency component of the vertical accelerations taken from $x = 60\ m$ (the third span) of the Kyung-bu bridge for a vehicle velocity of $88\ m/s$, the velocity for which the *Simple* model generates the largest accelerations. $f_{s,i}$ and $f_{f,i}$ refer to the ith mode generated by ABAQUS frequency analysis, for bridges neglecting and incorporating the vehicle mass respectively. f_{vi} are the ith harmonic of the resonant frequency based on repeating vehicle spacing
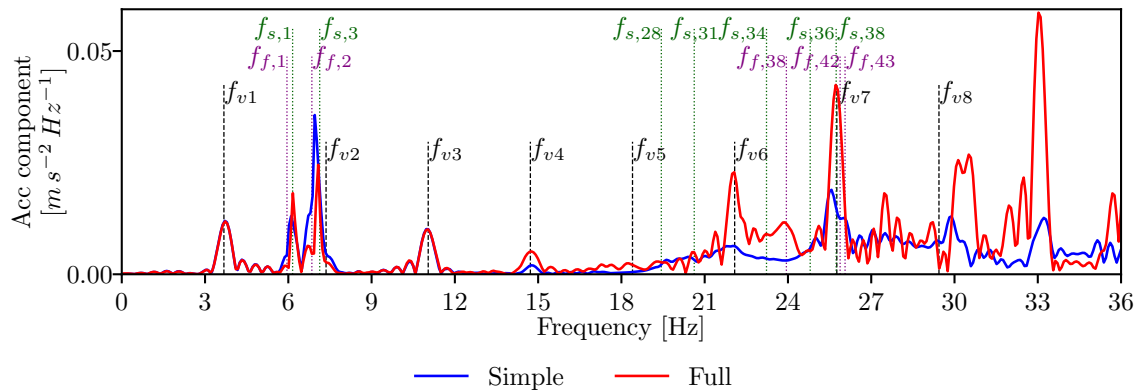
Figure 6.11: Frequency component of the vertical accelerations taken from midspan of the third span of the Kyung-bu bridge for a vehicle velocity of $92\ m/s$, the velocity for which the *Full* model generates the largest accelerations. $f_{s,i}$ and $f_{f,i}$ refer to the ith mode generated by ABAQUS frequency analysis, for bridges neglecting and incorporating the vehicle mass respectively. f_{vi} are the ith harmonic of the resonant frequency based on repeating vehicle spacing

(a) Mode shape of frequency $f_{s,31} = 20.6\,Hz$

(b) Mode shape of frequency $f_{s,38} = 25.7\,Hz$

(c) Mode shape of frequency $f_{f,38} = 23.9\,Hz$

(d) Mode shape of frequency $f_{f,42} = 25.9\,Hz$
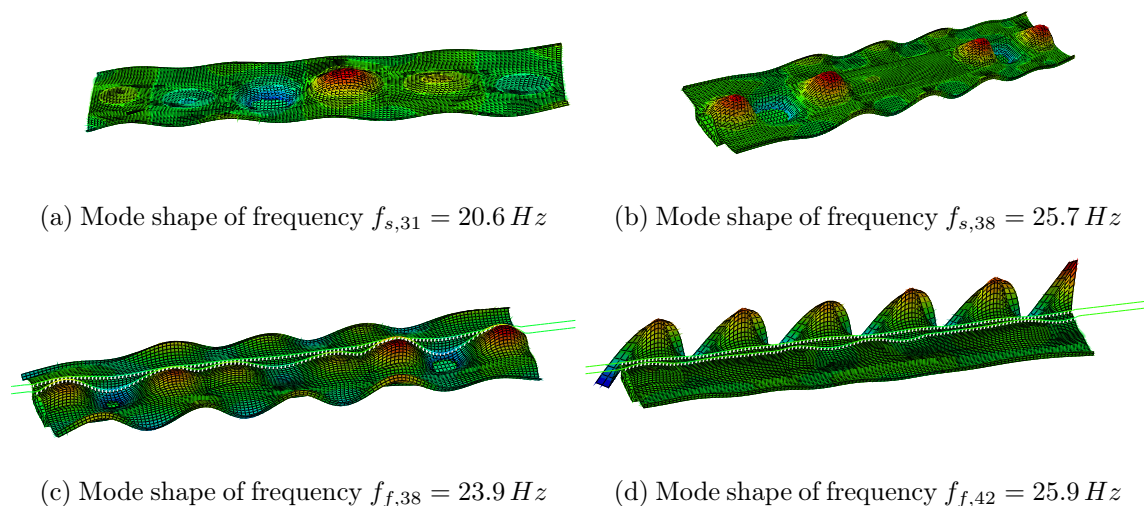
Figure 6.12: Other modal shapes of the Kyung-bu viaduct that have significant contributions to the vertical acceleration response. $f_{f,i}$ refers to modes incorporating vehicle mass and $f_{s,i}$ are modes without vehicle mass.

the first span, at the (x, y) coordinate (12.5, 0) on the top slab of the bridge are shown to vary with velocity as in Figure 6.13a. This shows similar variation between the *Simple* and *Full* models, as found in the previous chapter. The *Full* model does not pick up all the variation in displacement with velocity, compared to the *Simple* model, as fewer velocities are modelled because of the higher computational demand they require. At the same location, the lateral displacements also show good correlation between the *Simple* and *Full* models, but with smaller displacements (Figure 6.13b).

The variation of the vertical and lateral displacements under load are shown to vary along the centreline of the bridge for the velocity of $100\,m/s$ ($360\,km/h$) in Figure 6.14. This shows similar responses between the models vertically, with larger downward displacements due to the vertical vehicle load. It can be seen that there are some localised variation and peaks within each $25\,m$ span for the *Full* model, showing the influence of the higher frequency modes in the deflections. Laterally, the displacement mainly comes from twisting due to the eccentric load. As only one track is loaded in this analysis, the twisting here causes greater displacements in the positive direction (Figure 6.13b), however if the alternative track was loaded, the opposite would be true. It is also larger for the *Full* model, potentially due to the lateral forces that the vehicle introduces. The displacements are also larger at the ends, but the magnitude is small, so should not be a concern for the derailment of the vehicle.

From this study on the displacements, it appears that the *Simple* model is satisfactory in estimating the maximum lateral and vertical displacements in the bridge due to the vehicle load. With the maximum vertical displacement due to the vehicle loads being smaller than $1\,mm$, this is well below the project specific limit of $L/1700$, which corresponds to $14.7\,mm$

(a) Variation of the vertical deflection

(b) Variation of the lateral deflection
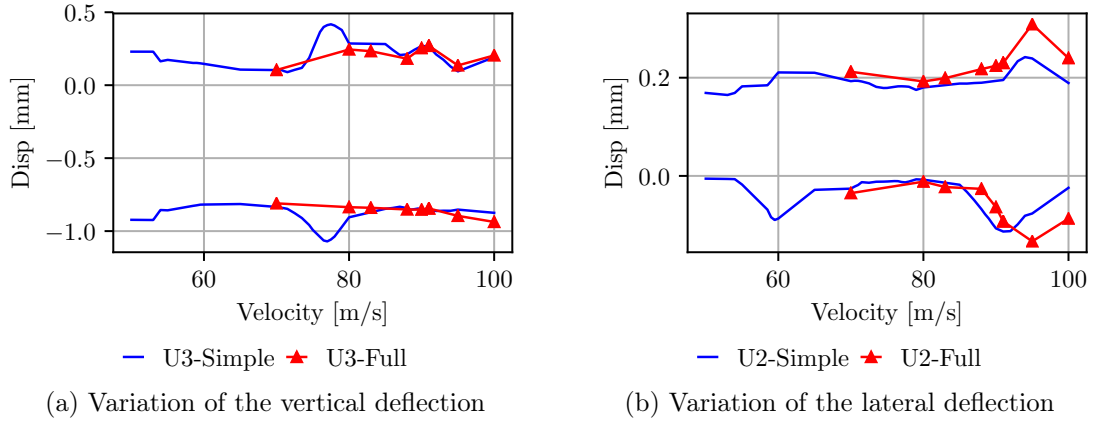
Figure 6.13: Variation of the displacements of the Kyung-bu bridge with velocity at the (x, y) coordinate $(12.5, 0)$

(a) Variation of the vertical deflection

(b) Variation of the lateral deflection
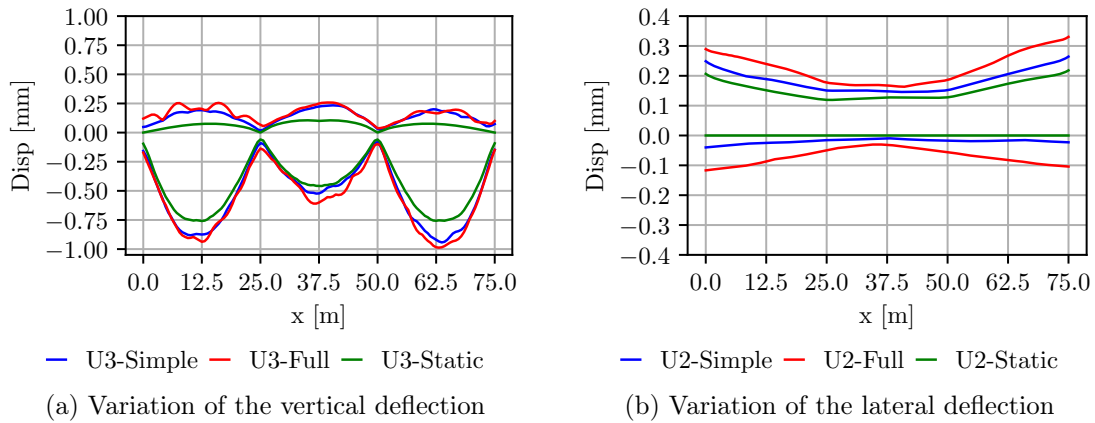
Figure 6.14: Variation of the displacements of the Kyung-bu bridge along the centreline of the bridge for a vehicle velocity of $100\,m/s$

(a) Variation of the S11 stress (normal stress in longitudinal direction)

(b) Variation of the S22 stress (normal stress in lateral direction)
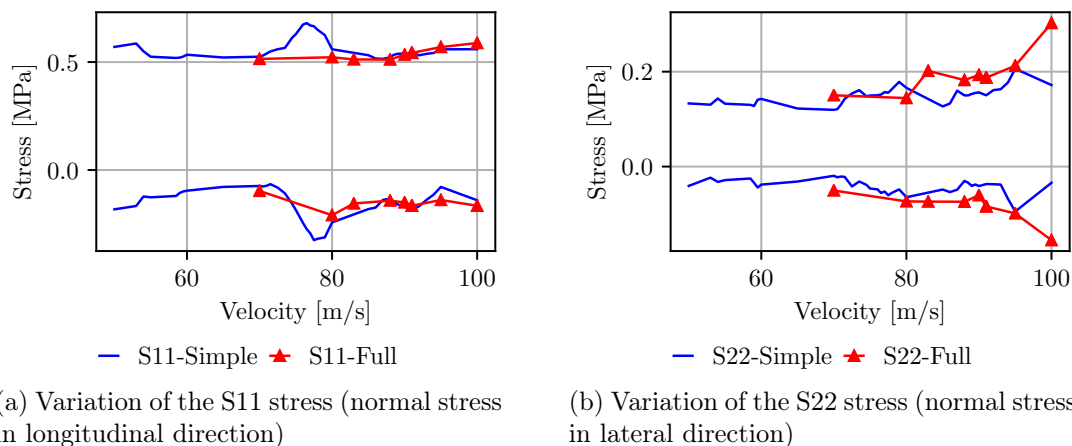
Figure 6.15: Variation of the stresses due to vehicular load, in the bottom flange of the Kyung-bu bridge with velocity at the (x, y) coordinate (12.5, 0)

of possible deflection.

6.1.3.3   Bridge Stress Variation

Consideration of the variation of the normal stresses due to vehicular load, in the bottom flange both longitudinally (S11) and laterally (S22), are shown in Figure 6.15. The S11 stress variation from the vehicular load was found to be larger, in part due to the larger vertical bending deflection. The *Simple* and *Full* models match well. For the S22 stress, the magnitude of variation is smaller than for S11, however there is some more variation in the stress between models particularly at $100 \, m/s$ where the stress variation in the *Full* model is 50 % larger than the *Simple* model. This is partly a reflection on the greater lateral displacements of the bridge for a *Full* vehicle model. In comparison with the benchmark case in the preceding chapters, the S22 stress variation is also higher, due to the wider bottom flange reducing the stiffness locally, which allows greater transverse bottom flange bending increasing the S22 stress.

Considering the variation in the S11 stress along the length of the bridge (Figure 6.16a), shows there is a compressive stress introduced along the bottom of the box girder in the intermediate support sections. This is because of a hogging moment due to the continuity of the bridge. Nonetheless the stress variation is well matched between the *Simple* and *Full* models. Considering the S22 stress variation (Figure 6.16b), over the support regions where it peaks, the *Simple* and *Full* models also match well. However, in the midspan the *Full* model produces greater variability into the stresses than the *Simple* model. This suggests that the S22 stress variation need to be studied for parametric analysis.

Study of these stress variations in the middle of the top slab at the midspan of the first span is shown to vary with velocity in Figure 6.17. The *Simple* model in both the S11 and S22

(a) Variation of the S11 stress (normal stress in longitudinal direction)

(b) Variation of the S22 stress (normal stress in lateral direction)
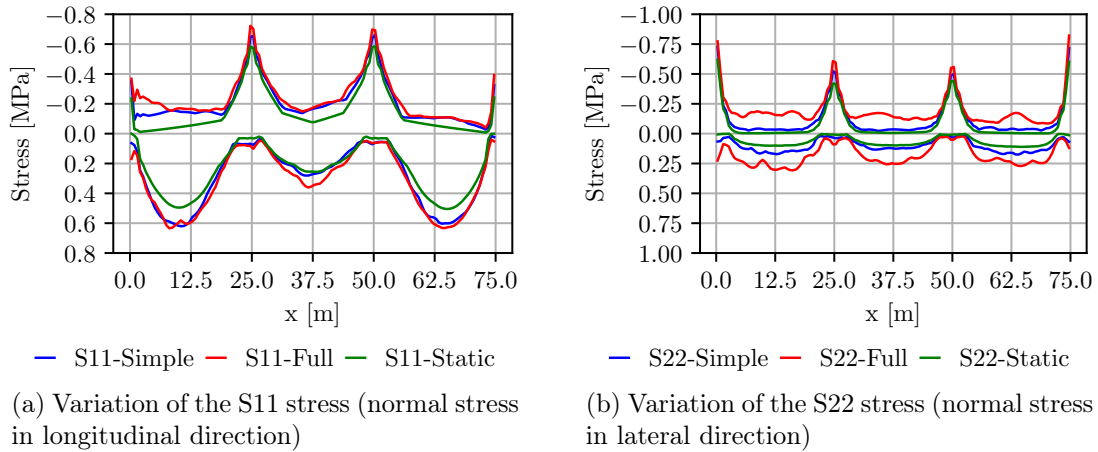
Figure 6.16: Variation of the stresses due to vehicular load in the bottom flange of the Kyung-bu bridge along the length of the bridge for a velocity of $100 m/s$

(a) Variation of the S11 stress (normal stress in longitudinal direction)

(b) Variation of the S22 stress (normal stress in lateral direction)
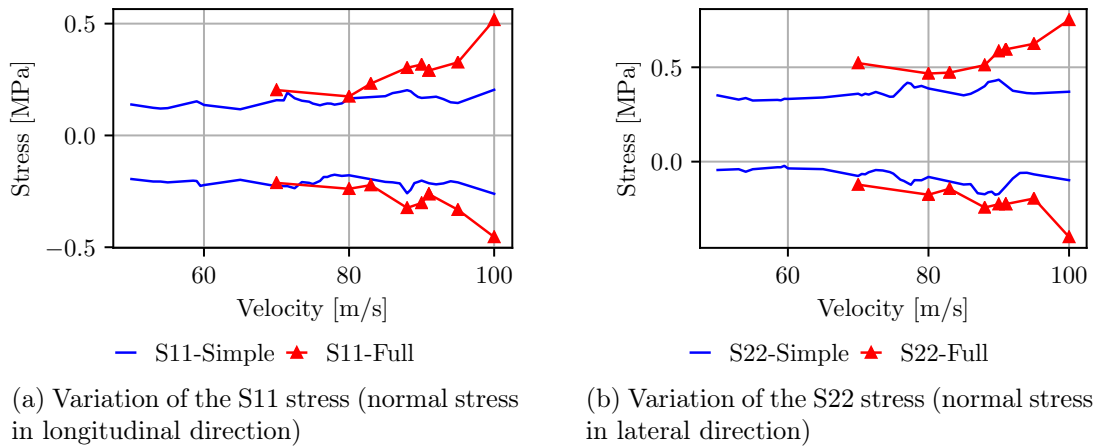
Figure 6.17: Variation of the stresses due to vehicular load, in the top slab of the Kyung-bu bridge with velocity at the (x, y) coordinate (12.5, 0)

stress directions seems to be relatively constant with velocity. However, for the *Full* model the stress variation increases, and for $100\,m/s$ the *Full* model S11 stress variation is double that of the *Simple* model. Considering the S22 direction, the stress variation is even higher. The increased S22 stress variation is a sign of the increased transverse bending that is introduced into the slab due to the loading from the train vehicle and the increased flexibility of the slab, which can lead to localised slab displacements increasing the stress.

Study of the stress variation across the length of the bridge in the slab also shows considerable variability between the *Simple* and *Full* models (Figure 6.18). The pattern of peaks, particularly for the S11 stress variation, is similar to that observed with the accelerations and displacements showing a direct link between the local deformations of the slab and the stress in the slab.

(a) Variation of the S11 stress (normal stress in longitudinal direction)

(b) Variation of the S22 stress (normal stress in lateral direction)
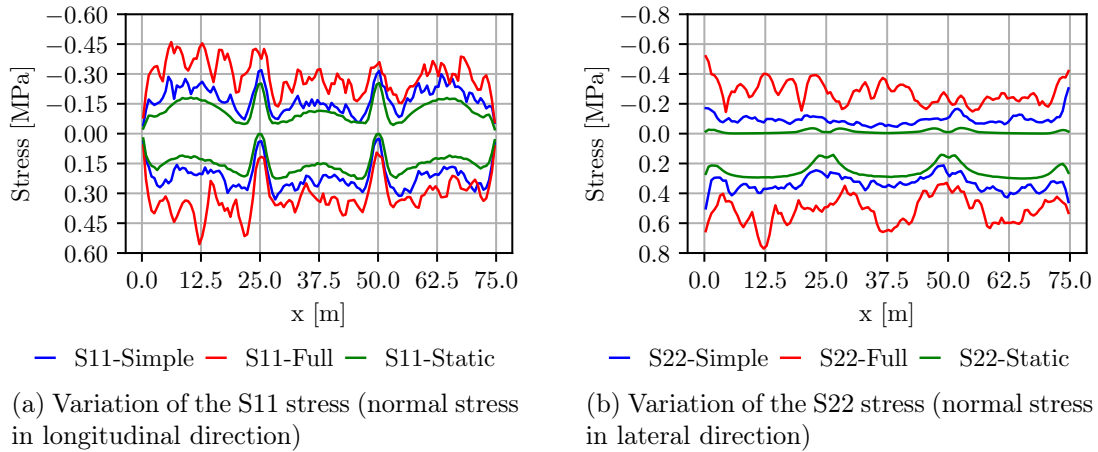
Figure 6.18: Variation of the stresses due to vehicle load, in the top slab of the Kyung-bu bridge along the length of the bridge for a velocity of $100m/s$

From this benchmark case analysis, it can be seen that the study of the variation in the stresses has to use the *Full* models, particularly in the slab, in order to get a good representation. For the S22 stress variation this is due to the reduced transverse stiffness leading to greater transverse bending and hence increasing the stress.

6.1.3.4   Conclusions to Benchmark Case Analysis of Kyung-Bu bridge

From study of the benchmark case, it is apparent that the higher frequency of the fundamental vertical bridge mode $(f_{s,1})$ leads to a reduced contribution to the response from this mode, as it does not become resonant under influence of the first resonant loading frequency (f_{v1}). The response is dominated by higher frequency modes. There is a difference between the *Simple* and *Full* model accelerations, with amplification of high frequency modes due to force variation when considering the *Full* model contributing to the larger accelerations of the *Full* model. As a result modelling with beam elements does not provide a good estimation due to the modes activated at high frequency containing sectional deformations not possible in beam element models. The displacements are found to be well matched between the *Simple* and *Full* model, as are stress variations in the bottom flange. However, the stress variations in the slab do not have good correlation between models. Hence, consideration of the *Full* model is required to accurately determine the stress variation due to the load.

6.1.4   Parametric study

The parametric study of the Kyung-bu models, tests the material savings made in the previous chapter, i.e. the web being 66 % of the original thickness and the bottom flange 75 % of its original thickness. This is applied as seen in Figure 6.19. As the top flange is also precast it is
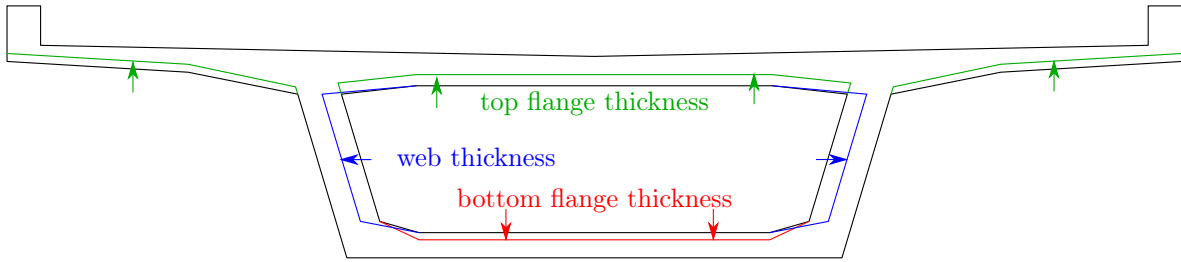
Figure 6.19: Variation of the geometry of the Kyung-bu viaducts for parametric analysis

Top flange thickness [%]	Bottom flange thickness [%]	Web thickness [%]	Concrete Strength [%]
100	75	66	178
90	75	66	180
80	75	66	187
75	75	66	188
70	75	66	190

Table 6.4: Properties of the models for the top flange variation for the Kyung-bu viaduct as a percentage of the benchmark case values
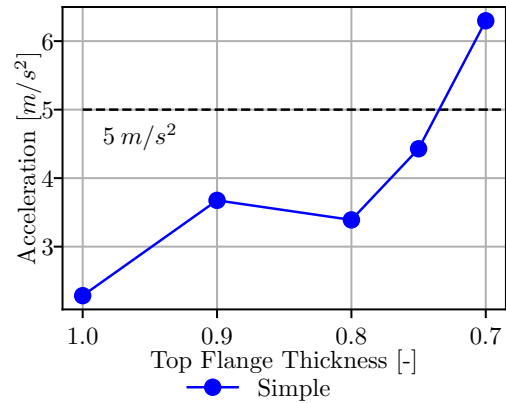
Figure 6.20: Maximum filtered accelerations of the *Simple* model of the Kyung-bu viaduct with top flange thickness variation

appropriate to apply a reduction to the thickness as well. To determine a possible top flange thickness variation, a small study using the *Simple* model was used to estimate an appropriate thickness to study further. Due to time constraints, the *Full* model was not chosen for this preliminary study, as it requires a significantly longer computational time. The thickness of the top flange was varied, with the web and bottom flange thickness modelled at their reduced thickness. This leads to the models in Table 6.4. The maximum accelerations found for any velocity for these models using the *Simple* model are shown in Figure 6.20. Here, for a top flange thickness of 70 %, the accelerations are unacceptable, and considering the accelerations of a *Full* model are higher, this would be unacceptable. The other reductions in top flange thickness are all acceptable for the *Simple* model. As a result, the thinnest acceptable top flange thickness 75 % of the original is progressed to the parametric analysis.

After the selection of the top flange thickness, the parametric analysis can be performed using the *Full* model. Through variation of the geometry and concrete strength, the properties at midspan are shown to vary with parameter in Figure 6.21. Here the moment resistance and EI_{yy} values are maintained to be at least the level of the benchmark case. There is some reduction in the shear capacity of the section, however calculations made found that there was redundancy in the shear capacity of the section. The properties used with respect to the
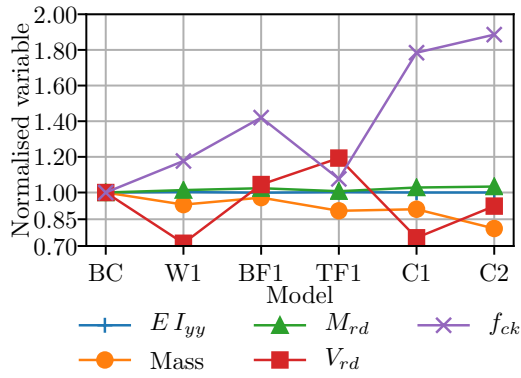
Figure 6.21: Variation of properties from parametric analysis, normalised with respect to the benchmark case model for the Kyung-bu viaduct

Model	Web thickness [%]	Bottom flange thickness [%]	Top flange thickness [%]	Concrete Strength [%]
BC	100	100	100	100
W1	66	100	100	117
BF1	100	75	100	142
TF1	100	100	75	108
C1	66	75	100	178
C2	66	75	75	188

Table 6.5: Variation of properties from parametric analysis for the Kyung-bu viaduct with respect to the original values of the benchmark case
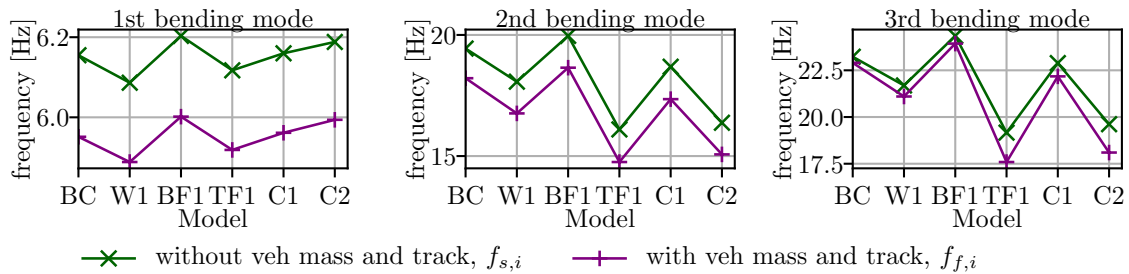
Figure 6.22: Change in frequency with parameter of the sinusoidal bending modes of the Kyung-bu Viaduct, as displayed in Figure 6.5

benchmark case values in each of the parametric cases are shown in Table 6.5.

Through changing the geometry and concrete strength, the frequencies of the modes also change. This is shown in Figure 6.22, where the change in the frequencies of the mode shapes of Figure 6.5 is shown (modes with one, two and three half sine waves). Obviously, for very similar values of $EIyy$, and a mass reduction between parameters, the fundamental mode would be expected to increase in frequency. However, this is not the case. Both the W1 and TF1 cases have lower frequencies than the benchmark case (BC). This is possible because of two reasons. Firstly, the boundary conditions are not applied at the centre of mass, and so although the stiffness of the section is maintained with respect to the centre of mass, this position changes between parameters, which influences the frequency. Secondly, although the mode shapes are very similar between parametric models, sectional deformations within the mode shapes due to thinner elements, can cause variation in the frequency at which they are found. The second reason is particularly relevant for the modes of higher frequency with a greater number of local deformations.
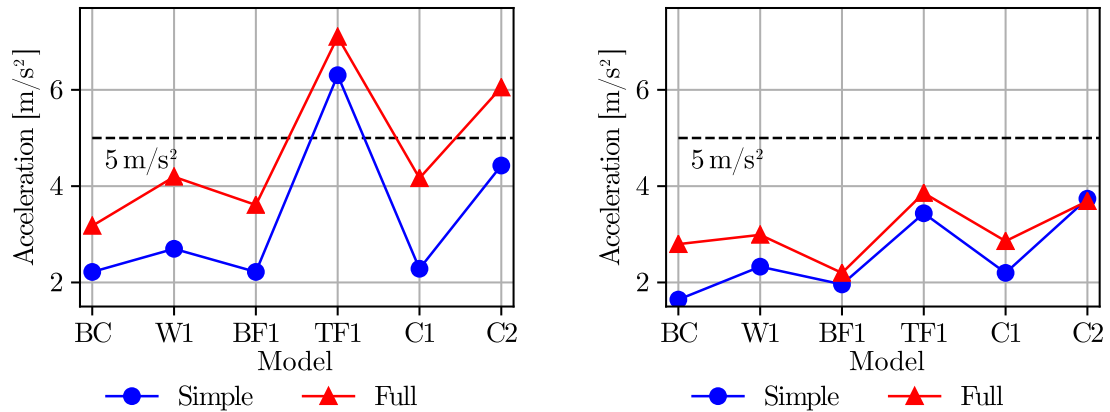
(a) Variation of maximum accelerations for the maximum magnitude in the bridge length

(b) Variation of maximum accelerations at midspan of the first span

Figure 6.23: Comparison of maximum vertical accelerations across all velocities for the Kyung-bu viaducts under parametric analysis

6.1.4.1 Vertical Bridge Accelerations

From the parametric analysis conducted, the maximum acceleration along the centre of the bridge for any velocity is compared for each parameter in Figure 6.23a. The chosen value for the top flange is shown to be unacceptable for accelerations, both for using the *Simple* and *Full* models when analysed as a change on its own (TF1) and for the *Full* model when combined with the web and bottom flange thickness changes (C2). Interestingly the accelerations found in the parametric model C2 are smaller than TF1, despite the lower mass of this model. This is due to coupling of modes in the TF1 case, such that multiple modes are activated at once. The accelerations of the other models are found to be acceptable for this bridge. Comparatively, the *Simple* model produced smaller results than the *Full* model, but they followed a similar pattern between parametric models.

Study of the accelerations at one location is shown in Figure 6.23b. This shows that the accelerations are below the maximum recorded in the bridge for both the *Simple* and *Full* models. This links back to Figures 6.8 and 6.9, which showed that in the benchmark case the high frequency components lead to maximum accelerations not necessarily at the centre of the span.

Comparison of the maximum accelerations along the length of the bridge for different velocities and parameters is shown in Figure 6.24. It can be clearly seen that the accelerations of the *Full* model are higher than the *Simple* model again. Changes to the top flange thickness shown by parameters TF1 and C2 indicate more and larger peaks, which coincides with a greater number of modes, due to the increased flexibility of the slab. This also leads to a greater chance of coupling of the bridge modes, particularly those with large top flange deformation

components, leading to large responses.

Study of frequency contributions of the acceleration for the location and velocity that lead to a maxima for each parameter is shown in Figure 6.25. Here, the fundamental modes are seen to have minimal contributions to the maximum acceleration. This is as the frequency of this mode is still above the first loading frequency, for all applicable velocities of this bridge. Coupling of modes can clearly be seen in the figure, particularly for the TF1 case, where the contribution to acceleration comes from two peaks, coinciding with the f_{v6} and f_{v7} frequencies. These frequencies coincide with bridge modes $f_{s,33}$ (a three half sine wave per span mode) and $f_{s,42}$ (a four half sine wave per span mode). Clearly the influence of the four half sine waves per span modes at frequencies lower than they were previously found at in the dual U-beam bridge, indicates that as expected the slab thickness is key to the accelerations in the slab, more so than the thickness of the web and bottom flange. When the top flange thickness is reduced, the larger number of modes in the studied frequency range increases the chance of the loading frequency to match a bridge frequency and trigger a resonant response. As the models incorporating top flange thickness changes (TF1 and C2) have lower stiffness of the top flange, a greater number of sine waves per span can be developed for the studied frequency range, leading to larger resonant response phenomena.

Similarly to the double U-beam bridge, for the velocities leading to the maximum acceleration, the resonant loading frequency f_{v7} has a very high contribution to activating these high frequency modes. This is as there is no change in the vehicle axle spacing and hence loading pattern between the bridges. The bridge modes that the f_{v7} frequency activates, for each parameter, for the vehicle velocity leading to the maximum response, are $f_{s,38}$ (BC: three half sine waves per span), $f_{s,47}$ (W1: four half sine waves per span), $f_{s,37}$ (BF1: three half sine waves per span), $f_{s,42}$ (TF1: four half sine waves per span), $f_{s,30}$ (C1: two half sine waves per span) and $f_{s,51}$ (C2: five half sine waves per span). Although the activated mode numbers may be similar, the shapes of mode may not be the same for the same mode number between models, as the geometry changes cause shifting frequencies and additional mode shapes. Also, multiple similar modes may be found at different frequencies, but have variations of the same shape, leading to it being more likely that the resonant loading frequency (f_{vi}), will match a bridge mode. This is a feature of the shell models, not replicated in the beam element models, which will tend to have one frequency for each mode shape. This effect adds to the complexity of the response of the shell element models, being a better representation of reality.

Comparison of the maximum accelerations against the span mass is shown in Figure 6.26. This uses mass normalised against the benchmark case. This shows that there is generally a relatively steady increase in the accelerations for reductions in the mass, as expected. However, the TF1 case, with reductions to the top flange thickness, leads to much higher accelerations than the C1 case, despite similar masses. This shows the importance of the local slab flexibility in the determination of the accelerations.
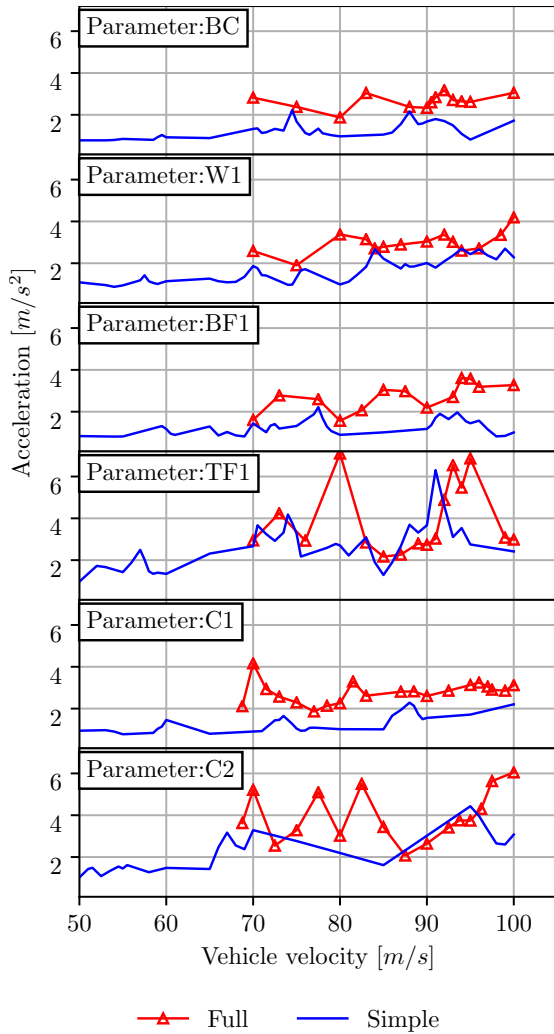
Figure 6.24: Maximum vertical acceleration (from the full length of the bridge) against velocity for the Kyung-bu viaducts under different parametric cases
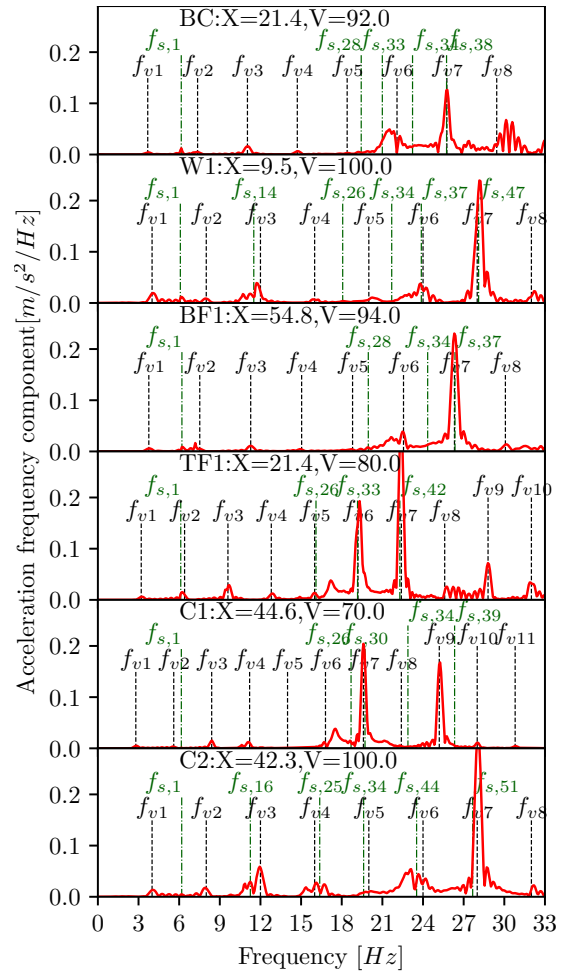
Figure 6.25: Analysis of the frequencies contributing to the maximum accelerations in the *Full* model for the Kyung-bu bridge parametric analysis
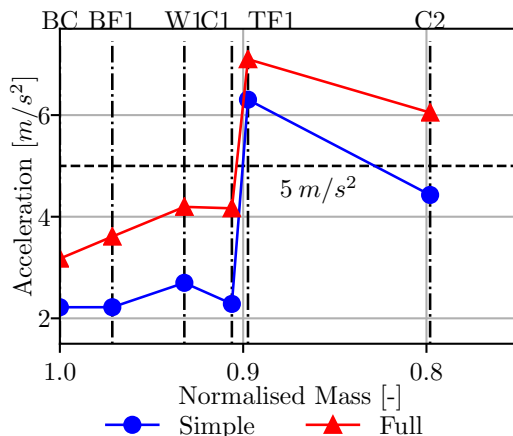
Figure 6.26: Maximum vertical acceleration found at any point along the bridge centreline for any velocity below $100\,m/s$, compared against the bridge mass normalised to benchmark case, for each parametric case of the Kyung-bu Viaduct

6.1.4.2   Bridge Displacements

Study of the displacements of the bridge in the bottom flange (Figure 6.27), shows that the displacements are relatively consistent both vertically and laterally between models. The DAF also decreases generally as the mass decreases for the lateral displacements, although it was originally very high due to the low magnitude of both the static and dynamic deflections. Considering the top flange deflections (Figure 6.28), the displacements are slightly higher than the bottom flange, both laterally and vertically, due to the local deformations caused by the flexibility of the slab. However, the maximum displacement between parametric models does not appear to be affected by the maximum accelerations found in TF1 and C2 cases, as the displacements are relatively consistent between models. For the deflections in both locations, the *Simple* model mostly provides slightly higher deflections, but in general similar to the *Full* model, allowing the *Simple* model to determine the bridge deflections.

6.1.4.3   Bridge Stress Variation

The bridge stress variation due to vehicular load, is studied at midspan of the first span, both in the bottom flange and the top flange. Firstly, the longitudinal normal stress variation (S11) in the bottom flange, where tensile stresses would be most critical, is shown in Figure 6.29. Here, it can be seen that the stress variation does increase slightly for the reduction in mass associated with the parametric cases, but the magnitude of this stress variation is relatively similar. The DAF is also shown to be quite constant. Interestingly, the *Simple* model generates bigger stress variation than the *Full* model, agreeing with the slightly larger vertical displacements of this model seen in Figure 6.27.
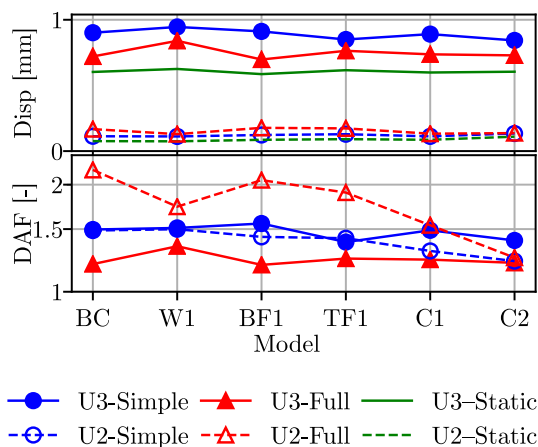
Figure 6.27: Variation of the actual and DAF of displacements in the bottom flange at midspan of the first span of the Kyung-bu Viaduct (DAF is shown using a logarithmic vertical scale)
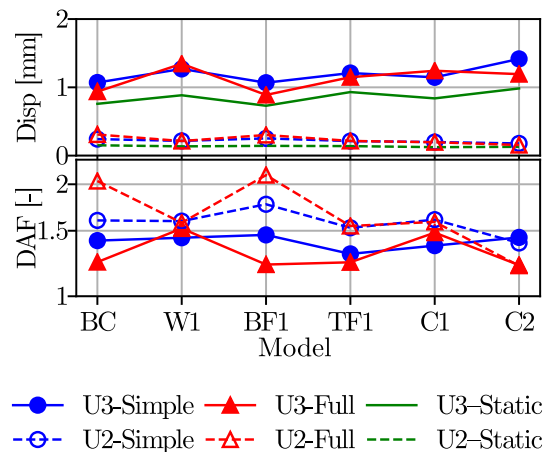
Figure 6.28: Variation of the actual and DAF of displacements in the centre of the slab at midspan of the first span of the Kyung-bu Viaduct (DAF is shown using a logarithmic vertical scale)

Study of the S11 stress variation in the top flange (Figure 6.30), shows the maximum stress stays relatively constant for the *Full* model between the studied parametric cases, although it does increase slightly with the reduced mass of these cases in the *Simple* model. The stress variation here is smaller and less critical than the bottom flange, as the vertical loading will tend to result in this part of the bridge sustaining compressive stresses. For all but the C2 case, the *Full* model leads to much larger stress variation than the *Simple* model, contradicting the displacement at this location which suggests the *Simple* model may have similar or larger stresses.

In the top flange, the S22 stress variation is larger than the S11 stress, as found in the benchmark case. In the slab, this corresponds to the stress variation in the lateral direction and is shown in Figure 6.31. It is larger for all parameters tested, and this is a result of the transverse bending of the slab, due to it only having two support points (the webs). In this case, the *Full* model generates larger stress variations than the *Simple* model for all but the C2 case. The high frequency modes activated by the *Full* model is the cause, considerably affecting the transverse top flange behaviour, inducing larger vibrations. These modes often have large contributions from the flanges and the slabs, hence activation of these modes leads to the high transverse bending and therefore high S22 stress variation. Despite the large values, the stress variation level remains similar between parametric cases and hence are not of particular concern.
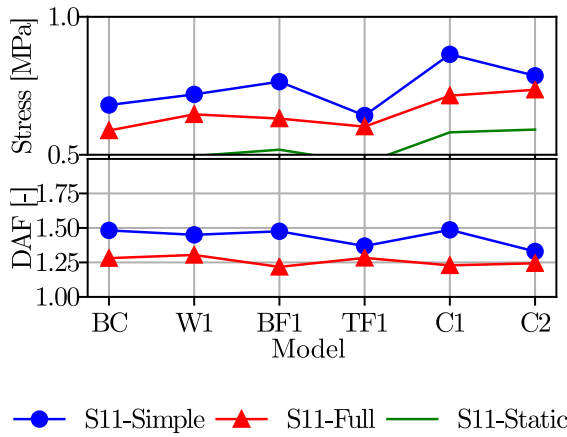
Figure 6.29: Variation of the actual and DAF of normal stress variation due to traffic load in the longitudinal direction (S11) in the bottom flange at midspan of the first span of the Kyung-bu Viaduct
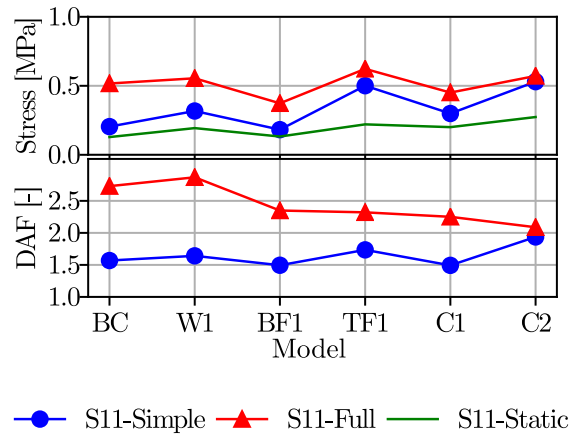
Figure 6.30: Variation of the actual and DAF of normal stress variation due to traffic load in the longitudinal direction (S11) at the centre of the slab at midspan of the of the first span of the Kyung-bu Viaduct
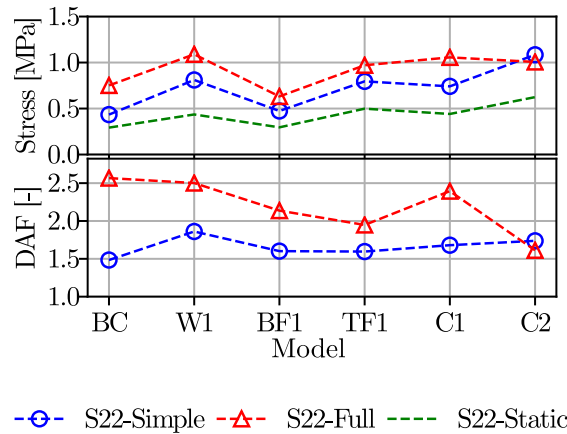
Figure 6.31: Variation of the actual and DAF of normal stresses due to vehicle load, in the lateral direction (S22) in the middle of the top flange at midspan of the Kyung-bu Viaduct
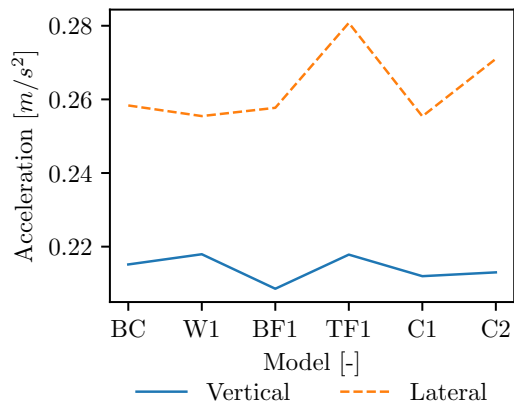
Figure 6.32: Variation of the Vehicle accelerations with model

	BC	C1
Concrete Strength [MPa]	40	71
Precast element Mass [$\times 10^3$ kg]	587	544
Non-Structural mass [$\times 10^3$ kg]	196	196
Total mass of span [$\times 10^3$ kg]	783	740

Table 6.6: Construction properties per span of the Kyung-bu viaducts

6.1.4.4   Vehicle Accelerations

The maximum vehicle accelerations at the centre of mass of any carriage and any velocity are recorded for each parameter, as displayed in Figure 6.32. Here, it shows the lateral accelerations are higher than the vertical, with the lateral acceleration peaking under the TF1 and C2 cases. The vertical accelerations of the vehicle are relatively consistent, and both accelerations are low and insignificant to the design as a result. They are also well below the $0.5\,m/s^2$ maximum vehicle accelerations prescribed by this project.

6.1.4.5   Construction Details

Through consideration of the parametric analysis the construction characteristics of the first combined case (C1) is compared to the benchmark case of the Kyung-bu bridge in Table 6.6. The characteristics of the second combined case (C2) is not expressed here, due to acceleration of the bridge associated with this model exceeding prescribed limits. The precast mass is reduced by 7.3 % per span, which could lead to smaller capacity transportation and lifting equipment being required. The total permanent mass is reduced by 5.5 %, which will influence the total load in the piers and hence allow them to be reduced in size. These are both considerable savings in terms of actual weight, even if the percentage is relatively small. This weight saving is achieved by a concrete strength increase of 77.5 % to counterbalance the reduction in the geometry.

6.1.4.6   Conclusions to the Kyung-bu Viaducts Parametric Analysis

Study of the parametric analysis has led to a suitable alternative section (C1), with a reduction in the precast mass of 7.3% for a concrete strength increase of 78%. Bridge accelerations for this case were below the limit allowed. In addition, the vehicle accelerations were also relatively consistent with those found in the benchmark case, and below the allowable level. For these cases, the bridge displacements and stress variations are relatively similar, and hence not of concern. In the cases where the top flange thickness are reduced (TF1 and C2), although the vehicle accelerations, stress variation and displacements are acceptable, the reduced stiffness of the slab leads to large unacceptable increases to the vertical bridge accelerations.

6.2   Piacenza Viaduct

There are two Piacenza viaducts found in Italy on the Milano-Bologna high speed line in the River Po region. One of the cross section solutions of these HSR viaducts is a double celled box girder (also known as a twin-box girder or triple webbed box girder). The whole section is precast and transported to location from the manufacturing plant by a gantry carrier. The section has a higher shear capacity than the Kyung-bu viaduct due to the introduction of this central web. Alternatively, similar cross sections have been achieved through precasting of two 'U' beams with one vertical side, allowing the beams to be adjacently located to each other and tied transversely with prestressing bars to keep the webs together, with a slab cast in-situ on top (Montaner Fraguet et al., 2014; Llombart Jaques et al., 2014a). The solution of the whole cross section being precast was studied due to the availability and completeness of the design drawings found in Miotti et al. (2003) and T.A.V. SpA (2006).

This bridge studied is a simply supported single span, with length $30.4\,m$. The cross section includes chamfers to corners, included to aid the release of formwork in the manufacturing process. In addition, the bottom flange is thickened over the $1.6\,m$ from each support region, from the standard thickness of $0.3\,m$ to $0.6\,m$. This enables anchoring of the prestress in the bottom flange and hence this thickness is maintained in parametric analysis.

6.2.1   Initial Design

The cross section in the support region is found in Figure 6.33, with the shape in the rest of the span indicated by a dashed line. This figure also shows the prestress arrangement at this location. The tendons are parabolic which can be seen in Figure 6.34. The bridge contains 24 tendons of two different types. In each web there are five, 19 strand tendons, carrying an initial prestress force assumed to be $3850\,kN$ (based on 78% characteristic breaking load). In the bottom flange the remaining nine, 12 strand tendons are found. Likewise, the same stress is assumed, leading to an initial prestress force of $2433\,kN$ per tendon. This prestress is introduced through post-tensioning. The prestress details and other selected properties of the bridge are shown in Table 6.8.

The viaduct is shown to have three bearings per support region. As this is a simply supported viaduct the horizontal load is transferred into the piers from each span. The articulation of the bridge is shown in Figure 6.35. The available motion of each bearing is assumed, as this is not specified by Miotti et al. (2003) and T.A.V. SpA (2006). The initial cross sectional properties of the bridge are shown in Table 6.7, including the sectional area (A_c), position of centroid from the base of the section ($\bar{z}$), and the second moments of area about the centroid in the y (I_{yy}) and z (I_{zz}) directions. The moment resistance (M_{rd}) is similar to that of the Kyung-bu viaduct, but the additional web has contributed to a significant increase in the
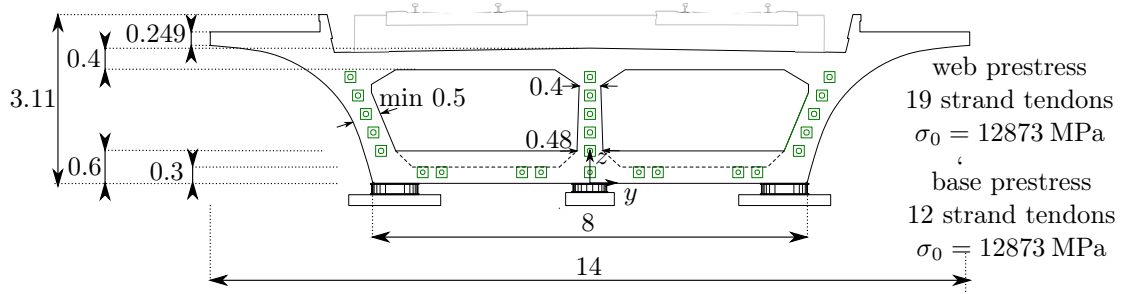
Figure 6.33: Cross section of the Piacenza viaduct, dimensions in m
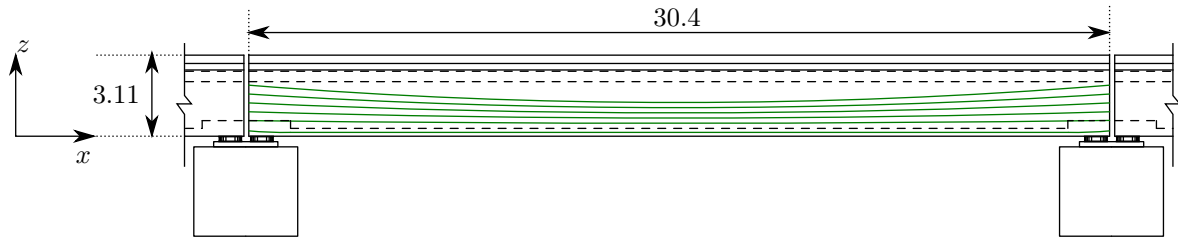
Figure 6.34: Longitudinal profile of the Piacenza viaduct, dimensions in m

uncracked shear resistance (V_{rd}) of the bridge. The bridge is modelled in this work with a slab track and hence will have a limit to the accelerations of $5\,m/s^2$.

6.2.2 Modelling of Piacenza viaduct

The modelling of this bridge follows the same process as in Section 6.1.2. However, the change in the cross section requires a different thicknesses of the shells to model the section accurately. This new shell thickness assignment is shown in Figure 6.36. This process was more difficult than for the double U-beam and Kyung-bu box girder. This was due to the curved outer edges and the additional central web creating more intersections between shells, which leads to more shell overlap. Therefore, larger adjustments were required to the position of intersection and thicknesses such that the area, centroid and second moments of area of the shell element cross section matches the real cross sectional properties.
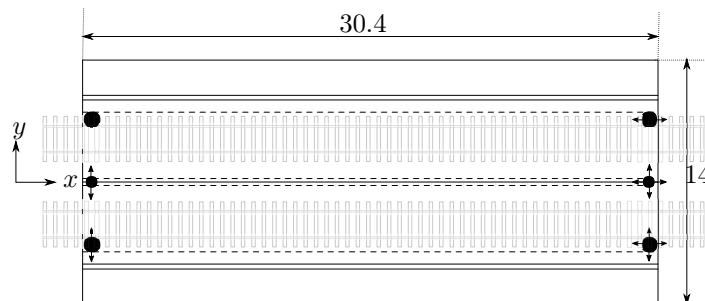
Figure 6.35: Articulation of the Piacenza viaduct. Arrows indicate unrestricted motion of the bearing, dimensions in m

M_{rd} [MNm]	135.2	I_{yy} [m^4]	10.28	A_c [m^2]	11.63
V_{rd} [MN]	12.03	I_{zz} [m^4]	151.3	$\bar{z}$ [m]	1.574

Table 6.7: Cross sectional properties of the bridge at midspan

Span length, L		30.4 m
Concrete strength, f_{ck}		35 MPa
Prestressing steel strength, f_{pk}		1860 MPa
Initial prestressing force	Webs	3850 kN
	Bottom Flange	2433 kN
Prestress Area	Webs	2660 mm^2
	Bottom Flange	1680 mm^2
Distance between track centrelines		5 m
Vehicle operating velocity		300 km/h
Span to Depth Ratio		9.77

Table 6.8: Selected data for Piacenza viaducts
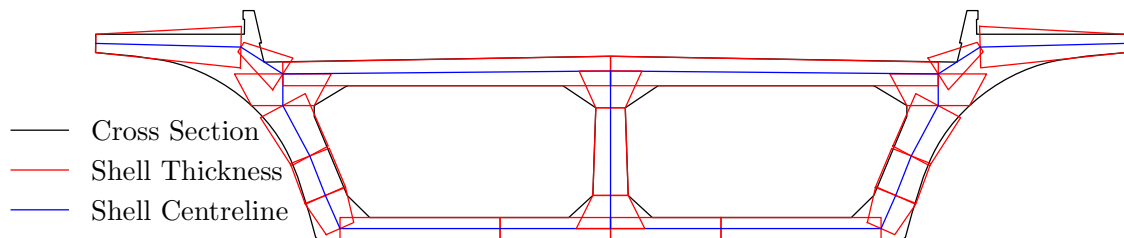
Figure 6.36: Shell thickness assignment of the Piacenza viaduct

Number of	Element Size [m]		Stress		Displacement		Fundamental Frequency	
Elements	X	YZ Plane	[MPa]	%	[mm]	%	[Hz]	%
1756	1/0.6	1	-2.13	3.49	-12.87	0.2	4.849	0.1
1791	0.6	1	-2.13	3.51	-12.87	0.2	4.849	0.1
2346	0.6	0.6	-2.16	2.11	-12.85	0.0	4.8516	0.0
86032	0.1	0.1	-2.20	-	-12.85	-	4.8532	-

Table 6.9: Mesh sensitivity of the Piacenza viaduct models. Prescribed element size is shown in the cross sectional plane (YZ Plane) and longitudinal direction (X)

(a) $f_{s,1} = 4.85$ Hz   (b) $f_{s,5} = 15.3$ Hz   (c) $f_{s,10} = 26.8$ Hz
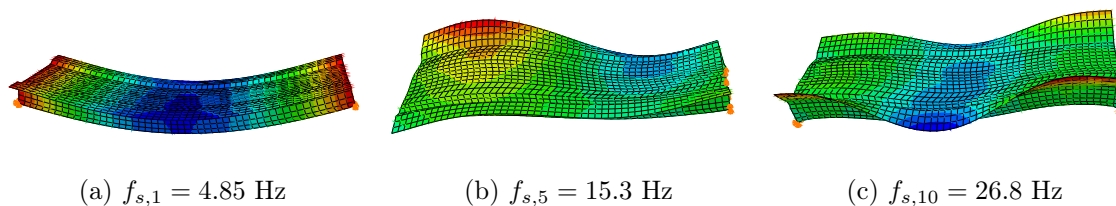
Figure 6.37: Modal shapes of first three sinusoidal bending modes of the Piacenza viaduct

Study of the mesh sensitivity is shown in Table 6.9. The mesh with 2346 elements was chosen, as it was more accurate than the coarser meshes, but the number of elements was not so large that the computational demand created models that were inefficient to run. The frequencies of the first three sinusoidal bending modes are shown in Figure 6.37. The bending mode with three half sine waves per span ($f_{s,10}$) is below $30\,Hz$, which indicates that the low pass frequency filter for the accelerations should stay at $30\,Hz$, following the requirements of BS EN 1991-2:2003 (2010), as outlined in Section 3.1.3. The addition of the web is shown to visibly reduce the flexibility of the top flange in the modal shapes, with the deformations of the top flange, web and bottom flanges all consistent and moving together, contrasting the independent flexibility shown by the top flange in the box girder of the Kyung-bu viaduct.

6.2.3 Benchmark Case Analysis

This section analyses in detail the original bridge. This allows identification of locations where parametric study should be focused, stopping unnecessary data from being collected in regions that the benchmark case identify as not of a concern, or of an interest.

6.2.3.1 Vertical Bridge Accelerations

Study of the bridge accelerations in the top flange of the bridge is shown in a contour plot in Figure 6.38, to identify the regions where accelerations are largest. This was modelled at the velocity of $66m/s$, which corresponds to the largest peak in acceleration, for the *Simple* model, when the maximum acceleration across the bridge is modelled against the vehicle velocity in Figure 6.39. From the contour plot, the largest accelerations appear to be on the outer edges of
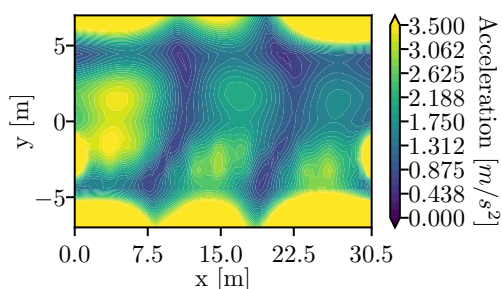
Figure 6.38: Contour plot of the maximum filtered vertical bridge acceleration from the *Simple* model for the velocity of 66 m/s for the Piacenza viaduct
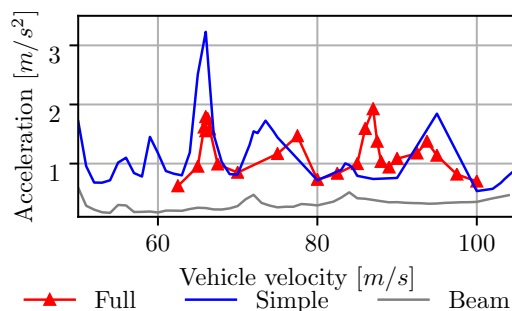
Figure 6.39: Variation of the maximum acceleration at any point on the bridge for each velocity in the benchmark case of the Piacenza viaduct

the top flange, however these regions are not of concern due to their distance from the tracks. Within the central proportion of the top slab, the highest accelerations are found around one sixth of the length of the bridge (around $5\,m$). The accelerations along the $y = 0\,m$ line is slightly lower than the surrounding areas due to the web here restricting the slab movement. Interestingly, study of the variation of the maximum accelerations with velocity in Figure 6.39, shows a much higher peak for the *Simple* model than the *Full* model, contradicting results of previous bridges.

To start to understand why the *Simple* model introduces larger accelerations than the *Full* model in this case, the maximum accelerations are plotted along the length of the bridge, for the velocity of $66\,m/s$ (Figure 6.40) and $87\,m/s$ (Figure 6.41), which are the velocities generating the largest response for the *Simple* and *Full* models respectively. For the velocity of $66\,m/s$ the *Full* and *Simple* models vary along the length of the bridge with similar shaped peaks in the acceleration, indicating a mode of three half sine waves per span, although the *Simple* model activates the mode with a greater amplitude. For the velocity of $87m/s$, the *Full* model also indicates a mode with three half sine waves being activated, and the *Simple* model shows a small amount of contribution from this mode, with three small peaks in acceleration.

Study of the frequency components of the maximum accelerations at $66\,m/s$ (Figure 6.42), indicates that the majority of the response for both the *Simple* and *Full* models comes from the combination of the tenth loading frequency (f_{v10}) and the tenth bridge frequency ($f_{s,10}$), which, as seen in Figure 6.37, is the mode with three half sine waves per span. Like in previous models, the inclusion of the vehicle mass in the calculation of the bridge frequencies ($f_{b,i}$), lowers the frequencies of the modes, but the peaks of the *Simple* and *Full* models occur at the same frequencies, indicating that the vehicular mass does not affect the frequency of the bridge response. Unlike most previous models, the peak acceleration component is not linked with the f_{v7} loading frequency. Due to the low speed where this resonance occurs, the f_{v10}
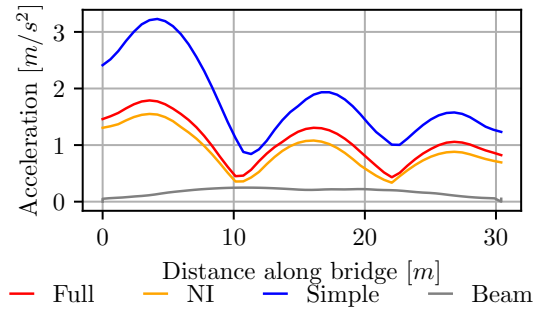
Figure 6.40: Variation of the maximum acceleration along the length of the Piacenza viaduct, for the velocity of $66\,m/s$. *Full* refers to the full vehicle-track model with irregularities, whereas NI is the full vehicle track model, but without irregularities
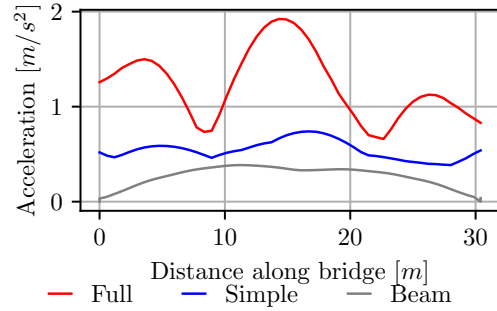
Figure 6.41: Variation of the maximum acceleration along the bridge centreline of the Piacenza viaduct, for the velocity of $87\,m/s$
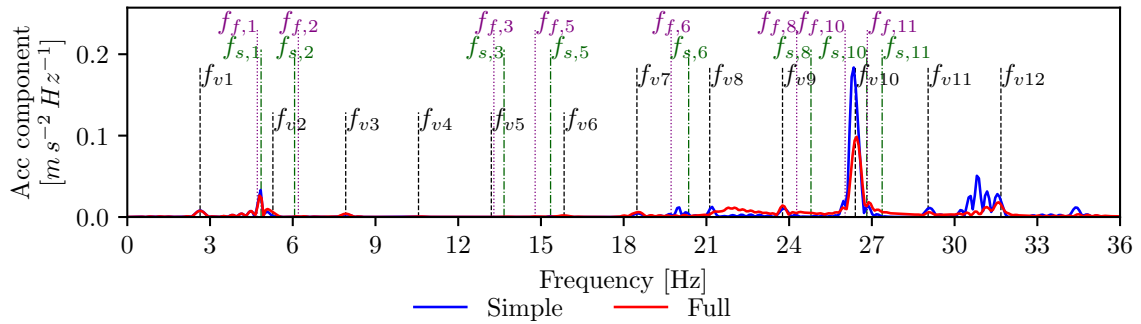
Figure 6.42: Frequency component of the Piacenza viaduct vertical accelerations at a velocity of $66\,m/s$

loading frequency is below the 30 Hz low pass filter. In the previous bridges studied, resonant problems tended to be at higher speeds, and hence this frequency associated with the axle spacing and velocity is above the filter. As can be seen in Figure 6.43a, this resonant loading frequency has the largest amplitude, considering the frequency components of the force-time history, at a single fixed point on the rail for the moving point loads. This suggests that it should induce a larger acceleration response when matching with a bridge frequency, than other resonant loading frequencies matching with the bridge modal frequencies. However, unlike in other cases where the *Full* model has the larger response, the *Simple* model response is larger and this is not explained solely by the large contribution of this resonant loading frequency.

When considering the *Full* model, the wheel forces are not constant as is assumed in Figure 6.43a, but rather they vary due to the irregularities in the rail. Hence, consideration of the force-time history experienced by different fixed points on the rail for the vehicle to travel
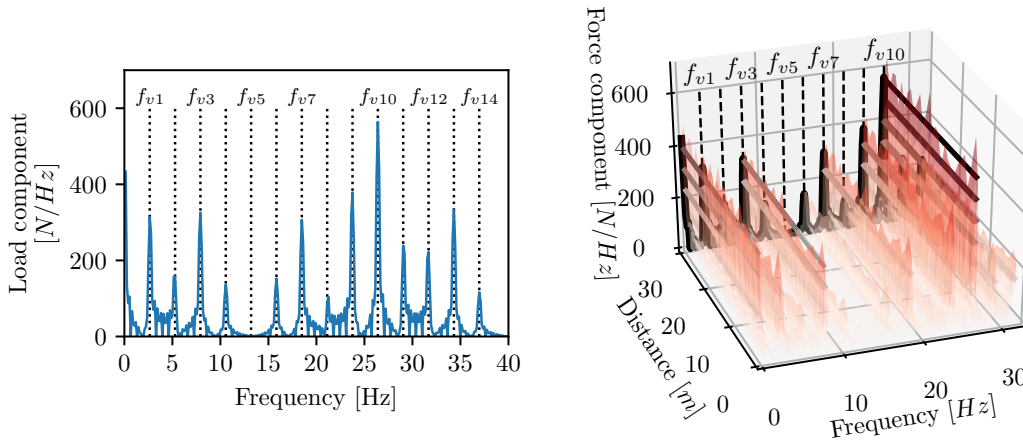
(a) Frequency decomposition of the force-time history of the moving point loads of fixed magnitude

(b) Frequency decomposition of the force-time history for the case where the real vehicle with irregularities passing over a fixed point, which due to the dynamic vehicle-rail-bridge interaction leads to variation in the magnitude of the force. The decomposition is performed at multiple locations along the distance of the bridge. Comparison of the contributions from the variable forces of the *Full* vehicle model (red shades), are made to the fixed magnitude loads of the point load model (black)

Figure 6.43: Frequency decomposition of the force-time history of a fixed point, as the vehicle or moving point loads crosses the point at the velocity of 66 m/s, with these plots showing the intensity of the force for each resonant frequency based on the axle spacings
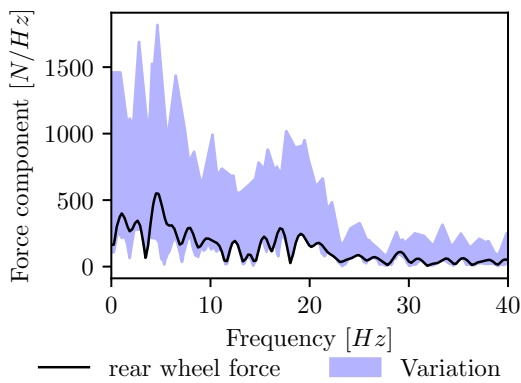
Figure 6.44: Variation of the force of one wheel as it moves along the track and bridge, split into the frequency domain, for a velocity of 66m/s. Also showing the variation of the other wheels as a filled region
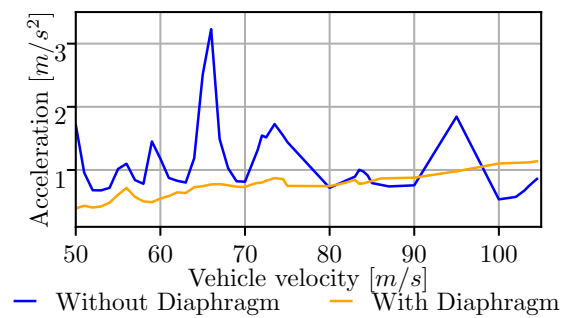
Figure 6.45: Comparison of the maximum vertical bridge accelerations between the *Simple* models at the maximum acceleration along the length of the bridge. It compares the accelerations for models with and without a diaphragm over the support sections

across, is split into the frequency domain for each point and shown in Figure 6.43b. This shows the resonant loading speeds of the *Full* vehicle model in the red shaded surfaces, with the equivalent loading speeds of a constant magnitude force shown in black (which is identical to Figure 6.43a). This indicates that the contribution of the f_{v10} frequency due to the spacing of the wheel forces at a fixed point, is very similar between the *Full* and *Simple* models. Due to the force variation, there are some small, but insignificant, deviations of frequency contributions representing the *Full* model (red) from the *Simple* model (black), purely due to changes in the wheel-rail force. The similar contribution at this mode indicates that the acceleration response should be similar between the *Simple* and *Full* model for this frequency, however it is seen that the *Simple* model leads to a larger response.

It was previously found that the frequency content of the wheel forces, which for a velocity of $100\,m/s$ leads to variation of the force for frequencies between 4 and 33 Hz (Figure 4.37 of Section 4.3.3), contributed to the amplification of the resonant modes. Here, the resonance occurs at $66\,m/s$, which corresponds to the frequency range of the wheel forces being between about 2.5 and 22 Hz. This is shown in Figure 6.44, where the force-time history of one wheel (as opposed to a fixed point on the rail where the wheel crosses as in Figure 6.43), is analysed in the frequency domain, and compared to variation of the other wheels (shaded region). The figure clearly shows large components of force variation is common for frequencies less than 22 Hz. This results in a smaller range of frequency content for the forces, and this 22 Hz is lower than the 26.5 Hz peak in contribution to the accelerations (Figure 6.42). This leads to the lack of amplification of this mode by the *Full* model in comparison with the *Simple* model. This is confirmed by the similar response of the model of the vehicle-track-bridge but with no irregularities (*NI*) in Figure 6.40, which shared a near identical response with the *Full* model, despite it having previously been shown (Section 4.3.3) that the force variations in the *NI* model are very small and the response is normally very similar to the *Simple* model. However, it does not explain the reason why the response is much lower in the *Full* model.

The reason behind the larger contribution of the *Simple* model in comparison with the *Full* model is found to be the track structure. The track is only used in the *Full* model, and it leads to a distribution of the load across the rail and adds a small amount of stiffness to the end of the slab. In the previous bridges studied, the presence of the diaphragm at the support sections means that this additional stiffness is negligible. However, in this bridge design, the end of the slabs over the support regions is not supported by diaphragms, such that in the *Full* model the stiffness of the track is not negligible. In addition, spreading of the load by the track in the *Full* model, leads to a more gradual increase in the force at the end span, whereas in the *Simple* model this increase is more sudden. This is not normally a problem as the load would be transferred straight into the bearings by the diaphragms, but the lack of these means the removal of the load spreading has a greater impact. This indicates the reasoning behind the smaller contribution of the $f_{s,10}$ bridge modes in the *Full* model in comparison with the *Simple* model. The introduction of diaphragms, each $1.6\,m$ thick over the support sections,

(a) Vertical Displacement (U3)   (b) Lateral Displacement (U2)
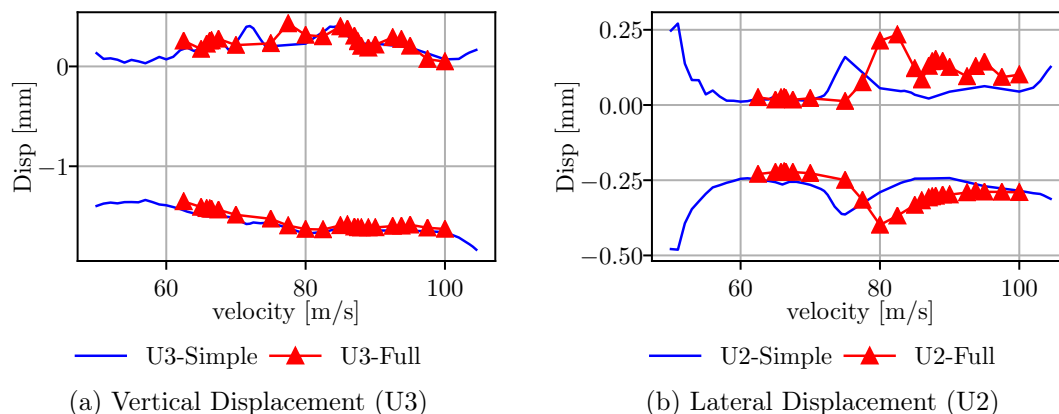
Figure 6.46: Variation of the displacements due to vehicle loading, taken from midspan for different velocities for the Piacenza viaduct

was tested for the *Simple* model and shown in Figure 6.45. This shows the impact on including the diaphragms, as the peak in acceleration at $66\,m/s$ is removed and the accelerations for all velocities are found to be lower.

As a result of this analysis it is clear that the *Simple* model produces larger accelerations. It is probable that the *Full* model provides more realistic accelerations, which are lower due to the stiffness and load spreading of the track structure, as well as more accurate due to the inclusion of irregularities, vehicle and wheel-rail interaction, which leads to more accurate representation of the wheel forces. The parametric analysis on this bridge will be performed without a diaphragm, as per the original bridge design, however the addition of the diaphragms have been shown to be important in the reduction of the accelerations, and it would be recommended for similar designs. In addition, the beam model in this bridge does not provide anywhere near the accelerations that the *Simple* or *Full* model do, due to the large sectional deformation and vibrations involving modes with a significant sectional deformation. Hence, it will not be compared in the parametric analysis.

6.2.3.2   Bridge Displacement

Considering the bridge displacement at midspan, it is found to vary with velocity as according to Figure 6.46. For the lateral displacements, there are some differences between the *Simple* and *Full* models. These lateral displacements due to vehicle load are relatively small, however there is significant difference between velocities due to resonant speeds. Considering the vertical displacements due to vehicle load, their magnitudes are larger than the lateral displacements. The *Full* and *Simple* models also have greater similarity. There does not appear to be a distinct peak, certainly not for a velocity corresponding to the peak vertical accelerations. This could be due to local top flange deformations influencing the bridge accelerations but not the displacement.

(a) Vertical Displacement (U3)   (b) Lateral Displacement (U2)
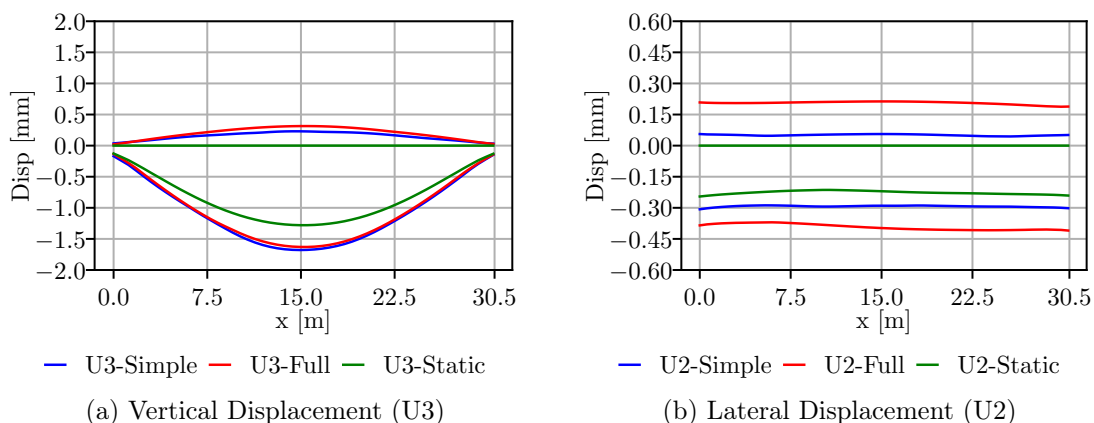
Figure 6.47: Variation of the displacements due to vehicle loading, along the length of the bridge for a vehicle velocity of $88\,m/s$ for the Piacenza viaduct

Due to the peak in the lateral and vertical displacements close to or at $80\,m/s$, the maximum displacements along the length of the bridge at this velocity are compared in Figure 6.47. Here, it can be seen that the lateral displacements are consistent along the length of the bridge, suggesting that the lateral displacement comes from distortion of the deck. This distortion would be significantly reduced by introducing diaphragms. Considering the vertical displacements the maximum as expected is found at midspan, with the *Simple* and *Full* models offering similar results.

Overall, the displacements due to load, both vertically and laterally, are similar or a bit larger than those of the Kyung-bu bridge. This could be due to the lack of diaphragms allowing greater distortion, despite the greater stiffness of this Piacenza bridge. The magnitude of the *Simple* model appears satisfactory to represent the *Full* model, especially for the vertical displacements, as the results between them are similar.

6.2.3.3 Bridge Stress Variation

Consideration of the longitudinal normal stress variation (S11) due to vehicle load, in the bottom flange is made at midspan, where it is found to be largest, in Figure 6.48. As expected this shows a very similar pattern to the vertical displacement at midspan with velocity in Figure 6.46a, as the S11 stress variation is linked to the vertical bending of the bridge. This also shows relatively good correlation between *Simple* and *Full* models.

When considering the normal stress variation under vehicle load in the lateral direction (S22), in the top flange of the bridge, as seen in Figure 6.49, it can be seen that the stress varies greatly with velocity. The *Simple* model displays much greater stress variation than the *Full* model for all velocities, whereas the *Full* model is smaller stress and more constant. The stress variation here is mainly caused by transverse bending, which for the *Simple* model, the lack
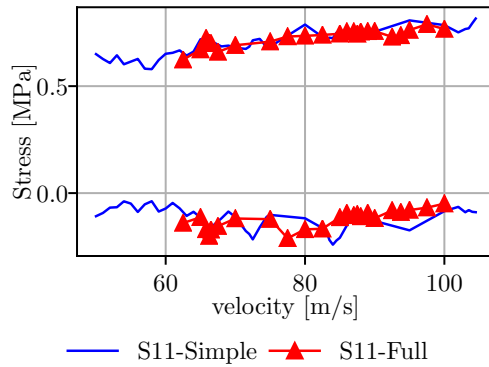
Figure 6.48: Variation due to vehicle loading of the bottom flange longitudinal normal stress (S11) in the Piacenza viaduct at midspan with velocity
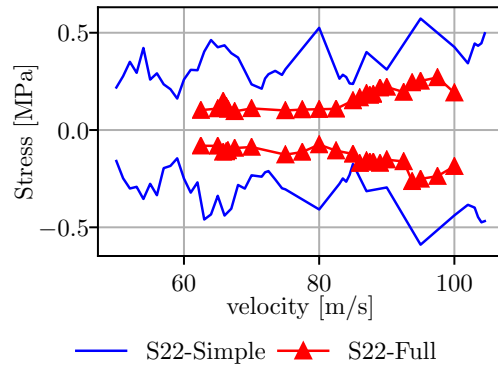
Figure 6.49: Variation due to vehicle loading of the top flange lateral normal stress (S22) in the Piacenza viaduct at midspan with velocity

of a track structure that distributes the loads, leads to larger stresses than in the *Full* model.

6.2.3.4   Conclusions to the Benchmark Case of the Piacenza Viaduct

It has been identified in the benchmark case that the accelerations are most critical under the *Simple* model loading at a velocity close to $66\,m/s$. The accelerations can be made lower by the easy introduction of diaphragms. The presence of a track structure in the *Full* model, increases the spreading of the load across the bridge, whilst also slightly increasing the stiffness of the top flange (due to rail continuity), which has the effect of reducing the accelerations in comparison with the *Simple* model. In terms of stress variation, the longitudinal normal value (S11) in the bottom flange varies very similarly to the vertical deflection with no significant difference between loading models. However, the influence of the transverse bending in the top flange leads to significantly higher S22 stress variations for the *Simple* model compared to the *Full* model. In terms of displacements, vertically it is highest at midspan, whereas laterally it is constant along the length. Variation between the models is larger in the lateral direction as previously seen, however this variation is small. As a result, in this bridge the most critical components are described by the *Simple* model, as it either matches or exceeds the deflections, accelerations and stresses of the *Full* model. However, the *Full* model may be more realistic of the bridge response due to the influence of the track in this model.

6.2.4   Parametric Analysis

For the parametric study of the Piacenza viaduct the same parametric percentage changes are modelled as for the Double U-beam and Kyung-bu viaducts for the web and the bottom flange, and the same top flange thickness changes made as in the Kyung-bu viaduct. This
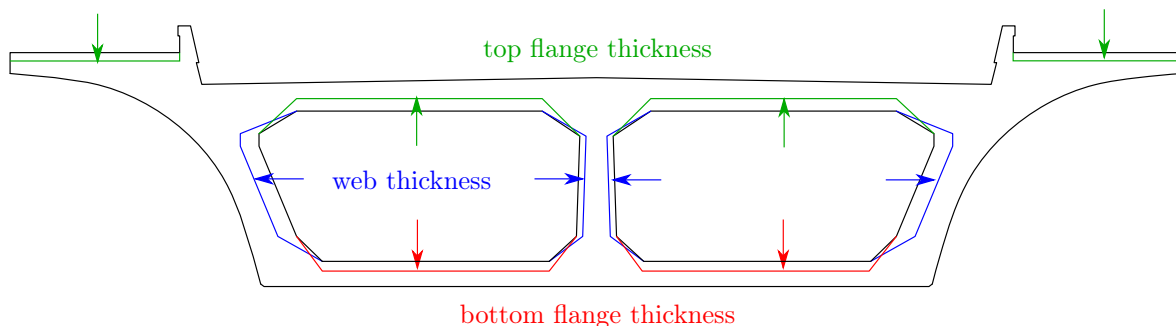
Figure 6.50: Variation of the Piacenza geometry for the parametric analysis
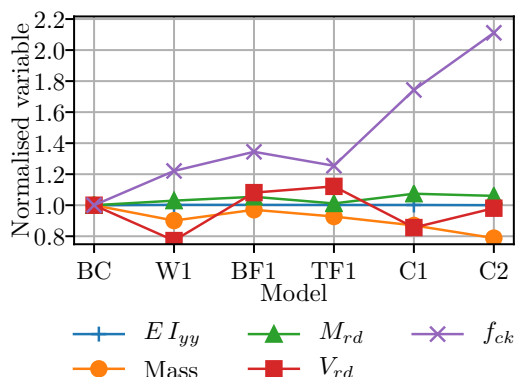
Figure 6.51: Variation of properties from parametric analysis, normalised with respect to the benchmark case model for the Piacenza viaduct

Model	Web thickness [%]	Bottom flange thickness [%]	Top flange thickness [%]	Concrete Strength [%]
BC	100	100	100	100
W1	66	100	100	122
BF1	100	75	100	134
TF1	100	100	75	125
C1	66	75	100	174
C2	66	75	75	211

Table 6.10: Geometrical properties of the parametric cases of the Piacenza viaduct with respect to the original values of the benchmark case

allows comparison between the models after the introduction of the central (or third) web to turn this bridge into a dual celled box girder. The parameters changed are shown in Figure 6.50, with each parameter as defined by Table 6.10. It is notable that a larger increase in the concrete strength is required for the changes in web and top flange thickness, to maintain the structural properties, than was required for the Kyung-bu viaducts. This is as the concrete strength initially is smaller, and although the geometry altered by the same proportions, the top flange and webs of this model are thicker, so more material is removed under the parametric analysis.

The variation of the concrete strength required to maintain the structural properties is shown in Figure 6.51. Here, it can be seen the capacity of the moment resistance (M_{rd}) and the second moment of area (EI_{yy}) are maintained or increased from the benchmark case at the midspan. The shear resistance (V_{rd}) is not necessarily maintained at midspan, however the reducing mass of the section will lead to a reduced shear demand. The resulting changes to the geometry and the mass of the bridge lead to changes to the frequency of the bridge modes containing one, two and three half sine waves per span as seen in Figure 6.52. For the fundamental mode in particular, the frequencies increase as the mass is reduced, as expected. For the two and
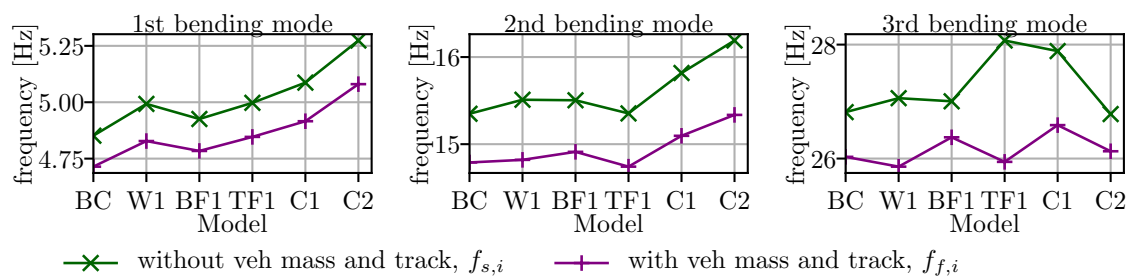
Figure 6.52: Variation of the frequencies of the modes displaying one, two and three half sine waves per span for the Piacenza viaduct. In the case of multiple modes displaying the shape, the mode with the lowest frequency of that shape is used

three half sine wave modes, the frequency generally increases with mass reduction, but due to sectional deformations affecting the mode shapes, some cases (for example C2 in the third bending mode), show a decrease of the frequency from the benchmark case. This is due to the complexity of the mode shapes with local deformations that are affected by the changing geometry.

6.2.4.1   Vertical Bridge Accelerations

Study of the accelerations, as shown by Figure 6.53a, immediately shows that most of the parametric cases exceed the accelerations allowed for the *Simple* model, but not for the *Full* model. This is unusual compared to the other bridges, as normally it is the *Full* model that exceeds the limits. The only viable change based on both models is the reduction to the bottom flange thickness, which shows similar accelerations to the benchmark case. However, as the *Full* model is assumed a more accurate model, a case can be made that all parametric cases satisfy the acceleration requirements. Considering the *Simple* model and parametric cases incorporating top flange changes, the accelerations are much higher than the limit, which can be put down to increased transverse flexibility. This reaction to the top flange thickness changes is similar to the higher response experienced by the Kyung-bu model under parametric analysis, despite the additional web reducing the flexibility of the top flange. Comparison with the accelerations at midspan (Figure 6.53b), shows that the maximum accelerations are not happening at midspan, particularly for the *Simple* model. This reflects well with the contour plot of the benchmark analysis, which showed a maximum for the *Simple* model in the first $5\,m$ of the span.

Considering the maximum response across the length of the bridge for the six parametric cases and how this acceleration changes with velocity is shown in Figure 6.54. It is clear from this figure that a similar mode is being activated to generate a maximum response at a velocity between 65 and 70 m/s. However, in the case of the BF1 this response is reduced. A second peak in the accelerations, with similar responses from both the *Simple* and *Full*
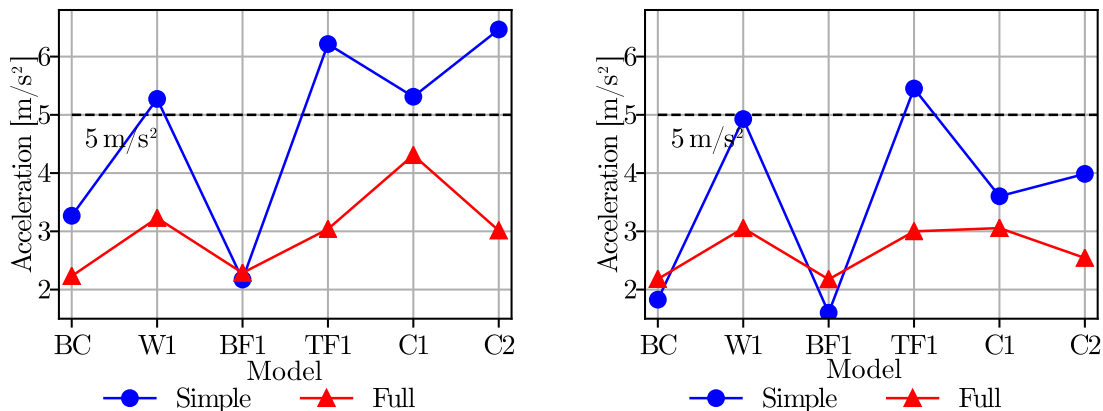
(a) Variation of maximum accelerations for the maximum magnitude in the span length

(b) Variation of maximum accelerations at midspan

Figure 6.53: Comparison of maximum vertical accelerations across all velocities for the Piacenza viaducts under parametric analysis

models occurs at a velocity between 90 and 100 m/s, which can be attributed to the $f_{s,10}$ mode being activated by the f_{v7} mode. This is the loading frequency that in previous bridges, led to increased responses by the *Full* model in comparison to the *Simple* model, when this frequency matched a bridge mode.

Consideration of the frequency components of the maximum acceleration response by the *Simple* model is shown in Figure 6.55. Here, it is seen that the contribution is consistently occurring under the convergence of the tenth loading frequency (f_{v10}) and the mode associated with three half sine waves per span which is $f_{s,10}$ in all cases except TF1 (where it is $f_{s,16}$). The location of the maximum tends to be at similar locations close to the end span in both cases. The contributions of this mode directly link to the magnitude of the maximum acceleration.

Comparison of the maximum accelerations against the span mass is shown in Figure 6.56, again using mass normalised against the benchmark case. This shows that there is generally a relatively steady increase in the accelerations for reductions in the mass, as expected especially for the *Full* model. In this model it can be seen that the TF1 case, does not lead to a large acceleration increase, which shows the effect of the additional stiffness as provided by the central web in this bridge in comparison with the Kyung-bu Viaducts.

6.2.4.2   Bridge Displacements

The variation of bridge displacements at midspan in the top slab, for different parametric cases is shown in Figure 6.57. From this figure both the lateral and vertical displacements stay relatively constant between the cases. In addition, good correlation is found between the *Simple* and *Full* models. The main difference found between cases is the DAF for the
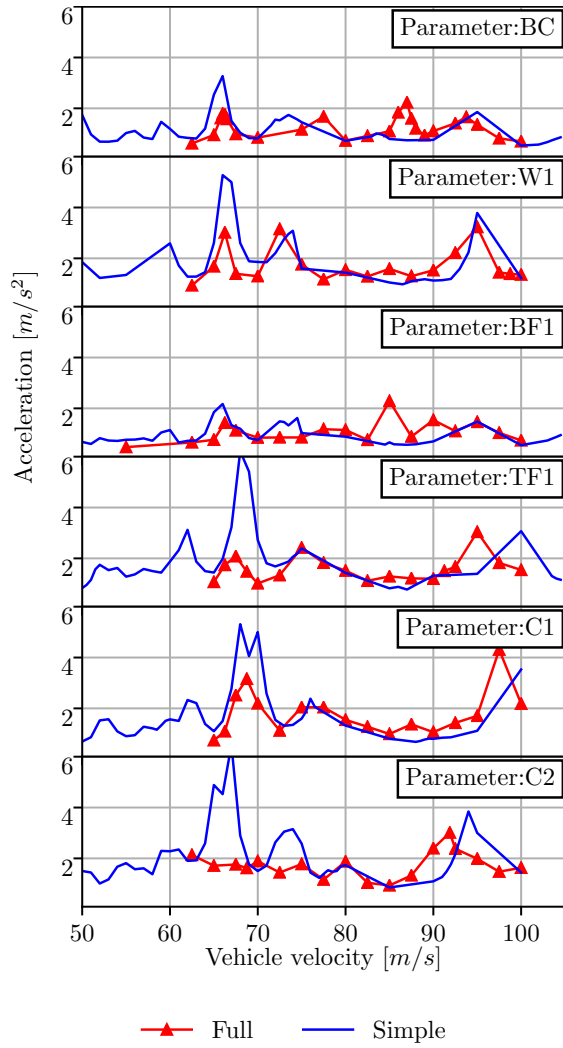
Figure 6.54: Variation of the maximum vertical acceleration along the length of the bridge with velocity for the Piacenza viaducts for different parametric cases
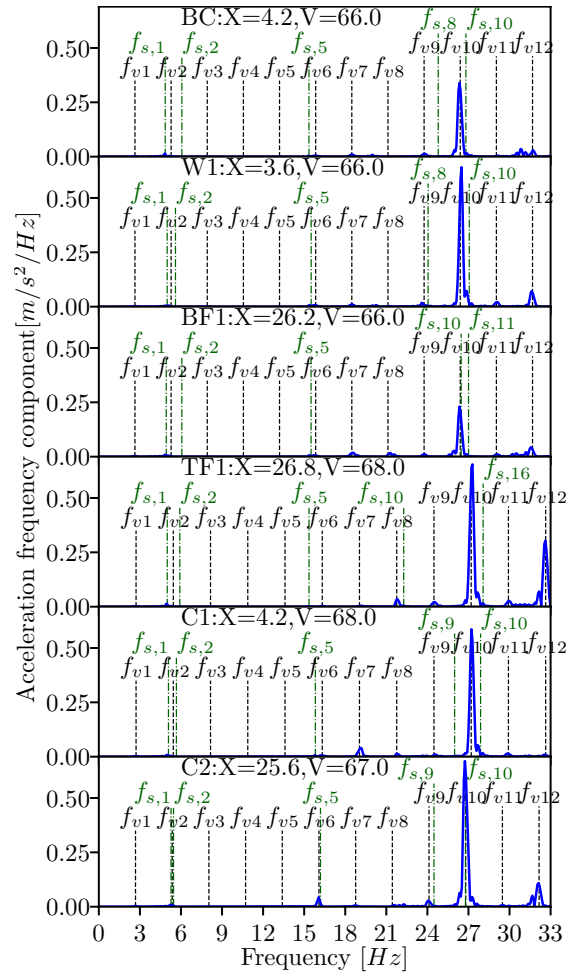
Figure 6.55: Analysis of the frequencies contributing to the maximum accelerations in the *Simple* model for the Piacenza bridge parametric analysis
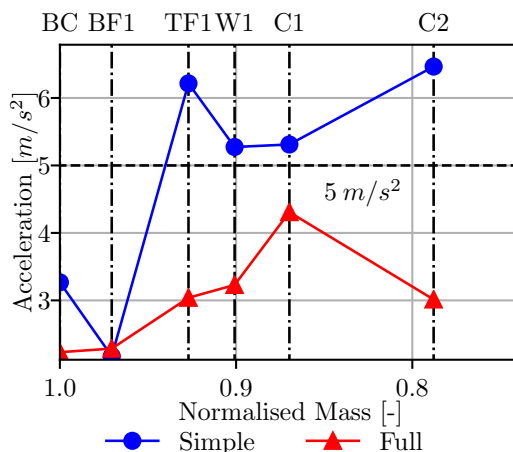
Figure 6.56: Maximum vertical acceleration found at any point along the bridge centreline for any velocity below $100\,m/s$, compared against the bridge mass normalised to benchmark case, for each parametric case of the Piacenza Viaduct

lateral deflections. However, this is particularly sensitive to small changes in displacement due to the small initial value of the static displacement. Overall, it can be determined that the displacements are not a concern during parametric analysis and that the *Simple* and *Full* models give good correlation.

6.2.4.3 Bridge Stress Variation

Considering the longitudinal normal stress variation in the bottom flange (Figure 6.58), it can be seen that the DAF and the actual stress variation follow very similar patterns. It can be seen that both models generally increase in stress variation with changes to the parameters, with the C1 and C2 cases that have the largest material savings, showing the larger stress variations. However, the increase is small and therefore not of concern due to the slightly increased bridge flexural capacity and lower bridge mass (Figure 6.51), such that the flexural demand should not exceed the capacity.

Considering the lateral normal stress variation (S22) from vehicular load, in the top flange (Figure 6.59), the stress variation is relatively constant between parametric cases, except for the *Simple* model in the cases where the top flange thickness is altered (TF1 and C2). In these cases the change in the thickness leads to a large increase in stress variation due to the increased transverse flexibility. In these cases the accelerations are higher as well, due to the greater activation of the higher modes. This leads to considerably higher stresses. However, in the more realistic *Full* model this increase is minimal and therefore it is acceptable.
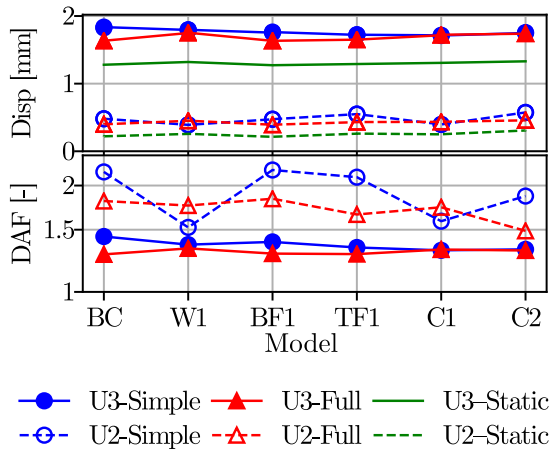
Figure 6.57: Variation of the actual and DAF of displacements in the centre of the slab at midspan of the first span of the Piacenza Viaduct (DAF is shown using a logarithmic vertical scale)
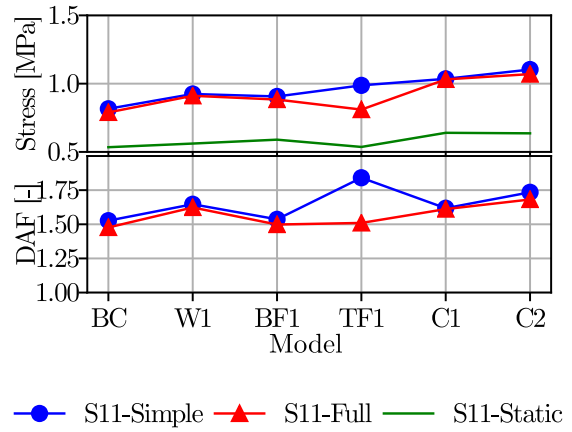
Figure 6.58: Actual and DAF of normal stress variation due to vehicle load, in the longitudinal direction (S11), in the bottom flange at midspan of the first span of the Piacenza Viaduct
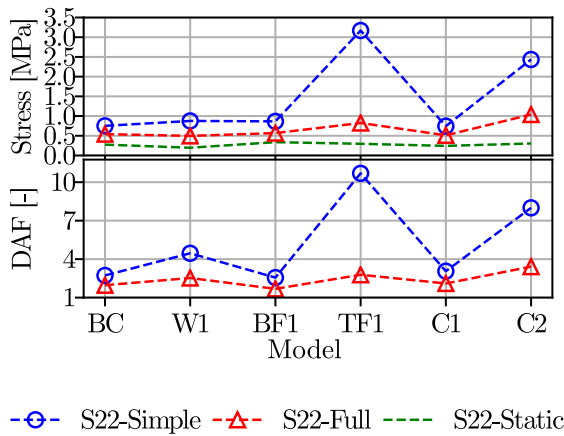
Figure 6.59: Actual and DAF of normal stress variation due to vehicle load in the lateral direction (S22) in the middle of the top flange at midspan of the Piacenza Viaduct
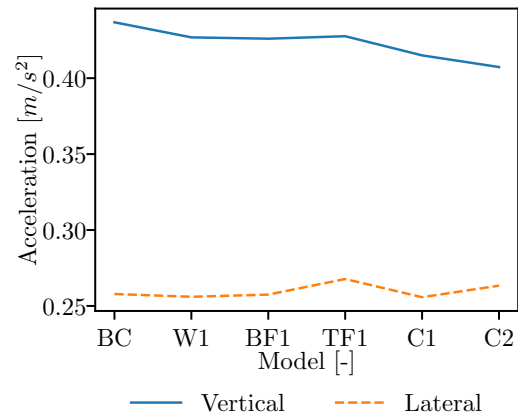
Figure 6.60: Variation of the Vehicle accelerations with parametric case

	BC	C1	C2
Concrete Strength	35	61	74
Precast element Mass [$\times 10^3$ kg]	862	750	680
Non-Structural mass [$\times 10^3$ kg]	198	198	198
Total mass of span [$\times 10^3$ kg]	1060	948	878

Table 6.11: Construction details of selected parametric cases of the Piacenza viaducts

6.2.4.4 Vehicle Accelerations

The comparison of vehicle accelerations both laterally and vertically is seen in Figure 6.60. In this figure it can be seen that the accelerations are relatively level, with higher vertical than lateral accelerations. The accelerations are far below levels of comfort and therefore are acceptable.

6.2.4.5 Construction Details

As can be seen from Table 6.11, the mass of this bridge is very high, both in terms of total permanent mass and precast mass. This means the reduction in mass is significant. The mass of the precast bridge can be reduced by 13% for C1 and 21% for C2 cases, with concrete strength increases of 75 and 111% respectively. This is a very significant amount and could lead to smaller capacity plant and site lifting elements being required. The total span weight is also reduced which will lead to reduced capacity being required in the foundations and piers. This bridge precast weight could be further reduced by splitting the beam into a slab, and two precast beams that are connected by transverse prestress bars.

6.2.4.6 Conclusions to the Piacenza Viaduct Parametric Analysis

From the parametric analysis it can be seen that all cases are viable when considering the more realistic *Full* vehicle-track-bridge model with irregularities. This can lead to reductions to the precast mass of 21% for an increase in concrete strength from 35 to 74 MPa. However, the parametric analysis also showed the drawbacks of using the *Simple* model leading to over design, as under this model, only savings to the bottom flange would have been practical of the cases studied, due to the large peak in accelerations (and S22 stress variation for top flange model cases) of the *Simple* model.

6.3   Modena Viaducts

The Modena viaducts, located on the Milan to Naples high speed rail line in Italy, are significantly different from the box girders studied. They have a cross sectional profile of a trough shape (also known as an 'Omega' profile). In these bridge types, the vehicle runs in the trough of the bridge, which lowers the running height of the vehicle, increasing aesthetic appeal and reducing noise pollution without the need for a noise barrier. A similar profile has been used in Belgium (Staquet et al., 2004). However, this type of cross section has been rarely used, as due to a lack of transverse stiffness, more advanced studies are required to verify the structure works. For example, the work by Macchi and Macchi (2003, 2010), studied this bridge for second order effects, to come up with the chosen cross section. Although these second order effects are not explained, by maintaining the sectional properties with an increase in concrete strength with geometry changes in the parametric analysis, the possibilities of using this section can be tested.

This bridge type utilises only one track per cross section, which in the Modena viaducts leads to multiple bridges placed next to each other to add further tracks. The bridges are simply supported and prestressed with parabolic tendons in the webs and straight tendons in the bottom flange. This bridge was chosen to be studied, despite the significant difference from the box girders, because it is similar to isolating the U-beam in the dual U-beam bridge, as it is composed of two webs and a bottom flange.

6.3.1   Initial Design

The cross section of the Modena viaduct is shown in Figure 6.61. It can be seen that there is an architectural fluting feature on the external surface, which was designed to mimic the Greek 'Doric column' style. This was introduced as it intended to aid the aesthetics by creating shadows that help reduce the appearance of the bridge depth (Macchi and Macchi, 2010). As a result, this feature will not be altered as part of the parametric design as it is a key feature of the bridge. The prestress is introduced via tendons of 12 strands. Four of these tendons follow a parabolic profile within each web, and the remaining 12 tendons are found in the bottom flange. This is shown in Figure 6.62. The initial prestressing load is assumed to be 78% of the characteristic breaking load. Further details are shown in Table 6.12.

The bridge is supported on two bearings at each support section, which are found on 'feet' to the cross-section. These feet are only found in the $2.1\,m$ from each end of the span. The Modena viaducts are modelled here as slab track, so hence limiting vertical bridge accelerations to $5\,m/s^2$. The thick elements of the cross section helps to contribute to properties in Table 6.13, which are comparable to the other cross sections studied in this chapter, despite being only supporting one track. Of the properties in this table, M_{rd} is the moment resistance, V_{rd}
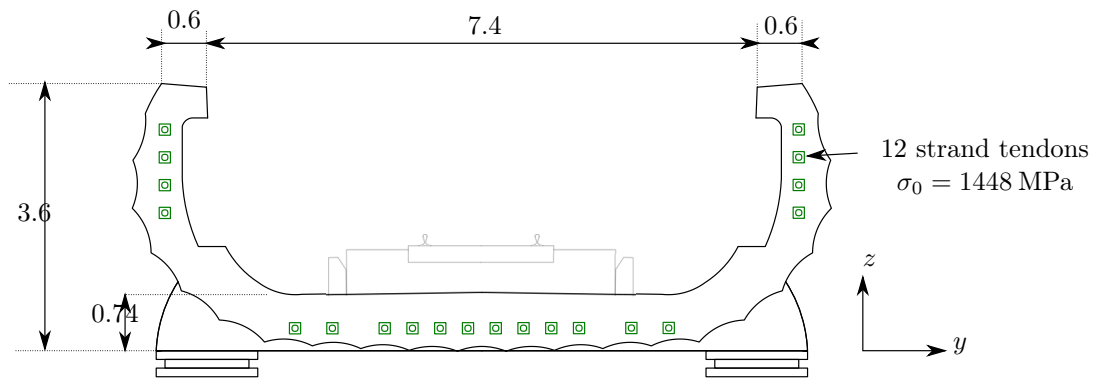
Figure 6.61: Cross section of the Modena viaduct at over the support region, dimensions in m
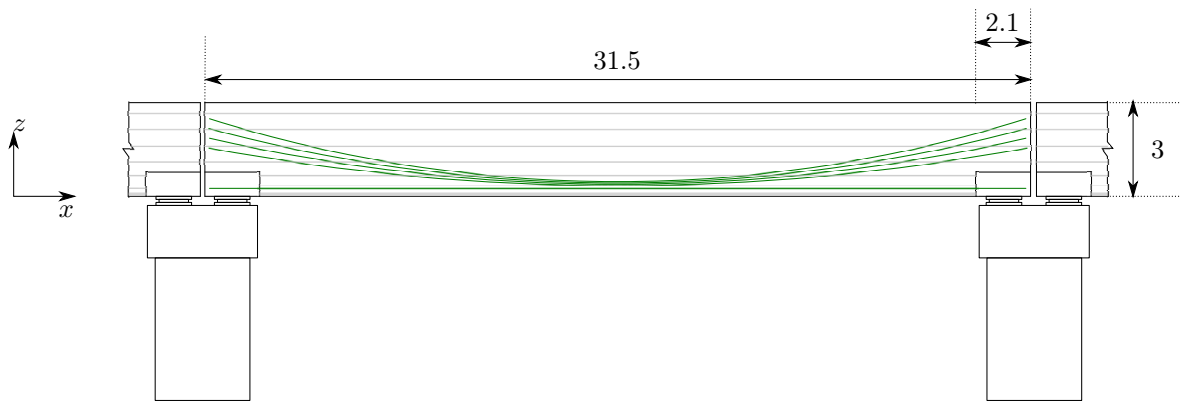
Figure 6.62: Longitudinal profile of the Modena viaduct, dimensions in m

Span length, L	31.5 m
Concrete strength, f_{ck}	35 MPa
Prestressing steel strength, f_{pk}	1860 MPa
Initial prestressing force	2430 kN
Prestress Area	1680 mm^2
Vehicle operating velocity	300 km/h
Span to Depth ratio	8.75

Table 6.12: Selected data for Modena viaducts
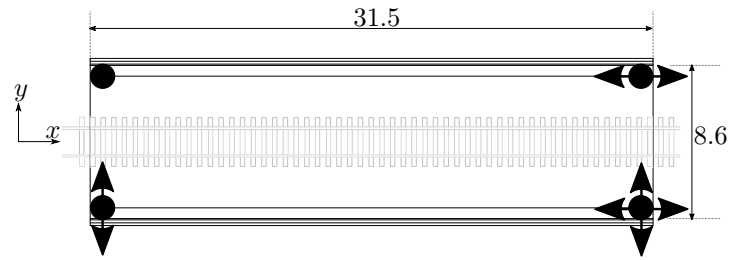
Figure 6.63: Articulation of the Modena viaduct. Arrows indicate unrestricted motion of the bearing, dimensions in m

M_{rd} [MNm]	119.0	I_{yy} [m^4]	8.567	A_c [m^2]	8.720
V_{rd} [MN]	27.59	I_{zz} [m^4]	83.89	$\bar{z}$ [m]	1.116

Table 6.13: Cross sectional properties of the Modena viaduct

the shear resistance, I_{yy} the second moment of area about the y axis centred around the centre of mass (with I_{zz} the same about the z axis), A_c the area of the precast concrete section, and $\bar{z}$ the distance from the bottom to the centroid.

6.3.2   Modelling of the Modena Viaducts

The bridge is modelled using the same methods as previously stated in this chapter. The estimation of the thicknesses of the shells was again difficult, due to the complex geometry of the cross section. The resulting shell position and thickness is shown in Figure 6.64, which gives representative structural properties of the real section. The centreline of the shell representing the webs is offset from the centre where there is an indent to the cross-section, as seen in Figure 6.64. This enables continuity of the shell elements, whilst still matching the profile properties.

Study of the mesh size is shown in Table 6.14. The model of 1084 elements was determined to be of sufficient accuracy, due to low variation from the fine mesh of the studied variables. The first instance of the bending modes with sinusiodal shape, up to three half sine waves are
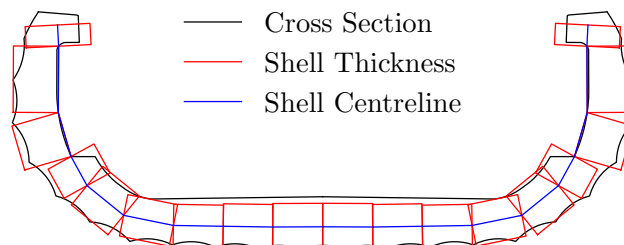
Figure 6.64: Shell location and thickness assignment of the Modena viaducts

Number of Elements	Element Size [m]		Stress		Displacement		Fundamental Frequency	
	X	YZ Plane	[MPa]	%	[mm]	%	[Hz]	%
958	1/0.6	1	1.14	2.9	-11.8	1.0	5.097	0.7
1084	0.6	0.6	1.13	1.4	-11.9	0.7	5.088	0.5
4522	0.3	0.3	1.10	0.6	-11.8	0.8	5.089	0.5
1591762	0.05	0.05	1.11	-	-11.9	-	5.064	-

Table 6.14: Mesh sensitivity of the Modena viaduct models. Prescribed element size is shown in the cross sectional plane (YZ Plane) and longitudinal direction (X)

(a) $f_1 = 5.13$ Hz   (b) $f_{s,7} = 19.5$ Hz   (c) $f_{s,9} = 24.7$ Hz
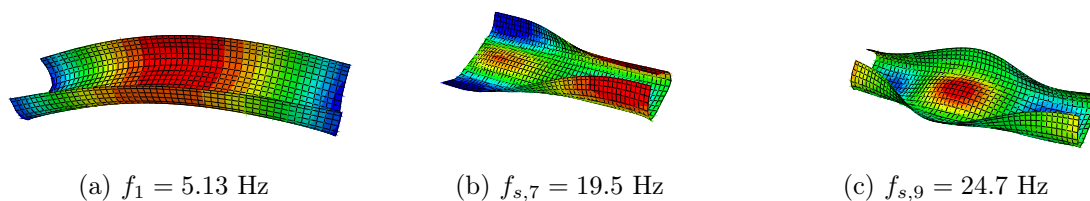
Figure 6.65: Modal shapes of first three sinusoidal bending modes of the Modena viaduct

shown in Figure 6.65. The second mode in particular shows considerable deformation of the webs, which is a result of the lack of transverse stiffness.

6.3.3   Benchmark Case Analysis

This subsection analyses the initial benchmark case of the Modena viaduct, to help identify the locations to further study, when conducting the parametric analysis.

6.3.3.1   Bridge Vertical Accelerations

A visualisation of the maximum filtered vertical accelerations of the initial model of the Modena viaducts, for a velocity of $87\,m/s$ ($313\,km/h$), across the whole bottom flange of the bridge (where the track is and the train runs), is shown in Figure 6.66. This was the velocity that generated the largest response by the *Simple* model. It shows that the vertical accelerations are relatively similar across the width of the bottom flange, with peaks at approximately one sixth, halfway and five sixths of the span length. Visualisation of the maximum acceleration along the centreline of the bridge ($y = 0\,m$) is shown in Figures 6.67 and 6.68, corresponding to the velocities leading to the maximum response for the *Simple* model ($87\,m/s$) and the *Full* model ($94\,m/s$) respectively.

Figure 6.67 shows a good match between the *Simple* and the *Full* model, with patterns of the peak acceleration displaying attributes of activation of a bending mode with three half sine waves, due to the peaks in the quarter span regions. On the contrary, Figure 6.68 displays significantly larger accelerations for the *Full* model. The shape of the peaks suggest that the
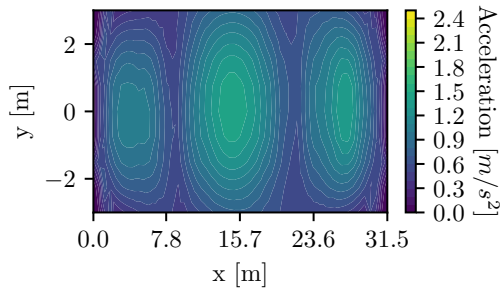
Figure 6.66: Contour plot of the maximum vertical filtered accelerations of the Modena viaduct at a vehicle velocity of 87 m/s for the *Simple* loading model
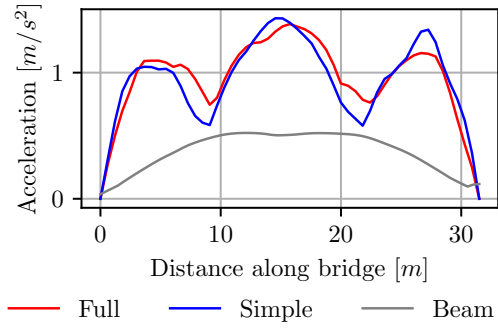
Figure 6.67: Maximum vertical filtered accelerations along the length of the Modena viaduct at a vehicle velocity of 87 m/s
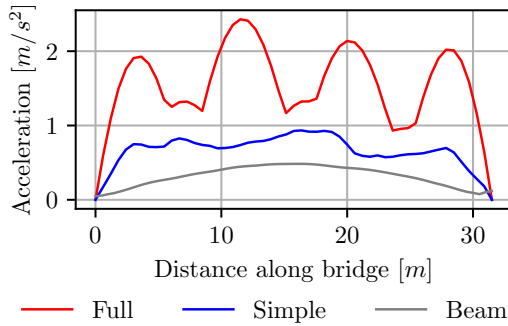
Figure 6.68: Maximum vertical filtered accelerations along the length of the Modena viaduct at a vehicle velocity of 94 m/s
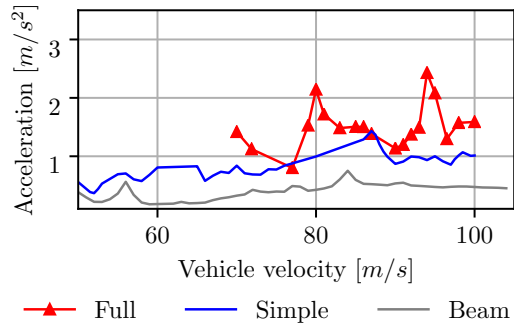
Figure 6.69: Maximum vertical filtered accelerations of the Modena viaduct for different vehicle velocities

contributions come from a high frequency bending mode with a shape containing 4 half sine waves, due to the four peaks.

Comparing the maximum filtered vertical acceleration found on the bridge with the velocity is shown in Figure 6.69. This shows that the peaks of the *Full* model are still significantly higher than the *Simple* model. As a result, it is seen to be important to use the *Full* model as some modes are still amplified by the inclusion of the vehicle and irregularities.

The frequency components of the acceleration at midspan for these two velocities are shown in Figures 6.70 and 6.71. The resonant frequencies associated with the spacing between loads is shown as f_{vi}, where i is the harmonic of the loading frequency. In addition, activated and relevant modal frequencies of the bridge are shown by $f_{s,i}$, where i is the mode number. Additional bridge modal frequencies, considering the vehicular mass as a distributed mass along the length of the track, are shown by $f_{f,i}$. The difference between these modal frequencies is small particularly for low frequency modes. In addition, the peaks in contribution to the
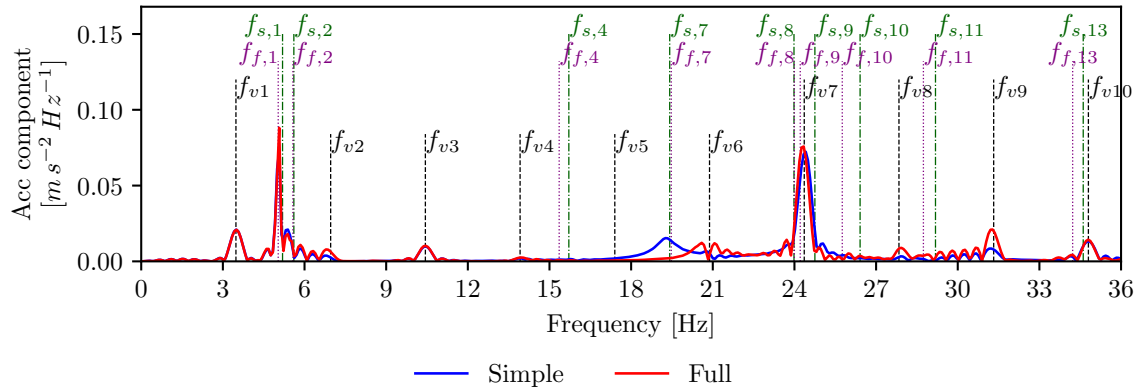
Figure 6.70: Frequency components of the maximum vertical filtered accelerations at the midspan of the Modena viaduct at a vehicle velocity of $87\,m/s$
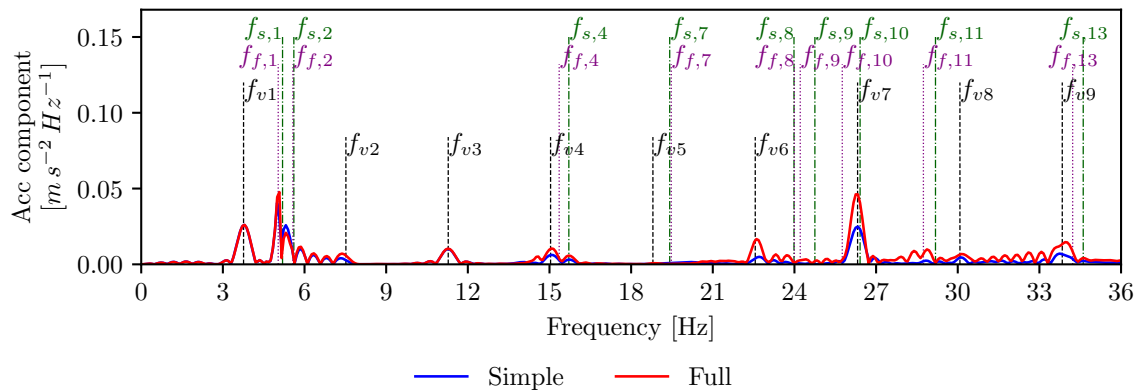
Figure 6.71: Frequency components of the maximum vertical filtered accelerations at the location $x = 12\,m$ of the Modena viaduct at a vehicle velocity of $94\,m/s$

accelerations for the *Full* model (the only dynamic model to incorporate the vehicle mass), correspond better to the $f_{s,i}$ frequencies. Hence, it is found that including the vehicle mass in the frequency analysis is not representative of the frequencies that the bridge oscillates at. This confirms findings previously made in this thesis. As in all the previous bridges, the f_{v7} bridge leads to large acceleration contributions. Figure 6.70 shows contribution is mainly from the first and the ninth bridge modes. The contributions between models are similar, hence the similar acceleration response. However, Figure 6.71 shows a smaller contribution from the first bridge mode, and activation around the tenth bridge mode/seventh loading frequency. This tenth mode shows an amplitude much larger for the *Full* model then the *Simple* model. The shape of this tenth mode displays three half sine waves, like the ninth mode, but with some inflexion of the webs within the shape.
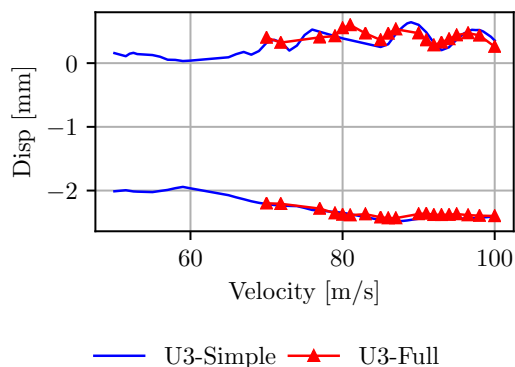
Figure 6.72: Vertical deflection of modena viaducts at midspan for different velocities
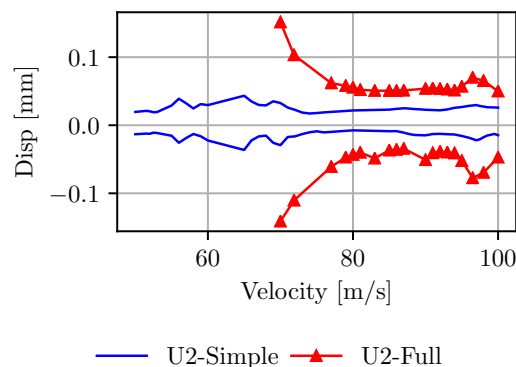
Figure 6.73: Lateral deflection of modena viaducts at midspan for different velocities

6.3.3.2 Bridge Displacement

Under study of the displacement of the bridge, the vertical displacement is maximum at midspan. Variation of the displacement in the bottom flange at the midspan with velocity shows similar responses between the *Full* and *Simple* models (Figure 6.72). The maximum variation from the static position is shown, with the upward deflection being much smaller than the downward (negative) deflections as expected. In general, the deflection is seen to increase with higher velocities. This suggests that the conclusion made in Section 5.5.3.6, that the deflection can be estimated by the *Simple* model for the *Full* model, holds true for this bridge type.

Laterally, the conclusions of Section 5.5.3.6 also hold true. The *Full* model is required to determine the full possible lateral deflection under dynamic loads. This is shown in Figure 6.73, which shows the larger deflections of the *Full* model, due to the lateral loads the vehicle introduces. The positive and negative displacements are relatively similar, reflecting the central location in the bottom flange that the data is taken from. The lateral deflections along the length of the bridge in the bottom flange are shown in Figure 6.74 and in the web in Figure 6.75. It can be seen here that the lateral deflection of the web is higher, which is due to them not being restrained by transverse elements. In addition, the maximum lateral deflection is not zero in either case at the supports which is due to only one bearing on each support restricting lateral motion, hence allowing some lateral movement, which also leads to small deflections under load.

6.3.3.3 Bridge Stress Variation

By ignoring the stresses generated by the dead load of bridge and track structure, as well as the stresses from the prestressing, the variation in stress generated by the vehicle loading
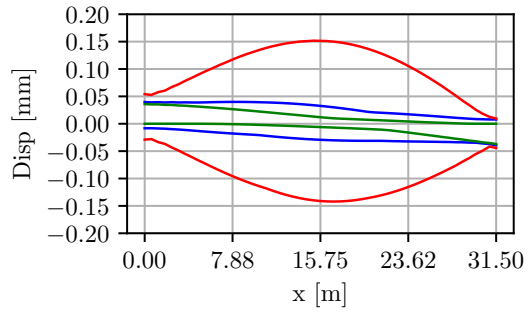
Figure 6.74: Maximum lateral deflection of Modena viaducts along the bridge centreline under vehicle load in the bottom flange for a velocity of $70\,m/s$
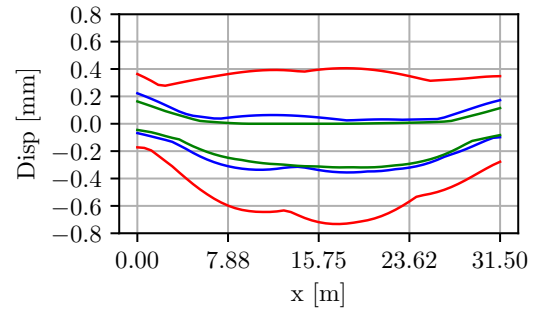
Figure 6.75: Maximum lateral deflection of Modena viaducts along the bridge for the location at the top of the web under vehicle load for a velocity of $70\,m/s$
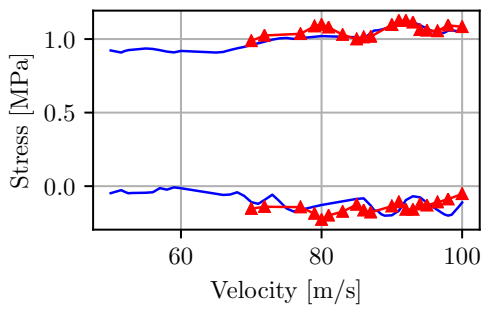
Figure 6.76: Variation of S11 stress with vehicle loading, in the bottom flange of the beam at midspan with velocity for the Modena Viaduct
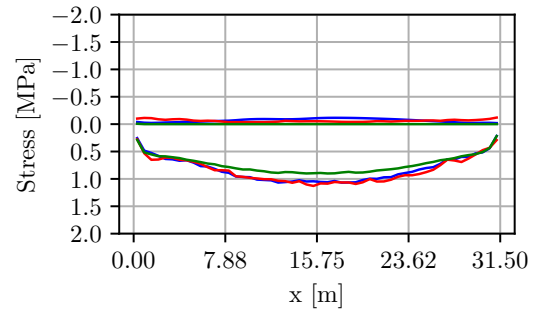
Figure 6.77: Variation of S11 stress with vehicle loading, in the bottom flange along the length of the beam for a velocity of $100\,m/s$

alone can be identified and plotted. The normal stress variation in the longitudinal x direction (S11) can be seen at midspan in the bottom flange for all velocities (Figure 6.76) to have a similar pattern to the vertical deflection at the same location (Figure 6.72). It can also be seen that the majority of the variation is positive, indicating a tensile stress. This is not a big problem because the prestress is designed to introduce a compressive stress in the bridge that will offset this. Study along the length of the bridge shows that the stress variation is maximum at midspan, with similar responses between the *Simple* and *Full* models, as per the conclusions of Section 5.5.3.6.

Unlike in Section 5.5.3.6, the S22 stress variations (normal stress perpendicular to longitudinal direction in the plane of the shell element), are not insignificant. These S22 stress variations are shown in Figure 6.78 at midspan of the bottom flange for all velocities studied. Here, the *Full* and *Simple* models are similar, which is unlike Section 5.5.3.6, where the S22 stress
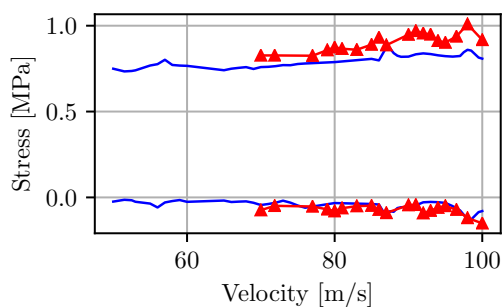
Figure 6.78: Variation of S22 stress due to vehicle loading in the bottom flange of the beam at midspan with velocity for the Modena Viaduct
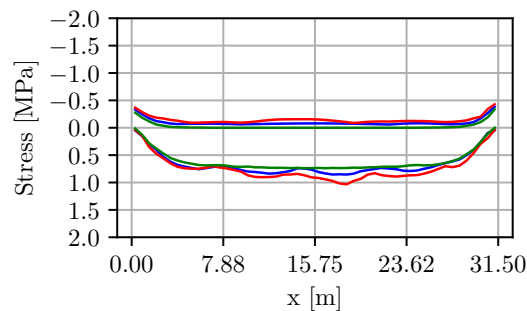
Figure 6.79: Variation of S22 stress due to vehicle loading in the bottom flange along the length of the beam for a velocity of $100 \, m/s$
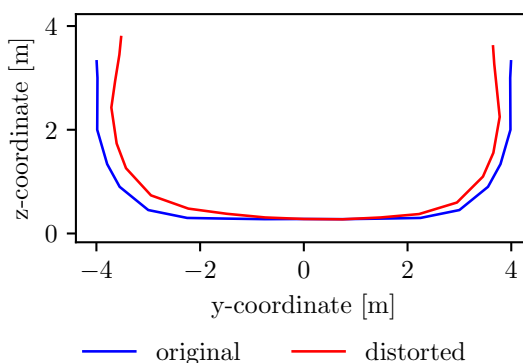
Figure 6.80: The distorted shape of the cross section at midspan of the Modena Viaduct

variation was dependent on the lateral displacement of the bridge and hence the *Full* model displayed higher stress variation than the *Simple* model. In this bridge, the magnitude of this stress variation is much higher than for the double U-beam bridge. The stress variation along the length of the beam in Figure 6.77, varies in a similar way to the S11 stress variation. From this it appears that the S22 stress variation is caused by an additional reason from the lateral displacement. This is identified as the transverse deformation of the cross section, such that there is two way bending in the bottom of the slab. The distortion of the cross section at midspan is shown in Figure 6.80. This bending under vertical load is predominantly inwards, however, some inflexion can occur during the dynamic analysis. The bending is as a result of the lack of transverse support, allowing the section to bend in ways that make the top of the webs closer or further from each other more easily. It is therefore important to maintain the levels of stress variation in the S22 direction under parametric analysis, for which the initial case is designed for.
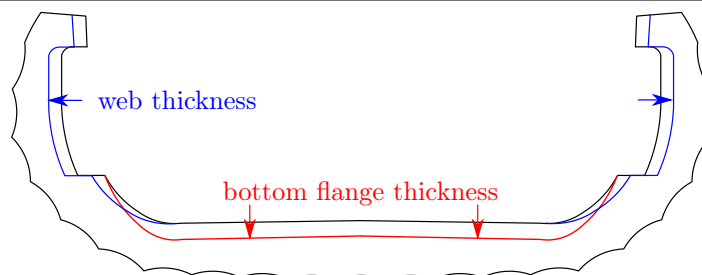
Figure 6.81: The pictorial implementation of the thickness changes to the Modena viaduct for parametric analysis

6.3.3.4   Conclusions to the Benchmark Case Analysis of the Modena Viaducts

From the benchmark case, it is identified that the bridge frequencies representing the response is best represented by the $f_{s,i}$ frequencies for both the *Simple* and *Full* vehicle models. The vertical bridge acceleration response was found to be higher for the *Full* model than the *Simple* model again, so the *Full* model is required. Considering the displacements, the *Simple* and *Full* models represent each other well vertically, however laterally, especially in the webs the deflection was much higher under the influence of the *Full* model and the lateral loads it introduces. Considering the stress variation, the *Simple* and *Full* models have good correlation, but as expected in an open section the S22 stress variation is larger here than seen in the double U-beam bridge, due to transverse bending. Finally, the location of the largest displacements and stresses are at the midspan, although this is not necessarily the case for the accelerations.

6.3.4   Parametric Analysis

The parametric analysis of this bridge compares three cases to the benchmark case. These test the conclusions of Section 5.5.3.6, and as such one case introduces a reduction to 66% of the original thickness of the web, another case studies reduction to 75% of the original bottom flange thickness and the final case considers a combination of them both. The introduction of these material savings, are performed as in Figure 6.81. Under the parametric analysis, in order to maintain the structural rigidity, the strength of the concrete is accordingly increased. The resulting variation in mass and concrete strength is shown, normalised with respect to the benchmark case scenario, in Figure 6.82, and the characteristics of each parametric case shown in Table 6.15. In this particular case, the reduction of the web thickness has very large implications on the flexural capacity, and therefore needs to be counterbalanced with large increments of the characteristic strength to maintain the initial flexural capacity

With variation in the geometry of the cross section, the frequencies of the modes change. This is from changes in the mass of the structure and also the local stiffness of components of the bridge. The variation of the frequency is shown in Figure 6.83. The frequency of the fundamental mode increases steadily with reducing mass, as expected due to the maintained
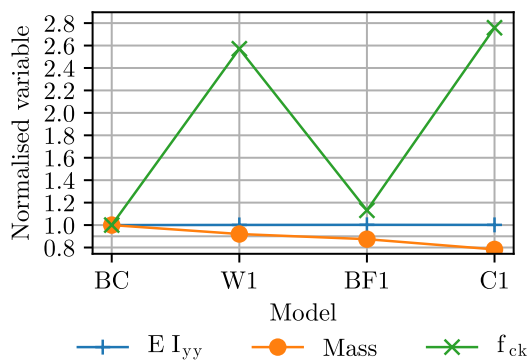
Figure 6.82: Variation of properties from parametric analysis, normalised with respect to the benchmark case model for the Modena viaduct

Model	Web thickness [%]	Bottom flange thickness [%]	Concrete Strength [%]
BC	100	100	100
W1	66	100	257
BF1	100	75	113
C1	66	75	275

Table 6.15: Geometric properties of the parametric cases for the Modena viaduct with respect to the original values of the benchmark case
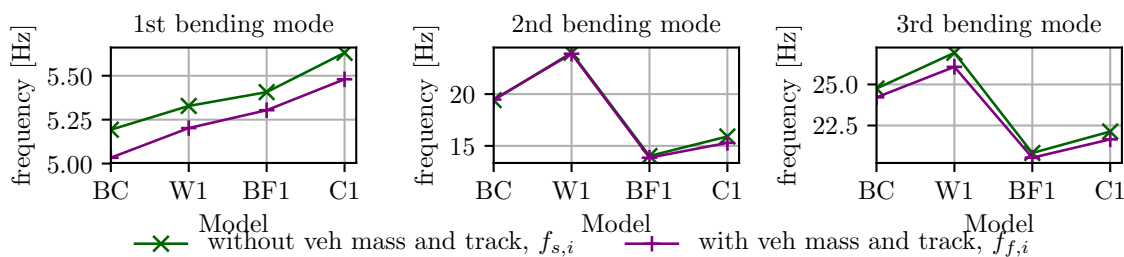
Figure 6.83: Variation of the frequency of the modes shown in Figure 6.65 with changing parameters

stiffness. However, due to local deformations in the modes, the second and third modes vary. As such, when reducing the bottom flange thickness, the local stiffness is reduced hence allowing more transverse bending, so the modal frequencies become considerably smaller.

6.3.5   Bridge Vertical Accelerations

Consideration of the bridge accelerations in Figure 6.84a, shows the maximum accelerations at any point along the centreline of the section (which is also the midpoint between the rails of the track), for any velocity studied. The greatest impact here appeared to be from changing the bottom flange thickness, with accelerations lower than the limit of $5 \ m/s^2$, being close to $3.5 \ m/s^2$ in both cases of reduced bottom flange thickness. The web thickness changes resulted in some increase in the accelerations, but these were smaller than for the bottom flange. This shows the effect of reducing the thickness of the running surface of the vehicle, leading to increased local flexibility and larger accelerations. The *Simple* model shows a similar relationship to the *Full* model, albeit with a smaller magnitude of acceleration. However, the combined case (C1) shows lower accelerations for the *Simple* model than the other two
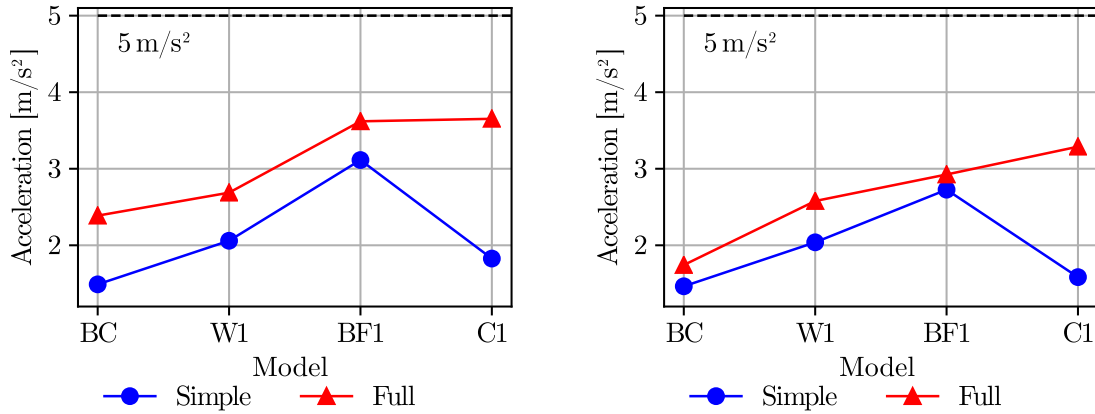
(a) Variation of maximum accelerations for the maximum magnitude in the span length

(b) Variation of maximum accelerations at midspan

Figure 6.84: Comparison of maximum vertical accelerations across all velocities for the modena viaducts under parametric analysis

parametric cases, due to some decoupling of modes and the reduced response of high frequency modes for the *Simple* model rather than *Full* model.

Focusing on the midspan accelerations the conclusions are similar, but again the accelerations are lower. This shows that the activation of modes with multiple acceleration peaks per span, leading to the maximum acceleration not being found at midspan. This was previously shown in Figure 6.68, where the midspan was a local minimum in accelerations for the *Full* model.

The variation of the accelerations with velocity are shown in Figure 6.85. It is evident the location of the maximum acceleration is changing with each parameter due to the shifting location of the velocity causing the peak. When considering the frequency components of the accelerations that cause each of these maxima, as in Figure 6.86, it is clear the contribution comes from considerably different frequencies for different speeds and parameters. It is also seen that the location is not always midspan, and is often closer to the one third or three quarter span locations. This is due to the high contribution from the high frequency modes which have peaks in these locations, and the low contribution from the fundamental mode. Some prominent peaks are in proximity to the bridge modes of $f_{s.3}$ for the BF1 case, which is a local mode involving large deflections of the bottom flange, and modes $f_{s,8}$ for the W1 case and $f_{s,10}$ for the C1 case, which are both three half sine wave per span modes. The activation of these modes, shows the continued importance of the *Full* model using the vehicle and irregularities.

Comparison of the maximum accelerations against the span mass is shown in Figure 6.87, again using mass normalised against the benchmark case. This shows that there is again a general increase in the maximum accelerations for reductions in the mass, as expected.
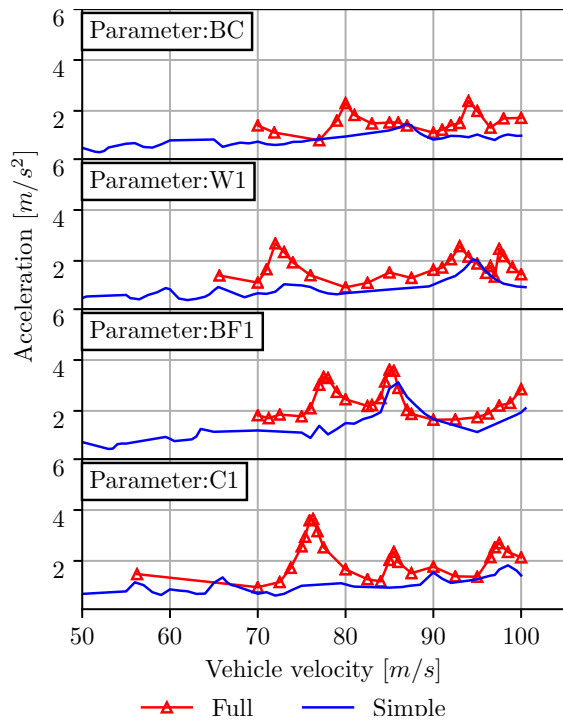
Figure 6.85: Variation of the maximum vertical acceleration along the length of the bridge with velocity for the Modena viaducts for different parametric cases
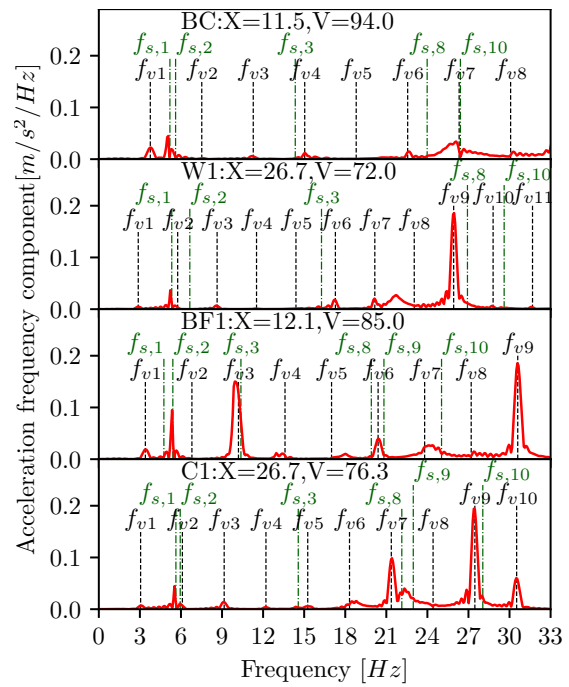
Figure 6.86: Analysis of the frequencies contributing to the maximum accelerations in the *Full* model for the Modena bridge parametric analysis
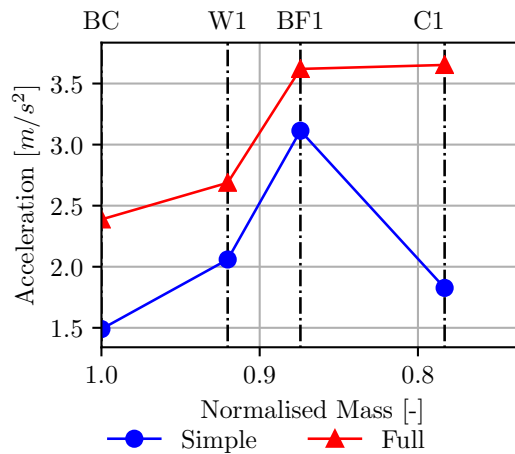
Figure 6.87: Maximum vertical acceleration found at any point along the bridge centreline for any velocity below $100\,m/s$, compared against the bridge mass normalised to benchmark case, for each parametric case of the Modena Viaduct
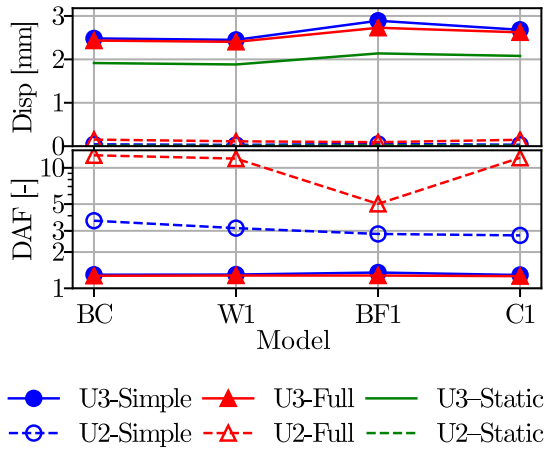
Figure 6.88: Variation of the actual and DAF of displacements in the bottom flange at midspan of the Modena Viaduct (DAF is shown using a logarithmic vertical scale)
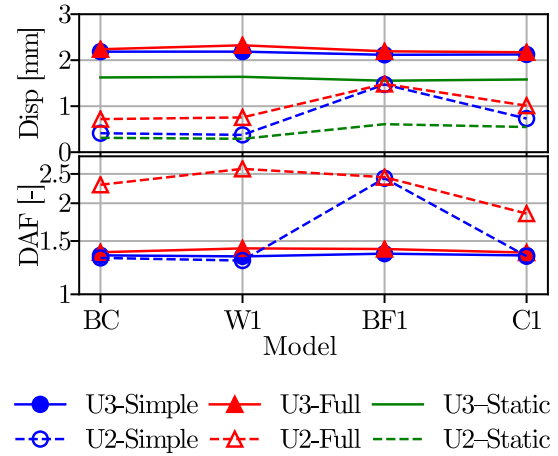
Figure 6.89: Variation of the actual and DAF of displacements in the top of the web at midspan of the Modena Viaduct (DAF is shown using a logarithmic vertical scale)

6.3.5.1 Bridge Displacements

The displacements of the bottom flange at midspan are shown to vary as in Figure 6.88. The lateral displacements here are very small resulting in large DAF. They also do not change significantly between models. Considering the vertical displacement, reductions in the bottom flange cause larger deflections. Studying the deflections at the top of the web at midspan is shown in Figure 6.89. The lateral deflections here may be of concern as they are much higher, however the DAF for the *Full* model stays relatively similar. The *Simple* model has lateral deflections similar to the *Static* model, apart from in the BF1 case, where it matches the *Full* model. Vertically the deflections are consistent between models. As a result it appears necessary to model the *Full* model to determine lateral web deflections, which as stated in Section 6.3 (Macchi and Macchi, 2003, 2010), were required to be subject to special analysis for study of second order effects.

6.3.5.2 Bridge Stress Variation

Consideration of the stress variation due to vehicle load is also carried out in two locations. Firstly, the longitudinal normal stress variation (S11) in the middle of the bottom flange is shown in Figure 6.90. Here the stress variation increases by up to 50%, but the DAF stays relatively constant. This increase in stress variation may be of concern, as it results in an increased flexural demand. However, the increment is small so this increase may be okay, and if not, a small incremental increase of the concrete strength or additional prestressing maybe required to increase the flexural capacity.
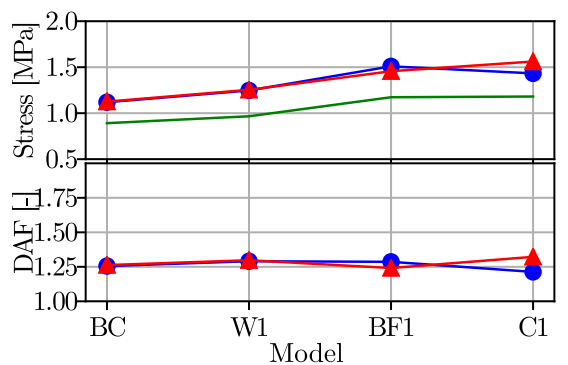
Figure 6.90: Variation of the DAF of normal stress with vehicle load in the longitudinal direction (S11) in the bottom flange at midspan of the Modena Viaduct
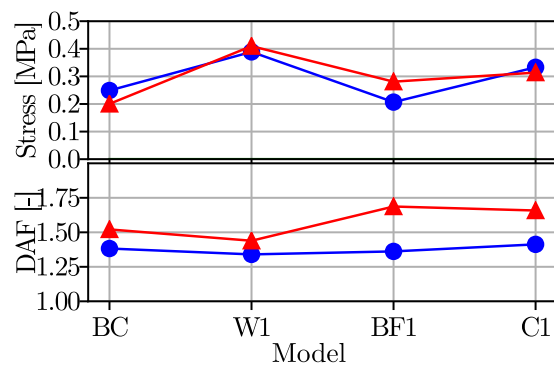
Figure 6.91: Variation of the DAF of normal stress with vehicle load in the longitudinal direction (S11) at the top of the web at midspan of the Modena Viaduct

The longitudinal stress variation in the top of the web is smaller (Figure 6.91). There is less variation between parametric cases, with the increase in stress between models varying no more than $0.2\,MPa$.

Considering the S22 stress variation, which increases with the transverse sectional deformations and is the stress induced in the plane of the shell perpendicular to the longitudinal direction, shows large changes with different parametric cases (Figure 6.92). In particular, when the bottom flange thickness is reduced, greater transverse bending in this section increases the S22 stress variation from the traffic loading. As a result, the stress variation in the bottom flange can be double that of the benchmark case, yet the concrete strength is not increased by double for the BF1 case, which shows the most critical stress variation. This would mean additional design may be required to ensure the bottom flange of the cross section stayed in compression under normal loading situations for this BF1 case. This phenomenon is similar to that seen in the previous bridges when the top flange was being reduced, as here it is the flange supporting the track.

Overall, the stress variations are very similar between the *Full* and *Simple* models. With relation to the DAF, the S11 stresses in the bottom flange have consistent values of about 1.25, whereas the web S11 and the bottom flange S22 stresses are less consistent between cases, and as a result have DAF values varying between 1.25 and 1.75.
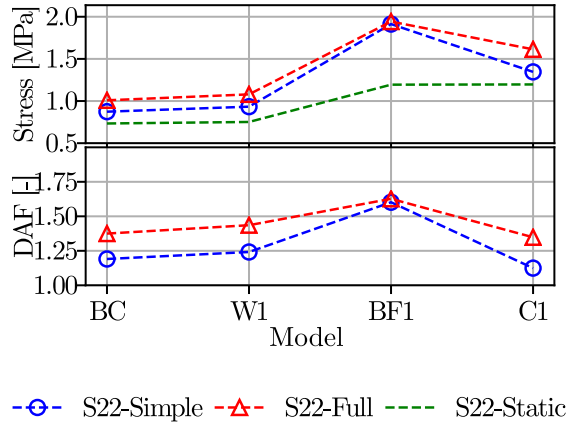
Figure 6.92: DAF of normal stress variation from vehicle load in the lateral direction (S22) in the bottom flange at midspan of the Modena Viaduct
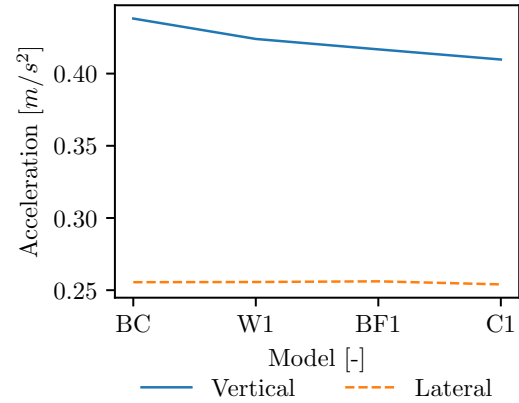
Figure 6.93: Variation of the Vehicle accelerations with model

6.3.5.3   Vehicle Accelerations

The maximum vehicle lateral (A2) and vertical (A3) accelerations for the worst case velocity, in any of the eight carriages, using the *Full* model with irregularities is compared between the models of the parametric analysis in Figure 6.93. Here, it is seen the lateral accelerations are smaller than the vertical and also relatively consistent between parametric cases. The vertical accelerations are shown to decrease slightly but also have relatively similar magnitudes. As a result the vehicle accelerations are allowable under the parametric analysis.

6.3.5.4   Construction Details

Considering the bridge under the combined parametric case, compared to the benchmark case, the details of what it possibly means for construction is shown in Table 6.16. This allows decisions on the viability of introducing the HPC into this type of structure, based on cost analysis of the material used, the capacity of piers required, and the capacity of the lifting equipment required. It shows a considerable saving in the bridge mass, but also with a large increase in concrete strength (2.74 times larger as the initial value was very small for a precast element). The precast elements are reduced in mass by 22%, which can reduce the capacity of lifting equipment required, and the total permanent mass per span reduced by 18%, which will impact the design of the piers, potentially saving material and money here.

	BC	C1
Concrete Strength [MPa]	35	96
Precast element Mass [$\times 10^3$ kg]	670	524
Non-Structural mass [$\times 10^3$ kg]	101	101
Total mass of span [$\times 10^3$ kg]	771	625

Table 6.16: Variation of construction details between benchmark (BC) and combined case (C1) of the Modena Viaducts. Non-structural mass refers to mass of track and other deck top permanent loads that are not a part of the structure

6.3.5.5 Conclusions to the Parametric Analysis of the Modena Viaduct

The parametric analysis of the Modena Viaduct has shown a viable option for the implementation of HPC into the bridge, reducing the geometry and mass as a result, without compromising the performance of the bridge or the safety of the train. It is found that the longitudinal stress variations in the concrete for the C1 case are of an acceptable level compared to the benchmark case, considering only small increases, hence the flexural demand is not increased significantly. If the flexural demand exceeds the capacity then additional prestressing or concrete strength increases can be introduced to increase the capacity. The vehicle accelerations are found to be consistent with the benchmark case, and hence of no concern. Likewise, the displacements of the bridge are very similar between cases. The bridge accelerations are considerably higher for the combined case, but below acceptable limits. As a result, the conclusions made in Section 5.5.3.6, which allowed the web and bottom flange thicknesses to be 66 and 75% of the original, providing the structural rigidity is maintained, holds true for this bridge type.

6.4 Comparison between the Bridge Models

This thesis has seen four different bridge cross sections analysed. In each, parametric analysis, through changing the geometry and then the concrete strength to maintain the structural rigidity is performed on each benchmark case. This leads to a series of parametric cases, some of which are viable and some of which are not. Comparison of the Modena, Piacenza, Kyung-bu and the three spanned dual U-beam bridges is shown in Figure 6.94. This shows for each parametric case for each bridge the comparison between the accelerations obtained by the *Simple* and *Full* models.

In Figure 6.94, it can be seen that the accelerations of the *Full* model are generally higher than that of the *Simple* model, except when modelling the Piacenza viaduct, for reasons previously explained in Section 6.2.3.1. For the Modena and Kyung-bu viaducts the accelerations appear to be up to 2 m/s^2 larger than the corresponding *Simple* model value. In the case of the dual U-beam bridge the accelerations of the *Full* model are significantly higher than the simple
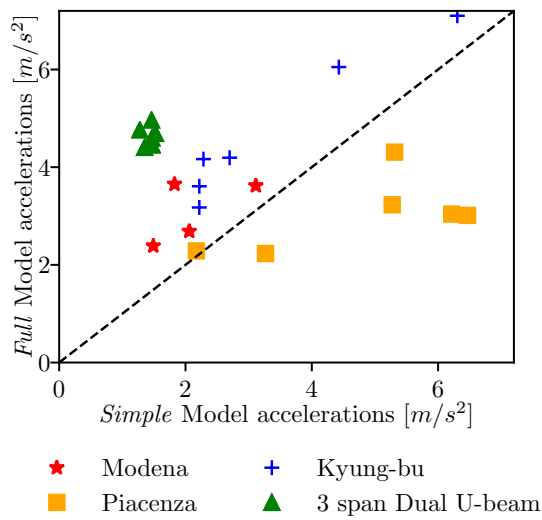
Figure 6.94: Comparison of the accelerations obtained by the *Simple* and *Full* models for each of the parametric cases for each bridge, using the maximum acceleration found along the centrelines for each bridge, considering the applicable range of velocities of each bridge
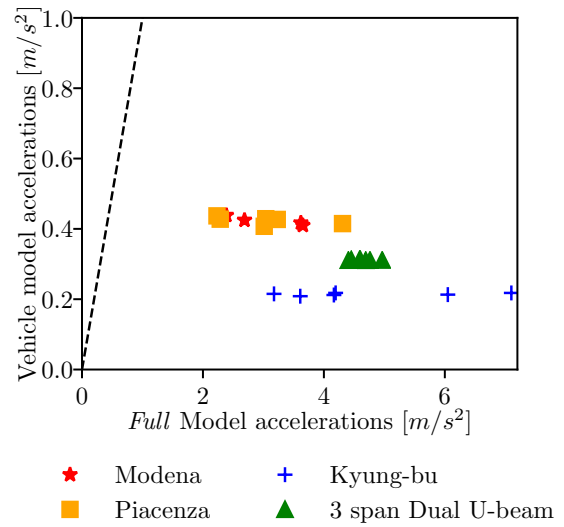
Figure 6.95: Comparison of the maximum vehicle accelerations against the maximum bridge deck accelerations for the *Full* model for each parametric case, of each bridge, using the maximum acceleration found along the centrelines for the bridge, and maximum vehicle acceleration at any carriage centre of mass, considering the applicable range of accelerations of each bridge

model, but the consistency between parametric cases is highlighted by the proximity of the points to each other. This is probably partly due to the lack of changes to the top flange thickness in this bridge, which as this chapter has found, the changes to the stiffness of the surface supporting the track has a high influence on the bridge accelerations.

Consideration of the maximum vehicular accelerations at the centre of mass of each carriage, in comparison with the bridge deck accelerations, both vertically, is shown in Figure 6.95. The dashed black line in this figure indicates the location of equal accelerations for the bridge and vehicle. It can be seen that all vehicle accelerations are much lower than the corresponding bridge accelerations, which is as expected due to the layers of suspension in the vehicle to aid comfort of passengers. What is notable is although each point for each bridge represents a different parametric case, there is no discernible difference in the vehicular accelerations attributed to each bridge. The points show that the bridge accelerations have little impact on the vehicular accelerations, hence they remain similar for all parametric cases of the bridge. The reasoning for the difference in accelerations between models is the differing deflections of the bridge. This links back to Section 4.1.6, where it was shown how different levels of prestress effected the accelerations in the vehicle, due to the change in the bridge profile. This means that for vehicle comfort over bridges, it is the displacements in the track that need to be controlled.

This section shows designers that the choice of model can severely impact the accelerations that are found in the bridge. It also shows the inadequacy of the *Simple* model in comparison with the *Full* model, especially considering current guidelines on bridge accelerations make no reference on the type of model to be used. Clearly allowance for the type of model should be made with different limits of accelerations in each case. This is especially apparent when the maximum bridge acceleration related to the *Full* model is 3.75 times greater than the equivalent *Simple* model acceleration. In addition, design for passenger comfort, (the vehicular accelerations) is strongly related to the running profile of the rails, impacted by both the irregularities and the bridge deflection, and so ensuring deviations from flat are kept small will help vehicle accelerations. Alternatively, the mean of all *Full* to *Simple* model accelerations is 1.76, with a standard deviation of 1.01. Considering this includes the models where the *Simple* model accelerations are higher than the *Full* model accelerations for the Piacenza viaduct, if these results are excluded then the mean becomes 2.1 and the standard deviation 0.9. These are both lower than the maximum value, but still significantly large that it necessitates a reconsideration of the limit to the accelerations.

6.5   Conclusions to the Analysis of Alternative Bridge Cross Sections

In this chapter, three alternative bridges have been studied, and the conclusions of the parametric analysis of Section 5.5.3.6 tested against these bridges. In general, it was found that under the *Full* vehicle, the bridges experienced larger acceleration responses due to the frequency variation of the wheel forces as a result of irregularities, in both the Kyung-bu and Modena viaducts. However, in the Piacenza viaduct the introduction of the track and *Full* model actually reduces the maximum bridge accelerations, due to a combination of the spreading of the load by the track and occurring at a velocity that has a narrow range of frequencies for the force variation that normally amplifies the response of resonant modes. This is a special case, due to the exclusion of a diaphragm in the design of this bridge.

In comparison with the design of the double U-beam bridge, the bridges in this chapter display larger S22 stress variations in regions studied. This is due to increased transverse flexibility in many of these bridges leading to increased sectional deformations. Moreover, this increased transverse flexibility has reduced the applicability of the beam model to estimate the response of the bridge as it consistently underestimates the bridge accelerations. The level of bridge accelerations are so low in the beam model in comparison to the *Full* vehicle model, that it must be recommended in future design codes that dynamic analysis is in the form of models that take into account the transverse flexibility of the section as this contributes significantly to the response.

Comparison between the Kyung-bu and Piacenza viaducts, indicates that by introducing an additional central web to the Kyung-bu viaduct, resulting in a cross section similar to the Piacenza viaduct, would enable larger reductions to the top flange thickness. This is due to the additional support and reduced transverse flexibility of the top flange. However, as a result, reductions to the web thickness result in larger increases to the accelerations, in comparison to when there were only two webs in the section.

Comparison of the different bridges in this chapter with the bridge of the previous chapter showed the inadequacy of the *Simple* model in comparison with the *Full* model. Maximum accelerations can be up to 3.75 times greater for the *Full* model than the *Simple* model, with a mean of the models showing amplification of the accelerations by the *Full* model being 2.1, which clearly shows the inadequacies of the acceleration limit being the same considering using a moving point load model and using a full vehicle model with irregularities.

Overall, parametric cases saving the precast mass by 7.3, 21 and 22% for the Kyung-bu, Piacenza and Modena Viaducts respectively, have been identified as potential solutions. This shows significant mass reductions can be achieved, which could possibly bring many benefits for the construction costs. These reductions can be achieved by the implementation of HPC,

using concrete strengths up to a maximum of 96 MPa. The implementation of higher strength concretes would lead to decks where the design is governed by the acceleration limits, rather than by sectional capacities.

Chapter 7

Conclusions

This chapter summarises the main conclusions of this thesis, splitting them up into conclusions related to modelling and conclusions related to the behaviour and design of HSR bridges. In addition, recommendations for the updating of codes to reflect the findings of this thesis are suggested, before presenting a summary of future work that can be undertaken both in an academic and industrial environment.

7.1 Conclusions for Modelling

This thesis incorporates very complex and realistic models for the bridge, track, wheel-rail interaction and train. These are models that previously are not found together in existing literature due to their complexity. This section will conclude some of the findings relating to the generation of these components of the model.

7.1.1 Conclusions related to Bridge Modelling

From the literature review (Section 2.1.6), it is initially concluded that the bridge should be modelled with shell elements, using beam element models to complement the results through quick to run simulations. It is also concluded that continuous bridges should lead to smaller accelerations than one spanned alternatives. Through this thesis, a detailed set of conclusions have been drawn in relation to these aspects. It was found that:

- A beam element model applied with the bridge's cross sectional properties does not generate the same bridge modal frequencies as a shell element model. This is due to two reasons:

    - The boundary conditions should be located at a realistic position (which is easier

       to implement when the deck is represented through shell elements), and not at
the centroid of the beam model. All current finite element packages already allow
the positioning of the boundary conditions away from the centroid using outrigger
systems (rigid or stiff beams).

   – The additional sectional deformation captured by the shell model which cannot be
captured through beam models, has an impact on the deck modal frequencies.

- A beam model with these adjusted boundary conditions, is able to predict velocities for
which the bridge will have resonant problems related to the fundamental mode, however
it does not accurately predict velocities for which higher frequency modes have resonance
problems.

- Generally the beam model is not able to provide a good representation of the dynamic
performance of these bridge types, as the sectional deformations are not negligible. The
shell models provide more accurate responses, and clearly more representative of reality.
If beam element models are used, they would lead to lower accelerations and unidentified
resonance of high frequency modes, contributing to poor design.

- As expected, it is shown in Section 4.1.3, that the use of one span bridges leads to larger
accelerations than continuous bridges with three or more spans. However, the use of
continuous bridges with two spans leads to similarly large bridge accelerations as single
span bridges.

In addition, some further conclusions related to the bridge model are as follows:

- Maximum accelerations are often found at the edges of the slab, where they are can-
tilevered, however these are not relevant to the potential derailment of the train and
hence the accelerations in the slab should be taken from appropriate regions (under the
rail track).

- Modelling of the prestressing tendons or strands are found to be important for incorpo-
rating their stiffness into the section. However, the stress in the tendons need not be
applied for the dynamic models as it does not significantly change the dynamic response
of the bridge.

- It is found that inclusion of the vehicular mass as a distributed non-structural mass
spread along the length of the bridge when studying the bridge frequencies, as expected
reduces the modal frequencies. However, these lower frequencies are not representative
of the frequency of oscillation of the bridge under vehicular load. Adding the traffic
mass is a normal design practice in footbridges, which should not be extended to HSR
bridges, as demonstrated in this work.

7.1.2   Conclusions related to the Track

In the literature review (Section 2.3.4), it is found that when the track is modelled, the majority of literature focus on ballasted tracks, although the current design tendancy is to move towards using slab track. After the literature review, it was determined that a comparison between tracks is required. In this thesis, ballasted track is compared to slab track in Section 4.2.3. It is found that ballasted models tend to lead to bridges with smaller accelerations, due to the higher mass and the greater deformability of the track structure causing greater distribution of the load. However, the models using ballasted track require more elements and hence are more computationally expensive. After considering the current drivers towards the use of slab track, these systems are modelled in all other cases in this thesis.

The literature identifies that the track has more influence on the vehicle than the bridge dynamics. From this work, it is found that the track stiffness has a significant impact on the bridge accelerations within one track system. However, the main contribution to the variation in the bridge acceleration response is the mass of the track. This highlights the need for consideration of a range of lifespan track masses, in particular for ballasted tracks, when dynamically designing a bridge.

7.1.3   Conclusions related to the Vehicle

The conclusions from the literature review (Section 2.2.8) identify a lack of train vehicle models being combined with a shell element model for the bridge. All the sophisticated vehicle models were using very simplistic bridge structural models, and the sophisticated bridge models used a very simplistic description of the traffic load through moving loads. This thesis incorporates these two models together. Comparison is made with the HSLM load models, but it is found that the *Full* vehicle model with irregularities generated bridge accelerations far greater than this load model. Siemens Velaro trains are modelled in this thesis, as their properties have been fully reported in literature. For most of the work, the train of eight carriages is used. This number of carriages generates 16 % smaller accelerations then a sixteen carriage train (both standard lengths), but is much more computationally efficient, with computational times less than half. Other conclusions relating to the vehicle include:

- Variation of the primary vehicle stiffness affects the bridge dynamics, but more significantly the vehicle dynamics, whereas secondary stiffness does not affect the bridge dynamics, but has significant consequences on the vehicle behaviour.

- The identification of vehicle accelerations by using the *Full* vehicle model are generally well within the limits of comfort for the irregularities and bridges modelled (using a representaive benchmark case from a built structure database).

- Running two vehicles simultaneously across the bridge in opposite directions can double the bridge accelerations, depending on the delay in entering of the two vehicles. An equation is proposed to determine whether any particular bridge mode is in resonant or cancellation behaviour based on the delay between the two trains entering the bridge.

7.1.3.1   Conclusions related to the Wheel-Rail Interaction

From the literature (Section 2.4.6) it is identified that the wheel-rail interaction is the most complicated part of the model, significantly increasing the computational time. In this thesis, for the modelling of the wheel-rail interaction, user elements are required in ABAQUS. These allow incorporation of an elastic contact method using Hertz non-linear contact theory to model the wheel-rail contact. In addition, irregularities are incorporated in the user element. This allows modelling of the motions and forces between the wheel and rail, representing a more realistic approach than using fixed magnitude wheel forces. As a result, the forces between the wheel and rail are able to be tested for comparison against derailment criteria, and are found to be well below the limits, so are not studied further for the rest of the parametric analysis in this thesis. It is identified in the literature review that a study on the tangential contact force models will be required. Based on representative wheel-rail contact force, ellipse sizes and creepages between the wheel and rail, the heuristic tangential force model is found to be the appropriate model.

One of the most significant findings of the modelling work occurs when using the wheel-rail interaction model. Its inclusion with irregularities leads to significant increases in accelerations in the bridge. It is in the case that when frequencies, specifically f_{v7}, relating to the axle distance and velocity of the train, match the frequencies of bridge modes, for velocities currently operated at by HSR trains, whilst in the presence of irregularities, that the accelerations are amplified dramatically, by up to a factor of 3.75. The irregularities cause force variations between the wheel and rail that cause amplification of the higher frequency bridge modes, in comparison with models without irregularities and moving point load models. Of the individual irregularity components, the cross level is the main contributor to increased lateral bridge accelerations, whereas vertical ones affect the vertical bridge accelerations. It is found that the irregularities would cause variations to the wheel-rail contact force.

7.2   Conclusions related to the Behaviour and Design of HSR Bridges

Four types of precast HSR bridge decks have been studied in this thesis considering four different types of cross sections. The most detailed analysis is performed on the bridge with two precast U-beams, topped with a cast insitu slab, which is the most common solution

for HSR bridges when precast elements are employed. Further analyses are performed on a fully-precast span-by-span single celled box girder (using the Kyung-bu benchmark case), fully-precast span-by-span double celled box girder (using the Piacenza viaduct benchmark case) and fully-precast span-by-span trough style (U-shaped) bridge (using Modena viaduct benchmark case). The general observations made with regard to these bridges are:

- Stresses in the non-running surfaces of the bridge (bottom flange and webs), are similar between the *Simple* point load and *Full* vehicle-irregularity-bridge models. Stresses in the running surface of the vehicle (top flange in all models but the trough style cross section bridge, where it is the bottom flange), can have greater disparity between the *Simple* and *Full* models due to activation of high frequency modes leading to greater transverse and vertical deformations in the bridge.

- Magnitudes of deflection under dynamic loads are similar between *Simple* and *Full* models vertically, with slightly higher lateral deformations with the *Full* model, due to increased deformation of the bridge and additional lateral loading introduced by the *Full* vehicle model.

- Bridge accelerations under the influence of the *Full* model are generally significantly higher than those of the *Simple* model, and these accelerations are often the most critical part of design. Therefore the *Full* model is required to take into account the accelerations. Current load models used by bridge designers (movable load models) clearly underestimate the value of the deck accelerations.

- Vehicle accelerations are not of concern for these bridges as they stay fairly constant, independent of the bridge models and their parametric cases.

Overall, it is found that the accelerations are as expected the most critical factor in the design of the bridges. However, cases have been found for each bridge tested, to enable saving up to 22% of the precast bridge structure mass, by implementing strength increases to high performance concretes of up to 96 MPa, enabling the structural rigidity and capacity to be maintained. This is achieved through reduction of combinations of the top flange, bottom flange and web thicknesses, with the accelerations particularly sensitive to the flexibility of the structure directly supporting the track (the top flange in all cases but the U-shaped trough style bridge). This high sensitivity to the flexibility of the track supporting surface leads to unsatisfactory accelerations exceeding the 5 m/s^2 limit for slab track for reductions tested in the fully precast box girder. In addition, reductions to the depth of the structure, whilst maintaining the span length, were found to be inappropriate in initial studies and hence were not widely applied under parametric analysis. The reductions in mass can lead to lower capacity lifting equipment being required for construction, also reducing the vertical capacity required of piers and abutments, which potentially reduces the amount of material required

here too. Further, specific details for each bridge cross section type under parametric analysis are outlined herein.

7.2.1 Conclusions Specific to the Double U-beam Bridge

A detailed parametric analysis was made on the double U-beam bridge. From this the following specific conclusions were made:

- The bridge is studied parametrically using both a one and three spanned case. The three spanned case shows smaller accelerations, as expected, than the single span model.

- Accelerations in the one span case are higher than the limit of $5\,m/s^2$ for all parametric cases including the benchmark case. However, under parametric analysis the level of accelerations stayed constant. For the three spanned continuous bridge, accelerations are below this limit.

- Reductions to the depth of the bridge are tested for the one span case only, but deemed to be inefficient, due to very large increases in concrete strength required to maintain the structural rigidity.

- Parametric analysis is applied to the U-beams by reducing the thickness of the web and bottom flange. These are tested individually and finally combined together. Overall, it is found that the web thickness can be reduced to 66% of the original thickness and the bottom flange to 75% of the original thickness. For this combined web and bottom flange case, reductions in thickness are combined with an increase in concrete strength of 56% (from 60 to 93.6 MPa). This leads to an 18% reduction in the mass of each precast beam and a reduction of 8% of the total bridge mass per span.

- Vertical displacements do not change significantly between parametric cases. The DAF of the lateral displacements can change significantly between *Simple* and *Full* models, and between parametric cases, however the magnitude of lateral deflections is very small and insignificant.

- The variation in the stress is larger in the bottom flange for normal stresses in the longitudinal direction than in the lateral direction, although stresses do not change significantly between parametric cases.

7.2.2 Conclusions Specific to the Fully Precast Span-by-span Single-Cell Box Girders

The Kyung-bu viaduct was selected as a benchmark case to illustrate the behaviour of this bridge type. For this bridge type, it is identified that:

- Reductions of the bottom flange and web thickness to 75% and 66% of the original thickness is viable both individually and combined together as the accelerations are below the limit.

- Reductions to 75% of the original thickness for the top flange is tested. It is found not to be viable due to large accelerations, due to reduced transverse stiffness of the slab. Therefore, for this bridge type the fact of precasting the whole section (in comparison with the previous bridge type in which the slab is built in-situ) does not allow for further reductions of the slab thickness.

- The combined bottom flange and web case is the most viable case with the biggest material savings. This leads to a 7.4% decrease in the precast mass of the bridge for a increase of 78% of the strength in the concrete (with a characteristic strengths up to 71 MPa).

- The variation of the displacements and stresses are relatively similar between parametric cases and hence not of concern for these parametric cases.

7.2.3 Conclusions Specific to the Fully Precast Span-by-span Double-Cell Box Girders

The Piacenza viaduct was selected as a benchmark case to illustrate the behaviour of this bridge type. For this bridge type, it is identified that:

- The lack of diaphragms in this bridge, leads to the high accelerations particularly in the *Simple* model. It shows the impact of diaphragms on reducing the slab accelerations. The use of diaphragms is recommended in this bridge type.

- The *Simple* model generates larger accelerations than the *Full* model leading to over-design and restraining the possibility of using thinner elements in the cross section. For instance, when using this load model, only the bottom flange thickness can be reduced to 75% of the original value.

- Considering the *Full* model, all cases studied lead to viable accelerations. This means that in the case of thickness of the webs, bottom flange and top flange being 66, 75 and 75% of the original, the increase in concrete strength to 74 MPa from the original 35 MPa is acceptable in maintaining the bridge structural rigidity and an acceptable level of accelerations. This leads to a 21% reduction in the precast mass of the bridge.

- The implementation of an intermediate web (double versus single box girder) allows a certain reduction in the acceleration in the top flange and further reductions in their thickness as highlighted above.

- The stresses and displacements are found to stay relatively similar between parametric cases. One exception is the longitudinal stress in the bottom flange which shows some small increase in stress variation for reductions in mass. Good correlation can also be found in all cases between the *Simple* and *Full* model, except for the stress in the top flange where reductions to this thickness lead to increased stresses in the *Simple* model.

- This bridge type can also be constructed in a different way, with two precast U-beams, positioned adjacently and tied transversely, with a cast in-situ slab at the top and transverse prestressing bars at the bottom. In this case the precast components can be altered in a similar way to the C1 case, with 66% of the original web thickness and 75% of the original bottom flange thickness. This would lead to acceptable accelerations in the *Full* model. This would enable a reduction in the bridge mass of 13% for a concrete strength increase of 61%.

7.2.4 Conclusions Specific to the Fully Precast Span-by-span Trough Style Bridge

The Modena viaduct was selected as a benchmark case to illustrate the behaviour of this bridge type. For this bridge type, it is identified that:

- The combined reductions to the web and bottom flange thickness of 66% and 75% of the original is a viable parametric case. This requires increases in concrete strength by 174% (up to 96 MPa), but it reduces the mass of the precast span by 22% and the total permanent load per span by 18%

- The variations in stresses from the dynamic loading in the longitudinal and lateral directions in the bottom of the slab are particularly affected by reductions to the bottom flange thickness due to the additional transverse bending that occurs.

- The deflections in the bridge are similar for all parametric cases, and also between *Simple* and *Full* models.

7.3   Recommendations for the Development of Codes

Much of the work in this thesis is made with or compared to BS EN 1991-2:2003 (2010). As a result, certain deficiencies are found, which require updating.

From this work it is identified that for all these bridge sections the accelerations cannot be accurately represented by models using beam elements (where all the bridge cross sectional properties are assigned to the beam element and the cross section is assumed to be undeformed under loading). This is due to the consistent underestimation of the accelerations

this model gives, due to the differences in the frequencies as a consequence of the unrealistic boundary conditions and lack of sectional deformations. The lack of transverse deformations is particularly a problem in the slab where the accelerations of the bridge are much higher due to the larger flexibility of the slab and the existence of sectional deformations. It is not defined in BS EN 1991-2:2003 (2010) what kind of bridge model is required to be modelled for dynamic analysis, so it should be clarified, with new limits to acceleration based on the type of model used, or recommending designers the use of shell elements, in particular when sectional deformations are expected, or when there is a significant difference between the frequencies obtained from the beam and shell models.

The high speed load models defined in BS EN 1991-2:2003 (2010) (HSLM A and B), which provide an envelope of the loading signatures to cover the resonant loading patterns generated by all possible trains, is inadequate for representing a real vehicle. Modelling of the vehicle with *Simple* moving point loads results in accelerations within the range generated by the HSLM model. However, the additional response generated by the inclusion of the *Full* vehicle, irregularities and the wheel-rail-interaction is not within this range.

Rail imperfections should be considered in the design, either by using *Full* models or by implementing safety coefficients that account for the simplicity of the models used in design (when movable load models are used, which cannot implement imperfections). A safety factor of 3.75 (using the maximum value) or 2.1 (using the mean value), developed from the ratio of the *Full* model and *Simple* model acceleration responses, has been shown to be enough for the consideration of imperfections on the basis of the results obtained from load models, for all the analyses considered in this thesis.

If irregularities are to become more commonly modelled, updating and clarification of expected irregularities is required, especially at high speeds. Currently, many researchers use an FRA model to model irregularities for HSR, when the definition of these irregularities is not made for such high speeds. Hence, the irregularities are unlikely to be realistic of a true HSR line. This thesis has used imperfections generated by a German PSD function, but comparison of these profiles was made with respect to the current track maintenance guidelines. This required significant time and work, for which it should not be expected for designers to be undertaking, hence clarification on appropriate models should be made in line with current track maintenance guidelines, such as BS EN 13848-5:2017 (2017).

It is found that the bridge accelerations are not reflected in the design of the vehicle accelerations. The bridge deck accelerations are much higher than the corresponding vehicle accelerations due to the vehicle suspension system. The vehicle accelerations are a reflection of the flatness of the track. This considers both the track imperfections and the bridge deflections. Controlling these is the best way to control the vehicle accelerations. Recommendations should be made that for the control of vehicular accelerations the combined bridge deflections and vertical irregularities should be considered and reduced if possible.

7.4   Further Work

After the work of this thesis, further work is identified in this section. The work would require strong collaboration with industry to ensure its continued applicability. Some of the further research relating to bridges include:

- Expansion of the parameters studied. For example a parametric study on all the bridge types for the span length, keeping constant slenderness, or altering the slenderness, altering the widths of the box girder components and the design of the piers can be developed. This will enable a more comprehensive parametric analysis.

- Study of segmental bridges. This thesis focuses on bridges with span length segments, which is restrictive to the total length of the bridge. Precast segmental bridges can allow more flexibility in span length, achieving longer spans, but extra study is required for the nonlinear analysis in the joints between segments.

- Inclusion of tuned mass dampers, as many bridges studied have seen particular bridge frequencies causing resonant problems, which TMD maybe able to be included and reduce the resonant effect. This may allow even further reductions to the bridge geometry.

- Study of the appropriateness of the acceleration limits considering both track types, the loading method (*Full* vehicle models with irregularities, moving point loads) and the bridge model type (shell or beam element) to find appropriate limits for each model with appropriate safety factors that consider the risk of derailment

- Performing more analysis on a wider range of bridges, trains and velocities in order to provide safety factor recommendations with good confidence.

In addition to further work on the bridge, further research can be made to develop the model, by the following work:

- An investigation in depth of the real rail irregularities found in existing infrastructure and how it evolves with use over the time, with particular study on the influence of supporting structure, such that irregularities common to bridges or to embankments are identified and can be appropriately modelled.

- Developing further understanding of the cause of the force variation between the wheel and rail as the wheel moves along the track. As this is found to be a cause in extra accelerations in the models including the *Full* vehicle and interaction between the wheel and rail, if the force variation can be modelled by a function of speed and irregularity, this will enable a better approximation of the *Full* model, but by using the computationally less expensive moving point load models.

- Developing a more efficient model, by a reduction in the number of elements. Currently, the inclusion of the vehicle requires lots of additional elements to model the wheel-rail-interaction. Although some elements are deactivated when not in use, the computational time is still large. Development of a more efficient user element model could potentially reduce the number of elements and the computational time.

- Developing a model with a nonlinear concrete model, accounting for greater changes in properties of the material, such as any potential change in the damping properties of the HPC.

- Modelling with further vehicles, as only one train vehicle was used here. As multiple types of vehicle exist, with different weights and characteristics, knowledge of further trains would make conclusions more valid for a range of vehicle, rather than just the one studied. However, realistically this would require the aforementioned efficiency gains to the model to enable multiple vehicles with enough resolution of velocities to correctly determine the bridge response.

Finally, a real world study should be studied, acquiring acceleration data from a HSR train passing over a bridge. This would require knowledge of the structural properties of the bridge and vehicle, as well as data on the track irregularities. This work would enable a better understanding of the effect of the irregularities on the bridge, validating the additional safety factor or lower acceleration limit required to be applied to the accelerations found by using a moving load model, rather than a *Full* vehicle model with irregularities.

Bibliography

Abad González, I., Santamaria Caballero, G., Antón Diaz, J., Martín Nieto, C., Niño Mendizábal, F., and Alcocer Olmos, P. (2011a). Viaductos de Ferrocarril en Ioannina-Igoumenitsa (Grecia). In *V Congreso de ACHE*, pages 1–10.

Abad González, I., Santamaria Caballero, G., Martín Nieto, C., Ontañón Carrera, G., and Izquierdo López, D. (2011b). Viaductos SG-25, SG-27 y SG-28 en la Nueva Línea de Alta Velocidad Atenas-Tesalónica (Grecia). In *V Congreso de ACHE*, pages 1–8.

AFGC (2013). *Ultra High Performance Fibre-Reinforced Concretes: Interim Recommendations*. AFGC, France.

Aied, H. and González, A. (2011). The Effect of Strain Rate on the Total Response of a Structure subject to a Moving Load. In *CIVILCOMP2011 The Thirteenth International Conference on Civil, Structural and Environmental Engineering Computing*.

Aitcin, P. C. (1998). *High-Performance Concrete*. E&FN Spon, London, UK, 1 edition.

Akin, J. E. and Mofid, M. (1989). Numerical Solution for Response of Beams with Moving Mass. *Journal of Structural Engineering*, 115(1):120–131.

Alamaa, A. (2016). *High-speed railway embankments - a comparison of different regulations*. Masters thesis, KTH Royal Institute of Technology.

Almansour, H. and Lounis, Z. (2011). Design of Prestressed UHPFRC Girder Bridges According to Canadian Highway Bridge Design Code. In *Designing and Building with UHPFRC*, pages 295–316. John Wiley & Sons, Inc.

Amarume, S., Taniguchi, S., Koizumi, K., Kondou, T., Arita, H., and Itou, A. (2003). Design and construction of the Shinkansen structure (eleven-span continuous PC box girder) that applied a highly efficient lightweight aggregate for the first time in the world. In *Structures for High-Speed Railway Transportation*, pages 124–125, Antwerp. IABSE.

Antolín, P. (2013). *Efectos Dinámicos Laterales en Vehículos y Puentes Ferroviarios sometidos a la Acción de Vientos Transversales*. PhD thesis, Universidad Politécnica de Madrid.

Antolin, P., Goicolea, J., Oliva, J., and Astiz, M. (2012). Nonlinear Train-Bridge Lateral Interaction Using a Simplified Wheel-Rail Contact Method Within a Finite Element Framework. *Journal of Computational and Nonlinear Dynamics*, 7(4):41014.

Antolín, P., Goicolea, J. M., and Astiz, M. Á. (2012). Strategies for Modelling Train-Bridge Lateral Dynamic Interaction. In Xia, H., De Roeck, G., and Goicolea, J. M., editors, *Bridge Vibration and Controls*, chapter 6, pages 195–235. Nova Science Publishers.

Antolín, P., Goicolea, J. M., Astiz, M. A., and Alonso, A. (2010). A methodology for analysing lateral coupled behavior of high speed railway vehicles and structures. *IOP Conference Series: Materials Science and Engineering*, 10:012001.

Antolín, P., Zhang, N., Goicolea, J. M., Xia, H., Astiz, M. Á., and Oliva, J. (2013). Consideration of nonlinear wheel–rail contact forces for dynamic vehicle–bridge interaction in high-speed railways. *Journal of Sound and Vibration*, 332(5):1231–1251.

Arenas de Pablo, J. J., Capellán Miguel, G., Sacristán Montesinos, M., and Fernandez Antón, J. (2011). Viaducto Sobre El Río Tinto en la Línea de Alta Velocidad Sevilla-Huelva. In *V Congreso de ACHE*, pages 1–10.

Aripov, N., Aliyev, R., Baratov, D., and Ametova, E. (2016). Features of Construction of Systems of Railway Automatics and Telemechanics at the Organization of High-Speed Traffic in the Republic of Uzbekistan. *Procedia Engineering*, 134:175–180.

Armisén Manterola, J., Astiz Suárez, M. Á., and Martínez Cutillas, A. (1999). Puentes de Ferrocarril de Alta Velocidad. *Revista de Obras Publicas*, 146(3386):43–77.

Arvidsson, T. (2018). *Train-Track-Bridge Interaction for the Analysis of Railway Bridges and Train Running Safety*. Doctoral thesis, KTH.

Au, F., Wang, J., and Cheung, Y. (2002). Impact study of cable-stayed railway bridges with random rail irregularities. *Engineering Structures*, 24(5):529–541.

Ayasse, J. and Chollet, H. (2005). Determination of the wheel rail contact patch in semi-Hertzian conditions. *Vehicle System Dynamics*, 43(3):161–172.

Bastin, R. (2006). Development of German non-ballasted track forms. *Proceedings of the Institute of Civil Engineers: Transport*, 159(1):25–39.

Bathe, K.-J. (1996). *Finite Element Procedures*. Prentice-Hall International, London, UK.

Bennett, D. (2007). Channel Tunnel Rail Link section 2: railway systems. *Proceedings of the Institution of Civil Engineers - Civil Engineering*, 160(6):49–53.

Berawi, A. R. B. (2013). *Improving Railway Track Maintenance Using Power Spectral Density (PSD)*. PhD thesis, Universidade do Porto.

Bezin, Y., Farrington, D., Penny, C., Temple, B., and Iwnicki, S. (2010). The dynamic response of slab track constructions and their benefit with respect to conventional ballasted track. *Vehicle System Dynamics*, 48(sup1):175–193.

Bowe, C. and Mullarkey, T. (2005). Wheel-rail contact elements incorporating irregularities. *Advances in Engineering Software*, 36(11-12):827–837.

BS EN 13674-1:2011+A1:2017 (2011). Railway applications. Track. Rail. Vignole railway rails 46 kg/m and above.

BS EN 13715:2006+A1:2010 (2011). Railway applications - Wheelsets and bogies - Wheels - Tread profile.

BS EN 13848-5:2017 (2017). Railway applications - Track - Track geometry quality- Part 5: Geometric quality levels - Plain line, switches and crossings.

BS EN 13848-6:2014 (2014). Railway applications — Track — Track geometry quality Part 6 : Characterisation of track geometry quality.

BS EN 14363:2016 (2016). Railway applications. Testing and Simulation for the acceptance of running characteristics of railway vehicles - Running Behaviour and stationary tests.

BS EN 1990:2002 +A1:2005 (2010). Eurocode - Basis of structural design.

BS EN 1991-2:2003 (2010). *Eurocode 1: Actions on structures - Part 2: Traffic loads on bridges.* BSI, 3 edition.

BS EN 1992-1-1:2004 (2004). *Design of concrete structures-Part 1-1: General rules and rules for buildings.* BSI, London, UK.

BS EN 1992-2:2005 (2005). Eurocode 2 : Design of concrete structures. Concrete bridges. Design and detailing rules.

BSI Group (2011). BSI Standards Publication Railway applications — Track — Rail. (January).

Buitelaar, P. (2004). Heavy Reinforced Ultra High Performance Concrete. In Schmidt, M., Fehling, E., and Geisenhansluke, C., editors, *Ultra High Performance Concrete (UHPC) Proceedings of the International Symposium on Ultra High Performance Concrete*, pages 25–36. Kassel University Press.

Calgaro, J., Tschumi, M., and Gulvanessian, H. (2010a). Combinations of actions for road bridges, footbridges and railway bridges. In Gulvanessian, H., editor, *Designers' Guide to Eurocode 1: Actions on Bridges*, chapter 8, pages 215–240. Thomas Telford Ltd, London, UK.

Calgaro, J., Tschumi, M., and Gulvanessian, H. (2010b). Traffic loads on railway bridges. In Gulvanessian, H., editor, *Designers' Guide to Eurocode 1: Actions on Bridges*, chapter 6, pages 145–190. Thomas Telford Limited, London.

Cantero, D., Arvidsson, T., Obrien, E., and Karoumi, R. (2016). Train – track – bridge modelling and review of parameters. *Structure and Infrastructure Engineering*, 12(9):1051–1064.

Capellán Miguel, G., Beade Pereda, H., Arenas de Pablo, J. J., García Arias, P., and Meana Martínez, I. (2014). Diseño del Puente Arco de Alta Velocidad sobre el Rio Almonte en el Embalse del Alcántara. In *VI Congreso de ACHE*, pages 1–10.

Chen, Y., Zhang, B., Zhang, N., and Zheng, M. (2015). A Condensation Method for the Dynamic Analysis of Vertical Vehicle–Track Interaction Considering Vehicle Flexibility. *Journal of Vibration and Acoustics*, 137(4):041010.

Claus, H. and Schiehlen, W. (1998). Modeling and Simulation of Railway Bogie Structural Vibrations. *Vehicle System Dynamics*, 29(sup1):538–552.

Combault, J. (2013). Design and construction of segmental bridges for high speed rail. *Aspire*, 7(4):18–21.

Commission Regulation (EU) (2014). The technical specifications for interoperability relating to the 'infrastructure' subsystem of the rail system in the European Union.

Corres Peiretti, H., Cuesta Allende, H., and Sánchez Delgado, J. (2011). Viaducto del Sar del Eje Atlántico de Alta Velocidad en Padrón (a Coruña). In *V Congreso de ACHE*, pages 1–9.

Cuadrado, M., Gonzalez, P., Goicolea, J. M., Nasarre, J., and Dias, R. (2008). Analysis of lateral displacements in large railway viaducts under traffic loads. Impact on ride safety and passenger comfort. *Proceedings of the 8th World Congress on Railway Research*, pages 1–12.

Dassault Systèmes SIMULIA Corp. (2014). ABAQUS FEA software.

De Man, A. (2002). *Dynatrack: A survey of dynamic railway track properties and their quality.* Doctoral thesis, Delft University.

de Villar Luengo, J. M., Del Valle Pérez, J. A., Carriazo Lara, Á., and Merino Martínez, R. M. (2011). Viaductos del Subtramo Silleda - Vedra - Boqueixón en el Corredor Norte-Noroeste de Alta Velocidad, Tramo Orense - Santiago. -Viaduucto Sobre El Río Ulla. In *V Congreso de ACHE*, pages 1–13.

del Valle Pérez, J. A., Carriazo Lara, Á., Gamino Palomo, J., Peset González, L., and Aja Chao, C. (2011). Construcción Del Viaducto Sobre El Rio Ulla. In *V Congreso de ACHE*, pages 1–14.

Delgado, R., Calcada, R., Ribeiro, D., Pinto, J., Figueiredo, H., and Faria, I. (2008). Assessment of the dynamic response of high-speed railway bridges in interoperable lines. In Delgado, R., Calcada, R., Goicolea, J. M., and Gabaldón, F., editors, *Dynamics of High-Speed Railway Bridges: Selected and revised papers from the Advanced Course on Dynamics of High-Speed Railway Bridges, Porto, Portugal, 20-23 September 2005*, pages 73–98, London, UK. CRC Press.

Delgado, R., Calcada, R., Ribeiro, D., Pinto, J., Figueiredo, H., and Faria, I. (2009). Assessment of the dynamic response of high-speed railway bridges in interoperable lines. In Delgado, R., Calçada, R., Goicolea, J. M., and Gabaldón, F., editors, *Dynamics of High-Speed Railway Bridges: Selected and revised papers from the Advanced Course on Dynamics of High-Speed Railway Bridges, Porto, Portugal, 20-23 September 2005*, pages 73–98, London, UK. CRC Press.

Delhez, R., Esveld, C., Godart, P., and Mijs, J. (1995). Avoidance of Expansion Joints in High-Speed CWR track on Long Bridges. *Rail Engineering International*, 3:7–9.

Dias, R., Goicolea, J. M., Gabaldón, F., Cuadrado, M., Nasarre, J., and Gonzalez, P. (2008). A study of the lateral dynamic behaviour of high speed railway viaducts and its effect on vehicle ride comfort and stability. In Koh and Frangopol, editors, *Bridge Maintenance, Safety, Management, Health Monitoring and Informatics*, pages 724–735. Taylor & Francis Group, London.

Dinh, V. N., Kim, K. D., and Warnitchai, P. (2009). Dynamic analysis of three-dimensional bridge-high-speed train interactions using a wheel-rail contact model. *Engineering Structures*, 31(12):3090–3106.

Doménech Monforte, A. (2014). *Influencia del modelo de vehículo en la predicción del comportamiento a flexión de puentes isostáticos de ferrocarril para tráfico de alta velocidad.* Doctoral thesis, Universitat Politécnica de Valéncia.

Dong Kang, K. and Suh, S. D. (2003). Experience with the Precast Span Method on the Korean High-Speed Rail Project. *Transportation Research Record: Journal of the Transportation Research Board*, 1825(1):15–21.

Durrant, D. W. (2015). The controversial discourse on speed in the case of HS2. *Proceedings of the Institution of Civil Engineers - Urban Design and Planning*, 168(5):241–250.

Esveld, C. (1997). Innovations in Railway Track.

Fagan, N. (2016). Choosing the Right Trackform for a High Speed Railway. In *Fixed Track Forms for High Speed Lines*, pages 4–8, Manchester, UK. Permenant Way Institute.

Fédération internationale du béton. Task Group 6.5. (2006). *Precast concrete railway track systems : state-of-art report*. International Federation for Structural Concrete.

FHWA (2005). *FHWA-PL-05-003: Prefabricated Bridge Elements and Systems in Japan and Europe*. Office of International Relations, Washington, USA, 1 edition.

FIB (2004). *Bulletin 29: Precast Concrete Bridges*. FIB, Lausanne, Switzerland.

FIB (2008). *Bulletin 42: Constitutive modelling of high strength/high performance concrete*. FIB, Lausanne, Switzerland.

Fries, R. H. and Coffey, B. M. (1990). A State-Space Approach to the Synthesis of Random Vertical and Crosslevel Rail Irregularities. *Journal of Dynamic Systems, Measurement, and Control*, 112(1):83–87.

Fritsch, M. (2003). The Valleybridge for the Taiwan high-speed transportation. In *Structures for High-Speed Railway Transportation*, pages 40–41, Antwerp. IABSE.

Frýba, L. (1996). *Dynamics of Railway Bridges*. Thomas Telford Publishing.

Frýba, L. (2001). A rough assessment of railway bridges for high speed trains. *Engineering Structures*, 23(5):548–556.

Fumey, M., Hofman, C., Schilder, Rudolph, Godart, P., Trevin, J. M., Simovic, T., Mißler, M., Kloisters, F., Crail, S., Fila, R., Marvillet, D., Porta, L., and Zuber, P. (2002). Feasibility Study: Ballastless Track. Technical report, UIC.

Gabaldón, F., Goicolea, J. M., Navarro, J. A., Riquelme, F., and Domínguez, J. (2008). Dynamic analysis of hyperestatic structures under high speed train loads. In *Bridges for High-Speed Railways: Revised Papers from the Workshop, Porto, Portugal, 3-4 June 2004*, page 143. CRC Press.

Gabaldon, F., Riquelme, F., Goicolea, J. M., and Arribas, J. (2008). Dynamic analysis of structures under high speed train loads: case studies in Spain. In Delgado, R., Calcada, R., Goicolea, J. M., and Gabaldón, F., editors, *Dynamics of High-Speed Railway Bridges: Selected and revised papers from the Advanced Course on Dynamics of High-Speed Railway Bridges, Porto, Portugal, 20-23 September 2005*, pages 113–132, London, UK. CRC Press.

Galvín, P., François, S., Schevenels, M., Bongini, E., Degrande, G., and Lombaert, G. (2010). A 2.5D coupled FE-BE model for the prediction of railway induced vibrations. *Soil Dynamics and Earthquake Engineering*, 30(12):1500–1512.

Garg, V. K. and Dukkipati, R. V. (1984). *Dynamics of railway vehicle systems*. Academic Press Canada, Toronto.

Garivaltis, D. S., Garg, V. K., and D'Souza, A. F. (1980). Dynamic Response of a Six-axle Locomotive to Random Track Inputs. *Vehicle System Dynamics*, 9(3):117–147.

Goicolea, J., Gabaldón, F., and Riquelme, F. (2006). Design issues for dynamics of high speed railway bridges. In *Bridge Maintenance, Safety, Management, Life-Cycle Performance and Cost*, pages 163–164, Taylor & Francis Group, 6000 Broken Sound Parkway NW, Suite 300, Boca Raton, FL 33487-2742. CRC Press.

Goicolea, J. M. and Antolín, P. (2011). Dynamic Effects of Railway Traffic due to Lateral Motion in Long Viaducts with High Piers. In Papadrakakis, M., Fragiadakis, M., and Plevris, V., editors, *COMPDYN 2011: 3rd ECCOMAS Thematic Conference on Computational Methods in Structural Dynamics and Earthquake Engineering*, pages 1–16, Corfu, Greece.

Goicolea, J. M. and Gabaldón, F. (2008). Design issues related to dynamic effects for high speed railway bridges in Spain. In Delgado, R., Calcada, R., Goicolea, J. M., and Gabaldón, F., editors, *Dynamics of High-Speed Railway Bridges: Selected and revised papers from the Advanced Course on Dynamics of High-Speed Railway Bridges, Porto, Portugal, 20-23 September 2005*, pages 9–18, London, UK. CRC Press.

Goicolea, J. M., Gabaldón, F., Dominguéz, J., and Navarro, J. A. (2008). Dynamic loads in new engineering codes for railway bridges in Europe and Spain. In *Bridges for High-Speed Railways: Revised Papers from the Workshop, Porto, Portugal, 3-4 June 2004*, page 31. CRC Press.

Goicolea-Ruigómez (2008). Service Limit States for Railway Bridges in new Design Codes IAPF and Eurocodes. In Calçada, R., Delgado, R., Campos e Matos, A., Goicolea, J. M., and Galbadon, F., editors, *Track-Bridge Interaction on High-Speed Railways: Selected and revised papers from the Workshop on Track-Bridge Interaction on High-Speed Railways, Porto, Portugal, 15-16 October, 2007*, pages 7–18, Boca Raton. CRC Press.

Grandío Noche, P., Cascales Fernández, J., Couto Worner, S., and Rico Rubio, R. (2014). Comportamiento Estructural Y Criterios de Diseño de Puentes continuos de Vigas Prefabricadas. In *VI Congreso de ACHE*, pages 1–10.

Gray, A., Gaby, P., Brown, G., Kirkcaldie, D., Cato, R., and Sweetman, P. (2003). New Standard Precast Concrete Bridge Beams Stage 1 - Research & Identify Proposed Standard Beam Shapes and Spans. Technical report, Transfund New Zealand.

Güttler, C., Heißelmann, D., Blum, J., and Krijt, S. (2012). Normal Collisions of Spheres: A Literature Survey on Available Experiments.

Hamid, A., Rasmussen, K., Baluja, M., and Yang, T. L. (1983). Analytical Descriptions of track geometry variations. Technical report, Federal Railroad Administration.

Hertz, H. (1882). Ueber die Berührung fester elastischer Körper. *J. Fur Reine und Angewandte Mathematik*, 92:156–171.

Hess, J. (2008). Rail expansion joints - the underestimated track work material? In *Track-Bridge Interaction on High-Speed Railways*. Taylor & Francis, London, UK.

Hseih, J. and Wu, F.-H. (2014). High-Speed Railway Bridges. In Chen, W.-F. and Duan, L., editors, *Bridge Engineering Handbook, Second Edition: Fundamentals*, chapter 8, pages 159–183. CRC Press, Boca Raton, 2 edition.

Iwnicki, S. (1998). The Manchester Benchmarks for rail simulators - an introduction. *Vehicle System Dynamics*, 29(sup1):717–722.

Jesús Pantaleón Prieto, M. J., Ramos Gutiérrez, Ó. R., Ortega Carreras, G., and Martínez García, J. M. (2011). Viaductos Sobre Río Deza Y Anzo 2. In *V Congreso de ACHE*, pages 1–10.

Ju, S. H. (2012). Nonlinear analysis of high-speed trains moving on bridges during earthquakes. *Nonlinear Dynamics*, 69(1-2):173–183.

Kalker, J. (1967). *On the rolling contact of two elastic bodies in the presence of dry friction.* Doctoral thesis, Delft University of Technology, Delft, Netherlands.

Kalker, J. (1982). A Fast Algorithm for the Simplified Theory of Rolling Contact. *Vehicle System Dynamics*, 11(1):1–12.

Kalker, J. (1991). Wheel-rail rolling contact theory. *Wear*, 144(1-2):243–261.

Kalker, J. J. (1979). The computation of three-dimensional rolling contact with dry friction. *International Journal for Numerical Methods in Engineering*, 14(9):1293–1307.

Kalker, J. J. (1990). *Three-Dimensional Elastic Bodies in Rolling Contact*, volume 2 of *Solid Mechanics and Its Applications*. Kluwer Academic Publishers, Dordrecht.

Kandge, G. M. (2007). *Influence of Mode Dependent Rayleigh Damping on Transient Stress Response.* Masters, Blekinge Institute of Technology.

Kargarnovin, M., Younesian, D., Thompson, D., and Jones, C. (2005). Ride comfort of high-speed trains travelling over railway bridges. *Vehicle System Dynamics*, 43(3):173–197.

Kim, S. I., Lee, J., and Kim, S. (2011). Dynamic behavior comparison of steel-composite and concrete high speed railway bridges. *International Journal of Steel Structures*, 11(4):445–455.

Kim, S.-I., Lee, Y.-N., Kim, I.-S., and Lee, W.-P. (2000). Automation of Bridge Construction by Precast Span Method in Korea High Speed Railway Project. In *Proceedings of the 17th ISARC*, pages 1–4, Taipei, Taiwan.

Kojundic, A. N. (2007). Great Salt Lake Causeway Railroad Bridge. *HPC Bridge Views*, 46:5.

Kouroussis, G., Verlinden, O., and Conti, C. (2012). Influence of some vehicle and track parameters on the environmental vibrations induced by railway traffic. *Vehicle System Dynamics*, 50(4):619–639.

Kufver, B. and Gåsemyr, H. (1999). Norwegian railways adapted for higher train speeds track aspects of tilting trains. In *2nd International conference Railway Engineering*, pages 1–10.

Kwark, J. W., Choi, E. S., Kim, Y. J., Kim, B. S., and Kim, S. I. (2004). Dynamic behavior of two-span continuous concrete bridges under moving high-speed train. *Computers and Structures*, 82(4-5):463–474.

Kwasniewski, L., Li, H., Wekezer, J., and Malachowski, J. (2006). Finite element analysis of vehicle-bridge interaction. *Finite Elements in Analysis and Design*, 42(11):950–959.

Laing O'Rourke (2016). River Tame Viaduct.

Leboeuf, M. (2018). *High Speed Rail: Fast Track to Sustainable Mobility*. UIC Passenger Department.

Lee, Y.-S. and Kim, S.-H. (2010). Structural analysis of 3D high-speed train-bridge interactions for simple train load models. *Vehicle System Dynamics*, 48(2):263–281.

Lei, X. and Noda, N. (2002). Analyses of dynamic response of vehicle and track coupling system with random irregularity of track vertical profile. *Journal of Sound and Vibration*, 258(1):147–165.

Lei, X. and Zhang, B. (2010). Influence of Track Stiffness Distribution on Vehicle and Track Interactions in Track Transition. *Proceedings of the Institution of Mechanical Engineers, Part F: Journal of Rail and Rapid Transit*, 224(6):592–604.

Li, G.-Q., Wang, Z.-L., Chen, S., and Xu, Y.-L. (2016). Field measurements and analyses of environmental vibrations induced by high-speed Maglev. *The Science of the total environment*, 568:1295–1307.

Li, Y., Qiang, S., Liao, H., and Xu, Y. (2005). Dynamics of wind-rail vehicle-bridge systems. *Journal of Wind Engineering and Industrial Aerodynamics*, 93(6):483–507.

Lin, C. C., Wang, J. F., and Chen, B. L. (2005). Train-Induced Vibration Control of High-Speed Railway Bridges Equipped with Multiple Tuned Mass Dampers. *Journal of Bridge Engineering*, 10(4):398–414.

Liu, K., De Roeck, G., and Lombaert, G. (2009a). The effect of dynamic train-bridge interaction on the bridge response during a train passage. *Journal of Sound and Vibration*, 325(1-2):240–251.

Liu, Z., Luo, S., Ma, W., and Song, R. (2009b). Application Research of Track Irregularity PSD in the High-Speed Train Dynamic Simulation. In Peng, Q., Wang, K. C. P., Qiu, Y., Pu, Y., Luo, X., and Shuai, B., editors, *International Conference on Transportation Engineering 2009*, pages 2845–2850, Reston, VA. American Society of Civil Engineers.

Llombart Jaques, J. A., Revoltós Fort, J., Carrero Martinez, J., and Catalán Martín, I. (2014a). Viaducto sobre el Río Arnoia. In *VI Congreso de ACHE*, pages 1–8.

Llombart Jaques, J. A., Revoltós Fort, J., Fernández Vega, J., and Catalán Martín, I. (2014b). Viaducto Sobre El Rio Oria. In *VI Congreso de ACHE*, pages 1–5.

Lou, P. (2005). A vehicle-track-bridge interaction element considering vehicle's pitching effect. *Finite Elements in Analysis and Design*, 41(4):397–427.

Lou, P. (2007). Finite element analysis for train-track-bridge interaction system. *Archive of Applied Mechanics*, 77(10):707–728.

Lou, P., Yu, Z., and Au, F. (2012). Rail-bridge coupling element of unequal lengths for analysing train-track-bridge interaction systems. *Applied Mathematical Modelling*, 36(4):1395–1414.

Lu, F., Kennedy, D., Williams, F., and Lin, J. (2008). Symplectic analysis of vertical random vibration for coupled vehicle-track systems. *Journal of Sound and Vibration*, 317(1-2):236–249.

Macalloy (2017). Macalloy Post Tensioning System. `https://www.macalloy.com/application/files/8115/0046/3186/POST_TENSIONING_SYSTEM_July_2017.PDF`. Last checked on Sep 1, 2019.

Macchi, G. and Macchi, S. (2003). Innovative Omega Profile for The Modena Viaducts of High Speed Railway. *IABSE Symposium Report, IABSE Symposium, Antwerp 2003: Structures for High-Speed Railway Transportation*, (7):43–49.

Macchi, G. and Macchi, S. (2010). Open Profile Bridges for High-Speed Trains, Italy. *Structural Engineering International*, 20(1):31–35.

Madrazo-Aguirre, F. (2016). *Behaviour and Design of Under-Deck Cable-Stayed Bridges with Steel-Concrete Composite Decks*. Doctoral thesis, Imperial College London.

Magalhães, H., Ambrósio, J., and Pombo, J. (2016). Railway vehicle modelling for the vehicle–track interaction compatibility analysis. *Proceedings of the Institution of Mechanical Engineers, Part K: Journal of Multi-body Dynamics*, 230(3):251–267.

Majka, M. and Hartnett, M. (2008). Effects of speed, load and damping on the dynamic response of railway bridges and vehicles. *Computers and Structures*, 86(6):556–572.

Majka, M. and Hartnett, M. (2009). Dynamic response of bridges to moving trains: A study on effects of random track irregularities and bridge skewness. *Computers and Structures*, 87(19-20):1233–1252.

Malveiro, J., Ribeiro, D., Calçada, R., and Delgado, R. (2014). Updating and validation of the dynamic model of a railway viaduct with precast deck. *Structure and Infrastructure Engineering*, 10(11):1484–1509.

Manterola Armisén, J., Martínez Cutillas, A., Martín Martínez, B., Gil Ginés, M. Á., Fuente García, S., Blanco Martín, L., and Faundez Velasco, H. (2014). Viaducto para Ferrocarril de Alta Velocidad Sobre el Río Tajo en el Embalse De Alcántara. In *VI Congreso de ACHE*, pages 1–10.

Marí, A. and Montaner, J. (2000). Continuous precast concrete girder and slab bridge decks. *Proceedings of the Institution of Civil Engineers - Structures and Buildings*, 140(3):195–206.

Martin, D. (2008). Railway bridges for high speed lines and Eurocodes. In Calcada, R., Delgado, R., and Campos e Matos, A., editors, *Bridges for High-Speed Railways: Revised Papers from the Workshop, Porto, Portugal, 3-4 June 2004*, pages 23–30. CRC Press.

Marx, S. and Seidl, G. (2011). Integral Railway Bridges in Germany. *Structural Engineering International*, 21(3):332–340.

Matsumoto, N. and Asanuma, K. (2008). Some experiences on track-bridge interaction in Japan. In Calcada, R., Delgado, R., Campos e Matos, A., Goicolea, J. M., and Gabaldón, F., editors, *Track-Bridge Interaction on High-Speed Railways*, pages 77–94, London, UK. CRC Press.

Matute Rubio, L., Torrico Liz, J., Martínez Agromayor, D., Sanz Manzanedo, C., and Encinas López, J. (2014). Viaductos de Alta Velocidad de Salubita, San Esteban, Oaska y Luzuriaga. In *VI Congreso de ACHE*, pages 1–8.

Millanes Mato, F., Matute Rubio, L., Martínez Agromayor, D., Gordo Monsó, C., and de Los Ríos Francisco, J. (2014a). Concepción y Proyecto del Viaducto sobre el Río Nervión. In *VI Congreso de ACHE*, pages 1–9.

Millanes Mato, F., Ortega Cornejo, M., Solera Pérez, P., Figueiredo, H., and Ugarte González, J. (2014b). Concepción y Proyecto del Viaducto de Alta Velocidad Sobre el Río Deba en la Y Vasca. In *VI Congreso de ACHE*, pages 1–10.

Miotti, A., Prevedini, C., and Zoratto, N. (2003). The Piacenza Viaduct for Milano-Bologna high-speed railway. In *Structures for High-Speed Railway Transportation*, pages 156–157, Antwerp. IABSE.

Miura, S., Takai, H., Uchida, M., and Fukada, Y. (1998). The Mechanism of Railway Tracks. *Japan Railway amd Transport Review*, 15:38–45.

Moliner, E., Martinez-Rodrigo, M. D., Lavado, J., and Castillo-Linares, A. (2012). Dynamic performance of existing simply supported high-speed railway bridges: influence of elastomeric bearings and transverse vibrations in the prediction of vertical acceleration levels. *Proceedings of ISMA2012 / USD2012*, pages 2853–2867.

Montagut, I. B. (2010). *Tipologia de Viaductos en las Lineas de Alta Velocidad en Espana*. PhD thesis, Universitat Politecnca de Catalunya, Barcelona, Spain.

Montaner Fraguet, J., Estaún Ibáñez, M., Osán Sarasa, F., and Bajo Pavía, C. J. (2014). Viaducto 2 Sobre el Río Pisuerga para la Línea del Ave en el Nudo Venta de Baños. Tramo: Valladolid-Burgos. In *VI Congreso de ACHE*, pages 1–8.

Montens, S. and Huyard, J. (2008). Last developments of dynamic analysis of bridges under moving train loads. In Delgado, R., Calcada, R., Goicolea, J. M., and Gabaldon, F., editors, *Dynamics of High-Speed Railway Bridges: Selected and revised papers from the Advanced Course on Dynamics of High-Speed Railway Bridges, Porto, Portugal, 20-23 September 2005*, pages 57–72, London, UK. CRC Press.

Morgan Girgis, A. F. and Tadros, M. K. (2007). Precast concrete bridge systems optimization. *Structural Control and Health Monitoring*, 14(3):522–536.

Nawy, E. G. (2001). *Fundamentals of high-performance concrete*. Wiley, New York ; Chichester, 2nd edition.

Nguyen, D.-V., Kim, K.-D., and Warnitchai, P. (2009). Simulation procedure for vehicle-substructure dynamic interactions and wheel movements using linearized wheel-rail interfaces. *Finite Elements in Analysis and Design*, 45(5):341–356.

Nguyen, K., Goicolea, J., and Galbadon, F. (2014). Comparison of dynamic effects of high-speed traffic load on ballasted track using a simplified two-dimensional and full three-dimensional model. *Proceedings of the Institution of Mechanical Engineers, Part F: Journal of Rail and Rapid Transit*, 228(2):128–142.

Nguyen Gia, K. (2013). *Effectos Dinámicos debidos al Tráfico de Ferrocarril sobre la Infraestructura de Vía y las Estructuras*. Phd, Universidad Politécnica de Madrid.

Nguyen Gia, K., Goicolea Ruigómez, J. M., and Gabaldón Castillo, F. (2015). Influence of rail track properties on vehicle–track responses. *Proceedings of the Institution of Civil Engineers - Transport*, 168(6):499–509.

Nielsen, J. and Oscarsson, J. (2004). Simulation of dynamic train-track interaction with state-dependent track properties. *Journal of Sound and Vibration*, 275(3):515–532.

Nurmikolu, A. (2012). Key aspects on the behaviour of the ballast and substructure of a modern railway track: research-based practical observations in Finland *. *Journal of Zhejiang University-SCIENCE A (Applied Physics & Engineering)*, 13(11):825–835.

Otero Vietez, F., Lozano Sáiz, J., and Caride Coello, J. (2011). Ultimas Tendencias en Viaductos Ferroviarios Prefabricados. In *V Congreso de ACHE*, pages 1–8.

Pacadar (2015). Puentes para Ave. http://www.pacadar.es/fichas/oc/puentes-para-ave. Last checked on Aug 01 2016.

Pantaleón Prieto, M. J., Ramos Gutiérrez, Ó. R., Martínez García, J. M., and De Vena Retuero, J. E. (2011). Viaducto Sobre Río Jauto. In *V Congreso de ACHE*, pages 1–10.

Pascal, J. and Sauvage, G. (1993). The Available Methods to Calculate the Wheel/Rail Forces in Non Hertzian Contact Patches and Rail Damaging. *Vehicle System Dynamics*, 22(3-4):263–275.

Pascal, J.-P. and Soua, B. (2016). Solving conformal contacts using multi-Hertzian techniques. *Vehicle System Dynamics*, 54(6):784–813.

Petrangeli, M., Usai, G., Magnorfi, F., Orlandini, M., and Geremia, G. (2006). Large Concrete Precast Box Girders along the New Italian High Speed Railway Lines. *IABSE Symposium Report*, 92(20):49–56.

Piotrowski, J. and Chollet, H. (2005). Wheel-rail contact models for vehicle system dynamics including multi-point contact. *Vehicle System Dynamics*, 437(6):455–483.

Podworna, M. (2014). Vibrations of Bridge / Track Structure / High-speed Train System with Vertical Irregularities of the Railway Track. *Procedia Engineering*, 91:148–153.

Polach, O. (1999). A Fast Wheel-Rail Forces Calculation Computer Code. In *16th International Association for Vehicle System Dynamics*, volume 33, pages 728–739.

Polach, O. (2005). Creep forces in simulations of traction vehicles running on adhesion limit. *Wear*, 258(7-8):992–1000.

Polo Orodea, T., Ramos Moreno, C., Aparicio Bengoechea, Á. C., and Ramos Schneider, G. (2011). Ingeniería de Construcción del Viaducto para Alta Velocidad sobre La Carretera C-66. In *V Congreso de ACHE*, pages 1–10.

Pombo, J. and Ambrósio, J. (2006). A New Approach to Study the Wheel-Rail Contact Problem in Railway Dynamics. In *7th World Congress on Railway Research*, pages 1–17, Montreal, Canada.

Proença, J. M., Casal, H., and Neves, M. (2011). Effect of the Type of Track on the Dynamic Behaviour of High Speed Railway Bridges. In Papadrakakis, M., Fragiadakis, M., and Plevris, V., editors, *3rd ECCOMAS Thematic Conference on Computational Methods in Structural Dynamics and Earthquake Engineering*, pages 1–18.

Quost, X., Sebes, M., Eddhahak, A., Ayasse, J.-B., Chollet, H., Gautier, P.-E., and Thouverez, F. (2006). Assessment of a semi-Hertzian method for determination of wheel-rail contact patch. *Vehicle System Dynamics*, 44(10):789–814.

Radiguet, B. (1999). The Avignon Viaducts. *Concrete Engineering International*, 3(1):38–41.

Railway Technology (2018). Siemens Velaro High Speed Trains - Railway Technology. `https://www.railway-technology.com/projects/siemens-velaro-high-speed-trains/`. Last checked on Nov 29 2018.

Ramondenc, P., Martin, D., and Schmitt, P. (2008). Track-Bridge interaction - the SNCF experience. In Calcada, R., Delgado, R., Campos e Matos, A., Goicolea, J. M., and Gabaldon, F., editors, *Track-Bridge Interaction on High-Speed Railways*, pages 63–76, London, UK. CRC Press.

Ramos Gutiérrez, Ó. R., De Vena Retuero, J., Ortega Carreras, G., and Jesús Pantaleón Prieto, M. J. (2014a). Viaductos del Tramo de Alta Velocidad los Gallardos-Sorbas. Nueva Estrategia para hacer Fente a las Acciones Horizontales. In *VI Congreso de ACHE*, pages 1–11.

Ramos Gutiérrez, Ó. R., Ortega Carreras, G., Martínez García, J. M., and Pantaleón Prieto, M. J. (2014b). Viaducto De San Benito En El Tramo Pontevedra - Cerponzons del Eje Atlántico de Alta Velocidad. In *VI Congreso de ACHE*, pages 1–10.

Ramos Gutiérrez, Ó. R., Ortega Carreras, G., Pereira da Sousa, R. R., Gaite González, C., Martínez García, J. M., and Pantaleón Prieto, M. J. (2014c). Viaducto Sobre Rio Guadalhorce y A-92 en la Línea de Alta Velocidad Antequera-Granada. In *VI Congreso de ACHE*, pages 1–10.

Reis, A. J., Lopes, N. T., and Ribeiro, D. (2008). Track-Structure interaction in long railway bridges. In Calcada, R., Delgado, R., Campos e Matos, A., Goicolea, J. M., and Gabaldon, F., editors, *Track-Bridge Interaction on High-Speed Railways*, pages 185–200, London, UK. CRC Press.

Resplendino, J. (2011). Introduction: What is a UHPFRC? In *Designing and Building with UHPFRC*, pages 3–14. John Wiley & Sons, Inc.

Rico Rubio, R., Couto Worner, S., and Cascales Fernández, J. (2014). Puentes de Ferrocarril Modulares Integrales como Alternativa al Tablero Isostítico. In *VI Congreso de ACHE*, pages 1–9.

Rigueiro, C., Rebelo, C., and Simões da Silva, L. (2010). Influence of ballast models in the dynamic response of railway viaducts. *Journal of Sound and Vibration*, 329(15):3030–3040.

Romero, A., Galvin, P., and Dominguez, J. (2012). Short span bridges dynamic behaviour account for the vehicle-track-structure-soil dynamic interaction. *Revista Internacional De Metodos Numericos Para Calculo Y Diseno En Ingenieria*, 28(1):55–63.

Rosignoli, M. (2014a). Full-span precasting for light-rail transit and high-speed railway bridges. *PCI Journal*, 59(2):49–61.

Rosignoli, M. (2014b). Full-Span Precasting of Railway Bridges. *Aspire*, 8(2):16–18.

Salcher, P., Pradlwarter, H., and Adam, C. (2014). Reliability of high-speed railway bridges with respect to uncertain characteristics. In Cunha, A., Caetano, E., Ribeiro, P., and Müller, G., editors, *Proceedings of the 9th International Conference on Structural Dynamics, EURODYN 2014*, pages 2729–2736.

Sayers, M. and Hedrick, J. (1977). Track Maintenance/Railcar Suspension Trade-Offs to Obtain Acceptable Ride Quality. *AMD*, 24:35–58.

Shabana, A. A. and Sany, J. R. (2001). An Augmented Formulation for Mechanical Systems with Non-Generalized Coordinates: Application to Rigid Body Contact Problems. *Nonlinear Dynamics*, 24(2):183–204.

Shabana, A. A., Tobaa, M., Sugiyama, H., and Zaazaa, K. E. (2005). On the Computer Formulations of the Wheel/Rail Contact Problem. *Nonlinear Dynamics*, 40(2):169–193.

Shabana, A. A., Zaazaa, K. E., Escalona, J. L., and Sany, J. R. (2004). Development of elastic force model for wheel/rail contact problems. *Journal of Sound and Vibration*, 269(1-2):295–325.

Shabana, A. A., Zaazaa, K. E., and Sugiyama, H. (2007). *Railroad Vehicle Dynamics: A Computational Approach*. CRC Press, Boca Raton.

Shen, Z. Y., Hedrick, J. K., and Elkins, J. A. (1983). A Comparison of Alternative Creep Force Models for Rail Vehicle Dynamic Analysis. *Vehicle System Dynamics*, 12(1-3):79–83.

Siemens (2018). Velaro - High-speed and Intercity trains - Siemens Global Website. `https://www.siemens.com/global/en/home/products/mobility/rail-solutions/rolling-stock/high-speed-and-intercity-trains/velaro.html`. Last checked on Sep 1 2019.

Simões, R., Calçada, R., and Delgado, R. (2008). Track-Bridge interaction in railway lines: Application to the study of the bridge over the River Moros. In Calcada, R., Delgado, R., Campos e Matos, A., Goicolea, J. M., and Gabaldón, F., editors, *Track-Bridge Interaction on High-Speed Railways*, pages 201–210, London, UK. CRC Press.

Six, K., Meierhofer, A., Müller, G., and Dietmaier, P. (2015). Physical processes in wheel-rail contact and its implications on vehicle-track interaction. *Vehicle System Dynamics*, 53(5):635–650.

Smith, J. (1988). *Vibration of Structures: Applications in civil engineering design*. Chapman and Hall, London.

Smith, R. A. (2003). The Japanese Shinkansen: Catalyst for the Renaissance of Rail. *The Journal of Transport History*, 24(2):222–347.

Song, M.-K., Noh, H.-C., and Choi, C.-K. (2003). A new three-dimensional finite element analysis model of high-speed train-bridge interactions. *Engineering Structures*, 25:1611–1626.

SSF Ingenieure (2016). Slab track systems on different substructures. `http://ssf.ro/en/downloads.html`. Last checked on May 1 2016.

Staquet, S., Espion, B., Rigot, G., and Detandt, H. (2004). Innovative composite precast prestressed precambered U-shaped concrete deck for belgium's high speed railway trains. *PCI Journal*, 49(6):94–134.

Sun, Y. and Dhanasekar, M. (2002). A dynamic model for the vertical interaction of the rail track and wagon system. *International Journal of Solids and Structures*, 39(5):1337–1359.

Sun, Y. Q., Dhanasekar, M., and Roach, D. (2003). A three-dimensional model for the lateral and vertical dynamics of wagon-track systems. *Proceedings of the Institution of Mechanical Engineers, Part F: Journal of Rail and Rapid Transit*, 217(1):31–45.

Tai, J. C., Jang, D., Gaffney, H., and Flint, J. (2010a). Full Span Precast and Launching Construction in Taiwan's High Speed Rail Project. In *Proceedings of the 2010 Joint Rail Conference*, pages 167–173, Urbana.

Tai, J. C., Jang, D., Gaffney, H., and Flint, J. (2010b). Full Span Precast and Launching Construction in Taiwan's High Speed Rail Project. In *2010 Joint Rail Conference, Volume 1*, pages 167–173. ASME.

Tang, M. C. (2004). High Performance Concrete - Past Present and Future. In Schmidt, M., Fehling, E., and Geisenhansluke, C., editors, *Ultra High Performance Concrete (UHPC) Proceedings of the International Symposium on Ultra High Performance Concrete*, pages 3–10. Kassel University Press.

T.A.V. SpA (2006). The Piacenza Viaduct. *L'industria Italiana del Cemento*, 76(820):492–497.

TECROC Products (2006). Technical Data: E140 Epoxy Grout. `https://www.arconsupplies.co.uk/uploads/EpoxygroutE140.pdf`. Last checked on Sep 1, 2019.

Tierra Armada (2012). Precast & Prestressed Beam Bridges. `http://www.tierraarmada.com/tae/index.php?option=com_docman&task=doc_download&gid=168&Itemid=&lang=es`. Last checked on May 06 2019.

Timoshenko, S. (1922). CV. On the forced vibrations of bridges. *Philosophical Magazine Series 6*, 43(257):1018–1019.

Torstensson, P. T. and Nielsen, J. C. (2011). Simulation of dynamic vehicle-track interaction on small radius curves. *Vehicle System Dynamics*, 49(11):1711–1732.

Turmo, J., Lozano-Galant, J., Mirambell, E., and Xu, D. (2015). Modeling composite beams with partial interaction. *Journal of Constructional Steel Research*, 114:380–393.

UIC (2019). HS Lines. `https://uic.org/high-speed-database-maps`. Last checked on Jun 21 2019.

UIC 510-2 (2004). Trailing stock: wheels and wheelsets. Condidtions concerning the use of wheels of various diameters.

Vale, C. and Calçada, R. (2014). A Dynamic Vehicle-Track Interaction Model for Predicting the Track Degradation Process. *Journal of Infrastructure Systems*, 20(3):04014016.

Varandas, J. N., Hölscher, P., and Silva, M. A. (2011). Dynamic behaviour of railway tracks on transitions zones. *Computers & Structures*, 89(13-14):1468–1479.

Viartola Laborda, L. M. (2002). Railway Bridges Constructed by ACS Proyectos, Obras y Construcciones. Construction Aspects. In Dolores, M., Pulido, G., and Sobrino, J. A., editors, *Railway Bridges: Design, Construction and Maintenance*, pages 54–103. Spanish Group of IABSE., Barcelona, Spain.

Vollebregt, E. (2016). User guide for CONTACT, Rolling and sliding contact with friction. Technical report, Vortech, Delft, Netherlands.

Wen, Z. F., Mao, G. W., Mao, X. B., Jin, X. S., and Zhu, M. H. (2009). Dynamic vehicle-track interaction and plastic deformation of rail at rail welds. *Engineering Failure Analysis*, 16(4):1221–1237.

White, R. and Cooperrider, N. (1981). Guideway-suspension tradeoffs in rail vehicle systems, Report ERC-R-78035. *Journal of Dynamic Systems, Measurement, and Control*, 103(3):237–244.

Wiriyachai, A., Chu, K.-H., and Garg, V. (1982). Bridge Impact due to Wheel and Track Irregularities. *Journal of the Engineering Mechanics Division*, 108(EM4):648–666.

Wu, T. X. and Thompson, D. J. (2002). A Hybrid Model for the Noise Generation due to Railway Wheel Flats. *Journal of Sound and Vibration*, 251(1):115–139.

Wu, Y.-S. and Yang, Y.-B. (2003). Steady-state response and riding comfort of trains moving over a series of simply supported bridges. *Engineering Structures*, 25:251–265.

Wu, Y.-S., Yang, Y.-B., and Yau, J.-D. (2010). Three-Dimensional Analysis of Train-Rail-Bridge Interaction Problems. *Vehicle System Dynamics*, 36(1):1–35.

Xia, H., Li, H. L., Guo, W. W., and De Roeck, G. (2014). Vibration Resonance and Cancellation of Simply Supported Bridges under Moving Train Loads. *Journal of Engineering Mechanics*, 140(5):04014015.

Xia, H., Wang, K., and Yu, Z. (2012). Dynamic Interaction Analysis of Coupled Train-Bridge System. In Xia, H., De Roeck, G., and Goicolea, J. M., editors, *Bridge Vibration and Controls*, chapter 1, pages 1–65. Nova Science Publishers.

Xia, H., Xu, Y., and Chan, T. (2000). Dynamic Interaction of Long Suspension Bridges with Running Trains. *Journal of Sound and Vibration*, 237(2):263–280.

Xia, H. and Zhang, N. (2005). Dynamic analysis of railway bridge under high-speed trains. *Computers & Structures*, 83(23-24):1891–1901.

Xia, H., Zhang, N., and De Roeck, G. (2003). Dynamic analysis of high speed railway bridge under articulated trains. *Computers & Structures*, 81(26-27):2467–2478.

Xia, H., Zhang, N., and Guo, W. W. (2006). Analysis of resonance mechanism and conditions of train-bridge system. *Journal of Sound and Vibration*, 297(3-5):810–822.

Xu, Y., Zhang, N., and Xia, H. (2004). Vibration of coupled train and cable-stayed bridge systems in cross winds. *Engineering Structures*, 26(10):1389–1406.

Yang, J., Wu, Y., and Yau, Y. (2004a). *Vehicle-Bridge interaction Dynamics: With Applications to High-Speed Railways*. World Scientific Publishing Co., Singapore.

Yang, Y. B., Lin, C. L., Yau, J. D., and Chang, D. W. (2004b). Mechanism of resonance and cancellation for train-induced vibrations on bridges with elastic bearings. *Journal of Sound and Vibration*, 269(1-2):345–360.

Yang, Y.-B. and Wu, Y.-S. (2001). A versatile element for analyzing vehicle-bridge interaction response. *Engineering Structures*, 23(5):452–469.

Zaazaa, K. E., Martin, T. P., Whitten, B., Marquis, B., Curtis, E., El-Sibaie, M., and Tajaddini, A. (2009). A Nonlinear Rail Vehicle Dynamics Computer Program Sams/Rail Part 3: Applications to Predict Railroad Vehicle-Track Interaction Performance. In *Proceedings of the ASME/IEEE Joint Rail Conference*, pages 165–173.

Zellner, W. and Saul, R. (1991a). Enz-Viaduct: a 1044 m long prestressed concrete box girder bridge. In *Bridge: Interaction Between Construction Technology and Design*, volume 64, pages 512–513, Leningrad. IABSE.

Zellner, W. and Saul, R. (1991b). Long Span Bridges of the new railroad lines in Germany. In *Bridges: interaction between construction technology and design*, pages 501–506, Leningrad. IABSE.

Zhai, W. (1996). Two Simple Fast Integration Methods for Large-Scale Dynamic Problems in Engineering. *International Journal for Numerical Methods in Engineering*, 39(24):4199–4214.

Zhai, W. and Sun, X. (1994). A Detailed Model for Investigating Vertical Interaction between Railway Vehicle and Track. *Vehicle System Dynamics*, 23(S1):603–615.

Zhai, W., Wang, K., and Cai, C. (2009). Fundamentals of vehicle–track coupled dynamics. *Vehicle System Dynamics*, 47(11):1349–1376.

Zhai, W., Wang, K., and Lin, J. (2004). Modelling and experiment of railway ballast vibrations. *Journal of Sound and Vibration*, 270(4-5):673–683.

Zhang, N., Xia, H., and Guo, W. W. (2008). Vehicle-bridge interaction analysis under high-speed trains. *Journal of Sound and Vibration*, 309(3-5):407–425.

Zhang, N., Xu, M., Chen, S., and Yu, Z. (2012). Dynamic Responses of a Simply-Supported beam Subjected to Various Moving Loads. In Xia, H., De Roeck, G., and Goicolea, J. M., editors, *Bridge Vibration and Controls*, pages 113–150. Nova Science Publishers.

Zhang, Q.-L., Vrouwenvelder, A., and Wardenier, J. (2001). Numerical simulation of train-bridge interactive dynamics. *Computers & Structures*, 79(10):1059–1075.

Zhang, Z., Lin, J., Zhang, Y., Zhao, Y., Howson, W., and Williams, F. (2010). Non-stationary random vibration analysis for train-bridge systems subjected to horizontal earthquakes. *Engineering Structures*, 32(11):3571–3582.

Zhaohua, F. and Cook, R. D. (1983). Beam Elements on Two-Parameter Elastic Foundations. *Journal of Engineering Mechanics*, 109(6):1390–1402.

Zhiping, Z. and Shouhua, J. (2009). PSD Analysis of Slab Ballastless Track Irregularity of Qinhuangdao-Shenyang Dedicated Passenger Railway Line. In Guerrero, J. E., editor, *2009 Second International Conference on Intelligent Computation Technology and Automation*, pages 669–672, Changsha, Hunan, China. IEEE.

Zhu, J. J., Ahmed, A. K. W., and Rakheja, S. (2007). An Adaptive Contact Model for Simulation of Wheel-rail Impact Load due to a Wheel Flat. In *13th National Conference on Mechanisms and Machines (NaCoMM07)*, pages 157–164, Bangalore, India.

Zhu, J. J., Ahmed, A. K. W., Rakheja, S., and Hu, Y. S. (2009). Impact load due to railway wheels with multiple flats predicted using an adaptive contact model. *Proceedings of the Institution of Mechanical Engineers, Part F: Journal of Rail and Rapid Transit*, 223(4):391–403.

Appendix A

Bridge Database

In this appendix, the bridge database is displayed. This database is compiled from various literature sources of HSR bridges. All of these bridges are constructed using concrete and are subsequently found in Table A.1. For this table a series of abbreviations have been used in the headings which are outlined in Table A.2, and a '?' is used where values are not reported for the particular property.

Source	Type	PC/CIS	Track	Number of Tracks	SS/C	Country	Span [m]	Depth [m]	Slab Width [m]	Web Thickness [m]	Bottom Flange Thickness [m]	Beam Width [m] (Top/Bot)	Slab Thickness [m] (max/min)	Concrete Strength [MPa]
Capellán Miguel et al. (2014)	a	CIS	Ballast	2	C	Spain	45.00	2.960	14.00	0.6	0.35	7.4/6	0.35/0.2	60
Llombart Jaques et al. (2014b)	c	CIS	Slab	2	C	Spain	49.00	4.560	14.00	0.5	0.3	6.5/6.5	0.4/0.25	?
Millanes Mato et al. (2014b)	a	CIS	Ballast	2	C	Spain	80.00	5.940	14.00	0.58	0.3	8.521/6.611	0.35/0.2	?
Millanes Mato et al. (2014a)	c	CIS	?	2	C	Spain	68.00	4.500	14.00	0.4	0.36	6.1/6.1	0.44/?	?
Matute Rubio et al. (2014)	a	CIS	Slab	2	C	Spain	57.00	3.940	14.00	0.45	0.35	6.8/6	0.4/0.2	45
Matute Rubio et al. (2014)	a	CIS	Slab	2	C	Spain	48.35	3.940	14.00	?	?	?/6	?/?	45
Matute Rubio et al. (2014)	a	CIS	Slab	2	C	Spain	50.00	3.940	14.00	?	?	?/6	?/?	45
Matute Rubio et al. (2014)	a	CIS	Slab	2	C	Spain	52.00	3.940	14.00	?	?	?/6	?/?	45
Llombart Jaques et al. (2014a)	a	CIS	Ballast	2	C	Spain	55.00	3.650	14.00	0.51	0.3	6.84/5.5	0.34/0.2	?
Llombart Jaques et al. (2014a)	d	PC	Ballast	2	C	Spain	37.00	2.300	14.00	0.235	0.223	3.91/3.31	0.35/0.2	?
Ramos Gutiérrez et al. (2014a)	a	CIS	Ballast	2	C	Spain	51.00	3.400	14.00	0.55	0.3	7.16/5.6	0.36/0.2	?
Ramos Gutiérrez et al. (2014b)	a	CIS	Ballast	2	C	Spain	84.00	6.500	14.00	0.6	0.3	6.5/6.3	0.3/0.2	?
Ramos Gutiérrez et al. (2014c)	a	CIS	Ballast	2	C	Spain	51.25	3.400	14.00	0.76	0.41	6.83/5.5	0.41/0.25	?
Montaner Fraguet et al. (2014)	d	PC	Ballast	2	C	Spain	45.00	3.210	14.00	0.2	0.2	3.977/2.48	0.34/0.213	?
Manterola Armisén et al. (2014)	a	CIS	Ballast	2	C	Spain	60.00	4.000	14.00	0.5	0.3	6.5/5	0.35/0.2	50
Grandío Noche et al. (2014)	b	PC	Ballast	2	C	Spain	42.00	2.990	14.00	0.18	0.28	3.58/1.74	0.39/0.25	?
Rico Rubio et al. (2014)	e	CIS	Ballast	2	C	Spain	21.50	1.350	14.00	n/a	n/a	7.2/6.1	n/a/n/a	?
Polo Orodea et al. (2011)	a	CIS	?	2	C	Spain	44.00	3.140	14.00	?	?	?/?	?/?	?
Jesús Pantaleón Prieto et al. (2011)	a	CIS	Ballast	2	C	Spain	75.00	4.500	14.00	0.55	0.4	6.8/?	0.4/?	?
Pantaleón Prieto et al. (2011)	b	PC	Ballast	2	C	Spain	15.00	1.240	14.00	0.195	0.25	4/2.55	0.34/0.2	?
Arenas de Pablo et al. (2011)	a	CIS	Ballast	2	C	Spain	54.00	3.750	14.00	0.5	0.35	7/6.05	0.35/0.2	?
Otero Vietez et al. (2011)	b	PC	Ballast	2	SS	Spain	33.75	2.750	14.00	?	?	?/1.72	?/0.25	?
Abad González et al. (2011b)	a	CIS	?	2	C	Greece	45.00	3.900	13.40	0.5	0.4	6.7/5.2	0.4/0.25	?
Abad González et al. (2011a)	a	CIS	?	1	C	Greece	45.00	3.850	8.60	0.5	0.45	4.9/4	0.4/0.2	?
Corres Peiretti et al. (2011)	a	CIS	?	2	C	Spain	55.00	3.750	14.00	0.5	0.3 to 0.6	7.5/6	0.4/0.2	?
de Villar Luengo et al. (2011); del Valle Pérez et al. (2011)	a	CIS	Ballast	2	C	Spain	52.00	3.890	14.00	0.5	0.25	7.5/5.5	0.35/0.2	?
Kwark et al. (2004); Lee and Kim (2010)	a	PC	Slab	2	C	Korea	40.00	3.500	14.00	0.6	0.35	7.4/5.6	?/0.35	?
Xia and Zhang (2005)	a	PC	Slab	2	SS	China	24.00	2.400	12.40	0.4	0.25	6.4/6.12	0.3/0.2	?
Tai et al. (2010a)	a	PC	Slab	2	SS	Taiwan	30.00	2.800	13.00	0.5	0.28	6.2/5.1	0.3/0.225	?
Marx and Seidl (2011)	a	CIS	Slab	2	C	Germany	58.00	4.750	13.80	0.6	0.3	6.4/5	0.3/0.3	?
Fritsch (2003)	a	PC	?	2	SS	Taiwan	45.00	4.400	13.00	0.55	0.35	6.2/5.2	?/0.25	?
Amarume et al. (2003)	a	PC	Slab	2	C	Japan	35.00	2.400	11.70	0.4	0.27	6.2/5.862	0.27/0.25	?
Malveiro et al. (2014)	a	PC	Ballast	1	SS	Portugal	21.00	1.480	7.20	0.2	0.18	?/3.3	0.28/0.22	?
Petrangeli et al. (2006)	b	PC	Ballast	2	SS	Italy	34.50	3.120	13.60	0.35	0.35	2.77/1.72	0.28/?	?
Viartola Laborda (2002)	a	PC	?	2	C	Spain	35.00	2.450	14.00	0.4	0.3	6/5.5	0.33/0.2	40
Dong Kang and Suh (2003)	a	PC	?	2	C	Korea	25.00	2.400	14.00	0.5	0.3	7/5.9	0.35/?	40
Armisén Manterola et al. (1999)	a	CIS	Ballast	2	C	France	48.00	3.500	12.30	0.5	?	?/5.5	?/?	?
Armisén Manterola et al. (1999)	a	CIS	Ballast	2	C	France	53.00	4.500	13.50	0.5	0.3	?/5.5	?/?	?
Armisén Manterola et al. (1999)	a	CIS	Ballast	2	C	France	100.0	6.500	12.96	?	?	?/5.5	?/?	?
Armisén Manterola et al. (1999)	a	CIS	Ballast	2	C	France	48.00	3.320	12.25	?	0.3	?/5.7	?/?	?
Armisén Manterola et al. (1999); Zellner and Saul (1991a)	a	CIS	Ballast	2	C	Germany	58.00	4.750	14.30	0.6	?	?/5.4	?/?	?
Armisén Manterola et al. (1999); Zellner and Saul (1991b)	a	CIS	Ballast	2	C	Germany	53.50	4.500	14.30	0.6	0.43	?/5.4	?/?	?
Armisén Manterola et al. (1999)	a	CIS	?	2	SS	Germany	58.00	5.000	14.90	0.6	0.35	?/5.4	?/?	?
Armisén Manterola et al. (1999)	a	CIS	Slab	2	SS	Germany	58.00	5.300	14.30	0.6	0.35	?/5	?/?	?
Armisén Manterola et al. (1999)	a	CIS	Slab	2	SS	Germany	44.00	4.000	14.30	0.6	0.35	?/5	0.3/0.28	?
Armisén Manterola et al. (1999)	a	CIS	Ballast	2	C	Spain	60.00	3.500	14.00	0.5	0.3	?/5	?/?	?
Armisén Manterola et al. (1999)	a	CIS	Ballast	2	C	Spain	45.00	2.800	14.00	0.45	0.3	?/5	?/?	?
Armisén Manterola et al. (1999)	a	CIS	Ballast	2	C	Spain	66.00	4.000	14.00	0.5	0.3	?/5	?/?	?
Miotti et al. (2003)	d	?	Ballast	2	SS	Italy	30.40	2.800	14.02	0.5	0.3	10/8	0.4/0.33	40
Laing O'Rourke (2016)	b	PC	Slab	2	C	UK	35.00	2.920	13.60	0.23	0.335	2.967/1.72	0.42/0.335	60

Table A.1: Database of bridges compiled from the literature

Source	Author(s) that published the data on the bridge
Type	Bridge cross section type. See Table A.3 for information
PC/CIS	Type of bridge construction: PC refers to precast and CIS to cast in-situ
Track	Type of track structure found to be used for the bridge
Number of tracks	Number of tracks placed on each bridge deck
SS/C	Definition of the continuity of the source bridge as either single span(SS) or continuous(C)
Country	Location of the country of construction
Span	Length of the span of the bridge
Depth	Depth of the cross section
Slab width	Width of the top flange (or slab)
Web thickness	Nominal thickness of the webs, for cross sections containing webs
Bottom Flange Thickness	Nominal thickness of bottom flange for cross sections with them
Beam Width	Transversal width of the beam or lower box of a box girder at the top and bottom
Slab Thickness	Thickness of the slab with min and max values to reflect the varying slab thickness
Concrete Strength	Published strength of concrete used in project

Table A.2: Definitions of the abbreviations used in Table A.1

cross section	name	key
	Box girder	a
	Dual U-Beam	b
	Straight sided box girder	c
	Triple webbed box girder	d
	Voided slab	e

Table A.3: Different types of cross section in the bridge database

Appendix B

Track Database

This appendix outlines the properties of some of the tracks modelled in literature. The majority of these values are shown in Table B.1.

The variation of the values in literature are shown pictorially in Figures B.1, which is where the sensitivity analysis values originate from in Section 4.2.

B.1 Longitudinal and Lateral Stiffness

Due to literature often focusing on two dimensional track models the longitudinal and lateral stiffnesses of the ballast and railpad are often excluded. However, in the case of both Rigueiro et al. (2010); Wu and Yang (2003), the value of longitudinal ballast stiffness is $10.4\,MN/m$, which is 10% of the vertical value. Contrastingly the ballast longitudinal damping is found to be $50\,kN\,s/m$ in both cases, the same as the vertical damping value in these cases. There are no values given for the lateral stiffness and damping of the ballast. In Sun and Dhanasekar (2002); Vale and Calçada (2014), the ballast damping and elastic stiffness is defined as 30% that of the vertical value.

For the railpad, the lateral coefficients are only included in the case of Zhai et al. (2009), where the stiffness value is $20\,MN/m$, and the damping value is $50\,kN\,s/m$. This compares to the vertical components as 27% and 66% respectively. No coefficients are given for the longitudinal stiffness of the railpad.

Source	Ballast Depth [m]	Ballast Vertical Stiffness MN/m]	Ballast Vertical Damping [kN s/m]	Ballast Density [kg/m³]	Ballast Mass [kg]	Railpad Vertical Stiffness [MN/m]	Railpad Vertical Damping [kN s/m]	Sleeper Spacing [m]	Sleeper Mass [kg]	Rail Stiffness [MN/m²]	Rail Mass per length [kg/m]
Romero et al. (2012)	0.7	?	?	1500	?	150	13.5	0.6	300	6.45	60.3
Nguyen Gia et al. (2015) Alonso Upper	?	200	?	?	?	500	?	?	?	?	?
Nguyen Gia et al. (2015) Alonso Lower	?	100	?	?	?	60	?	?	?	?	?
Nguyen Gia et al. (2015)	?	100	25	?	646	100	15	?	320	6.42	?
Cantero et al. (2016); Zhai (1996)	?	240	59	?	683	78	50	0.545	251	6.42	60.3
Cantero et al. (2016)	?	538	120	?	412	500	200	0.6	290	6.42	60.3
Cantero et al. (2016); Zhai et al. (2004)	?	138	58	?	531	65	75	0.545	251	6.42	60.3
Cantero et al. (2016); Lu et al. (2008)	?	480	?	?	1365	156	?	0.54	237	6.42	60.3
Cantero et al. (2016); Lei and Zhang (2010)	?	120	60	?	2718	80	50	0.57	340	6.42	60.3
Cantero et al. (2016); Nguyen et al. (2014)	?	100	25	?	646	100	15	0.6	320	6.42	60.3
Rigueiro et al. (2010) Model 1	?	104	50	2039	?	?	?	?	?	6.42	60.4
Rigueiro et al. (2010) Model 2	?	120	114	2039	?	300	80	0.6	300	6.42	60.4
Rigueiro et al. (2010) Model 3	?	538	120	?	412	500	200	0.6	290	6.42	60.4
Zhu et al. (2009)	?	40	50	?	?	200	30	0.6069	180	8.18	67.6
Lou et al. (2012)	?	225	60	?	?	60	75	0.625	340	6.63	60.6
Nielsen and Oscarsson (2004)	?	30	31	?	?	80	15	0.65	250	6.4	60
Sun and Dhanasekar (2002) Example 1	?	31	21	?	?	200	21.8	0.79	50	4.86	56
Sun and Dhanasekar (2002) Example 2	0.3	79	50	?	?	200	70	0.79	50	4.86	56
Sun and Dhanasekar (2002) Example 3	0.3	**	**	?	?	140	45	0.685	270	6.09	60
Kargarnovin et al. (2005)*	?	90	1125	?	?	220	700	?	125	6.42	60.4
Nguyen et al. (2014)	?	100	25	?	?	100	15	0.6	160	?	?
Nguyen Gia (2013)	?	29	70	?	?	140	45	0.685	270	6.09	60
Sun et al. (2003)	0.3	**	**	2600	?	140	45	0.685	?	?	?
Zhai et al. (2009)	0.45	**	**	1800	?	65	75	0.545	?	6.62	60.6
Kouroussis et al. (2012)	?	32	52	?	?	90	30	0.72	90.84	4.17	50.1

Table B.1: Comparison of the properties of the track used in literature. Where no data is provided a '?' is placed. * signifies that the stiffness is a defined in a nonlinear way and the linear component value is taken. ** signifies that this property is defined via an elastic modulus
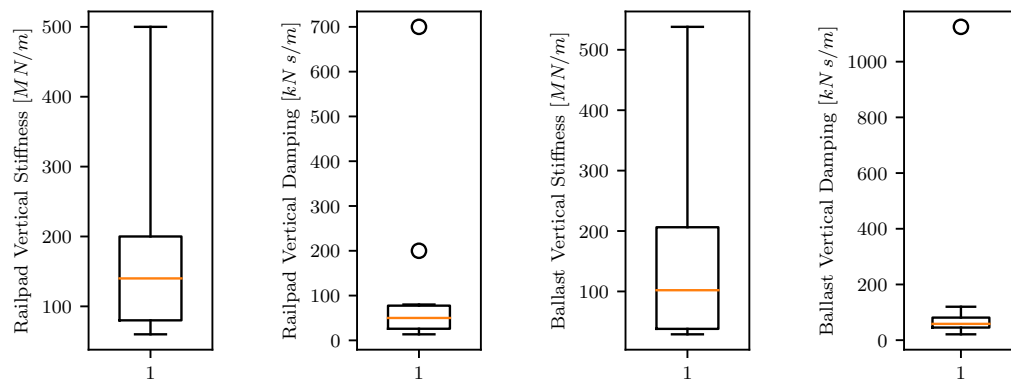
Figure B.1: Variation of the track properties in literature; Outliers represented by circles which were considered values not chosen as too dissimilar to the rest.

Appendix C

Vehicle Database

This appendix details the vehicle properties found in literature. It compares the mass properties of the vehicles as seen in Table C.3, and the suspension properties as seen in Table C.4. These values are used for the sensitivity analysis of the vehicles using the suspension data. Hence a comparison of the values is made in Figures C.2 and C.3. This appendix also details the Siemens Velaro train in more detail, that is used in this thesis.

C.1   Siemens Velaro Vehicle

The Siemens Velaro vehicle that is used in this thesis is outlined here. It uses data published by Antolin et al. (2012) and Antolín (2013) to describe the vehicle properties. The properties are shown in Tables C.1 and C.2. These correspond to the components shown in Figure C.1. Within the geometrical properties, h refers to the height of the centre of mass of the body above the contact point with rail, d is a longitudinal distance and b a width. d_c refers to the distance between carriages, and w_w is the distance between the initial contact points on the wheelset. The subscripts of c, b and w refer to the carriage, bogie and wheelset respectively. For the vehicle properties, k and c correspond to stiffness and damping coefficients, where the subscripts p and s are the primary and secondary suspension levels respectively. The directions x, y and z refer to the longitudinal, lateral and vertical directions respectively. The inertia of the carriage in this model depends on the mass of the carriage and the passengers within the carriage.
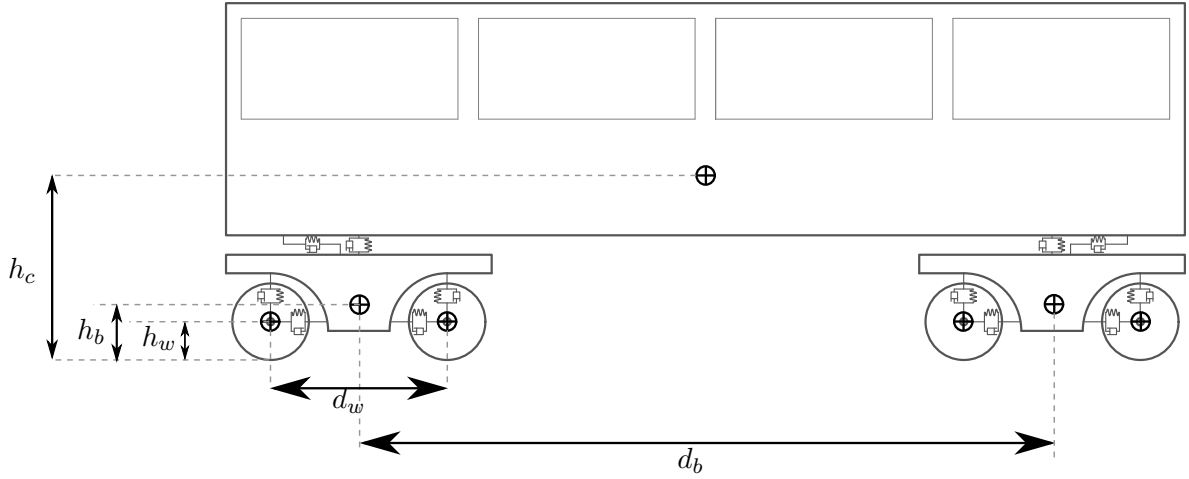
Figure C.1: Vehicle model

h_c	1.4 m	d_c	25.0 m		
h_b	0.5 m	d_b	17.375 m		
h_w	0.46 m	d_w	2.5 m	w_w	1.506 m

Table C.1: Siemens Velaro Geometrical Properties (all dimensions in m) (Antolin et al., 2012; Antolín, 2013)

Vehicle Property	Direction, i		
	x	y	z
Primary Stiffness $k_{p,i}$ $[kN/m]$	120×10^3	12.5×10^3	1200
Primary Damping $c_{p,i}$ $[kN \cdot s/m]$	27.9	9	10
Secondary Stiffness $k_{s,i}$ $[kN/m]$	12000	240	350
Secondary Damping $c_{s,i}$ $[kN \cdot s/m]$	600	30	20
Carriage mass Inertia $I_{c,i}$ $[kg \cdot m^2]$	70000	$49 \cdot m_c$	$49 \cdot m_c$
Bogie mass Inertia $I_{b,i}$ $[kg \cdot m^2]$	560	315	1715
Wheelset mass Inertia $I_{w,i}$ $[kg \cdot m^2]$	1000	100	1000
Carriage mass m_c $[kg]$	53500 +68 persons of mass 80 kg		
Bogie mass m_b $[kg]$	3500		
Wheelset mass m_w $[kg]$	1800		

Table C.2: Properties of the Siemens Velaro train as taken from Antolin et al. (2012) and Antolín (2013). Carriage mass related to passenger mass therefore $49 \cdot m_c = 2.89 \times 10^6 \ kg$

Source	Train Name	Type	Mass [kg]			Carriage Inertia [kg/m^2]			Bogie Inertia [kg/m^2]			Wheelset Inertia [kg/m^2]		
			Carriage	Bogie	Wheelset	vert	long	lat	vert	long	lat	vert	long	lat
Dias et al. (2008)	AVE S100		28740	3020	1580	981340	34270	981340	3790	2030	3200			
Doménech Monforte (2014)	AVE S103		53500	3500	1800			1690000			2802			
Dias et al. (2008)	AVE S103		33790	2800	1520	570000	88500	1540000	1316	2070	3052			
Lei and Zhang (2010)	CRH3		40000	3200	1200			547000			6800			
Zhang et al. (2010)	China star	P	40000	2100	1950	2560000	90000	2560000	2100	1701	2100	1248	1248	
Zhang et al. (2010)	China star	T	59364	5631	1844	1796565	130493	1723415	11233	2202	9488	1263	1263	
Liu et al. (2009a)	ETR500Y	T	34231	2760	1583									
Liu et al. (2009a)	ETR500Y	P	55976	3896	2059									
Doménech Monforte (2014)	Eurostar	T	51500	2200	1700			1050000			1900			
Doménech Monforte (2014)	Eurostar	P	22525	22900	1900			810000			2508			
Lin et al. (2005)	ICE-2		27000	3000	1800						4000			
Doménech Monforte (2014)	ICE2	T	60768	5600	2003			1344000			21840			
Doménech Monforte (2014)	ICE2	P	33930	2373	1728			2115000			1832			
Varandas et al. (2011)	ICR	P	60000	3400	750			902500			1857			
Varandas et al. (2011)	Koploper ICM	T	34500	2600	875			518938			1354			
Kwark et al. (2004)	Korean HST	PP	26000	3050	2000	971810	33940	971810	3790	2030	3200	1030	1030	0.8
Kwark et al. (2004)	Korean HST	T	48400	2514	2050	1694890	55500	1641510	3860	2070	3260	1030	1030	0.8
Kwark et al. (2004)	Korean HST	P	54960	2420	2050	1112900	59400	1132800	3068	1645	2593	1030	1030	0.8
Majka and Hartnett (2009)	LOCO141	T	37300	10390	2230	479800	22110	479800	27100	3645	27100			1535
Majka and Hartnett (2009)	LOCO201	T	63980	17320	2230	1295000	63980	1295000	45140	43190	6075			1535
Majka and Hartnett (2009)	Mark 4	P	42110	6820	1813	1837000	50870	1830000	7388	2420	5257			1120
Antolín et al. (2012)	Pioneer	P	44000	1700	1900	2740000	74000	2740000	1700	1600	1700			1067
Doménech Monforte (2014)	Pioneer	T	42400	3400	2200			1064400			7200			
Doménech Monforte (2014)	Pioneer	P	44000	1700	1900			2740000			1700			
Antolín et al. (2012)	Pioneer	T	42400	3400	2200	867200	101500	1064400	6800	3200	7200			1630
Lin et al. (2005)	SKS		20875	3040	1780						3930			
Wu and Yang (2003)	SKS-300		41750	3040	1780			2080000			3930			
Ju (2012)	SKS-700		38900	3000	1770	1267500	97200	1470000	3050	2470	3690	710	710	180
Antolín et al. (2013)	Seimens Velaro		53500	3500	1800	49m	70000	49m	1715	560	315	1800	1000	100
Romero et al. (2012)	TAV	P	24000	3040	2003			1480000			2680			
Romero et al. (2012)	TAV	T	55790	2380	2048			1480000			1150			
Lei and Noda (2002)	TGV		53500	3260	2000									
Lin et al. (2005)	TGV		27000	3000	1800						4000			
Galvín et al. (2010)	TGVA	T	55790	2380	2048			1150000			2680			
Galvín et al. (2010)	TGVA	P	24000	3040	2003			1480			2680			
Chen et al. (2015)			31994	3333	1650									
Antolin et al. (2012)			53500	3500	1800	2621500	70000	2621500	1715	560	315	1000	1000	100
Nguyen Gia (2013)			80600	3600		726426			1801					
Majka and Hartnett (2009)		F	63500	2219	1510	71880	11500	71880	3175	1736	1736		892	
Dinh et al. (2009)		T	54920	3434	1776	2505300	59400	2485400	2453	1766	4905	1138	1138	7.85
Dinh et al. (2009)		P	41750	3040	1776	2100000	23200	2080000	2344	1580	3934	1138	1138	7.85
Sun et al. (2003)			80600		1300									
Lou et al. (2012)			41750	3040	1780			2080000			3930			
Song et al. (2003)		T	54916	2446	2048	1112000	59400	1131900	3068	1645	2593	1030	1030	110
Song et al. (2003)		PP	42758	3076	2104	1697000	55570	1643620	3860	2070	3260	1030	1030	110
Song et al. (2003)		P	26373	3018	2104	981340	34270	981340	3790	2030	3200	1030	1030	110
Xu et al. (2004)		T	50000	15260	2670	1022549	119597	1255159	13147	5031	13665	2426	2426	
Xu et al. (2004)		P	48200	3086	1675	2999000	816720	2999000	4730	2132	4730	900	900	
Bowe and Mullarkey (2005)		T	90958	10175	4522									
Bowe and Mullarkey (2005)		P	33700	3150	1500									
Iwnicki (1998)			32000	2615	1813	1970000	56800	1970000	3067	1722	1476	1120	1120	112
Iwnicki (1998)			40770		1925	220000	35000	220000				950	950	150
Nguyen Gia et al. (2015)			53500	3500	1800									
Zhai et al. (2009)		T	59364.2	5630.8	1843.5	1796000	130500	1723000	11233	2202	9487	1285	1263	219
Zhai et al. (2009)		P	29600	1700	1900	2139000	58020	2139000	1700	1600	1700	1067	1067	140

Table C.3: Comparison of the mass properties of the vehicles modelled in literature. Type refers to the type of carriage modelled in the train:- P is passenger carriage; T is the traction or powered carriage; PP is a powered passenger car; F is a freight carriage. Vert=Vertical; Lat=Lateral; Long=Longitudinal

Source	Train name	type	Primary Stiffness [MN/m]			Primary Damping [kN/m]			Secondary Stiffness [MN/m]			Secondary Damping [$kN\,s/m$]		
			Vert	Long	Lat	Vert	Long	Lat	Vert	Long	Lat	Vert	Long	Lat
Dias et al. (2008)	AVE S100		1.650	110	22	12	48	22	0.3	0.1	0.1	6.6	240	30
Doménech Monforte (2014)	AVE S103		0.873			24			0.41			45		
Dias et al. (2008)	AVE S103		1.610		4.35	7.5		5.55	0.18		0.064	16.25		10
Lei and Zhang (2010)	CRH3		2.080			100			0.8			120		
Zhang et al. (2010)	China star	P	0.600		4.5	10		20	0.26		0.125	60		20
Zhang et al. (2010)	China star	T	2.400		4.878	30		80	0.886		0.316	45		50
Liu et al. (2009a)	ETR500Y	T	0.809			7.5			0.181			16.25		
Liu et al. (2009a)	ETR500Y	P	1.792			15.25			0.472			36.25		
Doménech Monforte (2014)	Eurostar	T	2.600			12			3.26			90		
Doménech Monforte (2014)	Eurostar	P	2.000			12			0.58					
Lin et al. (2005)	ICE-2		2.360			78.4			0.66			22.7		
Doménech Monforte (2014)	ICE2	T	4.800			108			1.76			152		
Doménech Monforte (2014)	ICE2	P	1.600			20			0.3			6		
Varandas et al. (2011)	ICR	P	1.800			10			0.8			35.4		
Varandas et al. (2011)	Koploper ICM	T	2.480			2.93			1.44			31.1		
Kwark et al. (2004)	Korean HST	PP	0.800	55	11	6			0.303	0.1	0.17			
Kwark et al. (2004)	Korean HST	T	1.250	40	9	10	0	0	0.37	0.1	0.15	20		30
Kwark et al. (2004)	Korean HST	P	1.250	40	9	10	0	0	1.27	0.303	0.303	20		100
Majka and Hartnett (2009)	LOCO141	T	1.488		2.12	7.5		1	0.53		0.16	15		32
Majka and Hartnett (2009)	LOCO201	T	1.470		2.12	4		1	0.63		0.16	20		32
Majka and Hartnett (2009)	Mark 4	P	3.185		10.13	32.41		0	0.566		0.211	26.24		41.44
Antolín et al. (2012)	Pioneer	P	0.700	15	5	38	0	0	0.35	0.21	0.21	40	300	15
Doménech Monforte (2014)	Pioneer	T	1.040			30			0.4			33		
Doménech Monforte (2014)	Pioneer	P	0.700			38			0.35			40		
Antolín et al. (2012)	Pioneer	T	1.040	9	1.32	30	0	0	0.4	0.24	0.24	33	120	30
Lin et al. (2005)	SKS		2.360			78.4			0.53			90.2		
Wu and Yang (2003)	SKS-300		1.180			39.2			0.53			90.2		
Ju (2012)	SKS-700		1.200	16	11	40	2.5	2.5	0.033	0.14	0.14	20	60	2500
Antolín et al. (2013)	Seimens Velaro		1.200	12.5	120	10	9	27.9	0.35	0.24	0.24	20	30	30
Romero et al. (2012)	TAV	P	1.400			10			0.82			48		
Romero et al. (2012)	TAV	T	2.450			20			2.45			40		
Lei and Noda (2002)	TGV		3.280			90			1.31			30		
Lin et al. (2005)	TGV		2.360			78.4			0.664			96.7		
Galvín et al. (2010)	TGVA	T	2.450			20			2.45			40		
Galvín et al. (2010)	TGVA	P	1.400			10			0.82			48		
Chen et al. (2015)			2.360			80			0.8			100		
Antolin et al. (2012)			1.200	120	12.5	10	27.9	9	0.35	12	0.24	20	600	30
Nguyen Gia (2013)			6.500			10			2.555			30		
Majka and Hartnett (2009)		F	1.500		2.12	4		1	0.35		0.16	20		32
Dinh et al. (2009)		T	1.226		2.453	29.43		98.1	1.246		0.297	98.1		98.1
Dinh et al. (2009)		P	0.590		2.35	19.62		58.86	0.045		0.039	0.42		1.23
Lou et al. (2012)			1.180			39.2			0.53			90.2		
Song et al. (2003)		T	1.225	40	9	10	22	10	1.268	0.302	0.302	20		30
Song et al. (2003)		PP	1.225	40	9	10	21	10	0.37	0.1	0.15	20		30
Song et al. (2003)		P	0.825	55	11	6	24	11	0.3	0.1	0.1	0		30
Xu et al. (2004)		T	16.000		3.74			120	0.5		0.072	100		72
Xu et al. (2004)		P	7.800		2.538			20	3.7		0.14	45		140
Bowe and Mullarkey (2005)		T	7.000			58.8			4.1			22		
Bowe and Mullarkey (2005)		P	0.700			5.88			0.41			2.2		
Iwnicki (1998)			1.220	31.391	3.884		15	2	0.43	0.16	0.16			
Iwnicki (1998)			1.800	12	0.64									
Nguyen Gia et al. (2015)			0.873			24			0.41			45		
Zhai et al. (2009)		T	2.400	30.8	4.878	30			0.886	0.316	0.315	45		50
Zhai et al. (2009)		P	0.873	24	5.1	30			0.41	1.2	0.3	108.7		25

Table C.4: Comparison of the stiffness properties of the vehicles modelled in literature. Type refers to the type of carriage modelled in the train:- P is passenger carriage; T is the traction or powered carriage; PP is a powered passenger car; F is a freight carriage. Vert=Vertical; Lat=Lateral; Long=Longitudinal
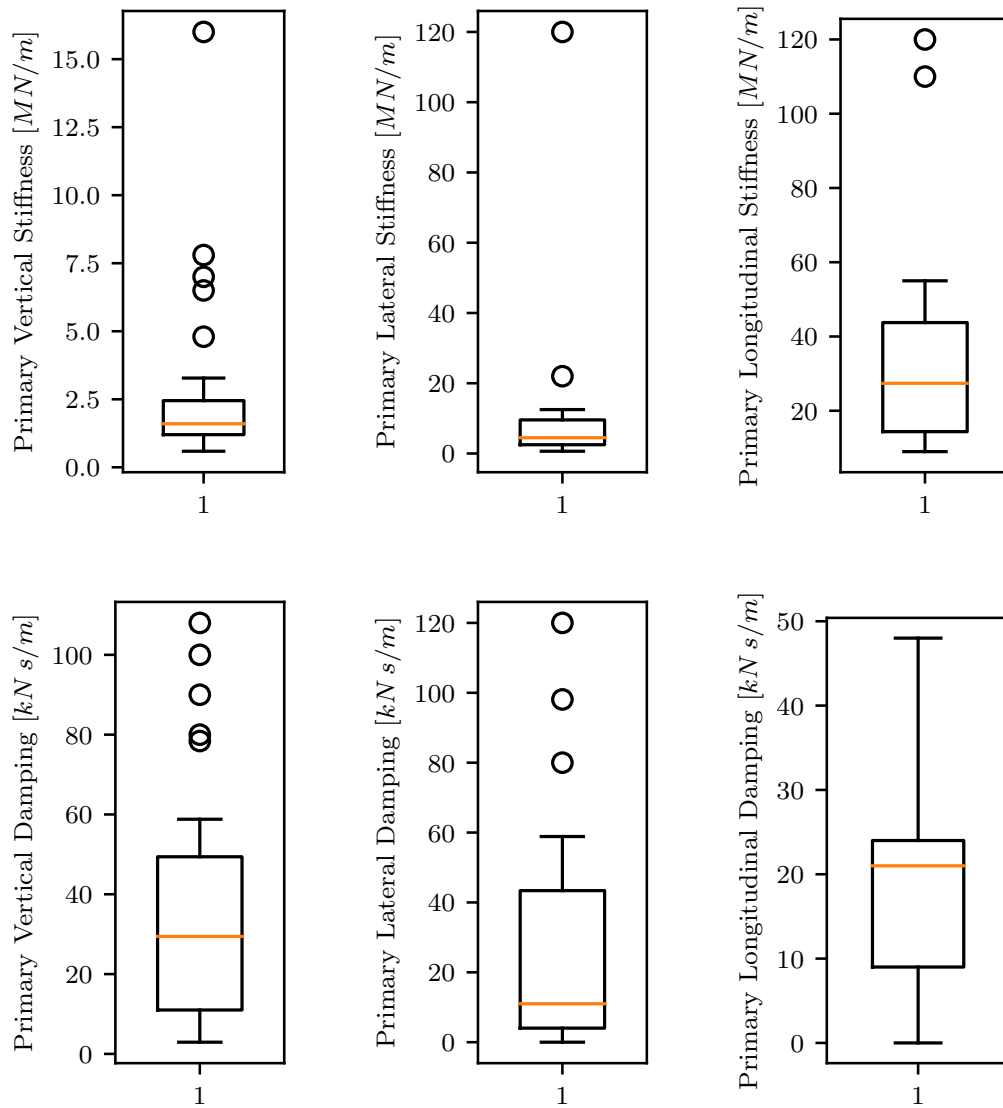
Figure C.2: Variation of the primary stiffness properties of the vehicles published in literature using box and whisker plots that display the median, upper and lower quartiles and outliers.
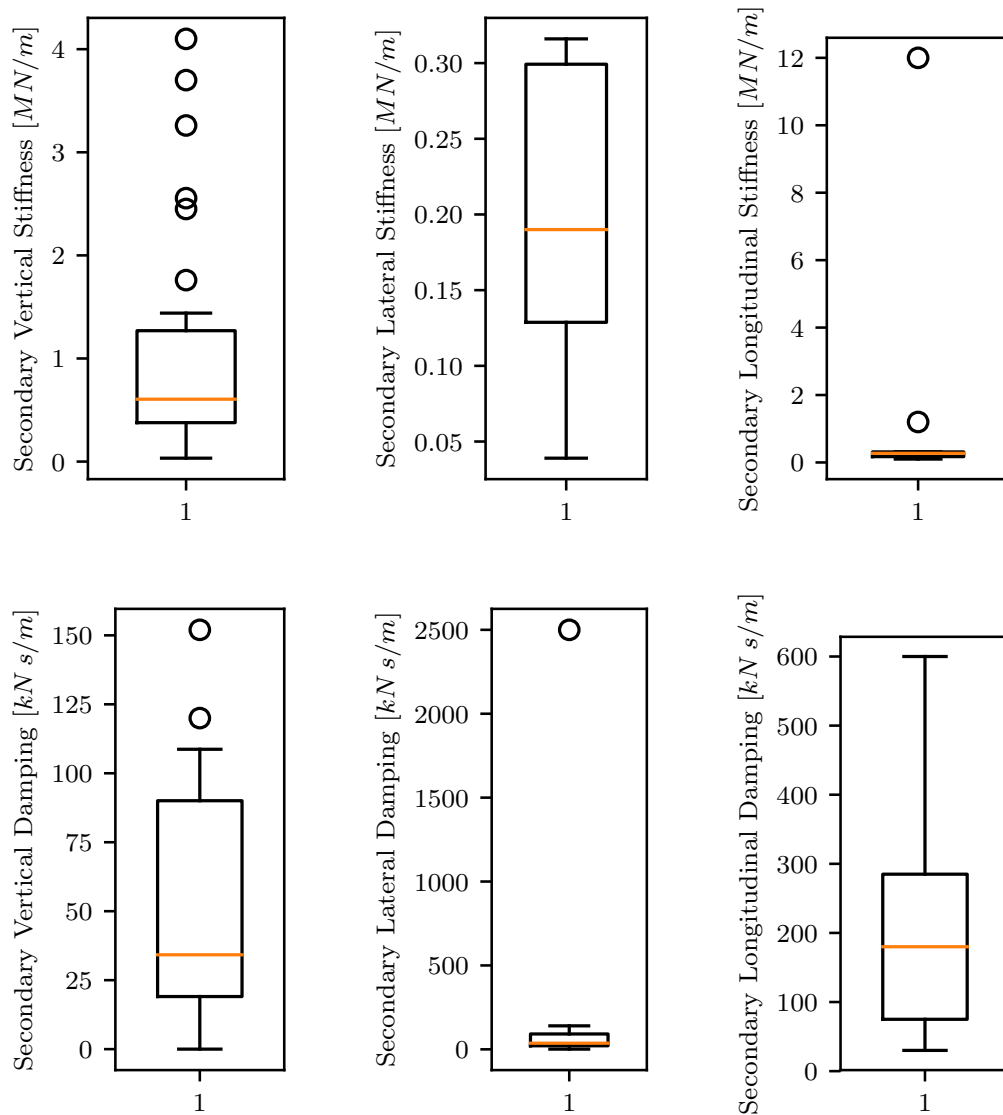
Figure C.3: Variation of the Secondary stiffness properties of the vehicles published in literature using box and whisker plots that display the median, upper and lower quartiles and outliers.

Appendix D

Wheel and Rail Geometry

The wheel geometry and the rail geometry used in this model take on the perfect geometries, as outlined in the source material (BS EN 13715:2006+A1:2010, 2011; BS EN 13674-1:2011+A1:2017, 2011). These geometries are outlined in this appendix, as well as the simplifications to geometry of the wheel for modelling purposes. These profiles do not take into account wear and changing of the profile shape.

D.1 Wheel Geometry

The wheel profile geometry is shown in Figure D.1. This comes from the source BS EN 13715:2006+A1:2010 (2011) as the commonly used S1002 wheel profile. The coordinates of the points in the model are found in Table D.1 (BS EN 13715:2006+A1:2010, 2011). In addition to the profile, the radius r_0 of the wheel is taken as $0.46\,m$, the location of which this is the radius is found at point C in Figure D.1. The distance from this point to the centre of the wheelset, y_0 is taken as $0.75\,m$.

From the profile shown, for modelling this is simplified into equations presented by UIC 510-2 (2004). These equations are shown in through Equations D.1-D.8.

$$f(S_{1W}) = 1.364323640 - 0.066666667 S_{1W} \tag{D.1}$$

$$
\begin{aligned}
f(S_{1W}) = &-3.358537058 \times 10^{-2} S_{1W} + 1.565681624 \times 10^{-3} S_{1W}^2 \\
&-2.810427944 \times 10^{-5} S_{1W}^3 + 5.844240864 \times 10^{-8} S_{1W}^4 \\
&-1.562379023 \times 10^{-8} S_{1W}^5 + 5.309217349 \times 10^{-15} S_{1W}^{6.0} \\
&-5.957839843 \times 10^{-12} S_{1W}^7 + 2.646656573 \times 10^{-13} S_{1W}^8
\end{aligned}
\tag{D.2}
$$
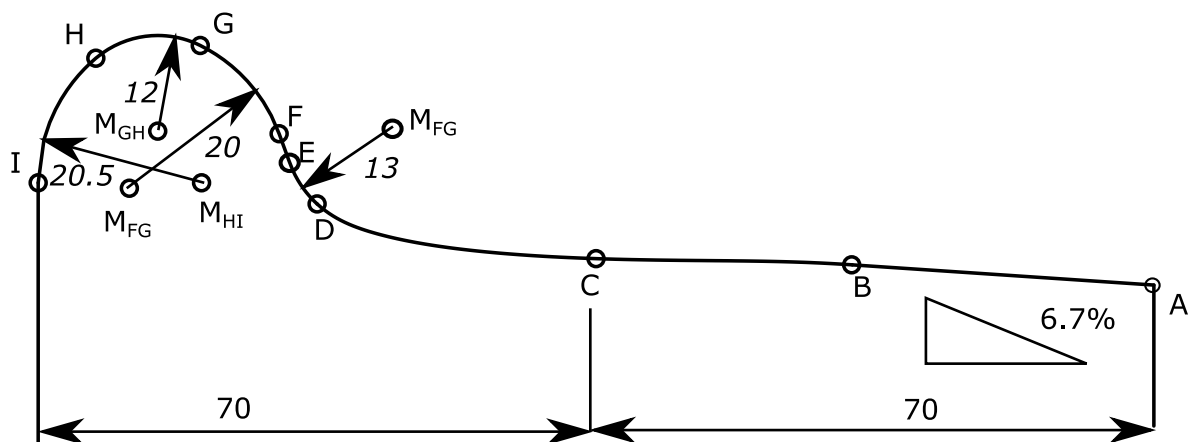
Figure D.1: Wheel profile geometry. All measurements in mm (BS EN 13715:2006+A1:2010, 2011)

Coordinate	S_{1W} [mm]	$f(S_{1W})$ [mm]
A	70.000	-3.315
B	32.158	-0.780
C	0.000	0.000
D	-35.000	6.867
E	-38.427	12.000
F	-39.765	15.675
G	-49.663	26.748
H	-62.765	25.149
I	-70.000	9.519
M_{DE}	-26.211	16.446
M_{FG}	-58.558	8.835
M_{GH}	-55.000	16.000
M_{HI}	-49.500	9.519

Table D.1: Coordinates for points in the wheel profile. Values in mm

Equation	Upper bound	lower bound
D.1	60.000	32.158
D.2	32.158	-26.000
D.1	-26.000	-35.000
D.4	-35.000	-38.427
D.5	-38.427	-39.764
D.6	-39.764	-49.663
D.7	-49.663	-62.765
D.8	-62.765	-70.000

Table D.2: Limits of validity for the each equation as a function of S_{1W}. Values in mm (BS EN 13715:2006+A1:2010, 2011)

$$
\begin{aligned}
f\left(S_{1W}\right) = & -4.320221263475584 \times 10^{3} - 1.038384035115286 \times 10^{3} S_{1W} \\
& -1.065501873 \times 10^{2} S_{1W}^{2} - 6.051367875 S_{1W}^{3} \\
& -2.054332446 \times 10^{-1} S_{1W}^{4} - 4.169739389 \times 10^{-3} S_{1W}^{5} \\
& -4.687195829 \times 10^{-5} S_{1W}^{6} - 2.252755540 \times 10^{-7} S_{1W}^{7}
\end{aligned} \tag{D.3}
$$

$$
f\left(S_{1W}\right) = 16.446 - \sqrt{13.0^{2} - \left(S_{1W} + 26.210665\right)^{2}} \tag{D.4}
$$

$$
f\left(S_{1W}\right) = -93.576667419 - 2.747477419 S_{1W} \tag{D.5}
$$

$$
f\left(S_{1W}\right) = 8.834924130 + \sqrt{20.0^{2} - \left(S_{1W} + 58.558326413\right)^{2}} \tag{D.6}
$$

$$
f\left(S_{1W}\right) = 16.0 + \sqrt{12.0^{2} - \left(S_{1W} + 55.0\right)^{2}} \tag{D.7}
$$

$$
f\left(S_{1W}\right) = 9.5192593020 + \sqrt{20.5^{2} - \left(S_{1W} + 49.50\right)^{2}} \tag{D.8}
$$

where the validity of each equation is outlined in Table D.2.

D.2 Rail Geometry

The rail geometry is shown in Figure D.2. This is the geometry for the commonly used UIC 60E1 rail (BS EN 13674-1:2011+A1:2017, 2011). The rail is angled, as commonly done in reality with a gradient of 1/40. This is shown in Figure D.3. Alternatives are 1/20, and no gradient which are not used. The rails point inwards towards the centre of the track.

To model the rail geometry, the geometry is converted into a series of equations. These model only the region for which contact can occur and are seen in Equation D.9:
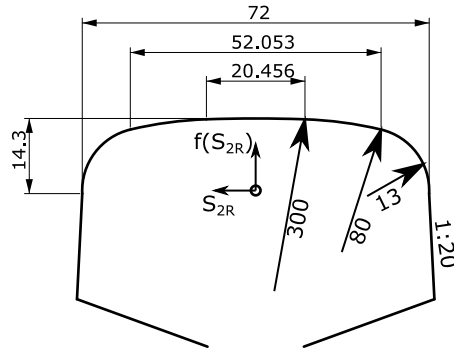
Figure D.2: Rail head profile geometry. All measurements in mm (BS EN 13674-1:2011+A1:2017, 2011)
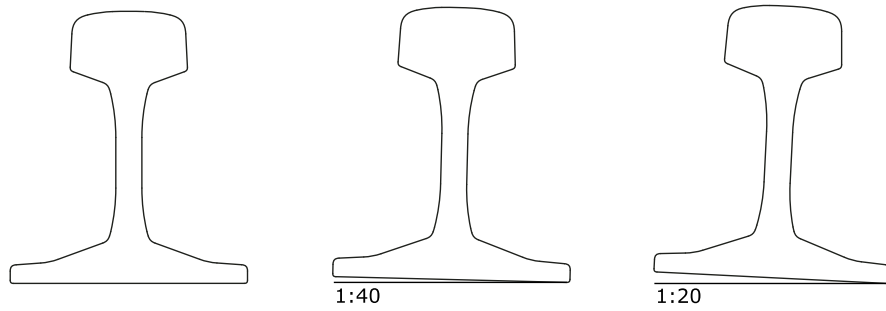
Figure D.3: Rail angle

$$
f\left(S_{2R}\right) =
\begin{cases}
-0.3 + \sqrt{0.3^2 - S_{2R}^2} & |S_{2R}| \leqslant 10.228 \\
-0.0801278 + \sqrt{0.08^2 - (S_{2R} - 0.0075005)^2} & 10.228 < S_{2R} \leqslant 26.0265 \\
-0.0149492 + \sqrt{0.013^2 - (S_{2R} - 0.0230162)^2} & 26.0265 < S_{2R} \leqslant 36.0 \\
-0.0801278 + \sqrt{0.08^2 - (S_{2R} + 0.0075005)^2} & -10.228 > S_{2R} \geqslant -26.0265 \\
-0.0149492 + \sqrt{0.013^2 - (S_{2R} + 0.0230162)^2} & -26.0265 > S_{2R} \geqslant -36.0
\end{cases}
$$

(D.9)

Appendix E

Pre-stress Losses Calculations

The benchmark case for the double U-beam bridge contains a series of pre-stressing tendons. The tendons are debonded over different distances from the end of the U-beam. Each tendon is 150 mm^2 with a diameter of 15.7 mm. The Young's modulus is 195 kN/mm, with the initial pre-stress being 219kN per strand, which is 78% of the characteristic breaking load.

Figure E.1 shows the layout of the pre-stressing tendons, including the longitudinal section in which the tendons are activated. For example, tendons highlighted as section 1, will be bonded throughout the length of the beam, whereas those highlighted as section 2 would begin being bonded in section 2 and so are unbonded in section 1. Likewise, those labelled section 3 become bonded in section 3 and are unbonded in sections 1 and 2.
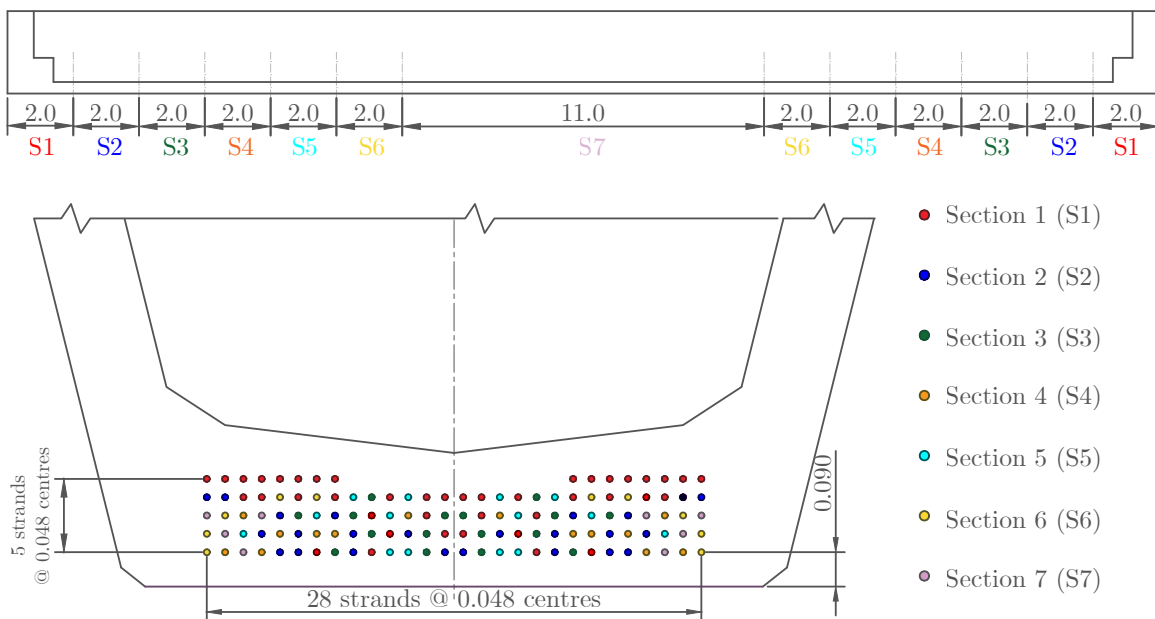
Figure E.1: Prestressing tendon arrangement and activation

E.1 Initial losses

For the calculation of the losses within the beam, study is made to the first span of the continuous three span bridge. The initial losses in the pre-stressing tendons are shown in Table E.1. The initial force comes from the initial tendon force. The elastic shortening of the concrete is calculated by the formula in Equation E.1 (BS EN 1992-1-1:2004, 2004).

$$\Delta P_i = \left(\frac{\sum_{j=1}^{N} P_j}{A_{C,H}} + \frac{\sum_{j=1}^{N} (P_j e_j) \, e_i}{I_{C,H}} \right) \frac{E_p}{E_C} A_{P,i} \tag{E.1}$$

The anchorage length (or transmission length) is calculated by Equation E.2. As it is a pretensioned bridge these are the only two initial losses. This results in a transmission length of 0.896565 m, which is reflected in Table E.1. The tendon forces can be calculated at x coordinates between the locations given by linear interpolation.

$$l_{pt} = \alpha_1 \alpha_2 \phi \sigma_{pm0} / f_{bpt} \tag{E.2}$$

where l_{pt} is the anchorage length, α_1 is 1.0 for gradual tendon release, α_2 is 0.19 for a seven wire strand, ϕ is the diameter of tendon ($= 15.7 \ mm$), σ_{pm0} is the tendon stress immediately after release and f_{bpt} is the constant concrete bond strength.

E.2 Time-dependent losses

The time dependent losses that affect this concrete structure are the concrete creep, concrete shrinkage and the tendon relaxation. In the sensitivity analysis of Chapter 4, two timescales were investigated: 30 days and 70 years (25567 days). An example of the pre-stressing forces after the time dependent losses are given for 30 days in this section.

The relaxation of the tendons comes from Equation E.3. The resultant loss of stress in each tendon in each tendon set based on where they are activated are expressed in Table E.2. The tendons are assumed to be of low relaxation and therefore a class 2 wire. Hence, the value of ρ_{1000} is 2.5. The derivation of the symbols can be found in BS EN 1992-1-1:2004 (2004).

$$\frac{\Delta \sigma_{pr}}{\sigma_{pi}} = 0.66 \rho_{1000} e^{9.1\mu} \left(\frac{t}{1000} \right)^{0.75(1-\mu)} 10^{-5} \tag{E.3}$$

The calculation of the creep forces requires the calculation of the bending moment diagram under long term loads. Equation E.4 is utilised to give the creep coefficient as used by Equation

x	Tendon force considering: $[kN]$								
location	Initial	Elastic	Anchorage in tendons bonded in:						
$[m]$		Shortening	S1	S2	S3	S4	S5	S6	S7
0	219	215	0	0	0	0	0	0	0
0.896565	219	215	215	0	0	0	0	0	0
2	219	217	217	0	0	0	0	0	0
2.896565	219	217	217	217	0	0	0	0	0
4	219	218	218	218	0	0	0	0	0
4.896565	219	218	218	218	218	0	0	0	0
6	219	218	218	218	218	0	0	0	0
6.896565	219	218	218	218	218	218	0	0	0
8	219	218	218	218	218	218	0	0	0
8.896565	219	218	218	218	218	218	218	0	0
10	219	218	218	218	218	218	218	0	0
10.89657	219	218	218	218	218	218	218	218	0
12	219	218	218	218	218	218	218	218	0
12.89657	219	218	218	218	218	218	218	218	218
17.5	219	218	218	218	218	218	218	218	218
22.10343	219	218	218	218	218	218	218	218	218
23	219	218	218	218	218	218	218	218	0
24.10343	219	218	218	218	218	218	218	218	0
25	219	218	218	218	218	218	218	0	0
26.10343	219	218	218	218	218	218	218	0	0
27	219	218	218	218	218	218	0	0	0
28.10343	219	218	218	218	218	218	0	0	0
29	219	218	218	218	218	0	0	0	0
30.10343	219	218	218	218	218	0	0	0	0
31	219	218	218	218	0	0	0	0	0
32.10343	219	217	217	217	0	0	0	0	0
33	219	217	217	0	0	0	0	0	0
34.10343	219	215	215	0	0	0	0	0	0
35	219	215	0	0	0	0	0	0	0

Table E.1: Forces in the tendons with different initial losses. The anchorage losses refer to the sections highlighted in Figure E.1 for the location of bonding of tendons

Location	Tendon stress loss under relaxation [MPa]						
[m]	S1	S2	S3	S4	S5	S6	S7
0.000	0	0	0	0	0	0	0
0.400	0.193	0	0	0	0	0	0
0.897	22.1	0	0	0	0	0	0
2.00	20.5	0	0	0	0	0	0
2.90	20.5	18.9	0	0	0	0	0
4.00	19.5	18.0	0	0	0	0	0
4.90	19.5	18.0	17.1	0	0	0	0
6.00	18.7	17.3	16.4	0	0	0	0
6.90	18.7	17.3	16.4	15.7	0	0	0
8.00	17.9	16.6	15.8	15.1	0	0	0
8.90	17.9	16.6	15.8	15.1	14.5	0	0
10.00	17.4	16.1	15.3	14.7	14.1	0	0
10.90	17.4	16.1	15.3	14.7	14.1	13.7	0
12.00	16.9	15.7	14.9	14.3	13.8	13.4	0
12.90	16.9	15.7	14.9	14.3	13.8	13.4	13.1
17.50	16.9	15.7	14.9	14.3	13.8	13.4	13.1
22.1	16.9	15.7	14.9	14.3	13.8	13.4	13.1
23.0	16.9	15.7	14.9	14.3	13.8	13.4	0
24.1	17.4	16.1	15.3	14.7	14.1	13.7	0
25.0	17.4	16.1	15.3	14.7	14.1	0	0
26.1	17.9	16.6	15.8	15.1	14.5	0	0
27.0	17.9	16.6	15.8	15.1	0	0	0
28.1	18.7	17.3	16.4	15.7	0	0	0
29.0	18.7	17.3	16.4	0	0	0	0
30.1	19.5	18.0	17.1	0	0	0	0
31.0	19.5	18.0	0	0	0	0	0
32.1	20.5	18.9	0	0	0	0	0
33.0	20.5	0	0	0	0	0	0
34.1	22.1	0	0	0	0	0	0
35.0	0	0	0	0	0	0	0

Table E.2: Losses of tendon stress due to relaxation of the tendons after 30 days

E.8. The equation originates in BS EN 1992-2:2005 (2005) and its components are further derived here. The relative humidity is assumed to be 80% for outside conditions, with a concrete strength of 60 MPa. it results in a creep coefficient after 30 days of 0.0251 and after 70 years of 1.0998.

$$\phi\left(t, t_0\right) = \phi_0 \beta_c\left(t, t_0\right) \tag{E.4}$$

The other loss for the calculation of time dependent losses is the calculation of the shrinkage in the concrete. Equations E.5, E.6 and E.7 are used to calculate these losses. The shrinkage comprises of the drying shrinkage strain and the autogenous shrinkage strain. Again these equations are taken from BS EN 1992-1-1:2004 (2004), so reference should be to this should further derivations be needed. The value of the total shrinkage strain after 30 days and 70 years is 9.82415×10^{-5} and 2.6462×10^{-4} respectively.

$$\epsilon_{cs} = \epsilon_{cd} + \epsilon_{ca} \tag{E.5}$$

$$\epsilon_{cd}\left(t\right) = \beta_{ds}\left(t, t_s\right) k_h \epsilon_{cd,0} \tag{E.6}$$

$$\epsilon_{ca} = \beta_{as}\left(t\right) \epsilon_{ca}\left(\infty\right) \tag{E.7}$$

In order to calculate the tendon forces displayed in Table E.3, the three time dependent losses are combined using Equation E.8. See BS EN 1992-1-1:2004 (2004) for more details and meaning of the symbols. The bending moment in the three span bridge is shown in Figure E.2. These bending moments are calculated under the quasi permanent loads and hence are used to determine the stresses used in Equation E.8.

$$\Delta P_{c+s+r} = A_p \Delta \sigma_{p,c+s+r} = A_p \frac{\epsilon_{cs} E_p + 0.8\Delta_{pr} + \frac{E_p}{E_{cm}} \phi\left(t, t_0\right) \sigma_{c,QP}}{1 + \frac{E_p}{E_{cm}} \frac{A_p}{A_c} \left(1 + \frac{A_c}{I_c} x_{cp}^2\right) \left[1 + 0.8\phi\left(t, t_0\right)\right]} \tag{E.8}$$

As a result of the losses calculated, Figure E.3 shows the tendon stresses in each of the tendon sets throughout the length of the bridge based on the combination of the losses. It shows both the tendon forces under the cases of 30 day losses as well as 70 year losses.

Location	Tendon force under combined time dependent losses [kN]						
[m]	S1	S2	S3	S4	S5	S6	S7
0	0.00	0.00	0.00	0.00	0.00	0.00	0.00
0.4	92.08	0.00	0.00	0.00	0.00	0.00	0.00
0.896565	206.38	0.00	0.00	0.00	0.00	0.00	0.00
2	204.61	0.00	0.00	0.00	0.00	0.00	0.00
2.896565	204.60	202.73	0.00	0.00	0.00	0.00	0.00
4	203.43	201.57	0.00	0.00	0.00	0.00	0.00
4.896565	203.42	201.56	200.37	0.00	0.00	0.00	0.00
6	202.41	200.55	199.36	0.00	0.00	0.00	0.00
6.896565	202.40	200.54	199.35	198.31	0.00	0.00	0.00
8	201.39	199.54	198.35	197.31	0.00	0.00	0.00
8.896565	201.38	199.53	198.34	197.31	196.32	0.00	0.00
10	200.66	198.82	197.63	196.60	195.61	0.00	0.00
10.89657	200.66	198.81	197.63	196.59	195.61	194.92	0.00
12	200.09	198.25	197.06	196.03	195.04	194.36	0.00
12.89657	200.08	198.24	197.06	196.02	195.04	194.36	193.80
17.5	200.08	198.24	197.06	196.02	195.04	194.36	193.80
22.10343	200.08	198.24	197.05	196.02	195.03	194.35	193.80
23	200.08	198.24	197.05	196.02	195.04	194.35	0.00
24.10343	200.65	198.80	197.62	196.58	195.60	194.91	0.00
25	200.65	198.81	197.62	196.59	195.60	0.00	0.00
26.10343	201.37	199.52	198.33	197.30	196.31	0.00	0.00
27	201.37	199.53	198.34	197.30	0.00	0.00	0.00
28.10343	202.38	200.53	199.34	198.30	0.00	0.00	0.00
29	202.39	200.53	199.34	0.00	0.00	0.00	0.00
30.10343	203.40	201.54	200.35	0.00	0.00	0.00	0.00
31	203.41	201.55	0.00	0.00	0.00	0.00	0.00
32.10343	204.57	202.71	0.00	0.00	0.00	0.00	0.00
33	204.59	0.00	0.00	0.00	0.00	0.00	0.00
34.10343	206.35	0.00	0.00	0.00	0.00	0.00	0.00
35	0.00	0.00	0.00	0.00	0.00	0.00	0.00

Table E.3: Tendon force in first span under combined time dependent losses after 30 days
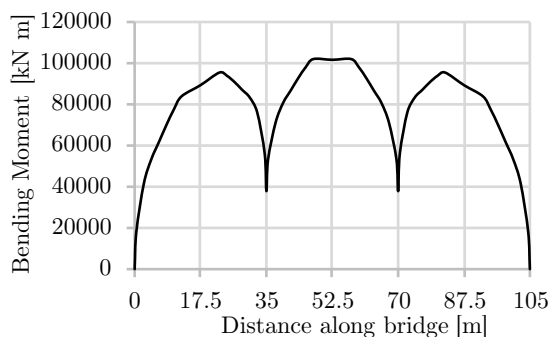
Figure E.2: Bending moment across the three continuous spans under permanent loads, for the calculation of the creep losses
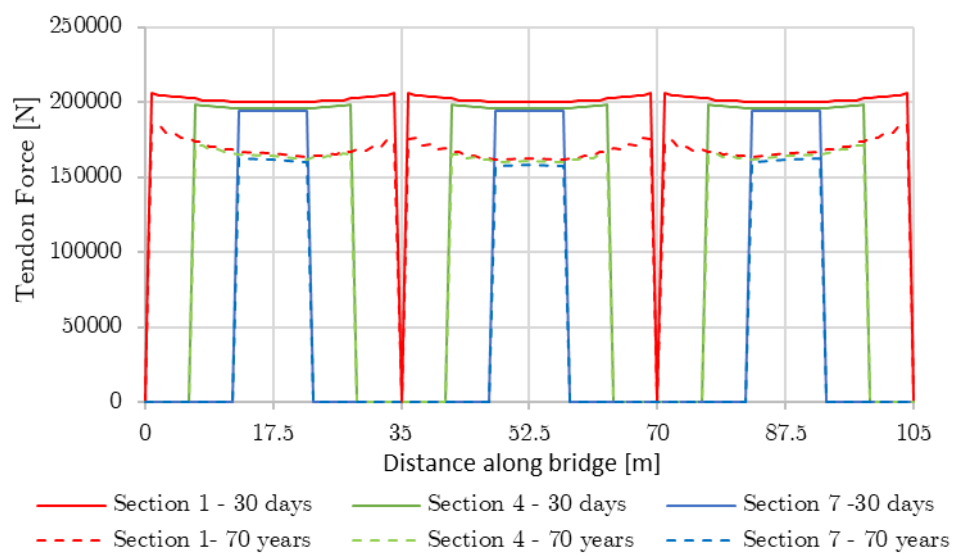
Figure E.3: Tendon forces across the three continuous spans under permanent loads, with all losses. Compares losses in the tendons activated in Sections 1, 4 and 7, at the ages of 30 days and 70 years.

Appendix F

Irregularities

Five specific country PSD functions were found in the literature study. Some only apply to the vertical irregularity (such as the SNCF and Braun PSDs), whereas other PSD functions (the FRA, German and Chinese functions), are set such that they can define all four types of irregularity, not just the vertical profile (Berawi, 2013). This appendix outlines the formulas used in generating these PSD functions.

F.1   FRA PSD Function

As mentioned in Section 2.5.2, these equations are the most commonly used in literature, utilising the class of tracks using proposed by the Federal Railroad Administration (FRA) (Hamid et al., 1983).

Despite claiming to use the FRA model, there appears to be three distinct PSD model formulations used in literature. The original is found in Hamid et al. (1983), which is also used by Garg and Dukkipati (1984), Frýba (1996), Au et al. (2002), Song et al. (2003) and Dinh et al. (2009). Alternative formulations, which use roughness coefficients to generate the PSD function that vary by up to 10 % from the original, are found in White and Cooperrider (1981) (later used by Fries and Coffey (1990), Yang et al. (2004a), Kargarnovin et al. (2005) and Majka and Hartnett (2009)) and Sayers and Hedrick (1977) (used by Garivaltis et al. (1980), Wiriyachai et al. (1982), Zhang et al. (2001), Lei and Noda (2002), Berawi (2013) and Podworna (2014)). These later two models have been found to vary due to rounding errors associated with conversion from imperial to metric units.

A slight variation of the Sayers and Hedrick (1977) model is introduced in the papers of Lei and Noda (2002), Berawi (2013) and Podworna (2014). Here, another constant is introduced, k, typically equal to 0.25, subsequently reducing the values of the PSD, but no reason is given

for them to be included. The source of this k constant appears to be Lei and Noda (2002). As a result both have been included in the comparisons between the models, which is shown in addition to the three models expressed previously in Table F.1. The value of A is a constant which differs between classes of track and is often referred to as a roughness parameter. The constants Ω_i, where i is an identifier to differentiate different constants, is sometimes referred to as a break frequency, and these break frequencies change between the different types of irregularity, but do not significantly change for different track classes. Each PSD tends to be valid over a certain wavelength of irregularities $(\lambda)[m]$.

Name	Equation	Ω equation	Use	Values	Sources
Hamid	$S(\Omega) = \frac{A\Omega_2^2(\Omega^2+\Omega_1^2)}{\Omega^4(\Omega^2+\Omega_2^2)}$ [$m^2/(cycle/m)$] $S(\Omega) = \frac{A\Omega_2^2}{(\Omega^2+\Omega_1^2)(\Omega^2+\Omega_2^2)}$ [$m^2/(cycle/m)$]	$\Omega = \frac{1}{\lambda}$ [$1/m$]	Profile	$A = 0.88 \times 10^{-8}$ [m^3] Ω_1=0.0233 [m^{-1}] Ω_2=0.131 [m^{-1}]	Hamid et al. (1983) Garg and Dukkipati (1984) Frýba (1996)
			Alignment	$A = 0.55 \times 10^{-8}$ [m^3] Ω_1=0.0328 [m^{-1}] Ω_2=0.1822 [m^{-1}]	
			Cross level	$A = 0.67 \times 10^{-8}$ [m^3] Ω_1=0.0233 [m^{-1}] Ω_2= 0.131 [m^{-1}]	
			Gauge	$A = 0.55 \times 10^{-8}$ [m^3] Ω_1=0.0293 [m^{-1}] Ω_2= 0.234 [m^{-1}]	
White	$S(\Omega) = \frac{A\Omega_c^2}{(\Omega^2+\Omega_r^2)(\Omega^2+\Omega_c^2)}$ [$m^2/(rad/m)$] $S(\Omega) = \frac{(A\Omega_c^2/l_a)\Omega^2}{(\Omega^2+\Omega_r^2)(\Omega^2+\Omega_c^2)(\Omega^2+\Omega_s^2)}$ [$m^2/(rad/m)$]	$\Omega = \frac{2\pi}{\lambda}$ [rad/m]	Profile	A= 1.5 $\times10^{-6}$ [m] Ω_c=0.825 [rad/m] Ω_r=2.06 $\times 10^{-2}$ [rad/m]	White and Cooperrider (1981) Fries and Coffey (1990) Yang et al. (2004a) Kargarnovin et al. (2005) Majka and Hartnett (2009)
			Alignment		
			Cross level	A= 1.5 $\times10^{-6}$ [m] Ω_c=0.825 [rad/m] Ω_r=2.06 $\times 10^{-2}$ [rad/m] Ω_s=0.438 [rad/m] l_a=0.763 [m]	
			Gauge		
Sayers	$S(\Omega) = \frac{2\pi A\Omega_c^2}{\Omega^2(\Omega^2+\Omega_c^2)}$ [$mm^2m/cycle$] $S(\Omega) = \frac{8\pi A\Omega_c^2}{(\Omega^2+\Omega_c^2)(\Omega^2+\Omega_s^2)}$ [$mm^2m/cycle$]	$\Omega = \frac{2\pi}{\lambda}$ [rad/m]	Profile Alignment Cross level Gauge	A= 3.365 [mm^2-rad/m] Ω_c=0.8242[rad/m] Ω_s=0.4395 [rad/m]	Sayers and Hedrick (1977) Garivaltis et al. (1980) Wiriyachai et al. (1982) Zhang et al. (2001)
Lei	$S(\Omega) = \frac{kA\Omega_c^2}{\Omega^2(\Omega^2+\Omega_c^2)}$ [$cm^2/(rad/m)$] $S(\Omega) = \frac{4kA\Omega_c^2}{(\Omega^2+\Omega_c^2)(\Omega^2+\Omega_s^2)}$ [$cm^2/(rad/m)$]	$\Omega = \frac{2\pi}{\lambda}$ [rad/m]	Profile Alignment Cross level Gauge	A= 0.0339 [cm^2rad/m] Ω_c=0.8245[rad/m] Ω_s=0.438 [rad/m] k=0.25 [-]	Lei and Noda (2002) Berawi (2013) Podworna (2014)

Table F.1: Comparison of the equations used for the FRA PSD functions ($S(\Omega)$), along with values for the class 6 irregularity, where λ is the wavelength of the irregularity

F.2   German Rail PSD Function

There are two types of German Spectra: the German Rail Spectrum of Low Irregularity (GRSLI) and German Rail Spectrum of High Irregularity (GRSHI). These can simulate the irregularities of modelling a bridge that runs HSR vehicles with design velocities up to $350 km/h$. The equations and values needed for the equations of the German PSD functions are shown in Table F.2. Some variation of the model exists with different coefficients given for the generation of the PSD, which are generated to match a real line with a Deutsche Bahn Train travelling at 250 km/h and referred to as ARGER/F models (Claus and Schiehlen, 1998; Cuadrado et al., 2008).

Type	Equation	Constants				
		Notation	GRSHI [ab]	GRSLI[ac]	ARGER/F High[d e]	ARGER/F Low [d e]
Profile	$S(\Omega) = \frac{A\Omega_c^2}{(\Omega^2+\Omega_\gamma^2)(\Omega^2+\Omega_c^2)}$ $[m^2/(rad/m)]$	$A_p\ [m^2 rad/m]$	10.8×10^{-7}	4.032×10^{-7}	15.9×10^{-7}	5.92×10^{-7}
		$\Omega_c\ [rad/m]$	0.82	0.82	0.8246	0.8246
		$\Omega_\gamma\ [rad/m]$	0.0206	0.0206	0.0206	0.0206
Alignment	$S(\Omega) = \frac{A\Omega_c^2}{(\Omega^2+\Omega_\gamma^2)(\Omega^2+\Omega_c^2)}$ $[m^2/(rad/m)]$	$A_a\ [m^2 rad/m]$	6.13×10^{-7}	2.12×10^{-7}	15.9×10^{-7}	5.92×10^{-7}
		$\Omega_c\ [rad/m]$	0.82	0.82	0.8246	0.8246
		$\Omega_\gamma\ [rad/m]$	0.0206	0.0206	0.0206	0.0206
Cross Level	$S(\Omega) = \frac{(A/b^2)\Omega_2^2\Omega^2}{(\Omega^2+\Omega_1^2)(\Omega^2+\Omega_2^2)(\Omega^2+\Omega_3^2)}$ $[m^2/(rad/m)]$	$A_p\ [m^2 rad/m]$	10.8×10^{-7}	4.032×10^{-7}	15.9×10^{-7}	5.92×10^{-7}
		$\Omega_c\ [rad/m]$	0.82	0.82	0.8246	0.8246
		$\Omega_\gamma\ [rad/m]$	0.0206	0.0206	0.0206	0.0206
		$\Omega_s\ [rad/m]$	0.438	0.438	0.438	0.438
		$b\ [m]$ [f]	0.75	0.75	0.75	0.75

Table F.2: Comparison of the PSD functions presented as the German spectra and the similar ARGER/F functions

[a] Valid for frequency range $0.06283 \leq \Omega \leq 2.513\ [rad/m]$

[b]Source: Zhang et al. (2010), Berawi (2013)

[c]Source: Li et al. (2005), Berawi (2013)

[d] Valid for frequency range $0.07 \leq \Omega \leq 2.1\ [rad/m]$

[e] Source: Claus and Schiehlen (1998), Cuadrado et al. (2008)

[f]half of the horizontal distance between two wheels

F.3   Other PSD functions

The Chinese PSD functions ahve only been found to be published in one English language source (Berawi, 2013). The function is applicable for specific speeds, with values given for the speeds of 200, 160 and 120 km/h. This means that it has a higher applicable line speed than the FRA class 6 track did (177 km/h), yet it is not widely used in literature. The same formula is used for each of the gauge, cross level, profile and alignment irregularities. Instead of using $\Omega = 2\pi/\lambda$ as in most of the the German and FRA spectra, the Chinese spectra uses $f = 1/\lambda$. Also provided is upper, general and lower bounds to the coefficients, representing a range in the track quality for a certain track operational speed. The Chinese PSD standard provided cannot be verified against other papers as it has not been found in another English language print. The equations for this PSD model at 200 km/h is shown in Table F.3.

Name	Irregularity Type	Equation	Values		
			Value	Upper	Lower
China PSD Standard (200km/h) [a][b]	Profile	$S(f) = \frac{af^2+b}{cf^2+df^4+ef^2+k}$ $[mm^2/(1/m)]$	a	0.0	0.0
			b	0.00353	0.00047
			c	0.0	0.0
			d	1.0	1.0
			e	0.00752	0.00783
			k	0.0	0.0
	Cross level		a	951.449	238.6205
			b	2.1747	0.5418
			c	47442.79	85347.970
			d	2121.780	3842.441
			e	25.473	45.8306
			k	0.0112	0.02
	Alignment		a	0.0	0.0
			b	0.00699	0.00097
			c	0.0	0.0
			d	1.0	1.0
			e	0.01893	0.1893
			k	0.00003	0.00003
	Gauge		a	362.2681	119.2536
			b	0.2393	0.0783
			c	15370.860	36295.990
			d	681.2174	1617.269
			e	10.2670	24.2936
			k	-0.0007	-0.0018
Braun [c][d]	Profile	$S(f) = A(\frac{f}{f_0})^{-w}$ $[m^3]$	w [-]	ranges between 1.5 and 3.5	ranges between 1.5 and 3.5
			A $[m^3]$	5.0×10^{-7}	1.0×10^{-7}
			f_0 $[1/m]$	$1/2\pi$	$1/2\pi$
SNCF [e][f]	Profile	$S(f) = \frac{A}{(1+\frac{f}{f_0})^3}$, $[m^3]$	A $[m^3]$	550×10^{-6}	160×10^{-6}
			f_0 $[m]$	0.307	0.307

Table F.3: Comparison of other PSD functions

[a]$f = 1/\lambda$ [1/m] Validity range not known
[b]Source: Berawi (2013)
[c]$f = 1/\lambda$, [1/m] where λ is the wavelength and f is the cyclic wavenumber. No wavelength range is given
[d]Source: Berawi (2013)
[e]$f = 1/\lambda$, [1/m] over the range of $0.025 \leq f \leq 0.5$
[f]Source: Frýba (1996); Berawi (2013)

According to Zhiping and Shouhua (2009), there are PSD functions for the countries of Britain, Czech Republic, India and Russia in addition to those seen (Frýba, 1996). However, these have not been able to be sourced. In Berawi (2013), reference is made towards the Braun and French SNCF PSD spectra that both only apply to the vertical profile. Braun is developed from a PSD spectra designed for highways, so is probably not as applicable as other sources. No further references can be found for this PSD, to confirm its viability. The SNCF PSD function is designed for the French railways and has a higher and lower quality level of irregularities (Frýba, 1996; Berawi, 2013). Both of these functions are shown in both Table F.3.